Title

Bottom-up Strategies towards Controlled Synthesis of Graphene Nanoribbons with Precise Edges and Structurally Aligned Semiconducting Polymers

Author

Li, Yolanda Lunn

Publication Date

2020

Peer reviewed|Thesis/dissertation

UNIVERSITY OF CALIFORNIA

Los Angeles

Bottom-up Strategies towards Controlled Synthesis of Graphene Nanoribbons with Precise Edges and Structurally Aligned Semiconducting Polymers

A dissertation submitted in partial satisfaction of the
requirements for the degree Doctor of Philosophy
in Chemistry

by

Yolanda Lunn Li

2020

ABSTRACT OF THE DISSERTATION

Bottom-up Strategies towards Controlled Synthesis of Graphene Nanoribbons with Precise Edges and Structurally Aligned Semiconducting Polymers

by

Yolanda Lunn Li
Doctor of Philosophy in Chemistry
University of California, Los Angeles 2020
Professor Yves F. Rubin, Chair

Chapter 1 provides an overview on the synthesis of graphene nanoribbons. Various types of edge structures and bottom-up synthetic strategies, on-surface and in-solution, are covered before discussing our group's third approach, solid-state. This is followed by a description of the effect of heteroatomic substitutions on electronic properties of GNRs. Lastly a brief discussion on other semiconducting polymer structure and charge transfer properties are introduced.

Chapter 2 details the synthesis of $N = 8$ armchair graphene nanoribbons (GNRs) using a two-step solid-state method. Four diarylbutadiyne precursors undergo topochemical polymerization to four distinct polydiacetylene (PDA) polymers, which subsequently cyclodehydrogenate and undergo side chain fragmentation to afford the same $N = 8$ armchair GNR. Various spectroscopic and imaging techniques are used to characterize this transformation, in addition to calculations of the cyclization process on a model system used to verify the mechanism.

Chapter 3 describes the synthesis of GNRs with a fjord-edge structure and site-specific nitrogen substitutions using the two-step approach above. Two dipyridylbutadiyne precursors polymerize and cyclize to afford N = 8 fjord-edge N-GNRs, with side chains still intact. Spectroscopic characterization, imaging and mechanistic calculations of a pyridyl model system verify the transformation from butadiyne to GNR.

Lower the barrier of Hopf cyclizations, a step towards GNRs in our solid-state approach, through introduction of strained cycloalkenes could lead to room temperature GNR syntheses. Chapter 4 details the synthesis of two polydiacetylene synthons containing norbornadiene, a bis(norbornadienyl)1,3-butadiyne and *trans*-bis(norbornadienyl)enediyne. Challenges towards synthesizing both monomer units and future applications of other *trans*-enediynes towards GNRs are discussed.

Chapter 5 describes the synthesis of an amphiphilic semiconducting polymer, poly(cyclopentadithiophene-alt-thiophene) (PCT), according to a set of design rules aimed at straightening the polymer backbone in order to reduce polymer disorder and increase conductivity. The design rules are 1) hydrophobic polymer backbone and hydrophilic side chains, 2) alternating co-polymer such that all the side chains reside on one side, 3) side chains branched off an sp^3 carbon to create a 3D wedge shape, and 4) complementary bond angles between monomer units to achieve a 180° dihedral angle. The solution phase of the polymer is characterized by small angle X-ray scattering (SAXS) and imaged using cryo-transition electron microscopy (TEM).

Applications of PCT towards controlling electron donor-acceptor complexes are explored in Chapter 6. PCT and poly(fluorene-alt-thiophene) (PFT), are complexed with two electron acceptors, a charged perylenediimide and a series of charged bis-pyrrolidium functionalized

fullerenes. The structure of these co-assemblies are characterized by small angle X-ray scattering and photoluminescence quenching, concluding that complementary geometries between the polymer micelle and acceptor shapes result in increased amounts of photoluminescence quenching.

The dissertation of Yolanda Lunn Li is approved.

William B. Gelbart

Ellen May Sletten

Sarah H. Tolbert

Yves F. Rubin, Committee Chair

University of California, Los Angeles

2020

TABLE OF CONTENTS

LIST OF FIGURES,TABLES AND SCHEMES

Chapter 1

Chapter 2

Chapter 3

Chapter 4

Chapter 5

Chapter 6

LIST OF ABBREVIATIONS

ACN	Acetonitrile
CP/MAS	Cross Polarization Magic Angle spinning
CV	Cyclic Voltammetry
DART MS	Direct analysis in real time mass spectrometry
DBBA	10,10'-dibromo-9,9'-bianthracene
DCC	Dicyclohexyldicarbodiimide
DCM	Dichloromethane
DFT	Density functional theory
DIPEA	Diisopropyl ethylamine
DMF	N,N-dimethylformamide
Et_3N	Triethylamine
Et_2O	Diethyl ether
FT-IR	Fourier transform-infrared
GIWAXS	Grazing incidence wide angle x-ray scattering
GNR	graphene nanoribbon
$_A$GNR	Armchair graphene nanoribbon
$_z$GNR	Zigzag graphene nanoribbon
HMPA	Hexamethylphosphoramide
HR-TEM	High resolution tunneling electron microscopy
LiHMDS	Lithium hexamethyldisilazide
MeI	Methyl iodide
n-BuLi	n-Butyl lithium
MEH-PPV	poly(2-methoxy-5-(2-ethylhexyloxy)-1,4-phenylenevinylene)
MeOH	Methanol
NMR	Nuclear magnetic resonance
PANi	poly(aniline)

PCC	Pyridinium chlorochromate
PCT	poly(cyclopentadithiophene-alt-thiophene)
PDA	Polydiacetylene
PDI	Perylenediimide
PEDOT	poly(3,4-ethylenedioxythiophene)
PFT	poly(fluorene-alt-thiophene)
PL	Photoluminescence
PTB7	poly[[4,8-bis[(2-ethylhexyl)oxy]benzo[1,2-b:4,5-b']dithiophene-2,6-diyl)[3-fluoro-2-[ethylhexyl)carbonyl]thieno[3,4-b]thiophenediyl
P3HT	poly(3-hexylthiophene)
TBAF	Tetrabutyl ammonium fluoride
TCNQ	Tetracyanoquinodimethane
TEM	Tunneling electron microscopy
THF	Tetrahydrofuran
TIPS	Triisopropylsilane
TLC	Thin layer chromatography
TMEDA	N,N,N',N'-tetramethyl ethylene diamine
TMS	Trimethylsilane
TTF	Tetrathiafulvalene
SAXS	Small angle x-ray scattering
STM	Scanning tunneling microscopy
UV	Ultraviolet
UV-Vis	Ultraviolet-visible
UV-Vis-NIR	Ultraviolet-visible-near infrared
XRD	X-ray diffraction
XPS	X-ray photoelectron spectroscopy

ACKNOWLEDGEMENTS

Firstly, I would like to thank my parents for supporting me through this journey. From patiently answering my questions from day one to asking me challenging ones now, you've helped shaped me as a person and scientist. Thanks for everything and letting me stray off the path of physics and engineering.

To my mentor Robert Jordan, thanks for taking the time to be a mentor both during graduate school and beyond. You showed me the creativity and work required to get to the end. To Dayanni Bhagwandin, I never thought I'd move across the country only to have another person from Jersey be my lab mate. It's been an adventure the last three years from building our own photoreactor to our debates over how to pronounce "lobster" and more. I hope you enjoy the role of senior grad student and all the fun it brings. Thanks Julia Chang for making the Rubin lab a tirelessly entertaining place to work, the dance sessions were much needed when my day was just back-to-back columns.

To our wonderful undergraduates Carter Faucher, Isabelle Winardi and Ethan Yang, having you in the group was beyond helpful. I'm sorry we never got to celebrate all the work you've done in lab, but your talents and help were much appreciated.

I would also like to thank Sarah, Ben and all my collaborators throughout the years. I've been fortunate to benefit from your mentorship and outlook on science. You've both made lasting impressions for years to come.

To Yves, this has been an adventure. Thank you for taking on a student with no synthetic experience and giving me the space to explore. It's been a pleasure to work with you these past few years, I never imagined the amount I would learn while here at UCLA when I first started. Thanks again for everything and I'm excited to see where the next adventure takes me. Let's go!

Chapter 2 is a version of [Jordan, R. S.; Li, Y. L.; Lin, C-W.; McCurdy, R. D.; Lin, J. B.; Brosmer, J. L.; Marsh, K. L.; Khan, S. I.; Houk, K. N.; Kaner, R. B.; Rubin, Y. Synthesis of $N = 8$ Armchair Graphene Nanoribbons from Four Distinct Polydiacetylenes. *J. Am. Chem. Soc.* **2017**, *139*, 15878-15890.] Robert Jordan assisted in the preparation and characterization of the compounds. Chang-Wei Lin acquired the HR-TEM images. Ryan McCurdy assisted in compound synthesis. Janice B. Lin performed DFT calculations. Jon Brosmer assisted in acquiring the Raman spectra. Kristopher Marsh performed the XPS studies.

Chapter 3 is a version of [Li, Y. L.; Zee, C.-T.; Lin, J. B.; Basile, V. M.; Muni, M.; Flores, M. D.; Kaner, R. B.; Houk, K. N.; Tolbert, S. H.; Rubin, Y. Fjord-edge Graphene Nanoribbons with Site-Specific Nitrogen Substitution. *In preparation*] Chih-Te Zee assisted in preparation of the crystals and acquired the X-ray diffraction. Janice B. Lin performed DFT calculations. Victoria M. Basile acquired the XPS spectra. Maria D. Flores assisted in the X-ray diffraction acquisition.

Chapter 5 is a version of [Winchell, K.J.;[*] Yee, P. Y.;[*] Li, Y. L.; Beren, C.; Thompson, R. J.; Jordan, R. S.; Gelbart, W. M.; Rubin, Y.; Tolbert, S. H. Design Rules for Straightening Conjugated Polymer Electrolyte Chains for OPV Applications. *In preparation*] K.J. Winchell and Patrick Yee acquired and modeled the SAXS data. Christian Beren imaged the micelles using cryo-EM. Robert Thompson and Robert Jordan assisted with the synthesis.

Chapter 6 is a version of [Wu, Y.;* Li, Y. L;*, Winchell, K.J.; Salamat, C.; Rubin, Y.; Tolbert, S. H. Design and control of amphiphilic polymer and small molecule acceptor co-assemblies to facilitate excited state electron transfer. *In preparation*] Yutong Wu acquired photoluminescence and SAXS data. KJ Winchell acquired SAXS data of the polymers. Charlene Salamat acquired CV data on the PDI acceptor.

FINANCIAL ACKNOWLEDGEMENT

This work was supported by the NSF Grant NSF-CHE-1608957 to YR. Solid state NMR work was supported by an instrumentation grant, Grant NSF-MRI-1532232. Y.L.L was also supported by the Saul Weinstein Fellowship from the Department of Chemistry and Biochemistry at UCLA.

Curriculum Vitae

Education

Cornell University 2015
B.A. Magna Cum Laude in Chemistry and Chemical Biology
B.A. in Economics

Research Experience and Internships

Graduate Researcher, UCLA 9/2015 – 6/2020

Synthesis and characterization of organic electronic materials including graphene nanoribbons, small molecule acceptors and semiconducting polymers

Undergraduate Researcher, Cornell University and Ithaca Beer Co. 1/2015 – 5/2015

Temperature dependence on hop oil expression during the dry hopping process

Research and Development Intern, Proctor and Gamble 6/2014 – 8/2014

Long term effects on the equilibrium of Zinc-Zincate in strong alkaline environments

Research and Development Intern, Unilever 6/2013 – 8/2013

Reformulation of exfoliating body washes: changing polyethylene beads for sustainable alternatives

Publications and Patents

Yolanda L. Li, Chih-Te Zee, Janice B. Lin, Victoria M. Basile, Mit Muni, Maria D. Flores, Richard B. Kaner, K. N. Houk, Sarah H. Tolbert, and Yves Rubin, "Fjord-edge Graphene Nanoribbons with Site-Specific Nitrogen Substitutions" *In preparation*

Yutong Wu,[†] Yolanda L. Li,[†] K.J. Winchell, Charlene Salamat, Yves Rubin, Sarah H. Tolbert, "Design and Control of Amphiphilic Co-assemblies to Facilitate Excited State Electron Transfer" *In preparation*

K.J. Winchell,[†] Patrick Y. Yee,[†] Yolanda L. Li, Christian Beren, Robert J. Thompson, William G. Gelbart, Yves Rubin, Sarah H. Tolbert, "Design Rules for Straightening Conjugated Polymer Electrolyte Chains for OPV Applications" *In preparation*

Erik P. Farr, Matthew, T. Fontana, Chen-Chen Zho, Peiqi Wu, Yolanda L. Li, Nicholas Knutson, Yves Rubin, and Benjamin J. Schwartz, "Bay-Linked Perylenediimides are Two Molecules in One: Insights from Ultrafast Spectroscopy, Temperature Dependence, and Time-Dependent Density Functional Theory Calculations" *J. Phys. Chem. C.* **2019**, *123*, 2127-2138.

Robert S. Jordan, Yolanda L. Li, Cheng-Wei Lin, Ryan D. McCurdy, Janice B. Lin, Jonathon L. Brosmer, Kristofer L. Marsh, Saeed I. Khan, K. N. Houk, Richard B. Kaner, and Yves Rubin, "Synthesis of *N*=8 Armchair Graphene Nanoribbons from Four Distinct Polydiacetylenes" *J. Am. Chem. Soc.* **2017**, 139, 15878-15890.

Yves Rubin, Robert S. Jordan, Yolanda L. Li, Ryan McCurdy, Simon Kervyn de Meerendré, "Synthesis of Graphene Nanoribbons from Monomeric Molecular Precursors Bearing Reactive Alkyne Moieties," International Patent No. US 0055735, filed Nov. 17, 2017, published Feb. 20, 2020.

Teaching Experience

UCLA 9/2015 – 6/2020

General Chemistry - Lecture

Organic Chemistry - Lab and Lecture

Instrumentation - Lab

Cornell University 7/2012 – 8/2015

General Chemistry - Lecture

Organic Chemistry - Lab and Lecture

Chapter 1: Introduction

Section 1.1. Graphene and Graphene Nanoribbons

One of the fundamental technologies required to power modern electronic devices is the transistor.[1] Often used as switches or amplifiers, these semiconducting devices rely on materials which possess an electronic band gap. This band gap prevents electrons from freely moving throughout the material and, crucially, creates on/off states for transistors. Current commercial transistors are predominantly made from germanium, silicon or gallium arsenide, and each exhibits a unique band gap that allows them to be used for different applications.[2] However, these static bandgaps are inherent to the elemental composition of the material and therefore cannot be tuned. Another limitation of current commercial transistors is the effect of size on their electronic properties.[3] As the size of these materials has gotten increasingly small, ~ 5 nm, these transistors begin to exhibit short channel effects such as current leakage in the off state, thereby limiting their ability to maintain on/off states.[4] While some hybrid materials have overcome these short channel effects, they possess static rather than tunable electronic bandgaps. Thus, a new hybrid would need to be prepared and tested for each new desired bandgap.[5] The demand for higher computing power with minimal size expansion requires the miniaturization of electronic devices, and thus a growing need for tunable semiconductors that do not exhibit short channel effects. As such, graphene nanoribbons (GNRs) are uniquely situated to meet this demand.

Graphene is a 2D sheet of sp^2 hybridized carbon atoms that has a zero electronic band gap, rendering it useless for transistors. Fortunately, in 1996 Fujita and Dresselhaus predicted that confining 2D sheets of graphene into 1D narrow ribbons would open an electronic bandgap. The

size of the bandgap was predicted to change depending on the edge structure and width of the ribbon, making GNRs an ideal material for tunable bandgaps.[6] Their work found that armchair and zigzag edged ribbons (Figure 1.1) displayed differing electronic properties. Armchair edge graphene nanoribbons ($_A$GNR) can be classified into three types depending on their width: N = 3p, 3p+1, and 3p+2 where N is the number of carbons across the short edge of the ribbon and p is an

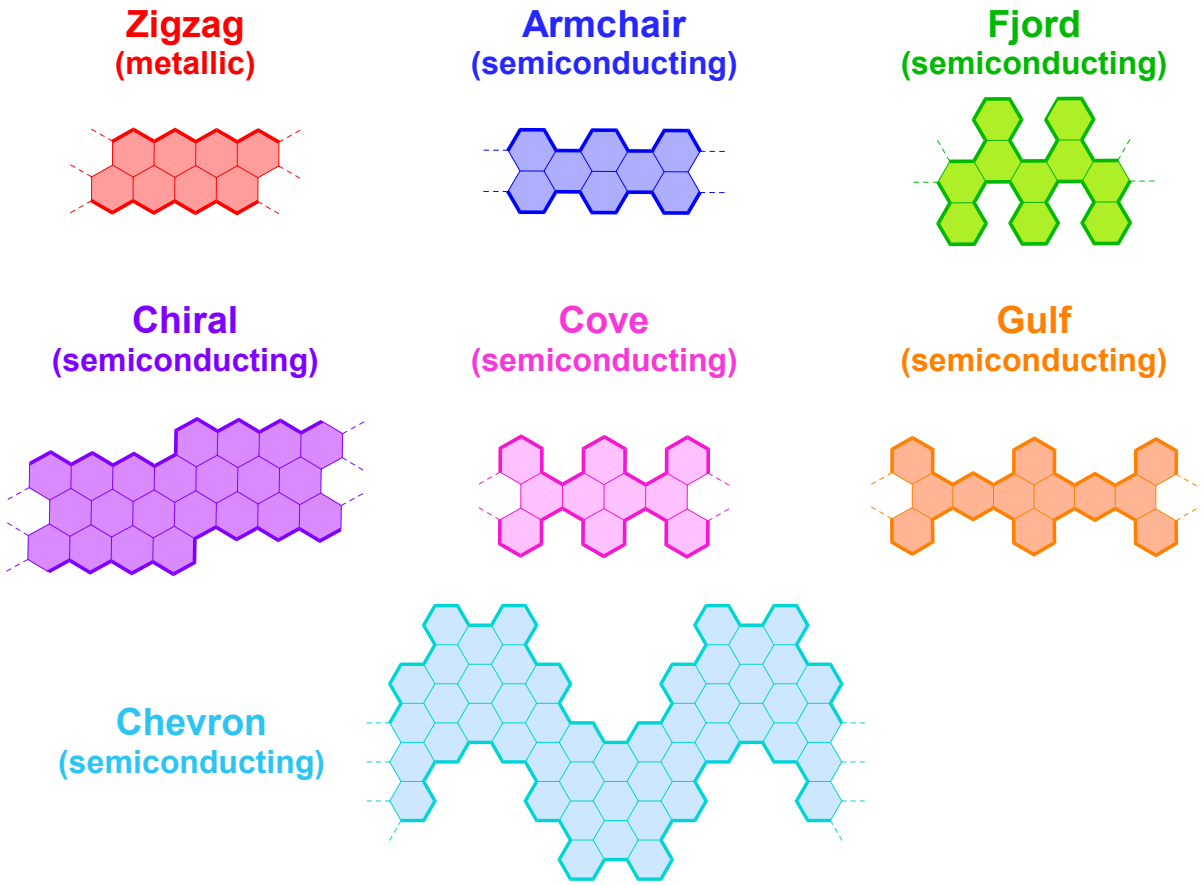

Figure 1.1. Examples of GNRs with various edge structures.

integer. Tight binding calculations revealed that ribbons with width <10 nm and N = 3p and 3p +1 should be semiconducting. For these two classes, the band gap size and ribbon width are inversely proportional. In contrast, $_A$GNR of N = 3p+2 and zigzag edges ($_Z$GNR) displayed metallic or

semimetallic properties with a near zero bandgap, regardless of ribbon width. While these calculations were incredibly important in outlining targets for synthetic efforts, it would not be until the next decade that a GNR synthesis was achieved.

In 2004 Novoselov *et al.* successfully isolated single-layer graphene from graphite.[7] Reproducible production of graphene eventually led to "top-down" GNR syntheses in which large sheets of graphene, and later carbon nanotubes, were cut into smaller graphitic ribbons via sonochemical exfoliation,[8,9] chemical oxidation,[10-12] and lithography.[13-17] While these early examples produced relatively narrow ribbons under 30 nm wide, researchers were unable to measure the electronic properties predicted by Fujita and Dresselhaus. Notably, top-down methods often produce GNRs which a) lack the structurally precise and uniform edges that are crucial to determining electronic states and b) are too wide to display large bandgaps. For example, in a sample of top-down produced GNRs, a single GNR might have sections of both armchair and zigzag edges with inconsistent widths along the ribbon. Additionally, lithographic methods are limited in resolution by the beam size and regularly produce GNRs that are tens of nm wide. These wider ribbons exhibit properties similar to 2D graphene instead of 1D GNRs and thus have minimal bandgaps, if at all. Unsatisfied with the irregularity of the GNRs produced by the top-down methods, researchers began to use a new strategy that sought to build structurally precise GNRs from a bottom-up method using molecular building blocks.

Bottom-up syntheses generally have a two-step mechanism that start from precise precursors to produce well-defined GNRs and are classified by their reaction medium: on-surface, in-solution and solid-state. The first step produces a highly conjugated polymer intermediate with pendant electron rich groups that can undergo oxidative or cyclodehydrogenative reactions. Step two cyclizes the backbone and pendant groups to yield fully fused GNRs. As the two-step process

utilizes robust organic transformations to produce structurally precise edges and widths, bottom-up methods are advantageous over top-down methods with their lack of uniformity and precision. On-surface, in-solution, and solid-state methodologies all adhere to this two-step mechanism, and each has its own advantages and disadvantages.

Section 1.2. On-Surface Syntheses of Graphene Nanoribbons

The first on-surface synthesis of GNRs used Au (111) as both the substrate and a reactive surface to produce $[7]_A$GNR and a chevron-GNR.[18] These GNRs were derived from the halogenated arenes 10,10'-dibromo-9,9'-bianthracene (DBBA) and 6,11-dibromo-1,2,3,4-tetraphenyltriphenylene respectively (Figure 1.2). To synthesize $[7]_A$GNR, DBBA was deposited on the Au (111) and heated to 200 °C to remove the bromines. The resultant bianthryl biradical then migrates along the surface and couples with other bianthryl biradicals to grow the polymeric anthracene shown in Figure 1.2. A final annealing step fuses between anthracene units to form an extended aromatic core, and thus, $[7]_A$GNR. The other precursor, 6,11-dibromo-1,2,3,4-tetraphenyltriphenylene, follows a similar process, but the asymmetric halogen substitution leads the radicals to couple into a chevron pattern. Annealing again cyclizes the phenyl units to give chevron GNR. Since this initial report, various halogenated arenes have been utilized to synthesize [5],[19] [6],[20] [9],[21,22] $[13]_A$GNR,[23] $[6]_z$GNR,[24] cove-GNR,[25] (3,1) chiral-GNR,[26] and [6] gulf-GNR.[27] Wider GNRs can also be formed on surfaces without the need to design new precursors through the edge-to-edge fusion between narrower GNRs. This strategy has been utilized to synthesize [8],[28] [9],[15] [10],[16] [12],[15] [15],[15] [18],[18] and $[21]_A$GNR.[18] The last decade has demonstrated the possibility of synthesizing a diverse array of GNR widths and edges on surfaces,

but unfortunately, the inherent nature of on-surface methods limits their bulk production, and thus, wide spread use.

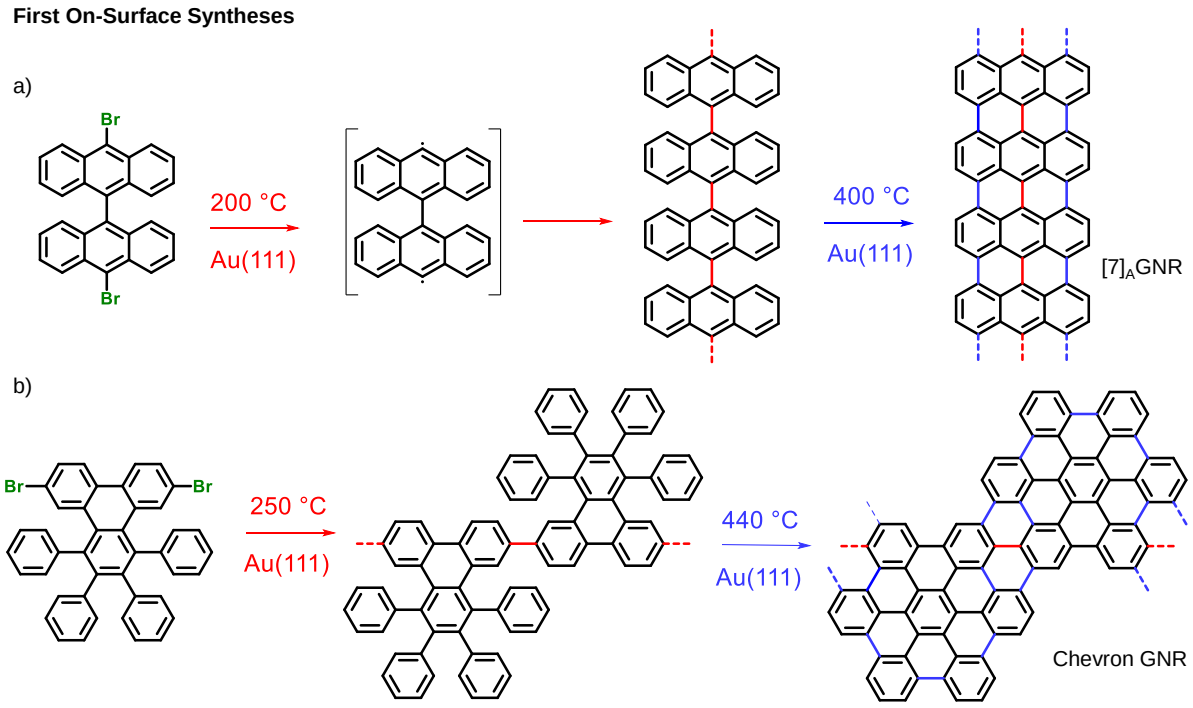

Figure 1.2. First on-surface syntheses of $[7]_A$GNR and a chevron GNR reported by Müllen and Fasel.[18]

On-surface syntheses require heavily specialized equipment, scanning tunneling microscopy (STM) or non-contact atomic force microscopy (nc-AFM) to deposit and monitor the formation of GNRs. These instruments are only compatible with relatively small substrates (~1 cm^2), which inherently limits the bulk amount of GNRs produced. The metallic substrates used to facilitate on-surface syntheses are incompatible with device fabrication, which requires the produced GNRs to be individually removed and deposited onto non-metallic substrates prior to use in devices. Chong *et al.*[29] demonstrated that individual GNRs could be lifted off Au (111) surfaces using an STM tip, but the removal process would be inefficient for mass production of

devices containing GNRs. As such, in-solution methods offer a partial solution to the above drawbacks.

Section 1.3. In-Solution Syntheses of Graphene Nanoribbons

Unlike on-surface syntheses, in-solution GNR syntheses are performed substrate-free. Therefore the length and amount of GNRs produced, is not limited by substrate size. Instead, these properties are controlled by the reaction conditions and efficiency. On-surface methods can be imaged throughout the synthesis to monitor reaction progress, but however, in-solution methods can only be characterized after completion, and therefore rely on high yielding reactions and good solubility to produce long and uniform GNRs. For example, a reaction yield of 60% at each reactive site propagated along results in a net 7.8% yield after five reactions. This rapidly results in a high number of defects along the length of the GNR. To combat this, in-solution syntheses use robust, high-yielding organic reactions.

Most in-solution methods utilize common transition-metal catalyzed carbon-carbon bond formations to generate polymeric precursors to GNRs. Unlike on-surface methods, which retain very little control over the length of GNRs, in-solution methods are able to control the length of GNRs by controlling length of the intermediate polymers. Careful design of highly soluble monomers and choice of polymerization conditions could lead to high molecular weight polymers with narrow polydispersity indices. Once purified, these polymers are subsequently graphitized using a variety of available methods (Figure 1.3): Scholl oxidation ([5],[30] [9],[31] [13],[32] $[18]_A$GNR,[33]

In-Solution Strategies

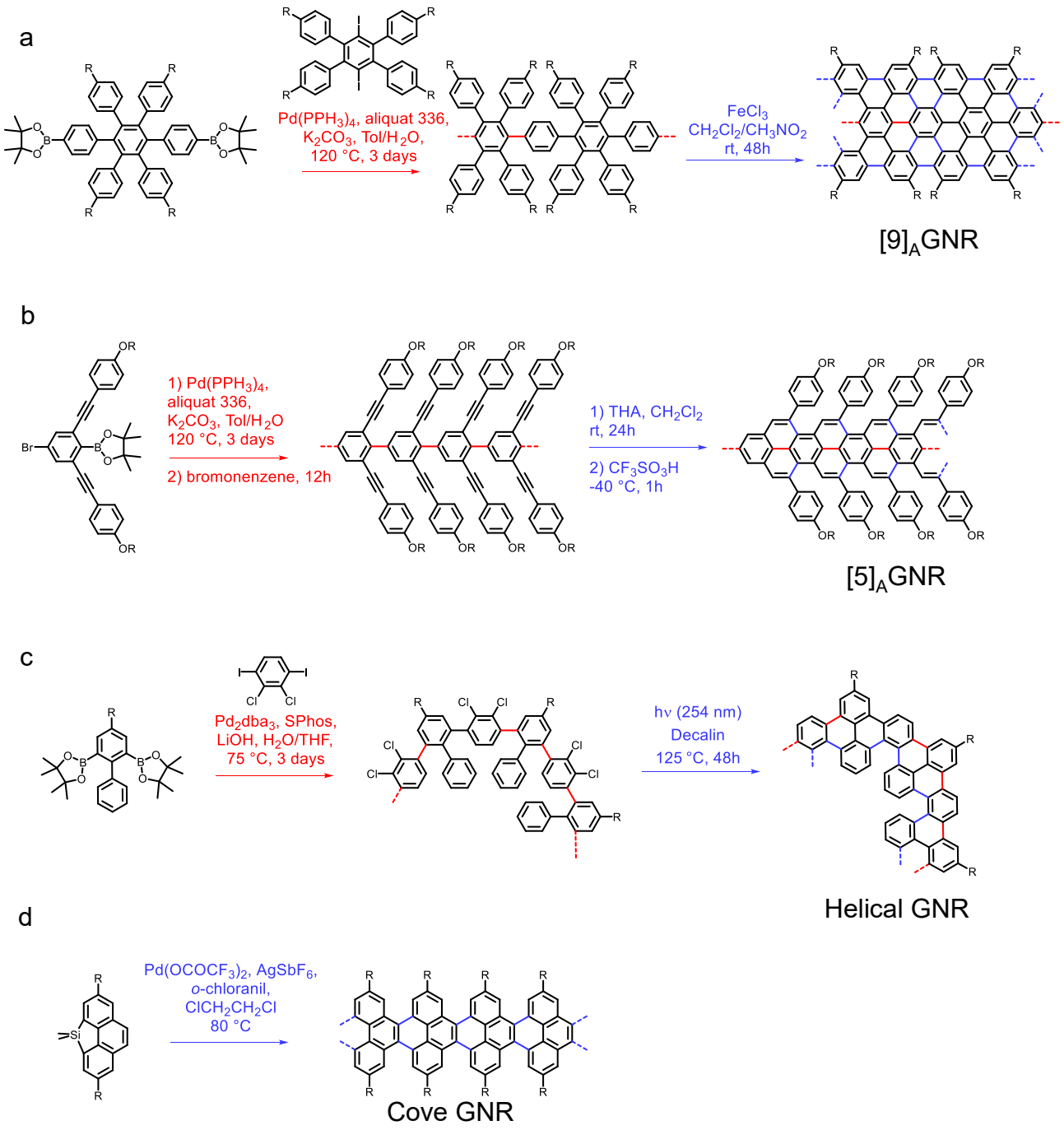

Figure 1.3. Strategies utilized to synthesize GNRs in-solution where R is a solubilizing hydrocarbon chain. a) Scholl oxidation utilized to produce $[9]_A$GNR.[31] b) Alkyne benzannulation utilized to synthesize $[5]_A$GNR.[39] c) Morin *et al*. utilized light induced cyclodehydrohalogenation to form a helical GNR.[40] d) Itami *et al.* recently reported on annulative π-extension (APEX) as a way to synthesize cove GNRs.[41]

chiral GNR,[34] chevron GNR,[35,36] [4],[37] [6],[38] [8]gulf-GNR),[37] alkyne benzannulation ($[5]_A$GNR),[39] light induced cyclodehydrochlorination (helical GNRs),[40] annulative π-extension (cove GNR,[41] [8]fjord GNR,[42] oligomeric length $[6]_A$GNR).[43] Again solubility is key to ensure complete graphitization. Since in-solution methods depend on high solubility in both steps to achieve high molecular weight polymers and sufficient graphitization, halogenated arene precursors contain solubilizing hydrocarbon chains (C_8-C_{16}) are often utilized. These sidechains are retained on the final GNR, producing free standing GNRswith relatively low solubility. Suspensions of these GNRs in solvents such as tetrahydrofuran, *o*-dichlorobenzene, 1,2,4-trichlorobenzene, N,N-dimethylformamide or N-methylpyrrolidine have yielded thin films and devices, making in-solution syntheses viable for manufacturing. In spite of the success of in-solution syntheses of soluble GNRs, the very low solubility of its precursors limits the quality of GNR produced.

Section 1.4. Solid-State Syntheses of Graphene Nanoribbons

Our group pioneered a third category of bottom-up GNR synthesis in 2016. This novel solid-state method utilizes light and heat as the only reagents to convert small bisaryl-1,3-butadiyne monomer units into GNRs. Similar to in-solution methods, our solid state-method produces bulk amounts of GNR, but is solvent-free, and thus advantageously removes the dependence of reaction yield on solubility. The first step of our process utilizes the topochemical polymerization of [n]oligoynes into polymers with an alternating enyne backbone, a reaction first reported by Wegner in 1972.[44] Specifically Wegner demonstrated that hexa-2,4-diyne-1,6-diyl bis(phenylcarbamate) polymerized into the corresponding polydiacetylene (PDA) polymer using UV light (Figure 1.4a). This reaction relies on close-contacts between neighboring butadiynes such

that the C_1 of one monomer is within van der Waals distance, 3.5 Å, of the C_4 on a neighboring monomer. The alkynes then react in a similar fashion to a 1,4-addition to produce the PDA. Any [n]oligoyne which is capable of packing into the required geometry can potentially undergo topochemical polymerization, thus produce a PDA backbone along the polymerization axis. The resulting polymers are generally blue or red depending on their morphology[45] and have been used

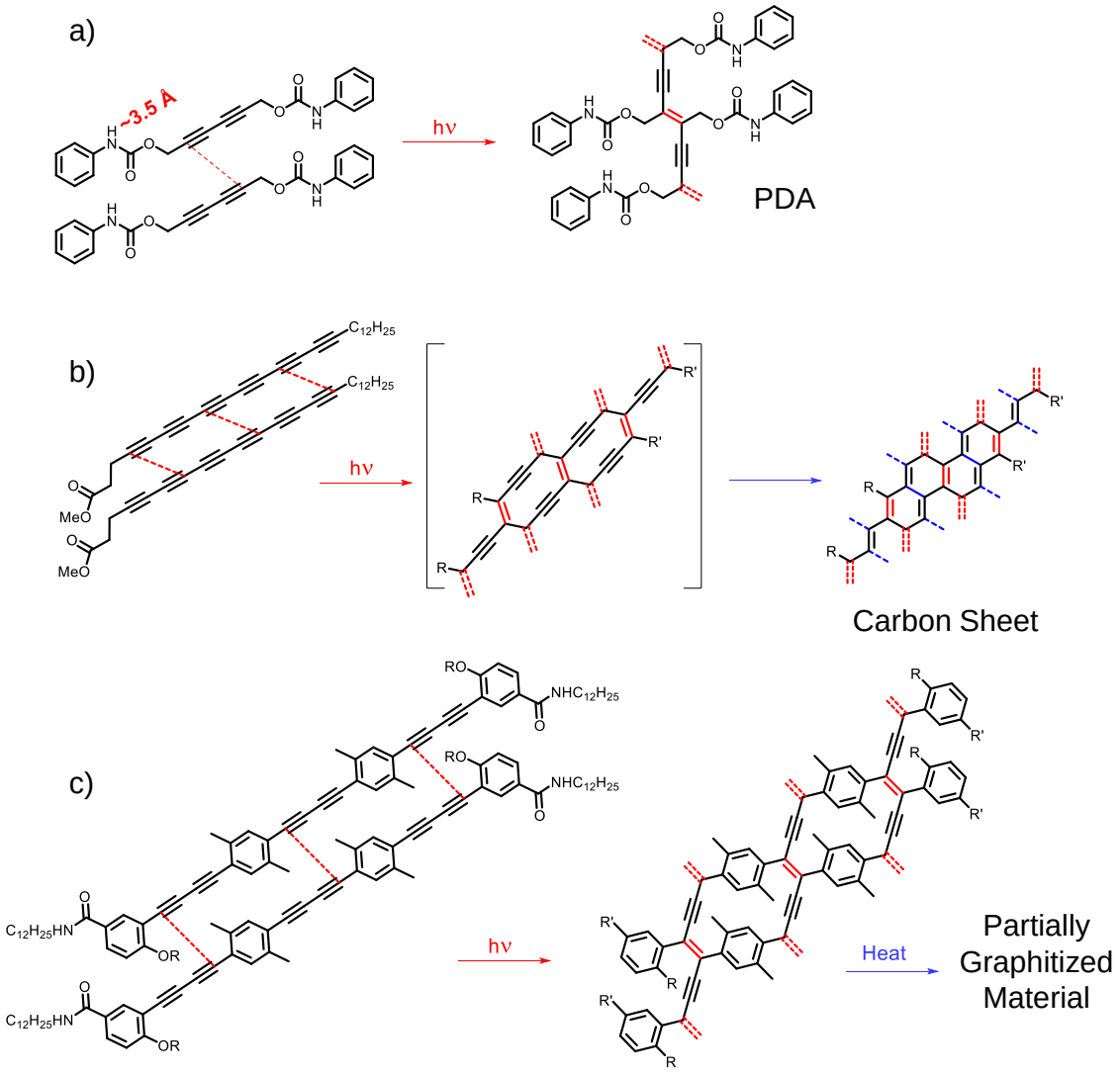

Figure 1.4. Examples of topochemical polymerization. a) The first system that Wegner reported which undergoes topochemical polymerization.[44] b) Frauenrath *et al.* utilized the reaction to as an intermediate towards carbonaceous sheets.[50] c) *Morin et al.* were able to obtain partially graphitized material upon heating their PDA.[51]

As sensors,[46,47] thermochromic ink,[48] and even gene therapy delivery systems.[49] Despite their broad range of applications, there has been relatively few attempts to utilize them as precursors for graphitic material.

In 2014, both Frauenrath *et al.*[50] and Morin *et al.*[51] reported partially graphitic nanosheets synthesized from PDA precursors (Figure 1.4). Frauenrath *et al.* utilized an aliphatic hexayne precursor to form self-assembled layers in a Langmuir film. The resultant PDA was unable to undergo further cyclization resulting in a highly conjugated but nonaromatic carbon sheet. The system used by Morin *et al.* contained pendant aromatic methyl groups that ideally would undergo cyclization after the PDA sheet was formed. However mild heating was unable to fully drive the cyclization reaction, and thus, resulted in only partially graphitized sheets. Imaging of their graphitic material revealed a layered 2D structure rather than the desired 1D ribbons.

The conversion of PDAs to GNRs was first demonstrated by our group with the synthesis of $[12]_A$GNR (Figure 1.5).[52] Starting with a bisnaphthylbutadiyne, we found that the methyl methoxy ether sidechains were crucial to inducing proper close packing between monomers. This anomeric effect was strong enough to ensure that the molecules could undergo topochemical polymerization, but flexible enough within the PDA to allow for movement during graphitization. Heating the PDA for 12 hours at 300 °C produced $[12]_A$GNR, which we characterized using Raman spectroscopy and X-ray photoelectron spectroscopy (XPS). We further confirmed the structure by imaging the GNRs using high-resolution tunneling electron microscopy (HR-TEM). Since our initial success we have demonstrated the versatility of our approach with simple modifications to the starting aryl[n]oligoynes. Expansion of the butadiyne core to longer [n]oligoynes would lead to wider GNRs, which still needs to be demonstrated. Alternatively, changing the terminal aryl groups from naphthalene to phenyl, pyridyl, other aryl rings, or highly

strained cyclic moieties should produce a library of diverse GNR widths, heteroatom doped GNRs, or GNRs with edge structures other than armchair.

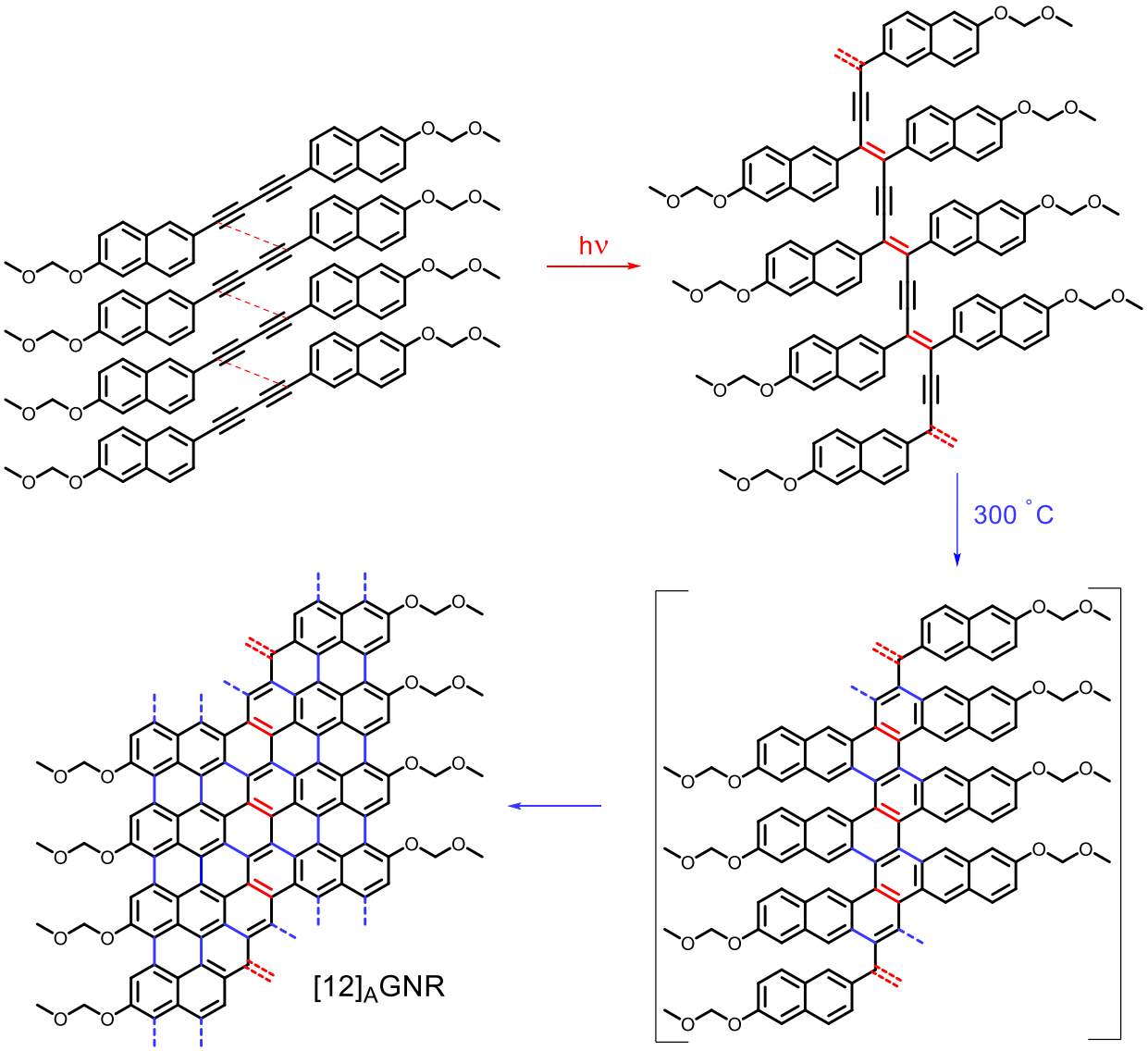

Figure 1.5. Synthesis of $[12]_A$GNR via topochemical polymerization and mild heating.

Section 1.5. Heteroatom Doped Graphene Nanoribbons

Heteroatom doped GNRs are of specific interest to our group because of their electronic properties, and the currently limited number of syntheses available. Similar to n- or p-doping in other semiconducting materials like silicon, introduction of dopants such as nitrogen or boron into the carbon backbone of GNRs was predicted to alter their electronic bandgap.[53,54] Specifically for GNRs, there exist two types of doping: edge, where heteroatoms sit along the GNR edges, and internal, where the heteroatoms lies within the basal plane (Figure 1.6). These types of substitutional doping have different effects on the bandgaps. Edge doping shifts the absolute energy placement of the bandgap while internal doping changes the size of the bandgap.[55,56] These two methods add another handle with which to tune GNR bandgaps. Together with the already established effect of GNR width and edge structure, the diversity of potential electronic bandgaps is vast. However, the current challenge lies with synthesizing these heteroatomic GNRs.

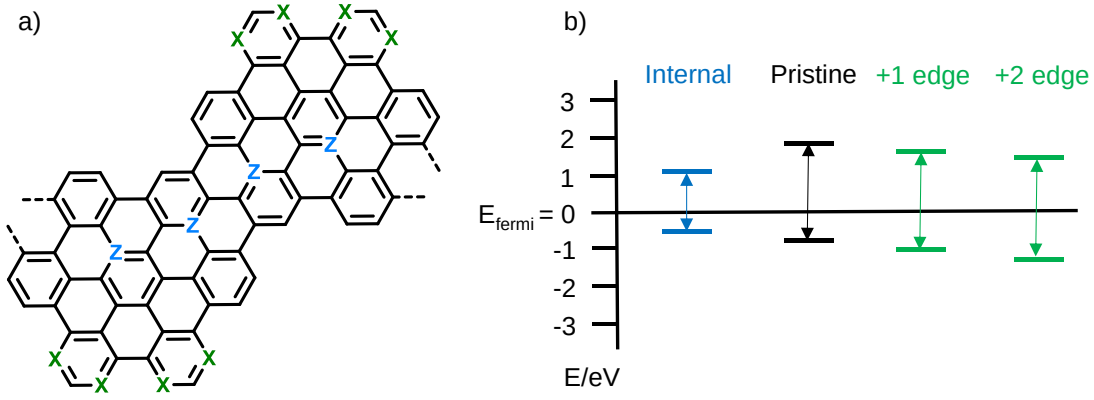

Figure 1.6. a) Example of internal (blue) and edge (green) doping sites. b) Possible bandgaps for GNRs with x or z sites replaced with nitrogens. The internally doped GNR is estimated (blue), pristine undoped GNR (black), one edge dopant (green) and two edge dopants (green) are experimentally measured bandgaps. Pristine, single nitrogen edge and dual nitrogen edge GNR bandgaps were experimentally determined to be 2.80 eV, 2.81 eV and 2.71 eV respectively.[61]

Most examples of bottom-up doped GNRs produced result in edge doped materials. This relationship is a direct result of the heterocyclic arene precursors used. As shown in the sections on on-surface and in-solution syntheses above, many of these precursors contain pendant phenyl or naphthyl groups which are ultimately cyclized into the GNR core. Thus replacing these groups with heterocyclic analogues such as thiophene, furan, or pyridine potentially provides heteroatom dopants without the need to redesign synthetic routes to the arene precursors. Indeed, such methods have been used to introduce sulfur,[57,58] oxygen,[59] oxygen-boron,[60] and nitrogen[61-65] dopants into armchair, chiral, and chevron edge GNRs (Figure 1.7a-c). Nitrogen-doped GNRs have been popular due to the diversity in aromatic nitrogen heterocycles. Specifically, the degree of heteroatom incorporation into the edge is reflected by whether pyridine, pyridazine or pyrimidine moieties are part of the monomer. The majority of the GNRs shown in **Figure 1.7** were produced on surfaces, with a select few in-solution synthesis.[62,64-65] In general, the bottom-up synthesis of edge-doped GNRs relies on careful choice of heterocyclic arene precursors, due to their more challenging synthesis, but can be achieved with relative ease using either the on-surface or in-solution methods outlined above.

In contrast, internally doped GNRs present a much greater synthetic challenge, as bond formation to dopant atoms needs to retain aromaticity of the overall GNR. The only bottom-up example to date utilizes a boron-doped trianthryl monomer to synthesize boron-doped $[7]_A$GNR on Au (111) (Figure 1.6d).[66] In this work, researchers introduced boron atoms into the interior of the graphitic lattice by pre-forming the bonds around the boron centers. Thus, the only cyclizations that needed to occur were between anthryl groups, which had been shown many times to be successful on Au (111). While this was a successful strategy, the lack of other examples of internally doped GNRs

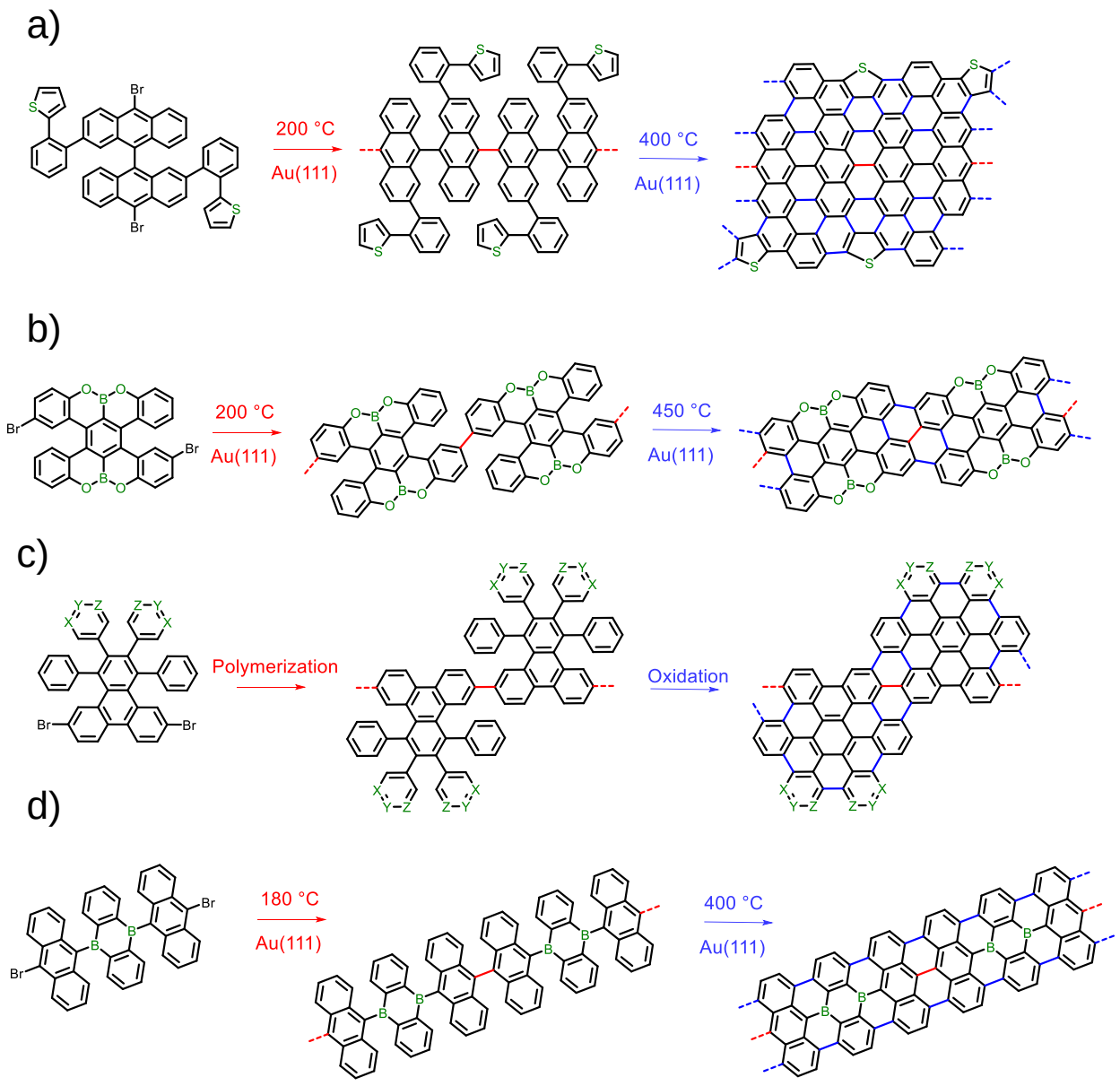

Figure 1.7. Examples of heteroatom doped GNRs. a) A sulfur edge-doped armchair-like GNR synthesized on Au (111).[57] b) Oxygen-boron doping on the edge of a chiral GNR.[60] c) Nitrogen-doped chiral GNRs made on-surface and in-solution. Precursors have included pyridine, pyridazine and pyrimidine pendant groups to introduce nitrogen dopants at edge sites denoted by X, Y, and Z.[61-65] d) One of the few examples of internal doping with boron in an armchair GNR.[66]

shows the limits of this approach. Notably, these arene precursors are highly symmetric and therefore cannot produce exceptionally narrow GNRs. Thus, the need for other successful routes to internally doped GNRs is critical as the need for GNRs with different electronic properties is still growing.

The work described herein details our efforts to expand the diversity of synthesized GNRs using our solid-state bottom-up methodology. We aim to develop GNRs of different widths, edge structures and dopants. Chapter 2 details the synthesis of $[8]_A$GNR from four distinct PDAs. The process is characterized by ^{13}C cross polarization magic angle spinning (CP/MAS) solid-state NMR, Fourier transform infrared spectroscopy (FT-IR), Raman spectroscopy, XPS, and TEM imaging.[67] Similar characterization methods are used to validate the synthesis of a heteroatom doped system, fjord-edge N_2[8] GNRs, as described in Chapter 3. Chapter 4 describes the synthesis of a bis(norbornyl) monomer unit as an example of an alternative PDA synthon to lower the very high reaction barrier of analogous aromatic butadiyne precursors.

Section 1.6. Amphiphilic Semiconducting Polymers and Electron Acceptors

Aside from GNRs, semiconducting polymers are another class of highly tunable organic electronic materials. These polymers characteristically contain a conjugated backbone, responsible for their electronic properties, and often have sidechains added to increase solubility (Figure 1.8).[68,69] Typically, polymers are either homopolymers or alternating copolymers of conjugated

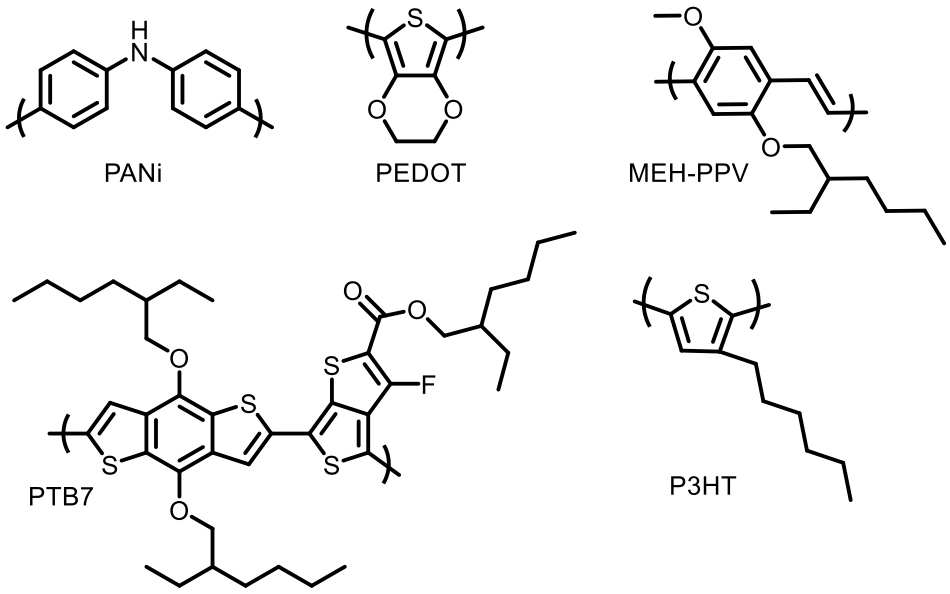

Figure 1.8. Examples of common semiconducting polymers: PANi = poly(aniline), PEDOT = poly(3,4-ethylenedioxythiophene), MEH-PPV = poly(2-methoxy-5-(2-ethylhexyloxy)-1,4-phenylenevinylene), PTB7 = poly(4,8-bis(5-(2-ethylhexyl)thiophene-2-yl)benzo([1,2-b;4,5-b']dithiophene-2,6-diyl-alt-(4-(2-ethylhexyl)-3-fluorothieno[3,4-b]thiophene-)-2-carboxylate-2-6-diyl)), and P3HT = poly(3-hexylthiophene).

monomer units, which can be either electron-rich, electron poor, or both. This allows for bandgap and absorption windows tuning across the entire UV, visible, and near-IR spectrum.[70,71] Absorption in the UV-vis-IR range makes these polymers useful for organic photovoltaic (OPV) devices and other excited state electron transfer complexes.[72,73] In designing these devices, there are two phenomena that affect polymer performance, processing conditions and chemical structure.[74,75] Both of these contribute to issues with semiconducting polymer devices' low conductivity by introducing bends and folds along the chain, which decreases the effective conjugation length of the polymer backbone. While much work has been done to control polymer morphology through casting conditions,[76,77] substrate choice,[78] rubbing,[79] and additives,[80] we chose to explore chemical structure as a handle to tune polymer morphology. By developing a set

of design rules, we could control polymer self-assembly as well as its assembly with other molecules capable of electron transfer.

We began by developing three design rules for amphiphilic semiconducting polymer assembly in aqueous solution. Water was our chosen assembly medium as it mimics excited state electron transfer environments found in nature, in addition to reducing the amount of organic solvent required to study these materials. Our three design rules were as follows: 1) a hydrophobic polymer backbone and hydrophilic sidechains, 2) an alternating co-polymer such that all the sidechains reside on one side of the polymer chain, and 3) sidechains branched off an sp^3 carbon to create a "pie-wedge" shape of occupied space. Using these rules, we synthesized the amphiphilic semiconducting polymer, poly(fluorene-alt-thiophene) (PFT) (Figure 1.9).[81] Terminal ammonium sidechains create the hydrophilic region, while fluorene and thiophene monomers comprise the hydrophobic backbone. The sidechains are attached to the sp^3 carbon on fluorene, which simultaneously positions all the sidechains to one side of the polymer, and also creates the "pie-wedge." As a result, PFT self-assembles in water to form worm-like cylindrical micelles, whose

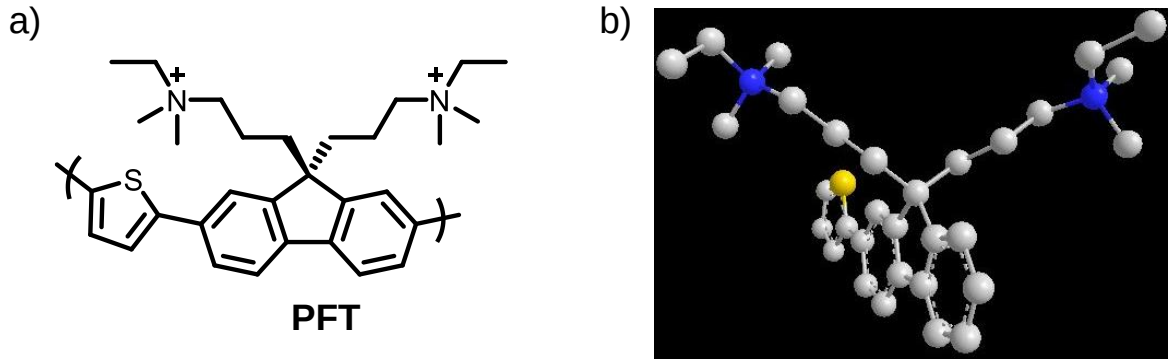

Figure 1.9. a) Structure of PFT and b) "pie-wedge" shape created by the sidechains of PFT shown for a single repeat unit of PFT. Structure was minimized using ChemDraw3D and hydrogens are omitted for clarity.

network can be relaxed or strengthened,[82] and is also capable of co-assembling with amphiphilic electron acceptors.[83] While these micelles were largely cylindrical, they also contained bends and kinks that could lead to inefficient assemblies with acceptors due to mismatched geometries. Thus we sought to design a new polymer that employed our previous design rules, but would also have a straighter backbone. This would reduce the number of kinks in the polymer micelle and therefore could also affect the co-assembly between polymer and electron acceptors. Chapter 5 details the synthesis and solution-state characterization of a new amphiphilic semiconducting polymer poly(cyclopentadithiophene-alt-thiophene) (PCT), according to our new design rule. Solution small angle x-ray scattering (SAXS), cryo-EM and modeling were used to characterize the structure of the new polymer micelles. The assembly of PCT micelles with amphiphilic acceptors is characterized in Chapter 6 along with their photoluminescence quenching.

References

[1] Chaudhari, P. Electronic and Magnetic Materials. *Scientific American* **1986**, *4*, 136-144.

[2] Brodsky, M. H. Progress in Gallium Arsenide Semiconductors. *Scientific American* **1990**, *2*, 68-75.

[3] Salahuddin, S.; Ni, K.; Datta, S. The Era of Hyper-Scaling in Electronics. *Nature Electronics* **2018**, *1*, 442-450.

[4] Lundstrom, M. Moore's Law Forever? *Science*, **2003**, *299*, 210-211.

[5] Desai, S. B.; Madhvapathy, S. R.; Sachid,A. B.; Llinas, J. P.;Wang, Q.;Ahn, G. H.; Pitner, G.; Kim, M. J.; Bokor, J.; H, C.; Wong, H.-S. P.; Javey, A. MoS_2 Transistors with 1-Nanometer Gate Lengths. *Science* **2016**, *354*, 99-102.

[6] Nakada, K.; Fujita, M.; Dresselhaus, G.; Dresselhaus, M. S. Edge State in Graphene Ribbons: Nanometer Size Effect and Edge Shape Dependence. *Phys. Rev. B* **1996,** *54*, 17954-17961.

[7] Novoselov, K. S.; Geim, A. K.; Morozov, S. V.; Jiang, D.; Zhang, Y.; Dubonos, S. V.; Grigorieva, I. V.; Firsov, A. A. Electric Field Effect in Atomically Thin Carbon Films. *Science* **2004**, *306*, 666-669.

[8] Li, X.; Wang, X.; Zhang, L.; Lee, S.; Dai, H. Chemically Derived, Ultrasmooth Graphene Nanoribbon Semiconductors. *Science*, **2008**, *319*, 1229-1232.

[9] Wu, Z.-S.; Ren, W.; Gao, L.; Liu, B.; Zhao, J.; Cheng, H.-M. Efficient Synthesis of Graphene Nanoribbons Sonochemically Cut from Graphene Sheets. *Nano Res* **2010**, *3*, 16-22.

[10] Kosynkin, D. V.; Higginbotham, A. L.; Sinitskii, A.; Lomeda, J.R.; Dimiev, A.; Price, B. K.; Tour, J. M. Longitudinal Unzipping of Carbon Nanotubes to Form Graphene Nanoribbons. *Nature* **2009**, *458*, 872-877.

[11] Kim, K.; Sussman, S.; Zettl, A. Graphene Nanoribbons Obtained by Electrically Unwrapping Carbon Nanotubes. *ACS Nano* **2010**, *4*, 1362-1366.

[12] Yu, W. J.; Zhae, S. H.; Perello, D.; Lee, S. Y.; Han, G. H.; Yun, M.; Lee, Y. H. Synthesis of Edge-Closed Graphene Ribbons with Enhanced Conductivity. *ACS Nano* **2010**, *4*, 5480-5486.

[13] Sommer, B.; Sonntag, J.; Ganczarczyk, A.; Braam, D.; Prinz, G.; Lorke, A.; Geller, M. Electron-beam Induced Nano-etching of Suspended Graphene. *Sci Rep*, **2015**, *5*, 7781.

[14] Fasoli, A.; Colli, A.; Lombardo, A.; Ferrari, A. C. Fabrication of Graphene Nanoribbons via Nanowire Lithography. *Phys. Status Solidi B* **2009**, *246*, 2514-1517.

[15] Sinitskii, A.; Tour, J. M. Patterning Graphene Nanoribbons using Copper Oxide Nanowires. *Appl. Phys.Lett.* **2012**, *100*, 103106.

[16] Tapasztó, L.; Dobrik, G.; Lambin, R.; Biró, L. Tailoring the Atomic Structure of Graphene Nanoribbons by Scanning Tunneling Microscope Lithography. *Nat. Nanotechnol.* **2008**, *3*, 397-401.

[17] Masubuchi, S.; Ono, M.; Yoshida, K.; Hirakawa, K.; Machida, T. Fabrication of Graphene Nanoribbon by Local Anodic Oxidation Lithography using Atomic Force Microscope. *Appl. Phys. Lett.* **2009**, *94*, 082107.

[18] Cai, J.; Ruffieux, P.; Jaafar, R,; Bieri, M.; Braun, T.; Blankenburg, S.; Muoth, M.; Seitsonen, A.P.; Saleh, M.; Feng, X.; Müllen, K.; Fasel, R. Atomically Precise Bottom-up Fabrication of Graphene Nanoribbons. *Nature* **2010**,*466*, 470-473.

[19] Zhang, H.; Lin, H.; Sun, K.; Chen, L.; Zagranyarski, Y.; Aghdassi, N.; Duhn, S.; Li, Q.; Zhong, D.; Li, Y.; Müllen, K.; Fuchs, H.; Chi, L. On-Surface Synthesis of Rylene-Type Graphene Nanoribbons. *J. Am. Chem. Soc.* **2015**, *137*, 4022-4025.

[20] Merino-Díez, N.; Garcia-Lekue, A.; Carbonell-Sanromà, E.; Li, Y.; Corso, M.; Colazzo, L.; Sedona, F.; Sánchez-Portal, D.; Pascual, J. I.; de Oteyza, D.; G. Width-Dependent Band Gap in Armchair Graphene Nanoribbons Reveals Fermi Level Pinning on Au(111). *ACS Nano* **2017**, *11*, 11661-11668.

[21] Talirz, A.; Söde, H.; Dumslaff, T.; Wang, S.; Sanchez-Valencia, J. R.; Liu, J.; Shinde, P.; Pignedoli, C. A.; Liang, L.; Meunier, V.; Plumb, N. C.; Shi, M.; Feng, X.; Narita, A.; Müllen, K.; Fasel, R.; Ruffieux, P. On-Surface Synthesis and Characterization of 9-Atom Wide Armchair Graphene Nanoribbons. *ACS Nano* **2017**, *11*, 1380-1388.

[22] Di Giovannantonio, M., Deniz, O.; Urgel, J. I.; Widmer, R.; Dienel, T.; Stolz, S.; Sánchez-Sánchez, C.; Muntwiler, M.; Dumslaff, T.; Berger, R.; Narita, A.; Feng, X.; Müllen, K.; Ruffieux, P.; Fasel, R. On-Surface Growth Dynamics of Graphene Nanoribbons: The Role of Halogen Functionalization. *ACS Nano* **2018**, *12*, 74-81.

[23] Chen, Y.-C.; de Oteyza, D. G.; Pedramrazi, Z.; Chen, C.; Fischer, F.R.; Crommie, M.; F. Tuning the Band Gap of Graphene Nanoribbons Synthesized from Molecular Precursors. *ACS Nano* **2013**, *77*, 1187-1190.

[24] Ruffieux, P.; Wang, S.; Yang, B.; Sánchez-Sánchez, C.; Liu, J.; Dienel, T.; Talirz, L.; Shinde, P.; Pignedoli, C. A.; Passerone, D.; Dumslaff, T.; Feng, X.; Müllen, K.; Fasel, R. On-Surface Synthesis of Graphene Nanoribbons with Zigzag Edge Topology. *Nature* **2016**, *531*, 489-493.

[25] Liu, J.; Li,B.-W.; Tan, Y.-Z.; Giannakopoulos, G.; Sánchez-Sánchez, C.; Beljonne, D.; Ruffieux, P.; Fasel,R.; Feng, X.; Müllen, K. Toward Cove-Edged Low Band Gap Graphene Nanoribbons. *J. Am. Chem. Soc.* **2015**, *137*, 6097-6103.

[26] Han, P.; Akahi, K.; Canova, F. F.; Mutoh, H.; Shiraki, S.; Iwaya, K.; Weiss, P.; Asao, N.; Hitosugi, T. Bottom-Up Graphene-Nanoribbon Fabrication Reveals Chiral Edges and Enantioselectivity. *ACS Nano* **2014**, *8*, 9181-9187.

[27] Sakaguchi, H.; Song, S.; Kojima, T.; Nakae, T. Homochiral Polymerization-driven Selective Growth of Graphene Nanoribbons. *Nat. Chem.* **2016**, *7*, 57-63.

[28] Sun, K.; Ji, P.; Zhang, J.; Wang, J.; Li, X.; Xu, X.; Zhang, H.; Chi, L. On-Surface Synthesis of 8-and10-Armchair Graphene Nanoribbons. *Small* **2019**, *15*, 1804526.

[29] Chong, M. C.; Afshar-Imani, N.; Scheurer, F.; Cardoso, C.; Ferretti, A.; Prezzi, D.; Schull, G. Bright Electroluminescence from Single Graphene Nanoribbon Junctions. *Nano Lett.* **2018**, *18*, 175-181.

[30] Jänsch, D.; Ivanov, I.; Zagranyarski, Y.; Duznovic, I.; Baumgarten, M.; Turchinovich, D.; Li, C.; Bonn, M.; Müllen, K. Ultra-Narrow Low-Bandgap Graphene Nanoribbons from Bromoperylenes-Synthesis and Terahertz-Spectroscopy. *Chem. Eur. J.* **2017**, *23*, 4870-4875.

[31] Yang, X.; Dou, X.; Rouhanipour, A.; Zhi, L.; Räder, J.; Müllen, K. Two-Dimensional Graphene Nanoribbons. *J. Am. Chem. Soc.* **2008**, *130*, 4216-4217.

[32] Gao, J.; Uribe-Romo, F. J.; Saathoff, J. D.; Arslan, H.; Crick, C. R.; Hein, S. J.; Itin, B.; Clancy, P.; Dichtel, W.R.; Loo, Y.-L. Ambipolar Transport in Solution-Synthesized Graphene Nanoribbons. *ACS Nano* **2016**, *10*, 4847-4856.

[33] El Gemayel, M.; Narita, A.; Dössel, L. F.; Sundaram, R. S.; Kiersnowski, A.; Pisula, W.; Hansen, M. R.; Ferrari, A. C.; Orgiu, E.; Feng, X.; Müllen, K.; Samori, O. Graphene Nanoribbon Blends with P3HT for Organic Electronics. *Nanoscale* **2014**, *6*, 6301-6314.

[34] Schwab, M. G.; Narita, A.; Hernandez, Y.; Balandina, T.; Mali, K.S.; De Feyter, S.; Feng, X.; Müllen, K. Structurally Defined Graphene Nanoribbons with High Lateral Extension. *J. Am. Chem. Soc.* **2012**, *134*, 18169-18172.

[35] Ho. T. V.; Shekhirev, M.; Kunkel, D. A.; Morton, M. D.; Berglund, E.; Kong, L.; Wilson, P. M.; Dowben, P. A.; Enders, A.; Sinitskii, A. Large-scale Solution Synthesis of Narrow Graphene Nanoribbons. *Nat. Commun.* **2014**, *5*, 3189.

[36] von Kugelgen, S.; Piskun, I.; Griffin, J. H.; Eckdahl, C. T.; Jarenwattananon, N. N.; Fischer, F. R. Templated Synthesis of End-Functionalized Graphene Nanoribbons through Living Ring-Opening Alkyne Metathesis Polymerization. *J. Am. Chem. Soc.* **2019**, *141*, 11050-11058.

[37] Narita, A.; Feng, X.; Hernandez, Y.; Jensen, S. A.; Bonn, M; Yang, H.; Verzhbitskiy, I. A.; Casiraghi, C.; Hansen, M. R.; Koch, A. H. R.; Fytas, G.; Ivasenko, A.; Li, B.; Mali, K. S.; Balandina, T.; Mahesh, S.; De Feyter, S.; Müllen, K. Synthesis of Structurally Well-defined and Liquid-phase-processable Graphene Nanoribbons. *Nat. Chem.* **2013**, *6*, 126-132.

[38] Hu, Y.; Xie, P.; De Corato, M.; Ruini, A.; Zhao, S.; Meggendorfer, F.; Straasø, L. A.; Rondin, L.; Simon, P.; Li, J.; Finley, J. J.; Hansen, M. R.; Lauret, J.-L.; Molinari, E.; Feng, X.; Barth, J. V.; Palma, C.-A.; Prezzi, D.; Müllen, K.; Narita, A. Bandgap Engineering of Graphene Nanoribbons by Control over Structural Distortion. *J. Am. Chem. Soc.* **2018**, *140*, 7803-7809.

[39] Yang, W.; Lucotti, A.; Tommasini, M.; Chalifoux, W. A. Bottom-Up Synthesis of Soluble and Narrow Graphene Nanoribbons Using Alkyne Benzannulations. *J. Am. Chem. Soc.* **2016**, *138*, 9137-9144.

[40] Daigle, M.; Miao, D.; Lucotti, A.; Tommasini, M.; Morin, J-F. Helically Coiled Graphene Nanoribbons. *Angew. Chem. Int. Ed.* **2017**, *56*, 6213-6217.

[41] Mitoma, N.; Yano, Y.; Ito, H.; Miyauchi, Y.; Itami, K. Graphene Nanoribbon Dielectric Passivation Layers for Graphene Electronics. *ACS Appl. Nano Mater*. **2019**, *2*, 4825-4851.

[42] Yano, Y.; Mitoma, N.; Matsushima, K.; Wang, F.; Matsui, K.; Takakura, A.; Miyauchi, Y.; Ito, H.; Itami, K. Living Annulative π-Extension Polymerization for Graphene Nanoribbon Synthesis. *Nature* **2019**, *571*, 387-392.

[43] Ito, H.; Segawa, Y.; Murakami, K.; Itami, K.; Polycyclic Arene Synthesis by Annulative π-Extension. *J. Am. Chem. Soc.* **2019**, *141*, 3-10.

[44] Wegner, G. *Makromolekul. Chem.* **1972**, *154*, 35-48.

[45] Patel, G. N.; Chance, R. R.; Witt, J. D. A Planar-Nonplanar Conformational Transition in Conjugated Polymer Solutions. *J. Chem. Phys.* **1979**, *70*, 4387-4392.

[46] Hong, J.; Park, D.-H.; Baek, S.; Song, S.; Lee, C. W.; Kim, J.-H. Polydiacetylene-Embedded Microbeads for Colorimetric and Volumetric Sensing of Hydrocarbons. *ACS Appl. Mater. Interfaces* **2015**, *7*, 8339-8343.

[47] Wang, M.; Wang, F.; Wang, Y.; Zhang, W.; Chen, X. Polydiacetylene-based Sensor for Highly Sensitive and Selective Pb^{2+} Detection. *Dyes Pigm.* **2015**, *120*, 307-313.

[48] Yoon, B.; Ham, D.-Y.; Yarimaga, O.; An, H.; Lee, C. W.; Kim, J.-M. Inkjet Printing of Conjugated Polymer Precursors on Paper Substrates for Colorimetric Sensing and Flexible Electrothermochromic Display. *Adv. Mater*. **2011**, *23*, 5492–5497.

[49] Morin, E.; Nothisen, M.; Wagner, A.; Remy, J.-S. Cationic Polydiacetylene Micelles for Gene Delivery. *Bioconjugate Chem.* **2011**, *22*, 1916-1923.

[50] Schrettl, S.; Stefaniu, C.; Schwieger, C.; Pasche, G.; Oveisi, E.; Fontana, Y; Morral, A. F. I.; Reguera, J.; Petraglia, R.; Corminboeuf, C.; Brezesinski, G.; Frauenrath, H. Functional Carbon

Nanosheets Prepared from Hexayne Amphiphile Monolayers at Room Temperature. *Nat. Chem.* **2014**, *6*, 468-476.

[51] Levesque, I.; Néabo, J. R.; Rondeau-Gagné, S.; Vigier-Carrière, Daigle, M.; Morin, J.-F. Layered Graphitic Materials from a Molecular Precursor. *Chem. Sci.* **2014**, *5*, 831-836.

[52] Jordan, R. S.; Wang, Y.; McCurdy, R. D.; Yeung, M. T.; Marsh, K. L.; Khan, S. I.; Kaner, R. B.; Rubin, Y. Synthesis of Graphene Nanoribbons via the Topochemical Polymerization and Subsequent Aromatization of a Diacetylene Precursor. *Chem* **2016**, *1*, 78-90.

[53] Yu, S. S.; Zheng, W. T.; Jiang, Q. Electronic Properties of Nitrogen-/Boron-Doped Graphene Nanoribbons with Armchair Edges. IEEE Trans Nanotechnol. **2010**, *9*, 78-81.

[54] Martin-Martinez, F. J.; Fias, S.; Van Lier, G.; De Proft, F.; Geerlings, P. Tuning Aromaticity and Electronic Properties of Armchair Graphene Nanoribbons with Chemical Edge Functionalization. *Phys. Chem. Chem. Phys.* **2013**, *15*, 12637-12647.

[55] Liu, W.; Zhang, K.; Wang, R.-Z.; Zhong, J.; Liu, L.-M. Modulation of the Electron Transportation Properties in Graphene Nanoribbons Doped with BN Chains. *AIP Advances* **2014**, *4*, 067123.

[56] Baildya, N.; Ghosh, N. N.; Chattopadhyay, A. P. Tailoring Electronic and Transport Properties of Edge-Terminated Armchair Graphene by Defect Formation and N/B Doping. *Phys. Lett. A* **2020**, *384*, 126194.

[57] Nguyen, G. D.; Toma, F. M.; Cao, T.; Pedramrazi, Z.; Chen, C.; Rizzo, D. J.; Joshi, T.; Bronner, C.; Chen, Y.-C.; Favaro, M.; Louie, S. G.; Fischer, F. R.; Crommie, M. F. Bottom-Up Synthesis of $N = 13$ Sulfur-Doped Graphene Nanoribbons. *J. Phys. Chem. C* **2016**, *120*, 2684-1687.

[58] Cao, Y.; Qi, J.; Zhang, Y.-F.; Huang, L.; Zheng, Q.; Lin, X.; Cheng, Z.; Zhang, Y.-Y.; Feng, X.; Du, S.; Pantelides, S. T.; Gao, H.-J. Tuning the Morphology of the Chevron-Type Graphene Nanoribbons by Choice of Annealing Temperature. *Nano Research* **2018**, *11*, 6190-6196.

[59] Durr, R. A.; Haberer, D.; Lee, Y.-L.; Blackwell, R.; Kalayjian, A. M.; Marangoni, T.; Ihm, J.; Louie, S. G.; Fisher, F. R. Orbitally Matched Edge-Doping in Graphene Nanoribbons. *J. Am. Chem. Soc.* **2018**, *140*, 807-813.

[60] Wang, X.-Y.; Urgel, J I.; Barin, G. B.; Eimre, E.; DiGiovannantonio, M. D.; Milani, A.; Tommasini, M.; Pignedoli, C. A.; Ruffieux, P.; Feng, X.; Fasel, R.; Müllen, K.; Narita, A. Bottom-Up Synthesis of Heteroatom-Doped Chiral Graphene Nanoribbons. *J. Am. Chem. Soc.* **2018**, *140*, 9104-9107.

[61] Bronner, C.; Stremlau, S.; Gille, M.; Braußе, F.; Haase, A.; Hecht, S.; Tegeder, P. Aligning the Band Gap of Graphene Nanoribbons by Monomer Doping. *Angew. Chem. Int. Ed.* **2013**, *52*, 4422-4425.

[62] Vo, T. H.; Perera, G. E.; Shekhirev, M.; Pour, M. M.; Kunkel, D. A.; Lu, H.; Gruverman, A.; Sutter, E.; Cotlet, M.; Nykypanchuk, D.; Zahl, P.; Enders, A.; Sinitskii, A.; Sutter. P. Nitrogen-Doping Induced Self-Assembly of Graphene Nanoribbon-Based Two-Dimensional and Three-Dimensional Metamaterials. *Nano Lett.* **2015**, *15*, 5770-5777.

[63] Zhang, Y.; Zhang, Y.; Li, G.; Lu, J.; Lin, X.; Du, S.; Berger, R.; Feng, X.; Müllen, K.; Gao, H.-J. Direct Visualization of Atomically Precise Nitrogen-Doped Graphene Nanoribbons. *Appl. Phys. Lett.* **2014**, *105*, 023101.

[64] Vo, T. H.; Shekhirev, M.; Kunkel, D. A.; Orange, D.; Guinel, M. J.-F.; Enders, A.; Sinitskii, A. Bottom-Up Solution Synthesis of Narrow Nitrogen-Doped Graphene Nanoribbons. *Chem. Commun.* **2014**, *50*, 4172-4174.

[65] Kim, K. T.; Lee, J. W.; Jo, W. H. Charge-Transport Tuning of Solution-Processable Graphene Nanoribbons by Substitutional Nitrogen Doping. *Macromol. Chem. Phys.* **2013**, *214*, 2768-2773.

[66] Kawai, S.; Saito, S.; Osumi, S.; Yamaguchi, S.; Foster, A. S.; Spijker, P.; Meyer, E. Atomically Controlled Substitutional Boron-Doping of Graphene Nanoribbons. *Nat. Commun.* **2015**, *6*, 8098.

[67] Jordan, R. S.; Li, Y. L.; Lin, C-W.; McCurdy, R. D.; Lin, J. B.; Brosmer, J. L.; Marsh, K. L.; Khan, S. I.; Houk, K. N.; Kaner, R. B.; Rubin, Y. Synthesis of *N* = 8 Armchair Graphene Nanoribbons from Four Distinct Polydiacetylenes. *J. Am. Chem. Soc.* **2017**, *139*, 15878-15890.

[68] Schenning, A. P. H. J; Meijer, E. W. Functional Conjugated Polymers, Molecular Design of: Architecture *Encyclopedia of Materials: Science and Technology* **2001**, 3400-3407.

[69] Fichou, D.; Horowitz, G. Molecular and Polymer Semiconductors, Conductors, and Superconductors: Overview *Encyclopedia of Materials: Science and Technology* **2001**, 5748-5758.

[70] Jung, J. W.; Jo, J. W.; Jung, E. H.; Jo, W. H. Recent Progress in High Efficiency Polymer Solar Cells by Rational Design and Energy Level Tuning of Low Bandgap Copolymers with Various Electron-Withdrawing Units. *Org. Electron.* **2016**, *31*, 149-170.

[71] Ma, Y.; Kang, Z.; Zheng, Q.; Recent Advances in Wide Bandgap Semiconducting Polymers for Polymer Solar Cells. *J. Mater. Chem. A.* **2017**, *5*, 1860-1872.

[72] Hoppe, H.; Sariciftci, N. S. Nanostructure and Nanomorphology Engineering in Polymer Solar Cells. *Nanostructured Materials for Solar Energy Conversion* **2006**, 277-318.

[73] Li, G.; Chang, W.-H.; Yang, Y. Low-bandgap Conjugated Polymers Enabling Solution-Processable Tandem Solar Cells. *Nat. Rev. Mater.* **2017**, *2*, 17043.

[74] Scharber, M. C.; Sariciftci, N. S. Efficiency of Bulk-Heterojunction Organic Solar Cells. *Prog. Polym. Sci.* **2013**, *38*, 1929-1940.

[75] Ferreira, A. S.; Aguirre, J. C.; Subramaniyan, S.; Jenekhe, S. A.; Tolbert, S. H.; Schwartz, B. J. Understanding How Polymer Properties Control OPV Device Performance: Regioregularity, Swelling, and Morphology Optimization Using Random Poly(3-butylthiophene-*co*-3-octylthiophene) Polymers. *J. Phys. Chem. C* **2016**, *120*, 22115-22125.

[76] Aubry, T.J.; Ferreira, A. S.; Yee, P. Y.; Aguirre, J. C.; Hawks, S. A.; Fontana, M. T.; Schwartz, B. J.; Tolbert, S. H. Processing Methods for Obtaining a Face-On Crystalline Domain Orientation in Conjugated Polymer-Based Photovoltaics. *J. Phys. Chem. C* **2018**, *122*, 15078-15089.

[77] Aguirre, J. C.; Hawks,S. A.; Ferreira, A. S.; Yee, P.; Subramaniyan, S.; Jenekhe, S. A.; Tolbert, S. H.; Schwartz, B. J. Sequential Processing for Organic Photovoltaics: Design Rules for Morphology Control by Tailored Semi-Orthogonal Solvent Blends. *Adv. Energy Mater.* **2015**, 1402020.

[78] Wu, D.; Kaplan, M.; Ro, H. W.; Engmann, S.; Fischer, D. A.; DeLongchamp, D. M.; Richter, L. J.; Gann, E.; Thomsen, L.; McNeill, C. R.; Zhang, X. Blade Coating Aligned, High-Performance, Semiconducting-Polymer Transistors. *Chem. Mater.* **2018,** *30*, 1924-1936.

[79] Biniek, L.; Pouget, S.; Djurado, D.; Gonthier, E.; Tremel, K.; Kayunkid, N.; Zaborova, E.; Crespo-Monteiro, N.; Boyron, O,; Leclerc, N.; Ludwigs, S.; Brinkmann, M. High-Temperature Rubbing: A Versatile Method to Align π-Conjugated Polymers without Alignment Substrate. *Macromol.* **2014**, *47*, 3871-3879.

[80] Nikolka, M.; Broch, K.; Armitage, J.; Hanifi, D.; Nowack, P. J.; Venkateshvaran, D.; Sadhanala, A.; Saska, J.; Mascal, M.; Jung, S.-H.; Lee, J.-K.; McCulloch, I.; Salleo, A.;

Sirringhaus, H. High-Mobility, Trap-Free Charge Transport in Conjugated Polymer Diodes. *Nat. Commun.* **2019**, *10*, 2122

[81] Clark, A. P.-Z.; Shi, C.; Ng, B. C.; Wilking, J. N.; Ayzner, A. L.; Stieg, A. Z.; Schwartz, B. J.; Mason, T. G.; Rubin, Y.; Tolbert, S. H. Self-Assembling Semiconducting Polymers – Rods and Gels from Electronic Materials. *ACS Nano* **2013**, *7*, 962-977.

[82] Huber, R. C.; Ferreira, A. S.; Aguirre, J. C.; Kilbride, D.; Toso, D. B.; Mayoral, K.; Zhou, H; Kopidakis, N.; Rubin, Y.; Schwartz, B. J.; Mason, T. G., Tolbert, S. H. Structure and Conductivity of Semiconducting Polymer Hydrogels. *J. Phys. Chem. B* **2016**, *120*, 6215-6224.

[83] Huber, R. C.; Ferreira, A. S.; Thompson, R.; Kilbride, D.; Knutson, N. S.; Devi, L. S.; Toso, D. B.; Challa, J. R.; Zhou, Z. H.; Rubin, Y.; Schwartz, B. J.; Tolbert, S. H. Long-Lived Photoinduced Polaron Formation in Conjugated Polyelectrolyte-Fullerene Assemblies. *Science* **2015**, *348*, 1340-1343.

Chapter 2: Synthesis of N = 8 Armchair Graphene Nanoribbons from Four Distinct Polydiacetylenes

Section 2.1. Abstract

We demonstrate a highly efficient thermal conversion of four differently substituted polydiacetylenes (PDAs **1** and **2a–c**) into virtually indistinguishable N = 8 armchair graphene nanoribbons ($[8]_A$GNR). PDAs **1** and **2a–c** are themselves easily accessed through photochemically initiated topochemical polymerization of diynes **3** and **4a–c** in the crystal. The clean, quantitative transformation PDAs **1** and **2a–c** into $[8]_A$GNR occurs via a series of Hopf pericyclic reactions, followed by aromatization reactions of the annulated polycyclic aromatic intermediates, as well as homolytic bond fragmentation of the edge functional groups upon heating up to 600 ˚C under an inert atmosphere. We characterize the different steps of both processes using complementary spectroscopic techniques (CP/MAS ^{13}C NMR, Raman, FT-IR, and XPS) and high-resolution transmission electron microscopy (HRTEM). This novel approach to GNRs exploits the combined power of crystal engineering and solid-state reactions by targeting very large organic structures through programmed chemical transformations. It also affords the first reported $[8]_A$GNR, which can now be synthesized on a large scale via two operationally simple and discrete solid-state processes.

Section 2.2. Introduction

While graphene displays a number of remarkable properties, its zero bandgap makes it unsuitable for most semiconductor applications.[1] However, graphene nanoribbons (GNRs), which are narrow strips of graphene with widths below 10 nm, display defined bandgaps in addition to ballistic charge transport thanks to the lateral confinement of charge carriers.[2] Not surprisingly, the designed synthesis of GNRs has quickly gained prominence in this field.

Graphene nanoribbons are classified as either armchair, zigzag, or chiral, depending on the topology of the repeating units within their long edges.[3] Armchair graphene nanoribbons ($_A$GNRs),[4] which are the most interesting type of GNR in terms of semiconductor applications, can be divided into three classes defined by the number of carbon atoms within their width. These classes comprise 3p, 3p + 1, and 3p + 2 carbon atoms, where p is in an integer. Armchair GNRs that fall into the 3p or 3p + 1 classes (e.g. [6] and [7]$_A$GNRs) are predicted to be semiconducting, with a bandgap that increases as ribbon width decreases, while the 3p + 2 class (e.g. [8]$_A$GNR) is predicted to have a significantly narrower bandgap.[5] The smallest member of the 3p + 2 class, [5]$_A$GNR, was first synthesized using on-surface chemistry, and subsequently, in-solution.[6-9] Since then, many graphene nanoribbons of the other classes have been synthesized, although the next smallest member of the 3p + 2 class, [8]$_A$GNR, has yet to be reported via either solution or surface chemistry.

Although graphene nanoribbons are quickly gaining importance, there is only a limited number of methods to generate them. These methods fall either into “top-down” or “bottom-up” strategies.[10] Top-down strategies include cutting a large piece of graphene with an electron beam, unzipping of carbon nanotubes, or sonochemical tearing of graphene sheets.[11-13] A major limitation

of the top-down strategies is that they do not provide homogeneous ultra-narrow ribbon widths (<10 nm) as well as atomically precise edges. By contrast, bottom-up strategies rely on the precision and control afforded by synthetic chemistry to construct ribbons molecule-by-molecule. Until recently, only two marginally differing bottom-up approaches had been described: (1) Surface assisted coupling and cyclodehydrogenation of dihalo polycyclic arenes, or (2) metal-catalyzed solution-phase polymerization of similar precursors, including alkynylarenes, to form polyarylene backbone polymers, followed by their subsequent, typically oxidative, aromatization to GNRs (Figure 2.1).[7,14-18] Recently, the groups of Dichtel and Chalifoux have described key strategic innovations in this area. Their approaches both utilize benzannulation reactions performed after metal-catalyzed polymerization.[7,19]

In the conceptual elaboration of our project, we identified that diphenyl polydiacetylene polymers should produce $[8]_A$GNR if they could be triggered to undergo internal backbone cyclization and cyclodehydrogenation (Figure 2.2). While the broad bandgap semiconducting polydiacetylene polymers (PDAs) have a rich history of synthetic design, spectroscopy, and applications in materials science, with a recent focus on their thermochromic properties,[20-22] synthetic strategies that directly utilize their poly- enyne backbone functionality for further synthetic transformations have only been described recently and are still rare.[23-25] Following our initial studies seeking the formation of nanotubular PDAs through topochemical polymerization of [24]dehydroannulenes,[26,27] our approach to GNRs originated from the intriguing prospect of exploiting the rehybridization energy of *sp* carbons within the alkyne units of aryl-substituted polydiacetylenes. By coercing them to expand their coordination using known thermal reactions involving the aryl substituents, the rehybridization and aromatization energies gained from each cyclizing alkyne unit should be energetically favorable and give polycyclic aromatic structures.

We first exploited this strategy to target the synthesis of $[12]_A$GNRs from naphthyl-substituted PDAs.[28] Here, we have extended this strategy to access $[8]_A$GNRs for the first time. We have also investigated the conversion steps in great detail using complementary spectroscopic techniques (CP/MAS ^{13}C NMR, Raman, FT-IR, and XPS), as well as high-resolution transmission electron microscopy (HRTEM).

As demonstrated below, the diphenyl polydiacetylene motif has proven itself to be an ideal platform to access these graphene nanoribbons. We show that four differently substituted diphenyl PDA polymers with either *para*- or *meta*-substituents (PDAs **1** and **2a**) all produce pristine $[8]_A$GNRs quantitatively via simple heating. This process is readily applicable to bulk synthesis thanks to the inherent ease with which solid-state transformations can be scaled up. This operationally simple, two-step synthesis of $[8]_A$GNRs does not require any external reagents or solvents and should be applicable to a range of device manufacturing techniques. Furthermore, these transformations are not limited by edge substituents and should ultimately provide access to a variety of different edges and widths, including the incorporation of heteroatoms.

Section 2.3. Results and Discussion

To generate $[8]_A$GNRs, we postulated that the phenyl substituents on the PDA backbone should engage their adjacent *trans*-dienyne moieties into a series of Hopf pericyclic reactions to provide annulated polycyclic aromatic intermediates (Figure 2.2).[28,29] Full cyclodehydrogenation of the resulting adjacent polycyclic aromatic rings, which would initially be a random mix of 2-

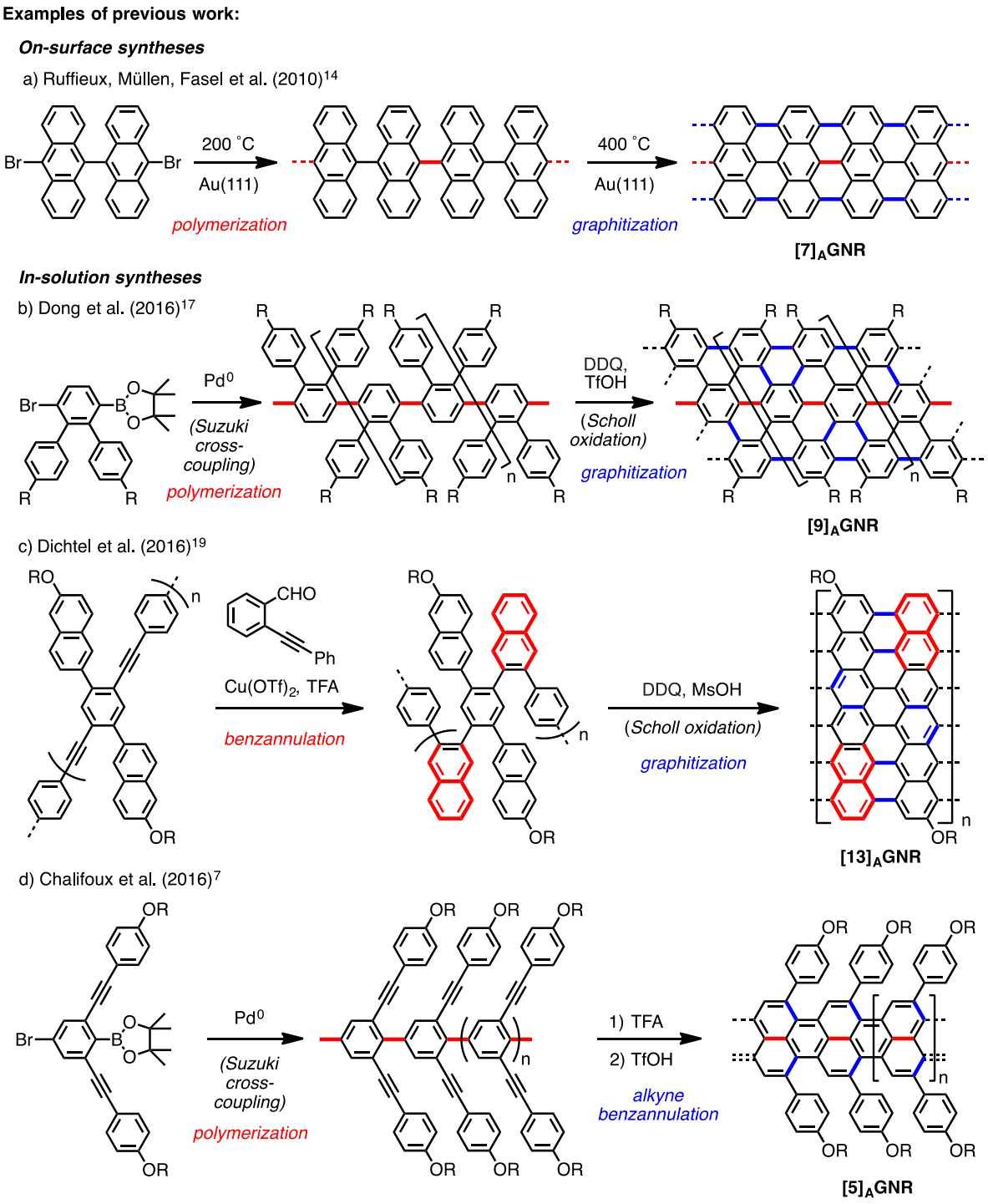

Figure 2.1. Examples of bottom-up syntheses of GNRs. a,b) Most approaches take advantage of the metal-catalyzed polymerization of arene monomers, either on-surface or in-solution, and subsequent oxidation of the ensuing polymers to the corresponding GNRs. c,d) By contrast, Dichtel and Chalifoux have developed ingenious new benzannulation strategies to access GNRs.

phenylnaphthalene, chrysene, 1,2-diphenylethene units, or larger, should ultimately fully aromatize to 8-armchair graphene nanoribbons (Figure 2.2). Hopf cyclizations have been experimentally shown to take place via three distinct mechanisms dependent on the reaction temperature: 1) 6π electrocyclization, 2) rearrangement of the alkyne to a vinylidene carbene followed by aryl C-H insertion, and 3) cyclization via initial radical addition to the alkyne.[30] Hopf has shown that electrocyclization is the predominant mechanism for a gas phase reaction below 550 ˚C.[30] All polymers discussed here undergo backbone cyclizations below 500 ˚C in the solid state, therefore it is likely that the backbone cyclization process occurs via a 6π electrocyclization pathway.

Thus, to model the energetics of the Hopf cyclization stage for PDAs **1** and **2a**, we performed DFT calculations on the *trans*-enediynes **5** and **6** as model systems for the keto and amido functionalized PDAs **1** and **2a** (Figure 2.3). We based our mechanistic study on previous work by Hopf *et al.*,[29] in which the thermal cycloisomerization pathway of *cis*-hexa-1,3-dien-5-yne was explored computationally. As noted above, the authors established that the Hopf cyclization proceeds through the initial 6π-electrocyclization, which is followed by two consecutive [1,2]-H shifts, with the first H-shift being the rate-determining step. Structures were optimized in the gas-phase using B3LYP/6-31G(d),[31] and single-point calculations were performed using M06-2X/6-311+G(d,p)[31d] to obtain free energy values.[32] Transition state geometries of the Hopf cyclization (**5a**, **6a,c**) and first H-shift (**5b**, **6b,d**) steps are shown in Figure 2.3.

The activation free energies are 52.6 and 58.4 kcal mol^{-1} for **5a** and **5b**, respectively. Similar reaction barriers of 52.5 and 57.5 kcal mol^{-1} are found for the *meta*-amide model system undergoing cyclization *para* to its amide sidechain (**6a,b**). The barriers to *ortho* cyclization (**6c,d**)

are higher than for *para* cyclization by 2.9 and 6.8 kcal mol^{-1}, respectively. In all cases, the barriers for the first H-shift are higher than that for the Hopf cyclization, a finding that is in line with the work of Hopf *et al.*[29]

The geometries of each of the transition structures are similar. The π-system of the alkynes is planar in each of the Hopf cyclization transition states, while the flanking aryl groups are out of plane by approximately 30˚. In the H-shift step, the forming naphthyl ring is planar, and the C6-H1 bond stretches to about 1.23-1.25 Å from its normal C-H bond length of 1.09 Å (Figure 2.3d,f,h). In both *ortho* transition states **6c** and **6d**, the close proximity of the amide and methyl groups at the forming C-C bond leads to higher barriers. This results in an intrinsic preference for the *para* pathway over the *ortho* pathway by 6.8 kcal mol^{-1}.

For both models **5** and **6**, the reaction barriers of the rate-determining H-shift are >14 kcal mol^{-1} higher than that of *cis*-hexa-1,3-dien-5-yne. This increase in reaction barrier can be attributed to the benzannulation within the π-systems of **5** and **6** compared to *cis*-hexa-1,3-dien-5-yne, which requires disrupting the aromatic π-system at the transition state.[33] In addition, while these gas-phase energies are useful for understanding the intrinsic barriers to cyclization, we acknowledge the limit of these simple models in accounting for the solid-state behavior and polymer conformational influence on the large scale graphitization process within PDAs **1** and **2a**.

Monomer Synthesis: A key to our methodology was to identify monomers that have: 1) phenyl substituents at both ends of the butadiyne unit, and 2) undergo the proper crystalline-state organization that promotes topochemical polymerization. In our previous investigations of the solid-state packing of [24]-dehydroannulenes, we noted that carbamate groups could be exploited to achieve tight, in-register crystal packing of the internal butadiyne units.[27] While designing

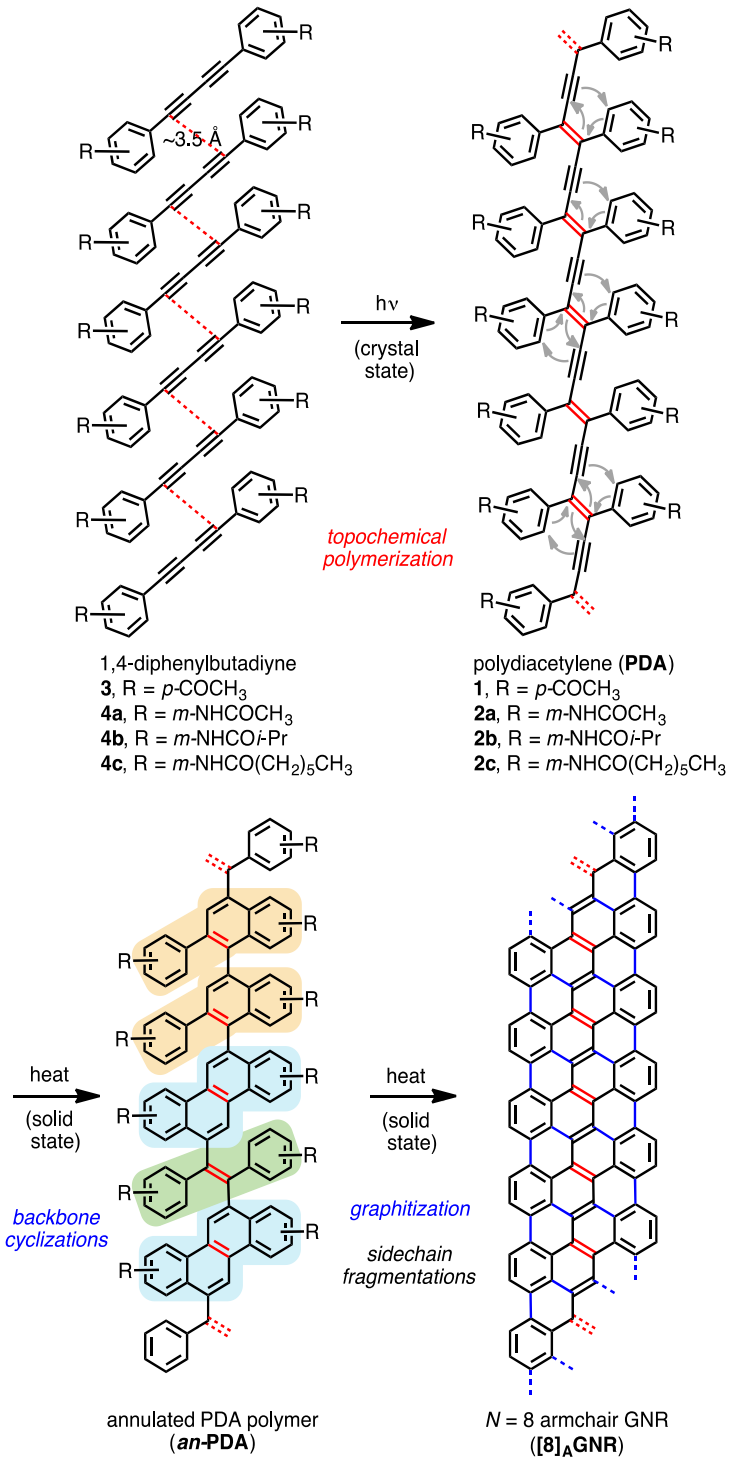

Figure 2.2. Our synthetic approach to $[8]_A$GNR from substituted 1,4-diphenylbutadiynes via the crystalline-state topochemical polymerization of substituted 1,4-diphenylbutadiynes, followed by a separate solid-state thermal aromatization and fragmentation of side-chains. Likely steps in the series of random Hopf cyclizations include the formation of 2-phenylnaphthalene units (orange shaded area), as well as chrysene (cyan) and 1,2-diphenylethene units (green).

monomers to access $[8]_A$GNRs, we anticipated that either amide, carbamate, or urea functionalities would be suitable to promote tight, in-register packing of simple diphenylbutadiynes, as discovered previously.[34-36] Our own synthesis and characterization of both **3**, **4a** and **4c** confirmed their predisposition to undergo topochemical polymerization. We also synthesized a range of diphenylbutadiynes containing a number of different amide substituents in their *meta* position and were delighted to find that many of them, including amide **4b**, provide crystals that undergo topochemical polymerization.

While diynes **3** and **4a–c** differ in their substitution, the position and nature of these substituents is not critical in the PDA to GNR conversion process. For diyne **3**, there is only one possible Hopf cyclization pathway because of the inherent axial symmetry of its *para*-substitution (Figure 2.3). For diynes **4a–c**, the *meta*-amido group is predicted, as discussed above, to have a significant *para*-directing effect in preference to *ortho* in the Hopf cyclizations. Thus, annulated polymers with primarily *edge* amido substituents should be formed initially according to our calculations. However, should a small fraction of Hopf cyclization reactions take place at *ortho* positions, this should not be an issue because all side-chains are ultimately lost in the final conversion of PDAs **1** or **2a–c** to $[8]_A$GNR. Thanks to this design feature, nearly any emergent edge group can be used to promote organization of the internal butadiyne monomer units without worry of its effect on the resulting GNR structure. In addition, GNRs with heteroatom doping (B, N, O, or S) can be targeted through the specific incorporation of heteroaromatic rings as substituents of the butadiyne, which we are currently pursuing.

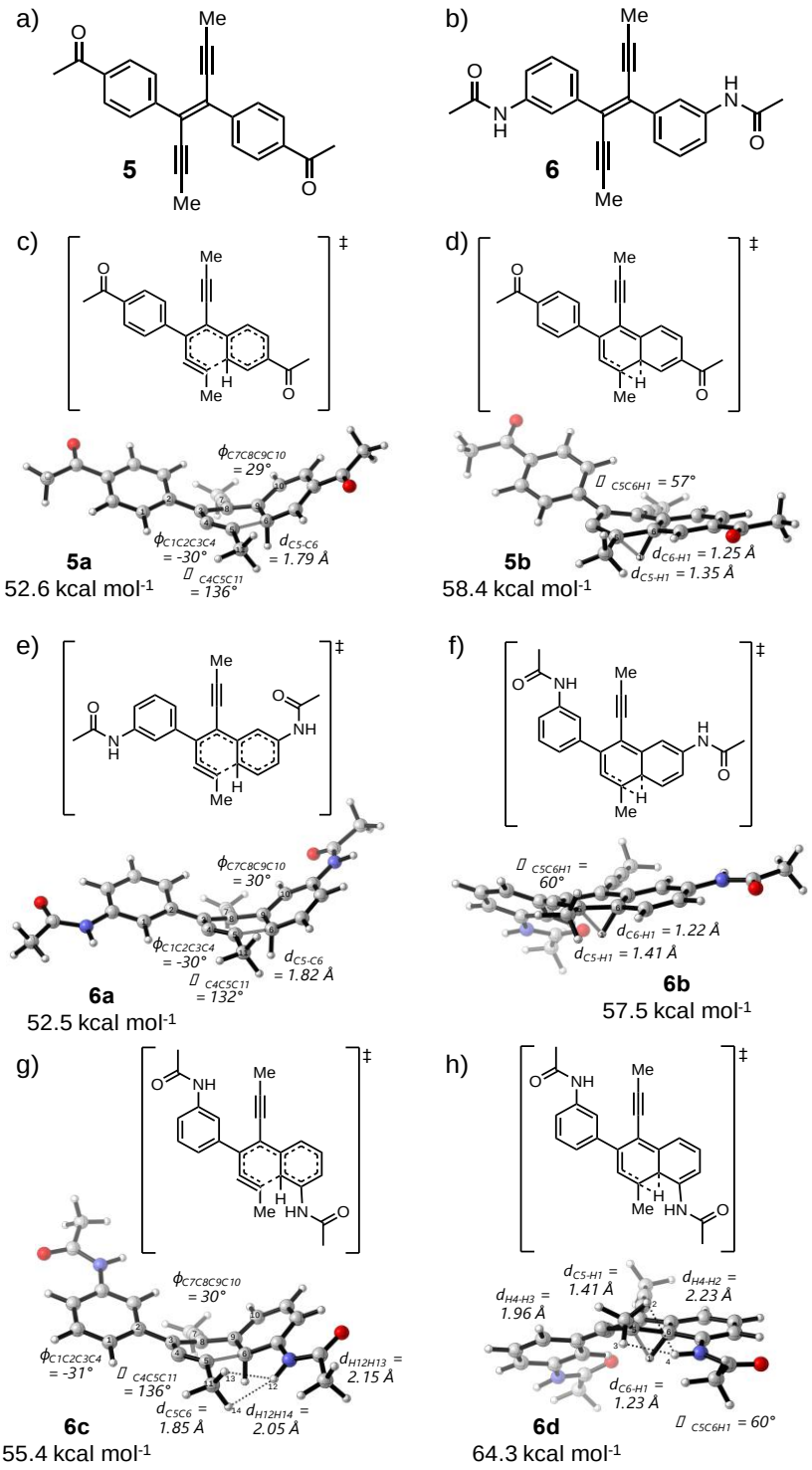

Figure 2.3. Transition state geometries and free activation energies of the 6π-electrocyclization and subsequent H-shift for model systems **5** and **6**. Structures were optimized in the gas phase using B3LYP/6-31G(d) and single-point energies were performed using M06-2X/6-311+G(d,p). Frequency analysis was performed at 350 ˚C.

The synthesis of monomer **3** was carried out in three steps from commercially available 4-bromoacetophenone following the method of Szafert et al.[34] Crystals of monomer **3** turn rapidly blue upon standing, which is indicative of their propensity to undergo topochemical polymerization. Monomeric amides **7a–c** were synthesized in two steps from commercially available 3-ethynylaniline (Scheme 2.1). Amide bond formation between the amino group and either acetyl chloride, isobutyric acid (via activation with *N,N'*-dicyclohexylcarbodiimide (DCC)), or heptanoic anhydride, produced the highly crystalline amides **7a–c**. Oxidative dimerization of these alkynyl aryl amides under the Hay conditions produced the corresponding butadiynes monomers (**4a–c**) in good yields. Recrystallization from an appropriate solvent gave crystals suitable for topochemical polymerization in each case.[33] All syntheses are very efficient (66%, 69%, 71%, and 84% overall yields for monomers **3**, **4a**, **4b** and **4c**, respectively, from the commercially available starting materials) and allowed us to generate tens of grams of the respective diynes **3** and **4a–c** within a few days.

*Topochemical Polymerization of Diynes **3** and **4a–c***: For butadiyne units to undergo topochemical polymerization, their termini need to be within close to van-der-Waals contact (≤3.5 Å), and also offset by a short repeat distance (≤5 Å).[37] As can be seen from the X-ray crystal packing structures (Figure 2.4a–d), diynes **3** and **4a–c** all display ideal close-contacts between the terminal carbons of their butadiyne units, which should favor topochemical polymerization.

Accordingly, all four crystalline diynes (**3** and **4a–c**) readily undergo topochemical polymerization at room temperature upon exposure to ambient light. Polymerization is clearly noted by the deep blue color that appears within the crystals upon standing in an unshielded container. Topochemical polymerization can be accelerated by irradiation of the crystals with a

high powered Hanovia lamp, typically overnight, producing a deep purple/black color within the crystals. Dissolution of the polymerized crystals to dissolve any unreacted monomer provides the pristine polydiacetylenes **1** and **2a–c** as bulk fibrous powders after filtration. The recovered monomer solutions can be concentrated, recrystallized and subjected again to irradiation to provide further amounts of PDA. Repeating this process allowed us to produce gram quantities of PDAs **1** and **2a–c** in only a few days. As an example, the recycling polymerization reaction of the lowest yielding diyne **3** produced 24% of PDA **1** overall after four cycles (first cycle: 7%).

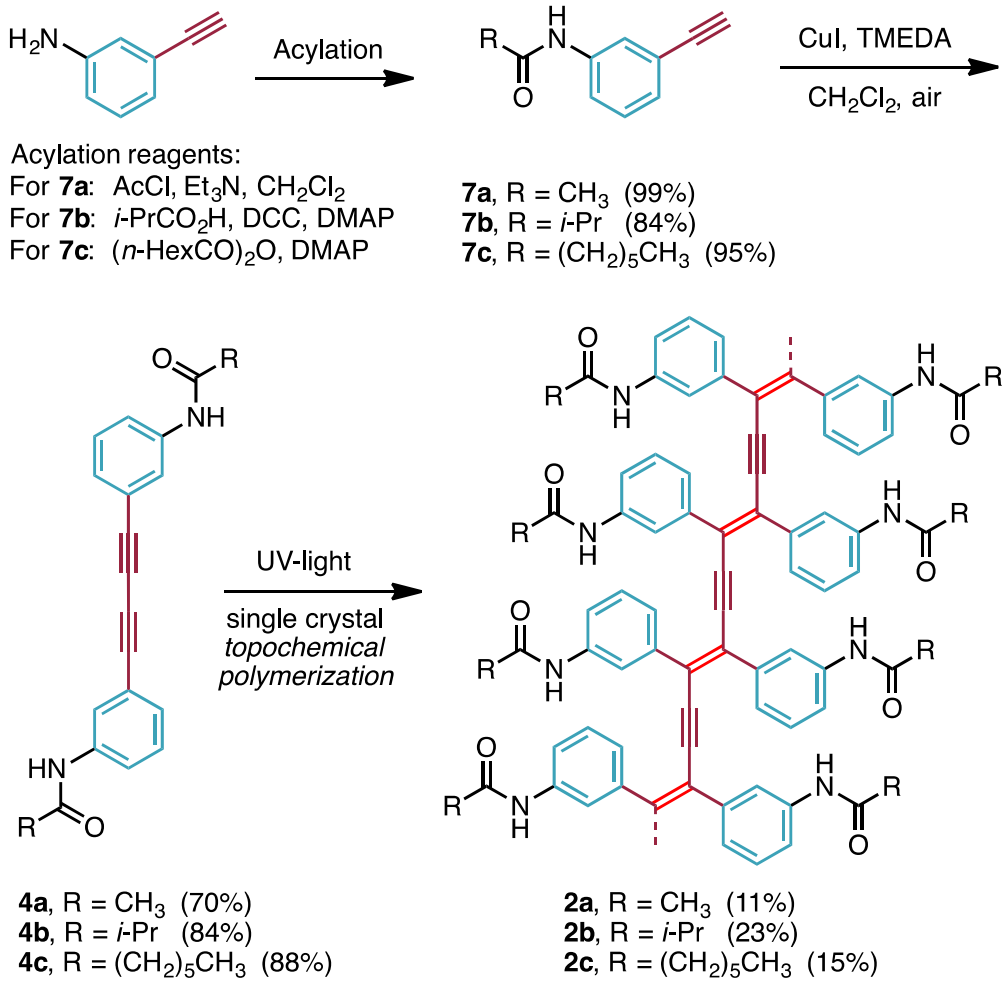

Scheme 2.1. Syntheses of the PDAs **2a–c**.

Characterization of the Polydiacetylenes: Polydiacetylene polymers **1** and **2a–c** were characterized by solid state CP/MAS ^{13}C NMR, XPS, IR, and Raman spectroscopy. Utilizing cross-polarization magic angle spinning (CP/MAS) ^{13}C NMR spectroscopy, the structure and purity of all four polymers could be established unequivocally. While full assignment of each carbon of the aryl or alkyl groups is difficult via solid-state NMR due to the inherently large ^{1}H dipolar couplings in this method, key features can be identified (Figure 2.5).

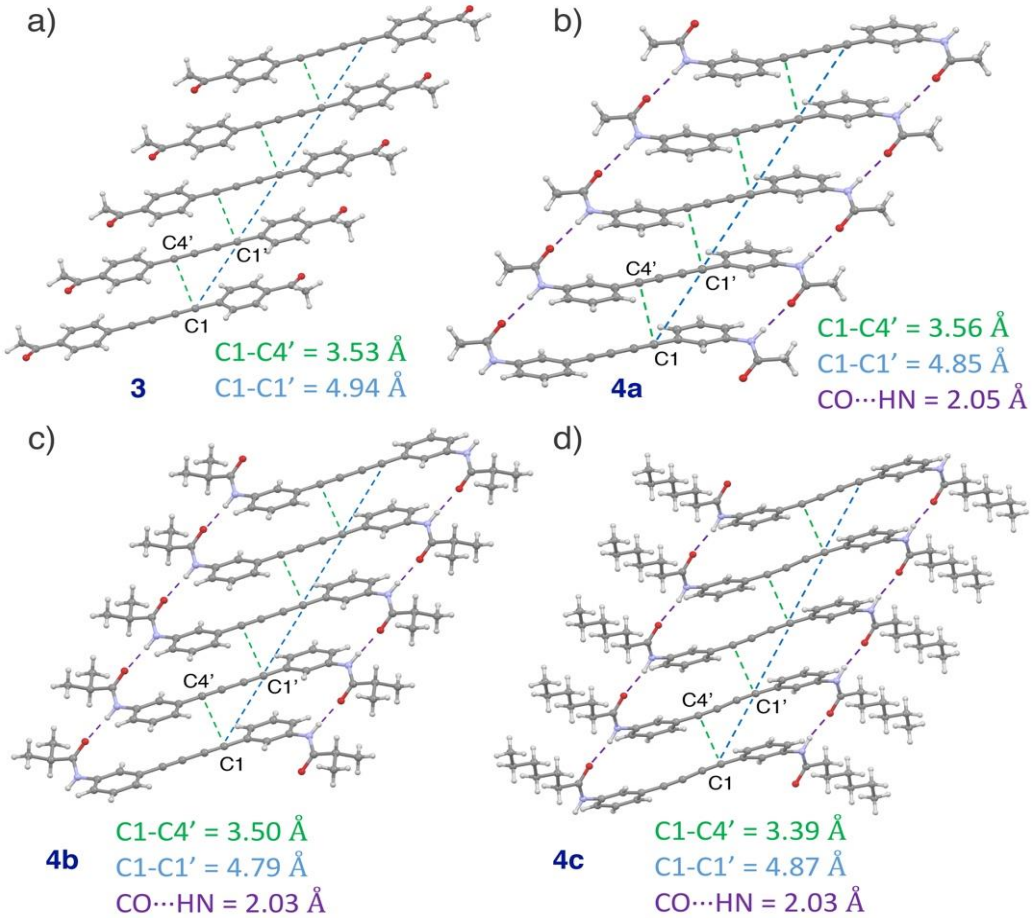

Figure 2.4. Crystal packing structures of diynes **3** and **4a–c** showing close contact distances C1–C4' (≤3.5 Å) and C1–C1' (≤5 Å) crucial for topochemical polymerization.[38]

For example, the alkyne carbons in the PDA backbone can be clearly seen at 102 ppm for **1**, and 101 ppm for **2a**, **2b**, and **2c**. The position of these peaks matches well with other reported PDAs and supports the symmetric structure of the polymer backbone.[39,40] Other discernable features of PDA **1** are the ketone carbonyl carbon, appearing at 198 ppm, and the methyl carbon present at 26 ppm. On the other hand, the carbonyl carbon for the amide containing PDAs **2a–c** appears at 169, 177, and 172 ppm, respectively. The alkyl sidechains in these amides appear as discrete carbon peaks in the alkyl region (10-50 ppm).

Further investigation of the PDA structure was carried out by analysis of the infrared absorption spectra of all four polymers (Figures 2.6, A1-A8). As will be discussed later, detailed assignment of the unreacted PDAs' IR spectra was key to determining subtle structural changes within the polymers upon heating. PDA **1** displays a strong absorption at 1676 cm^{-1} corresponding to the carbonyl stretch of its ketone functional group. Furthermore, strong absorption bands centered around 831 cm^{-1} correspond to the in-phase out-of-plane (oop) C-H wagging motion of two adjacent C–H bonds on the *para*-substituted phenyl rings.[41] A medium strength in-plane ring bending mode can be identified at 1400 cm^{-1}, attributed to the *para*-substituted phenyl ring in PDA **1**. Infrared analysis of PDAs **2a–c** reveals a medium strength N-H stretch centered around 3300 cm^{-1}, as well as strong carbonyl absorptions at 1665, 1652 and 1660 cm^{-1}, respectively, confirming the presence of the amide sidechains (Figure 2.6). The well-defined in-phase oop C–H wagging motion of the *meta*-substituted phenyl ring can be identified by the strong absorptions at 888, 783, and 694 cm^{-1} for PDA **2a**, 873, 774, and 698 cm^{-1} for PDA **2b**, and 870, 783, and 698 cm^{-1} for PDA **2c**, respectively.[41] The stretching vibration at ~ 880 cm^{-1} corresponds to the oop C-H wagging motion of a single, isolated aromatic C–H bond, whereas the stretching vibration at ~ 780 cm^{-1} results from the oop C-H wagging motion of the three adjacent hydrogens between the *meta*

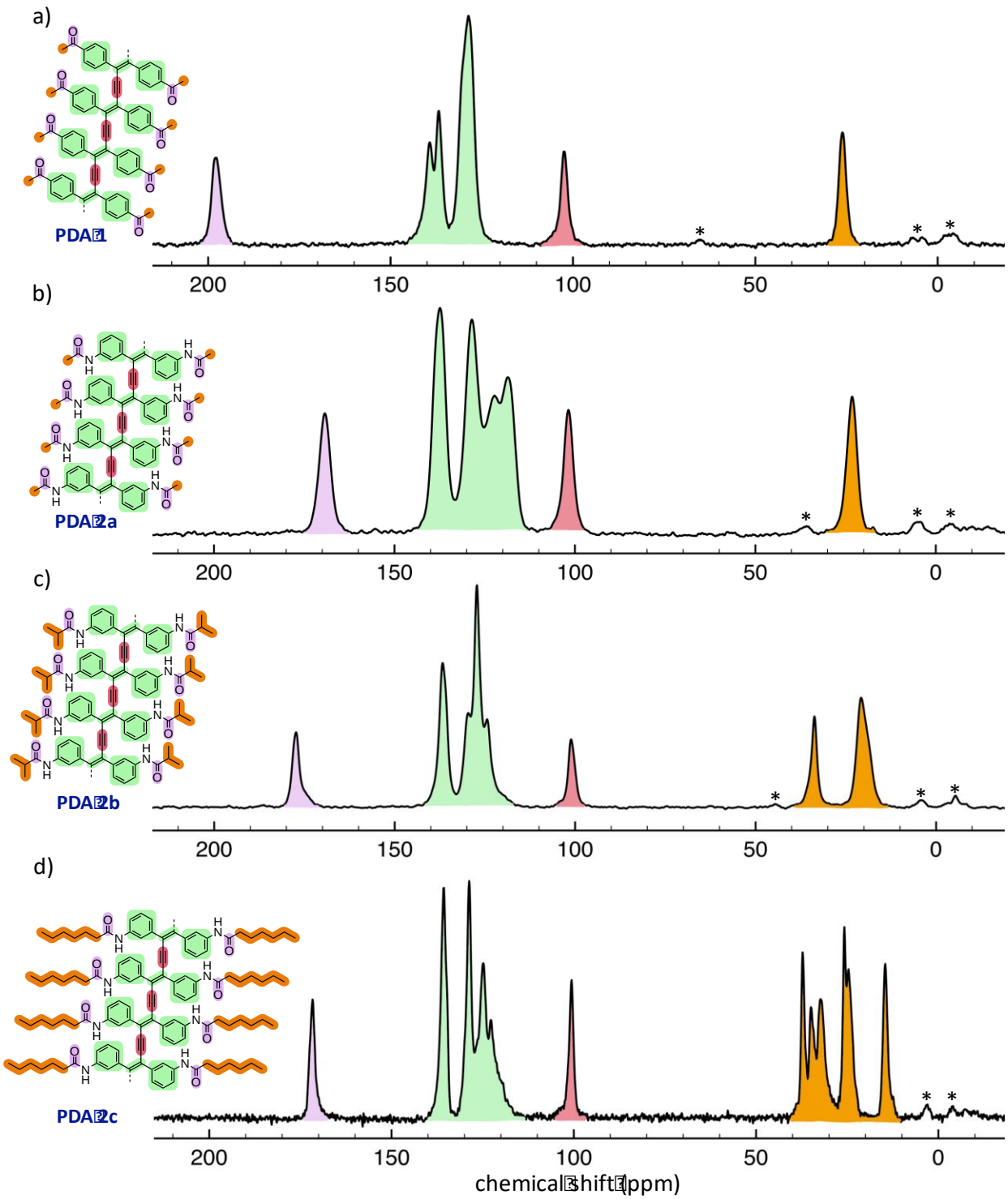

Figure 2.5. Cross polarization magic angle spinning (CP/MAS) solid state ^{13}C NMR spectra of PDAs **1** and **2a–c**. Characteristic regions are color-shaded to guide the eye. Asterisks denote spinning sidebands (10 kHz).

substituents.[41] The strong absorption at ~700 cm^{-1} is a ring bending mode characteristic of asymmetrically substituted (*meta*) phenyl rings.[41] In combination, these stretches provide strong support for the *meta*-substituted nature of the aryl rings in PDAs **2a–2c**.

Due to the symmetric nature of the PDA backbone, Raman spectroscopy is another technique of choice for its characterization. Excitation of the polymers in the form of pressed pellets using a 514 nm Argon laser produces intense peaks at 1466 cm^{-1} and 2113 cm^{-1} for PDA **1**, 1471 cm^{-1} and 2120 cm^{-1} for PDA **2a,** 1483 cm^{-1} and 2133 cm^{-1} for PDA **2b,** and 1480 cm^{-1} and 2110 cm^{-1} for PDA **2c** (Figure 2.7). These peaks correspond to symmetric stretching vibrations for the alkene (1466, 1471, 1483, and 1480 cm^{-1}) and alkyne (2113, 2120, 2133 and 2110 cm^{-1}) moieties of the polydiacetylene backbone. Importantly, lack of any absorption at 2200 cm^{-1}, corresponding to monomeric butadiynes **3** and **4a–c**, confirms the absence of any monomer contamination in the polymer samples.

X-ray photoelectron spectroscopy analysis of PDAs **1** and **2a–c** shows distinct C1s spectra with two well defined peaks (Figures A9-A12).[33] The single peaks centered at 284.5, 284.7, 284.6 and 284.5 eV in the spectra of PDAs **1**, **2a**, **2b** and **2c**, respectively, reflect the combination of sp, sp^2, and sp^3 hybridized carbons engaged in the carbon-carbon bonding throughout the structure. The peaks centered at 287.2, 287.9, 287.7, and 287.5, respectively, correspond to the sp^2 hybridized carbonyl carbon of the PDA sidechains.

Thermal Conversion of the Polydiacetylenes to Graphene Nanoribbons: With large quantities of the PDA polymers easily available, their conversion to $[8]_A$GNR was carried out by heating of the bulk polymers in a programmable tube furnace under argon flow. PDA polymers **1** and **2a–c** were placed in an aluminum oxide boat within a quartz tube and heated at various temperatures for 1

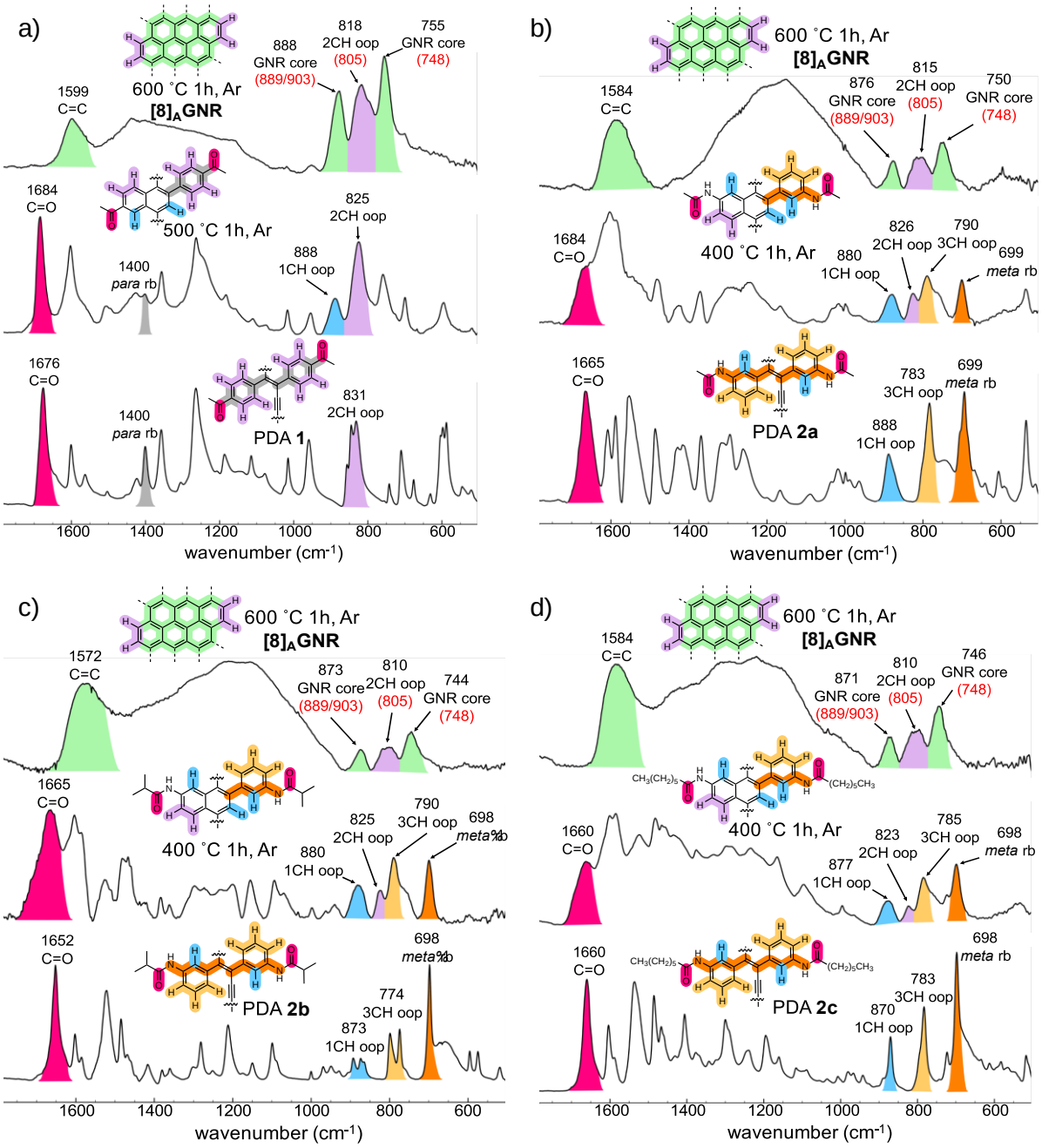

Figure 2.6. Detailed infrared analysis of the conversion of PDAs **1** and **2a–2c** to [8]AGNR via annulated intermediate polymers. Characteristic stretches have been denoted and colored to guide the eye. Experimentally measured vibrations have been marked in black with corresponding calculated (DFT) vibrational modes[33] denoted in red where applicable.

hour. The resulting materials were characterized by CP/MAS ^{13}C NMR, Raman, XPS and FT-IR to follow the PDA to GNR conversion process (Figures 2.5–2.8, A1-A16).[33] transformation of the PDAs to $[8]_A$GNR relies on three thermally promoted reactions, namely (1) backbone Hopf cyclization, (2) exhaustive cyclodehydrogenation of the nanoribbon core, and (3) removal of the edge groups (ketone or amide). From the gathered spectroscopic data, we can conclude that for all PDAs presented here, Hopf cyclizations along the poly-enyne backbone are completed before the other two steps at the range of temperature between 400 and 500 ˚C. Accordingly, we present below spectroscopic evidence for all three steps of the PDA to GNR pathway.

Initial Step, Backbone Cyclization (Hopf reaction): As described above, the CP/MAS ^{13}C NMR spectra provide unambiguous assignments for the internal alkyne carbons of each PDA (101-102 ppm). Heating of the PDA polymers to either 500 ˚C (**1**) or 400 ˚C (**2a–c**) for 1h results in complete loss of the backbone alkyne carbons in the CP/MAS ^{13}C NMR spectra (Figure 2.8). Concomitant with this change is a transformation of the aryl region (100-150 ppm) from the well-defined spectra of the unheated PDAs to a broader cluster with two main peaks at 127 and 135 ppm for **1**, and 127 and 137 ppm for **2a–c**, respectively. Interestingly, the spectra of the heated polymers are remarkably similar, which highlight a common cyclization pathway among all of the polymers.

Raman analysis of the heated polymers also confirms the absence of any remaining backbone alkynes (Figures A13-A16).[33] Most importantly, analysis of the IR spectra obtained for these heated polymers details discrete changes in their out-of-plane (oop) bending modes (Figure 2.6). The oop bending modes are the key spectroscopic signatures of the substitution patterns within the aryl rings in the starting material, intermediate structures, and final $[8]_A$GNR product.[7,17] The IR data for PDA **1** heated to 500 ˚C shows the appearance of a new C–H oop bending

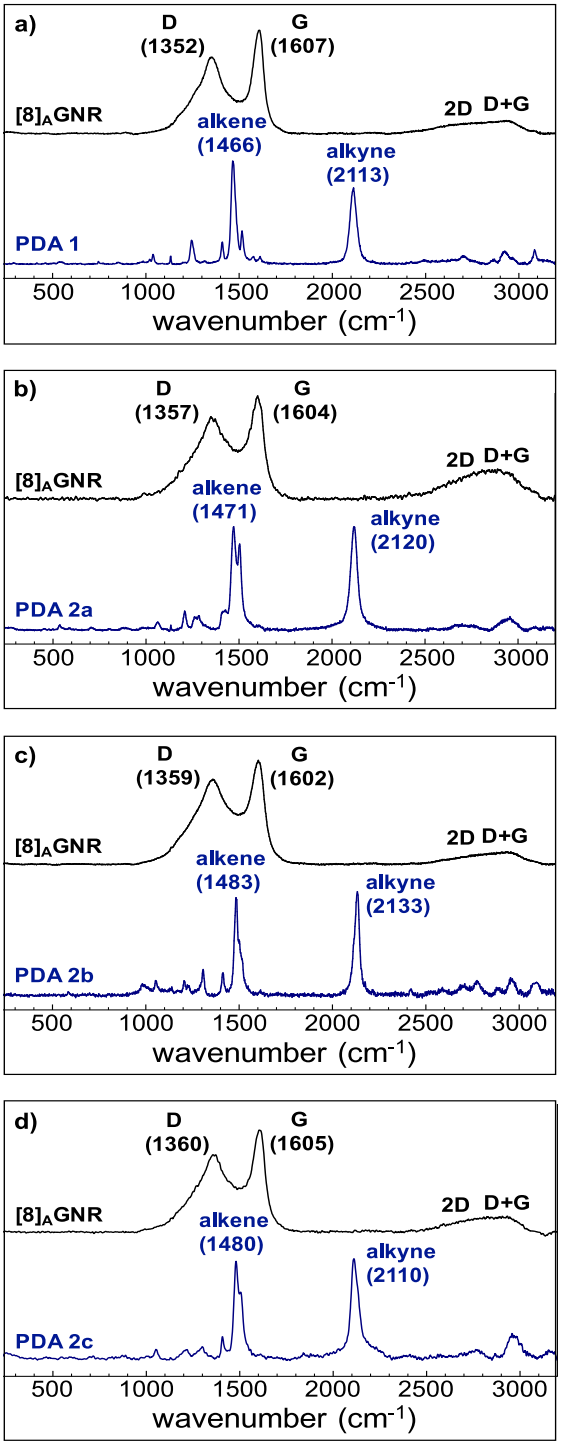

Figure 2.7. Raman spectra of PDAs **1** and **2a-2c** and the corresponding $[8]_A$GNR samples produced after thermal conversion. Specific vibrations corresponding to the enyne backbone of the PDA polymers, as well as the D and G peaks characteristic of GNRs, are labeled.

absorption at 888 cm^{-1}, characteristic of a lone aryl C–H with no adjacent hydrogens, which can only appear if an annulated ring such as naphthalene or chrysene is formed, which is also supported by our frequency calculations (Figures 2.2 and 2.6a).[33,41] Furthermore, the strong phenyl ring bending mode characteristic of *para* substituted rings at 1400 cm^{-1} has been attenuated, lending further support to an annulated intermediate structure. Very similar changes can be noted in the IR spectra of samples of **2a–c** heated to 400 ˚C (Figures 2.6b-d). In all three IR spectra, a new oop C–H bend characteristic of two adjacent aryl hydrogens appears at 826, 825, and 813 cm^{-1} for PDAs **2a**, **2b**, and **2c**, respectively.[41] Importantly, this specific oop C–H bend should only occur if polymers **2a–c** underwent cyclization *para* to their amido substituents.

The combined CP/MAS ^{13}C NMR, IR, and Raman data provide strong evidence that the PDA polymers have undergone successful cyclization of the backbone alkyne units to form annulated polycyclic aromatic structures (Figure 2.2). While the spectroscopic data does not directly point to a specific mechanism of backbone cyclization, it is highly likely that formal Hopf (dienyne) cyclizations are occurring as designed.

Steps 2 and 3, Exhaustive Cyclodehydrogenation and Sidechain Removal: The remaining two thermal steps, cyclodehydrogenation of the nanoribbon core and sidechain removal, both occur upon heating of PDAs **1** and **2a–c** up to 600 ˚C for 1h. Evidence for thermal cyclodehydrogenation is again found through analysis of the CP/MAS ^{13}C NMR, IR and Raman data (Figures 2.6–2.8). The CP/MAS ^{13}C NMR spectra obtained after heating PDAs **1** and **2a–c** to 600 ˚C for 1h show a clean convergence to the uniform spectra of $[8]_A$GNR (Figure 2.8).[42] In all spectra, resonances corresponding to the carbonyl and alkyl carbons of the PDA sidechains are absent, indicating complete removal. Furthermore, the aryl region has simplified dramatically and all spectra of $[8]_A$GNR exhibit a principal peak centered at 126 ppm, along with a prominent shoulder at 137 ppm.

The position of the principal peak is in good agreement with calculated and experimental data for graphene-like systems.[43]

In this context, reagent-less, thermal cyclodehydrogenation reactions to produce annulated polycyclic aromatic hydrocarbons have been shown to occur in polycyclic aromatic systems upon simple heating. For example, Clar synthesized hexabenzocoronene via a high-yielding thermal cyclodehydrogenation of a penultimate intermediate at 482 ˚C.[44] Coronene was also shown to undergo dimerization, ultimately leading to polymerization, through cyclodehydrogenation at its edges upon heating to 530 ˚C.[45]

The spectra of $[8]_A$GNR produced from the different PDAs vary slightly with respect to their peak width at half height (Figure 2.8), which we attribute to the differences in morphology of the samples as further discussed in the IR analysis below. In CP/MAS experiments, the intensities of carbon peaks are directly related to the amount of cross-polarization that they experience. In all our CP/MAS experiments, we used a long cross-polarization contact time (5 ms) to eliminate any distance dependence and its effect on the height or ratio between individual peaks. The relative ratio of the shoulder at 137 ppm to the main peak at 126 ppm in all three spectra is ~1:3 (Table1). Due to the highly symmetric nature of the graphene nanoribbons, there should be only four carbons with distinct chemical shifts in $[8]_A$GNR; which include the edge C–H carbons and three quaternary interior carbons (Figures A17 and A18).[33] Deconvolution of the experimental spectra of $[8]_A$GNR obtained from PDAs **1** and **2a** using four equal intensity curves provides the values shown in Table 2.1. The chemical shifts of the individual carbons of $[8]_A$GNR produced from PDA **1** are centered at 137.6, 129.8, 126.4, and 121.8, while the $[8]_A$GNR produced from PDA **2a** has chemical shifts of 136.3, 128.9, 124.9, and 119.5 respectively. The shoulder peak (137

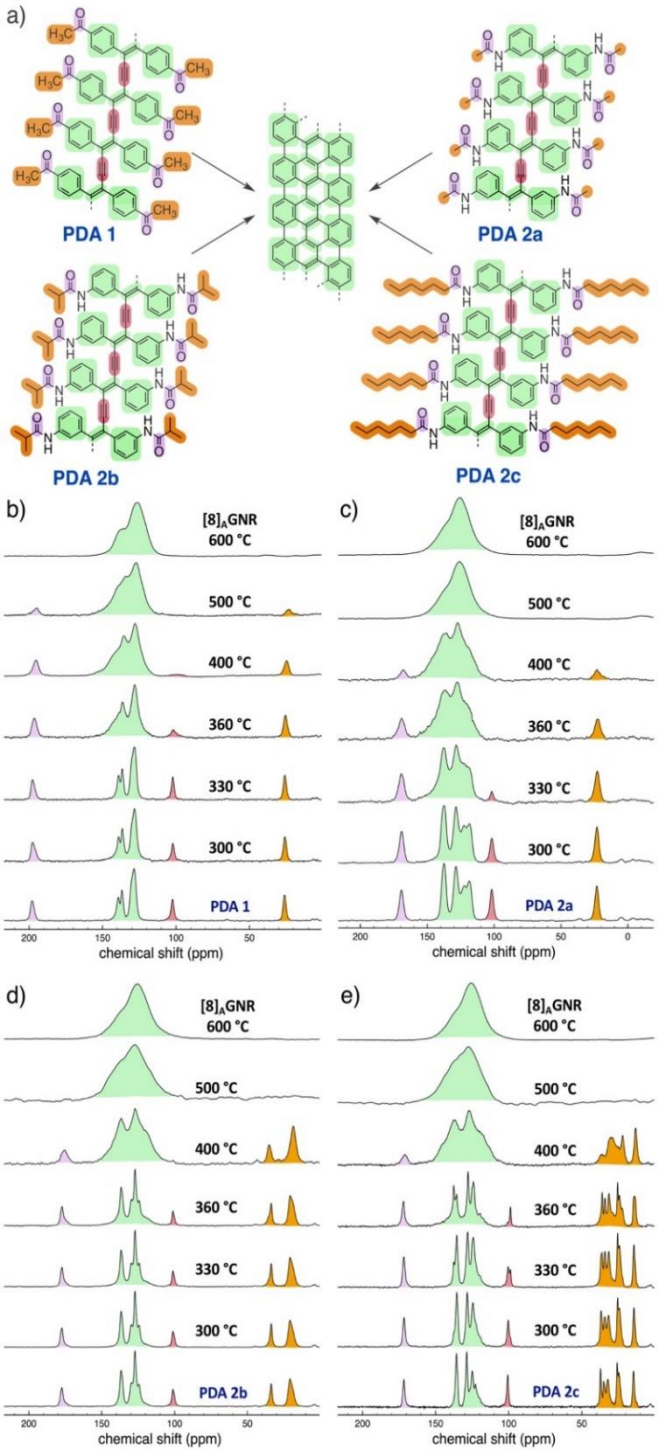

Figure 2.8. CP/MAS ^{13}C NMR spectra for the conversion of PDAs **1**, **2a–2c** to $[8]_AGNR$. a) Overview of the thermal conversions of PDAs **1**, **2a–2c** to $[8]_AGNR$. b–e) Spectra corresponding to the different samples obtained after heating at the temperatures shown, each for one hour. All spectra are normalized for comparison, and spectral acquisition data are included in the SI.

ppm) can be attributed to the quaternary carbon of the bay region (second row), similar to other well-known polycyclic aromatic hydrocarbons,[46] which is also evidenced by the calculated model for a large section of $[8]_A$GNR (B3LYP//6-31G* level of theory) (Table 2.1 and Figure A19).[33] The NMR shielding tensors were computed with the Gauge-Independent Atomic Orbital (GIAO) method. Overall, the calculated chemical shifts are in rather good agreement with the deconvoluted chemical shifts for the four types of carbons (Table 2.1 and Figure A19).[33]

As was detailed earlier, analysis of the oop CH wag region (1000-700 cm^{-1}) for heated samples of the PDAs confirms the successful cyclization of alkynes on the backbone of PDAs **1** and **2a–c**. Upon heating of the polymers to 600 ˚C, we obtain IR spectra with remarkably similar features which we assign to $[8]_A$GNR (Figure 2.6). The CH oop region is transformed further upon heating to 600 ˚C, producing three distinct peaks. The intensity and shape of the peaks are similar in all samples of $[8]_A$GNR and occur at similar wavenumbers. Critically, all samples of $[8]_A$GNR display an oop CH wagging mode for two adjacent (*ortho*) hydrogens at 818, 815, 810, and 810 cm^{-1} for $[8]_A$GNR produced from PDAs **1** and **2a-c**, respectively. This stretch is consistent with the presence of two adjacent hydrogens at the edges of $[8]_A$GNR. The two other distinguishable peaks in the oop region are centered around 875 cm^{-1} and 750 cm^{-1} for all samples. Frequency analysis calculation performed on a model system slightly shorter than that shown in Table 2 gives a fingerprint region similar to the experimental spectrum (Figure A22).[33] Analysis of the calculated vibrational modes provides insight into the molecular origin of the three fingerprint stretches observed in all experimental spectra. The experimental absorption at ~750 cm^{-1} can be attributed to an asymmetric ring stretching mode for the C=C bonds within the $[8]_A$GNR core, calculated to occur at 748 cm^{-1}. Furthermore, the oop CH wagging mode for the edge protons is calculated to occur at 805 cm^{-1} and is observed experimentally around 815 cm^{-1}. Finally, the strong absorption

at ~ 875 cm^{-1} is calculated as two modes at 905 and 890 cm^{-1}, which are in-plane rocking modes for the edge CH bonds. Another common feature in all spectra of $[8]_A$GNR is the presence of a broad range of absorptions (hump) between 1000 and 1400 cm^{-1}. Our calculations predict this region to contain a number of frequencies arising from the in- or out-of-plane modes for edge C-H bonds, as well as in-plane bending modes for C–C and C=C stretches within the fused rings of the GNR core. Broad absorbance in this region has been ascribed to large networks of delocalized, conjugated π bonds.[47]

Further confirmation of successful cyclodehydrogenation and side-chain removal is evidenced by the Raman spectra of the respective samples of $[8]_A$GNR (Figure 2.7). Raman spectra of all PDA polymers after heating to 600 ˚C for 1h clearly exhibit D and G peaks, which are spectroscopic signatures for GNRs (Figures 2.7 and A13-A16).[33,48] The $[8]_A$GNRs produced from either **1** or **2a**, **2b** or **2c** display a large D peak at 1352, 1357, 1359, and 1360 cm^{-1} and a base G peak at 1607, 1604, 1602 and 1605 cm^{-1}, respectively. In all four cases, the G peak is slightly upshifted and broadened compared to the G peak for pristine few-layer graphene, which occurs at 1581 cm^{-1}.[49] This shift is consistent with a narrowing of a graphene sheet into "nanographene".[50] Additionally, the overtone 2D and D+G peaks can clearly be identified, but display significant broadening. The broadening of these peaks can be attributed to strong π-π* interactions between multiple layers, a consequence of the highly stacked nature of our GNRs in bulk samples (see below for TEM section).[51] While this broadening is most likely a consequence of the tight graphitic stacking of our GNRs in the bulk, it is also possible that defects within the formed ribbons are contributing to this effect. One consequence of the crystal-phase topochemical polymerization of diynes **3** and **4a–c** is that the resulting PDA polymers **1** and **2a–c** are strongly organized in columnar stacks. These stacks are likely to have a templating effect during the graphitization step

affording the GNRs. Nevertheless, the appearance of the D and G peaks and their overtones provides spectroscopic evidence that exhaustive cyclodehydrogenation has taken place along the PDA nanoribbons to give the $[8]_A$GNRs.

Table 2.1. Comparison of the fitted experimental spectral curves with calculated ^{13}C NMR chemical shifts (B3LYP/6-31G(d)) for the model $[8]_A$GNR molecule shown in a). b) Deconvolution analysis of the ^{13}C CP/MAS NMR spectrum $[8]_A$GNR obtained from PDA **1** using a set of four curves with equal heights.[52]

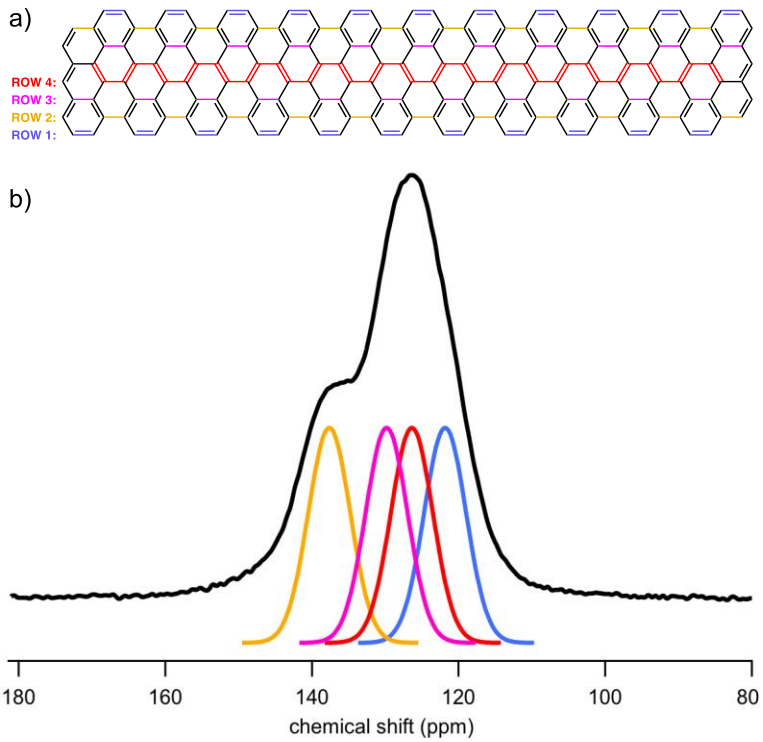

Carbon row	1	2	3	4
Deconvoluted δ (ppm) (PDA **1**)	136.3	128.9	124.9	119.5
Deconvoluted δ (ppm) (PDA **2a**)	137.6	129.8	126.4	121.8
Calculated δ (B3LYP) Structure a)	130.0	125.2	124.4	122.5

All four samples of $[8]_A$GNR produced from PDAs **1** and **2a–c** to $[8]_A$GNR were also examined by XPS to ensure the complete removal of side-chains as evidenced by the loss of a C=O peak (Figures A9-A12).[33] All C1s spectra of $[8]_A$GNRs display a single peak centered at 284.6 eV, characteristic of sp^2 hybridized carbons engaged in C-C and C-H bonding. All spectra also show significant narrowing of their main C1s peak, due to the absence of any sp or sp^3 hybridized carbons, further confirming that backbone cyclization and side-chain removal is complete.

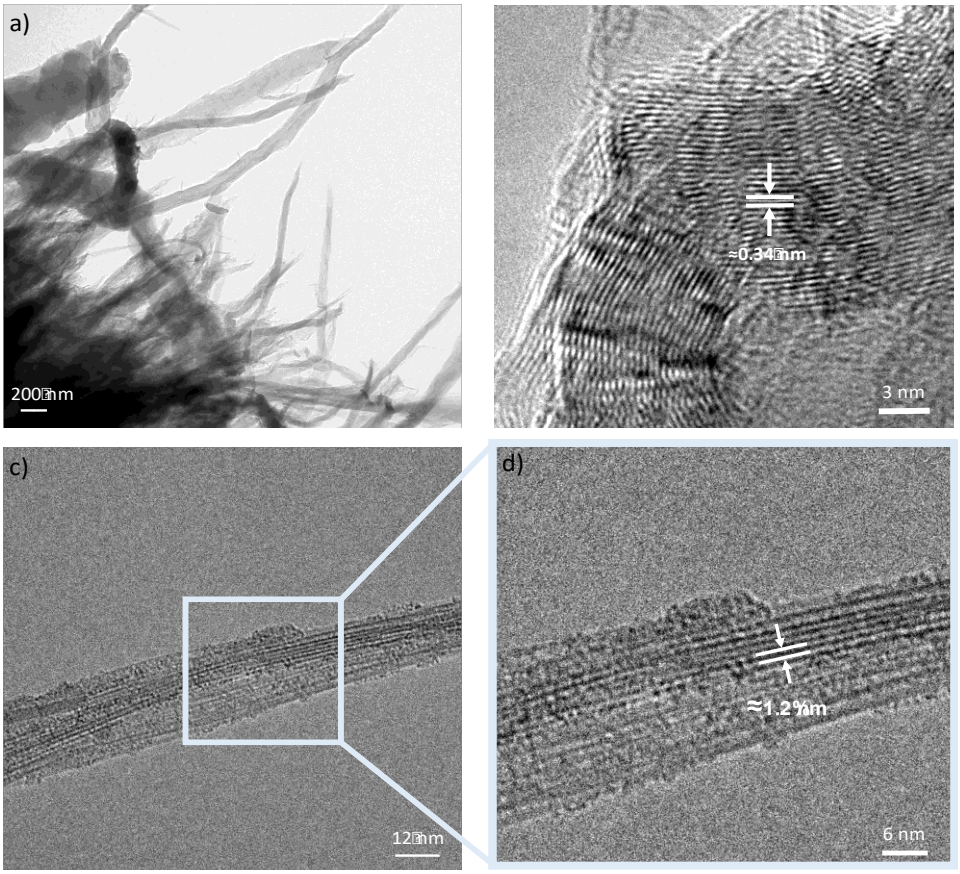

Figure 2.9. TEM and HRTEM analysis of PDA polymers and the $[8]_A$GNRs produced from their solid-state graphitization. a) TEM analysis of PDA polymer **1** showing the thin, layered and fibrous nature of the polymer. b) HRTEM analysis of the resulting $[8]_A$GNR produced from heating of PDA **1**. The tight (0.34 nm) co-facial π-π (002) graphitic stacking of the GNRs can clearly be seen. c,d) HRTEM analysis of $[8]_A$GNR produced from PDA **2b**. Individual GNRs of width ≈ 1.2 nm can clearly be seen.

Transmission Electron Microscopy: The morphology of the PDA polymers and the ensuing GNRs was investigated by high-resolution transmission electron microscopy (HRTEM, Figure 2.9). All four PDA polymers have a thin fibrous nature with uniform thickness, and show large regions of agglomeration (Figure 2.9a). After thermal aromatization to $[8]_A$GNR, all samples display tight (0.34 nm) co-facial graphitic stacking and can clearly be seen by HRTEM (Figure 2.9b). Additionally, the long length and flexibility of the stacked GNRs can be distinctly visualized. The stacked nature of our GNR samples appears reinforced by the initial preorganization of the PDA polymers as they are formed within crystals, which leads to in-register columnar stacks that remain strongly associated after aromatization. This supports the Raman data gathered from the samples and helps to explain the broadening of the 2D and D+G bands as a consequence of tight nanoribbon stacking.[52] Importantly, individual ribbons can be identified and measured (Figures 2.9c,d). Figure 2.9c clearly shows a number of individual $[8]_A$GNRs, produced from thermal aromatization of PDA **2b**, aligned horizontally with respect to each other. Their uniform width (1.2 nm) is confirmed through a plot profile of pixel intensities across a number of GNR bundles (see Figure A23).[33] This value is in close agreement with their calculated width of 1.3 nm.[33]

Section 2.4. Conclusion

We have described parallel synthetic routes to $[8]_A$GNRs from four distinct, differently substituted 1,4-diphenyl polydiacetylenes. PDA polymers **1** and **2a–2c** can be readily synthesized in bulk quantities via a solid-state topochemical polymerization. Heating of all four PDAs between 500 and 600 ˚C under Ar for 1h promotes their conversion to $[8]_A$GNR in the solid state, without the need for additional reagents. This process occurs via a cascade of thermally promoted reactions

including (1) backbone cyclization, (2) exhaustive cyclodehydrogenation, and finally (3) sidechain thermolysis, as highlighted by the spectroscopic data. This solid-state reaction cascade is remarkably efficient, as evidenced by the yields in the PDA **1** and **2a–2c** to GNR conversions being quantitative in all cases. Accordingly, the quality of this complex transformation can be viewed as a highlight of designed solid-state reaction pathways. Our approach should be expandable to GNRs of different widths and structure (including heteroatoms) via judicious design of the starting diarylbutadiyne monomers. Further studies on the synthetic and mechanistic aspects of these conversions are currently underway and will be communicated in due time.

Section 2.5. Experimental Details

General Procedures: Unless stated otherwise, reactions were performed under an argon atmosphere in flame-dried glassware. Tetrahydrofuran (THF), methylene chloride (CH_2Cl_2), diethyl ether (Et_2O), toluene (C_7H_8), and acetonitrile (CH_3CN) were passed through activated alumina columns prior to use. Chemical reagents were obtained from commercial sources and used without further purification. Reaction temperatures were controlled using an IKA magnetic stirring plate with a temperature modulator and silicone oil bath. Procedures were performed at 25 ˚C unless otherwise indicated. Column chromatography was performed on Silicycle (Siliflash P60) silica gel 60 (240-400 mesh). Thin layer chromatography utilized pre-coated plates from E. Merck (silica gel 60 PF254, 0.25 mm).

4’-Ethynylacetophenone and compounds **3**, **7c**, and **4c** were prepared according to their previously reported syntheses.[34,35] All spectra of known compounds matched their reported values

and are tabulated below. For new compounds that were synthesized for this study (namely compounds **7a**, **4a**, **7b**, and **4b**), their ^{1}H and ^{13}C NMR spectra are included in Section 2(viii) (Figures **A28–A35**).

4'-Ethynylacetophenone

4'-Bromoacetophenone (10.5 g, 52.8 mmol, 1 eq) was added to a round bottom flask with a magnetic stirring bar under argon. THF (160 mL) was added, followed by bis(triphenylphosphine) palladium dichloride (1.85 g, 2.6 mmol, 0.05 eq) and copper(I) iodide (1.01 g, 5.28 mmol, 0.1 eq) in one portion. This mixture was sparged with argon for 30 min and then trimethylsilylacetylene (10.4 g, 105 mmol, 2 eq) was added and the mixture heated to reflux until judged complete by ^{1}H NMR of the crude (typically overnight). The mixture was cooled to 25 ˚C and KF (6.13 g, 105 mmol, 2 eq) was added along with MeOH (110 mL), and the mixture allowed to stir open in the air for 30 min. Once the TMS deprotection was complete as judged by NMR, the mixture was filtered over celite and concentrated. The crude residue was purified by filtration over SiO_2 eluting with CH_2Cl_2. Evaporation on the Rotavap afforded 6.2 g (81%) of 4'-ethynylacetophenone as a deep yellow oil. ^{1}H NMR (400 MHz, $CDCl_3$): 2.60 (s, 3H), 3.24 (s, 1H), 7.57 (d, J = 8.6 Hz, 2H), 7.90 (d, J = 8.6, 2H); ^{13}C NMR (100 MHz, $CDCl_3$): 26.65, 80.35, 82.76, 126.93, 128.20, 132.31, 136.80, 197.27. HRMS (DART) Calculated for $C_{10}H_8O$ [$M^{\bullet+}$]: 144.05751; found 144.05872.

1,1'-(Buta-1,3-diyne-1,4-diylbis(4,1-phenylene))bis(ethan-1-one) (3)

4'-Ethynylacetophenone (6.2 g, 43 mmol, 1 eq) was added to a round bottom flask with a magnetic stirring bar and dissolved in CH_2Cl_2 (200 mL, 0.2M). To this mixture was added copper(I) iodide (820 mg, 4.3 mmol, 0.1 eq) and TMEDA (500 mg, 4.3 mmol, 1 eq) in one portion. Air was bubbled into the mixture and allowed to react at 25 ˚C until complete as indicated by TLC (SiO_2, CH_2Cl_2). Upon completion, the mixture was diluted with water and partitioned via a separatory funnel. The aqueous layer was extracted with fresh CH_2Cl_2 three times, organics pooled, washed with 0.5M HCl, brine, dried over $MgSO_4$, and filtered and concentrated *in vacuo* to give the crude product as a crystalline solid. The crude product was immediately recrystallized from boiling ethanol via hot filtration and the receiving flask protected from ambient light to limit polymerization of the forming crystals. A total of 5.1 g (83%) of **3** was obtained as clear crystals which rapidly turn blue upon standing in ambient light. ^{1}H NMR (500 MHz, $CDCl_3$): 2.61 (s, 3H), 7.62 (d, J = 8.6 Hz, 2H), 7.94 (d, J = 8.6, 2H); ^{13}C NMR (125 MHz, $CDCl_3$): 26.67, 76.56, 81.98, 126.26, 128.31, 132.71, 137.12, 197.06. HRMS (DART) Calculated for $C_{20}H_{14}O_2$ [$M^{\bullet+}$]: 286.09938; found 286.098676.

N-(3-Ethynylphenyl)acetamide (7a)

Acetyl chloride (4.15 g, 78.5 mmol, 1.2 eq) dissolved in CH_2Cl_2 (20 mL) was added to a solution of 3-ethynylaniline (5.20 g, 44.4 mmol, 1.0 eq) and triethylamine (5.83 g, 57.7 mmol, 1.3 eq) in CH_2Cl_2 (150 mL) at 0^{o}C. The mixture was allowed to warm to 25 ˚C and stirred until complete by TLC (SiO_2, CH_2Cl_2/hexanes 1:1). The reaction mixture was washed twice with an aqueous $NaHCO_3$ solution before passing the organic layer over a SiO_2 plug. A total of 7.23 g (99%) of **7a**

was recovered as a yellow solid. ^{1}H NMR (400 MHz, $CDCl_3$): 2.17 (s, 3H), 3.05 (s, 1H), 7.2-7.3 (m, 2H), 7.43 (br s, 1H), 7.53 (d, *J* = 8.0 Hz, 1H), 7.61 (s, 1H); ^{13}C NMR (100 MHz, $CDCl_3$): 24.71, 77.59, 83.28, 120.56, 122.94, 123.37, 128.15, 129.16, 138.06, 168.60; HRMS (DART) Calculated for $C_{10}H_9NO$ [$M^{\bullet+}$]: 160.07569; found 160.07540.

N,N'-(Buta-1,3-diyne-1,4-diyl-bis(1,3-phenylene))diacetamide (4a)

N-(3-Ethynylphenyl)acetamide (**7a**, 7.07 g, 44.4 mmol, 1.0 eq), copper (I) iodide (845 mg, 4.44 mmol, 0.1 eq) and TMEDA (2.58 g, 22.2 mmol, 0.5 eq) was dissolved in CH_2Cl_2 (135 mL, 0.33M). Air was bubbled through the mixture, which was stirred at 25 ˚C overnight. The insoluble product was filtered and washed with water before recrystallization from acetone. A total of 4.91 g (70%) of **4a** was isolated as clear crystals which rapidly turn blue. ^{1}H NMR (500 MHz, DMSO): 2.06 (s, 3H), 7.27 (d, *J* = 7.8 Hz, 1H), 7.36 (t, *J* = 8.0 Hz, 1H), 7.56 (d, *J* = 8.0 Hz, 1H), 7.87 (s, 1H), 10.1 (br s, 1H); ^{13}C NMR (125 MHz, DMSO): 24.05, 73.14, 81.80, 120.58, 122.10, 127.04, 129.49, 139.67, 168.71; HRMS (DART) Calculated for $C_{20}H_{16}N_2O_2$ [$M^{\bullet+}$]: 317.12845; found 317.12841.

N-(3-Ethynylphenyl)isobutyramide (7b)

3-Ethynylaniline (5.00 g, 42.7 mmol, 1.0 eq), isobutyric acid (3.75 g, 42.7 mmol, 1.0 eq), N,N'-dicyclohexylcarbodiimide (8.79 g, 42.7 mmol, 1.0 eq) and DMAP (677 mg, 5.55 mmol, 0.13 eq) were dissolved in CH_2Cl_2 (200 mL, 0.22M) and stirred at 25 ˚C overnight. The resulting mixture was filtered and the filtrate concentrated *in vacuo* before purification by column chromatography with SiO_2 eluting with CH_2Cl_2. Recovered 6.67 g (84%) of **7b**. ^{1}H NMR (500 MHz, $CDCl_3$): 1.26

(d, *J* = 6.9 Hz, 6H), 2.50 (sept, *J* = 6.9 Hz, 1H), 3.06 (s, 1H), 7.10 (br, 1H), 7.2-7.3 (m, 2H), 7.57 (d, *J* = 7.9 Hz, 1H), 7.64 (s, 1H); ^{13}C NMR (125 MHz, $CDCl_3$): 19.72, 36.90, 77.55, 83.27, 120.42, 122.97, 123.26, 128.01, 129.18, 138.16, 175.35; HRMS (DART) Calculated for $C_{12}H_{13}NO$ [$M^{\bullet+}$]: 187.09917; found 187.09986.

N,N'-(Buta-1,3-diyne-1,4-diyl-bis(1,3-phenylene))bis(2-methylpropanamide) (4b)

N-(3-Ethynylphenyl)isobutyramide (**7b**, 659 mg, 3.52 mmol, 1.0 eq) was dissolved in CH_2Cl_2 (10 mL, 0.33M) before copper (I) iodide (67 mg, 0.35 mmol, 0.1 eq) and TMEDA (41 mg, 0.35 mmol. 0.1 eq) were added to the flask. Air was bubbled through the mixture and allowed to stir at 25 ˚C overnight. The insoluble dimerization product was filtered and washed with water before recrystallization by hot filtration from THF. A total of 549 mg (84%) of **4b** was recovered as clear crystals which rapidly turn blue in ambient light. ^{1}H NMR (500 MHz, DMSO): 1.10 (d, *J* = 6.9 Hz, 6H), 2.59 (sept, *J* = 6.9 Hz, 1H), 7.27 (dt, *J* = 8.0, 1.0 Hz, 1H), 7.36 (t, *J* = 8.0 Hz, 1H), 7.64 (ddd, *J* = 8.0, 2.0, 1.0 Hz, 1H), 7.89 (t, *J* = 2.0 Hz, 1H), 10.0 (br s, 1H); ^{13}C NMR (125 MHz, DMSO): 19.48, 35.07, 73.18, 81.83, 120.61, 120.85, 122.34, 127.08, 129.53, 139.83, 175.72; HRMS (DART) Calculated for $C_{24}H_{24}N_2O_2$ [$M^{\bullet+}$]: 372.1833; found 372.17976.

***N*-(3-Ethynylphenyl)heptanamide (7c)**

3-Ethynylaniline (3.5 g, 30 mmol, 1 eq) was added to a round bottom flask with a magnetic stirring bar and reflux condenser, pyridine (150 mL, 0.2M) was added followed by heptanoic anhydride (10.9 g, 45 mmol, 1.5 eq), and finally dimethylaminopyridine (DMAP) (367 mg, 3 mmol, 0.1 eq).

The resulting mixture was heated to 100 °C. After stirring overnight, the reaction was complete as indicated by TLC (SiO_2, CH_2Cl_2/hexanes 1:1). The mixture was concentrated *in vacuo*, partitioned between Et_2O/H_2O, aqueous extracted twice with Et_2O, washed twice with 0.5M HCl, then brine, dried over $MgSO_4$, filtered and concentrated *in vacuo* to give a crude residue. The residue was purified by column chromatography on SiO_2 utilizing a gradient up to 20% of EtOAc in hexanes. Recovered 6.6 g (95%) of **7c** as an oil. ^{1}H NMR (500 MHz, $CDCl_3$): 0.88 (t, *J* = 7.0 Hz, 3H), 1.2-1.4 (m, 6H), 1.7 (quint, *J* = 7.3 Hz, 2H), 2.34 (t, *J* = 7.3 Hz, 2H), 3.05 (s, 1H), 7.2-7.3 (m, 2H), 7.37 (br s, 1H), 7.55 (d, *J* = 7.6 Hz, 1H), 7.63 (s, 1H); ^{13}C NMR (125 MHz, $CDCl_3$): 14.15, 22.62, 25.66, 29.04, 31.67, 37.90, 77.52, 83.30, 120.52, 122.92, 123.34, 127.99, 129.12, 138.13, 171.76. HRMS (DART) Calculated for $C_{15}H_{19}NO$ [$M^{\bullet+}$]: 229.14666; found 229.14354.

***N,N'*-(Buta-1,3-diyne-1,4-diylbis(3,1-phenylene))diheptanamide (4c)**

N-(3-Ethynylphenyl)heptanamide (**7c**, 6.6 g, 29 mmol, 1 eq) was added to a round bottom flask with a magnetic stirring bar and dissolved in CH_2Cl_2 (100 ml, 0.33M). To this mixture was added copper(I) iodide (550 mg, 2.8 mmol, 0.1 eq), followed by TMEDA (325 mg, 2.8 mmol, 0.1 eq). Air was bubbled through the mixture and allowed to react at 25 ˚C overnight. The insoluble product **4c** formed overnight was filtered over a fritted funnel. The filtrate was added back to the reaction flask and allowed to continue to react. The combined solids were washed with CH_2Cl_2 and dried. The product was recrystallized from boiling isopropanol via hot filtration, and the receiving flask was protected from ambient light during cooling. Recovered 5.8 g (88%) of **4c** as clear crystals which rapidly turn blue upon standing in ambient light. ^{1}H NMR (500 MHz, DMSO): 0.86 (t, *J* = 7.2 Hz, 3H), 1.29 (m, 6H), 1.58 (quint, *J* = 7.3, 2H), 2.31 (t, *J* = 7.3 Hz, 2H), 7.26 (d, *J* = 7.8 Hz,

1H), 7.36 (t, *J* = 8.0 Hz, 1H), 7.61 (d, *J* = 8.0 Hz, 1H), 7.89 (s, 1H), 10.04 (s, 1H); ^{13}C NMR (125 MHz, DMSO): 13.94, 21.99, 24.97, 28.31, 31.04, 36.43, 73.12, 81.77, 120.56, 120.64, 122.14, 126.97, 129.46, 139.69, 171.66. HRMS (DART) Calculated for $C_{30}H_{36}N_2O_2$ [$M^{\bullet+}$]: 456.27768; found 456.27679

General procedure for topochemical polymerizations:

The crystals to be irradiated were placed into a suitable Erlenmeyer flask and suspended in hexanes with a stir bar. The flask was capped and placed inside a photoreactor equipped with a water-jacketed quartz immersion well with a high-powered Hanovia lamp inside. The flask was placed on a stirplate with stirring to ensure the crystals would mix in the liquid to expose all faces to UV light. The lamp was turned on and the crystals were allowed to react overnight. In the morning, the crystals typically took on a deep purple or black color. The crystals were filtered to remove hexanes and then dissolved in a solvent that readily dissolved the monomer. This solution was boiled to ensure complete dissolution of the monomer from the crystals, resulting in a suspension of the PDA polymer. The hot mixture was filtered over a Buchner funnel with a filter paper and the polydiacetylene "paper" produced was further washed with fresh solvent. The PDA paper could be easily peeled away from the filter paper and further dried under vacuum to give pure polymer. Due to the insolubility of the polymers, their purity was routinely checked by CP/MAS ^{13}C NMR, as the internal alkyne carbon (≈100 ppm) can easily be distinguished from the monomeric butadiyne (≈70-80 ppm). Utilizing the above procedure, specifically, boiling of the solvent while dissolving the reacted crystals, we rarely observed any monomer impurities in our recovered polymer samples. The recovered monomer solution was concentrated and recrystallized

to produce more monomer crystals for further polymerization. As an example, 11.6 g of diyne **3** was subjected to UV irradiation overnight, dissolved and filtered to produce 807 mg (7 %) of PDA **1**. The dissolved monomer solution was concentrated and recrystallized to produce 10.6 g of crystalline diyne **3**. Repetition of this process 3 more times produced a total of 2.8 g (24 % overall yield) of PDA **1** from 11.6 g of diyne **3**.

Diyne 3:

Polymerization yield: 960 mg of PDA **1** was recovered from 14.0 g of crystals (7%)

Solvent: Boiling $CHCl_3$ is an ideal solvent for dissolution of the monomer

Recrystallization: Boiling ethanol and hot filtration

Diyne 4a:

Polymerization yield: 185 mg of PDA **2a** was recovered from 1.70 g of crystals (11%)

Solvent: Boiling THF is an ideal solvent for dissolution of the monomer followed by additional boiling of the crude PDA in DMF, filtering, and washing with diethyl ether

Recrystallization: Boiling acetone and hot filtration

Diyne 4b:

Polymerization yield: 363 mg of PDA **2b** was recovered from 1.56 g of crystals (23%)

Solvent: Boiling in a 1:1 solution of THF/acetone is ideal for dissolution of the monomer followed by additional boiling of the crude PDA **2b** in DMF, filtering, and washing with diethyl ether

Recrystallization: Boiling THF and hot filtration

Diyne 4c:

Polymerization yield: 540 mg of PDA **2c** was recovered from 3.6 g of crystals (15%)

Solvent: Boiling THF is an ideal solvent for dissolution of the monomer

Recrystallization: Boiling isopropanol and hot filtration

General procedure for the graphitization experiments:

For the conversion of the PDA polymers **1** and **2a–c** to $[8]_A$GNR, a programmable tube furnace (MTI OTF-1200X-S-NT) was used. A quartz tube with internal diameter of 2 inches was used, and the PDA to be heated was placed in an alumina boat inside the quartz tube in the middle of the hot zone. End caps were clamped onto the tube to provide a positive flow of Argon. The program used for the heating experiments is as follows: heat over 40 min to the target temperature, hold at target temperature for 1 h, then cool to room temp over 40 min. Due to the thermal mass of the tube, cooling of the system from higher temperatures (>400 ˚C) could take long times, but the system rapidly cooled from the higher temperatures (>400 ˚C) to below 250 ˚C at the end of the 40 min cooling period. After the system had cooled to 25 ˚C, the material was removed from

the alumina boat and immediately weighed to quantify mass loss and yield, as reported in Table S1.

The yields for the graphitization process were determined by measuring the amount of material recovered after thermal aromatization of the respective PDAs (Table S1). The expected theoretical mass recovery after complete graphitization of the PDAs **1**, and **2a-2c** was 68%, 62%, 53%, and 43% respectively. After heating of PDAs **1**, and **2a–2c** to 600 ˚C for 1h under argon, the experimental mass recovery matched the theoretical mass recovery in all cases. This implies that the yield for the overall PDA to GNR conversion process is quantitative for all cases presented here.

Section 2.6. Appendix A

Table A1. Mass and percent mass recovery for the thermal conversions of PDAs **1** and **2a–c** to $[8]_A$GNR.

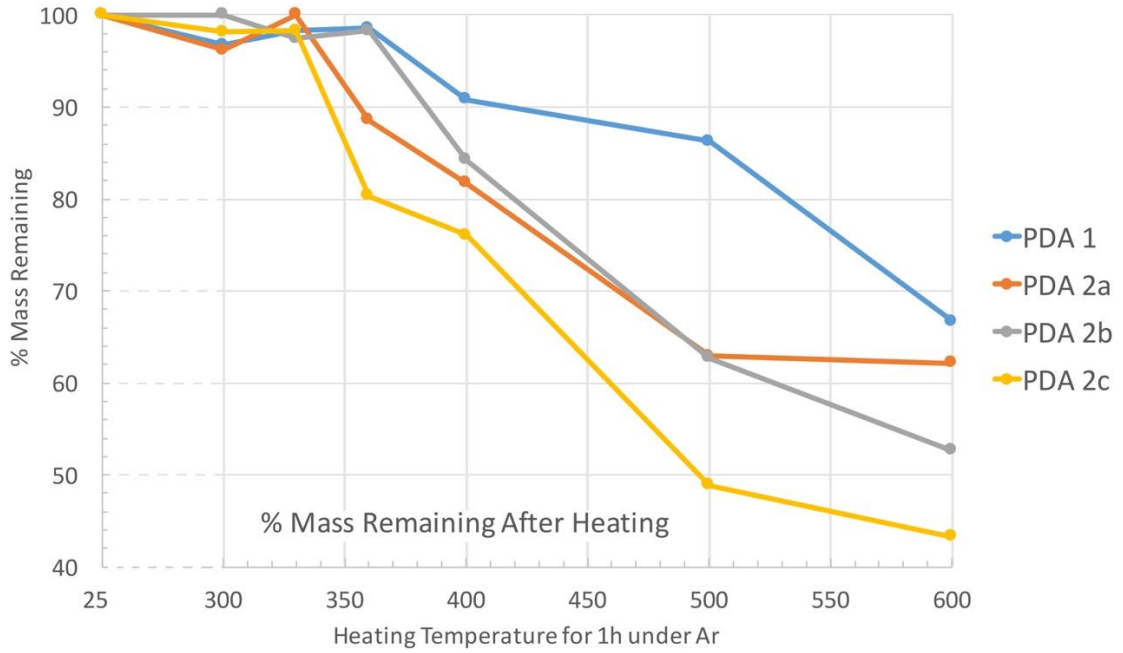

Temperature (˚C)	Amount (mg) at:	1	2a	2b	2c
25	starting mass	62	52	66	53
300	final mass	60	50	66	52
	mass % remaining[1]	97%	96%	100%	98%
25	starting mass	57	37	78	59
330	final mass	56	37	76	58
	mass % remaining[1]	98%	100%	97%	98%
25	starting mass	71	35	59	66
360	final mass	70	31	58	53
	mass % remaining[1]	99%	89%	98%	80%
25	starting mass	76	93	76	71
400	final mass	69	76	64	54

	mass % remaining[1]	91%	82%	84%	76%
25	starting mass	80	143	134	135
500	final mass	69	90	840	66
	mass % remaining[1]	86%	63%	63%	49%
25	starting mass	318	148	76	141
600	final mass	212	92	40	61
	mass % remaining[1]	67%	62%	53%	43%
	theoretical mass % remaining[2]	68%	62%	53%	43%
	$[8]_A$GNR yield[3]	99%	100%	100%	100%

[1] The mass percent remaining was calculated by dividing material mass before and after a heating experiment.

[2] The theoretical mass percent remaining was calculated by comparing the molecular weight of a pristine PDA monomer unit to that of $[8]_A$GNR (after undergoing side-chain loss and exhaustive cyclodehydrogenation).

[3] The overall yield for the PDA to $[8]_A$GNR process was determined by dividing the experimental and theoretical mass percentages for product remaining after heating to 600 ˚C.

Section 2: Supplementary spectroscopic data for PDAs **1**, **2a–2c** and $[8]_A$GNR

i) Stack plots of the infrared spectra at full width, as well as in the fingerprint region, for the conversions of PDAs **1** and **2a–2c** to $[8]_A$GNR.

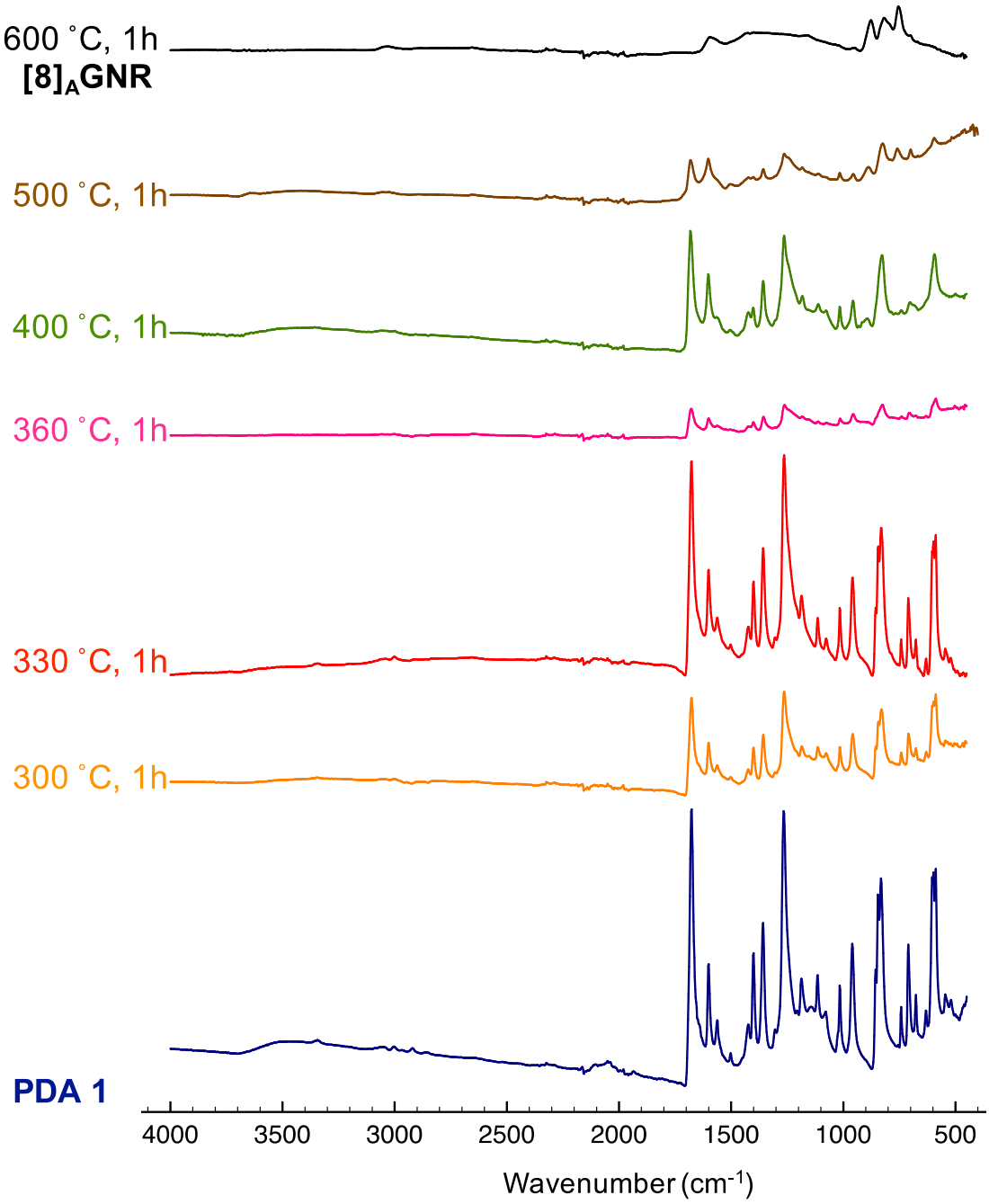

Figure A1. Full width infrared spectrum detailing the conversion of PDA **1** to $[8]_A$GNR, *without* baseline correction.

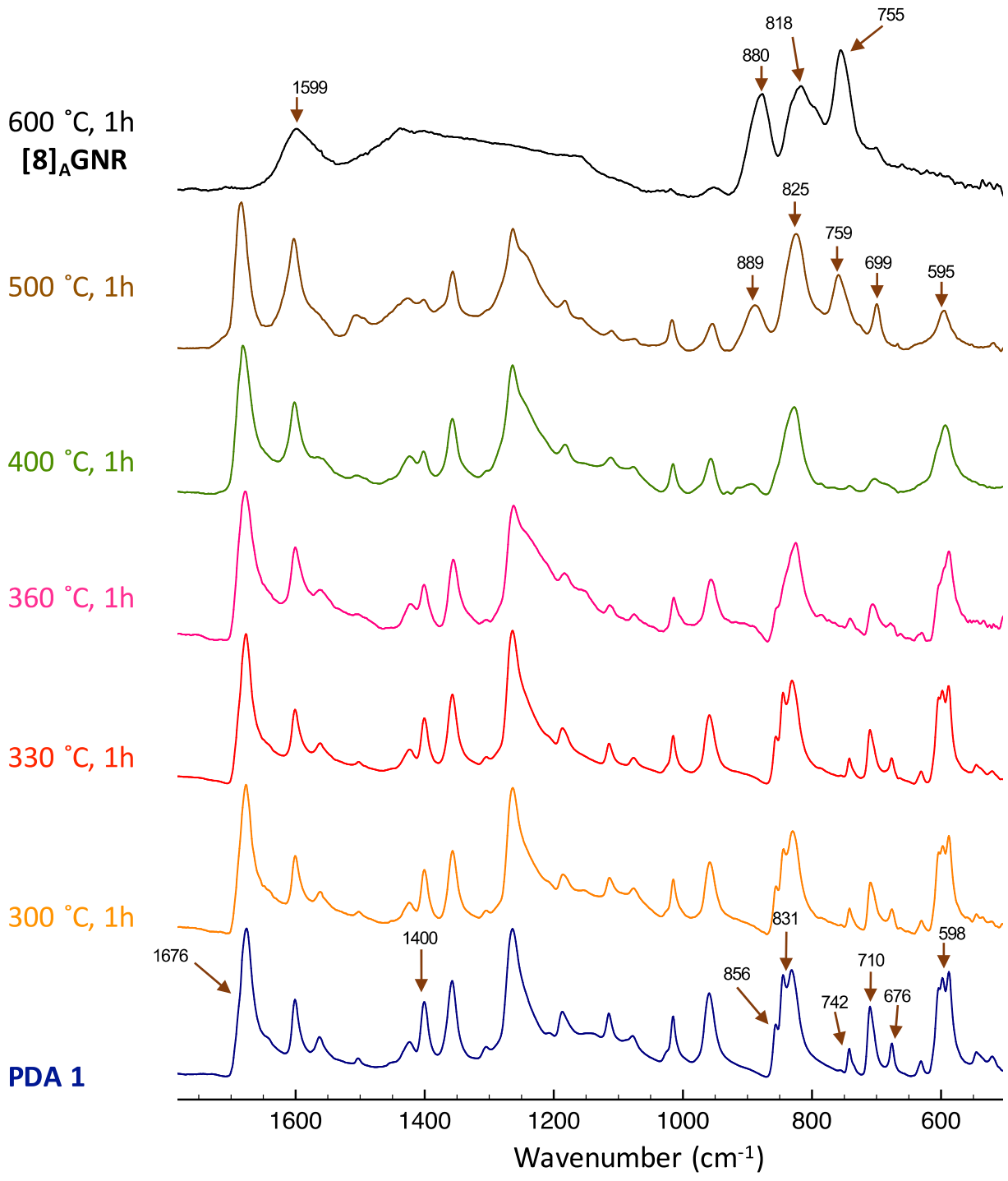

Figure A2. Fingerprint region expansion of infrared spectrum detailing the conversion of PDA **1** to $[8]_A$GNR, *with* baseline correction.

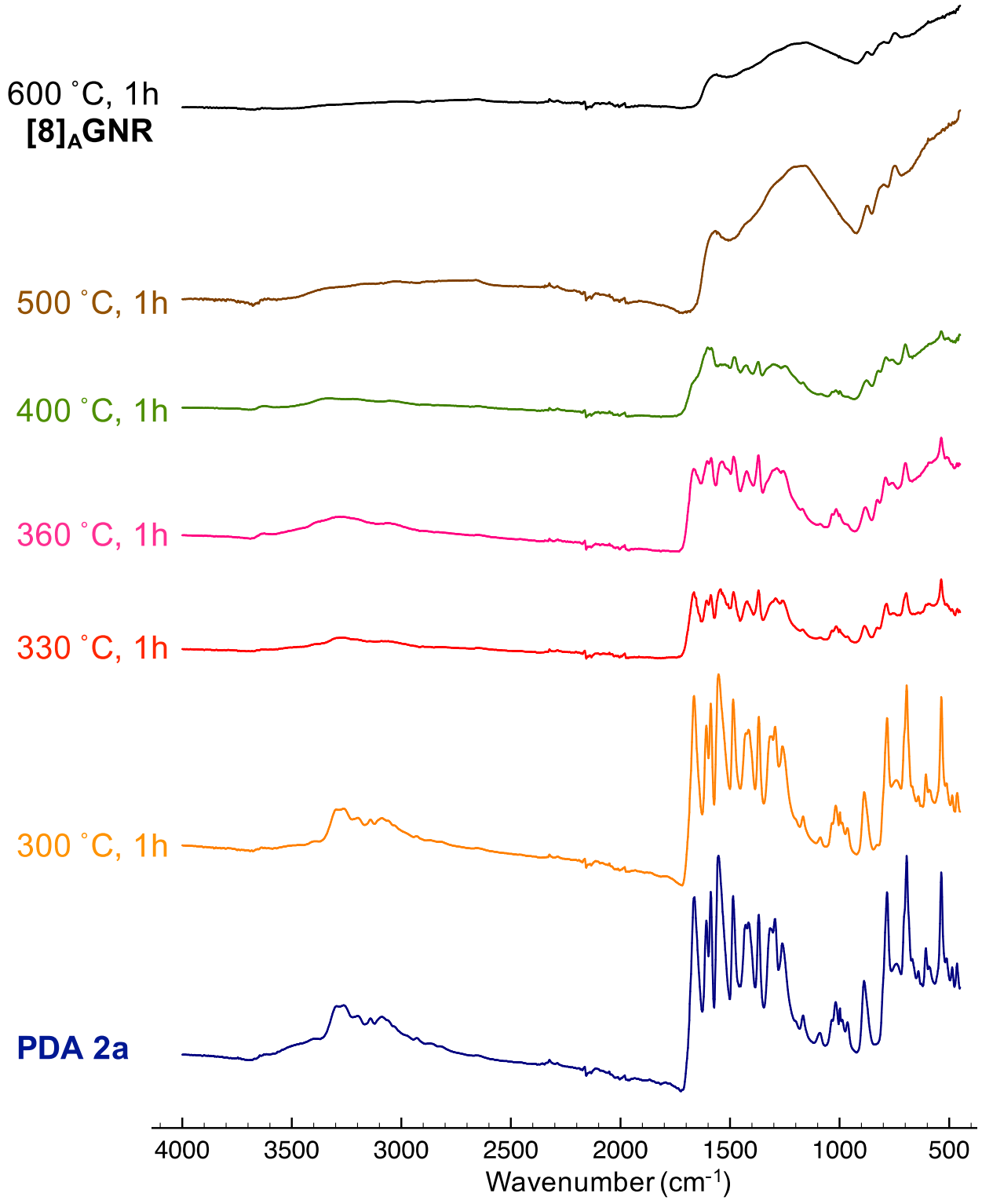

Figure A3. Full width infrared spectrum detailing the conversion of PDA **2a** to [8]$_A$GNR, *without* baseline correction.

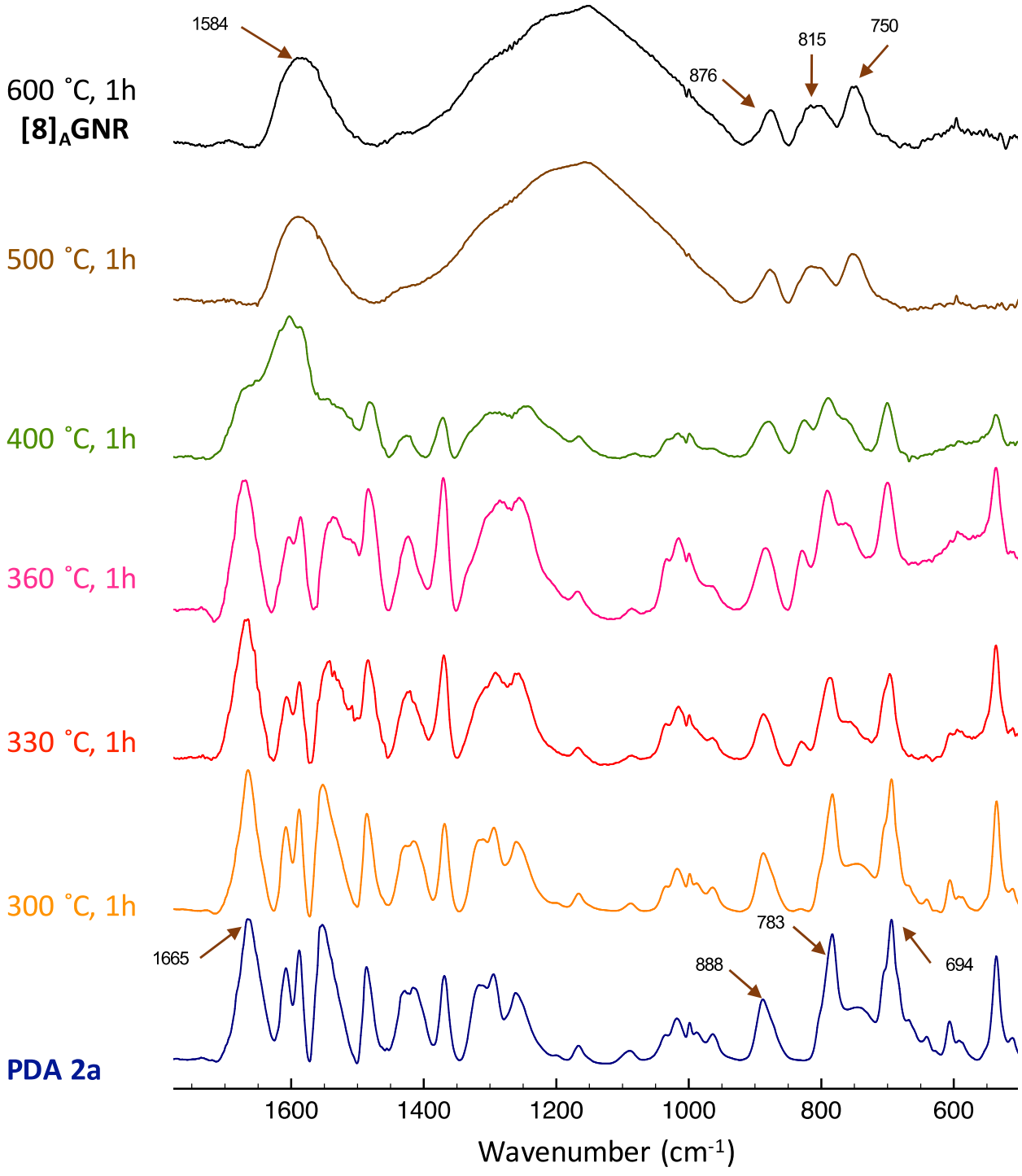

Figure A4. Fingerprint region expansion of infrared spectrum detailing the conversion of PDA **2a** to $[8]_A$GNR, *with* baseline correction.

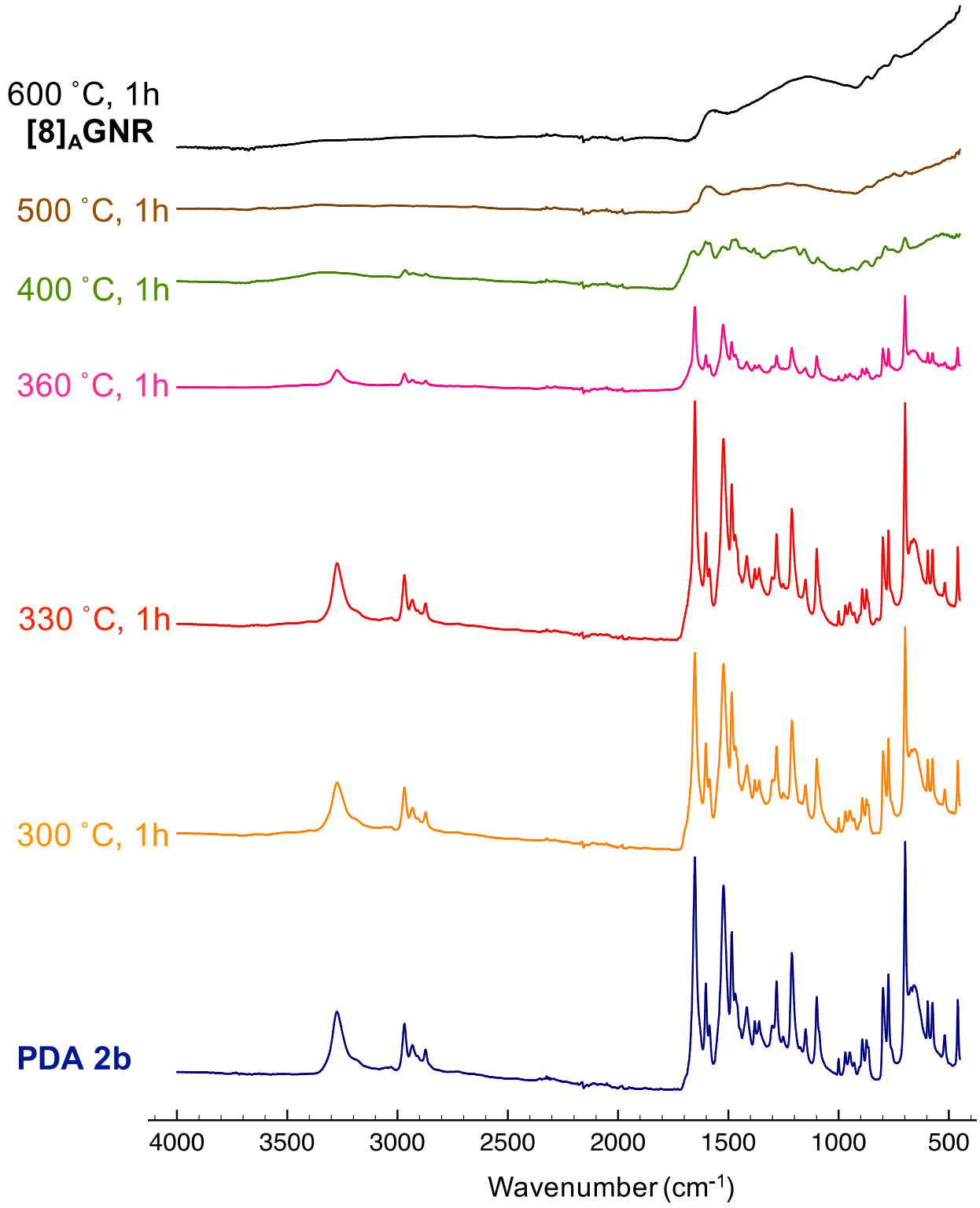

Figure A5. Full width infrared spectrum detailing the conversion of PDA **2b** to $[8]_A$GNR, *without* baseline correction.

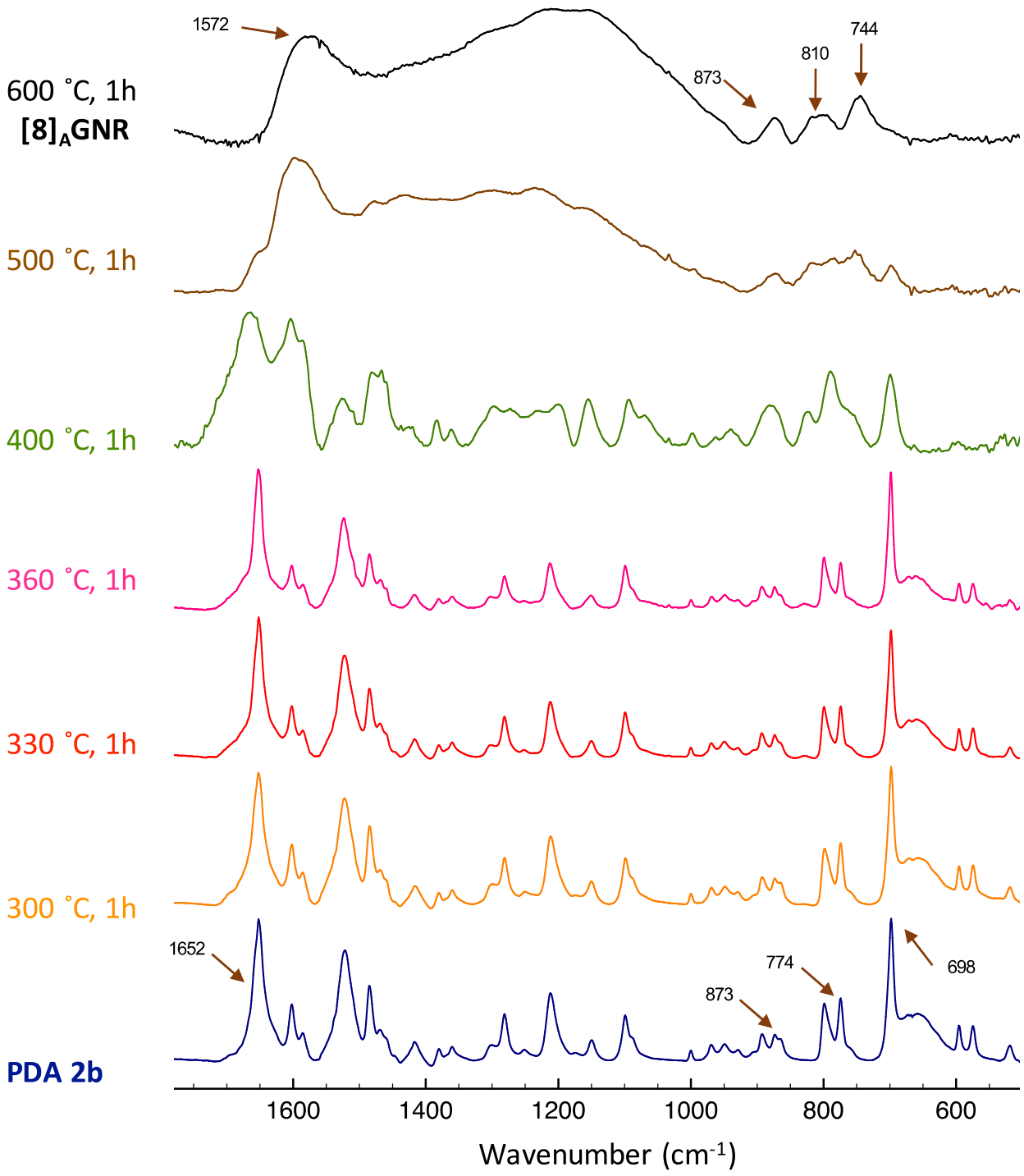

Figure A6. Fingerprint region expansion of infrared spectrum detailing the conversion of PDA **2b** to $[8]_A$GNR, *with* baseline correction.

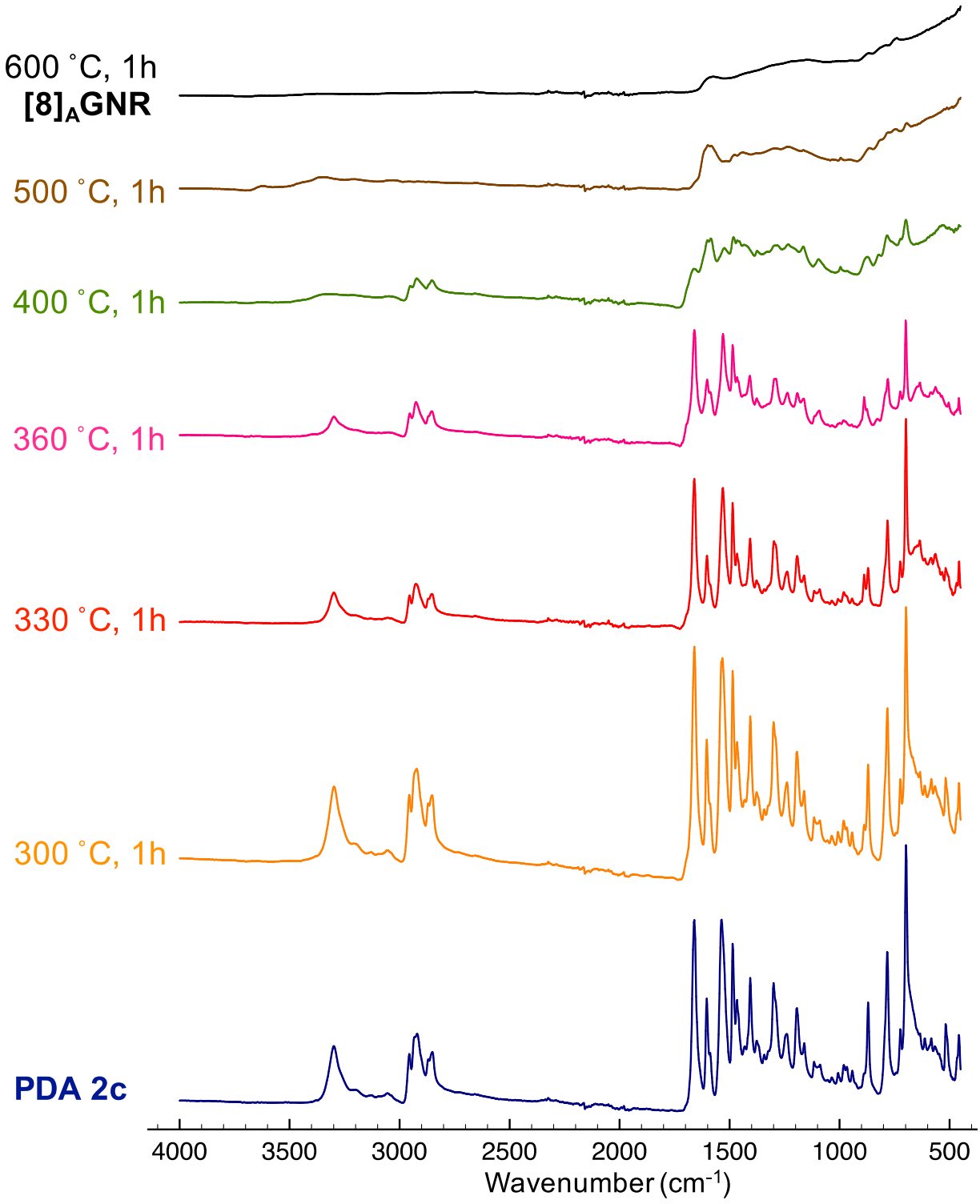

Figure A7. Full width infrared spectrum detailing the conversion of PDA **2c** to [8]$_A$GNR, *without* baseline correction.

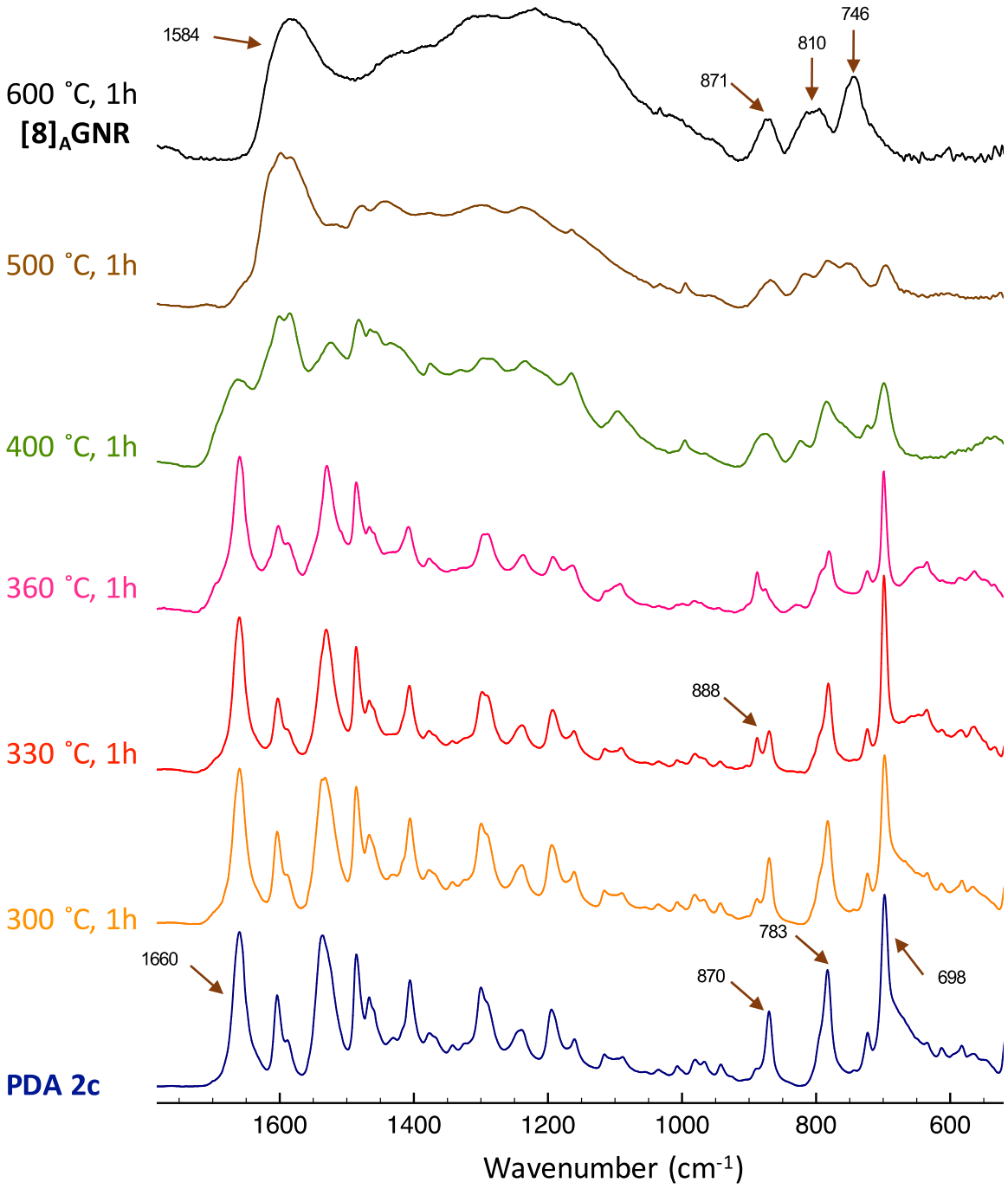

Figure A8. Fingerprint region expansion of infrared spectrum detailing the conversion of PDA **2c** to [8]$_A$GNR, *with* baseline correction.

ii) Plots of the XPS spectra of PDAs **1**, **2a–2c**, and the resulting $[8]_A$GNR for each experiment.

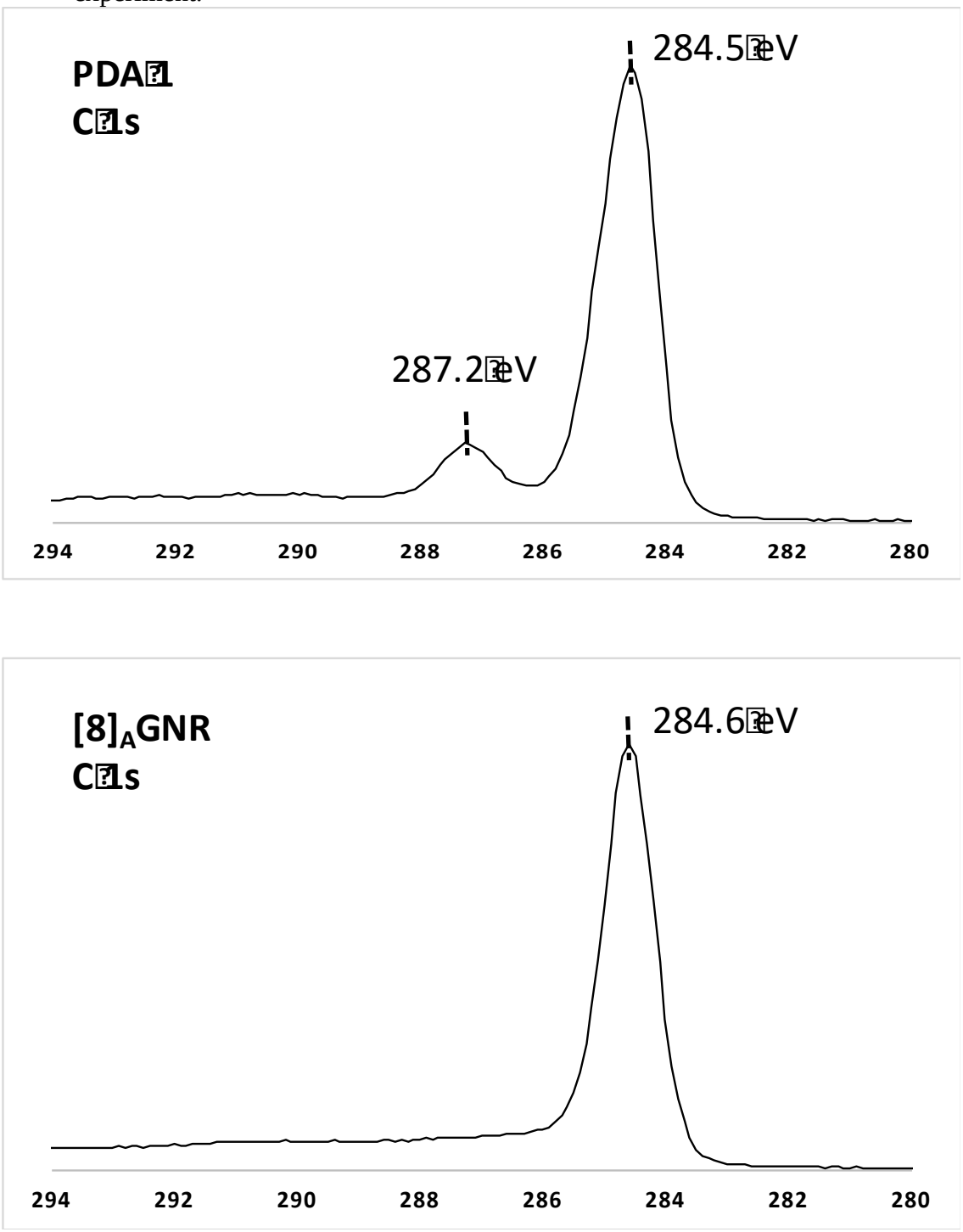

Figure A9. XPS spectra showing the conversion of PDA **1** to $[8]_A$GNR.

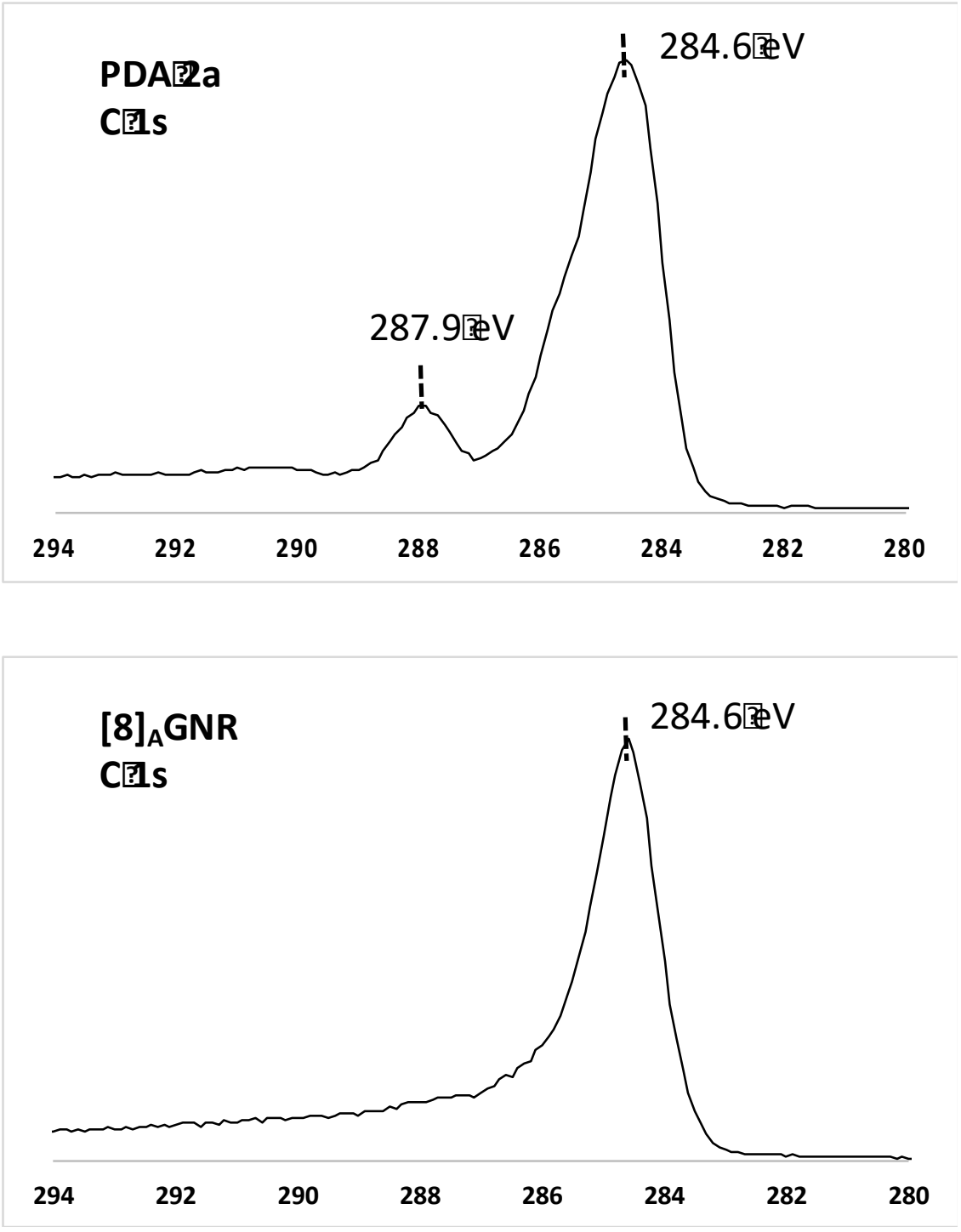

Figure A10. XPS spectra showing the conversion of PDA **2a** to $[8]_A$GNR.

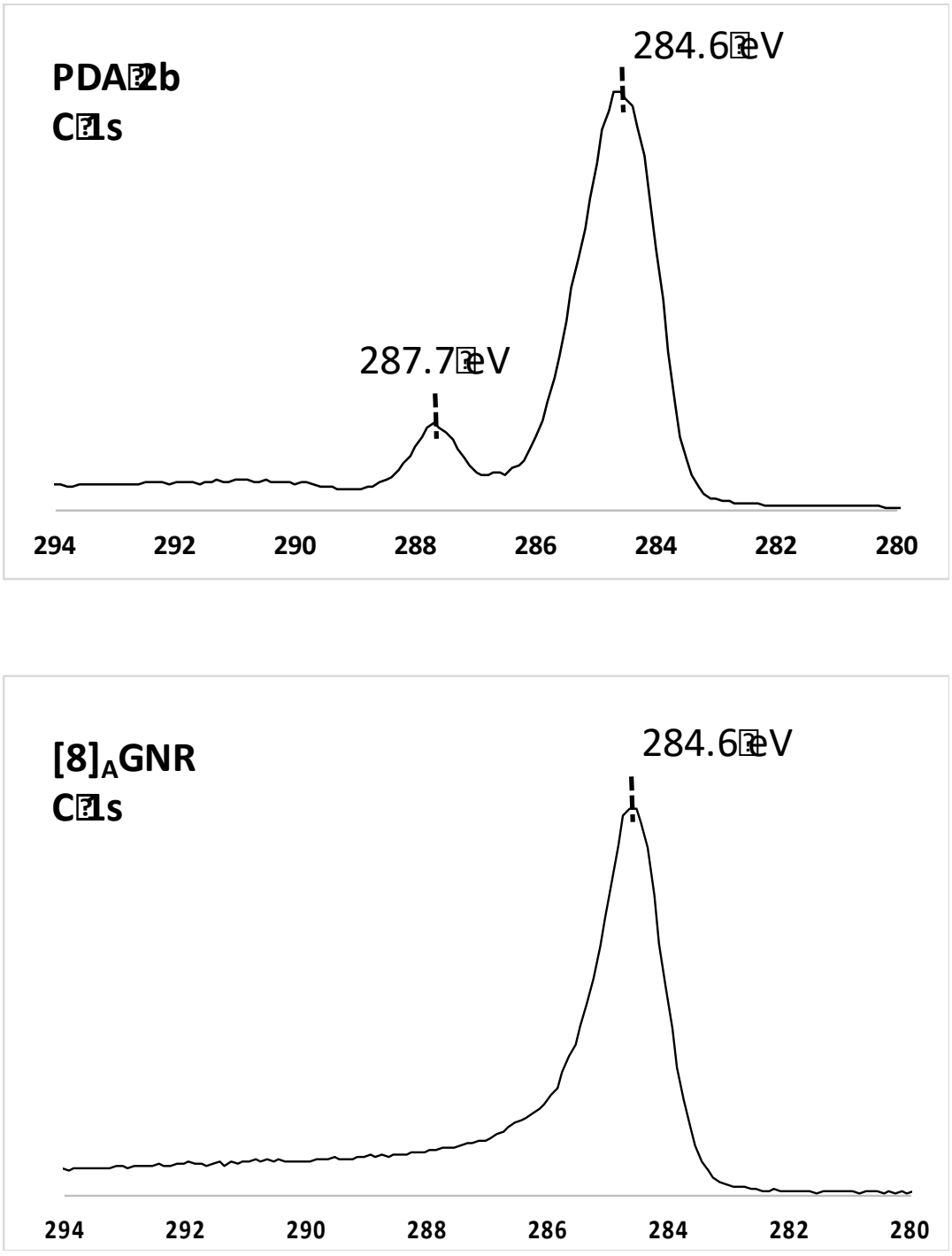

Figure A11. XPS spectra showing the conversion of PDA **2b** to $[8]_A$GNR.

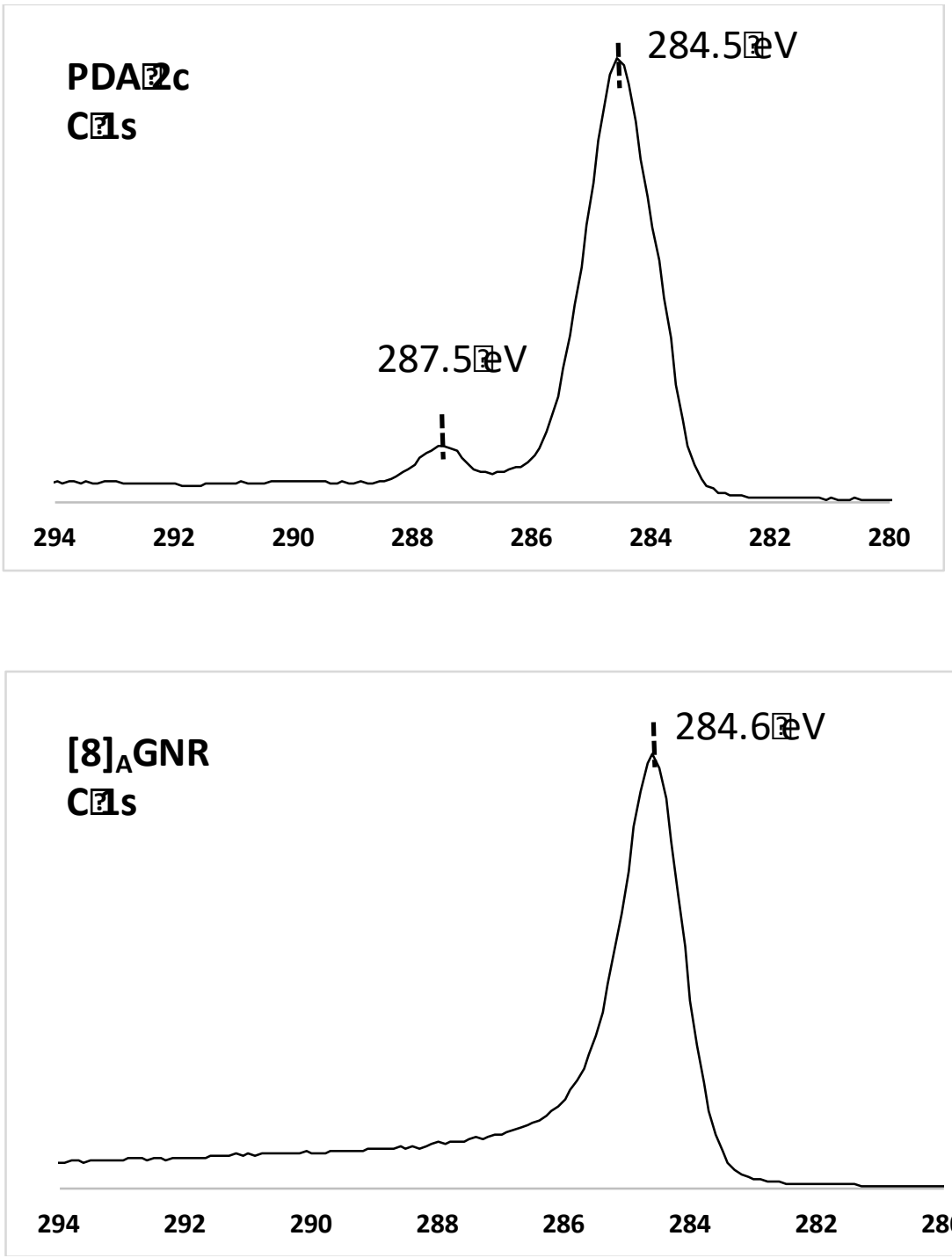

Figure A12. XPS spectra showing the conversion of PDA **2c** to $[8]_A$GNR.

iii) Stacked plots of the Raman spectra acquired for PDAs **1**, **2a**–**2c**, and the resulting samples heated at the temperatures indicated for one hour

Spectra are displayed stacked without baseline correction to highlight the photoluminescence background that occurs in a number of the annulated intermediate polymers produced upon heating. We attribute this background to the formation of larger polycyclic aromatic moieties (naphthalene, chrysene, etc) along the polymeric backbone. Such polycyclic aromatic compounds have been shown to fluoresce at the excitation wavelength (514 nm) and interfere with Raman measurements.[52] Noticeably, upon full graphitization to $[8]_A$GNR upon heating to 600 ˚C for 1h, the photoluminescence decreases to a large extent in all cases due to fusion of the isolated polycyclic aromatic units along the polymer backbone into $[8]_A$GNR.

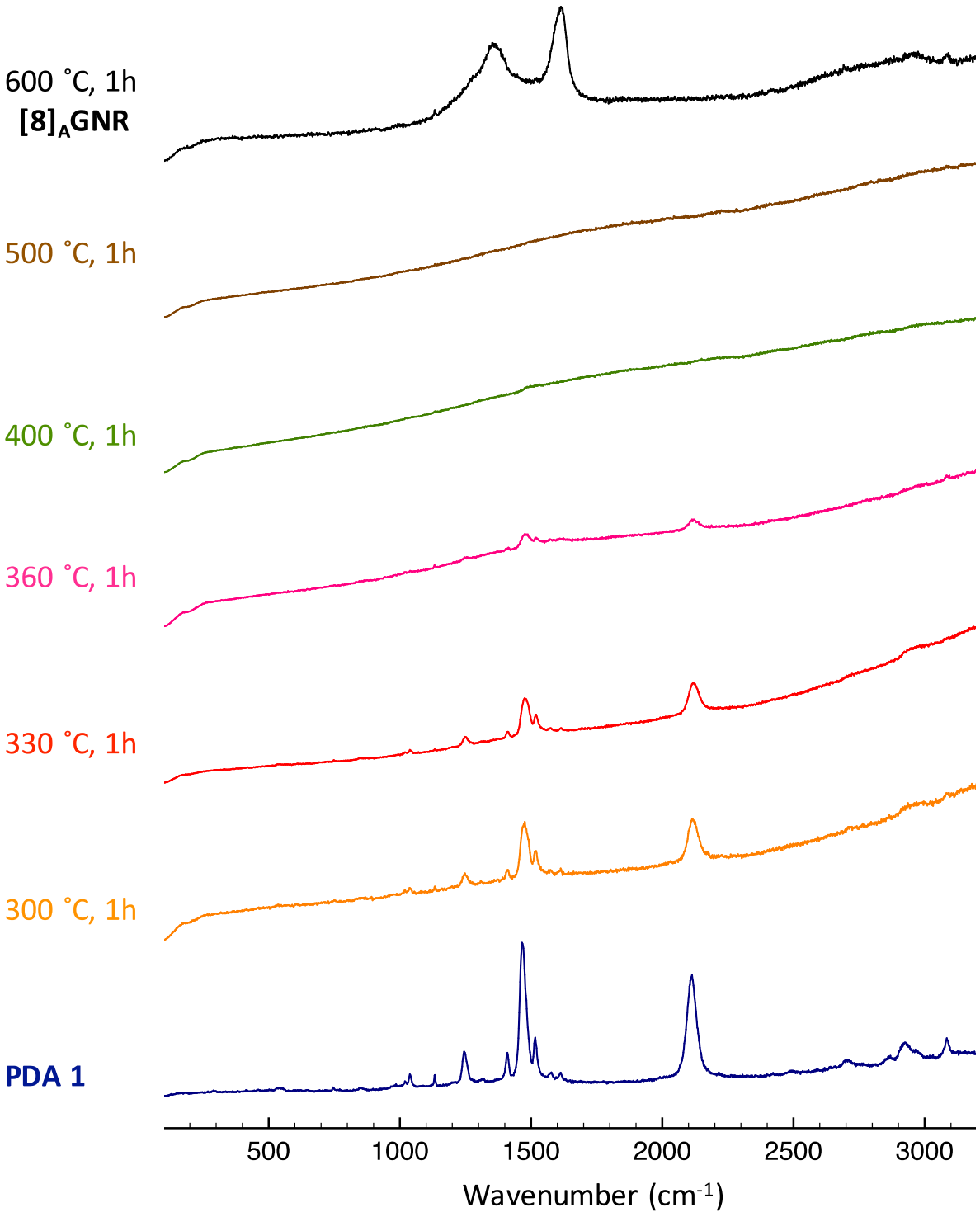

Figure A13. Raman spectra (514 nm excitation wavelength) showing the conversion of PDA **1** to $[8]_A$GNR.

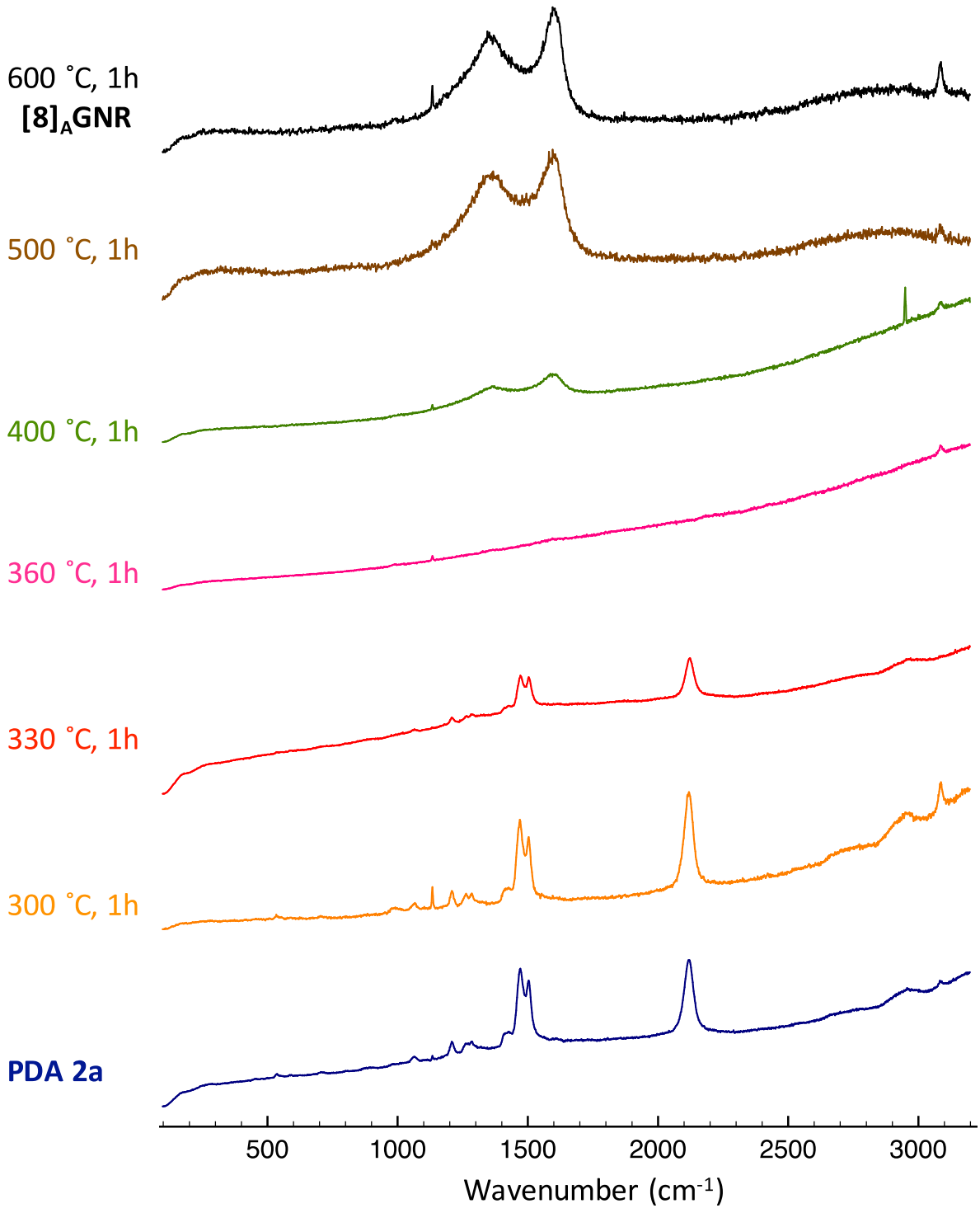

Figure A14. Raman spectra (514 nm excitation wavelength) showing the conversion of PDA **2a** to $[8]_A$GNR.

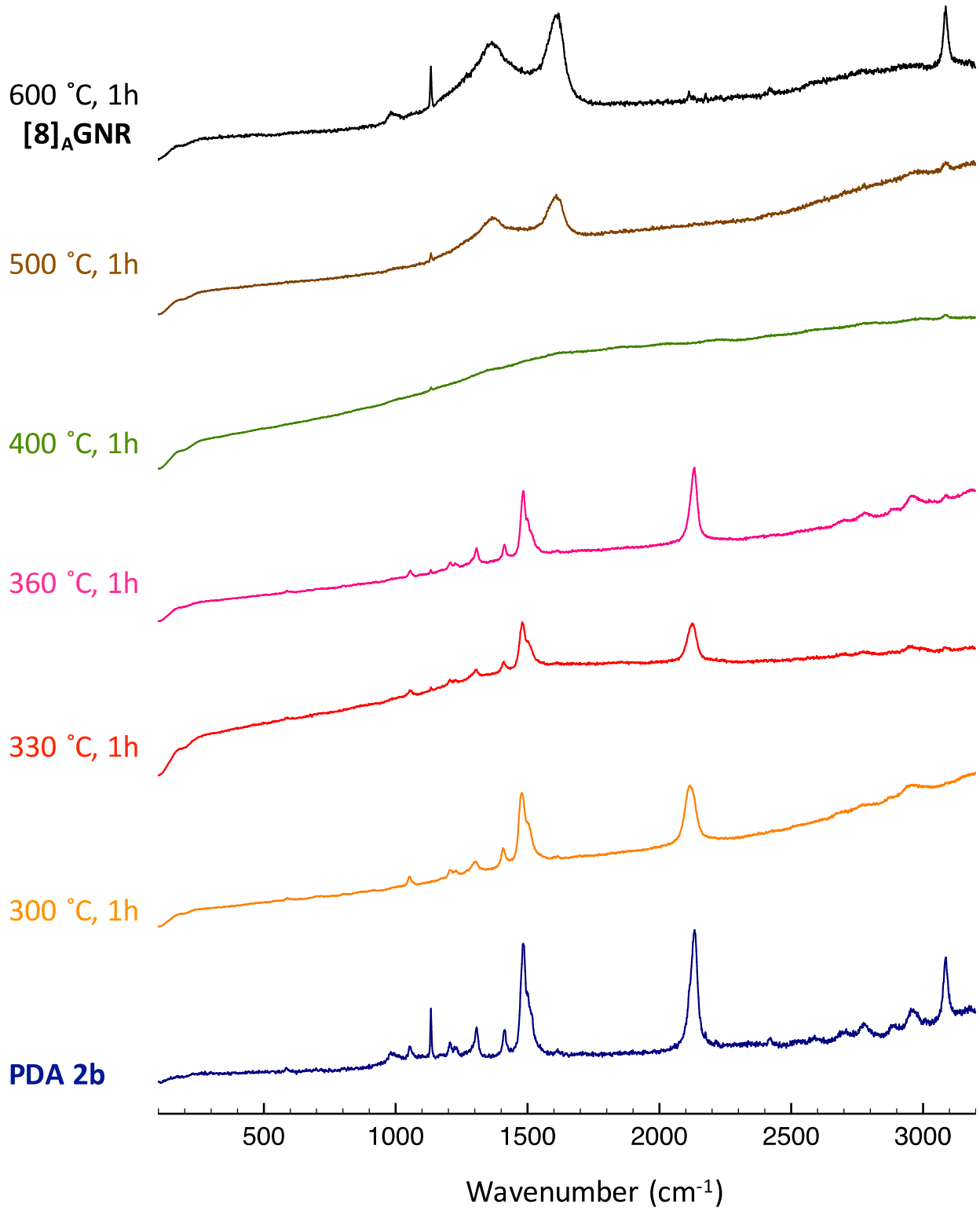

Figure A15. Raman spectra (514 nm excitation wavelength) showing the conversion of PDA **2b** to $[8]_A$GNR.

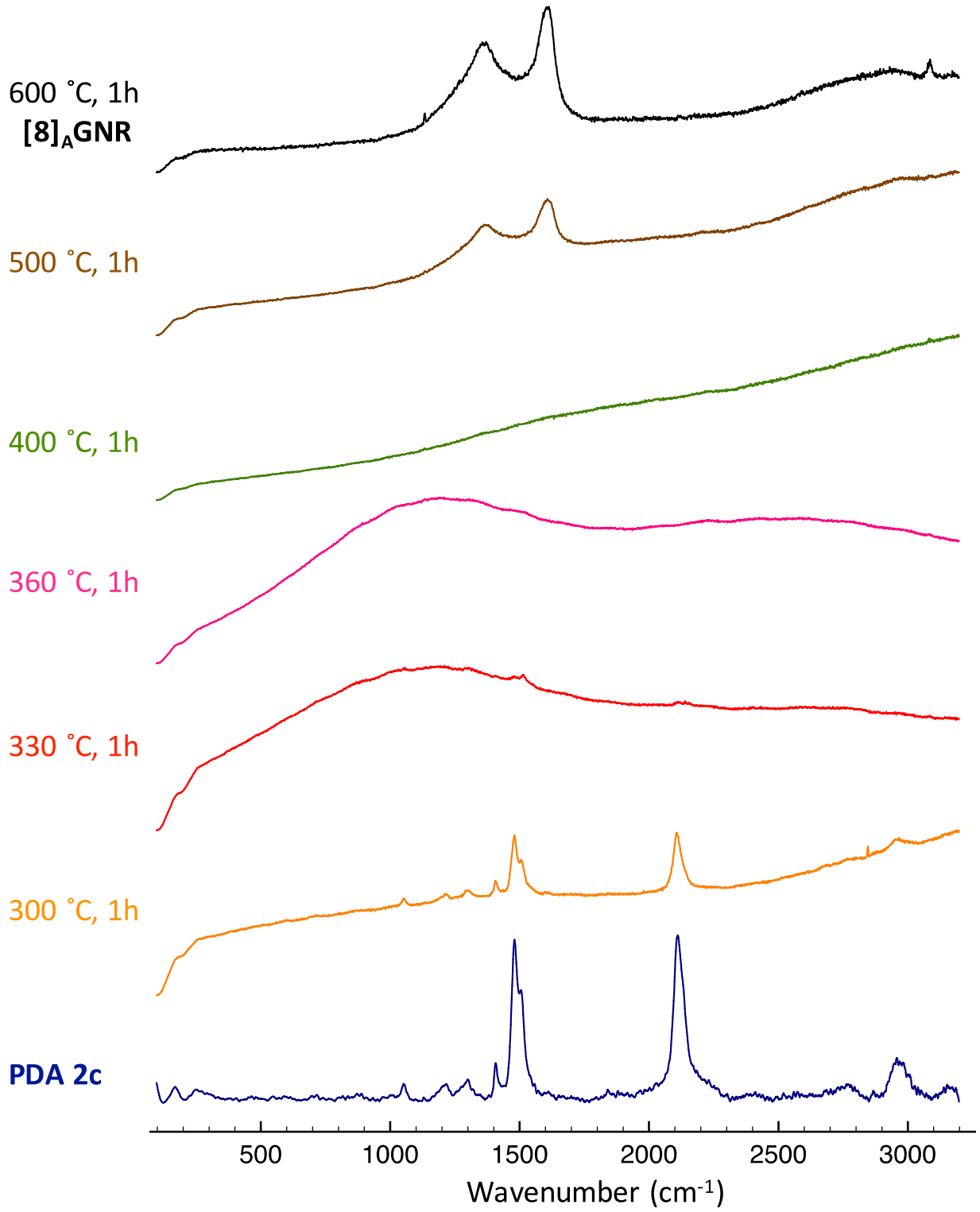

Figure A16. Raman spectra (514 nm excitation wavelength) showing the conversion of PDA **2c** to $[8]_A$GNR.

iv) Calculated curve fits of the CP/MAS ^{13}C NMR aromatic region for $[8]_A$GNR produced from thermal aromatization of either PDAs **1** or **2a**

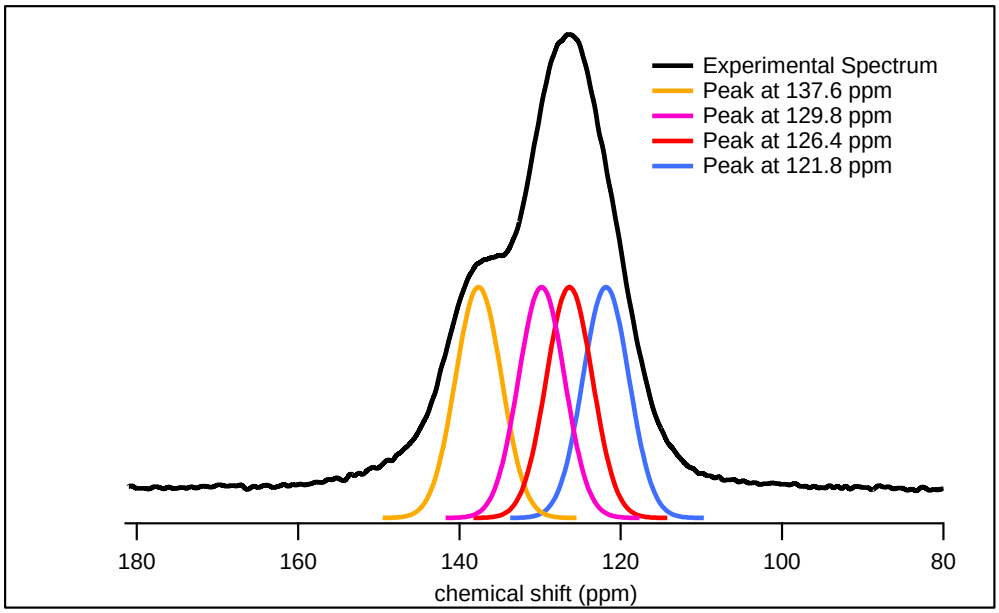

Figure A17. Calculated curve fitting of CP/MAS ^{13}C NMR data for $[8]_A$GNR produced from thermal aromatization of PDA **1**.

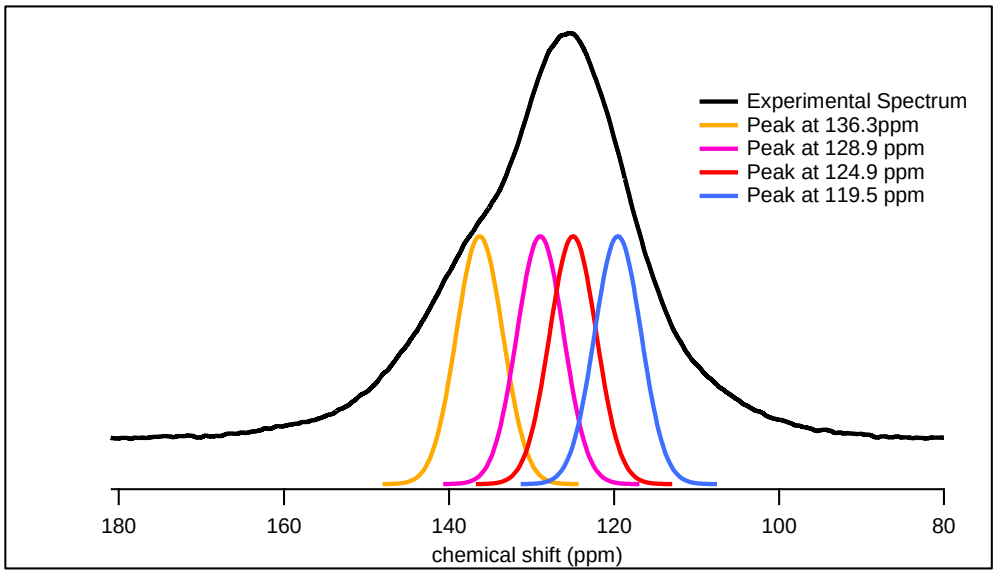

Figure A18. Calculated curve fitting of CP/MAS ^{13}C NMR data for $[8]_A$GNR produced from thermal aromatization of PDA **2a**.

Peak fitting was accomplished using the Multipeak Fitting 1.4 package in Igor Pro 6.37. The experimental spectra were fit to four peaks over the region of interest using a Gaussian line shape. As each GNR is composed of four distinct carbons of equal weighting, the amplitude and width of each fit was held constant during the fitting process. The results show four distinct functions whose centers were taken to be the chemical shift of the carbons in question.

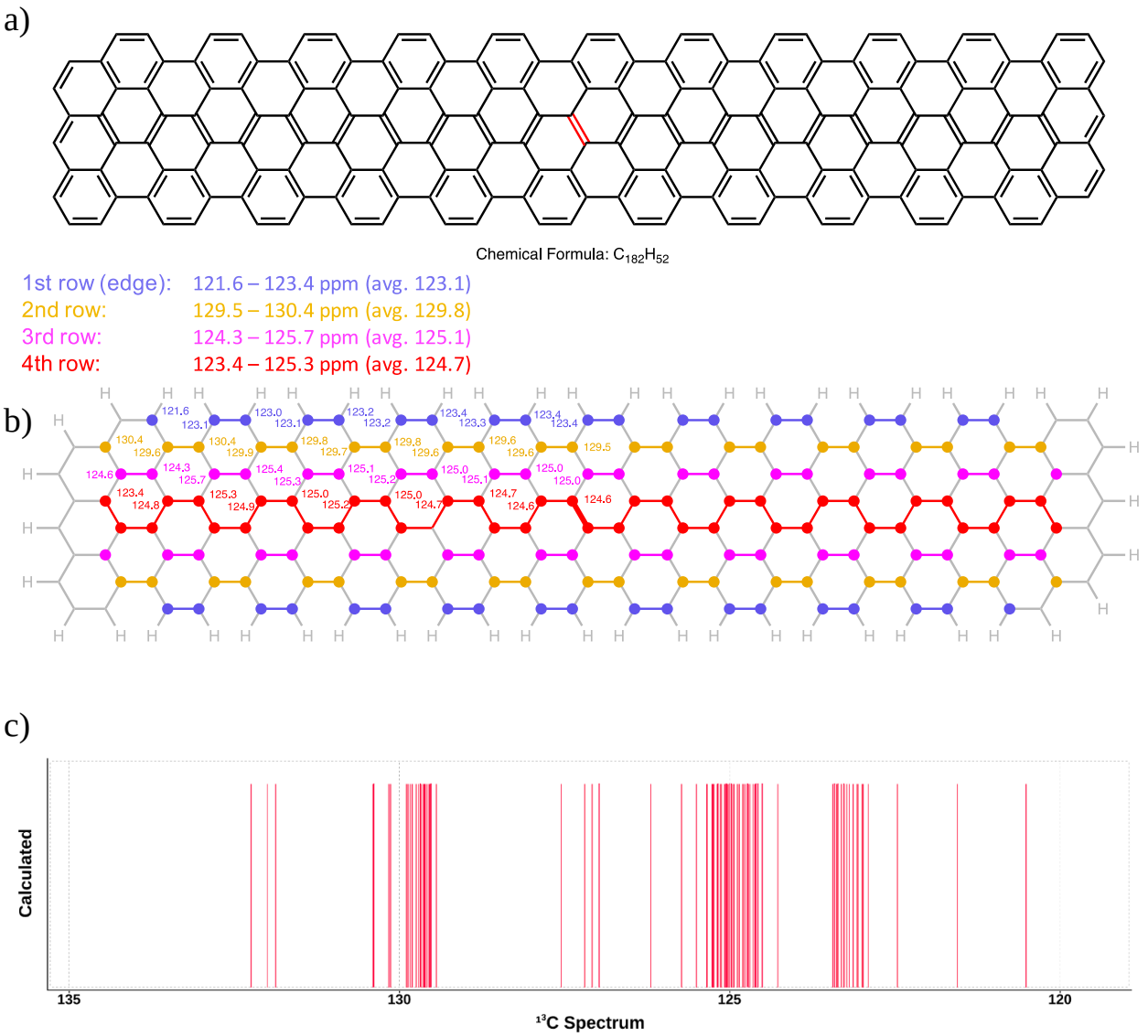

Figure A19. a) Chemical structure with listed range of calculated ^{13}C NMR chemical shifts for each row of non-symmetrically related carbons, and b) ^{13}C NMR chemical shifts δ (ppm) for a large section of $[8]_A$GNR calculated at the B3LYP//6-31G* level of theory. NMR shielding tensors were computed with the Gauge-Independent Atomic Orbital (GIAO) method. The

calculation was performed with the MacSpartan 16 package.[53] The ^{13}C NMR chemical shifts that are displayed here are all within ±1 ppm of each other in each of the four different rows of carbons. Thus, the 2nd row of carbons should roughly have a relative intensity of 1:3 with those carbons within rows 1, 3, and 4. c) Plot of all the ^{13}C NMR chemical shifts obtained in the B3LYP//6-31G* calculation for this model compound using Spartan 16.

v) Comparison of calculated IR spectra with experimental data for PDA **1** at various stages of thermal conversion. The starting PDA structure, the likely annulated structure (PDA **1-annul**), and the $[8]_A$GNR final stage are shown in Figure A20–S22. Frequency calculation methods and lists of frequencies are described in Section 3(xi).

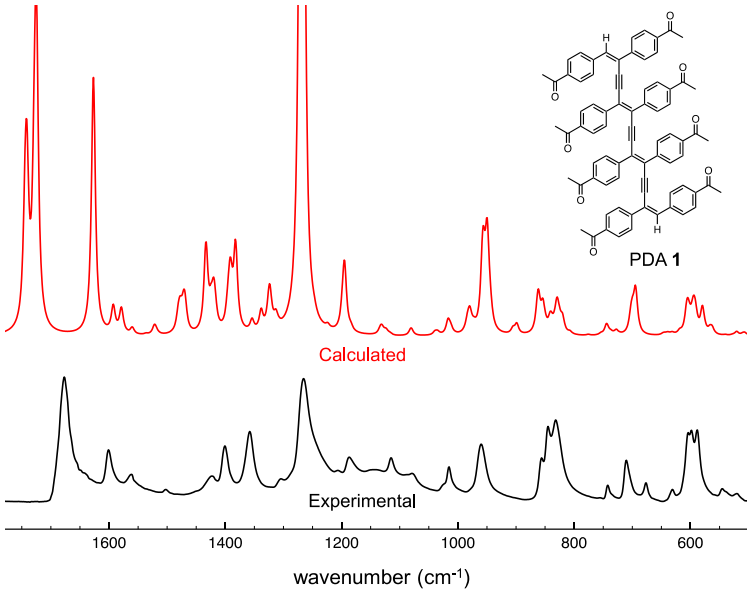

Figure A20: Comparison of calculated and experimental IR spectra for PDA polymer **1**.

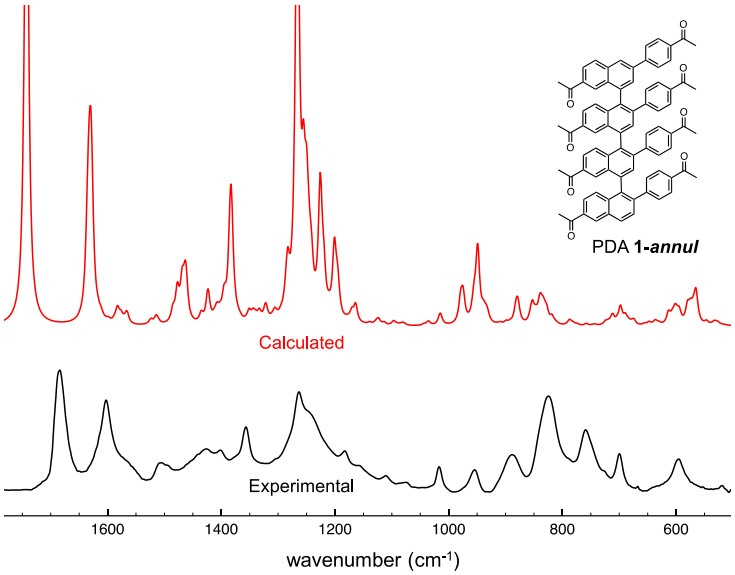

Figure A21: Comparison of calculated IR spectra of a possible structure for the annulated polymer (PDA ***an*-PDA**) resulting from thermal treatment of PDA **1** and comparison to experimental data.

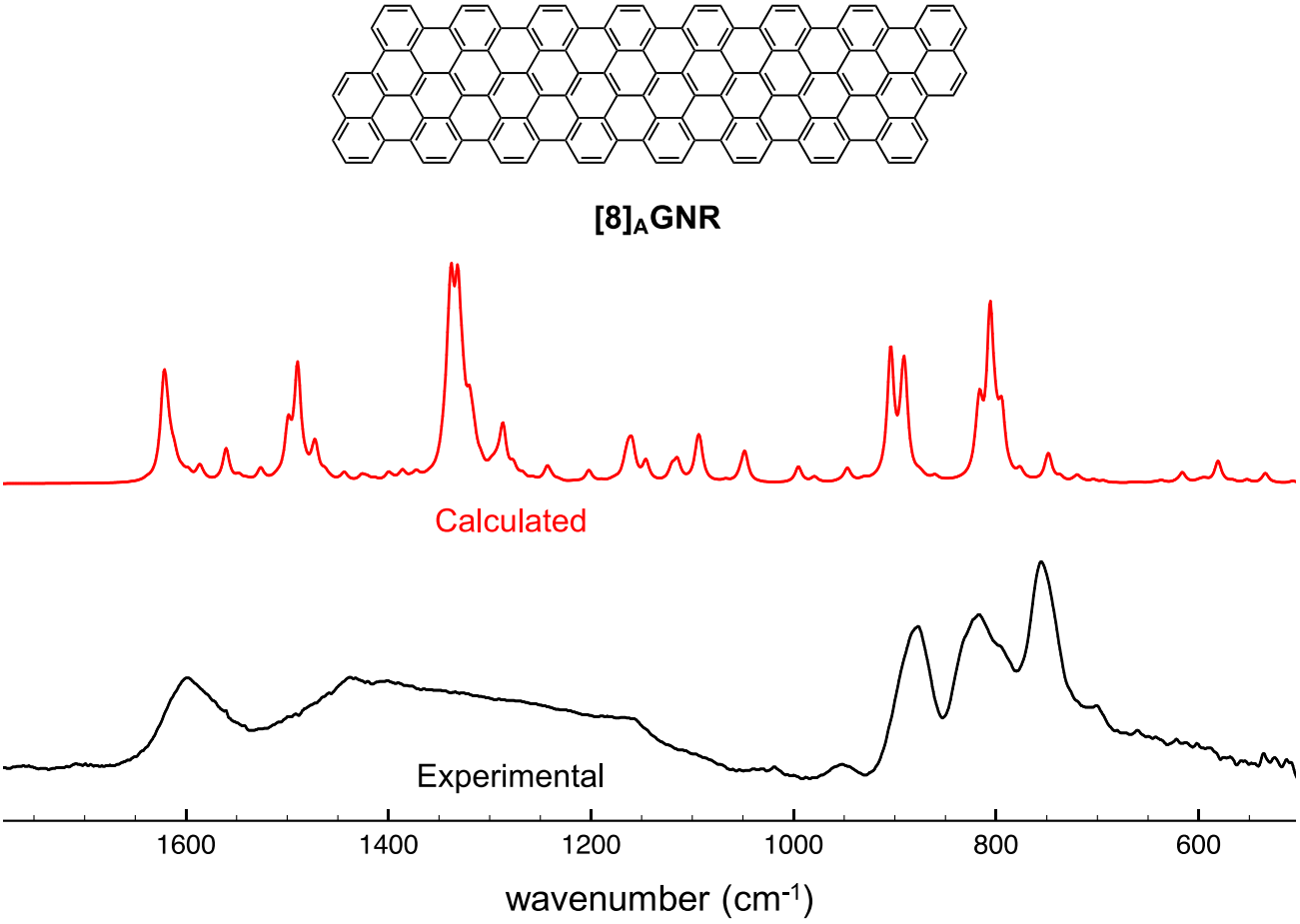

Figure A22. Comparison of calculated and experimental IR spectra for $[8]_A$GNR produced from thermal aromatization of PDA **1**. In light of available computational resources, a section of $[8]_A$GNR was used as a surrogate for the spectrum calculation in lieu of the corresponding infinite ribbon. The ribbon is 34 carbons in length and its structure is shown above the spectra.

vi) Width calculation of $[8]_A$GNR and plot profile analysis of the HRTEM image for $[8]_A$GNR.

The width of an individual $[8]_A$GNR ribbon was calculated using the optimized geometry of the model segment described in Fig. S22. Distance from the center of an edge hydrogen to the center of the edge hydrogen horizontally across the ribbon was measured using GaussView as 10.47 Å. To account for the Van der Waals radii of the edge hydrogen (1.2 Å), 2.4 Å was added to the measured width to produce the calculated ribbon width of ≈12.9 Å (~1.3 nm).

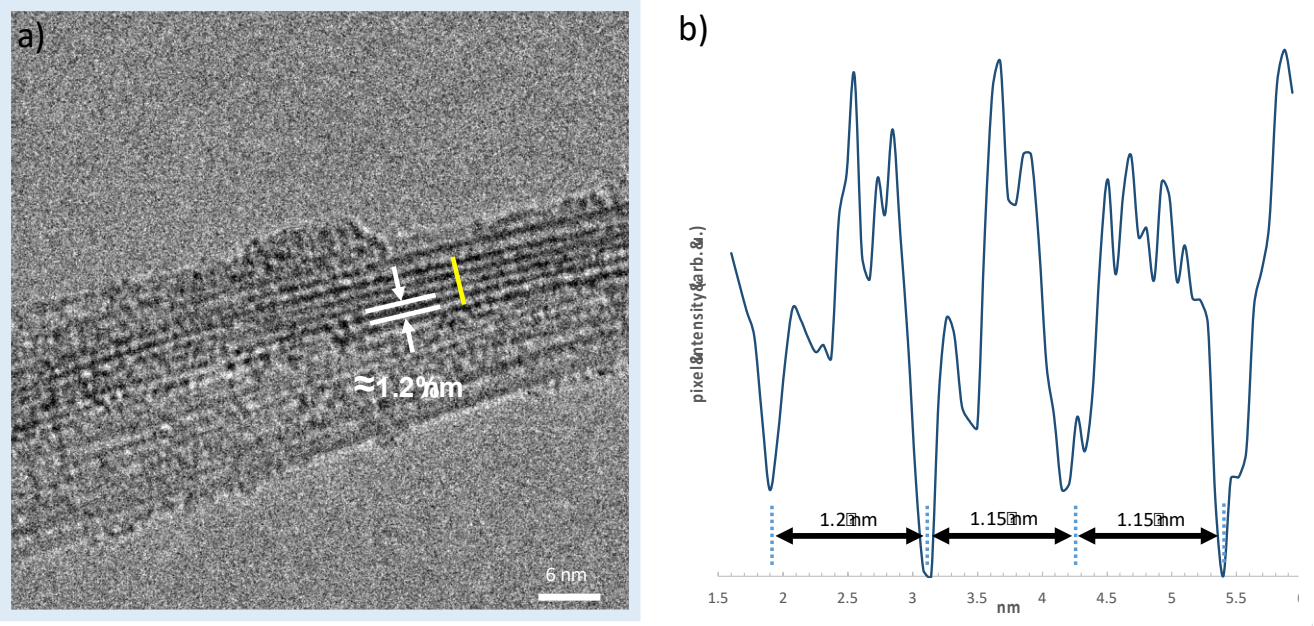

Figure A23. Plot profile analysis (yellow line) of HRTEM image of $[8]_A$GNR produced from thermal graphitization of PDA **2b**.

vii) Spectroscopic details of the CP/MAS ^{13}C NMR experiments

CP/MAS ^{13}C NMR experiments were performed on a Bruker DSX300 operating at 300 MHz and at 298 K. A 4mm zirconia rotor with a Kel-F cap was used spinning at 10 KHz in all experiments. A 5 ms cross-polarization contact time was utilized in all experiments. To ensure that a good signal-to-noise ratio was achieved for all spectra, the number of scans collected was increased as necessary. Below is a table listing the specific number of scans collected for all spectra described in Fig 8 of the paper. A 50 Hz line broadening was applied to all spectra except for the spectra of PDAs **2b** and **2c** after heating to 500 ˚C where a 100 Hz line broadening was used.

PDA	No heating (# of scans)	300 ˚C, 1h (# of scans)	330 ˚C, 1h (# of scans)	360 ˚C, 1h (# of scans)	400 ˚C, 1h (# of scans)	500 ˚C, 1h (# of scans)	600 ˚C, 1h (# of scans)
1	2048	2048	2048	2048	19456	12288	12288
2a	2048	2048	2048	2048	24576	24576	24576
2b	2048	2048	2048	2048	24576	24576	24576
2c	2048	2048	2048	2048	17408	40960	32768

Interestingly, amide-containing PDAs **2a–2c** underwent a dramatic loss of CP/MAS signal upon conversion to the annulated intermediate polymers (heating to either 400 or 500 ˚C, see Figure 2.2) en-route to $[8]_A$GNR. The CP/MAS signal returned upon final aromatization to $[8]_A$GNR. This behavior was not noted in *para*-acetophenone PDA **1**. To showcase this phenomenon, a series of spectra were acquired where the number of scans was held constant at 2048 and peak heights were not normalized. These four series of spectra are shown in Figures A24–A27 below. The origin of this phenomenon is currently under investigation in our group.

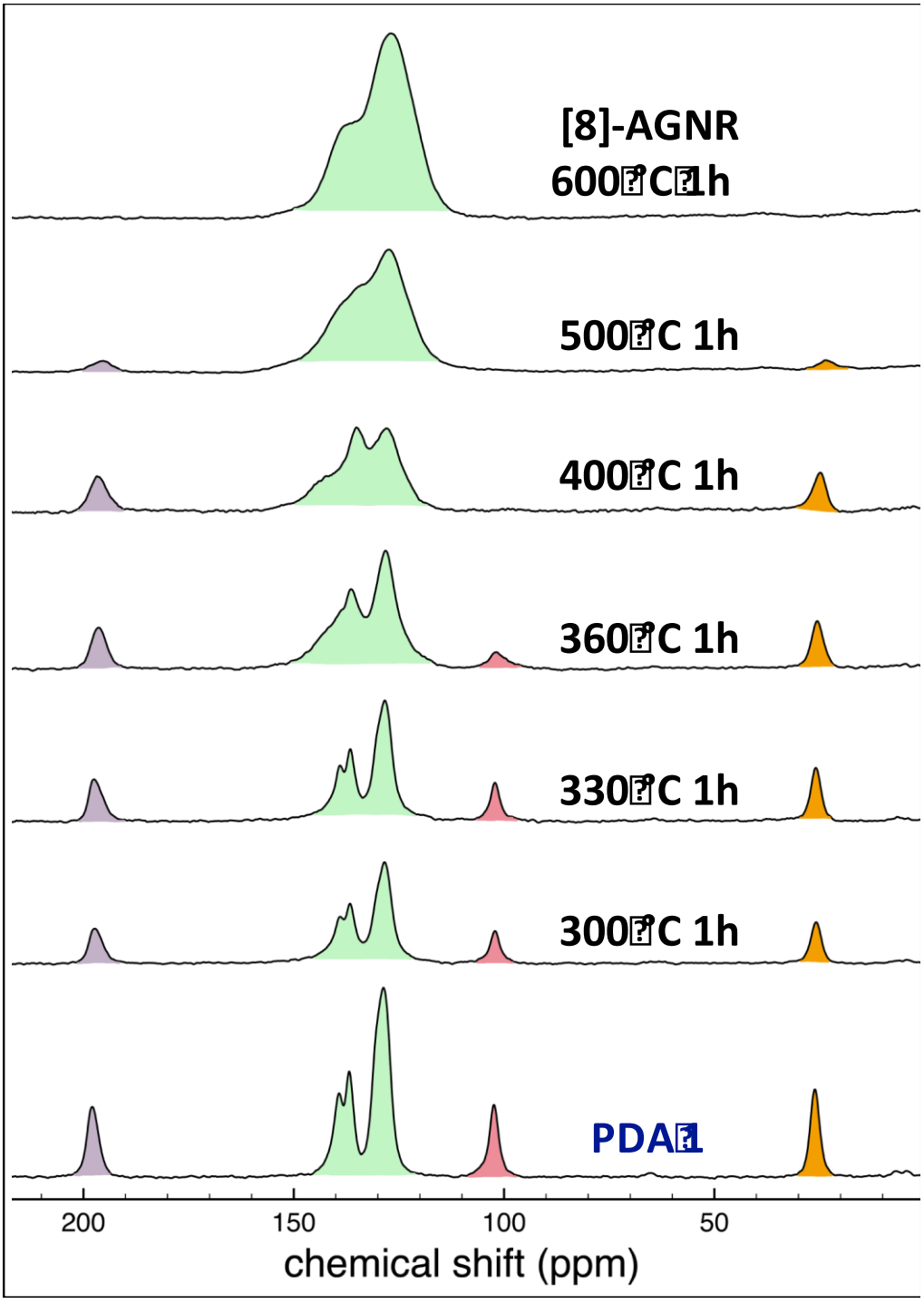

Figure A24. Stacked CP/MAS ^{13}C NMR spectra of the conversion of PDA **1** to $[8]_A$GNR with constant number of scans (2048) and no peak height normalization. No significant loss of signal was noted at these temperatures within this system.

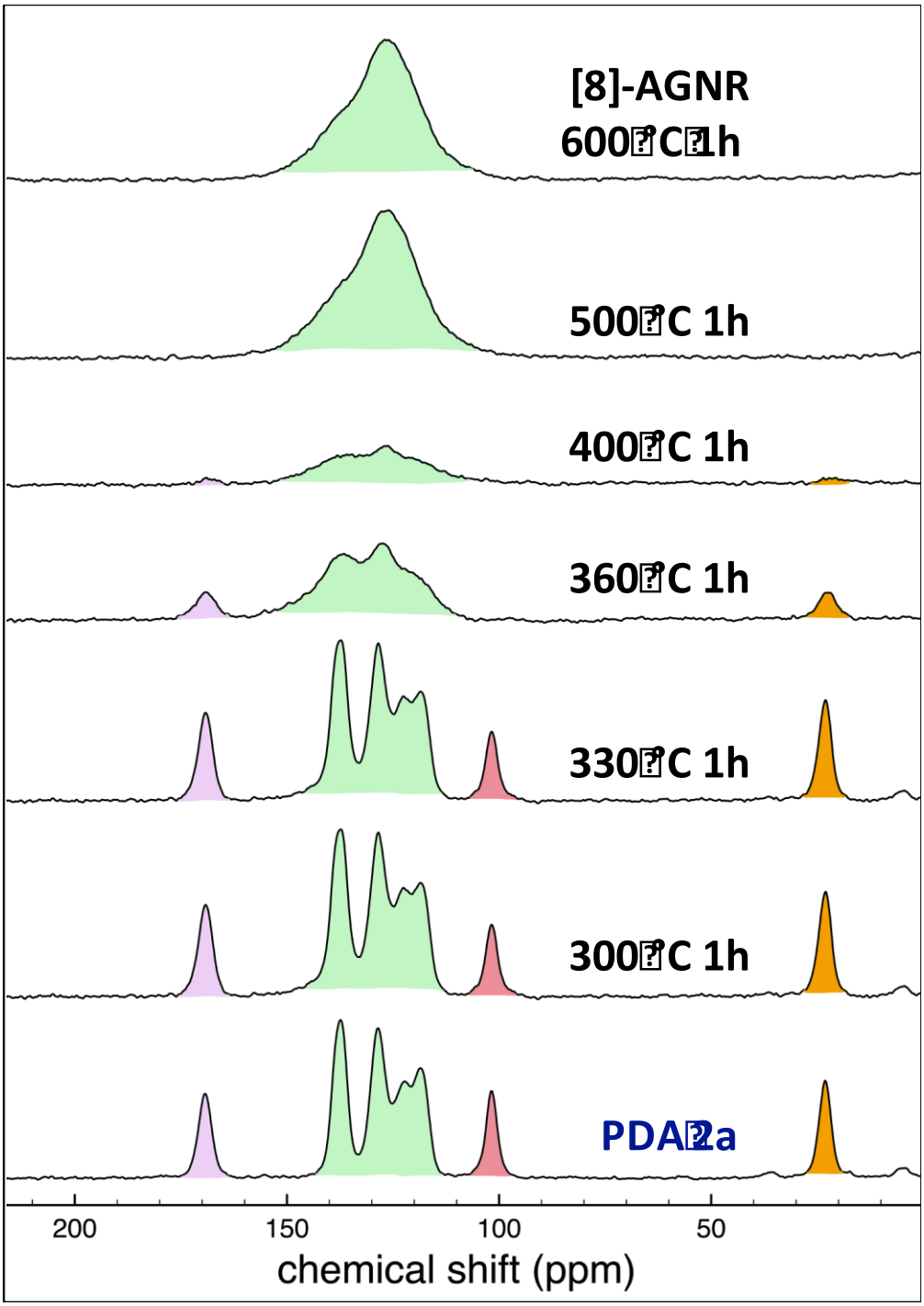

Figure A25. Stacked CP/MAS ^{13}C NMR spectra of the conversion of PDA **2a** to $[8]_A$GNR with constant number of scans (2048) and no peak height normalization. Note the large reduction and recovery of signal for samples heated at 360, 400, and 500 ˚C.

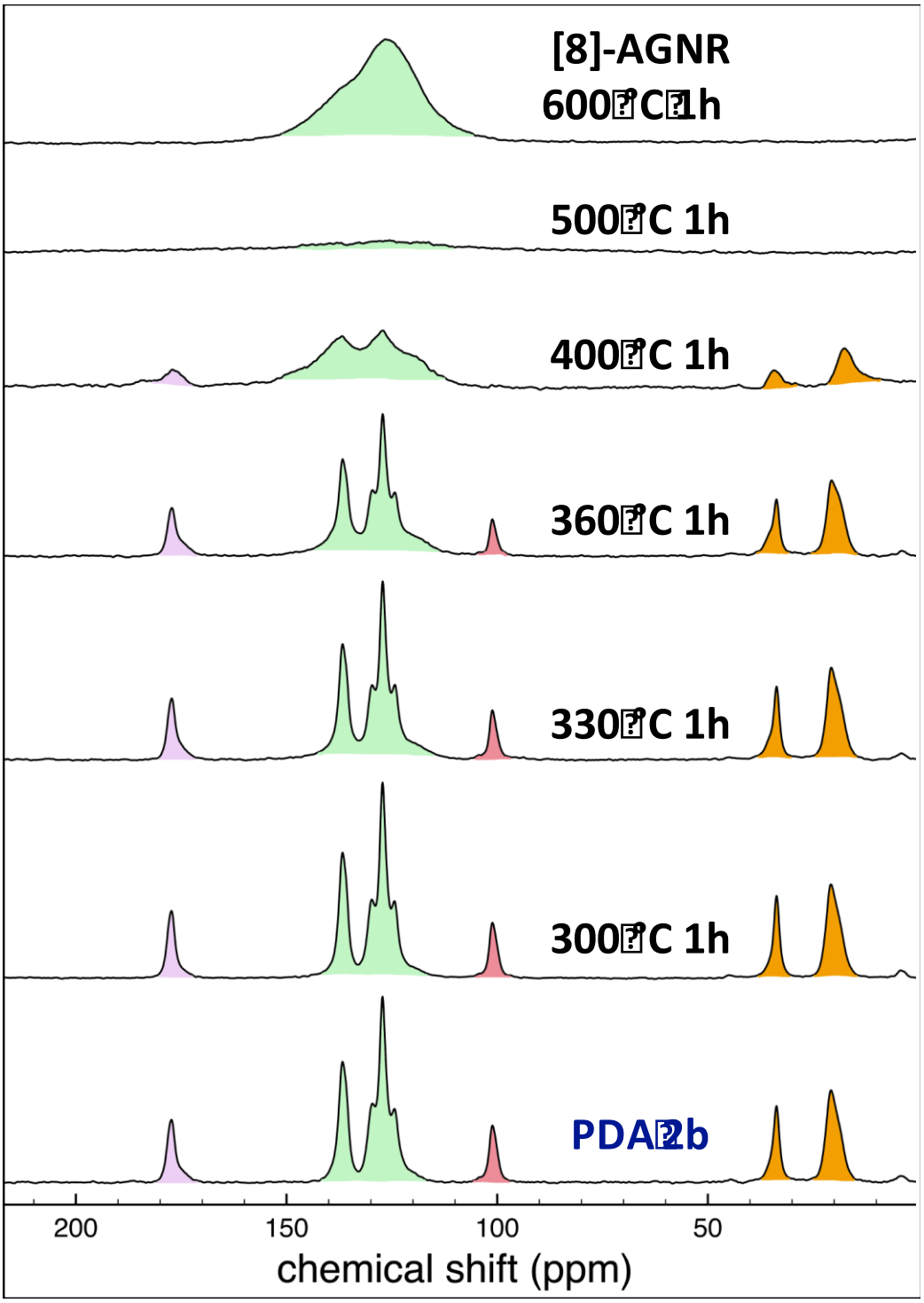

Figure A26. Stacked CP/MAS ^{13}C NMR spectra of the conversion of PDA **2b** to $[8]_A$GNR with consistent number of scans (2048) and no peak height normalization. Note the dramatic loss and recovery of signal for samples heated at 400, 500, and 500 ˚C.

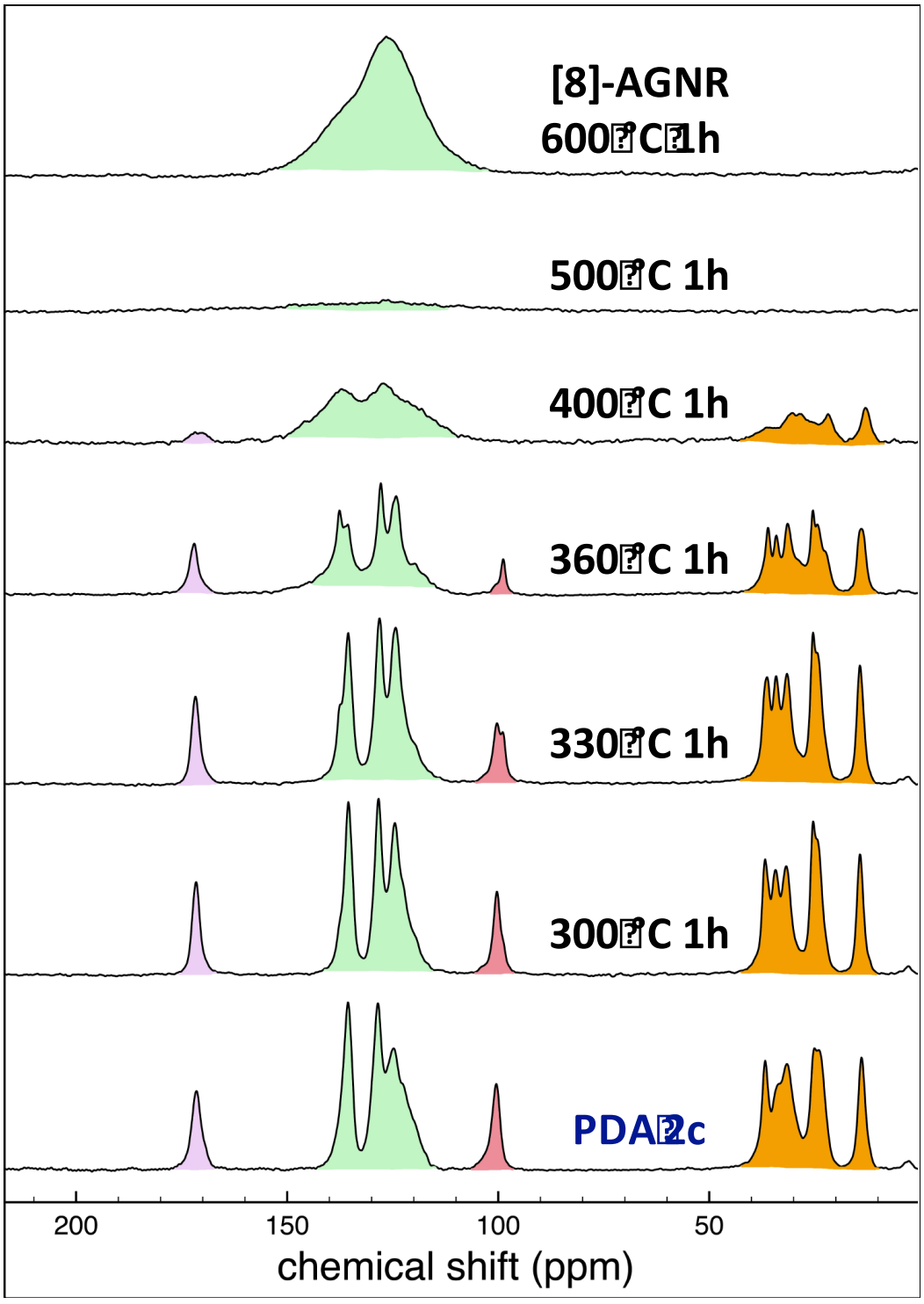

Figure A27. Stacked CP/MAS ^{13}C NMR spectra of the conversion of PDA **2c** to $[8]_AGNR$ with consistent number of scans (2048) and no peak height normalization. Note the dramatic loss and recovery of signal for samples heated at 400, 500, and 500 ˚C.

viii) ^{1}H and ^{13}C NMR spectra for compounds **7a**, **4a**, **7b and 4b**.

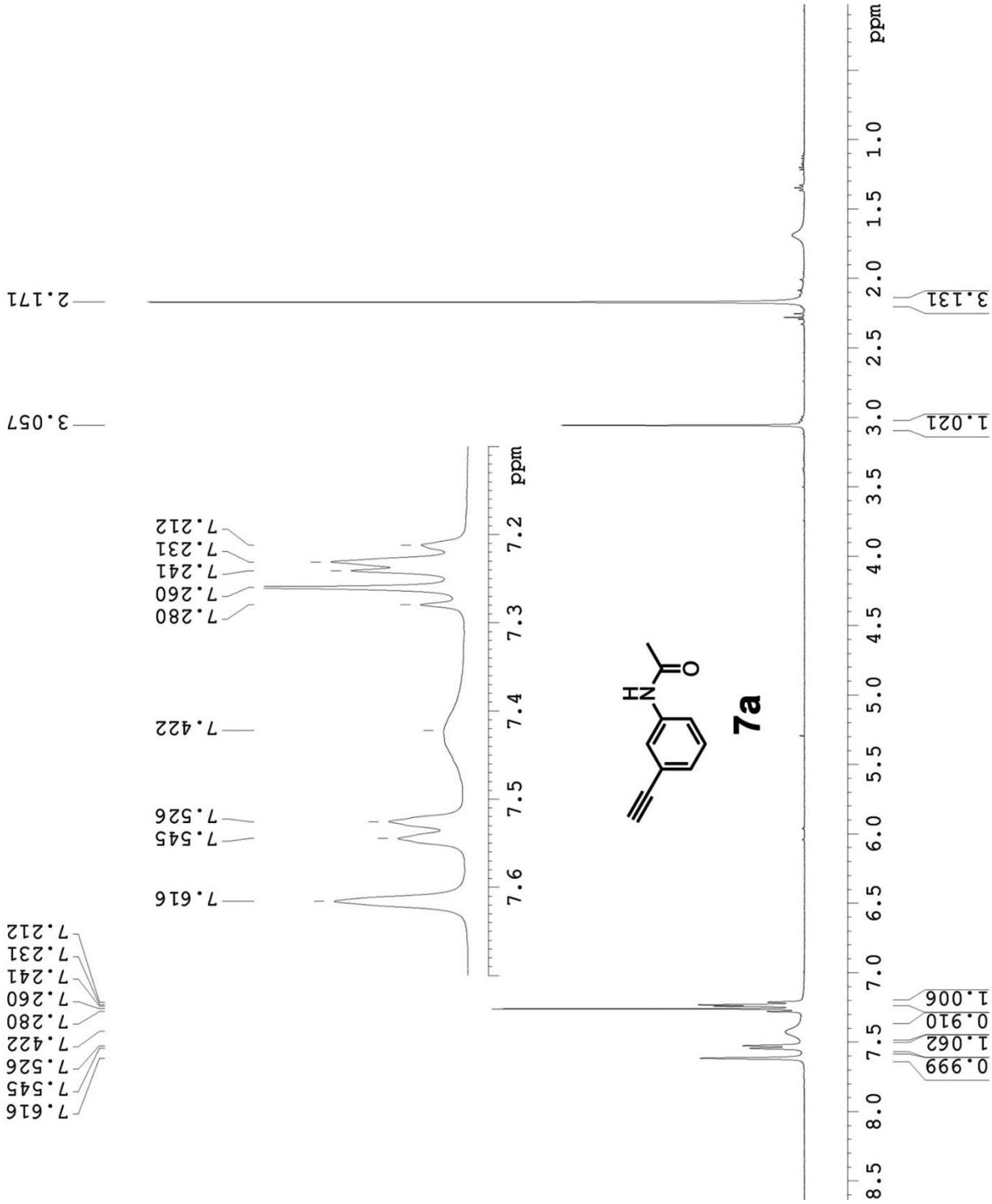

Figure **A28**: ^{1}H NMR spectrum of compound **7a**.

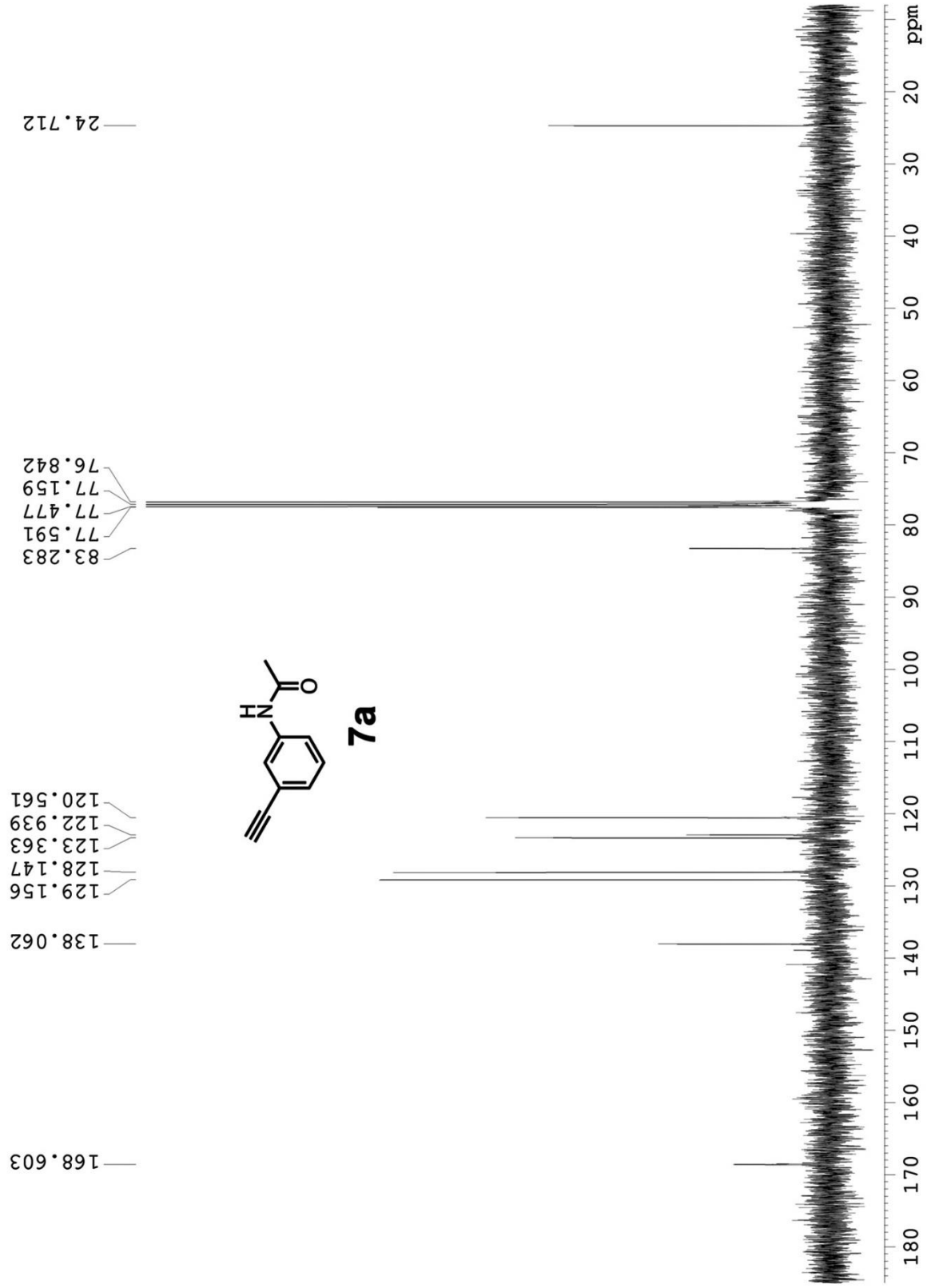

Figure A**29**: ^{13}C NMR spectrum of compound **7a**.

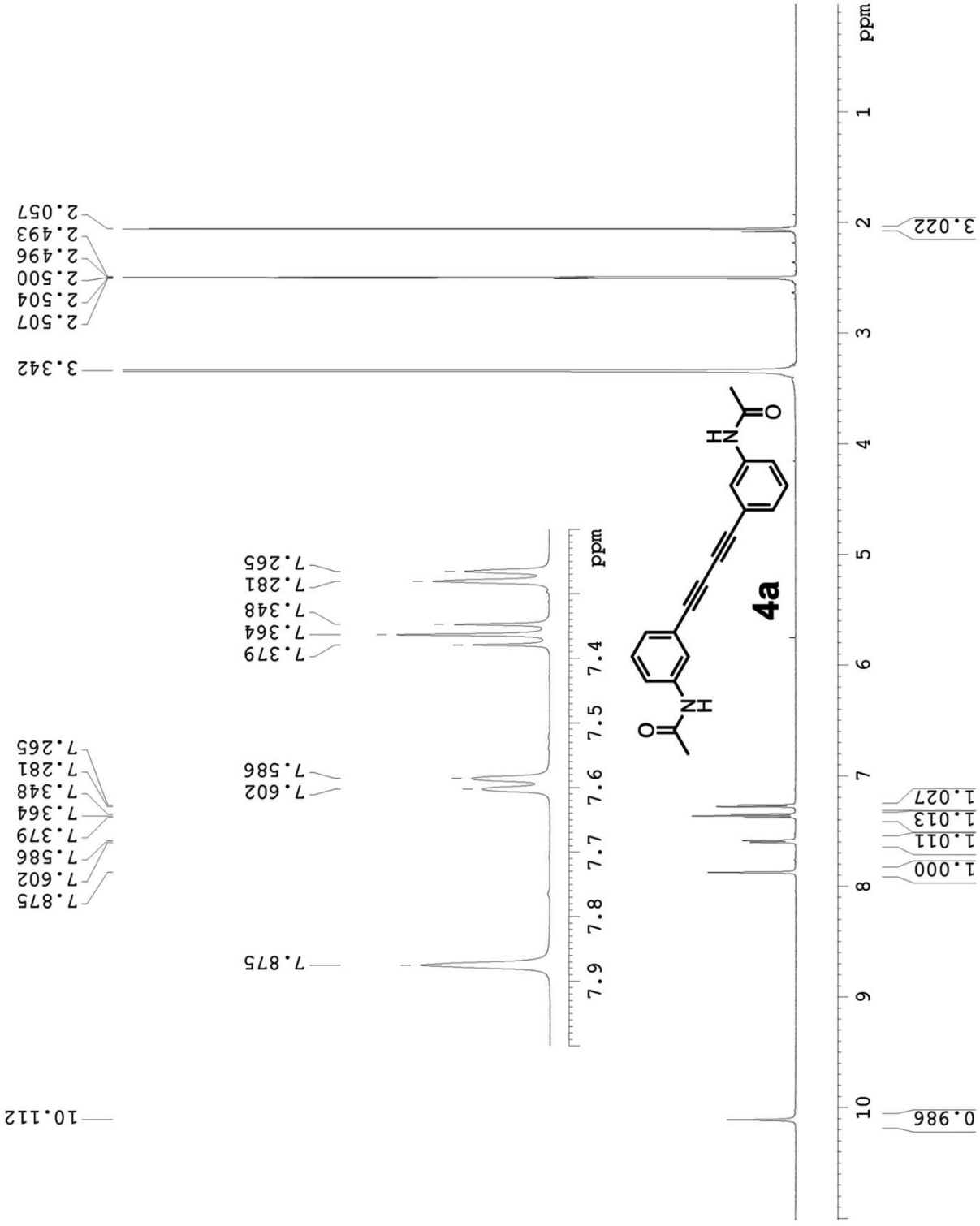

Figure **A30**: [1]H NMR spectrum of compound **4a**.

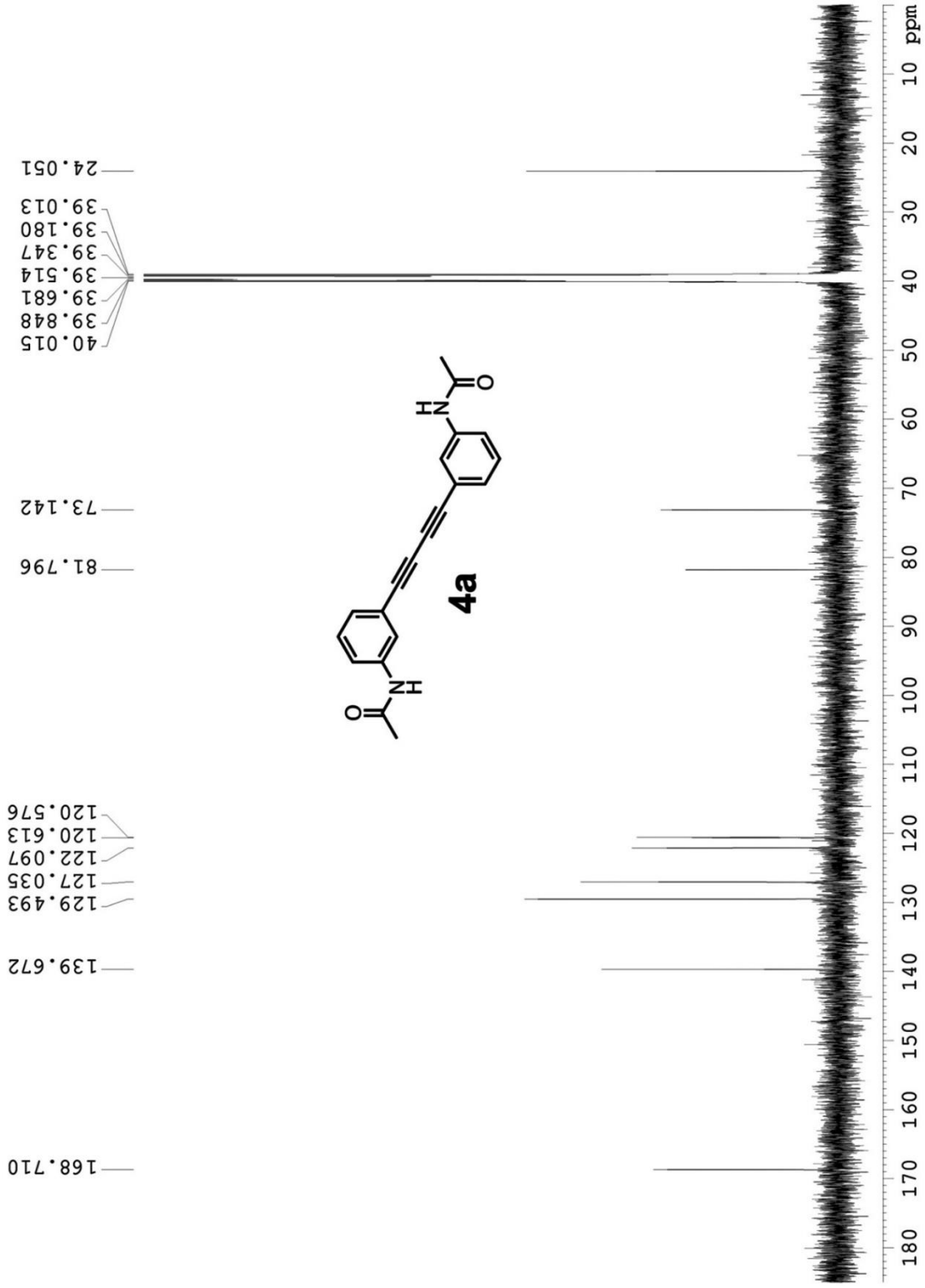

Figure **A31**: ^{13}C NMR spectrum of compound **4a**.

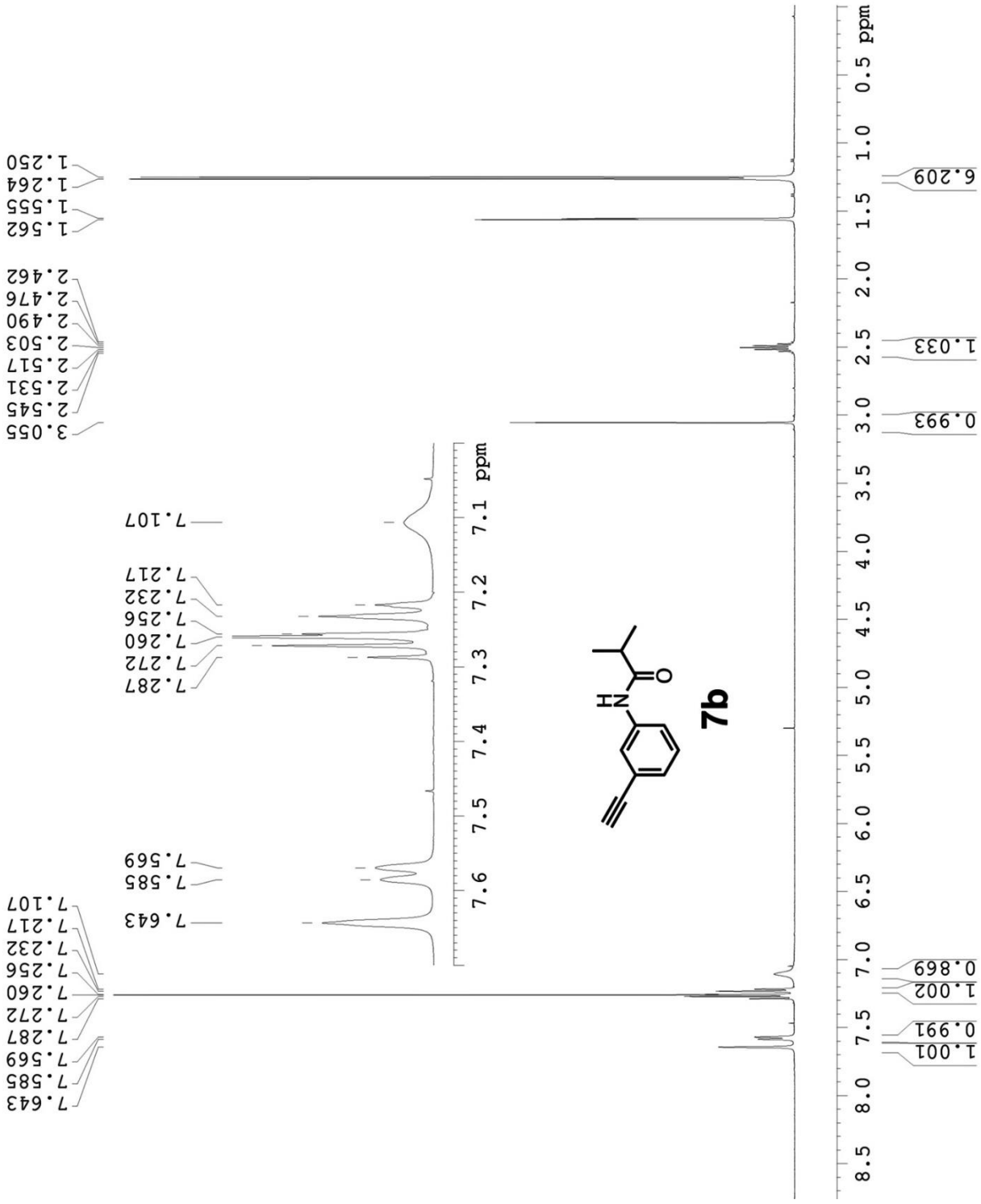

Figure **A32**: ^{1}H NMR spectrum of compound **7b**.

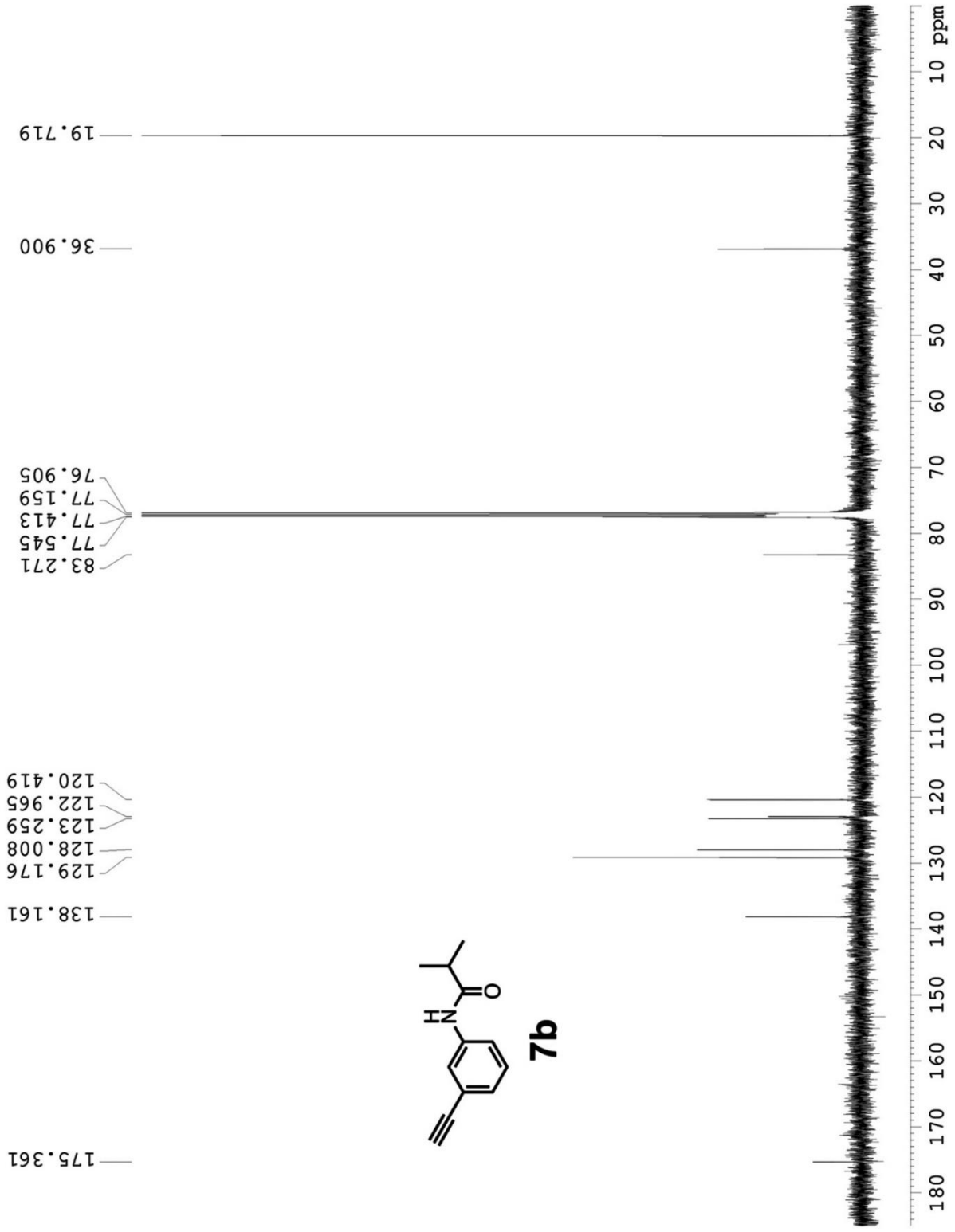

Figure A33: ^{13}C NMR spectrum of compound **7b**.

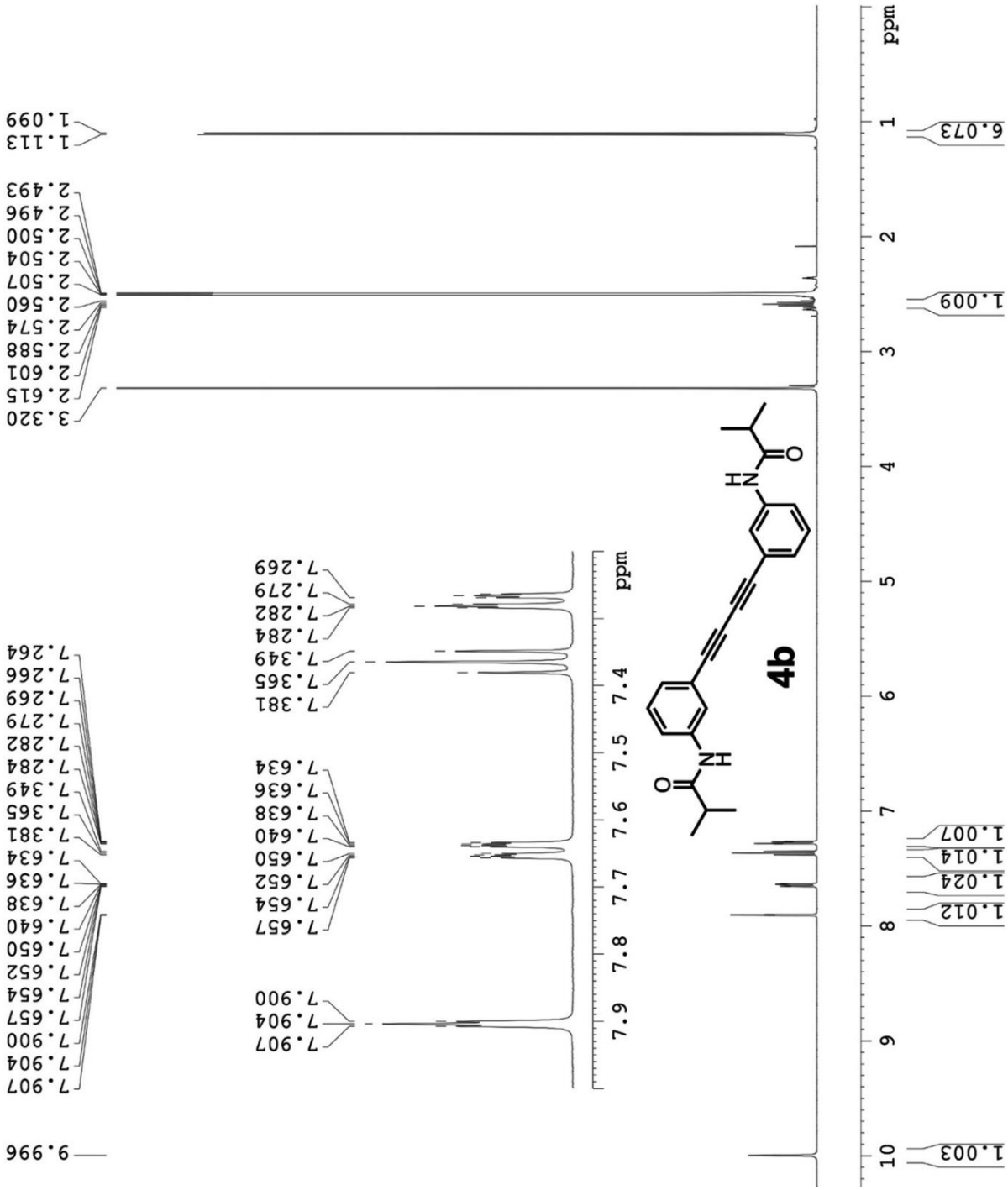

Figure A34: ^{1}H NMR spectrum of compound **4b**.

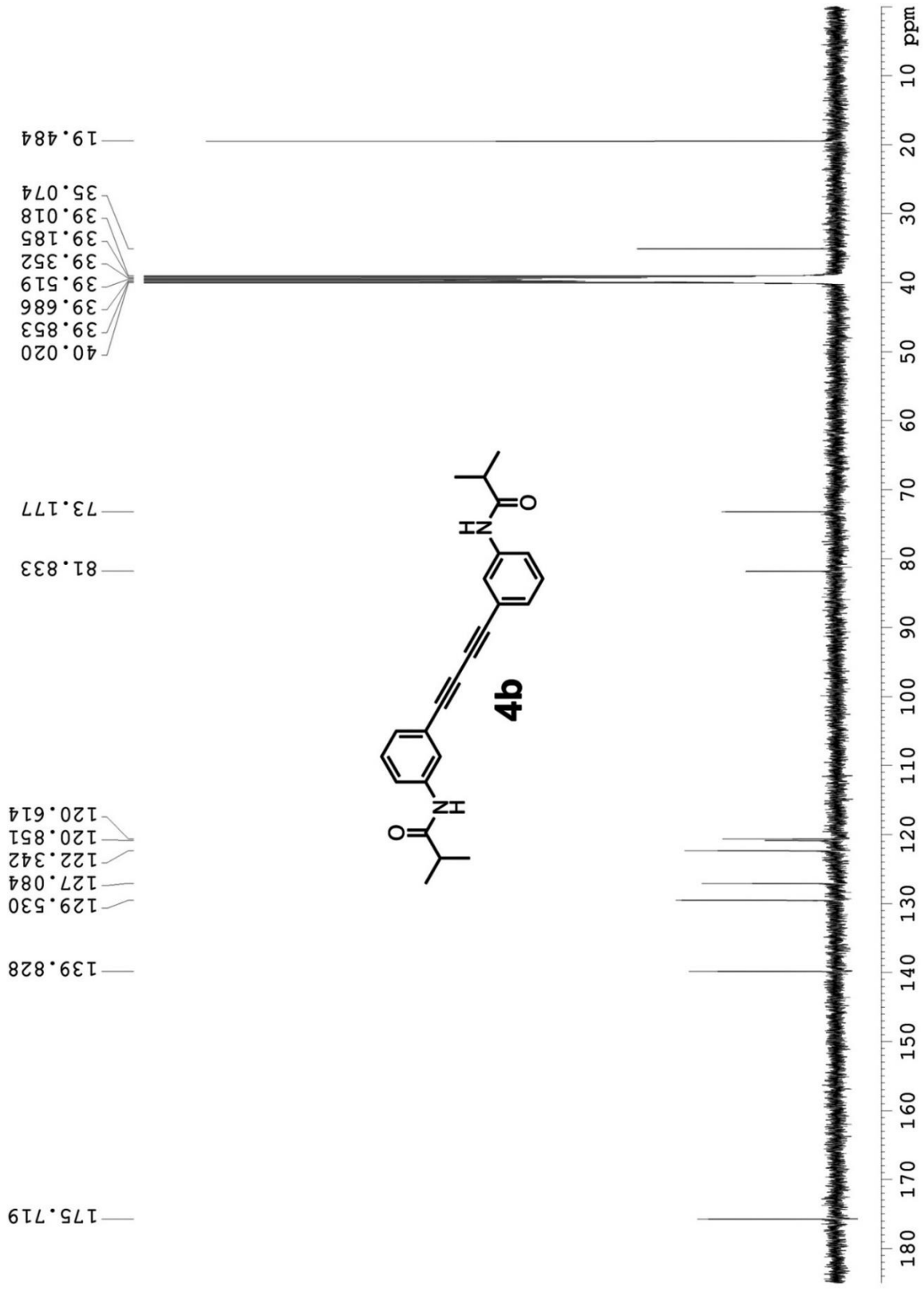

Figure A35: ^{13}C NMR spectrum of compound **4b**.

***Section 3**: Details of Computational Investigations*

All geometries were fully optimized at the B3LYP/6-31G(d) level of theory in the gas phase.[31] All optimized geometries were verified by frequency computations as minima (no imaginary frequencies) or transition structures (one imaginary frequency). Frequency analysis was performed at 623.15 K, and frequency values discussed in the text were scaled using a factor 0.98.[54,55] Free energy corrections were calculated using Truhlar's quasiharmonic approximation, which sets all the real vibrational frequencies that are lower than 100 cm^{-1} to 100 cm^{-1} to correct entropies for the breakdown of the harmonic oscillator approximation.[56,57] Subsequent single-point energy calculations on the optimized structures were performed using the M06-2X/6-311+G(d,p) level of theory. The thermal corrections calculated from the scaled vibrational frequencies at the B3LYP/6-31G(d) level on the optimized geometries were then added to the M06-2X/6-311+G(d,p) electronic energies to obtain the Gibbs free energies. All quantum chemical computations were performed using Gaussian 09.[32] All graphics on optimized structures were generated with CYLview.[58]

Conformational searches were carried out with *MacroModel* from *Schrödinger* using OPLS_2005 and an energy window of 10.0 kcal mol^{-1}. A redundant conformer elimination was performed using an energy window of 10.0 kcal mol^{-1} and a maximum atom deviation cutoff of 0.5 Å. The lowest energy conformers were optimized with B3LYP/6-31G(d) to locate the global minimum for each reaction.

ix) Model systems

The cycloisomerization of PDA model compounds **5** and **6** is expected to proceed through a 6-π electrocyclization pathway, the favored pathway of dienynes for reaction temperatures under 550°C.[30] Previously, Prall *et al.*[29] computed the mechanistic pathway of the thermal cyclization of hexa-1,3-dien-5-yne **8a** (Scheme S1). The initial 6π electrocyclization forms isobenzene intermediate **8a-*cycl***, which subsequently undergoes two consecutive [1,2]-H shifts and rearomatizes to the final product benzene. This study established the first [1,2]-H shift (**8a-*H-shift***) from the allenic intermediate as the rate-determining step, with an enthalpic barrier of 38.4 kcal mol^{-1} relative to the starting dienyne (computed using BCCD(T)/cc-pVCZ//BLYP/6-31G(d)). The results are tabulated in Table S2.

Scheme A1. Mechanistic pathway of hexa-1,3-dien-5-yne (**8a**).

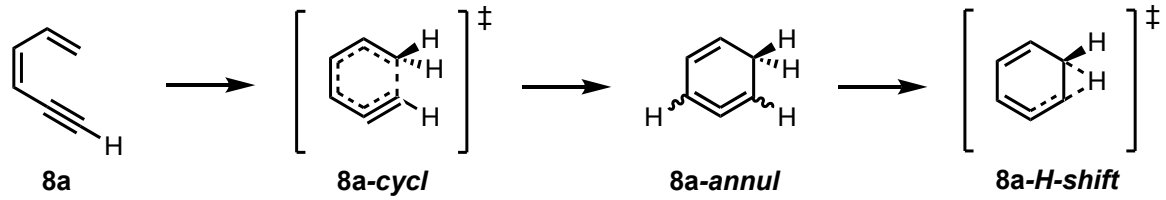

We sought to explore a set of four test structures **8a**–**11a**, the former two in order to validate our method compared to calculations by Prall *et al*. (Schemes S1 and S2), and the latter two to probe the effect of π-extension of **8a** on reaction barriers (Schemes S3 and S4). We computed the reaction barriers to **8a-*cycl*** and **8a-*H-shift***, which are 40.2 and 44.0 kcal mol^{-1}, respectively (Table S2). For the benzannulated system **9a** (Scheme S2), the barriers for **9a-*cycl*** and **9a-*H-shift*** increase to 46.6 and 51.1 kcal mol^{-1}, respectively, as would be expected to due to the breaking of aromaticity necessary for cyclization to occur. Enthalpies of rate-determining barriers for **8a** and **9a** are within 3 kcal mol^{-1} of those calculated by Prall *et al*.

Scheme A2. Mechanistic pathway of 1-ethynyl-2-vinylbenzene (**9a**).

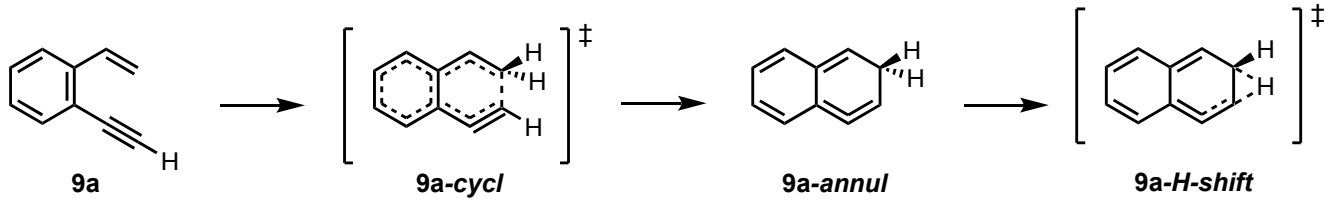

Next, we explored the effect of extending the π-system, as is the case in the PDAs. Phenyl fusion at the 3,4-positions of (*E*)-hexa-3,5-dien-1-yn-3-ylbenzene (**10a**) does not affect the reaction barriers, which stay approximately the same as those for **8a** (37.6 and 46.3 kcal mol^{-1} for **10a-*cycl*** and **10a-*H-shift***, respectively). However, (*Z*)-but-1-en-3-yn-1-ylbenzene **11a** (Scheme S4) has much high reaction barriers of 54.1 and 58.4 kcal mol^{-1} for **11a-*cycl*** and **11a-*H-shift***, respectively. The increases in the energetic barriers of the rate-determining steps of **9a** and **11a** are due to the necessity to interrupt the aromaticity of the benzene ring.

Scheme A3. Mechanistic pathway of (*E*)-hexa-3,5-dien-1-yn-3-ylbenzene (**10a**).

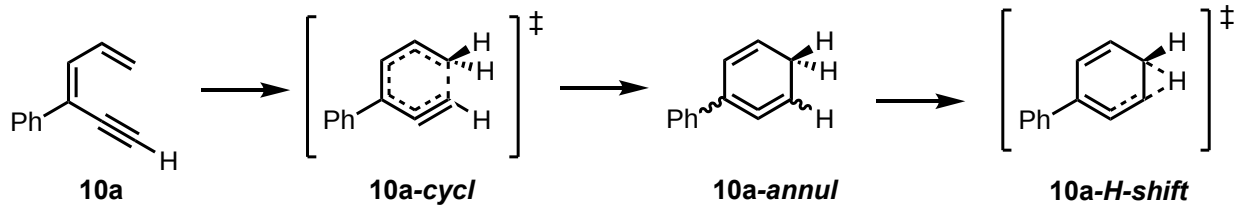

10a **10a-*cycl*** **10a-*annul*** **10a-*H-shift***

Scheme A4. Mechanistic pathway of *cis*-2-ethynyl-1-phenylethene (**11a**).

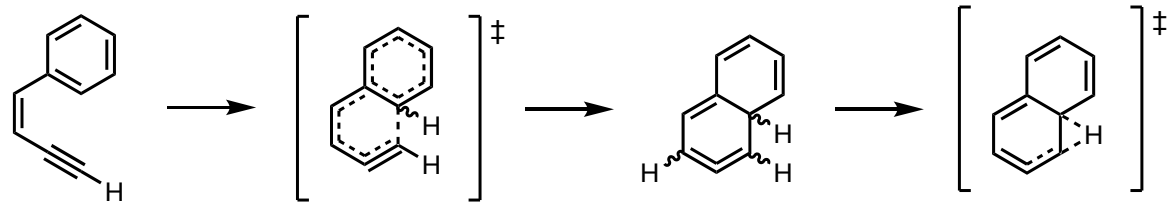

11a **11a-*cycl*** **11a-*annul*** **11a-*H-shift***

Table A2. Computed energetics of pathway intermediates in kcal mol^{-1} relative to starting dienynes **8a**, **9a**, **10a**, and **11a**.

		cycl	***annul***	***H-shift***
8a	$\Delta H/\Delta H^{\neq}$ [a]	31.7	7.9	39.4
	$\Delta H/\Delta H^{\neq}$	34.5	11.8	36.7
	$\Delta G/\Delta G^{\neq}$	40.2	17.5	44
9a	$\Delta H/\Delta H^{\neq}$ [a]	36.4	25.5	46
	$\Delta H\Delta H^{\neq}$	41.3	32.9	44.4
	$\Delta G/\Delta G^{\neq}$	46.6	37.6	51.1
10a	$\Delta H\Delta H^{\neq}$	32.4	34	39.7
	$\Delta G/\Delta G^{\neq}$	37.6	39.3	46.3
11a	$\Delta H\Delta H^{\neq}$	48.9	44.7	52.7

	$\Delta G/\Delta G^{\neq}$	54.1	48.4	58.4

[a] Computed by Prall et al[17] using BCCD(T)/cc-pVDZ//BLYP/6-31G(d).

x) *trans*-Enediyne 5

Scheme A5. Mechanistic pathway for the *trans*-enediyne **5** model system.

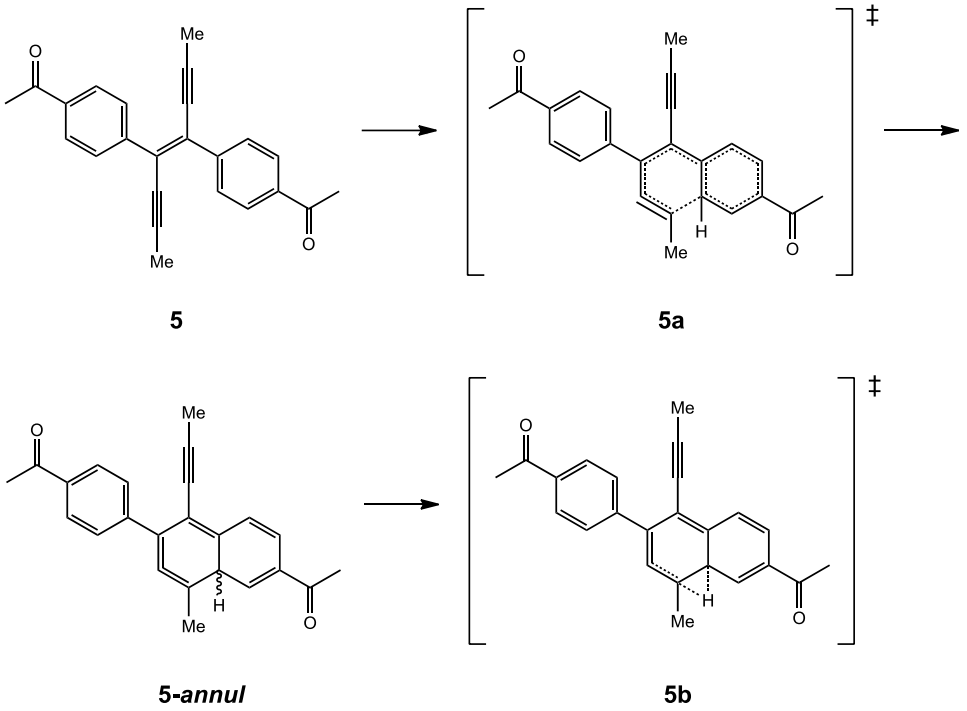

Table A3. Computed energetics in kcal mol^{-1} relative to *trans*-enediyne 5.

Structure	$\Delta H/\Delta H^{\neq}$	$\Delta G/\Delta G^{\neq}$
5a	47.5	52.6
5-*annul*	41.6	45.5
5b	52.9	58.4

xi) *trans*-Enediyne **6**.

Scheme A6. Mechanistic pathway of *trans*-enediyne **6** model system.

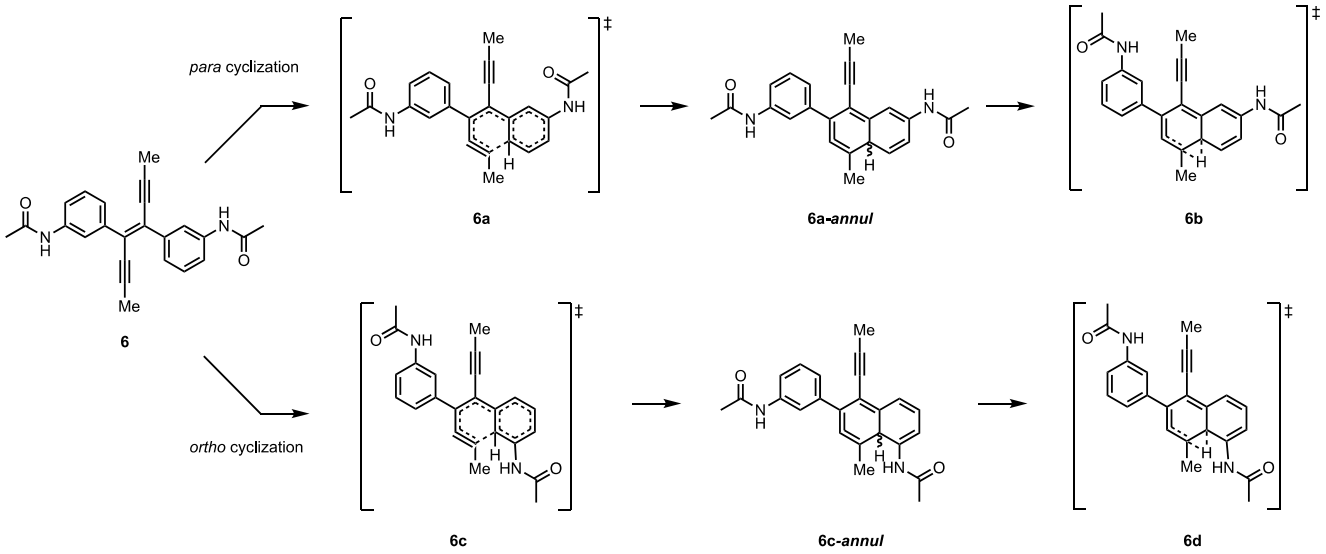

Table A4. Computed energetics in kcal mol^{-1} relative to *trans*-enediyne **6**.

Structure	$\Delta H/\Delta H^{\neq}$	$\Delta G/\Delta G^{\neq}$
6a	48.2	52.5
6a-*annul*	38.6	42.0
6b	52.3	57.5
6c	50.5	55.4
6c-*annul*	37.8	41.5
6d	58.8	64.3

Frequencies and IR intensities

Calculated IR spectra were obtained using DFT. Optimization of ground state structures were performed in the gas phase using B3LYP/6-31G(d), and subsequent frequency calculations were performed at the same level of theory. Frequency values were subsequently scaled according to the previously determined scale factor of 0.98 for B3LYP/6-31G(d).[9,10] Each frequency (cm^{-1}), scaled frequency (cm^{-1}), IR intensity, and vibrational mode symmetry for $[8]_A$GNR, PDA **1**, and PDA **1-*annul*** is tabulated below.

$[8]_A$GNR model system (computed structure described in Fig. S22)

3.7591, 3.6839, 0.0126, A
10.8839, 10.6662, 0.0000, B
11.6690, 11.4356, 0.0000, A
14.5886, 14.2968, 0.0000, B
18.2999, 17.9339, 0.0038, A
23.2288, 22.7642, 0.0201, A
26.4301, 25.9015, 0.0000, B
33.9612, 33.282, 0.0000, B
35.1583, 34.4551, 0.0002, A
42.0545, 41.2134, 0.0011, A
42.6379, 41.7851, 0.0000, B
43.8158, 42.9395, 0.0763, B
47.5128, 46.5625, 0.0000, B
48.2518, 47.2868, 0.0003, A
49.4408, 48.452, 0.1252, A
49.7479, 48.7529, 0.0000, B
76.1991, 74.6751, 3.0455, A
80.3517, 78.7447, 0.0000, B
86.2615, 84.5363, 0.6570, A
93.5868, 91.7151, 0.0000, A
93.9562, 92.0771, 0.0000, B
99.5475, 97.5566, 0.0000, A
104.1331, 102.0504, 0.5201, A
114.0138, 111.7335, 0.0000, B
122.5015, 120.0515, 0.0074, A
135.5879, 132.8761, 0.0000, B
152.5565, 149.5054, 0.1740, B
153.7651, 150.6898, 0.1639, A
168.9970, 165.6171, 0.0000, B
177.5502, 173.9992, 0.1212, A
182.4801, 178.8305, 0.0000, B
184.1532, 180.4701, 0.9670, A
185.2072, 181.5031, 0.0000, B
188.9498, 185.1708, 0.0397, A
192.6506, 188.7976, 5.9351, B
192.6852, 188.8315, 0.0018, B
194.3778, 190.4902, 0.0000, B
194.4768, 190.5873, 0.0105, A
203.9246, 199.8461, 0.0000, A
232.8023, 228.1463, 0.0121, A

233.3387, 228.6719, 0.0000, B
245.9956, 241.0757, 0.0000, B
249.1636, 244.1803, 0.0000, A
249.7145, 244.7202, 0.3948, B
249.9368, 244.9381, 0.9146, A
264.1529, 258.8698, 0.1562, A
272.5594, 267.1082, 0.0000, B
276.9627, 271.4234, 1.4216, B
279.7361, 274.1414, 0.0000, A
286.7408, 281.006, 0.0000, A
287.4821, 281.7325, 0.0000, B
294.9906, 289.0908, 0.7120, A
310.9867, 304.767, 0.0000, A
313.5329, 307.2622, 0.0000, B
313.9190, 307.6406, 0.3408, A
316.4644, 310.1351, 0.1147, B
329.5677, 322.9763, 1.0994, A
333.8510, 327.174, 0.0000, B
334.8777, 328.1801, 1.2636, B
338.1115, 331.3493, 0.0000, A
341.6509, 334.8179, 0.0705, A
345.2419, 338.3371, 0.0000, B
346.2704, 339.345, 7.1672, B
349.9989, 342.9989, 0.0000, B
350.2446, 343.2397, 0.0044, A
350.2551, 343.25, 4.9191, B
350.5981, 343.5861, 0.0000, A
352.2443, 345.1994, 0.0000, B
357.0980, 349.956, 0.0000, A
357.1480, 350.005, 5.7770, A
361.1008, 353.8788, 1.0260, A
366.6995, 359.3655, 0.2860, A
367.2729, 359.9274, 0.0000, B
369.6219, 362.2295, 0.0000, A
376.4362, 368.9075, 0.0000, B
381.8717, 374.2343, 4.8560, B
386.3403, 378.6135, 0.0243, A
388.6468, 380.8739, 0.0001, B
393.1716, 385.3082, 1.8966, B
401.1684, 393.145, 0.0000, B
401.6419, 393.6091, 0.0091, A
401.7257, 393.6912, 0.0001, A
404.3065, 396.2204, 0.5854, B
406.5664, 398.4351, 0.3339, A
422.3602, 413.913, 0.0000, A
440.1450, 431.3421, 0.0000, B
446.7792, 437.8436, 0.0000, A
452.3757, 443.3282, 0.0000, A
453.5989, 444.5269, 0.1769, B
456.4595, 447.3303, 0.2985, B
459.2374, 450.0527, 0.2156, A
462.3576, 453.1104, 0.0000, B
471.9556, 462.5165, 1.7063, B
476.0943, 466.5724, 0.0012, A
477.3425, 467.7956, 0.7125, B
478.5801, 469.0085, 0.0000, A
496.6771, 486.7436, 0.0001, B
497.4026, 487.4545, 5.0884, B
498.7857, 488.81, 0.0000, A
498.9805, 489.0009, 0.0001, B
499.2230, 489.2385, 0.4767, A
500.2216, 490.2172, 0.0000, A
501.3032, 491.2771, 0.3861, A
507.0061, 496.866, 0.0000, B

509.6238, 499.4313, 0.0000, B
513.2479, 502.9829, 0.0372, A
515.5001, 505.1901, 0.0035, A
517.5113, 507.1611, 2.8243, B
520.3471, 509.9402, 0.0000, B
521.8552, 511.4181, 0.0000, A
528.7574, 518.1823, 0.0000, B
529.6322, 519.0396, 0.0148, A
530.0907, 519.4889, 0.0000, B
533.3298, 522.6632, 0.4724, B
540.9562, 530.1371, 0.0593, A
543.2185, 532.3541, 0.0000, A
545.1332, 534.2305, 13.1894, B
549.1266, 538.1441, 0.0000, B
550.7969, 539.781, 0.0000, A
552.1976, 541.1536, 0.0004, A
555.8190, 544.7026, 0.0000, B
560.9573, 549.7382, 0.0114, A
563.5558, 552.2847, 4.2220, B
565.3737, 554.0662, 0.0000, A
570.0412, 558.6404, 0.0126, A
570.2190, 558.8146, 0.0000, B
573.6140, 562.1417, 0.0034, A
576.1594, 564.6362, 0.0000, B
577.8978, 566.3398, 2.7637, B
580.4089, 568.8007, 0.0000, B
583.6118, 571.9396, 0.0000, A
584.2918, 572.606, 0.1380, B
587.0477, 575.3067, 0.5039, B
589.1559, 577.3728, 0.0000, A
589.3474, 577.5605, 0.1026, A
592.7261, 580.8716, 28.8549, B
593.1048, 581.2427, 0.0000, A
593.1269, 581.2644, 0.0000, B
603.9262, 591.8477, 0.0000, A
604.7560, 592.6609, 1.8705, B
605.8853, 593.7676, 0.1025, A
607.8722, 595.7148, 3.1958, A
610.4395, 598.2307, 0.0000, A
610.7472, 598.5323, 0.0000, B
611.7044, 599.4703, 2.2019, A
613.5443, 601.2734, 0.0000, B
615.2864, 602.9807, 0.5971, B
618.1732, 605.8097, 0.1081, A
619.0734, 606.6919, 0.0000, B
623.6230, 611.1505, 0.2398, A
625.1653, 612.662, 0.0583, A
625.6214, 613.109, 0.0000, B
628.7107, 616.1365, 13.6543, B
629.0733, 616.4918, 0.0000, A
635.1430, 622.4401, 1.1676, B
638.9920, 626.2122, 0.0000, A
639.1632, 626.3799, 0.0000, B
643.0124, 630.1522, 0.0000, A
643.5365, 630.6658, 0.1967, B
644.7215, 631.8271, 0.0000, B
648.4611, 635.4919, 0.0000, A
649.7076, 636.7134, 3.0663, B
652.1903, 639.1465, 0.0000, A
653.7435, 640.6686, 0.8471, A
658.5373, 645.3666, 0.4219, A
658.6728, 645.4993, 0.6009, B
659.4952, 646.3053, 0.0000, B
660.6409, 647.4281, 0.0000, B

661.8493, 648.6123, 0.1538, A
665.3076, 652.0014, 0.0000, A
670.5431, 657.1322, 0.2593, A
671.9723, 658.5329, 0.8113, B
673.7102, 660.236, 0.0000, B
678.8123, 665.2361, 0.0000, B
679.6176, 666.0252, 1.1043, A
688.1951, 674.4312, 0.0000, A
693.5983, 679.7263, 0.0673, B
695.4233, 681.5148, 0.2805, A
695.4700, 681.5606, 0.0000, B
708.1646, 694.0013, 2.6308, B
709.3357, 695.149, 0.0000, A
715.5111, 701.2009, 0.0000, B
717.8584, 703.5012, 2.1038, A
718.5596, 704.1884, 1.6357, A
720.5653, 706.154, 0.0000, B
720.7186, 706.3042, 0.0299, A
721.4551, 707.026, 0.0000, B
721.7214, 707.287, 0.0000, A
723.8436, 709.3667, 0.2435, A
725.9343, 711.4156, 0.0000, B
726.8826, 712.3449, 0.0000, B
728.6187, 714.0463, 1.3008, B
728.6614, 714.0882, 0.1145, A
734.3201, 719.6337, 0.0012, A
734.5021, 719.8121, 8.6358, A
736.8139, 722.0776, 0.0000, B
738.7250, 723.9505, 1.2750, A
745.2001, 730.2961, 0.0000, B
747.7613, 732.8061, 0.0000, A
751.6202, 736.5878, 6.0615, B
755.6521, 740.5391, 0.0000, A
758.3163, 743.15, 0.4256, B
763.0804, 747.8188, 24.8056, A
763.0809, 747.8193, 0.0001, B
764.9479, 749.6489, 13.9904, B
778.0750, 762.5135, 0.4567, B
785.8264, 770.1099, 0.0000, A
789.8066, 774.0105, 0.0000, A
792.0736, 776.2321, 0.0000, B
792.0754, 776.2339, 12.3643, A
802.7927, 786.7368, 2.0508, B
808.6675, 792.4941, 0.0003, A
810.4191, 794.2107, 69.0274, A
810.4347, 794.226, 0.0000, B
810.9817, 794.7621, 5.3575, A
811.2008, 794.9768, 0.0000, B
812.2162, 795.9719, 0.0000, B
812.7188, 796.4644, 3.7300, A
814.1237, 797.8412, 7.2283, A
814.8360, 798.5393, 0.0000, B
816.7531, 800.418, 0.0000, B
817.6703, 801.3169, 29.8940, A
819.8887, 803.4909, 0.0725, A
820.4873, 804.0776, 0.0000, B
821.9562, 805.5171, 0.0000, B
821.9674, 805.5281, 0.7357, B
822.4023, 805.9543, 208.1540, A
832.8949, 816.237, 0.0001, B
832.8985, 816.2405, 80.8806, A
835.8092, 819.093, 19.3441, B
837.5469, 820.796, 0.0001, A
860.1695, 842.9661, 0.0000, A

867.6021, 850.2501, 0.0016, B
873.7732, 856.2977, 0.0000, A
875.5550, 858.0439, 0.0013, A
875.6173, 858.105, 0.0000, B
877.8762, 860.3187, 5.5877, B
890.8357, 873.019, 0.0000, B
890.8543, 873.0372, 2.6255, A
893.4871, 875.6174, 0.0000, A
893.8305, 875.9539, 4.6603, B
899.0747, 881.0932, 0.0982, A
900.9841, 882.9644, 0.0000, A
902.3163, 884.27, 0.0001, B
908.4103, 890.2421, 113.3481, B
908.9469, 890.768, 0.0030, B
910.7514, 892.5364, 52.2533, B
911.4576, 893.2284, 0.1425, A
920.2437, 901.8388, 0.0010, A
922.1167, 903.6744, 0.0010, B
922.5767, 904.1252, 169.6376, B
926.8561, 908.319, 0.0000, A
930.7609, 912.1457, 0.0000, A
930.8569, 912.2398, 0.0000, B
932.2854, 913.6397, 0.1347, A
939.5236, 920.7331, 0.0855, A
940.6880, 921.8742, 0.0000, B
943.8008, 924.9248, 0.0000, A
945.4834, 926.5737, 0.0000, B
946.5485, 927.6175, 0.1256, A
947.9434, 928.9845, 0.8612, A
948.4752, 929.5057, 0.0000, B
949.9708, 930.9714, 2.2446, B
963.7810, 944.5054, 0.0000, B
963.7840, 944.5083, 0.2602, A
963.8266, 944.5501, 0.0000, A
966.2117, 946.8875, 17.2154, B
970.4424, 951.0336, 1.0751, A
970.4428, 951.0339, 0.0000, B
975.4580, 955.9488, 0.5992, B
978.6605, 959.0873, 0.0000, A
987.4800, 967.7304, 0.0000, A
999.3008, 979.3148, 7.2191, B
1002.6138, 982.5615, 0.0000, A
1015.5149, 995.2046, 21.1473, B
1047.5127, 1026.5624, 0.0000, A
1069.5069, 1048.1168, 38.9335, B
1073.6857, 1052.212, 7.4746, B
1074.5941, 1053.1022, 0.0000, A
1087.7803, 1066.0247, 0.0000, A
1089.0046, 1067.2245, 2.8861, B
1097.5181, 1075.5677, 0.3876, B
1099.9257, 1077.9272, 0.0000, A
1104.9907, 1082.8909, 0.0000, A
1114.6829, 1092.3892, 34.7705, B
1117.2137, 1094.8694, 34.8758, B
1128.2744, 1105.7089, 0.0000, A
1131.8029, 1109.1668, 0.0000, A
1137.4547, 1114.7056, 25.4519, B
1142.9855, 1120.1258, 16.8871, B
1151.9990, 1128.959, 0.0000, A
1162.3133, 1139.067, 0.0000, A
1169.1535, 1145.7704, 26.0421, B
1177.1845, 1153.6408, 0.5399, B
1177.5009, 1153.9509, 0.0000, A
1182.5447, 1158.8938, 0.0000, A

1182.8531, 1159.196, 39.6620, B
1184.6902, 1160.9964, 0.0000, A
1186.7207, 1162.9863, 28.7250, B
1190.0209, 1166.2205, 13.9881, B
1191.8305, 1167.9939, 0.0000, A
1196.5315, 1172.6009, 0.0000, A
1199.1930, 1175.2091, 1.9384, B
1203.3881, 1179.3203, 1.8250, B
1205.6390, 1181.5262, 0.0000, A
1210.9321, 1186.7135, 0.0000, A
1213.5536, 1189.2825, 1.6277, B
1215.6452, 1191.3323, 0.0000, A
1216.3527, 1192.0256, 0.2796, B
1222.6826, 1198.2289, 0.0000, A
1226.6485, 1202.1155, 15.2653, B
1231.2560, 1206.6309, 0.0000, A
1237.5004, 1212.7504, 0.0000, A
1238.9580, 1214.1788, 0.7622, B
1242.5889, 1217.7371, 0.6213, B
1249.8837, 1224.886, 0.0000, A
1255.9049, 1230.7868, 0.0000, A
1257.1945, 1232.0506, 2.5414, B
1258.9315, 1233.7529, 0.0000, A
1264.7923, 1239.4965, 3.4302, B
1265.6432, 1240.3303, 0.0000, A
1268.5556, 1243.1845, 18.9320, B
1282.9896, 1257.3298, 3.1079, B
1284.4752, 1258.7857, 0.0000, A
1289.1254, 1263.3429, 0.0132, B
1293.3587, 1267.4915, 6.8945, B
1294.0897, 1268.2079, 0.0000, A
1297.0894, 1271.1476, 0.4350, B
1302.7669, 1276.7116, 16.5782, B
1304.6400, 1278.5472, 0.0000, A
1306.0261, 1279.9056, 0.0000, A
1310.6189, 1284.4065, 0.0000, A
1313.1087, 1286.8465, 65.0143, B
1315.1584, 1288.8552, 0.0001, A
1316.6596, 1290.3264, 8.0458, B
1319.5037, 1293.1136, 0.0000, A
1320.3052, 1293.8991, 9.9251, B
1324.5322, 1298.0416, 10.2248, B
1326.9308, 1300.3922, 0.0000, A
1328.8131, 1302.2368, 2.3175, B
1328.9346, 1302.3559, 0.0000, A
1335.0010, 1308.301, 0.0000, A
1335.5571, 1308.846, 12.4717, B
1338.5499, 1311.7789, 0.0000, A
1340.7402, 1313.9254, 0.0000, A
1342.5504, 1315.6994, 31.3160, B
1346.8417, 1319.9049, 66.8891, B
1350.6821, 1323.6685, 0.0000, A
1353.8896, 1326.8118, 60.0231, B
1358.5438, 1331.3729, 0.0000, A
1358.6516, 1331.4786, 196.8522, B
1361.5338, 1334.3031, 0.0000, A
1365.4517, 1338.1427, 199.1285, B
1368.3878, 1341.02, 0.0000, A
1368.8014, 1341.4254, 47.2962, B
1372.7546, 1345.2995, 11.4972, B
1373.4538, 1345.9847, 5.6660, B
1374.2603, 1346.7751, 0.0000, A
1376.1652, 1348.6419, 2.5696, B
1378.6128, 1351.0405, 0.0000, A

1381.0600, 1353.4388, 0.0000, A
1382.2668, 1354.6215, 0.7467, B
1382.5636, 1354.9123, 0.0000, A
1387.3889, 1359.6411, 2.1722, B
1387.6301, 1359.8775, 0.0000, A
1388.4527, 1360.6836, 0.2734, B
1392.9599, 1365.1007, 0.0000, A
1393.7515, 1365.8765, 0.7431, B
1393.8438, 1365.9669, 0.0000, A
1396.1704, 1368.247, 0.2078, B
1396.9490, 1369.01, 0.0000, A
1398.7897, 1370.8139, 0.0000, A
1400.5694, 1372.558, 8.9656, B
1400.7835, 1372.7678, 0.0000, A
1406.1442, 1378.0213, 1.9332, B
1406.9554, 1378.8163, 0.0000, A
1413.1813, 1384.9177, 0.0000, A
1414.4529, 1386.1638, 12.2458, B
1418.4415, 1390.0727, 0.5499, B
1420.3349, 1391.9282, 0.0000, A
1420.8634, 1392.4461, 0.0000, A
1421.4269, 1392.9984, 0.0707, B
1423.7956, 1395.3197, 0.2105, B
1425.0740, 1396.5725, 1.4918, B
1425.2167, 1396.7124, 0.0000, A
1428.5485, 1399.9775, 10.1056, B
1431.7669, 1403.1316, 0.0000, A
1434.3617, 1405.6745, 0.0000, A
1442.3443, 1413.4974, 3.2183, B
1443.6929, 1414.819, 0.0000, A
1450.0418, 1421.041, 4.6558, B
1455.2953, 1426.1894, 7.8157, B
1458.6523, 1429.4793, 0.0000, A
1469.1562, 1439.7731, 0.0000, A
1473.0274, 1443.5669, 11.0348, B
1473.1459, 1443.683, 0.0000, A
1477.1706, 1447.6272, 0.2998, B
1481.6713, 1452.0379, 0.0000, A
1484.4928, 1454.8029, 0.0000, A
1487.7470, 1457.9921, 0.2651, B
1488.1902, 1458.4264, 1.5294, B
1489.6459, 1459.853, 0.0000, A
1492.5818, 1462.7302, 9.0163, B
1495.7817, 1465.8661, 0.0143, B
1496.6593, 1466.7261, 0.0000, A
1500.9506, 1470.9316, 0.0000, A
1502.3548, 1472.3077, 43.7952, B
1504.5719, 1474.4805, 0.0000, A
1505.3468, 1475.2399, 5.3686, B
1510.6054, 1480.3933, 0.0000, A
1512.8061, 1482.55, 6.6379, B
1514.0615, 1483.7803, 0.0000, A
1520.0573, 1489.6562, 147.5679, B
1524.2614, 1493.7762, 0.0000, A
1529.5547, 1498.9636, 0.0000, A
1529.6481, 1499.0551, 66.0466, B
1539.9529, 1509.1538, 2.7353, B
1543.0544, 1512.1933, 0.8943, B
1543.7699, 1512.8945, 0.0000, A
1555.6949, 1524.581, 0.0000, A
1557.3576, 1526.2104, 16.4498, B
1558.6531, 1527.48, 0.0000, A
1568.1594, 1536.7962, 0.0000, A
1568.4291, 1537.0605, 0.3749, B

1571.5742, 1540.1427, 2.5076, B
1578.8337, 1547.257, 0.0000, A
1579.1334, 1547.5507, 7.1232, B
1581.5180, 1549.8876, 0.0000, A
1585.1600, 1553.4568, 0.0338, B
1588.4618, 1556.6926, 0.0000, A
1592.1882, 1560.3444, 43.6554, B
1601.1842, 1569.1605, 0.0000, A
1605.4974, 1573.3875, 0.0000, A
1606.6057, 1574.4736, 0.0692, B
1608.1387, 1575.9759, 0.0000, A
1610.1695, 1577.9661, 0.1981, B
1612.2536, 1580.0085, 0.0000, A
1613.0396, 1580.7788, 0.4667, B
1613.4623, 1581.1931, 0.0000, A
1617.1418, 1584.799, 5.5943, B
1619.0062, 1586.6261, 15.1028, B
1624.3643, 1591.877, 0.0000, A
1627.9112, 1595.353, 0.0000, A
1630.1975, 1597.5936, 9.4375, B
1636.3458, 1603.6189, 6.6330, B
1636.8688, 1604.1314, 0.0000, A
1640.0849, 1607.2832, 2.9227, B
1640.3931, 1607.5852, 0.0000, A
1644.2835, 1611.3978, 22.5058, B
1645.4007, 1612.4927, 0.0000, A
1647.6527, 1614.6996, 0.0000, A
1648.2624, 1615.2972, 16.0325, B
1649.7827, 1616.787, 0.0000, A
1651.6518, 1618.6188, 25.4206, B
1653.3032, 1620.2371, 36.9385, B
1654.3689, 1621.2815, 0.0000, A
1655.1440, 1622.0411, 93.8649, B
1655.4873, 1622.3776, 0.0000, A
1657.7648, 1624.6095, 0.0000, A
1657.9144, 1624.7561, 0.0674, B
1659.5137, 1626.3234, 0.0000, A
1659.5592, 1626.368, 0.9751, B
1671.6004, 1638.1684, 0.0000, A
1671.6013, 1638.1693, 2.0077, B
3184.0417, 3120.3609, 18.8822, B
3184.0443, 3120.3634, 0.0000, A
3187.7679, 3124.0125, 16.4511, B
3187.7682, 3124.0128, 0.0000, A
3193.1555, 3129.2924, 200.2975, B
3193.1844, 3129.3207, 0.0000, A
3201.7053, 3137.6712, 349.5977, B
3201.7414, 3137.7066, 0.0001, A
3212.8041, 3148.548, 0.0000, A
3212.8206, 3148.5642, 133.4451, B
3214.1214, 3149.839, 1.2382, B
3214.1485, 3149.8655, 0.0000, A
3216.2432, 3151.9183, 0.0000, A
3216.2606, 3151.9354, 0.9699, B
3219.1951, 3154.8112, 5.2449, B
3219.2157, 3154.8314, 0.0000, A
3222.4551, 3158.006, 0.0000, A
3222.5026, 3158.0525, 6.2913, B
3224.0510, 3159.57, 7.4216, B
3224.1058, 3159.6237, 0.0000, A
3226.5668, 3162.0355, 0.0000, A
3226.5875, 3162.0557, 12.9654, B
3229.7148, 3165.1205, 3.0521, B
3229.7189, 3165.1245, 0.0000, A

3235.7129, 3170.9986, 20.5269, B
3235.7151, 3171.0008, 0.0000, A
3238.3680, 3173.6006, 19.6238, B
3238.3739, 3173.6064, 0.0000, A
3241.5840, 3176.7523, 0.0000, A
3241.5855, 3176.7538, 22.5947, B
3244.6125, 3179.7203, 5.7147, B
3244.6283, 3179.7357, 0.0000, A
3246.3930, 3181.4651, 0.0000, A
3246.4202, 3181.4918, 193.9567, B
3247.4700, 3182.5206, 53.2751, B
3247.5289, 3182.5783, 0.0001, A
3249.3532, 3184.3661, 0.0000, A
3249.3746, 3184.3871, 147.3290, B
3250.5959, 3185.584, 246.8701, B
3250.7269, 3185.7124, 0.0001,

PDA **1**

4.6611, 4.5679, 0.1432, A
6.9889, 6.8491, 0.1551, A
8.4223, 8.2539, 0.2416, A
11.2147, 10.9904, 0.0676, A
15.9201, 15.6017, 0.0423, A
17.2367, 16.892, 0.4053, A
19.9120, 19.5138, 0.2877, A
22.7655, 22.3102, 0.3102, A
24.7994, 24.3034, 0.5824, A
26.1330, 25.6103, 0.2746, A
26.6106, 26.0784, 1.6231, A
27.5668, 27.0155, 1.1030, A
30.8649, 30.2476, 1.4259, A
31.9242, 31.2857, 0.4138, A
32.8979, 32.2399, 0.2513, A
36.9863, 36.2466, 1.3351, A
37.9438, 37.1849, 0.5224, A
39.9331, 39.1344, 1.7550, A
42.7919, 41.9361, 0.7399, A
49.4646, 48.4753, 0.9346, A
52.8586, 51.8014, 0.6203, A
57.2596, 56.1144, 1.8237, A
59.5767, 58.3852, 2.3638, A
61.7084, 60.4742, 3.4279, A
64.5021, 63.2121, 1.0637, A
68.5749, 67.2034, 4.1255, A
71.3683, 69.9409, 6.8983, A
72.0762, 70.6347, 0.7919, A
72.2683, 70.8229, 1.5959, A
73.5206, 72.0502, 0.2642, A
76.0208, 74.5004, 1.3786, A
76.3257, 74.7992, 2.4876, A
80.7638, 79.1485, 0.2770, A
81.8660, 80.2287, 5.0401, A
84.2358, 82.5511, 1.4147, A
92.1781, 90.3345, 3.4734, A
94.2099, 92.3257, 3.0242, A
95.7170, 93.8027, 0.0759, A
102.6371, 100.5844, 0.3992, A
105.4323, 103.3237, 0.6977, A

112.0857, 109.844, 1.0698, A
121.6466, 119.2137, 0.0693, A
127.5331, 124.9824, 0.2949, A
128.2857, 125.72, 1.6831, A
130.8528, 128.2357, 0.8744, A
136.5965, 133.8646, 0.1351, A
143.8584, 140.9812, 1.6345, A
156.4861, 153.3564, 0.4246, A
157.4803, 154.3307, 1.1386, A
157.6735, 154.52, 0.3313, A
162.1909, 158.9471, 0.4960, A
165.0440, 161.7431, 0.1726, A
166.0414, 162.7206, 0.7245, A
168.0929, 164.731, 0.5047, A
173.6145, 170.1422, 0.8725, A
179.7704, 176.175, 7.2593, A
180.9681, 177.3487, 1.6059, A
184.3473, 180.6604, 2.1135, A
188.7399, 184.9651, 2.2571, A
190.6164, 186.8041, 1.1757, A
191.9129, 188.0746, 4.7408, A
192.7503, 188.8953, 0.5714, A
199.1083, 195.1261, 0.8099, A
204.9374, 200.8387, 0.5593, A
217.3462, 212.9993, 9.4053, A
221.7300, 217.2954, 9.2414, A
237.0731, 232.3316, 0.0966, A
237.4538, 232.7047, 1.1926, A
254.5843, 249.4926, 0.8490, A
256.5080, 251.3778, 3.6165, A
258.2755, 253.11, 5.1298, A
265.4718, 260.1624, 1.1031, A
271.7238, 266.2893, 0.6194, A
277.4337, 271.885, 0.5136, A
287.6564, 281.9033, 6.1052, A
291.5157, 285.6854, 0.5849, A
297.7980, 291.842, 0.5739, A
311.7958, 305.5599, 10.6864, A
329.4237, 322.8352, 0.4911, A
333.1340, 326.4713, 4.9412, A
337.5218, 330.7714, 0.1651, A
344.7567, 337.8616, 0.4447, A
353.7960, 346.7201, 1.5385, A
360.3043, 353.0982, 5.2101, A
370.8439, 363.427, 2.2679, A
380.2675, 372.6621, 2.4773, A
387.0991, 379.3571, 1.8672, A
394.3452, 386.4583, 0.7524, A
396.2100, 388.2858, 0.4000, A
398.7017, 390.7277, 0.2609, A
403.7919, 395.7161, 3.8771, A
409.7537, 401.5586, 6.3715, A
414.3535, 406.0664, 1.3617, A
415.4895, 407.1797, 1.0483, A
418.3759, 410.0084, 0.1768, A
419.1456, 410.7627, 0.6729, A
419.8822, 411.4846, 0.8331, A
419.9500, 411.551, 0.2172, A
420.1854, 411.7817, 0.4413, A
422.8413, 414.3845, 0.7174, A
426.5569, 418.0258, 1.2153, A
440.5194, 431.709, 0.3222, A
452.3853, 443.3376, 0.9774, A
454.4641, 445.3748, 6.7723, A

460.7995, 451.5835, 1.4564, A
461.8428, 452.6059, 1.9097, A
469.6513, 460.2583, 26.9171, A
473.2693, 463.8039, 8.9460, A
475.0057, 465.5056, 3.2815, A
484.1454, 474.4625, 0.8802, A
485.5634, 475.8521, 0.9719, A
493.2098, 483.3456, 2.9618, A
499.2543, 489.2692, 1.1880, A
501.1894, 491.1656, 2.4494, A
502.2351, 492.1904, 1.0896, A
516.4907, 506.1609, 0.9765, A
517.3357, 506.989, 4.8329, A
520.8802, 510.4626, 2.9511, A
531.1625, 520.5393, 8.7468, A
537.1812, 526.4376, 0.9857, A
539.5837, 528.792, 0.6194, A
550.9635, 539.9442, 1.4156, A
567.1835, 555.8398, 0.2542, A
574.1083, 562.6261, 13.0643, A
578.0839, 566.5222, 11.1328, A
587.7841, 576.0284, 4.1786, A
591.2547, 579.4296, 57.9544, A
601.3561, 589.329, 1.7322, A
602.9898, 590.93, 22.6235, A
603.8055, 591.7294, 4.8560, A
605.8601, 593.7429, 38.9255, A
607.9779, 595.8183, 7.1272, A
608.5258, 596.3553, 19.6409, A
609.8583, 597.6611, 2.4052, A
611.3455, 599.1186, 3.0884, A
614.2037, 601.9196, 14.3990, A
616.4718, 604.1424, 24.4403, A
617.9568, 605.5977, 20.0635, A
618.2376, 605.8728, 2.8352, A
619.3540, 606.9669, 25.1313, A
631.1694, 618.546, 6.8207, A
642.5164, 629.6661, 0.3713, A
643.8167, 630.9404, 0.5237, A
644.4060, 631.5179, 2.8992, A
644.7500, 631.855, 0.6533, A
647.9449, 634.986, 0.5477, A
650.6292, 637.6166, 1.2343, A
651.5834, 638.5517, 1.1590, A
653.2073, 640.1432, 2.5908, A
657.6755, 644.522, 2.4111, A
660.4957, 647.2858, 2.8113, A
701.0040, 686.9839, 0.6059, A
706.1887, 692.0649, 6.9051, A
707.8782, 693.7206, 9.9042, A
708.6981, 694.5241, 82.5468, A
713.7312, 699.4566, 36.0434, A
716.8679, 702.5305, 31.7452, A
736.1078, 721.3856, 0.9703, A
742.3104, 727.4642, 9.8947, A
746.9639, 732.0246, 1.0419, A
751.9708, 736.9314, 4.6666, A
754.2210, 739.1366, 0.1012, A
755.4094, 740.3012, 1.1095, A
756.2115, 741.0873, 0.7087, A
758.5064, 743.3363, 4.4754, A
759.2257, 744.0412, 2.9629, A
759.7905, 744.5947, 17.5212, A
769.3279, 753.9413, 3.5351, A

769.9218, 754.5234, 0.0492, A
791.6188, 775.7864, 2.0249, A
823.7488, 807.2738, 5.4698, A
836.0588, 819.3376, 10.1550, A
837.0800, 820.3384, 22.3693, A
842.3471, 825.5002, 20.8920, A
845.9993, 829.0793, 20.7626, A
846.5669, 829.6356, 39.9115, A
849.6474, 832.6545, 6.4286, A
849.7397, 832.7449, 3.1100, A
851.5339, 834.5032, 3.2063, A
854.5880, 837.4962, 2.5369, A
856.6754, 839.5419, 15.1487, A
858.7037, 841.5296, 20.4111, A
860.3099, 843.1037, 1.4303, A
866.7581, 849.4229, 7.0895, A
867.6269, 850.2744, 0.2874, A
869.0145, 851.6342, 4.0286, A
871.1197, 853.6973, 42.0998, A
872.1741, 854.7306, 14.2831, A
878.5369, 860.9662, 39.0246, A
879.5294, 861.9388, 32.1607, A
880.9884, 863.3686, 27.1989, A
917.1040, 898.7619, 23.2102, A
923.7518, 905.2768, 12.3740, A
963.0479, 943.7869, 23.5152, A
965.7197, 946.4053, 10.3983, A
967.6088, 948.2566, 41.7741, A
968.0763, 948.7148, 6.6036, A
968.4749, 949.1054, 2.7432, A
969.0256, 949.6451, 16.5436, A
969.3529, 949.9658, 137.0426, A
969.5738, 950.1823, 5.5017, A
969.8311, 950.4345, 1.1983, A
971.1226, 951.7001, 4.1552, A
974.1332, 954.6505, 7.9629, A
974.5022, 955.0122, 17.4174, A
974.9962, 955.4963, 31.8086, A
975.9404, 956.4216, 18.9600, A
976.4220, 956.8936, 53.0014, A
976.8046, 957.2685, 1.5403, A
977.5117, 957.9615, 81.9414, A
991.6370, 971.8043, 7.4751, A
993.0078, 973.1476, 2.7177, A
994.5560, 974.6649, 1.3567, A
996.9542, 977.0151, 0.9900, A
997.1829, 977.2392, 4.6863, A
999.5738, 979.5823, 38.7077, A
1002.3730, 982.3255, 5.7206, A
1003.6809, 983.6073, 19.3875, A
1008.3651, 988.1978, 1.6665, A
1026.1797, 1005.6561, 0.5957, A
1032.1113, 1011.4691, 4.0064, A
1032.3890, 1011.7412, 4.6345, A
1034.0591, 1013.3779, 5.7551, A
1035.9730, 1015.2535, 2.3043, A
1037.4591, 1016.7099, 20.8913, A
1038.3914, 1017.6236, 8.6576, A
1039.0048, 1018.2247, 0.8570, A
1050.1174, 1029.1151, 0.3107, A
1055.3918, 1034.284, 1.9696, A
1055.5795, 1034.4679, 1.8432, A
1056.2848, 1035.1591, 1.6781, A
1056.5551, 1035.424, 1.2747, A

1058.6999, 1037.5259, 0.8409, A
1059.5499, 1038.3589, 1.3359, A
1060.8270, 1039.6105, 2.9793, A
1061.1525, 1039.9294, 2.7916, A
1095.5135, 1073.6032, 0.1935, A
1099.9300, 1077.9314, 0.7882, A
1101.3904, 1079.3626, 2.3885, A
1101.4213, 1079.3929, 2.7215, A
1102.7284, 1080.6738, 5.1198, A
1102.8964, 1080.8385, 4.1270, A
1103.6960, 1081.6221, 3.5456, A
1104.2441, 1082.1592, 0.1151, A
1120.5983, 1098.1863, 0.0730, A
1139.6666, 1116.8733, 2.7295, A
1144.6506, 1121.7576, 2.3217, A
1146.6587, 1123.7255, 6.6166, A
1147.8611, 1124.9039, 1.8603, A
1152.0561, 1129.015, 2.5970, A
1152.7594, 1129.7042, 3.4008, A
1154.2002, 1131.1162, 1.7019, A
1155.0417, 1131.9409, 12.8989, A
1157.6768, 1134.5233, 5.4310, A
1207.9576, 1183.7984, 8.3764, A
1215.5517, 1191.2407, 1.5673, A
1216.3227, 1191.9962, 0.9874, A
1218.7952, 1194.4193, 37.1387, A
1219.1142, 1194.7319, 28.7602, A
1219.5999, 1195.2079, 82.6519, A
1221.2486, 1196.8236, 0.6786, A
1221.6477, 1197.2147, 6.7604, A
1223.0658, 1198.6045, 27.4695, A
1243.9742, 1219.0947, 0.1638, A
1248.8517, 1223.8747, 8.3748, A
1264.0039, 1238.7238, 0.0905, A
1271.6201, 1246.1877, 5.4431, A
1274.4871, 1248.9974, 4.5609, A
1287.7182, 1261.9638, 42.8027, A
1289.7508, 1263.9558, 127.5961, A
1290.3690, 1264.5616, 388.7070, A
1291.7158, 1265.8815, 76.9464, A
1292.6704, 1266.817, 124.7521, A
1294.0472, 1268.1663, 425.7966, A
1295.7343, 1269.8196, 1046.7376, A
1298.0948, 1272.1329, 100.1248, A
1299.6289, 1273.6363, 100.3767, A
1307.8967, 1281.7388, 4.2105, A
1334.7958, 1308.0999, 2.4176, A
1337.7380, 1310.9832, 1.3309, A
1339.7118, 1312.9176, 23.8071, A
1340.7762, 1313.9607, 2.4856, A
1342.6355, 1315.7828, 0.8135, A
1346.6428, 1319.7099, 1.0092, A
1348.0185, 1321.0581, 5.8251, A
1349.1268, 1322.1443, 3.6962, A
1349.9258, 1322.9273, 11.5897, A
1350.8091, 1323.7929, 61.5903, A
1351.1234, 1324.1009, 3.9746, A
1351.8376, 1324.8008, 0.9118, A
1351.9241, 1324.8856, 0.3401, A
1353.1035, 1326.0414, 20.4506, A
1365.6397, 1338.3269, 44.0619, A
1366.7922, 1339.4564, 0.4074, A
1381.6433, 1354.0104, 25.8289, A
1409.4997, 1381.3097, 56.8591, A

1410.6895, 1382.4757, 76.2982, A
1411.1928, 1382.9689, 64.3224, A
1417.9754, 1389.6159, 25.8964, A
1418.9936, 1390.6137, 32.2588, A
1419.6142, 1391.2219, 14.0296, A
1420.7739, 1392.3584, 34.0241, A
1420.8633, 1392.446, 33.1540, A
1423.5955, 1395.1236, 11.5090, A
1424.7096, 1396.2154, 23.5278, A
1445.7740, 1416.8585, 13.6075, A
1447.0079, 1418.0677, 18.7845, A
1448.5137, 1419.5434, 32.0286, A
1449.5069, 1420.5168, 40.3911, A
1453.6416, 1424.5688, 37.5928, A
1454.6036, 1425.5115, 3.8674, A
1461.4853, 1432.2556, 57.0713, A
1462.9107, 1433.6525, 149.1810, A
1498.3358, 1468.3691, 10.7375, A
1498.6904, 1468.7166, 10.0286, A
1499.3743, 1469.3868, 8.1869, A
1499.5501, 1469.5591, 20.0370, A
1501.0461, 1471.0252, 2.8043, A
1501.2655, 1471.2402, 6.6791, A
1501.3408, 1471.314, 25.8852, A
1502.7393, 1472.6845, 13.9769, A
1506.3002, 1476.1742, 8.6311, A
1506.3465, 1476.2196, 9.1804, A
1507.8556, 1477.6985, 9.4889, A
1508.2305, 1478.0659, 11.1410, A
1508.9928, 1478.8129, 13.9714, A
1510.6728, 1480.4593, 8.2092, A
1511.0636, 1480.8423, 9.4407, A
1511.9571, 1481.718, 12.5694, A
1521.9665, 1491.5272, 0.5904, A
1545.9839, 1515.0642, 0.7125, A
1548.4646, 1517.4953, 0.6344, A
1548.7018, 1517.7278, 0.7270, A
1550.9028, 1519.8847, 1.2698, A
1551.1889, 1520.1651, 7.5789, A
1552.9133, 1521.855, 0.4111, A
1553.0734, 1522.0119, 9.4095, A
1553.6534, 1522.5803, 6.0641, A
1567.7824, 1536.4268, 2.2642, A
1590.9462, 1559.1273, 5.2846, A
1592.3478, 1560.5008, 10.3129, A
1609.1593, 1576.9761, 0.6070, A
1610.2790, 1578.0734, 14.2555, A
1610.7168, 1578.5025, 22.3548, A
1611.5468, 1579.3159, 19.7975, A
1612.3328, 1580.0861, 1.0684, A
1614.0411, 1581.7603, 1.1719, A
1624.2226, 1591.7381, 20.1976, A
1625.6437, 1593.1308, 42.0803, A
1657.8240, 1624.6675, 8.2370, A
1658.4727, 1625.3032, 7.0945, A
1658.8222, 1625.6458, 13.8556, A
1659.2359, 1626.0512, 15.8032, A
1659.6480, 1626.455, 1.4245, A
1659.9772, 1626.7777, 467.4437, A
1660.6475, 1627.4345, 68.6613, A
1661.2540, 1628.0289, 23.3909, A
1759.5342, 1724.3435, 352.8441, A
1760.5105, 1725.3003, 277.2710, A
1762.6843, 1727.4306, 62.9877, A

1763.6760, 1728.4025, 113.8520, A
1763.8246, 1728.5481, 97.7625, A
1776.6349, 1741.1022, 217.7765, A
1777.0752, 1741.5337, 94.6879, A
1779.8486, 1744.2516, 207.1766, A
2211.4741, 2167.2446, 2.0712, A
2246.5795, 2201.6479, 0.4329, A
2270.7382, 2225.3234, 0.1384, A
3050.6327, 2989.62, 5.1142, A
3050.6381, 2989.6253, 5.1693, A
3051.7490, 2990.714, 3.3968, A
3052.7112, 2991.657, 2.5292, A
3053.7404, 2992.6656, 3.5168, A
3053.7550, 2992.6799, 4.1883, A
3054.0480, 2992.967, 1.9999, A
3054.1715, 2993.0881, 2.0008, A
3111.5048, 3049.2747, 3.3068, A
3111.8323, 3049.5957, 9.5237, A
3112.3344, 3050.0877, 3.9259, A
3113.3949, 3051.127, 8.4099, A
3113.4871, 3051.2174, 8.4079, A
3113.6879, 3051.4141, 5.6188, A
3114.3783, 3052.0907, 3.0920, A
3116.4048, 3054.0767, 3.7908, A
3168.2014, 3104.8374, 9.5317, A
3168.3342, 3104.9675, 17.9799, A
3168.4470, 3105.0781, 9.7947, A
3169.0672, 3105.6859, 15.3489, A
3169.3328, 3105.9461, 12.7755, A
3170.5188, 3107.1084, 16.3888, A
3170.8761, 3107.4586, 16.2145, A
3171.2687, 3107.8433, 15.1233, A
3179.6531, 3116.06, 4.0531, A
3180.4029, 3116.7948, 7.3286, A
3187.0201, 3123.2797, 14.7124, A
3187.2261, 3123.4816, 16.6014, A
3199.4268, 3135.4383, 4.6180, A
3199.9361, 3135.9374, 2.6707, A
3201.1184, 3137.096, 3.2931, A
3203.5706, 3139.4992, 2.7060, A
3204.0637, 3139.9824, 2.6636, A
3204.6299, 3140.5373, 2.8632, A
3207.4012, 3143.2532, 2.2185, A
3209.9895, 3145.7897, 6.9993, A
3211.7659, 3147.5306, 32.0251, A
3212.3499, 3148.1029, 32.5491, A
3214.5589, 3150.2677, 3.8754, A
3215.5274, 3151.2169, 4.1164, A
3215.8070, 3151.4909, 15.9850, A
3218.6523, 3154.2793, 0.1258, A
3219.9440, 3155.5451, 9.3879, A
3221.0442, 3156.6233, 8.0698, A
3221.1906, 3156.7668, 1.2631, A
3223.7432, 3159.2683, 0.8166, A
3224.2032, 3159.7191, 5.4049, A
3225.2085, 3160.7043, 0.7384, A
3225.7057, 3161.1916, 3.9348, A
3226.9990, 3162.459, 3.0012, A
3228.4107, 3163.8425, 7.4397, A
3229.3958, 3164.8079, 4.8466, A
3230.2679, 3165.6625, 0.8412, A
3232.0032, 3167.3631, 0.3714, A
3235.5490, 3170.838, 2.1028, A
3235.7740, 3171.0585, 0.3845, A

3259.4131, 3194.2248, 1.2606, A

3266.6129, 3201.2806, 0.7875, A

PDA **1-*annul***

3.6990, 3.625, 0.0067, A

6.4261, 6.2976, 0.0042, A

7.7767, 7.6212, 0.0054, A

9.2040, 9.0199, 0.0721, A

11.5251, 11.2946, 0.0045, A

18.6093, 18.2371, 0.0620, A

19.7030, 19.3089, 0.4385, A

20.4653, 20.056, 0.1143, A

22.7231, 22.2686, 0.3915, A

24.6340, 24.1413, 0.6540, A

25.6647, 25.1514, 0.2612, A

27.6193, 27.0669, 0.5064, A

31.6870, 31.0533, 0.2823, A

32.4531, 31.804, 1.8834, A

33.3181, 32.6517, 2.9664, A

34.8188, 34.1224, 1.5982, A

37.4829, 36.7332, 0.8401, A

40.3281, 39.5215, 0.7745, A

43.2525, 42.3874, 0.2316, A

45.4552, 44.5461, 4.4539, A

47.8029, 46.8468, 3.1652, A

52.3504, 51.3034, 0.9327, A

53.3620, 52.2948, 3.2635, A

57.8376, 56.6808, 3.5628, A

60.1065, 58.9044, 1.7061, A

70.6514, 69.2384, 0.3589, A

71.2225, 69.798, 2.4686, A

73.9062, 72.4281, 1.7276, A

75.6217, 74.1093, 0.7060, A

78.1840, 76.6203, 1.0184, A

80.3886, 78.7808, 0.0440, A

81.0384, 79.4176, 0.6016, A

84.5693, 82.8779, 0.2490, A

85.0017, 83.3017, 0.6013, A

98.5413, 96.5705, 0.5766, A

103.3541, 101.287, 1.6494, A

111.7429, 109.508, 0.2065, A

113.3812, 111.1136, 0.1212, A

122.0081, 119.5679, 0.7158, A

136.7481, 134.0131, 4.6313, A

146.8561, 143.919, 0.3248, A

156.6741, 153.5406, 1.4895, A

159.8334, 156.6367, 0.7602, A

161.0790, 157.8574, 1.3524, A

162.4748, 159.2253, 0.1651, A

163.9000, 160.622, 0.2513, A

167.2836, 163.9379, 0.1798, A

167.9330, 164.5743, 0.2354, A

171.9608, 168.5216, 0.1904, A

173.5558, 170.0847, 0.2965, A

173.8815, 170.4039, 0.0878, A

174.1959, 170.712, 0.3664, A

176.0461, 172.5252, 0.0589, A

177.0714, 173.53, 0.4036, A

183.0668, 179.4055, 1.4113, A

183.5250, 179.8545, 0.4135, A

185.8077, 182.0915, 0.2235, A
187.3008, 183.5548, 0.9907, A
189.7467, 185.9518, 0.4775, A
191.6464, 187.8135, 2.5262, A
197.7306, 193.776, 1.6008, A
203.7805, 199.7049, 3.6838, A
210.5878, 206.376, 4.0402, A
216.5005, 212.1705, 3.0565, A
224.8797, 220.3821, 0.3653, A
238.3021, 233.5361, 1.1799, A
246.5290, 241.5984, 1.3881, A
254.1450, 249.0621, 5.0520, A
260.2631, 255.0578, 2.6028, A
264.7205, 259.4261, 2.0051, A
268.3638, 262.9965, 0.4787, A
282.7096, 277.0554, 1.0344, A
300.7009, 294.6869, 1.3339, A
304.1110, 298.0288, 1.3232, A
316.6868, 310.3531, 2.5107, A
320.5860, 314.1743, 0.9402, A
331.4440, 324.8151, 0.0135, A
337.6106, 330.8584, 0.2975, A
339.3336, 332.5469, 0.6476, A
339.4858, 332.6961, 0.7123, A
358.2759, 351.1104, 0.5204, A
368.8766, 361.4991, 0.4760, A
386.7953, 379.0594, 6.1161, A
395.2633, 387.358, 4.9172, A
402.9035, 394.8454, 1.9195, A
409.1514, 400.9684, 0.9044, A
412.5883, 404.3365, 0.4140, A
416.7775, 408.4419, 0.6078, A
417.5625, 409.2113, 0.1944, A
417.7736, 409.4181, 0.4684, A
418.1406, 409.7778, 0.9285, A
418.4007, 410.0327, 0.0831, A
422.2569, 413.8118, 0.4236, A
427.2582, 418.713, 0.6712, A
432.4326, 423.7839, 1.1434, A
439.0194, 430.239, 0.9802, A
448.7198, 439.7454, 2.6860, A
456.0316, 446.911, 0.4394, A
462.4606, 453.2114, 5.7821, A
474.0200, 464.5396, 2.9262, A
478.4097, 468.8415, 0.8018, A
482.4837, 472.834, 6.3149, A
483.5819, 473.9103, 1.4518, A
487.1557, 477.4126, 2.8426, A
489.3905, 479.6027, 0.4392, A
492.6220, 482.7696, 1.0942, A
501.9325, 491.8938, 1.3688, A
505.3613, 495.2541, 0.5170, A
507.3735, 497.226, 0.4424, A
509.8872, 499.6895, 0.2394, A
522.9137, 512.4554, 1.0216, A
527.9845, 517.4248, 1.3933, A
533.4026, 522.7345, 0.9530, A
534.0230, 523.3425, 0.0739, A
535.9272, 525.2087, 1.5901, A
538.5531, 527.782, 5.5637, A
541.4092, 530.581, 0.8246, A
543.8548, 532.9777, 7.6026, A
549.6522, 538.6592, 0.9661, A
557.6524, 546.4994, 8.1115, A

573.2366, 561.7719, 4.7738, A
576.6745, 565.141, 69.6451, A
581.2382, 569.6134, 22.7758, A
586.2132, 574.4889, 30.0851, A
591.1581, 579.3349, 20.4268, A
592.3083, 580.4621, 19.8049, A
602.4563, 590.4072, 1.2422, A
605.9063, 593.7882, 2.7557, A
606.5967, 594.4648, 18.5751, A
607.1666, 595.0233, 4.5591, A
610.5074, 598.2973, 9.0434, A
613.0303, 600.7697, 4.9528, A
613.6521, 601.3791, 18.9132, A
615.5955, 603.2836, 7.0472, A
616.7598, 604.4246, 2.8060, A
619.2586, 606.8734, 12.8486, A
623.7080, 611.2338, 2.4225, A
626.0629, 613.5416, 25.2471, A
643.0337, 630.173, 4.3626, A
648.4614, 635.4922, 6.3707, A
650.0234, 637.0229, 0.0526, A
650.5954, 637.5835, 4.4316, A
654.0530, 640.9719, 0.8710, A
660.7145, 647.5002, 6.9782, A
668.9073, 655.5292, 3.8331, A
687.9169, 674.1586, 6.0418, A
688.7078, 674.9336, 6.4138, A
692.6949, 678.841, 3.0487, A
697.6557, 683.7026, 6.1325, A
699.9225, 685.924, 0.9524, A
703.4379, 689.3691, 18.5646, A
711.6127, 697.3804, 24.3510, A
712.5595, 698.3083, 17.8056, A
718.2738, 703.9083, 6.5220, A
726.2987, 711.7727, 21.1534, A
729.4942, 714.9043, 3.6579, A
734.3058, 719.6197, 4.8877, A
739.0688, 724.2874, 7.6165, A
756.1431, 741.0202, 0.9339, A
756.8690, 741.7316, 0.2802, A
759.2082, 744.024, 1.8798, A
763.6211, 748.3487, 1.0101, A
773.6572, 758.1841, 4.3766, A
789.4735, 773.684, 2.3735, A
791.1472, 775.3243, 0.8872, A
795.6536, 779.7405, 2.2671, A
799.2396, 783.2548, 4.1767, A
803.2526, 787.1875, 5.7459, A
803.8987, 787.8207, 5.2144, A
807.0501, 790.9091, 1.0892, A
825.7002, 809.1862, 1.6088, A
829.2643, 812.679, 3.3359, A
834.9948, 818.2949, 16.5821, A
843.7891, 826.9133, 11.8045, A
845.1379, 828.2351, 16.1627, A
848.3082, 831.342, 11.5646, A
851.0248, 834.0043, 27.5122, A
854.9518, 837.8528, 6.4991, A
855.3865, 838.2788, 27.3069, A
857.7613, 840.6061, 25.6275, A
864.0426, 846.7617, 16.1551, A
865.8582, 848.541, 2.6247, A
870.1474, 852.7445, 15.4298, A
870.2684, 852.863, 26.2590, A

873.8868, 856.4091, 10.4640, A
894.7537, 876.8586, 4.4860, A
896.0663, 878.145, 35.7566, A
898.2777, 880.3121, 18.4319, A
900.3028, 882.2967, 21.7496, A
909.8198, 891.6234, 4.1231, A
917.2427, 898.8978, 6.6245, A
927.7628, 909.2075, 3.4062, A
930.3759, 911.7684, 0.3856, A
931.9017, 913.2637, 0.9222, A
949.7887, 930.7929, 10.6426, A
952.8361, 933.7794, 19.2589, A
956.9516, 937.8126, 3.8000, A
957.3138, 938.1675, 15.7313, A
959.5834, 940.3917, 7.8307, A
967.4408, 948.092, 49.9975, A
968.5353, 949.1646, 52.6478, A
968.6845, 949.3108, 53.4424, A
968.7998, 949.4238, 21.5398, A
970.9757, 951.5562, 1.1474, A
971.6784, 952.2448, 0.4238, A
971.9760, 952.5365, 0.3371, A
973.6190, 954.1466, 1.7498, A
973.6996, 954.2256, 1.2633, A
974.6441, 955.1512, 39.9063, A
976.5967, 957.0648, 5.1075, A
977.3902, 957.8424, 2.0459, A
978.6969, 959.123, 3.9004, A
980.2614, 960.6562, 0.5047, A
993.3640, 973.4967, 2.1068, A
994.1592, 974.276, 36.6707, A
995.0286, 975.128, 20.5748, A
995.8049, 975.8888, 4.2620, A
996.6580, 976.7248, 1.8028, A
997.6967, 977.7428, 2.0614, A
998.8533, 978.8762, 34.1694, A
999.4472, 979.4583, 15.5076, A
1034.7468, 1014.0519, 6.7845, A
1034.7741, 1014.0786, 5.2686, A
1035.5317, 1014.8211, 7.3039, A
1036.5921, 1015.8603, 10.4096, A
1055.9804, 1034.8608, 1.3025, A
1056.0939, 1034.972, 0.7746, A
1056.4472, 1035.3183, 0.8401, A
1056.6942, 1035.5603, 0.8260, A
1056.8131, 1035.6768, 1.6385, A
1056.8699, 1035.7325, 1.1780, A
1056.9418, 1035.803, 1.2867, A
1057.0552, 1035.9141, 1.3087, A
1059.5969, 1038.405, 0.9561, A
1060.6525, 1039.4394, 0.0872, A
1065.0875, 1043.7858, 3.0246, A
1081.4237, 1059.7952, 0.2564, A
1097.1824, 1075.2388, 0.1583, A
1098.1631, 1076.1998, 0.1209, A
1099.6971, 1077.7032, 1.6438, A
1101.4087, 1079.3805, 1.9284, A
1103.6351, 1081.5624, 3.1010, A
1104.5170, 1082.4267, 1.1371, A
1108.5811, 1086.4095, 1.3308, A
1112.9692, 1090.7098, 2.4209, A
1119.2299, 1096.8453, 10.0957, A
1136.1628, 1113.4395, 5.2300, A
1146.4029, 1123.4748, 11.2674, A

1147.3627, 1124.4154, 1.0192, A
1147.6971, 1124.7432, 1.3236, A
1150.8549, 1127.8378, 4.8545, A
1162.4289, 1139.1803, 4.1750, A
1187.4123, 1163.6641, 41.4323, A
1194.0953, 1170.2134, 21.7298, A
1198.4782, 1174.5086, 2.6844, A
1199.8202, 1175.8238, 0.9073, A
1203.4560, 1179.3869, 3.5912, A
1218.9629, 1194.5836, 22.5670, A
1219.4818, 1195.0922, 34.2280, A
1219.6392, 1195.2464, 2.2411, A
1221.3359, 1196.9092, 25.7841, A
1225.6091, 1201.0969, 160.3739, A
1235.2144, 1210.5101, 9.9931, A
1244.5162, 1219.6259, 82.8407, A
1249.6650, 1224.6717, 84.0947, A
1251.2303, 1226.2057, 231.6436, A
1266.8449, 1241.508, 88.3159, A
1271.3034, 1245.8773, 72.1270, A
1275.3684, 1249.861, 205.1784, A
1276.1487, 1250.6257, 11.5074, A
1280.5561, 1254.945, 92.8939, A
1281.1684, 1255.545, 136.2324, A
1282.5414, 1256.8906, 29.9352, A
1290.5598, 1264.7486, 169.8789, A
1291.1017, 1265.2797, 297.8894, A
1291.5106, 1265.6804, 52.1725, A
1292.5698, 1266.7184, 551.5905, A
1295.0162, 1269.1159, 86.6705, A
1308.9222, 1282.7438, 58.5266, A
1309.8623, 1283.6651, 43.7348, A
1312.5850, 1286.3333, 21.8634, A
1321.2030, 1294.7789, 5.2787, A
1332.0726, 1305.4311, 16.8179, A
1333.5762, 1306.9047, 1.2299, A
1335.6481, 1308.9351, 2.8992, A
1337.2513, 1310.5063, 2.0154, A
1347.9915, 1321.0317, 6.9933, A
1348.5596, 1321.5884, 8.4480, A
1348.6813, 1321.7077, 16.7778, A
1350.6509, 1323.6379, 8.3251, A
1360.2542, 1333.0491, 21.9753, A
1367.0197, 1339.6793, 10.3987, A
1371.4454, 1344.0165, 18.8270, A
1378.5187, 1350.9483, 22.6996, A
1382.1199, 1354.4775, 1.9369, A
1394.8783, 1366.9807, 3.0823, A
1398.5477, 1370.5767, 4.5696, A
1402.1531, 1374.11, 2.6542, A
1404.8991, 1376.8011, 3.0014, A
1407.3936, 1379.2457, 2.4182, A
1409.2658, 1381.0805, 34.0166, A
1409.9741, 1381.7746, 50.2152, A
1410.4154, 1382.2071, 43.9769, A
1410.7639, 1382.5486, 39.0445, A
1411.7243, 1383.4898, 93.0019, A
1412.1850, 1383.9413, 39.2989, A
1413.4856, 1385.2159, 35.6222, A
1413.7763, 1385.5008, 20.1657, A
1421.7120, 1393.2778, 11.3872, A
1423.9424, 1395.4636, 44.5812, A
1430.8993, 1402.2813, 15.0603, A
1435.3435, 1406.6366, 5.5268, A

1436.6960, 1407.9621, 21.7271, A
1441.1824, 1412.3588, 9.0427, A
1452.2115, 1423.1673, 60.3113, A
1453.1922, 1424.1284, 10.4471, A
1454.2009, 1425.1169, 7.6839, A
1464.4961, 1435.2062, 21.2916, A
1491.6551, 1461.822, 62.1177, A
1492.4412, 1462.5924, 29.4861, A
1494.2566, 1464.3715, 40.6804, A
1498.4837, 1468.514, 22.3973, A
1498.5567, 1468.5856, 5.3391, A
1498.5736, 1468.6021, 7.6355, A
1498.6535, 1468.6804, 9.0692, A
1498.8158, 1468.8395, 14.4919, A
1499.1917, 1469.2079, 6.7815, A
1499.4756, 1469.4861, 9.0572, A
1499.6688, 1469.6754, 8.7948, A
1506.4871, 1476.3574, 8.6736, A
1507.0662, 1476.9249, 9.4025, A
1507.2521, 1477.1071, 9.5081, A
1507.5772, 1477.4257, 9.4495, A
1507.5939, 1477.442, 8.0866, A
1507.7029, 1477.5488, 9.9935, A
1507.8401, 1477.6833, 9.8252, A
1507.8602, 1477.703, 9.1387, A
1515.4291, 1485.1205, 27.9216, A
1541.0073, 1510.1872, 3.1241, A
1543.2146, 1512.3503, 3.3931, A
1544.8808, 1513.9832, 1.6616, A
1545.7341, 1514.8194, 15.4945, A
1554.2987, 1523.2127, 5.4191, A
1554.4784, 1523.3888, 1.6912, A
1554.7501, 1523.6551, 0.6661, A
1555.9238, 1524.8053, 4.4851, A
1597.6179, 1565.6655, 22.9323, A
1599.8455, 1567.8486, 5.0627, A
1602.3012, 1570.2552, 4.5335, A
1608.5090, 1576.3388, 18.3715, A
1613.5466, 1581.2757, 5.1814, A
1614.9203, 1582.6219, 22.4421, A
1615.7329, 1583.4182, 8.0721, A
1620.2262, 1587.8217, 4.7315, A
1631.3367, 1598.71, 5.8946, A
1636.1827, 1603.459, 0.4612, A
1644.1638, 1611.2805, 11.8861, A
1649.9832, 1616.9835, 10.4355, A
1659.9117, 1626.7135, 63.2932, A
1660.8477, 1627.6307, 7.7528, A
1661.2870, 1628.0613, 1.2364, A
1661.7487, 1628.5137, 35.8611, A
1662.2173, 1628.973, 164.2694, A
1662.8668, 1629.6095, 101.0912, A
1665.9620, 1632.6428, 233.2598, A
1669.3028, 1635.9167, 105.8606, A
1776.5894, 1741.0576, 119.5989, A
1777.2221, 1741.6777, 122.2058, A
1777.4571, 1741.908, 220.8851, A
1777.7285, 1742.1739, 373.1200, A
1778.2156, 1742.6513, 95.7929, A
1778.6065, 1743.0344, 231.3459, A
1779.2949, 1743.709, 107.3472, A
1781.3921, 1745.7643, 140.4035, A
3052.3956, 2991.3477, 2.4043, A
3052.5248, 2991.4743, 2.7417, A

3052.6382, 2991.5854, 2.5008, A
3052.6731, 2991.6196, 2.5753, A
3053.4234, 2992.3549, 2.8031, A
3053.6112, 2992.539, 2.3929, A
3053.9813, 2992.9017, 2.2559, A
3054.0101, 2992.9299, 2.5184, A
3111.2609, 3049.0357, 7.5568, A
3111.4477, 3049.2187, 6.3915, A
3111.5482, 3049.3172, 7.8762, A
3111.6251, 3049.3926, 7.9459, A
3112.2261, 3049.9816, 10.2101, A
3112.9646, 3050.7053, 8.3231, A
3113.1159, 3050.8536, 8.6230, A
3113.1992, 3050.9352, 7.6434, A
3169.9700, 3106.5706, 19.9513, A
3170.3161, 3106.9098, 14.2802, A
3170.5280, 3107.1174, 12.4851, A
3170.5952, 3107.1833, 20.7420, A
3170.6551, 3107.242, 8.7583, A
3170.7807, 3107.3651, 16.2824, A
3170.9601, 3107.5409, 12.2899, A
3170.9934, 3107.5735, 16.6361, A
3186.9809, 3123.2413, 4.4334, A
3190.4108, 3126.6026, 7.1175, A
3190.9632, 3127.1439, 9.5153, A
3193.3696, 3129.5022, 11.5511, A
3193.6781, 3129.8045, 4.7095, A
3195.9346, 3132.0159, 6.8117, A
3197.1500, 3133.207, 8.7792, A
3197.7994, 3133.8434, 8.6572, A
3199.6562, 3135.6631, 7.6506, A
3204.9159, 3140.8176, 5.7693, A
3205.4139, 3141.3056, 7.0089, A
3206.0615, 3141.9403, 4.4658, A
3207.8090, 3143.6528, 6.0549, A
3208.6014, 3144.4294, 1.8883, A
3208.7423, 3144.5675, 6.8195, A
3209.8156, 3145.6193, 13.2218, A
3209.9586, 3145.7594, 4.2433, A
3210.3217, 3146.1153, 3.3826, A
3212.3436, 3148.0967, 6.9902, A
3214.5523, 3150.2613, 7.2762, A
3217.1559, 3152.8128, 24.2294, A
3217.2863, 3152.9406, 4.6816, A
3222.4174, 3157.9691, 5.7174, A
3222.8669, 3158.4096, 6.1385, A
3225.8221, 3161.3057, 1.4723, A
3226.2174, 3161.6931, 1.3714, A
3226.5742, 3162.0427, 1.9263, A
3227.1881, 3162.6443, 4.1579, A
3228.6509, 3164.0779, 1.8079, A
3228.7657, 3164.1904, 4.0620, A
3229.8703, 3165.2729, 11.5973, A
3230.4286, 3165.82, 8.1191, A
3231.3708, 3166.7434, 9.0718, A
3240.1361, 3175.3334, 0.2289, A

xii) Computed structures of model systems **8a**-**11a** and *trans*-enediynes **5** and **6.**

8a	**10a-*cycl***	**5-*annul***
8a-*cycl*	**10a-*annul***	**5b**
8a-*annul*	**10a-*H-shift***	**6**
8a-*H-shift*	**11a**	**6a**
9a	**11a-*cycl***	**6a-*annul***
9a-*cycl*	**11a-*annul***	**6b**
9a-*annul*	**11a-*H-shift***	**6c**
9a-*H-shift*	**5**	**6c-*annul***
10a	**5a**	**6d**

8a

C	0.85140	1.05021	0.15302
C	-0.48259	1.21077	-0.00210
C	-1.54317	0.23936	-0.27690
C	1.73185	-0.12226	-0.00506
C	1.46713	-1.40263	-0.20157
C	-1.70647	-0.96486	0.28868
H	-1.02632	-1.34106	1.04669
H	0.62226	-2.06801	-0.29824
H	1.40808	1.96201	0.36601
H	2.79293	0.14589	0.02759
H	-0.83601	2.24186	0.05087
H	-2.55640	-1.59345	0.03749
H	-2.31343	0.58925	-0.96690

SCF energy: -232.086400774 hartree

Zero-point correction: 0.093293 hartree

Enthalpy correction: 0.118480 hartree

Free Energy correction: 0.015218 hartree

Quasiharmonic Free Energy correction: 0.016069 hartree

8a-*cycl*

C	1.33065	-0.64496	0.00925
C	1.17036	0.73851	0.16029
C	-0.06582	1.36979	-0.07520
C	0.18962	-1.43244	-0.04445
C	-1.06120	-1.24066	-0.11102
C	-1.33195	0.77277	0.05111
H	-1.62539	0.38837	1.02446
H	-1.98079	-1.68391	0.23237
H	2.31176	-1.02413	-0.26822
H	2.06879	1.35251	0.12334
H	-2.16091	1.25706	-0.46798
H	-0.00347	2.33207	-0.58390

SCF energy: -232.028325883 hartree

Zero-point correction: 0.093140 hartree

Enthalpy correction: 0.115378 hartree

Free Energy correction: 0.022025 hartree

Quasiharmonic Free Energy correction: 0.022025 hartree

8a-*annul*

C	1.24096	-0.78486	0.16536
C	1.24185	0.64816	-0.21400
C	0.07210	1.30149	-0.05671
C	0.06168	-1.37752	-0.02418
C	-1.15488	-0.86631	-0.18065
C	-1.25238	0.59112	0.24495
H	-1.53242	0.78576	1.29461
H	-1.92984	-1.29915	-0.80972
H	2.04942	-1.17950	0.77852
H	2.16618	1.18335	-0.41932
H	-2.05220	1.04832	-0.35281
H	0.04283	2.38875	-0.09992

SCF energy: -232.0668176 hartree

Zero-point correction: 0.095286 hartree

Enthalpy correction: 0.117757 hartree

Free Energy correction: 0.024329 hartree

Quasiharmonic Free Energy correction: 0.024329 hartree

8a-*H-shift*

C	1.20183	0.68315	0.04767
C	0.00365	1.38799	-0.03404
C	-1.19938	0.65696	-0.06751
C	1.22626	-0.72290	-0.01300
C	0.09008	-1.56467	-0.04582
H	-0.01674	2.47222	-0.07701
H	-1.23801	-0.04363	1.01504
C	-1.12825	-0.82649	-0.01829
H	-2.09899	-1.32731	0.00518
H	-2.16304	1.15290	-0.18065
H	2.13530	1.24289	0.10493
H	2.21629	-1.18134	-0.08159

SCF energy: -232.022839771 hartree

Zero-point correction: 0.092172 hartree

Enthalpy correction: 0.113358 hartree

Free Energy correction: 0.022563 hartree

Quasiharmonic Free Energy correction: 0.022563 hartree

9a

C	-2.47978	0.53132	-0.00003
C	-0.03671	0.77542	0.00002
C	1.07445	1.74076	-0.00007
C	2.39986	1.54171	0.00013
C	0.07462	-0.64411	0.00004
C	1.31751	-1.35126	-0.00004
C	-1.33472	1.32063	-0.00005
H	0.73047	2.77538	-0.00027
H	3.07088	2.39623	0.00002
C	-2.35929	-0.85904	0.00004
C	-1.09300	-1.43270	0.00007
H	-1.43654	2.40311	-0.00009
H	-3.46037	0.99923	-0.00007

H	-3.24207	-1.49200	0.00006
H	-0.98137	-2.51255	0.00009
C	2.31341	-2.04039	-0.00011
H	3.20607	-2.62366	-0.00012
H	2.85471	0.56022	0.00039

SCF energy: -385.717403355 hartree

Zero-point correction: 0.139785 hartree

Enthalpy correction: 0.176506 hartree

Free Energy correction: 0.046969 hartree

Quasiharmonic Free Energy correction: 0.049497 hartree

9a-*cycl*

C	-2.44480	0.72394	0.06479
C	0.00122	0.68850	0.07209
C	1.23233	1.35220	-0.20234
C	2.49373	0.79979	0.07112
C	-0.04590	-0.77044	0.03307
C	1.18011	-1.47804	0.00832
C	-1.23150	1.38752	0.09963
H	1.17115	2.23400	-0.83847
H	3.34880	1.26849	-0.41971
C	-2.48310	-0.67731	-0.04553
C	-1.30163	-1.40086	-0.08204
H	-1.21185	2.47155	0.17937
H	-3.37141	1.28977	0.11301
H	-3.43804	-1.19306	-0.09489
H	-1.32051	-2.48376	-0.15418
C	2.39005	-1.07430	-0.03913
H	3.36455	-1.45949	0.21938
H	2.71428	0.56653	1.11567

SCF energy: -385.648220935 hartree

Zero-point correction: 0.139373 hartree

Enthalpy correction: 0.173141 hartree

Free Energy correction: 0.054553 hartree

Quasiharmonic Free Energy correction: 0.054553 hartree

9a-*annul*

C	2.43451	0.71146	0.04634
C	0.00448	0.69551	0.00288
C	-1.22268	1.38589	-0.09943
C	-2.42438	0.67587	-0.05165
C	0.00062	-0.75496	-0.01304
C	-1.18300	-1.56379	-0.03034
C	1.24309	1.39793	0.04913
H	-1.23248	2.46530	-0.22190
H	-2.44881	0.04935	1.03093
C	2.45064	-0.70561	-0.01290
C	1.26771	-1.40870	-0.04952
H	1.23303	2.48518	0.09074
H	3.37399	1.25730	0.08276
H	3.40291	-1.22914	-0.02685
H	1.25118	-2.49374	-0.08564
C	-2.37779	-0.83411	0.02598
H	-3.35664	-1.30806	0.10643
H	-3.38232	1.17706	-0.18123

SCF energy: -385.663816316 hartree

Zero-point correction: 0.141176 hartree

Enthalpy correction: 0.175386 hartree

Free Energy correction: 0.055793 hartree

Quasiharmonic Free Energy correction: 0.055793 hartree

9a-*H-shift*

C	-2.44096	0.69551	0.07760
C	-0.01100	0.70249	0.17083
C	1.16112	1.31200	-0.17979
C	2.47104	0.58555	-0.33374
C	-0.01595	-0.78483	0.10514
C	1.19593	-1.40391	0.28722
C	-1.28319	1.38451	0.27916
H	1.15006	2.36632	-0.45041
H	2.86457	0.74432	-1.35450
C	-2.42359	-0.71013	-0.22658
C	-1.25385	-1.42161	-0.22023
H	-1.29885	2.44659	0.51188
H	-3.39786	1.20697	0.14138
H	-3.36528	-1.21482	-0.42501
H	-1.24956	-2.49661	-0.37735
C	2.39978	-0.83967	0.19901
H	3.28723	-1.24398	0.68376
H	3.21370	1.07181	0.31854

SCF energy: -385.641337517 hartree

Zero-point correction: 0.138366 hartree

Enthalpy correction: 0.171267 hartree

Free Energy correction: 0.054843 hartree

Quasiharmonic Free Energy correction: 0.054843 hartree

10a

C	-3.52508	-0.17372	-0.02276
C	-2.77440	-1.27647	0.38964
C	-2.86857	0.99560	-0.41049
C	-1.47669	1.06012	-0.39351
C	-1.38257	-1.21349	0.40583
C	0.78255	0.01765	-0.01572
C	1.53283	-1.09450	-0.26771
C	2.97698	-1.28332	-0.31049
C	1.35773	1.30316	0.21970
C	1.77754	2.42217	0.42074
C	3.96267	-0.42987	0.02020
H	5.00087	-0.73710	-0.06890
H	-0.81427	-2.06584	0.76599
H	-3.44159	1.86292	-0.72788
H	-0.97303	1.97342	-0.69461
C	-0.70812	-0.04869	-0.00051
H	-3.27362	-2.18536	0.71527
H	0.96623	-1.99281	-0.50054
H	2.17069	3.39655	0.60312
H	-4.61061	-0.22182	-0.03041
H	3.27137	-2.27416	-0.65592
H	3.77478	0.57236	0.38436

SCF energy: -463.10241976 hartree

Zero-point correction: 0.172961 hartree

Enthalpy correction: 0.217754 hartree

Free Energy correction: 0.069287 hartree

Quasiharmonic Free Energy correction: 0.072079 hartree

10a-*cycl*

C	-3.58784	0.00522	-0.12818
C	-2.88055	-1.19702	-0.21525
C	-2.89045	1.19773	0.06994
C	-1.50300	1.18613	0.19375
C	-1.49263	-1.20787	-0.10765
C	0.69622	0.03093	0.22778
C	1.48350	-1.11980	0.42266
C	2.82258	-1.20703	0.00451
C	1.40203	1.20926	-0.05020
C	2.58267	1.55089	-0.34060
C	3.72910	-0.14341	-0.12787
H	3.95652	0.45822	0.74721
H	-0.96334	-2.14852	-0.22406
H	-3.42871	2.13928	0.14130
H	-0.95929	2.10844	0.37522
C	-0.77456	-0.01537	0.10581
H	-3.41207	-2.12988	-0.38462
H	0.96546	-2.05758	0.61174
H	3.26935	2.37139	-0.22257
H	-4.67098	0.01041	-0.21538
H	3.11491	-2.17589	-0.40230
H	4.60581	-0.31383	-0.75473

SCF energy: -463.047680368 hartree

Zero-point correction: 0.172750 hartree

Enthalpy correction: 0.214658 hartree

Free Energy correction: 0.075697 hartree

Quasiharmonic Free Energy correction: 0.077304 hartree

10a-*annul*

C	3.51072	0.01952	0.29520
C	2.77845	1.20881	0.27452
C	2.86034	-1.19507	0.05908
C	1.49428	-1.21867	-0.20253
C	1.40827	1.18749	0.02360
C	-0.70545	-0.09194	-0.45428
C	-1.52626	1.12909	-0.65724
C	-2.69764	1.17935	0.00718
C	-1.45974	-1.19986	-0.27478
C	-2.71759	-1.30746	0.14099
C	-3.30923	-0.02980	0.71211
H	-3.22151	0.10851	1.80368
H	0.84723	2.11694	0.03972
H	3.42410	-2.12437	0.06365
H	0.98624	-2.15309	-0.42277
C	0.73943	-0.02874	-0.21316
H	3.27571	2.15724	0.46068
H	-1.13084	2.00316	-1.17008
H	-3.38046	-2.13102	-0.11882
H	4.58052	0.03962	0.48506
H	-3.24445	2.11798	0.07913
H	-4.39013	-0.05134	0.51557

SCF energy: -463.047680368 hartree

Zero-point correction: 0.175277 hartree

Enthalpy correction: 0.217183 hartree

Free Energy correction: 0.078686 hartree

Quasiharmonic Free Energy correction: 0.080044 hartree

10a-*H-shift*

C	-3.56733	-0.01513	0.10598
C	-2.84251	-1.19900	0.26217
C	-2.88841	1.18418	-0.12405
C	-1.49846	1.20016	-0.20921
C	-1.45150	-1.18316	0.18019
C	0.72554	0.06518	-0.15561
C	1.44448	-1.10322	-0.46757
C	2.82444	-1.15827	-0.17957
C	1.38716	1.31922	0.04308
C	2.77196	1.27009	0.21737
C	3.51051	0.06285	0.23969
H	3.02514	-0.86846	1.06658
H	-0.89992	-2.10550	0.34219
H	-3.44624	2.10973	-0.24305
H	-0.94462	2.11656	-0.38489
C	-0.75565	0.01478	-0.06552
H	-3.36097	-2.13373	0.46052
H	0.96772	-1.99132	-0.87560
H	3.35379	2.18978	0.30903
H	-4.65250	-0.02745	0.16912
H	3.41497	-2.05267	-0.35686
H	4.58127	0.01698	0.43132

SCF energy: -463.033762525 hartree

Zero-point correction: 0.171357 hartree

Enthalpy correction: 0.212317 hartree

Free Energy correction: 0.075910 hartree

Quasiharmonic Free Energy correction: 0.077237 hartree

11a

C	2.23238	-1.06461	0.00021
C	0.91851	-1.39546	0.00029
C	-0.28851	-0.56749	0.00015
C	2.82545	0.22464	-0.00014
C	3.41581	1.28395	-0.00050
C	-0.28841	0.84210	0.00042
H	0.65255	1.37837	0.00066
H	3.91365	2.22679	-0.00068
H	2.94533	-1.88827	0.00028
H	0.71524	-2.46530	0.00036
C	-1.53359	-1.22800	-0.00025
C	-2.73068	-0.51739	-0.00037
C	-2.71214	0.87844	-0.00009
H	-3.67673	-1.05220	-0.00069
C	-1.48683	1.55057	0.00030
H	-3.64347	1.43839	-0.00018
H	-1.46458	2.63727	0.00051
H	-1.55396	-2.31555	-0.00045

SCF energy: -385.721282245 hartree

Zero-point correction: 0.140578 hartree

Enthalpy correction: 0.176707 hartree

Free Energy correction: 0.048771 hartree

Quasiharmonic Free Energy correction: 0.050886 hartree

11a-*cycl*

C	-2.42634	-0.69522	-0.24200

C	-1.30849	-1.34331	0.27338
C	-0.04831	-0.68908	0.33433
C	-2.41301	0.69879	-0.37337
C	-1.45617	1.53602	-0.14576
C	0.04097	0.77453	0.44549
H	-0.33177	1.13161	1.41660
H	-1.45151	2.58142	0.13484
H	-3.21903	-1.30323	-0.67519
H	-1.31190	-2.43193	0.31533
C	1.12876	-1.42666	0.05151
C	1.32136	1.37871	0.11393
C	2.39834	0.62276	-0.25975
H	3.33804	1.10192	-0.52241
C	2.31562	-0.79686	-0.25604
H	1.06103	-2.51127	0.00742
H	1.40914	2.45993	0.19143
H	3.18955	-1.38642	-0.51841

SCF energy: -385.639673951 hartree

Zero-point correction: 0.139756 hartree

Enthalpy correction: 0.173075 hartree

Free Energy correction: 0.055512 hartree

Quasiharmonic Free Energy correction: 0.055512 hartree

11a-*annul*

C	2.54217	0.52317	0.12789
C	1.34705	1.34621	-0.13768
C	0.13098	0.75017	0.01393
C	2.35572	-0.77454	-0.13519
C	1.22489	-1.46250	-0.27341
C	0.04792	-0.77275	0.37228
H	0.14552	-0.77932	1.47823
H	1.06824	-2.25879	-1.00100
H	3.39204	0.94481	0.66149
H	1.42081	2.42044	-0.29341
C	-1.12308	1.47005	-0.04245
C	-1.30183	-1.39062	0.09052
C	-2.40196	-0.63172	-0.04607
H	-3.37635	-1.09323	-0.18641
C	-2.31651	0.82467	-0.05029
H	-3.23874	1.39624	-0.11531
H	-1.08719	2.55361	-0.13258
H	-1.35652	-2.47670	0.07172

SCF energy: -385.648570857 hartree

Zero-point correction: 0.140757 hartree

Enthalpy correction: 0.175166 hartree

Free Energy correction: 0.055373 hartree

Quasiharmonic Free Energy correction: 0.055373 hartree

11a-*H-shift*

C	2.46984	0.66443	-0.08367
C	1.28770	1.37077	0.09429
C	0.02857	0.72763	0.08528
C	2.56140	-0.75466	-0.19292
C	1.36605	-1.43010	-0.00777
C	0.00612	-0.72064	0.10830
H	0.62206	-1.06593	1.10720
H	1.28765	-2.51416	0.09254
H	3.37555	1.25958	-0.22006

H	1.29926	2.46042	0.13619
C	-1.20622	1.42515	0.01463
C	-1.26240	-1.39864	0.01260
C	-2.42096	-0.67624	-0.08964
H	-3.37257	-1.19272	-0.18353
C	-2.39935	0.74736	-0.07660
H	-3.33408	1.29567	-0.14734
H	-1.18661	2.51224	0.01418
H	-1.27578	-2.48554	0.01383

SCF energy: -385.631734333 hartree

Zero-point correction: 0.138075 hartree

Enthalpy correction: 0.171114 hartree

Free Energy correction: 0.054335 hartree

Quasiharmonic Free Energy correction: 0.054335 hartree

5

C	4.74218	-0.09486	-0.07201
C	3.94099	0.78983	-0.81016
C	4.11592	-1.11983	0.65287
C	2.73098	-1.25136	0.64132
C	2.55769	0.66777	-0.81194
C	0.44233	-0.52326	-0.07009
C	-0.44234	0.52324	0.07000
C	-1.92591	0.34947	0.07447
C	0.00017	-1.86791	-0.24294
C	-0.29050	-3.03391	-0.41811
C	-2.55766	-0.66787	0.81186
C	-3.94095	-0.78994	0.81015
C	-4.74217	0.09483	0.07213
C	-4.11598	1.11988	-0.65269
C	-2.73104	1.25141	-0.64120
H	-2.26006	2.05688	-1.19609
H	-4.70628	1.82548	-1.22926
H	-1.95853	-1.35286	1.40031
H	1.95861	1.35271	-1.40050
H	4.70615	-1.82539	1.22958
H	2.25997	-2.05676	1.19627
C	1.92589	-0.34949	-0.07449
C	0.29048	3.03390	0.41792
C	-0.00019	1.86789	0.24280
C	0.68382	4.42237	0.62816
H	0.54835	4.71850	1.67594
H	1.73849	4.57878	0.37129
H	0.08342	5.10371	0.01285
C	-0.68385	-4.42236	-0.62841
H	-1.73799	-4.57923	-0.36965
H	-0.55030	-4.71783	-1.67663
H	-0.08209	-5.10390	-0.01465
H	-4.43219	-1.56728	1.38641
H	4.43225	1.56712	-1.38647
C	-6.22768	-0.09292	0.10365
C	6.22769	0.09294	-0.10351
C	7.10674	-0.87067	0.67843
H	6.86192	-0.85094	1.74718
H	6.96843	-1.90160	0.33104
H	8.14987	-0.58066	0.54178
C	-7.10661	0.87076	-0.67831
H	-8.14979	0.58099	-0.54156
H	-6.96802	1.90171	-0.33105
H	-6.86184	0.85085	-1.74707

O	-6.72770	-1.00475	0.74611
O	6.72766	1.00479	-0.74600

SCF energy: -1076.75960768 hartree

Zero-point correction: 0.357835 hartree

Enthalpy correction: 0.455985 hartree

Free Energy correction: 0.171968 hartree

Quasiharmonic Free Energy correction: 0.192017 hartree

5a

C	-4.56731	-0.39550	0.56719
C	-3.71355	0.66721	0.90858
C	-4.05140	-1.44582	-0.20511
C	-2.72797	-1.42505	-0.63310
C	-2.39335	0.68877	0.48520
C	-0.46079	-0.42989	-0.74327
C	0.38685	0.70615	-0.90094
C	1.79298	0.53893	-0.64545
C	0.13648	-1.68987	-0.86391
C	1.34716	-2.11524	-0.95613
C	2.48597	-0.72905	-0.92443
C	3.76852	-0.92982	-0.28522
C	4.35032	0.02161	0.52013
C	3.72051	1.29520	0.64484
C	2.50178	1.54706	0.05263
H	2.01810	2.50701	0.20026
H	4.18755	2.07635	1.23589
H	2.54441	-0.92093	-2.00493
H	-1.75187	1.50712	0.78793
H	-4.68146	-2.28490	-0.48406
H	-2.33527	-2.23423	-1.24020
C	-1.87041	-0.35724	-0.30371
C	-0.54031	3.15533	-1.22420
C	-0.12977	2.02834	-1.03286
C	-1.06999	4.49620	-1.44579
H	-2.07263	4.60245	-1.01385
H	-0.42614	5.25993	-0.99308
H	-1.14512	4.72003	-2.51738
C	2.01024	-3.36633	-1.42664
H	2.62747	-3.19048	-2.31874
H	2.66990	-3.78582	-0.65616
H	1.25362	-4.11577	-1.67262
H	4.30966	-1.85483	-0.46004
H	-4.11272	1.46596	1.52529
C	-5.98368	-0.35613	1.05055
C	5.66295	-0.30545	1.17276
C	6.34717	0.76238	2.00970
H	6.56708	1.65361	1.40941
H	5.70695	1.08054	2.84153
H	7.27869	0.35454	2.40552
C	-6.91284	-1.50714	0.69743
H	-7.89423	-1.30886	1.13158
H	-7.01219	-1.61570	-0.38927
H	-6.52940	-2.45806	1.08635
O	-6.38910	0.58396	1.71896
O	6.17164	-1.40722	1.03316

SCF energy: -1076.680287 hartree

Zero-point correction: 0.356840 hartree

Enthalpy correction: 0.452307 hartree

Free Energy correction: 0.182927 hartree

Quasiharmonic Free Energy correction: 0.196489 hartree

5-*annul*

C	-4.31239	-0.56099	0.65555
C	-3.43016	0.44060	1.09546
C	-3.90220	-1.40297	-0.38929
C	-2.65575	-1.23858	-0.98281
C	-2.18210	0.60097	0.51289
C	-0.43437	-0.15777	-1.16054
C	0.44974	1.01178	-1.02000
C	1.77331	0.70533	-0.70677
C	0.16312	-1.25486	-1.70338
C	1.44025	-1.59076	-1.80785
C	2.39836	-0.63455	-1.06053
C	3.40429	-1.11482	-0.06847
C	4.04690	-0.24848	0.75726
C	3.69821	1.16094	0.71922
C	2.62283	1.61413	0.01400
H	2.31222	2.65129	0.09577
H	4.26679	1.86437	1.31897
H	3.02592	-0.37119	-1.94326
H	-1.51377	1.36830	0.88589
H	-4.56041	-2.18468	-0.75660
H	-2.35048	-1.87022	-1.81096
C	-1.76564	-0.24044	-0.54010
C	-0.47609	3.48084	-0.97102
C	-0.04108	2.34680	-0.96703
C	-1.01857	4.83499	-0.97534
H	-2.08697	4.83222	-0.72801
H	-0.50714	5.47277	-0.24416
H	-0.90667	5.30500	-1.96055
C	2.03125	-2.58103	-2.77456
H	2.76914	-2.11117	-3.44031
H	2.55081	-3.39671	-2.25184
H	1.24369	-3.02750	-3.38741
H	3.69233	-2.16214	-0.06511
H	-3.74967	1.08067	1.91146
C	-5.64745	-0.67666	1.32173
C	5.10747	-0.79558	1.67384
C	5.83973	0.16722	2.59270
H	6.36523	0.93941	2.01723
H	5.13886	0.68188	3.26139
H	6.56252	-0.39420	3.18693
C	-6.60829	-1.76070	0.85848
H	-6.85732	-1.64118	-0.20276
H	-6.16723	-2.75735	0.97972
H	-7.52105	-1.69510	1.45306
O	-5.96314	0.08493	2.22491
O	5.37376	-1.98701	1.68007

SCF energy: -1076.69151475 hartree

Zero-point correction: 0.357847 hartree

Enthalpy correction: 0.454264 hartree

Free Energy correction: 0.181844 hartree

Quasiharmonic Free Energy correction: 0.196334 hartree

5b

C	-4.69019	-0.34522	0.45588
C	-3.80783	0.61700	0.97522
C	-4.17254	-1.34912	-0.37662

C	-2.81763	-1.38180	-0.69027
C	-2.45691	0.58654	0.66165
C	-0.48951	-0.51647	-0.50647
C	0.36305	0.63389	-0.55233
C	1.75377	0.45831	-0.29980
C	0.03845	-1.79772	-0.73332
C	1.41036	-2.02166	-0.73285
C	2.33708	-0.87599	-0.34134
C	3.70589	-1.04832	0.05921
C	4.48876	0.02994	0.39849
C	3.93265	1.34638	0.34822
C	2.62143	1.54704	-0.00023
H	2.20480	2.54853	-0.01455
H	4.54994	2.20294	0.59780
H	2.12778	-1.20227	-1.52520
H	-1.79378	1.32732	1.09469
H	-4.82679	-2.11115	-0.78981
H	-2.40803	-2.15871	-1.32631
C	-1.93355	-0.41090	-0.18599
C	-0.54650	3.06535	-1.03386
C	-0.13050	1.95102	-0.78866
C	-1.08954	4.38909	-1.31617
H	-0.97821	4.64441	-2.37741
H	-2.15748	4.43700	-1.07180
H	-0.57533	5.16343	-0.73411
C	2.01562	-3.38024	-1.02519
H	2.96655	-3.32755	-1.56997
H	2.20523	-3.92536	-0.09122
H	1.30006	-3.96368	-1.60929
H	4.14485	-2.03952	0.09061
H	-4.21079	1.37798	1.63575
C	-6.13826	-0.25372	0.82153
C	5.91381	-0.23669	0.80310
C	6.79183	0.93768	1.19727
H	6.88518	1.65485	0.37263
H	6.36622	1.47776	2.05173
H	7.78132	0.56221	1.46277
C	-7.10011	-1.30038	0.28012
H	-7.10613	-1.30222	-0.81644
H	-6.81177	-2.30699	0.60574
H	-8.10314	-1.07531	0.64661
O	-6.54642	0.64520	1.54355
O	6.35165	-1.37617	0.81422

SCF energy: -1076.66931677 hartree

Zero-point correction: 0.354557 hartree

Enthalpy correction: 0.449956 hartree

Free Energy correction: 0.181560 hartree

Quasiharmonic Free Energy correction: 0.194812 hartree

6

C	4.46146	0.82345	0.54123
C	3.66477	1.85923	1.02858
C	3.83783	-0.33623	0.05752
C	2.44044	-0.42985	0.07301
C	2.27428	1.77417	1.03276
C	0.15569	0.45973	0.54710
C	-0.71125	1.44239	0.12270
C	-2.20214	1.31630	0.14698
C	-0.30304	-0.79979	1.02855
C	-0.62090	-1.89773	1.43880
C	-2.97184	2.43695	0.50188

C	-4.36140	2.35707	0.52607
C	-5.00474	1.17092	0.18683
C	-4.24928	0.05053	-0.18786
C	-2.85087	0.12458	-0.21387
H	-2.28561	-0.74125	-0.51977
H	-2.47432	3.36557	0.76062
H	1.67878	2.58773	1.42960
H	1.95670	-1.33559	-0.28544
C	1.64317	0.62139	0.54075
C	0.10496	3.74838	-0.87123
C	-0.22760	2.68246	-0.39429
C	0.55344	5.01479	-1.43921
H	0.40007	5.04155	-2.52554
H	0.00592	5.86276	-1.00896
H	1.62197	5.17622	-1.25083
C	-1.08849	-3.20586	1.88003
H	-1.43592	-3.17241	2.92073
H	-1.92243	-3.53506	1.24878
H	-0.29145	-3.95738	1.82311
H	-4.95013	3.22441	0.81214
H	4.14664	2.75099	1.42115
H	-6.09138	1.11192	0.20947
H	5.53981	0.89244	0.53666
N	-4.96676	-1.11484	-0.55146
N	4.54864	-1.44648	-0.45157
C	-4.51055	-2.39829	-0.73615
C	5.90770	-1.61945	-0.58962
H	-5.96621	-0.98532	-0.62524
H	3.96671	-2.21304	-0.75964
O	-3.33612	-2.73345	-0.64466
O	6.74462	-0.78788	-0.26721
C	-5.59511	-3.41184	-1.07936
H	-5.58516	-4.20438	-0.32465
H	-6.60430	-2.99217	-1.13812
H	-5.34904	-3.87453	-2.04006
C	6.31344	-2.95768	-1.19548
H	7.00962	-3.45303	-0.51211
H	6.85222	-2.77035	-2.12976
H	5.47660	-3.63299	-1.40023

SCF energy: -1187.49759135 hartree

Zero-point correction: 0.392521 hartree

Enthalpy correction: 0.499013 hartree

Free Energy correction: 0.199530 hartree

Quasiharmonic Free Energy correction: 0.216757 hartree

6a

C	-4.03841	-1.64402	-0.80623
C	-2.77656	-2.23588	-0.89195
C	-4.13677	-0.34260	-0.29525
C	-2.98009	0.32534	0.12515
C	-1.62510	-1.57540	-0.47607
C	-0.53936	0.53570	0.45893
C	0.69353	-0.01723	0.89008
C	1.90802	0.73779	0.65306
C	-0.60667	1.93106	0.28422
C	0.27047	2.87164	0.30760
C	1.90981	2.20150	0.70498
C	3.06942	2.86502	0.14373
C	4.10909	2.16721	-0.39956
C	4.13415	0.74322	-0.33383
C	3.05741	0.05261	0.21052

H	3.07034	-1.02737	0.21709
H	1.67634	2.57534	1.71019
H	-0.66018	-2.05418	-0.58282
H	-3.04485	1.33440	0.52449
C	-1.71250	-0.27239	0.04987
C	0.98560	-2.50785	1.70832
C	0.82556	-1.37767	1.29383
C	1.15745	-3.87557	2.18399
H	2.12413	-4.28369	1.86500
H	1.12194	-3.92423	3.27985
H	0.36917	-4.53347	1.79751
C	0.24799	4.35519	0.46364
H	0.72398	4.67598	1.40162
H	0.78096	4.85687	-0.35522
H	-0.78553	4.71151	0.46449
H	-2.69605	-3.23733	-1.30694
H	4.95369	2.69582	-0.83882
H	-4.93057	-2.16333	-1.12580
N	-5.35983	0.35491	-0.17013
C	-6.63176	-0.05663	-0.49752
C	-7.71718	0.97984	-0.23204
H	-8.47021	0.53594	0.42607
H	-7.35419	1.90831	0.22023
H	-8.21226	1.21863	-1.17861
H	-5.27396	1.28758	0.20913
O	-6.90225	-1.15355	-0.96657
N	5.27161	0.11402	-0.86804
H	5.94376	0.74011	-1.28975
C	5.59205	-1.23060	-0.90215
O	4.89005	-2.11119	-0.42965
C	6.90290	-1.54357	-1.61084
H	7.54239	-0.67022	-1.77479
H	7.44994	-2.28112	-1.01825
H	6.68205	-2.00060	-2.58194
H	3.11016	3.95033	0.17918

SCF energy: -1187.41718818 hartree

Zero-point correction: 0.391039 hartree

Enthalpy correction: 0.495425 hartree

Free Energy correction: 0.200235 hartree

Quasiharmonic Free Energy correction: 0.219980 hartree

6a-*annul*

C	4.21186	-1.43421	-1.00711
C	2.96888	-2.02857	-1.22967
C	4.26958	-0.24639	-0.26064
C	3.09055	0.31122	0.24388
C	1.79183	-1.47633	-0.73255
C	0.63275	0.39636	0.50311
C	-0.71278	-0.25558	0.55744
C	-1.76232	0.51865	0.09264
C	0.58583	1.71884	0.78018
C	-0.43391	2.56731	0.62367
C	-1.48736	1.99325	-0.31838
C	-2.74036	2.80430	-0.51516
C	-3.95086	2.23652	-0.60669
C	-4.13386	0.79622	-0.42600
C	-3.08543	-0.00903	-0.07540
H	-3.25470	-1.05923	0.11636
H	-1.03969	1.92384	-1.32984
H	0.83950	-1.95453	-0.92864
H	3.12155	1.21676	0.84591

C	1.83972	-0.28185	0.00996
C	-1.01924	-2.74197	1.37276
C	-0.88626	-1.59695	0.98856
C	-1.18239	-4.11517	1.83712
H	-0.36999	-4.75843	1.47623
H	-1.18377	-4.16948	2.93347
H	-2.12913	-4.54113	1.48344
C	-0.67005	3.82076	1.41404
H	-0.63903	4.72267	0.78503
H	-1.66097	3.80494	1.88946
H	0.09371	3.93020	2.18924
H	-2.62751	3.87682	-0.64893
H	2.92466	-2.94700	-1.80931
H	-4.83025	2.84917	-0.80096
H	5.12406	-1.87295	-1.38546
N	-5.45204	0.35210	-0.60809
N	5.47570	0.42974	0.03156
C	-5.96080	-0.93185	-0.50779
C	6.76541	0.09835	-0.31846
C	-7.44308	-1.04692	-0.83552
H	-7.96671	-0.08672	-0.88457
H	-7.55551	-1.55503	-1.79969
H	-7.91865	-1.67450	-0.07747
C	7.82595	1.05972	0.20443
H	8.45269	0.53131	0.93055
H	8.47000	1.35353	-0.62916
H	7.42345	1.96063	0.67852
H	-6.11390	1.07017	-0.86791
H	5.36271	1.26807	0.58446
O	-5.29011	-1.90462	-0.20305
O	7.06884	-0.88314	-0.98213

SCF energy: -1187.43470494 hartree

Zero-point correction: 0.392484 hartree

Enthalpy correction: 0.497709 hartree

Free Energy correction: 0.200504 hartree

Quasiharmonic Free Energy correction: 0.220784 hartree

6b

C	5.03562	1.29262	0.55984
C	4.33402	2.39503	1.04156
C	4.34299	0.23676	-0.04871
C	2.94802	0.28576	-0.15986
C	2.94877	2.45330	0.92705
C	0.75493	1.51448	0.21464
C	-0.09719	0.38626	0.31351
C	-1.50231	0.52641	0.03952
C	0.25018	2.84411	0.09499
C	-1.07176	3.01096	-0.28390
C	-2.01218	1.79931	-0.42028
C	-3.42054	1.91408	-0.68945
C	-4.28085	0.86493	-0.49375
C	-3.77056	-0.38893	-0.05306
C	-2.41190	-0.53681	0.19270
H	-2.01899	-1.49312	0.52624
H	-1.36510	2.17980	-1.38110
H	2.38465	3.31566	1.26296
H	2.43414	-0.53054	-0.64349
C	2.23890	1.39038	0.34190
C	0.73066	-1.99243	1.10906
C	0.36187	-0.89225	0.75163

C	1.28483	-3.28961	1.47939
H	0.57091	-4.10204	1.29623
H	2.18729	-3.48349	0.88729
H	1.55479	-3.31822	2.54274
C	-1.68404	4.36843	-0.55080
H	-2.11239	4.46591	-1.55718
H	-2.48975	4.58248	0.16573
H	-0.89827	5.11673	-0.43802
H	-3.81267	2.86274	-1.03916
H	4.87653	3.21406	1.50647
H	-5.34188	0.96932	-0.67041
H	6.11973	1.24962	0.65130
N	-4.59312	-1.51063	0.14990
N	5.12104	-0.83625	-0.55368
C	-5.95486	-1.64708	-0.04383
C	4.72848	-2.10285	-0.90851
C	-6.49587	-3.03632	0.26338
H	-6.86899	-3.48126	-0.66500
H	-5.76395	-3.71659	0.70990
H	-7.34788	-2.93495	0.94148
C	5.86256	-3.01039	-1.36997
H	6.85573	-2.55263	-1.32085
H	5.85862	-3.91582	-0.75550
H	5.66752	-3.31725	-2.40245
H	-4.10514	-2.33362	0.47651
H	6.11476	-0.65558	-0.58296
O	-6.68433	-0.74919	-0.43693
O	3.57010	-2.50203	-0.87889

SCF energy: -1187.40835091 hartree

Zero-point correction: 0.389131 hartree

Enthalpy correction: 0.493117 hartree

Free Energy correction: 0.203835 hartree

Quasiharmonic Free Energy correction: 0.219140 hartree

6c

C	4.30107	-2.01096	0.03799
C	3.34942	-2.85668	0.60579
C	3.92475	-0.70060	-0.29892
C	2.61773	-0.26415	-0.05346
C	2.04863	-2.42594	0.85050
C	0.25583	-0.70964	0.75089
C	-0.17808	0.62738	0.95808
C	-1.48668	1.01460	0.48105
C	-0.74509	-1.67322	0.62366
C	-2.02345	-1.65294	0.49038
C	-2.63483	0.08892	0.48296
C	-3.79885	0.48767	-0.32144
C	-3.80349	1.65561	-1.05601
C	-2.71937	2.55042	-0.94169
C	-1.61600	2.26392	-0.16475
H	-0.78136	2.95487	-0.12664
H	-2.93805	-0.14756	1.51151
H	1.31657	-3.08770	1.30087
H	2.33348	0.74322	-0.34022
C	1.66324	-1.11146	0.52763
C	1.44447	2.53648	1.78950
C	0.72242	1.65707	1.36398
C	2.33153	3.57273	2.30722
H	2.13160	3.77346	3.36742
H	3.38421	3.27627	2.22091
H	2.20296	4.51766	1.76473

C	-3.07413	-2.67541	0.79374
H	-3.73471	-2.36315	1.61862
H	-3.70010	-2.90721	-0.07760
H	-2.58974	-3.60535	1.10242
H	3.63680	-3.87210	0.86567
H	-4.66642	1.90501	-1.65649
H	5.31246	-2.34174	-0.15015
N	4.80578	0.22629	-0.90136
C	6.12589	0.06518	-1.25998
C	6.74925	1.28424	-1.92904
H	7.68919	1.51730	-1.42087
H	6.99350	1.03003	-2.96581
H	6.11245	2.17472	-1.92729
H	4.39265	1.12463	-1.10970
O	6.76893	-0.95915	-1.07958
N	-4.92015	-0.35527	-0.24148
C	-6.14849	-0.23764	-0.86762
H	-4.82648	-1.14043	0.38406
O	-6.43372	0.64411	-1.66322
H	-2.75359	3.48335	-1.49781
C	-7.15597	-1.30744	-0.46799
H	-7.91957	-0.85560	0.17506
H	-7.65799	-1.66454	-1.37073
H	-6.71762	-2.16077	0.05953

SCF energy: -1187.41375492 hartree

Zero-point correction: 0.391428 hartree

Enthalpy correction: 0.495594 hartree

Free Energy correction: 0.202564 hartree

Quasiharmonic Free Energy correction: 0.221280 hartree

6c-*annul*

C	3.91947	-2.78192	0.14871
C	2.89626	-3.44808	-0.52238
C	3.78928	-1.41722	0.44620
C	2.62447	-0.72884	0.08509
C	1.74772	-2.76630	-0.90623
C	0.33285	-0.73515	-0.96096
C	0.09478	0.74843	-0.85705
C	-1.13535	1.12197	-0.35129
C	-0.79903	-1.38824	-1.28533
C	-2.07526	-1.03705	-1.12005
C	-2.17105	0.00628	-0.00542
C	-3.55068	0.51172	0.38626
C	-3.80659	1.83202	0.55033
C	-2.76645	2.80769	0.31299
C	-1.51010	2.48203	-0.09761
H	-0.76936	3.25385	-0.28229
H	-1.77316	-0.45278	0.91847
H	0.96284	-3.26702	-1.46462
H	2.53477	0.31819	0.32967
C	1.59277	-1.40175	-0.59367
C	2.00577	2.45846	-1.45180
C	1.10293	1.68909	-1.18880
C	3.13742	3.34276	-1.70341
H	3.51913	3.22694	-2.72588
H	2.86181	4.39584	-1.56876
H	3.95101	3.11003	-1.00523
C	-3.17712	-1.30808	-2.10697
H	-3.99095	-1.92585	-1.70206

H	-3.63955	-0.36560	-2.43057
H	-2.77307	-1.82509	-2.98199
H	3.00956	-4.50198	-0.76179
H	-4.78478	2.15529	0.87701
H	4.82780	-3.31400	0.42535
N	4.86655	-0.80296	1.12791
C	5.12698	0.53543	1.31746
C	6.42017	0.82535	2.06936
H	7.02019	-0.06195	2.29496
H	7.02146	1.51891	1.47428
H	6.17393	1.33107	3.00861
H	5.57674	-1.44305	1.45484
O	4.39617	1.43999	0.93749
H	-3.01835	3.85306	0.47194
N	-4.45183	-0.52621	0.66031
C	-5.74864	-0.44407	1.13712
H	-4.08651	-1.45749	0.51724
C	-6.42748	-1.78898	1.35519
H	-7.33691	-1.82548	0.74741
H	-5.80293	-2.65359	1.10928
H	-6.73414	-1.86114	2.40331
O	-6.32008	0.61035	1.36587

SCF energy: -1187.43627485 hartree

Zero-point correction: 0.393102 hartree

Enthalpy correction: 0.497995 hartree

Free Energy correction: 0.205810 hartree

Quasiharmonic Free Energy correction: 0.221618 hartree

6d

C	4.19604	-2.58249	0.12699
C	3.20804	-3.33720	-0.49977
C	3.93746	-1.25020	0.48235
C	2.68724	-0.68362	0.21079
C	1.96771	-2.77539	-0.78646
C	0.33659	-0.89740	-0.69872
C	0.06699	0.50007	-0.84347
C	-1.24510	0.97716	-0.54190
C	-0.71978	-1.79884	-0.88717
C	-2.04252	-1.38844	-0.76648
C	-2.33203	0.03590	-0.28167
C	-3.63141	0.56250	0.13663
C	-3.83675	1.92691	0.18027
C	-2.77892	2.81295	-0.12111
C	-1.52336	2.36325	-0.45507
H	-0.71603	3.05953	-0.65082
H	-2.02365	-0.83668	0.53311
H	1.18590	-3.34182	-1.27962
H	2.50047	0.33716	0.50641
C	1.69423	-1.44138	-0.43558
C	1.92816	2.22332	-1.56942
C	1.06510	1.43310	-1.24503
C	3.03025	3.12428	-1.88469
H	3.45837	2.89897	-2.86972
H	2.70454	4.17149	-1.89610
H	3.82145	3.01633	-1.13280
C	-3.15119	-2.31931	-1.21230
H	-3.59314	-2.92537	-0.40664
H	-3.95579	-1.79811	-1.74381
H	-2.67455	-3.03653	-1.88712
H	3.41551	-4.36783	-0.77560

H	-4.80759	2.30286	0.46731
H	5.17110	-3.02004	0.33467
N	4.97855	-0.54353	1.13433
C	5.12534	0.81115	1.31647
C	6.41778	1.21823	2.01393
H	7.07809	0.38224	2.26570
H	6.95966	1.91542	1.36749
H	6.16493	1.75645	2.93277
H	5.75657	-1.11734	1.42824
O	4.30251	1.64788	0.96692
H	-2.96870	3.88128	-0.06445
N	-4.62099	-0.35814	0.52605
C	-5.86533	-0.11224	1.08411
H	-4.40285	-1.33175	0.38674
C	-6.66842	-1.37056	1.38516
H	-7.07442	-1.28819	2.39683
H	-7.51774	-1.42149	0.69521
H	-6.09663	-2.30053	1.30374
O	-6.31315	1.00026	1.31041

SCF energy: -1187.39790182 hartree

Zero-point correction: 0.389022 hartree

Enthalpy correction: 0.492993 hartree

Free Energy correction: 0.203882 hartree

Quasiharmonic Free Energy correction: 0.219582 hartree

xiii) Computed structures of $[8]_A$GNR, PDA **1**, PDA **1-annul** for frequency calculations

$[8]_A$GNR (computed structure described in Fig. S22)

PDA **1**

PDA **1-*annul***

$[8]_A$GNR			
C	0.55650	16.86421	0.00769
C	4.28665	14.69804	0.00487
C	4.28755	13.30577	0.00353
C	3.09106	12.57962	0.00300
C	1.85091	13.28860	0.00376
C	1.85480	14.71814	0.00519
C	3.09202	15.39450	0.00571
C	0.59830	15.43700	0.00604
C	-0.61884	14.71890	0.00525
C	-1.86482	15.43164	0.00600
C	-3.10666	14.73148	0.00513
C	-4.29501	15.47334	0.00592
C	-4.28927	16.87115	0.00756
C	-3.09121	17.56216	0.00841
C	-1.86934	16.86058	0.00764
C	-0.61436	13.27708	0.00371
C	4.27513	10.38040	0.00110
C	4.27487	9.00167	-0.00020
C	3.08018	8.26456	-0.00099
C	1.84959	8.97740	-0.00036
C	1.85069	10.41043	0.00098
C	3.08314	11.12013	0.00167
C	0.60892	11.12761	0.00162
C	-0.61094	10.41311	0.00090
C	-1.85300	11.12990	0.00147
C	-3.08307	10.41550	0.00065
C	-4.27928	11.14949	0.00106
C	-4.28300	12.52904	0.00246
C	-3.09407	13.27091	0.00348
C	-1.85737	12.56247	0.00290
C	0.60789	12.56785	0.00306
C	-0.62298	17.54879	0.00847
C	-0.61040	0.35788	-0.00521
C	-4.27571	2.54089	-0.00549
C	-4.27516	3.91784	-0.00477
C	-3.07934	4.65705	-0.00397
C	-1.84841	3.94599	-0.00419
C	-1.84876	2.51345	-0.00489
C	-3.07991	1.80160	-0.00542
C	-0.61007	1.79529	-0.00498
C	0.61078	2.51158	-0.00476
C	1.84958	1.79342	-0.00514
C	3.08067	2.50516	-0.00522
C	4.27647	1.76572	-0.00586
C	4.27613	0.38877	-0.00610
C	3.08018	-0.35071	-0.00570
C	1.84928	0.36080	-0.00537
C	0.61087	3.94917	-0.00411

C	-4.27513	6.84602	-0.00219	C	-0.61087	-3.94917	-0.00411
C	-4.27516	8.22347	-0.00105	C	4.27513	-6.84602	-0.00219
C	-3.08067	8.96273	-0.00054	C	4.27516	-8.22347	-0.00105
C	-1.84886	8.25321	-0.00108	C	3.08067	-8.96273	-0.00054
C	-1.84848	6.82072	-0.00224	C	1.84886	-8.25321	-0.00108
C	-3.07938	6.10825	-0.00285	C	1.84848	-6.82072	-0.00224
C	-0.60943	6.10298	-0.00272	C	3.07938	-6.10825	-0.00285
C	0.61057	6.81947	-0.00218	C	0.60943	-6.10298	-0.00272
C	1.84948	6.10070	-0.00278	C	-0.61057	-6.81947	-0.00218
C	3.08032	6.81201	-0.00234	C	-1.84948	-6.10070	-0.00278
C	4.27580	6.07327	-0.00319	C	-3.08032	-6.81201	-0.00234
C	4.27604	4.69585	-0.00426	C	-4.27580	-6.07327	-0.00319
C	3.08063	3.95641	-0.00448	C	-4.27604	-4.69585	-0.00426
C	1.84961	4.66800	-0.00381	C	-3.08063	-3.95641	-0.00448
C	0.61010	8.25843	-0.00100	C	-1.84961	-4.66800	-0.00381
C	-0.60960	4.66486	-0.00368	C	0.60960	-4.66486	-0.00368
C	0.61040	-0.35788	-0.00521	C	-0.55650	-16.86421	0.00769
C	-0.61022	8.97306	-0.00043	C	-4.28665	-14.69804	0.00487
C	4.27571	-2.54089	-0.00549	C	-4.28755	-13.30577	0.00353
C	4.27516	-3.91784	-0.00477	C	-3.09106	-12.57962	0.00300
C	3.07934	-4.65705	-0.00397	C	-1.85091	-13.28860	0.00376
C	1.84841	-3.94599	-0.00419	C	-1.85480	-14.71814	0.00519
C	1.84876	-2.51345	-0.00489	C	-3.09202	-15.39450	0.00571
C	3.07991	-1.80160	-0.00542	C	-0.59830	-15.43700	0.00604
C	0.61007	-1.79529	-0.00498	C	0.61884	-14.71890	0.00525
C	-0.61078	-2.51158	-0.00476	C	1.86482	-15.43164	0.00600
C	-1.84958	-1.79342	-0.00514	C	3.10666	-14.73148	0.00513
C	-3.08067	-2.50516	-0.00522	C	4.29501	-15.47334	0.00592
C	-4.27647	-1.76572	-0.00586	C	4.28927	-16.87115	0.00756
C	-4.27613	-0.38877	-0.00610	C	3.09121	-17.56216	0.00841
C	-3.08018	0.35071	-0.00570	C	1.86934	-16.86058	0.00764
C	-1.84928	-0.36080	-0.00537	C	0.61436	-13.27708	0.00371

C	-4.27513	-10.38040	0.00110
C	-4.27487	-9.00167	-0.00020
C	-3.08018	-8.26456	-0.00099
C	-1.84959	-8.97740	-0.00036
C	-1.85069	-10.41043	0.00098
C	-3.08314	-11.12013	0.00167
C	-0.60892	-11.12761	0.00162
C	0.61094	-10.41311	0.00090
C	1.85300	-11.12990	0.00147
C	3.08307	-10.41550	0.00065
C	4.27928	-11.14949	0.00106
C	4.28300	-12.52904	0.00246
C	3.09407	-13.27091	0.00348
C	1.85737	-12.56247	0.00290
C	0.61022	-8.97306	-0.00043
C	-0.60789	-12.56785	0.00306
C	0.62298	-17.54879	0.00847
C	-0.61010	-8.25843	-0.00100
H	1.47901	17.43129	0.00842
H	5.22961	15.23783	0.00526
H	5.24203	12.79458	0.00285
H	3.12600	16.47659	0.00672
H	-5.25429	14.96952	0.00530
H	-5.23284	17.40988	0.00816
H	-3.07539	18.64908	0.00968
H	5.23393	10.88403	0.00172
H	5.23236	8.49593	-0.00056
H	-5.23575	10.64166	0.00026
H	-5.24188	13.03304	0.00277
H	-0.62627	18.63591	0.00974
H	-5.23345	2.03529	-0.00602
H	-5.23247	4.42383	-0.00481
H	5.23424	2.27127	-0.00610
H	5.23342	-0.11729	-0.00652
H	-5.23262	6.34001	-0.00248
H	-5.23293	8.72850	-0.00047
H	5.23355	6.57893	-0.00301
H	5.23357	4.19018	-0.00485
H	5.23345	-2.03529	-0.00602
H	5.23247	-4.42383	-0.00481
H	-5.23424	-2.27127	-0.00610
H	-5.23342	0.11729	-0.00652
H	5.23262	-6.34001	-0.00248
H	5.23293	-8.72850	-0.00047
H	-5.23355	-6.57893	-0.00301
H	-5.23357	-4.19018	-0.00485
H	-1.47901	-17.43129	0.00842
H	-5.22961	-15.23783	0.00526
H	-5.24203	-12.79458	0.00285
H	-3.12600	-16.47659	0.00672
H	5.25429	-14.96952	0.00530
H	5.23284	-17.40988	0.00816
H	3.07539	-18.64908	0.00968
H	-5.23393	-10.88403	0.00172
H	-5.23236	-8.49593	-0.00056
H	5.23575	-10.64166	0.00026
H	5.24188	-13.03304	0.00277
H	0.62627	-18.63591	0.00974

SCF energy: -4978.77060971 hartree

Zero-point correction: 1.249321 hartree

Enthalpy correction: 1.324765 hartree

Free Energy correction: 1.143176 hartree

PDA **1**

C	-6.45855	4.35630	0.30470
C	-7.56343	5.13226	-0.08147
C	-8.76276	4.47391	-0.39894
C	-8.83647	3.08685	-0.36071
C	-7.71700	2.29811	-0.01358
C	-6.52943	2.97340	0.34450
C	-7.36076	-1.58267	-0.13638
C	-6.64070	-2.59094	0.52370
C	-7.00828	-3.92856	0.40413
C	-8.10781	-4.29981	-0.38167
C	-8.83171	-3.29403	-1.04107
C	-8.46353	-1.96044	-0.92604
C	-2.88915	4.15778	-0.80763
C	-2.15573	4.72784	0.24302
C	-1.68803	3.89340	1.26949
C	-1.93233	2.52676	1.24202
C	-2.64515	1.95105	0.17764
C	-3.13081	2.78626	-0.83940
C	-2.22648	-1.93519	0.29818
C	-3.15270	-2.54466	-0.56590
C	-3.43327	-3.90056	-0.45490
C	-2.79238	-4.69249	0.51065
C	-1.82912	-4.09785	1.33949
C	-1.55158	-2.73787	1.23182
C	8.40650	-4.48221	-1.25953
C	7.24565	-5.12104	-0.79303
C	6.28723	-4.35220	-0.11300
C	6.45772	-2.98939	0.07089
C	7.60414	-2.33091	-0.42443
C	8.58321	-3.11708	-1.07080
C	7.50884	1.52155	0.12254
C	6.74026	2.63537	-0.26089
C	7.23173	3.92544	-0.11303
C	8.50415	4.15115	0.43498
C	9.26700	3.04431	0.83566
C	8.77514	1.75130	0.68837
C	2.64552	-4.14110	-0.61055
C	2.92119	-2.78463	-0.76950
C	2.67513	-1.88180	0.27359
C	2.17348	-2.36852	1.49092
C	1.89362	-3.72065	1.64587
C	2.11660	-4.62380	0.59512
C	2.24723	1.97686	-0.14827
C	1.71836	2.93957	0.72240
C	1.93501	4.29785	0.50069
C	2.67382	4.72583	-0.61120
C	3.18851	3.76321	-1.49364
C	2.98303	2.40769	-1.26595
H	-5.53865	4.86468	0.57126
H	-5.66252	2.40874	0.65770
H	-6.41705	-4.68369	0.91145
H	-9.67179	-3.58986	-1.66106
H	-3.27082	4.77911	-1.61145
H	-4.15913	-4.37060	-1.10946
H	9.17532	-5.04702	-1.77772
H	9.48511	-2.63720	-1.44293
H	6.64097	4.78316	-0.41835
H	10.24574	3.18504	1.28380
H	2.83864	-4.81966	-1.43513
H	3.32503	-2.42005	-1.70919
H	1.50086	5.02189	1.18252
H	5.40332	-4.84989	0.26923

H	5.70715	-2.42909	0.61219	H	8.98300	-7.40517	-1.05145
H	-3.69922	2.35625	-1.65838	C	-2.59183	7.15623	-0.57343
H	-1.14139	4.34442	2.09103	H	-2.42159	6.93557	-1.63450
H	-9.64249	5.04089	-0.68771	H	-2.24709	8.17030	-0.36361
H	3.73966	4.10769	-2.36288	H	-3.67213	7.09011	-0.39292
H	9.36682	0.91475	1.04696	C	-2.44963	-7.02468	1.60894
H	-3.65234	-1.95321	-1.32479	H	-2.83122	-8.04264	1.51137
H	-0.81059	-2.28625	1.88249	H	-2.61380	-6.68062	2.63820
H	-1.28647	-4.69353	2.06629	H	-1.36672	-7.01318	1.44189
H	-5.78106	-2.32301	1.12832	C	-8.61685	7.47929	-0.43923
H	-9.01061	-1.20664	-1.48446	H	-9.41167	7.30323	0.29509
H	1.50216	-4.10511	2.58208	H	-9.03099	7.25187	-1.42913
C	-8.53100	-5.72806	-0.57058	H	-8.31885	8.52858	-0.40901
O	-9.49354	-5.99541	-1.27518	C	-7.74393	-6.82209	0.12658
C	-7.39983	6.61731	-0.14912	H	-8.17702	-7.78734	-0.14174
O	-6.30277	7.13412	0.02100	H	-7.79085	-6.69812	1.21593
C	-1.82955	6.18991	0.31084	H	-6.68437	-6.80230	-0.15498
O	-0.96317	6.58627	1.08140	C	2.25491	-7.09769	-0.18502
C	-3.19146	-6.13292	0.63192	H	1.94562	-8.08733	0.15595
O	-4.12199	-6.57212	-0.03332	H	3.34726	-7.06227	-0.27849
H	2.00891	-1.67845	2.31333	H	1.83513	-6.92009	-1.18324
C	1.75083	-6.06296	0.80083	C	10.36537	5.81716	1.15816
O	1.05472	-6.38574	1.75656	H	10.44682	5.42285	2.17840
C	2.92936	6.17637	-0.91371	H	10.54511	6.89337	1.17366
O	3.51907	6.49235	-1.93645	H	11.14024	5.32800	0.55585
C	6.97680	-6.57851	-0.99244	C	2.45537	7.22618	0.07317
O	5.90735	-7.07036	-0.65441	H	2.93165	7.07890	1.05049
C	8.98029	5.56493	0.58302	H	1.37192	7.17600	0.23408
O	8.26801	6.49883	0.24827	H	2.72474	8.21148	-0.31122
C	8.05116	-7.44478	-1.62787	H	1.13322	2.61878	1.57803
H	8.28165	-7.10283	-2.64417	C	-6.93710	-0.15403	-0.02203
H	7.69271	-8.47458	-1.66882	C	-7.86999	0.84927	-0.05135

H	-8.90256	0.51977	-0.13915
C	-5.53833	0.07123	0.07049
C	-4.31945	0.16933	0.10644
C	-2.94158	0.48472	0.16082
C	-1.94312	-0.47066	0.24035
C	-0.57787	-0.09365	0.25653
C	0.61981	0.15134	0.20629
C	1.97954	0.52479	0.07651
C	2.98046	-0.42436	0.10095
C	4.35760	-0.11748	0.00770
C	5.57763	-0.03342	-0.01412
C	6.98705	0.13447	-0.05290
H	5.75102	2.48335	-0.67887
C	7.85472	-0.90234	-0.28333
H	3.36924	1.67414	-1.96702
H	-1.58379	1.89546	2.05327
H	-9.76974	2.59395	-0.62182
H	8.89426	-0.61922	-0.42976

SCF energy: -3608.89483372 hartree

Zero-point correction: 1.133001 hartree

Enthalpy correction: 1.214160 hartree

Free Energy correction: 1.001313 hartree

PDA **1-*annul***

C	5.55520	-5.25313	1.71968
C	4.16291	-4.97648	1.80309
C	3.67404	-3.79295	1.27296
C	4.52512	-2.84697	0.65423
C	5.92960	-3.13106	0.58284
C	6.40944	-4.35335	1.12831
C	6.80568	-2.19046	-0.01186
C	6.33775	-0.99399	-0.52655
C	7.25648	-0.00422	-1.13940
C	7.04822	1.37469	-0.96705
C	7.91186	2.30503	-1.53884
C	9.01081	1.88611	-2.30221
C	9.22200	0.50946	-2.47700
C	8.36086	-0.41843	-1.90786
C	4.94017	-0.72572	-0.45503
C	1.33468	-3.34482	-2.73928
C	-0.04451	-3.00916	-2.75883
C	-0.52265	-2.09342	-1.83906
C	0.32153	-1.48225	-0.88236
C	1.71029	-1.84484	-0.84884
C	2.18039	-2.77989	-1.81451
C	2.58597	-1.25880	0.12511
C	2.07862	-0.31928	1.02006
C	2.91412	0.36262	2.05147
C	2.95886	1.76814	2.09551
C	3.70731	2.42882	3.06177
C	4.42638	1.70670	4.02629
C	4.37326	0.30575	3.99421
C	3.62941	-0.35673	3.02070
C	4.04440	-1.60780	0.11152
C	-3.87403	3.98840	2.65162
C	-3.83387	5.26959	2.08230
C	-4.60197	5.51871	0.93470
C	-5.38648	4.51740	0.37681
C	-5.42041	3.22727	0.93745
C	-4.65365	2.98195	2.08707
C	-6.30397	2.18523	0.33883
C	-5.84707	0.92731	-0.05549

C	-6.76316	-0.01101	-0.64159	H	-10.09298	-0.31602	-1.47900
C	-8.14370	0.34614	-0.79263	H	-6.90020	-3.13468	-2.01549
C	-9.04508	-0.57911	-1.36760	H	-1.14349	1.57060	-5.37461
C	-8.62638	-1.82355	-1.80314	H	-2.45171	0.51616	-3.58123
C	-7.25428	-2.16873	-1.66980	H	-2.48955	-2.80295	3.70879
C	-6.35453	-1.29186	-1.11005	H	-9.61938	1.90091	-0.48463
C	-4.39471	0.56267	0.03092	C	-8.57193	1.63286	-0.37348
C	-0.87236	1.76169	-4.34087	C	-7.67851	2.52243	0.16329
C	-1.62001	1.16723	-3.32658	H	-4.56579	6.51110	0.49716
C	-1.29509	1.37668	-1.97701	H	-5.97199	4.72469	-0.51497
C	-0.20848	2.21433	-1.67246	H	3.23077	-3.04737	-1.81869
C	0.53378	2.81032	-2.68364	H	-1.57738	-1.84698	-1.86771
C	0.21646	2.58949	-4.03282	H	2.60822	-3.60518	1.34537
C	-2.13115	0.75818	-0.90710	H	7.86950	-2.41160	-0.02934
C	-1.61680	-0.10963	0.05307	H	4.56316	0.19631	-0.88655
C	-2.49673	-0.66870	1.03923	H	-5.78858	-0.61905	2.05503
C	-2.03550	-1.58370	2.02806	H	-5.31253	-1.57936	-1.02835
C	-2.88393	-2.10800	2.97435	H	-8.01505	3.50155	0.49080
C	-4.25680	-1.74848	2.99526	H	2.41313	2.34185	1.35089
C	-4.73495	-0.87555	2.03332	H	3.59199	-1.44103	3.02131
C	-3.89211	-0.32605	1.03670	H	4.90967	-0.28101	4.73358
C	-0.17208	-0.50958	0.04711	H	6.21903	1.72141	-0.35727
C	-3.51857	1.07018	-0.90258	H	8.52416	-1.47833	-2.08113
C	0.70242	0.03818	0.95933	H	-3.89186	1.74915	-1.66322
H	5.95273	-6.17696	2.12753	H	1.36904	3.46399	-2.45425
H	7.47427	-4.56541	1.07187	C	9.97232	2.84093	-2.94490
H	7.72482	3.36229	-1.37915	O	10.92099	2.42271	-3.59149
H	10.06879	0.19291	-3.07719	C	3.18649	-5.91454	2.45040
H	1.73502	-4.05255	-3.45828	O	2.00237	-5.62366	2.53291
H	3.75316	3.51266	3.09135	C	-1.01464	-3.59433	-3.74208
H	-3.30135	3.76760	3.54726	O	-2.18623	-3.24534	-3.74741
H	-4.68295	2.00292	2.55350	C	5.21525	2.47254	5.04610

O	5.23152	3.69402	5.02837
H	0.03877	2.40958	-0.63404
H	0.33082	0.76279	1.67843
C	1.06076	3.25334	-5.07880
O	2.01665	3.94426	-4.75904
C	-5.22198	-2.27788	4.01635
O	-6.39093	-1.92393	4.01171
C	-3.01121	6.38889	2.64513
O	-3.00304	7.48618	2.10751
C	-9.64453	-2.74632	-2.40520
O	-10.81176	-2.40170	-2.51469
C	-2.18702	6.13706	3.89770
H	-2.82597	5.83540	4.73637
H	-1.65854	7.05545	4.15854
H	-1.45872	5.33303	3.73738
C	-0.51298	-4.62983	-4.73446
H	0.27602	-4.21376	-5.37275
H	-1.34832	-4.95201	-5.35831
H	-0.08839	-5.49877	-4.21735
C	5.99409	1.70364	6.10086
H	6.50493	2.41845	6.74802
H	6.73400	1.03894	5.63916
H	5.32678	1.07874	6.70656
C	3.69741	-7.23432	3.00410
H	4.44895	-7.07010	3.78591
H	4.17111	-7.83580	2.21884
H	2.85572	-7.78702	3.42455
C	9.74544	4.33418	-2.77897
H	10.53402	4.86859	-3.31118
H	9.76353	4.62161	-1.72076
H	8.76981	4.63213	-3.18135
C	0.70831	3.05236	-6.54361
H	1.42266	3.60710	-7.15414
H	-0.30630	3.40905	-6.75762
H	0.74540	1.99096	-6.81688
C	-9.19647	-4.11943	-2.87736
H	-8.42690	-4.03744	-3.65452
H	-10.06071	-4.65091	-3.27918
H	-8.76458	-4.69862	-2.05226
C	-4.71520	-3.26215	5.05737
H	-3.91344	-2.81970	5.66102
H	-4.30588	-4.16253	4.58344
H	-5.54511	-3.54135	5.70856
H	-0.99063	-1.87162	2.03173

SCF energy: -3685.36777794 hartree

Zero-point correction: 1.153329 hartree

Enthalpy correction: 1.232052 hartree

Free Energy correction: 1.024117 hartre

References

[1] Allen, M. J.; Tung, V. C.; Kaner, R. B. Honeycomb Carbon:A Review of Graphene. *Chem. Rev*. **2010**, *110*, 132–145.

[2] Nakada, K.; Fujita, M.; Dresselhaus, G.; Dresselhaus, M. S. Edge State in Graphene Ribbons: Nanometer Size Effect and Edge Shape Dependence. *Phys. Rev. B* **1996**, *54*, 17954– 17961.

[3] Dutta, S.; Pati, S. K. Novel Properties of GrapheneNanoribbons: A Review. *J. Mater. Chem.* **2010**, *20*, 8207–8223.

[4] We are proposing the use of a modified nomenclature for the armchair (A) or zigzag (Z) topologies of graphene nanoribbons, in which the A or Z letters are subscripted in front of the GNR acronym. The established convention for GNR width, indicated by the number of carbons within the GNR width, is placed in between brackets at the front of the $_{A}$GNR or $_{Z}$GNR terms. Thus, $N = 8$ armchair graphene nanoribbons are designated as $[8]_{A}$GNR rather than the current designation (8-AGNR), while $N = 12$ zigzag graphene nanoribbons would be designated as $[12]_{Z}$GNR (instead of 12-ZGNR). However, the current nomenclature for graphene nanoribbons with 2D "chirality" can be retained, as it is defined by the [n,m] numerals (n = zigzag edge repeat carbons, m = armchair edge repeat carbons) in front of the GNR abbreviation.

[5] Yang, L.; Park, C.-H.; Son, Y.-W.; Cohen, M. L.; Louie, S. G. Quasiparticle Energies and Band Gaps in Graphene Nanoribbons. *Phys. Rev. Lett.* **2007**, *99*, 186801.

[6] Kimouche, A.; Ervasi, M. M.; Drost, R.; Halonen, S.; Harju, A.; Joensuu, P. M.; Sainio, J.; Liljeroth, P. Ultra-narrow Metallic Armchair Graphene Nanoribbons. *Nat. Commun.* **2015**, 10177.

[7] Yang, W.; Lucotti, A.; Tommasini, M.; Chalifoux, W. A. Bottom-up Synthesis of Soluble and Narrow Graphene Nanoribbons using Alkyne Benzannulations. *J. Am. Chem. Soc.* **2016**, *138*, 9137–9144.

[8] Jänsch, D.; Ivanov, I.; Zagranyarski, Y.; Duznovic, I.; Baumgarten, M.; Turchinovich, D.; Li, C.; Bonn, M.; Müllen, K. Ultra-Narrow Low-Bandgap Graphene Nanoribbons from Bromoperylenes-Synthesis and Terahertz-Spectroscopy. *Chem. Eur. J.* **2017**, *23*, 4870–4875.

[9] Zhang, H.; Lin, H.; Sun, K.; Chen, L.; Zagranyarski, Y.; Aghdassi, N.; Duhm, S.; Li, Q.; Zhong, D.; Li, Y.; Müllen, K.; Fuchs, H.; Chi, L. On-Surface Synthesis of Rylene-Type Graphene Nanoribbons. *J. Am. Chem. Soc.* **2015**, *137*, 4022–4025.

[10] Tour, J. M. Top-Down versus Bottom-up Fabrication of Graphene-Based Electronics. *Chem. Mater.* **2014**, *26*, 163–171.

[11] Sommer, B.; Sonntag, J.; Ganczarczyk, A.; Braam, D.; Prinz, G.; Lorke, A.; Geller, M. Electron-Beam Induced Nano-Etching of Suspended Graphene. *Sci. Rep.* **2015**, *5*, 7781.

[12] Kosynkin, D. V.; Higginbotham, A. L.; Sinitskii, A.; Lomeda, J. R.; Dimiev, A.; Price, B. K.; Tour, J. M. Longitudinal Unzipping of Carbon Nanotubes to form Graphene Nanoribbons. *Nature* **2009**, *458*, 872–876.

[13] Li, X.; Wang, X.; Zhang, L.; Lee, S.; Dai, H. Chemically Derived, Ultrasmooth Graphene Nanoribbon Semiconductors. *Science* **2008**, *319*, 1229–1232.

[14] Cai, J.; Ruffieux, P.; Jaafar, R.; Bieri, M.; Braun, T.; Blankenburg, S.; Muoth, M.; Seitsonin, A. P.; Saleh, M.; Feng, X.; Müllen, K.; Fasel, R. Atomically Precise Bottom-Up Fabrication of Graphene Nanoribbons. *Nature* **2010**, *466*, 470–473.

[15] Ruffieux, P.; Wang, S.; Yang, B.; Sánchez-Sánchez, C.; Liu, J.; Dienel, T.; Talirz, L.; Shinde, P.; Pignedoli, C. A.; Passerone, D.; Dumslaff, T.; Feng, X.; Müllen, K.; Fasel, R. On-Surface Synthesis of Graphene Nanoribbons with Zigzag Edge Topology. *Nature* **2016**, *531*, 489–492.

[16] Yang, X.; Dou, X.; Rouhanipour, A.; Zhi, L.; Räder, J.; Müllen, K. Two-Dimensional Graphene Nanoribbons. *J. Am. Chem. Soc.* **2008**, *130*, 4216–4217.

[17] Li, G.; Yoon, K-Y.; Zhong, X.; Zhu, X.; Dong, G. Efficient Bottom-Up Preparation of Graphene Nanoribbons by Mild Suzuki-Miyaura Polymerization of Simple Triaryl Monomers. *Chem. Eur. J.* **2016**, *22*, 9116-9120.

[18] Narita, A.; Verzhbitskiy, I. A.; Frederick, W.; Mali, K. S.; Jensen, S. A.; Hansen, M. R.; Bonn, M.; De Feyter, S.; Casiraghi, C.; Feng, X.; Müllen, K. Bottom-Up Synthesis of Liquid-Phase-Processable Graphene Nanoribbons with Near-Infrared Absorption. *ACS Nano* **2014,** *8*, 11622–11630.

[19] Gao, J.; Uribe-Romo, F. J.; Saathoff, J. D.; Arslan, H.; Crick, C. R.; Hein, S. J.; Itin, B.; Clancy, P.; Dichtel, W. R.; Loo, Y-L. Ambipolar Transport in Solution-Synthesized Graphene Nanoribbons. *ACS Nano*, **2016**, *10*, 4847–4856.

[20] Park, I. S.; Park, H. J.; Kim, J.-M. A Soluble, Low-Temperature Thermochromic and Chemically Reactive Polydiacetylene. *ACS Appl. Mater. Interfaces* **2013**, *5*, 8805–8812.

[21] Lauher, J. W.; Fowler, F. W.; Goroff, N. S. Single-Crystal-to-Single-Crystal Topochemical Polymerizations by Design. *Accts. Chem. Res.* **2008**, *41*, 1215–1229.

[22] Ishijima, Y.; Okaniwa, M.; Oaki, Y.; Imai, H. Two-Exfoliation Approaches for Organic Layered Compounds: Hydrophilic and Hydrophobic Polydiacetylene Nanosheets. *Chem. Sci.* **2017**, *8*, 647–653.

[23] Luo, L.; Wilhelm, C.; Young, C. N.; Grey, C. P.; Halada, G. P.; Xiao, K.; Ivanov, I. N.; Howe, J. Y.; Geohegan, D. B.; Goroff, N. S. Characterization and Carbonization of Highly Oriented Poly(diiododiacetylene) Nanofibers. *Macromolecules* **2011**, *44*, 2626–2631.

[24] Luo, L.; Resch, D.; Wilhelm, C.; Young, C. N.; Halada, G. P.; Gambino, R. J.; Grey, C. P.; Goroff, N. S. Room-Temperature Carbonization of Poly(diiododiacetylene) by Reaction with Lewis Bases. *J. Am. Chem. Soc.* **2011**, *133*, 19274–19277.

[25] Levesque, I.; Néabo, J. R.; Rondeau-Gagné, S.; Vigier-Carrière, C.; Diagle, M.; Morin, J.-F. Layered Graphitic Materials from a Molecular Precursor. *Chem. Sci.* **2014**, *5*, 831–836.

[26] Suzuki, M.; Comito, A.; Khan, S. I.; Rubin, Y. Nanochannel Array within a Multilayered Network of a Planarized Dehydro[24]annulene. *Org. Lett.* **2010**, *12*, 2346–2349.

[27] Suzuki, M.; Khosrowabadi Kotyk, J. F.; Khan, S. I.; Rubin, Y. Directing the Crystallization of Dehydro[24]annulenes into Supramolecular Nanotubular Scaffolds. *J. Am. Chem. Soc.* **2016**, *138*, 5939–5956.

[28] Jordan, R. S.; Wang, Y.; McCurdy, R. D.; Yeung, M. T.; Marsh, K. L.; Khan, S. I.; Kaner, R. B.; Rubin, Y. Synthesis of Graphene Nanoribbons via the Topochemical Polymerization and Subsequent Aromatization of a Diacetylene Precursor. *Chem* **2016**, *1*, 78–90.

[29] Prall, M.; Krüger, A.; Shreiner, P. R.; Hopf, H. The Cyclization of Parent and Cyclic Hexa-1,3-dien-5-ynes –A Combined Theoretical and Experimental Study. *Chem. Eur. J.* **2001**, *7*, 4386–4394.

[30] Zimmerman, G. Cycloaromatization of Open and Masked 1,3-Hexadien-5-ynes –Mechanistic and Synthetic Aspects. *Eur. J. Org. Chem.* **2001**, 457–471.

[31] (a) Becke, A. D. Density-Functional Thermochemistry. III. The Role of Exact Exchange. *J. Chem. Phys.* **1993**, *98*, 5648−5652. (b) Lee, C.; Yang, W.; Parr, R. G. Development of the

Colle-Salvetti Correlation-Energy Formula Into a Functional of the Electron Density. *Phys. Rev. B* **1988**, *37*, 785−789. (c) Stephens, P. J.; Devlin, F. J.; Chabalowski, C. F.; Frisch, M. J. Ab Initio Calculation of Vibrational Absorption and Circular Dichroism Spectra using Density Functional Force Fields. *J. Phys. Chem.* **1994**, *98*, 11623−11627. (d) Vosko, S. H.; Wilk, L.; Nusair, M. Accurate Spin-Dependent Electron Liquid Correlation Energies for Local Spin Density Calculations: A Critical Analysis. *Can. J. Phys.* **1980**, *58*, 1200−1211.

[32] All calculations described here were performed using Gaussian 09: Frisch, M. J.; Trucks, G. W.; Schlegel, H. B.; Scuseria, G. E.; Robb, M. A.; Cheeseman, J. R.; Scalmani, G.; Barone, V.; Mennucci, B.; Petersson, G. A.; Nakatsuji, H.; Caricato, M.; Li, X.; Hratchian, H. P.; Izmaylov, A. F.; Bloino, J.; Zheng, G.; Sonnenberg, J. L.; Hada, M.; Ehara, M.; Toyota, K.; Fukuda, R.; Hasegawa, J.; Ishida, M.; Nakajima, T.; Honda, Y.; Kitao, O.; Nakai, H.; Vreven, T.; Montgomery, J. A., Jr.; Peralta, J. E.; Ogliaro, F.; Bearpark, M.; Heyd, J. J.; Brothers, E.; Kudin, K. N.; Staroverov, V. N.; Kobayashi, R.; Normand, J.; Raghavachari, K.; Rendell, A.; Burant, J. C.; Iyengar, S. S.; Tomasi, J.; Cossi, M.; Rega, N.; Millam, N. J.; Klene, M.; Knox, J. E.; Cross, J. B.; Bakken, V.; Adamo, C.; Jaramillo, J.; Gomperts, R.; Stratmann, R. E.; Yazyev, O.; Austin, A. J.; Cammi, R.; Pomelli, C.; Ochterski, J. W.; Martin, R. L.; Morokuma, K.; Zakrzewski, V. G.; Voth, G. A.; Salvador, P.; Dannenberg, J. J.; Dapprich, S.; Daniels, A. D.; Farkas, Ö.; Foresman, J. B.; Ortiz, J. V.; Cioslowski, J.; Fox, D. J. *Gaussian 09, Revision B.01*; Gaussian, Inc.: Wallingford, CT, 2009.

[33] See Appendix for further details.

[34] Osowska, K.; Lis, T.; Szafert, S. Protection/Deprotection-Free Syntheses and Structural Analysis of (Keto-aryl)diynes. *Eur. J. Org. Chem.* **2008**, 4598–4606.

[35] Tanphibal, P.; Tashiro, K.; Chirachanchai, S. Constructing π-Electron-Conjugated Diarylbutadiyne-Based Polydiacetylene under Molecular Framework Controlled by Hydrogen Bond and Side-Chain Substituent Position. *Macromol. Rapid Commun.* **2016**, *37*, 685– 690.

[36] Wegner, G. Topochemical Reactions of Monomers with Conjugated Triple Bonds. III. Solid-State Reactivity of Derivatices of Diphenyldiacetylene. *J. Polym. Sci. Pol. Lett.* **1971**, *9*, 133-144.

[37] Wegner, G. *Makromol. Chem.* **1972**, *154*, 35–48.

[38] The crystal packing representation for compound **4c** was generated from CCDC database crystal structure number = 1434545.

[39] Nava, A. D.; Thakur, M.; Tonelli, A. E. Carbon-13 NMR Structural Studies of a Soluble Polydiacetylene, Poly(4BCMU). *Macromolecules* **1990**, *23*, 3055–3063.

[40] Cholli, A. L.; Sandman, D. J. Structural Investigation of Polydiacetylenes: A Variable Temperature Solid State ^{13}C CP/MAS NMR Study. *Bull. Mater. Sci.* **1999**, *22*, 691–695.

[41] Colthup, N. B.; Daly, L. H.; Wiberley, S. E. *Introduction to Infrared and Raman Spectroscopy*, 3rd ed.; Academic Press: San Diego, 1990.

[42] Interestingly, a dramatic loss of CP/MAS signal was observed in samples heated between 400 and 500 ˚C for PDAs **2a**–**2c** (S25-S27). Performing acquisition at –100 ˚C did not lead to a significant recovery of signal. The exact nature of this phenomenon is currently under investigation, but could be due to partial doping (air oxidation) of the GNRs prepared at 500 ˚C.

[43] de Souza, F. A. L.; Ambrozio, A. R.; Souza, E. S.; Cipriano, D. F.; Scopel, W. L.; Freitas, J. C. C. NMR Spectral Parameters in Graphene, Graphite, and Related Materials : Ab Initio Calculations and Experimental Results. *J. Phys. Chem. C* **2016**, *120*, 27707–27716.

[44] Clar, E.; Ironside, C. T.; Zander, M. J. The Electronic Interaction Between Benzenoid Rings in Condensed Aromatic Hydrocarbons. 1 :12-2 :3-4 :5-6 :7-8 :9-10 :11-hexabenzocoronene, 1 :2-3 :4-5 :6-10 :11-tetrabenzoanthanthrene, and 4 :5-6 :7-11 :12-13 :14-tetrabenzoperopyrene. *J. Chem. Soc.* **1959**, 142–147.

[45] Talyzin, A. V.; Luzan, S. M.; Leifer, K.; Akhtar, S.; Fetzer, J.; Cataldo, F.; Tsybin, Y. O.; Tai, C. W.; Dzwilewski, A.; Moons, E. Coronene Fusion by Heat Treatment : Road to Nanographenes. *J. Phys. Chem. C* **2011**, *115*, 13207–13214.

[46] Hansen, P. E. ^{13}C NMR of Polycyclic Aromatic Compounds: A Review. *Org. Magn. Reson.* **1979**, *12*, 109–142.

[47] Ferrari, A. C.; Rodil, S. E.; Robertson, Interpretation of Infrared and Raman Spectra of Amorphous Carbon Nitrides. J. *Phys. Rev. B.* **2003**, *67*, 155306.

[48] Ryu, S.; Maultzsch, J.; Han, M. Y.; Kim, P.; Brus, L. E. Raman Spectroscopy of Lithographically Patterned Graphene Nanoribbons. *ACS Nano* **2011**, *5*, 4123–4130.

[49] Graf, D.; Molitor, F.; Ensslin, K.; Stampfer, C.; Jungen, A.; Hierold, C.; Wirtz, L. Spatially Resolved Raman Spectroscopy of Single-and Few-Layer Graphene. *Nano Lett.* **2007**, *7*, 238–242.

[50] Ferrari, A. C.; Robertson, J. Interpretation of Raman Spectra of Disordered and Amorphous Carbon. *Phys. Rev. B.* **2000**, *61*, 14095–14107.

[51] Bottari, G.; Herrans, M. Á.; Wibmer, L.; Volland, M.; Rodrígues-Pérez, L.; Guldi, D. M.; Hirsch, A.; Martín, N.; D'Souza, F.; Torres, T. Chemical Functionalization and Characterization of Graphene-Based Materials *Chem. Soc. Rev.* **2017**, *46*, 4464–4500.

[52] Alajital, A. I.; Edwards, H. G. M.; Elbagerma, M. A.; Scowen, I. J. The Effect of Laser Wavelength on the Raman Spectra of Phenanthrene, Chrysene, and Tetracene: Implications

for Extra-Terrestrial Detection of Polyaromatic Hydrocarbons. *Spectrochim. Acta Mol. Biomol. Spectrosc.* **2010**, *76*, 1-5.

[53] Spartan, Wavefunction, Inc. Irvine, CA. Except for molecular mechanics and semi-empirical models, the calculation methods used in Spartan have been documented in: Y. Shao, L.F. Molnar, Y. Jung, J. Kussmann, C. Ochsenfeld, S.T. Brown, A.T.B. Gilbert, L.V. Slipchenko, S.V. Levchenko, D.P. O'Neill, R.A. DiStasio Jr., R.C. Lochan, T. Wang, G.J.O. Beran, N.A. Besley, J.M. Herbert, C.Y. Lin, T. Van Voorhis, S.H. Chien, A. Sodt, R.P. Steele, V.A. Rassolov, P.E. Maslen, P.P. Korambath, R.D. Adamson, B. Austin, J. Baker, E.F.C. Byrd, H. Dachsel, R.J. Doerksen, A. Dreuw, B.D. Dunietz, A.D. Dutoi, T.R. Furlani, S.R. Gwaltney, A. Heyden, S. Hirata, C-P. Hsu, G. Kedziora, R.Z. Khalliulin, P. Klunzinger, A.M. Lee, M.S. Lee, W.Z. Liang, I. Lotan, N. Nair, B. Peters, E.I. Proynov, P.A. Pieniazek, Y.M. Rhee, J. Ritchie, E. Rosta, C.D. Sherrill, A.C. Simmonett, J.E. Subotnik, H.L. Woodcock III, W. Zhang, A.T. Bell, A.K. Chakraborty, D.M. Chipman, F.J. Keil, A.Warshel, W.J. Hehre, H.F. Schaefer, J. Kong, A.I. Krylov, P.M.W. Gill and M. Head-Gordon, *Phys. Chem. Chem. Phys*. **2006,** *8,* 3172–3191.

[54] Bauschlicher, C. W., Jr.; Partridge, H. A Modification of the Gaussian-2-Approach using Density Functional Theory. *J. Chem. Phys.* **1995**, *103,* 1788-1791.

[55] Wong, M. W. Vibrational Frequency Prediction using Density Functional Theory. *Chem. Phys. Lett.* **1996**, *256*, 391-399.

[56] Zhao, Y.; Truhlar, D. G. Computational Characterization and Modeling of Buckyball Tweezers: Density Functional Study of Concave-Convex π-π Interactions. *Phys. Chem. Chem. Phys.* **2008**, *10*, 2813-2818.

[57] Ribeiro, R. F.; Marenich, A. V.; Cramer, C. J.; Truhlar, D. G. Use of Solution-Phase Vibrational Frequencies in Continuum Models for the Free Energy of Solvation. *J. Phys. Chem. B* **2011**, *115*, 14556-14562.

[58] Legault, C. Y. *CYLview, 1.0 b*; *Université de Sherbrooke* (http://www.cylview.org), 2009.

[59] Watts, K. S.; Dalal, P.; Tebben, A. J.; Cheney, D. L.; Shelley, J. C. J. Chem. Inf. Model. 2014, 54, 2680.

Chapter 3: Fjord-edge Graphene Nanoribbons with Site-Specific Nitrogen Substitution

Section 3.1. Abstract

The synthesis of graphene nanoribbons (GNRs) having site-specifically substituted backbone heteroatoms is one of the essential goals to achieving control over the electronic properties of these next generation organic materials. Here, we exploit our recently reported solid-state topochemical polymerization/cyclization-aromatization strategy to convert the simple 1,4-bis(3-pyridyl)butadiynes **3a,b** into the fjord-edge nitrogen-doped graphene nanoribbon structures **1a,b** (fjord-edge N_2[8]GNRs). Their structural assignment is unambiguously confirmed by CP/MAS ^{13}C NMR, Raman, and XPS spectroscopy, as well as by high-resolution transmission electron microscopy (HRTEM). Fjord-edge N_2[8]GNRs **1a,b** are exciting potential precursors for the novel backbone nitrogen-substituted $N_2[8]_A$GNRs **2a,b**, which should display an unusual bonding topology.

Section 3.2. Introduction

Graphene nanoribbons (GNRs) are expected to usher the ultimate nanosizing of electronics[1-4] and sensors[5,6] for next generation devices. The electronic properties of GNRs can be exquisitely tuned by modification of their width, backbone, and edge structure.[7-10] In the last decade, both on-surface and in-solution bottom-up syntheses have achieved precise control over

these benchmarks.[11-15] Early bottom-up syntheses of these materials have focused on armchair[16-19] or zigzag[20] edged GNRs. More recently, intricate edge or interior configurations such as chevron,[11,21-23] cove,[24-26] fjord[27] or holey[28] have been obtained. These novel topologies significantly alter the electronic and magnetic properties of GNRs, as does the atomically precise[29] substitution of carbons with heteroatoms such as boron,[30,31] sulfur,[32,33] or nitrogen.[34,35] Crucially, site-specific doping at the GNR *backbone* achieves dramatic alteration of its electronics, making such structures the most desirable targets for synthesis.[29,36-38] Nitrogen doped GNRs are of particular interest as they produce p-doped materials.[34,35] Hence, the opportunity to synthesize novel edge or backbone-doped structures remains wide open.[23,39-42]

Herein, we describe the first 8-atom wide, fjord-edge nitrogen-doped graphene nanoribbons **1a,b** (fjord-edge N_2[8]GNR; Figure 3.1). GNRs **1a,b** were synthesized in a facile two-step process: a) topochemical polymerization of the corresponding dipyridyl diynes **3a,b** to the polydiacetylenes (PDAs) **4a,b** and b) thermal treatment of **4a,b** to afford GNRs **1a,b**. The Hopf cyclization step from PDAs **4a,b** to GNRs **1a,b** were confirmed by cross-polarization magic angle spinning (CP/MAS) solid state ^{13}C NMR. X-ray photoelectron spectroscopy (XPS) was used to verify the bonding state of the nitrogen atoms (see below). Finally, the morphology of the fjord-edge N_2[8]GNRs **1a,b** was confirmed using Raman and high resolution tunneling electron microscopy (HR-TEM).

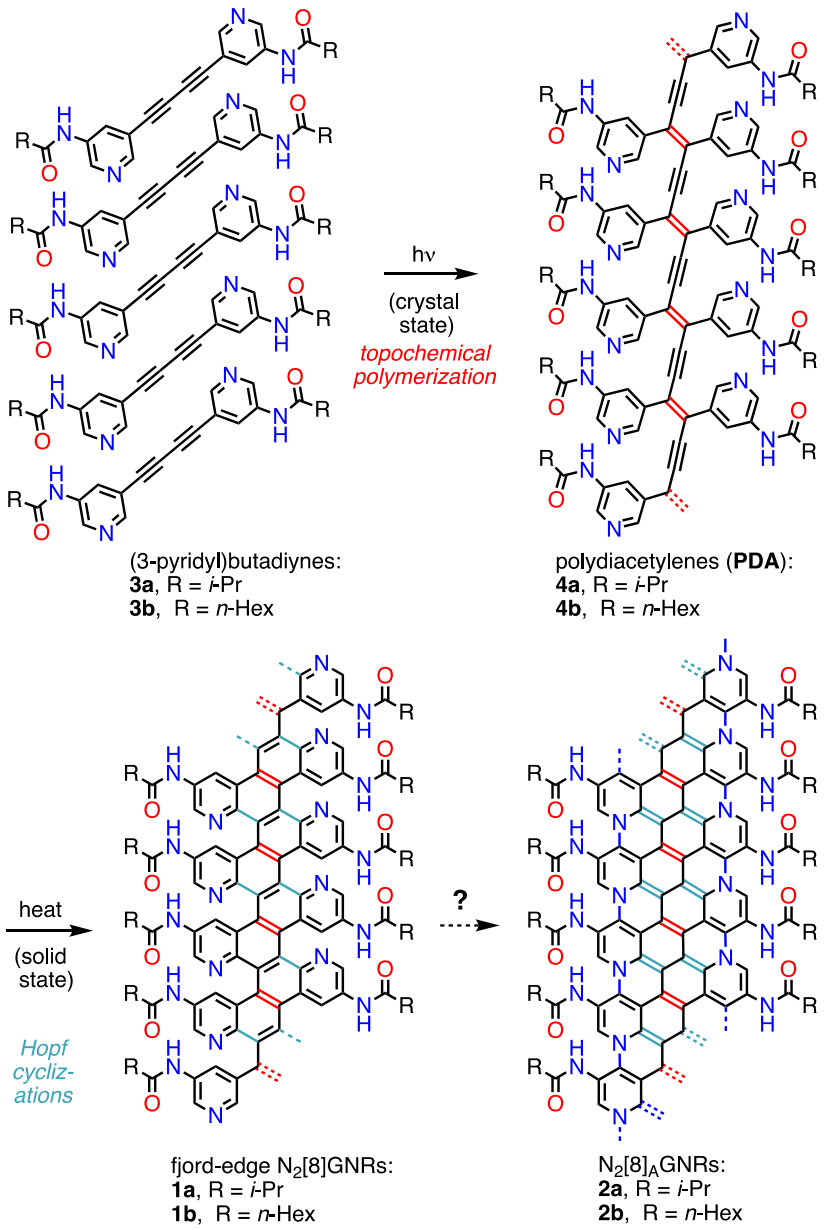

Figure 3.1. Synthesis of fjord-edge nitrogen-doped graphene nanoribbons **1a,b** (fjord-edge N_2[8]GNRs).

Section 3.3. Results and Discussion

Diyne monomer synthesis: Solid-state topochemical polymerizations require the appropriate packing of precursor monomers in a crystal to favor subsequent polymerization.[43-45] Here, the

dipyridyl diyne units of **3a–c** need to position their diyne 1,4-carbons within van-der-Waals contact distance (~3.5 Å), which promotes a facile formation of new bonds occurring already under ambient light.[46,47] While we synthesized several isomeric dipyridyl diyne systems,[48] only one series based on 3-amino-5-alkynylpyridine gave polymerizable diynes **3a,b**. Accordingly, 3-amino-5-bromopyridine was coupled with trimethylsilylacetylene under Sonogashira conditions, followed by acylation of the product with the corresponding acid chlorides (R = *i*-Pr, *n*-Hex, Me, respectively). Removal of the trimethylsilyl protecting group gave alkynyl amides **6a–c** in good to excellent yields (Scheme 3.1). Oxidative coupling under the Hay conditions afforded diyne amides **3a–c** in good to high yields. Crude diyne **3a** afforded single crystals after slow evaporation from methanol (Figures A28a,b). X-ray diffraction at the Brookhaven Synchroton X-ray source (Figure A29) afforded a 1.0 Å resolution crystal structure (Figure 3.2 and Table A1).

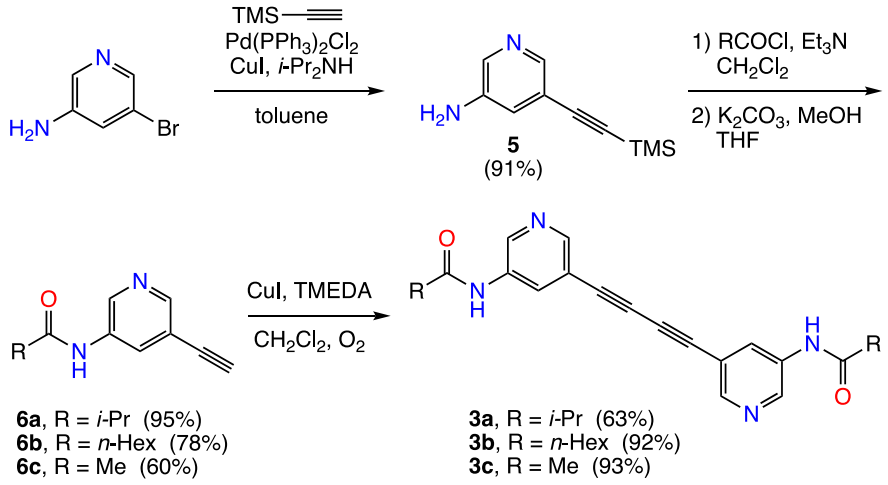

Scheme 3.1. Synthesis of 1,4-bis(3-pyridyl)butadiynes **3a–c**.

The crystallographic packing geometry for molecules of diyne **3a** corroborates the desired short C1–C4' distance of 3.45 Å (Figure 3.2a). The hydrogen bonds between the carbonyl oxygens and amide hydrogens have an optimal distance of 2.00 Å (Figure 3.2a), connecting the dipyridyl

diyne units of **3a** along the unit cell vector *a*. The relative strength of these intermolecular interactions is reflected in the crystal morphology and powder diffraction (Figures A28 and A30). To accommodate the H-bonding motif, the polymer growth axis exhibits a horizontal offset between each molecule, organizing the diynes into an optimal arrangement for topochemical polymerization (Figure 3.2b). Powder diffraction of **3b** displayed similar packing arrangements as **3a** (Figure A31).

Both dipyridyl diynes **3a,b** easily polymerized to dipyridyl PDAs **4a,b** when subjected to UV light, as well as in ambient light, while diyne amide **3c** did not. The polymerizations were carried out by irradiation of fine dispersions of the crystals in hexanes using a medium pressure Hanovia lamp (Pyrex filter), typically for 12 h, producing deep purple/black crystals. Dissolution of unreacted monomer from the polymerized crystals afforded the pristine polydiacetylenes **4a,b** (18 and 4%, respectively) as fibrous powders after filtration. The single-step, low polymerization yield for **3b** appears to be inherent to this derivative, since repeated attempts to increase yields by using microcrystalline material could not raise the conversion yield for this step.

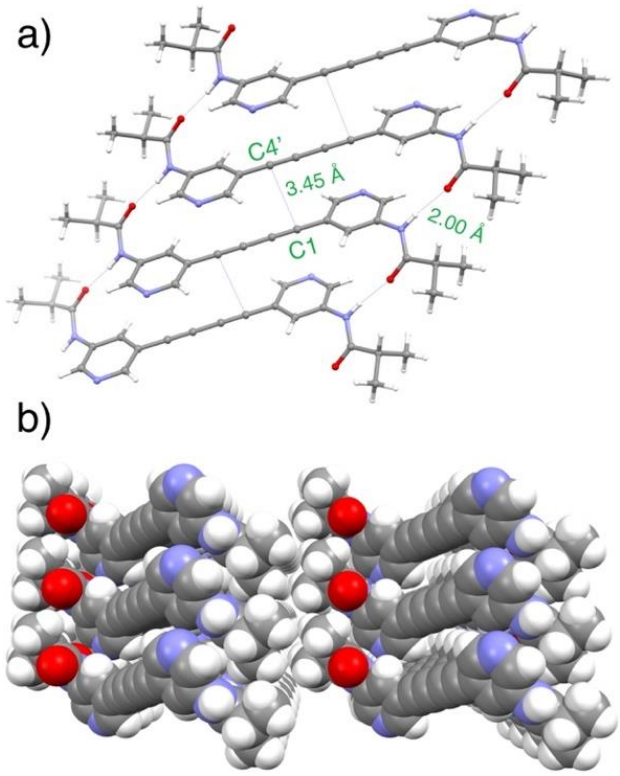

Figure 3.2. a) Crystal packing structure for diyne diamide **3a** displaying the short C1-C4' distance driven by the C=O···H–N hydrogen-bonded network. b) View of **3a** down the H-bonding axis.

*Characterization of the PDA and graphitization process***:** Once the PDA was successfully synthesized, the conversion from polymer to GNR could be studied by incremental heating of the PDA under argon. Our prior work underwent a two-step process, Hopf cyclization followed by cyclodehydrogenation and sidechain fragmentation, to form $N = 8$ armchair GNRs.[47] In contrast, pyridyl GNRs **1a,b** form in a one-step concomitant Hopf cyclization and aromatization transformation to yield a fjord-edge GNR upon heating without loss of sidechains. By using CP/MAS ^{13}C solid state NMR, we could observe the transformation by focusing on four distinct types of carbon signals that correspond to the four functional groups of interest: amide carbonyl, alkynl carbons, aryl carbons and amide sidechains (Figure 3.3). As PDAs **4a,b** were heated at

increasingly higher temperature for 1h, the distinct ^{13}C NMR signals tracked an initial Hopf cyclization, followed by full aromatization to the fjord-edge N_2[8]GNRs **1a** and **1b**.

The one-step transformation towards our fjord-edge GNRs involves a series of Hopf cyclizations between the pyridyl rings with the alkyne units along the PDA polymer backbone. For both **4a** and **4b**, significant reduction in the alkynyl signal can be seen after heating to 300 ˚C, indicating that this cyclization occurs more readily for the pyridyl PDAs than for their phenyl analogs.[47] Subsequent heating at 330 ˚C and 360 ˚C results in complete loss of the alkynyl carbon signal, which indicates complete Hopf cyclization along the backbone of **4a** and **4b**, respectively.

Concomitant with the loss of signal at ~100 ppm is the convergence of the aryl signals between 120-150 ppm into a broad peak with an underlying intensity ratio of 1:2:1 for both **1a** and **1b** at 330 ˚C and 360 ˚C, respectively. This ratio of intensities maps well onto what is expected from a structurally ideal fjord-edge heterocyclic GNR. Such an GNR would be expected to have

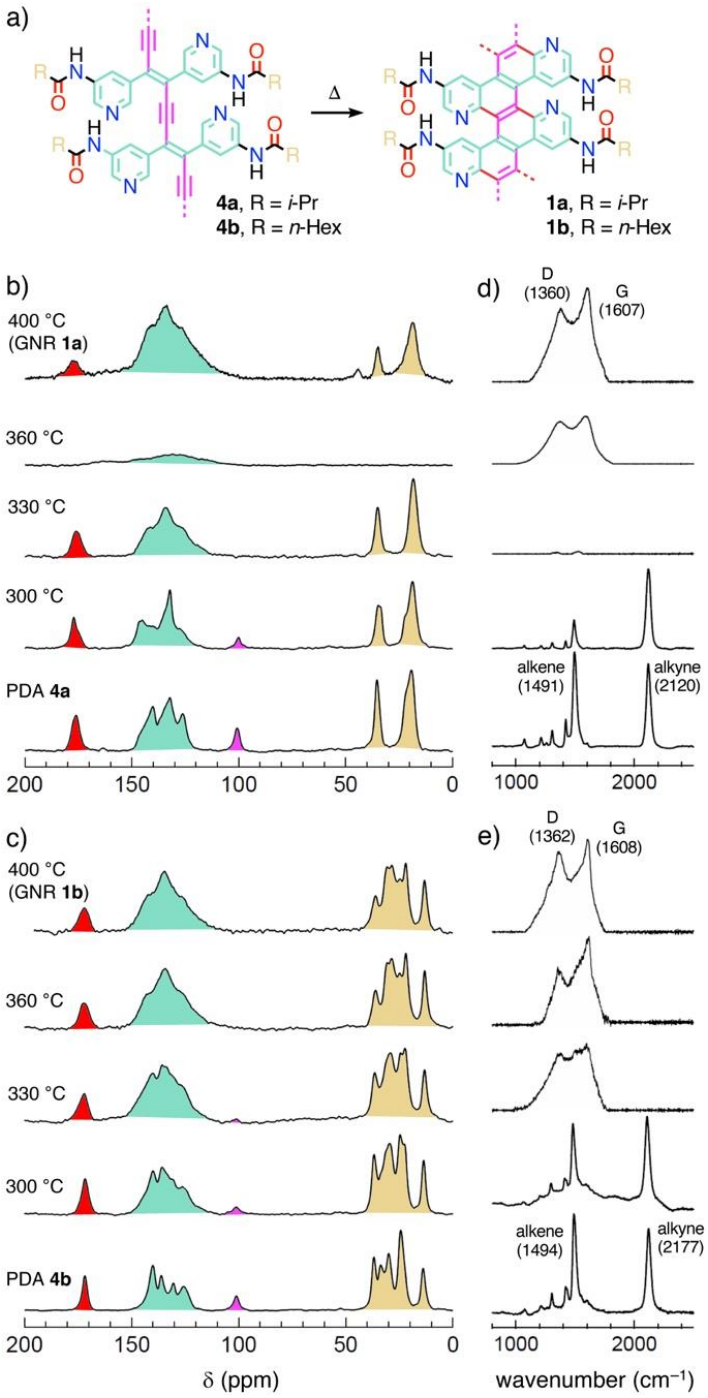

Figure 3.3. CP/MAS solid state ^{13}C NMR and Raman spectra for the products obtained by heating PDAs **4a,b**. Each heating experiment was carried out for 1h using a fresh sample of PDA. a) PDAs **4a,b** and GNRs **1a,b** are color-coded by chemical shift region to reflect spectral changes in b) and c). b) PDA **4a** conversion to fjord-edge N_2[8]GNR **1a**, and c) PDA **4b** conversion to fjord-edge N_2[8]GNR **1b**. The very broad weak signal for the sample heated at 360 ˚C in b) is due to the presence of an air-stable π-radical impurity.[49] Raman spectra for the conversion of d) PDA **4a** to fjord-edge N_2[8]GNR **1a**, and e) PDA **4b** to fjord-edge N_2[8]GNR **1b**.

seven distinct aryl carbon shifts with an overall profile of 1:2:1 (Table 3.1). By deconvoluting the experimental spectrum into seven individual signals of equal relative intensity, we can compare the experimental and calculated ^{13}C NMR chemical shifts. These values are in fair agreement with the calculated carbon shifts and support the assignment of a fjord edge to our GNRs. Similarly, the convergence of both **4a** and **4b** to matching aryl peaks indicates that these PDAs both undergo identical processes to form the same core fjord-edge N2[8]GNR. Subsequent heating to temperatures as high as 400 ˚C shows no change in the ^{13}C CP/MAS spectra, suggesting that the fjord-edge N2[8]GNR has fully formed at 330 ˚C and 360 ˚C for 4**a** and **4b** respectively. These mild temperatures retain the sidechains throughout the conversion to GNRs **1a,b**, as discussed below, and highlight an advantage of our bottom-up, solid-state methodology.

The retention of sidechains during the aromatization process up to 400 ˚C has potential impact on the processability of these GNRs. The relative intensities of the sidechain peaks to the aryl peaks remain constant throughout higher heating, indicating that neither a) further edge-to-edge cyclization of fjord-edge N2[8]GNR nor b) deformation of the fjord-edge due new C-N bonds formation occurs. In addition to the constant intensity, the presence of sidechains after aromatization increases the solubility of these materials without the need for additional surfactants. GNRs **1a,b** could be sonicated in N-methyl-2-pyrrolidone then passed through a 0.2 μm filter. The resulting solutions were colored and UV-vis spectra of the filtrate (Figure A27) indicated that these GNRs were soluble. Such solution-phase processability of these GNRs shows promise for future large scale processing conditions or device fabrication.

Determining the bonding environment of nitrogen: Although the CP/MAS ^{13}C NMR data supports the formation of fjord edges, it is possible to envision two possible Hopf cyclization pathways that both afford a fjord-edge GNR. Unlike our prior work on $[8]_AGNR$,[47] which forms a symmetric

Table 3.1. Comparison of Experimentally Fitted ^{13}C CP/MAS Chemical Shifts with Calculated Shifts for a fjord-edge N_2[8]GNR model.[48] a) Deconvolution of the experimental ^{13}C CP/MAS spectral absorptions in the aromatic range of 110-160 ppm. b) Comparison of fitted and calculated chemical shifts (ppm).

a)

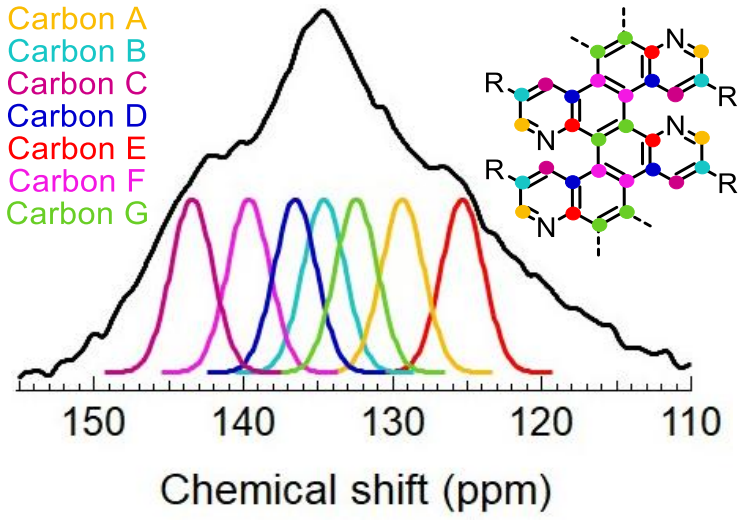

b)

Carbon	A	B	C	D	E	F	G
Fitted δ	129.4	134.5	143.5	136.5	125.4	139.7	132.5
Calc. δ	128.5	131.3	142.6	132.6	125.7	138.0	130.6

structure regardless of initial cyclization pathway at the 4- or 6-position, cyclization of the pyridyl PDA at the 4- or 6- position results in differing fjord-GNRs (Figure 3.4). Cyclization at the 4-position would yield a twisted "edge-like" doped GNR due to large steric overlap of the amide

sidechain and nearby isoquinoline unit. Potential further aromatization to an edge doped armchair GNR would require loss of sidechains and is not observed by ^{13}C NMR. Alternative cyclization at the 6-position produces a flatter "internal-like" doped material with amide sidechains pointed away from neighboring quinoline units. Both calculations on the mechanistic pathway and XPS data support cyclization at the 6-position to yield GNRs **1a,b**.

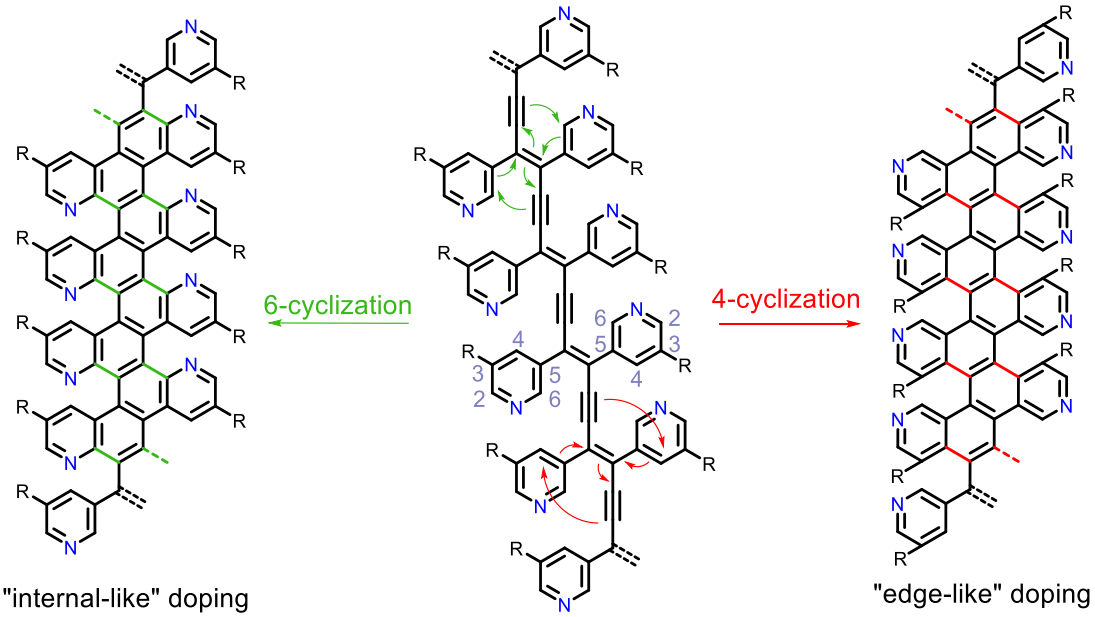

Figure 3.4. Hopf cyclization of the PDA dienyne systems at either the 4- or 6-position of the pyridyl rings, leading to "edge-like" and "internal-like" nitrogen doped fjord-GNRs, respectively.

We base our mechanistic investigation on previous work by Prall et al.[50] and our groups[47] that support a Hopf cyclization pathway for this class of systems. The Hopf cyclization proceeds through an initial 6π-electrocyclization, followed by two consecutive [1,2]-H shifts, with the first H-shift as the rate-determining step. For our model system **7** (Figure 3.5), we hypothesized a regioselective cyclization, with cyclization at the 6- (or *para* to the amide group) position (n) as the favored pathway over the 4- (or *ortho*) position (n') due to the steric bulk of the amide group. Using density functional theory (DFT), we computed the geometries of the transition state for the

initial 6π electrocyclization **8** and **8'**, the annulated allene intermediates **9** and **9'**, and the transition states for the 1,2-shift structures **10** and **10'**. Structures were optimized in the gas-phase using B3LYP/6-31G(d), and single-point calculations were performed using M06-2X/6-311+G(d,p) to obtain free energy values. The potential energy surfaces for the two cyclization pathways are shown in Figure 3.5.

The energetic trends for this pyridyl system are similar to the all-carbon systems studied by our groups previously. As we expected, the barriers for *ortho* cyclization are higher than those for *para* cyclization. The activation free energies of the favored transition states **8** and **10** are 48.1 and 54.7 kcal mol^{-1}, and the analogous transition states **6'** and **8'** have higher barriers of 51.3 and 60.0 kcal mol^{-1}. Like the all-carbon PDAs previously studied, the 1,2-shift following electrocyclization is the rate-determining step in both pathways, and the preference for the *para* pathway is a significant (5.3 kcal mol^{-1}).

The geometries of the transition structures **8** and **8'** are similar to each other and to their all-carbon variants. In **8** and **8'**, the π-system of the alkynes is planar, while the flanking aryl groups are out of plane by approximately 30˚. The slightly higher barrier of **8'** is likely due to the close proximity of the amide oxygen and methyl group on the forming C-C bond. More differences can be seen between the rate-determining states **10** and **10'**. In **10**, the quinoline is planar, and the C6-H1 bond stretches to 1.22 Å from its normal C-H bond length of 1.09 Å. However, in the unfavored transition state **10'**, the bulky amide group forces the quinoline out of plane, largely due to unfavorable interactions between the amide oxygen and the shifting hydrogen and adjacent methyl group, which accounts for the intrinsic preference for *para* cyclization.

Calculations for the unsubstituted variant (no amide groups) were also computed to probe the intrinsic preference for the 6-position (see Appendix B). The barrier of the rate-determining

1,2-shift for the unsubstituted system is 53.7 and 55.7 kcal mol^{-1} for the 6- and 4-positions, respectively, with only a preference of 2.0 kcal mol^{-1} for the 6-position. The increased preference for the 6-position with the substituted system **7** can be attributed to the unfavorable steric interactions from the substituent that would occur in **10'**.

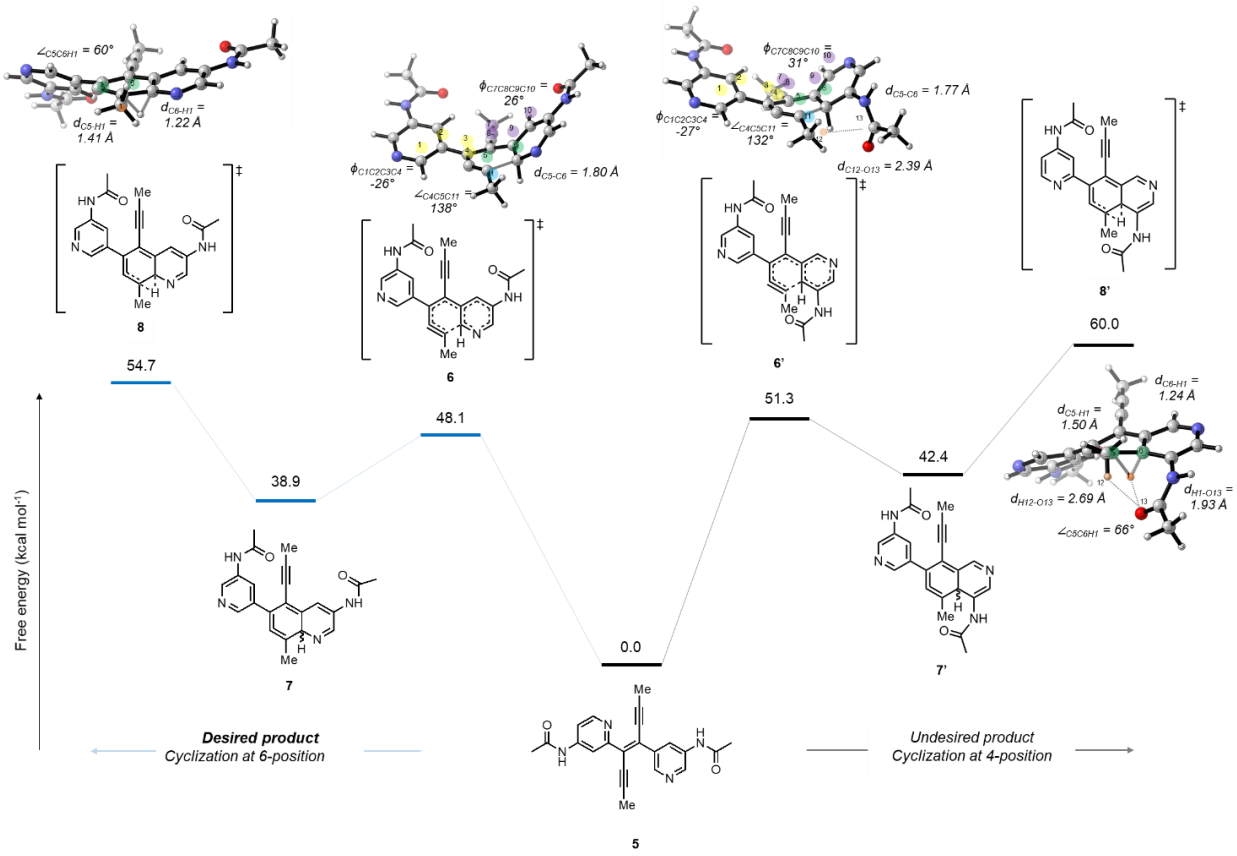

Figure 3.5. Free energy surface of pathways to desired product (left) and undesired product (right) relative to starting structure 7. Energies are free energies in kcal mol^{-1}

We note that the barrier of the rate-determining step in this pyridyl system **7** is only ~3 kcal mol^{-1} lower than that of the all-carbon system, which does not directly correlate with the ~100°C lower conversion temperature of this N-based system. We acknowledge that while these gas-phase calculations are useful in understanding the intrinsic regioselectivity of this system, they do not

account for other interactions that would arise in the full-length system in the solid state. Particularly, the pyridine nitrogen would be likely to cause differential behavior and packing compared to the all-carbon system.

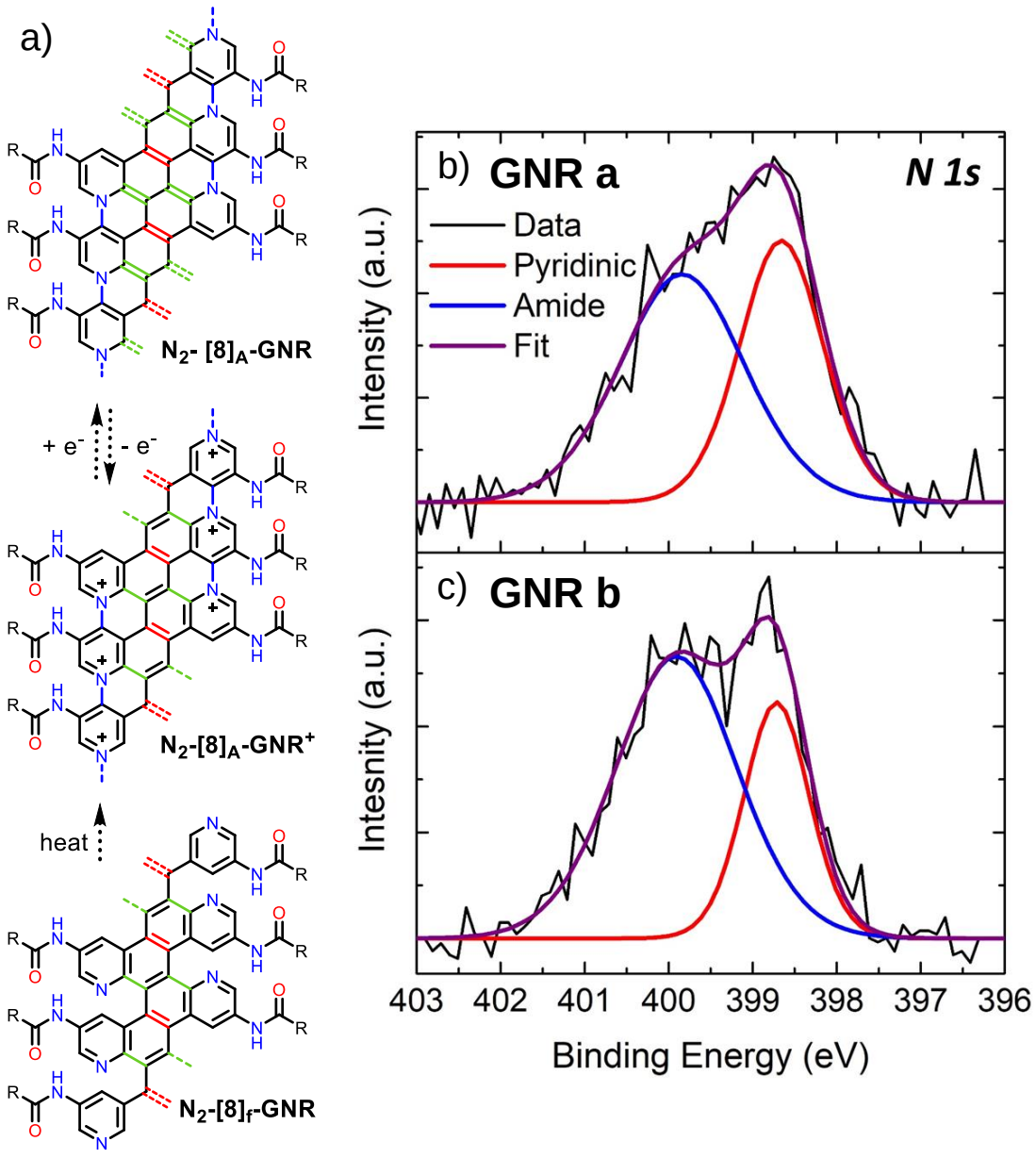

Figure 3.6. a) Paths to graphitization of fjord-GNRs to armchair GNRs. b) N 1s XPS for **GNR a** and c) N 1s XPS for **GNR b** with pyridinic and amido nitrogens centered at 398.7 and 399.7 eV, respectively.

In addition to questions about the Hopf cyclization pathway, it is worth considering whether a second cyclization occurs at higher temperatures beyond 330 and 360 °C. Further reaction could result in an internally doped armchair GNR, **N_2-[8]$_A$-GNR$^+$** or **N_2-[8]$_A$-GNR** (Figure 3.6). Although lack of additional oxidants makes the formation of these armchair GNRs unlikely, structural confirmation of fjord or armchair edge can be determined using XPS.

If an armchair edge were synthesized, the dominant nitrogen species within **N_2-[8]$_A$-GNR** would be internal, graphitic nitrogens which exhibit a N 1s binding energy of 401.8 ± 0.3 eV.[51-54] Similarly, **N_2-[8]$_A$-GNR$^+$** contains pyridinium species, which exhibit binding energies of 402.3 - 402.7 eV.[55,56] However, XPS spectra of GNRs **1a,b** display no signal at those binding energies (Figure 3.6). Deconvolution of our N 1s signal yields binding energies of 398.7 ± 0.3 eV and 399.7 ± 0.2 eV. These energies correspond to pyridinic[12,13] and amido[57] nitrogens respectively, without evidence of any higher energy species. Specifically, the lack of pyridinium signal negates the possibility of a secondary cyclization to an armchair edge and thus corroborates the presence of fjord edge structures in GNRs **1a,b**.

*Graphitic properties of GNRs **1a,b***: The graphitic nature of our fjord-edge N2[8]GNR systems were further verified using Raman spectroscopy and imaged using HR-TEM. PDAs **4a,b** both exhibit strong alkene, 1494 and 1491 cm^{-1} respectively, and alkyne peaks, 2117 and 2120 cm^{-1} respectively, which characteristically identify the enyne backbone of the PDAs (Figure 3.3). Upon heating, these signals disappear while the signature D and G peaks of GNRs **1a,b** appear (Figure 3.3). The Raman spectra show D peaks at 1360 and 1362 cm^{-1} and G peaks at 1607 and 1608 cm^{-1}, respectively, for GNRs **1a,b**. Relative to large sheets of graphene, the G peaks of these GNRs are upshifted due to the confined nature of GNRs, while prior reports of GNRs show similar shifts

in the D peak as well.[58] Specifically, the broad feature of the observed D peaks can be attributed to the fjord edge structure and the high levels of site-specific heteroatom substitutions as discussed below.

Broadening of the D peak is generally caused by defects within the graphene lattice.[59-61] Bond vacancies, atom vacancies, and heteroatoms distort the lattice away from perfect sp^2 graphitic carbon, which are reflected in the D peak. Fjord-edge GNRs with site-specific nitrogen substitutions thus have two structural features that inherently broaden the D peak beyond previously reported GNR examples. Specifically, fjord-edges represent bond vacancies along the edge of pristine graphene which mimic the effect of holey graphene.[62] Broad D and G peaks with higher (I_D / I_G) ratios represent large numbers of defects, which characteristically describe holey graphene and such broadened D peaks can be seen in other fjord edge GNRs.[27]

Further broadening of the D peaks is caused by nitrogen dopant distortion of the lattice. Reports for both nitrogen doped graphene sheets and top-down synthesized doped GNRs have shown this broadening with various levels of dopant.[63-64,69] The bottom-up approach of our synthesis incorporates high levels of nitrogen doping, 12.5 % at., which further accounts for the broad D peak relative to other examples with doping under 5% at.[65]

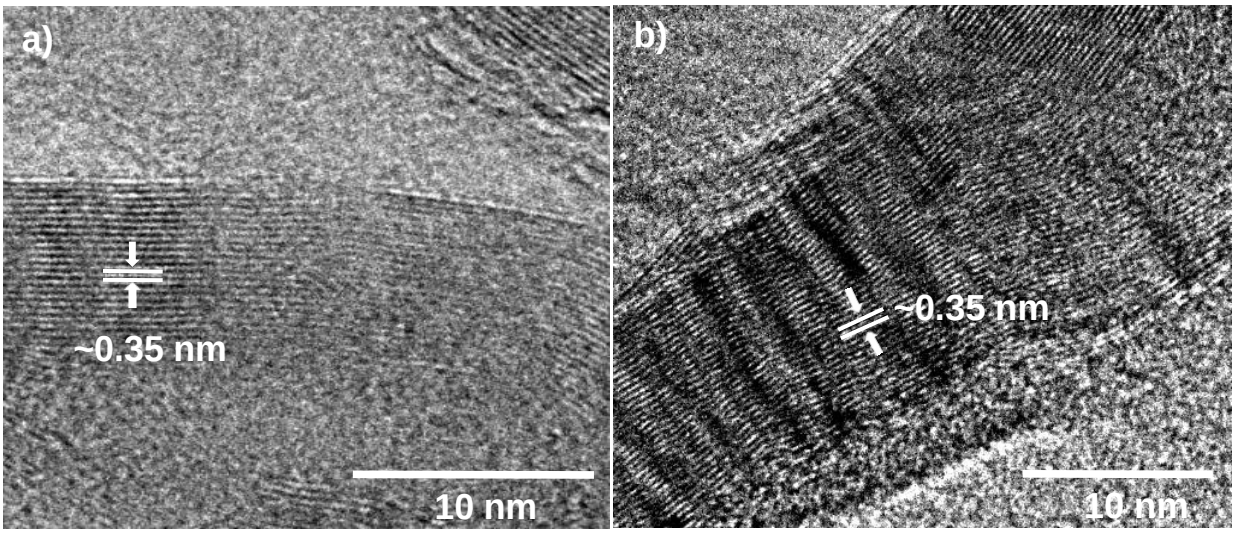

Figure 3.7. HR-TEM images of a) GNR **1a,** and b) GNR **1b**. The spacing between nanoribbon striations corresponds to the π-stacking distance between fjord edged ribbons.

HR-TEM imaging of both GNRs **1a,b** show tight bundles of stacked ribbons (Figure 3.7). Ribbons within the bundles have a stacking distance of ~0.35 nm, indicating cofacial π-π stacking. This is the expected π-stacking distance for graphitic materials, thus indicating ideal packing between GNRs despite their non-planar structure**.**

Section 3.4. Conclusion

In summary, we have demonstrated the synthesis of a novel fjord-edge GNR with site-specific nitrogen substitutions, GNRs **1a,b**. The stepwise conversion from dipyridyl diynes to heteroatomic PDA via topochemical polymerization followed by Hopf cyclization to the GNR proceeded at mild temperatures of 330-360 ˚C. The formation of the GNRs was confirmed via CP/MAS ^{13}C NMR, XPS, Raman and HR-TEM. Retention of the sidechains throughout this process yields soluble N-GNRs, which could be used in solution processing. The success of our

bottom-up method demonstrates the versatility of this solid-state method to incorporate heteroatom substitutions and synthesize diverse GNR edge structures.

Section 3.5. Experimental Details

Diynes that successfully polymerized:

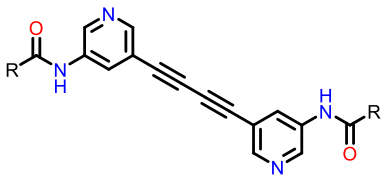

3a, R = *i*Pr
3b, R = $(CH_2)_5CH_3$

Diynes that did not polymerize topochemically:

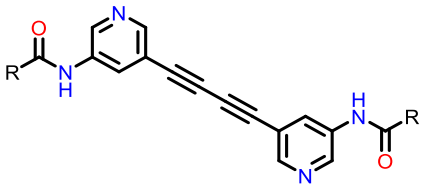

3c, R = Me

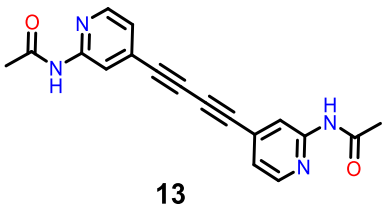

13

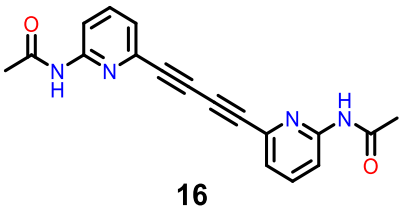

16

General procedures: Chemical reagents were obtained from commercial sources and used without further purification. Unless otherwise noted, all reactions were performed under argon at 25 °C. Silicycle (Siliflash P60) silica gel 60 (240-400 mesh) was used for all column chromatography.

Solution NMR spectra were obtained on a Bruker AV500 instrument. CP/MAS ^{13}C NMR spectra were obtained on a Bruker AV600 using a 3.2 mm zirconia rotor spinning at 18 kHz. A 514 nm excitation laser was used on pellets of material to obtain Raman spectra. The x-ray photoelectron spectroscopy (XPS) was performed using a Kratos Axis Ultra DLD spectrometer with a monochromatic Al Kα radiation source. A pass energy of 20 eV was used with a step size of 0.1 eV, a dwell time of 300 ms, and a charge neutralizer filament. The obtained spectra were calibrated to the advantageous carbon 1s peak at 284.8 eV and analysis of the spectra was performed using CasaXPS.

3-Amino-5-((trimethylsilyl)ethynyl)pyridine (5).

3-Amino-5-bromopyridine (5.00 g, 28.9 mmol, 1.0 eq) was added to a round-bottomed flask with a stirring bar under argon. Toluene (75 mL), bis(triphenylphosphine) palladium dichloride (507 mg, 0.722 mmol, 0.025 eq) and copper(I) iodide (79 mg, 0.72 mmol, 0.025 eq) were added and the mixture was sparged with argon for 15 minutes. Trimethylsilylacetylene (5.37 g, 57.7 mmol, 2.0 eq) and diisopropylamine (5.84 g, 57.7 mmol, 2.0 eq) were added before refluxing overnight. After reaction completion as ascertained by ^{1}H NMR of the crude, the mixture was cooled to 25 ˚C, filtered over Celite and concentrated on the Rotavap. Purification by flash column chromatography with SiO_2 yielded 5.02 g (91%) of **3** as a pale tan solid. ^{1}H NMR (400 MHz, $CDCl_3$): δ (ppm) 0.25 (s, 9H), 3.68 (br s, 2H), 7.03 (dd, *J* = 2.7, 1.9 Hz, 1H), 8.00 (d, *J* = 2.7 Hz, 1H), 8.10 (d, *J* = 1.9 Hz, 1H); ^{13}C NMR (125 MHz, $CDCl_3$): δ (ppm) 0.0, 97.5, 102.0, 120.28, 124.0, 137.0, 141.8, 143.1; HRMS (DART) Calculated for $C_{10}H_{14}N_2Si$ [M+H]: 191.09902; found 191.10066.

N-(5-Ethynyl-3-pyridyl)isobutyramide (6a).

3-Amino-5-((trimethylsilyl)ethynyl)pyridine **3** (5.02 g, 26.4 mmol, ~1.0 eq) was added to a round-bottomed flask with a stirring bar under argon and dissolved in anhydrous CH_2Cl_2 (75 mL). Triethylamine (5.34 g, 52.8 mmol, 2.0 eq) was added and the flask was cooled to 0 ˚C. Isobutryl chloride (4.22 g, 39.6 mmol, 1.5 eq) was dissolved in CH_2Cl_2 (15 mL) and added dropwise. The mixture was allowed to warm to 25 ˚C while stirring. Upon completion by TLC, the reaction was washed with an aqueous solution of $NaHCO_3$ and extracted twice with CH_2Cl_2. Organic layers were combined and washed with brine before drying over $MgSO_4$ and concentrating *in vacuo*. The crude product was then dissolved in MeOH and THF (each 130 mL), anhydrous K_2CO_3 added (~0.5 g) and stirred at 25 ˚C until completion by TLC. The solvents were removed *in vacuo* before partitioning between water and CH_2Cl_2. The aqueous layer was extracted with CH_2Cl_2 twice, organic layers combined, washed with brine, dried over $MgSO_4$ and concentrated. A total of 4.73 g (95% over 2 steps) of amide **4a** was collected as pale yellow crystals. ^{1}H NMR (400 MHz, $CDCl_3$): δ (ppm) 1.26 (d, *J* = 6.9 Hz, 6H), 2.58 (sept, *J* = 6.9 Hz, 1H), 3.19 (s, 1H), 7.56, (br s, 1H), 8.30 (dd, *J* = 2.6, 1.9 Hz, 1H), 8.43 (d, *J* = 1.9 Hz, 1H), 8.52 (d, *J* = 2.6, 1H); ^{13}C NMR (125 MHz, $CDCl_3$): δ (ppm) 19.5, 36.6, 79.9, 80.9, 129.9, 133.6, 134.4, 140.3, 147.9, 175.7; HRMS (DART) Calculated for $C_{11}H_{12}N_2O$ [$M^{\bullet+}$]: 188.09496; found 188.10645. (Note: the NH proton is completely missing in the spectrum, in a very unusual occurrence)

N,N'-(Buta-1,3-diyne-1,4-diylbis(pyridine-5,3-diyl))bis(2-methylpropanamide) (3a).

N-(5-ethynyl-3-pyridyl)isobutyramide **4a** (3.33 g, 17.7 mmol, 1.0 eq) was dissolved in CH_2Cl_2 (53 mL) before adding N,N,N'N'-tetramethylethylene-1,2-diamine (TMEDA) (205 mg, 1.77 mmol,

0.1 eq) and copper(I) iodide (337 mg, 1.77 mmol, 0.1 eq). Air was bubbled through the mixture for 15 minutes before allowing to stir overnight open to air. The product was filtered and washed with water to give 2.07 g (63%) of diyne **1a**. The material was then recrystallized from MeOH to yield clear colorless needles which rapidly turn deep blue upon exposure to light. ^{1}H NMR (400 MHz, DMSO): δ (ppm) 1.08 (d, *J* = 6.9 Hz, 12H), 2.58 (sept, *J* = 6.9 Hz, 2H), 8.26 (dd, *J* = 1.8, 1.4 Hz, 2H), 8.45 (d, *J* = 1.4 Hz, 2H), 8.74 (d, *J* = 1.8 Hz, 2H), 10.24 (s, 2H); ^{13}C NMR (125 MHz, DMSO): δ (ppm) 19.8, 35.4, 76.1, 80.0, 117.7, 128.9, 136.2, 141.8, 147.3, 176.7; HRMS (DART) Calculated for $C_{22}H_{22}N_4O_2$ [$M^{\bullet+}$]: 374.1743; found 374.1596.

N-(5-Ethynyl-3-pyridyl)heptanamide (6b).

3-Amino-5-((trimethylsilyl)ethynyl)pyridine **3** (4.90 g, 25.8 mmol, ~1.0 eq) was added to a round-bottomed flask with a stirring bar under argon and dissolved in anhydrous CH_2Cl_2 (72 mL). Triethylamine (5.21 g, 52.0 mmol, 2.0 eq) was added and the flask cooled to 0 ˚C. Heptanoyl chloride (5.74 g, 38.6 mmol, 1.5 eq) was dissolved in CH_2Cl_2 (15 mL) and added dropwise. The mixture was allowed to warm to 25 ˚C while stirring. Upon completion by TLC, the reaction was washed with an aqueous solution of $NaHCO_3$ and extracted twice with CH_2Cl_2. Organic layers were combined and washed with brine before drying over $MgSO_4$ and concentrating *in vacuo*. The crude product was then dissolved in MeOH (100 mL) and THF (100 mL), anhydrous K_2CO_3 added (~0.5 g) and the solution stirred at 25 ˚C until reaction completion (desilylation) as monitored by TLC. The solvents were removed *in vacuo* before partitioning between water and CH_2Cl_2. The aqueous layer was extracted with CH_2Cl_2 twice, organic layers combined, washed with brine, dried over $MgSO_4$ and concentrated. A total of 4.65 g (78% over 2 steps) of amide **5b** was collected as

pale yellow crystals. ^{1}H NMR (400 MHz, $CDCl_3$): δ (ppm) 0.88 (t, *J* = 7.0 Hz, 3H), 1.31 (m, 4H), 1.36 (t, *J* = 7.0 Hz, 2 H), 1.72 (quint, *J* = 7.5 Hz, 2H), 2.38 (t, *J* = 7.5 Hz, 2H), 3.19 (s, 1H), 7.37 (br s, 1H), 8.29 (dd, *J* = 2.6, 1.6 Hz, 1H), 8.42 (d, *J* = 1.6 Hz, 1H), 8.50 (d, *J* = 2.6 Hz, 1H); ^{13}C NMR (125 MHz, $CDCl_3$): δ (ppm) 14.0, 22.5, 25.4, 28.9, 31.5, 80.0, 80.9, 119.5, 129.9, 134.5, 140.3, 147.8, 172.1; HRMS (DART) Calculated for $C_{14}H_{18}N_2O$ [$M^{\bullet+}$]: 230.1419; found 230.1312.

N,N'-(Buta-1,3-diyne-1,4-diylbis(pyridine-5,3-diyl))diheptanamide (3b).

N-(5-Ethynyl-3-pyridyl)heptanamide **3** (3.92 g, 17.0 mmol, 1.0 eq) was dissolved in CH_2Cl_2 (50 mL) before adding N,N,N'N'-tetramethylethylene-1,2-diamine (TMEDA) (197 mg, 1.70 mmol, 0.1 eq) and copper(I) iodide (324 mg, 1.70 mmol, 0.1 eq). Air was bubbled through the mixture for 15 minutes before allowing to stir overnight open to air. The product was filtered and washed with water to give 3.60 g (92%) of diyne **1b**. The material was then recrystallized from isopropanol to yield clear needles which rapidly turn blue upon exposure to light. ^{1}H NMR (500 MHz, DMSO): δ (ppm) 0.86 (t, *J* = 7.0, 6H), 1.28 (m, 6H), 1.59 (quint, *J* = 7.0 Hz, 4H), 2.34 (t, *J* = 7.5 Hz, 4H), 8.28 (dd, *J* = 2.3, 1.4 Hz, 2H), 8.48 (d, *J* = 1.4 Hz, 2H), 8.73 (d, *J* = 2.3, 2H), 10.31 (s, 2H); ^{13}C NMR (125 MHz, DMSO): δ (ppm) 19.1, 27.2, 30.0, 33.5, 36.2, 41.5, 80.8, 84.7, 122.4, 133.6, 140.8, 146.4, 152.1, 177.6; HRMS (DART) Calculated for $C_{28}H_{34}N_4O_2$ [$M^{\bullet+}$]: 458.2682; found 458.3872.

N-(5-Ethynyl-3-pyridyl)acetamide (6c).

3-Amino-5-((trimethylsilyl)ethynyl)pyridine **5** (11.00 g, 57.8 mmol, 1.0 eq) was added to a round-bottomed flask with a stirring bar under argon and dissolved in anhydrous THF (115 mL). Acetic anhydride (8.843 g, 86.7 mmol, 1.5 eq) was added slowly at 0 ˚C. The mixture was allowed to warm to 25 ˚C while stirring overnight. The reaction was washed with an aqueous solution of $NaHCO_3$ and extracted twice with CH_2Cl_2. Organic layers were combined and washed with brine before drying over $MgSO_4$ and concentrating *in vacuo*. The residue was dissolved in methanol and THF (85 mL each) before adding anhydrous potassium carbonate (17.53 g, 126.8 mmol, 3.0 eq) and stirring until completion. The aqueous layer was extracted with CH_2Cl_2 twice, organic layers combined, washed with brine, dried over $MgSO_4$ and concentrated to yield 4.559 g (60%) of **4c**. ^{1}H NMR (400 MHz, $CDCl_3$): δ (ppm) 8.49 (br s, 1H), 8.45 (br s, 1H), 8.26 (s, 1H), 7.15 (br s, 1H), 3.21 (s, 1H), 2.22 (s, 3H).

N,N'-(Buta-1,3-diyne-1,4-diylbis(pyridine-5,3-diyl))diacetamide (3c).

N-(5-ethynyl-3-pyridyl)acetamide **6c** (4.559 g, 34.7 mmol, 1.0 eq) was dissolved in CH_2Cl_2 (105 mL) before adding N,N,N'N'-tetramethylethylene-1,2-diamine (TMEDA) (403 mg, 3.47 mmol, 0.1 eq) and copper(I) iodide (661 mg, 3.47 mmol, 0.1 eq). Air was bubbled through the mixture for 15 minutes before allowing to stir overnight open to air. The product was filtered and washed with water to give 5.156 g (94%) of diyne **1c**. ^{1}H NMR (400 MHz, d_6-DMSO): δ (ppm) 10.35 (br s, 2H), 8.69 (s, 2H), 8.46 (s, 2H), 8.24 (s, 2H), 2.07 (s, 6H); ^{13}C NMR (125 MHz, d_6-DMSO): δ (ppm) 169.84, 147.4, 141.6, 136.0, 128.9, 117.6, 79.9, 76.1, 24.4.

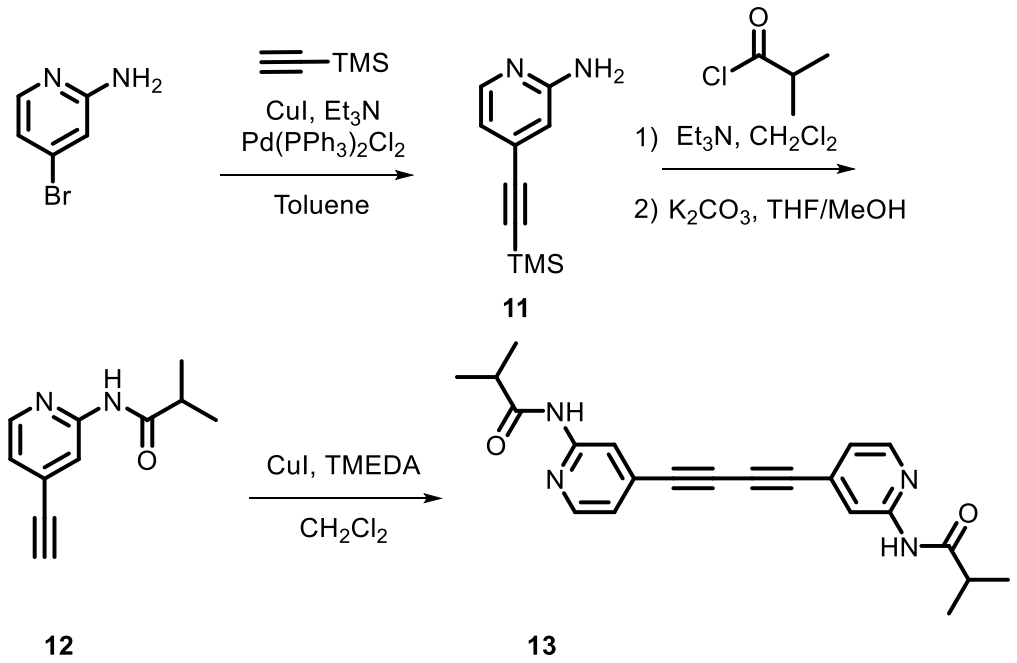

Scheme 3.2. Synthesis of 2,4-disubstituted dipyridyl diyne **13**.

2-Amino-4-((trimethylsilyl)ethynyl)pyridine (11).

2-Amino-4-bromopyridine (20.0 g, 115 mmol, 1.0 eq) was added to a round-bottomed flask fitted with a stirring bar. Toluene (250 mL), bis(triphenylphosphine) palladium dichloride (4.06 g, 5.78 mmol, 0.05 eq) and copper(I) iodide (2.20 g, 11.5 mmol, 0.1 eq) were added, then the mixture was sparged with argon for 15 minutes. Trimethylsilylacetylene (22.7 g, 231 mmol, 2.0 eq) and triethylamine (23.4g, 231 mmol, 2.0 eq) were added before refluxing overnight. After reaction completion as ascertained by ^{1}H NMR of the crude, the mixture was cooled to 25 ˚C, then filtered over Celite. The filtrate was then washed with water and acidified with HCl to pH = 1. The aqueous phase was then washed with CH_2Cl_2, followed by neutralization to pH = 7 using aqueous $NaHCO_3$. The aqueous phase was extracted with CH_2Cl_2 three times before all the organic layers were

combined, dried over $MgSO_4$ and concentrated. The product **11**, 18.8 g (86%), was obtained as a tan colored solid. ^{1}H NMR (400 MHz, $CDCl_3$): δ (ppm) 8.00 (d, *J* = 2.6 Hz, 1H), 6.67 (dd, *J* = 2.6, 0.6 Hz, 1H), 6.54 (d, *J* = 0.6 Hz, 1H), 4.42 (br s, 2H), 0.24 (s, 9H); ^{13}C NMR (125 MHz, $CDCl_3$): δ (ppm) 158.2, 148.2, 132.5, 116.4, 110.8, 102.6, 98.2, 0.3.

N-(4-Ethynyl-2-pyridyl)isobutyramide (12).

2-Amino-4-((trimethylsilyl)ethynyl)pyridine **11** (500 mg, 2.63 mmol, 1.0 eq) was added to a round-bottomed flask fitted with a stirring bar under argon. After dissolution into anhydrous CH_2Cl_2 (8 mL), triethylamine (663 mg, 6.57 mmol, 2.5 eq) was added. The flask was cooled to 0 ˚C, then isobutyryl chloride (616 mg, 5.78 mmol, 2.2 eq), dissolved in CH_2Cl_2 (2.3 mL), was added dropwise. The mixture was allowed to warm to 25 ˚C while stirring. Upon completion by TLC, the reaction was washed with an aqueous solution of $NaHCO_3$ and extracted twice with CH_2Cl_2. Organic layers were combined and washed with brine before drying over $MgSO_4$ and concentrating *in vacuo*. The crude product was then dissolved in methanol and THF (10 mL each), anhydrous K_2CO_3 (868 mg, 6.29 mmol, 3.0 eq) was added and the mixture was stirred at 25 ˚C until the removal of the trimethylsilyl group was completed, as judged by TLC. The solvents were removed *in vacuo* before partitioning between water and CH_2Cl_2. The aqueous layer was extracted with CH_2Cl_2 twice, organic layers combined, washed with brine, dried over $MgSO_4$ and concentrated to yield 286 mg (59%). ^{1}H NMR (400 MHz, $CDCl_3$): δ (ppm) 8.35 (t, *J* = 1.1 Hz, 1H), 8.21 (dd, *J* = 2.6, 0.4 Hz, 1H), 7.84 (br s, 1H), 7.07 (dd, *J* = 2.6, 0.8 Hz, 1H), 3.26 (s, 1H), 2.54 (septet, *J* = 6.9 Hz, 1H), 1.26 (d, *J* = 6.9 Hz, 6H). ^{13}C NMR (125 MHz, $CDCl_3$): δ (ppm) 175.5, 151.5, 147.8, 132.2, 122.2, 116.4, 81.7, 81.1, 36.8, 19.4.

N,N'-(buta-1,3-diyne-1,4-diylbis(pyridine-4,2-diyl))bis(2-methylpropanamide) (13).

N-(4-Ethynyl-2-pyridyl)isobutyramide **12** (290 mg, 1.54 mmol, 1.0 eq) was dissolved in CH_2Cl_2 (5 mL) before adding N,N,N'N'-tetramethylethylene-1,2-diamine (TMEDA) (17.8 mg, 0.154 mmol, 0.1 eq) and copper(I) iodide (29 mg, 0.154 mmol, 0.1 eq). Air was bubbled through the mixture for 15 minutes before allowing to stir overnight open to air. The product was filtered and washed with water to give 253 mg (88%) of diyne **13**. ^{1}H NMR (400 MHz, d_6-DMSO): δ (ppm) 10.64 (br s, 2H), 8.38 (dd, *J* = 2.6, 0.3 Hz, 2H), 8.23 (t, *J* = 1.1Hz, 2H), 7.28 (dd, *J* = 2.6 Hz, 2H), 2.74 (septet, *J* = 6.9 Hz , 2H), 1.07 (d, *J* = 6.9 Hz, 12H); ^{13}C NMR (125 MHz, d_6-DMSO): δ (ppm) 177.1, 153.0, 149.3, 129.9, 121.8, 115.9, 81.2, 76.2, 34.9, 19.8.

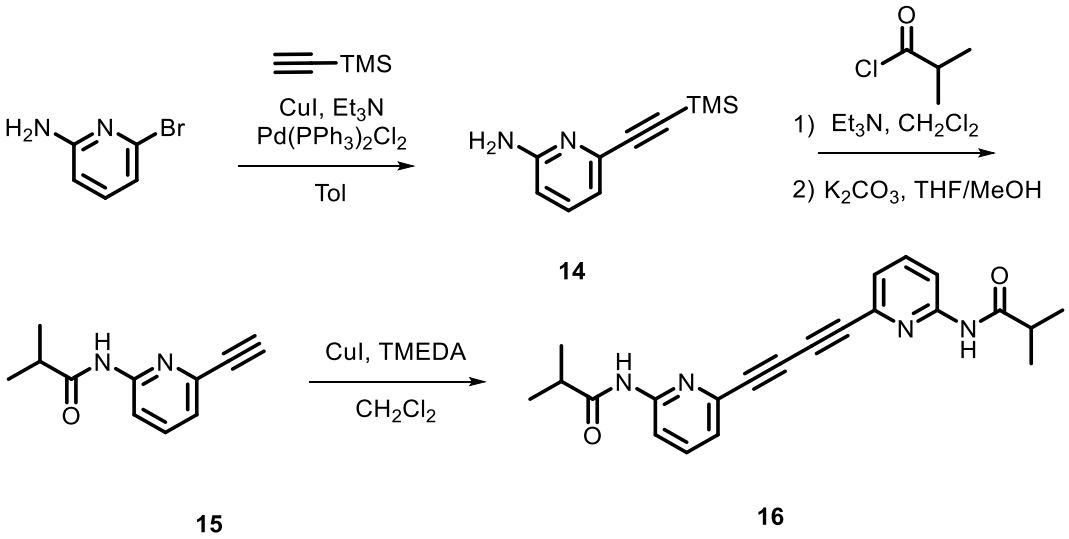

Scheme 3.3. Synthesis of 2,6-disubstituted dipyridyl diyne **16**.

2-Amino-6-((trimethylsilyl)ethynyl)pyridine (14).

2-Amino-6-bromopyridine (1.00 g, 5.78 mmol, 1.0 eq) was dissolved in toluene (15 mL) under argon along with bis(triphenylphosphine) palladium dichloride (203 mg, 0.289 mmol, 0.05 eq) and copper(I) iodide (110 mg, 0.589 mmol, 0.1 eq) before sparging with argon for 15 minutes. Trimethylsilylacetylene (1.14 g, 11.5 mmol, 2.0 eq) and triethylamine (1.17 g, 11.5 mmol, 2.0 eq) were added before refluxing overnight. After reaction completion as ascertained by ^{1}H NMR of the crude, the mixture was cooled to 25 ˚C, filtered over Celite. The filtrate was then washed with water and acidified with HCl to pH = 1. The aqueous phase was then washed with CH_2Cl_2 then neutralized using aqueous $NaHCO_3$. The aqueous phase was then extracted with CH_2Cl_2 three times before organic layers were combined, dried over $MgSO_4$ and concentrated. 767 mg (70%) of the title compound. ^{1}H NMR (400 MHz, $CDCl_3$): δ (ppm) 7.36 (dd, *J* = 4.4, 3.6 Hz, 1H), 6.85 (dd, *J* = 3.7, 0.4 Hz, 1H), 6.64 (dd, J = 4.1, 0.4 Hz, 1H), 4.48 (br s, 2H), 0.25 (s, 9H); ^{13}C NMR (125 MHz, $CDCl_3$): δ (ppm) 158.1, 140.9, 137.7, 118.1, 108.8, 104.0, 93.5, 0.2.

N-(6-ethynyl-2-pyridyl)isobutyramide (15)

2-Amino-6-((trimethylsilyl)ethynyl)pyridine **14** (200 mg, 1.05 mmol, 1.0 eq) was dissolved in anhydrous CH_2Cl_2 (3 mL) under argon along with triethylamine (319 mg, 2.63 mmol, 3.0 eq) at 0° C. A solution of isobutryl chloride (280 mg, 2.63 mmol, 2.5 eq) in CH_2Cl_2 (1 mL) was added dropwise. The mixture was allowed to warm to 25 ˚C while stirring, then washed with an aqueous solution of $NaHCO_3$ and extracted twice with CH_2Cl_2. Organic layers were combined and washed with brine before drying over $MgSO_4$ and concentrating *in vacuo*. The residue was dissolved in methanol and THF (7 mL each) before adding anhydrous potassium carbonate (601 mg, 4.35

mmol, 3.0 eq). After stirring at room temperature for 3 hours, the mixture was concentrated and partitioned between water and CH_2Cl_2. The aqueous layer was further extracted with CH_2Cl_2 before the organic layers were combined and washed with water and brine. After drying over $MgSO_4$ and concentrating, 210 mg (99%) of the product was obtained as an off-white solid. ^{1}H NMR (400 MHz, $CDCl_3$): δ (ppm) 8.24 (dd, *J* = 4.3, 0.4 Hz, 1H), 7.95 (br s, 1H), 7.67 (t, *J* = 8.0 Hz, 1H), 7.21 (dd, *J* = 3.8, 0.4 Hz, 1H), 3.14 (s, 1H), 2.52 (septet, *J* = 6.9 Hz, 1H), 1.25 (d, *J* = 6.9 Hz, 6H); ^{13}C NMR (125 MHz, $CDCl_3$): δ (ppm) 175.7, 151.5, 139.9, 138.7, 123.3, 114.2, 82.2, 77.1, 36.8, 19.4.

N,N'-(buta-1,3-diyne-1,4-diylbis(pyridine-6,2-diyl))bis(2-methylpropanamide) (16)

A solution of N-(6-ethynyl-2-pyridyl)isobutyramide **15** (210 mg, 1.12 mmol. 1.0 eq) in CH_2Cl_2 (4 mL), N,N,N'N'-tetramethylethylene-1,2-diamine (TMEDA) (22 mg, 0.11 mmol, 0.1 eq), and copper(I) iodide (13 mg, 0.11 mmol, 0.1 eq) was stirred at room temperature. Air was bubbled through the reaction for 15 minutes before being left open to air overnight. The product was filtered and washed with water to give 200 mg (96%) of **11**. ^{1}H NMR (400 MHz, $CDCl_3$): δ (ppm) 8.29 (dd, *J* = 4.2, 0.4 Hz, 1H), 7.96 (br s, 1H), 7.70 (t, *J* = 8.1 Hz, 1H), 7.28 (d, *J* = 3.8 Hz, 1H), 2.54 (septet, *J* = 6.9 Hz, 1H), 1.25 (d, *J* = 6.9 Hz, 6H); ^{13}C NMR (125 MHz, $CDCl_3$): δ (ppm) 175.8, 151.7, 139.3, 138.8, 124.3, 114.8, 85.8, 80.4, 36.8, 19.4.

General procedure for the topochemical polymerizations:

Crushed crystals were suspended in hexanes in a capped Erlenmeyer flask. This was placed in a photoreactor and stirred overnight under exposure to a high-powered Hanovia mercury lamp. Solids were then filtered off and subsequently boiled in the appropriate solvent to remove residual monomeric starting material. The remaining PDA solids could be filtered over filter paper and peeled off as a film. The recovered filtrate was evaporated *in vacuo* and the starting material was recrystallized to repeat the polymerization process.

PDA 4a:

Polymerization yield: 587 mg of PDA from 3.30 g of **3a** (18%)

Solvent: Boiling in ethanol and filtration followed by additional boiling in DMF, filtering and washing with diethyl ether.

PDA 4b:

Polymerization yield: 130 mg of PDA from 2.97 g of **3b** (4%)

Solvent: Boiling in chloroform and filtration followed by additional boiling in DMF, filtering and washing with diethyl ether.

General procedure for the graphitization of PDAs 4a,b:

All heating experiments were done using a quartz tube and programmable tube furnace (MTI OTF-1200X0S0NT). PDAs **4a** and **4b** were placed in an alumina boat and heated under positive argon flow. The furnace was programmed to ramp from 25 ˚C to the desired temperature over 40 minutes, remaining at the desired temperature for 1 hour, then cooled back to 25 ˚C over 40 minutes. Once fully cooled, the samples were removed from the furnace and massed.

Section 3.6. Appendix B

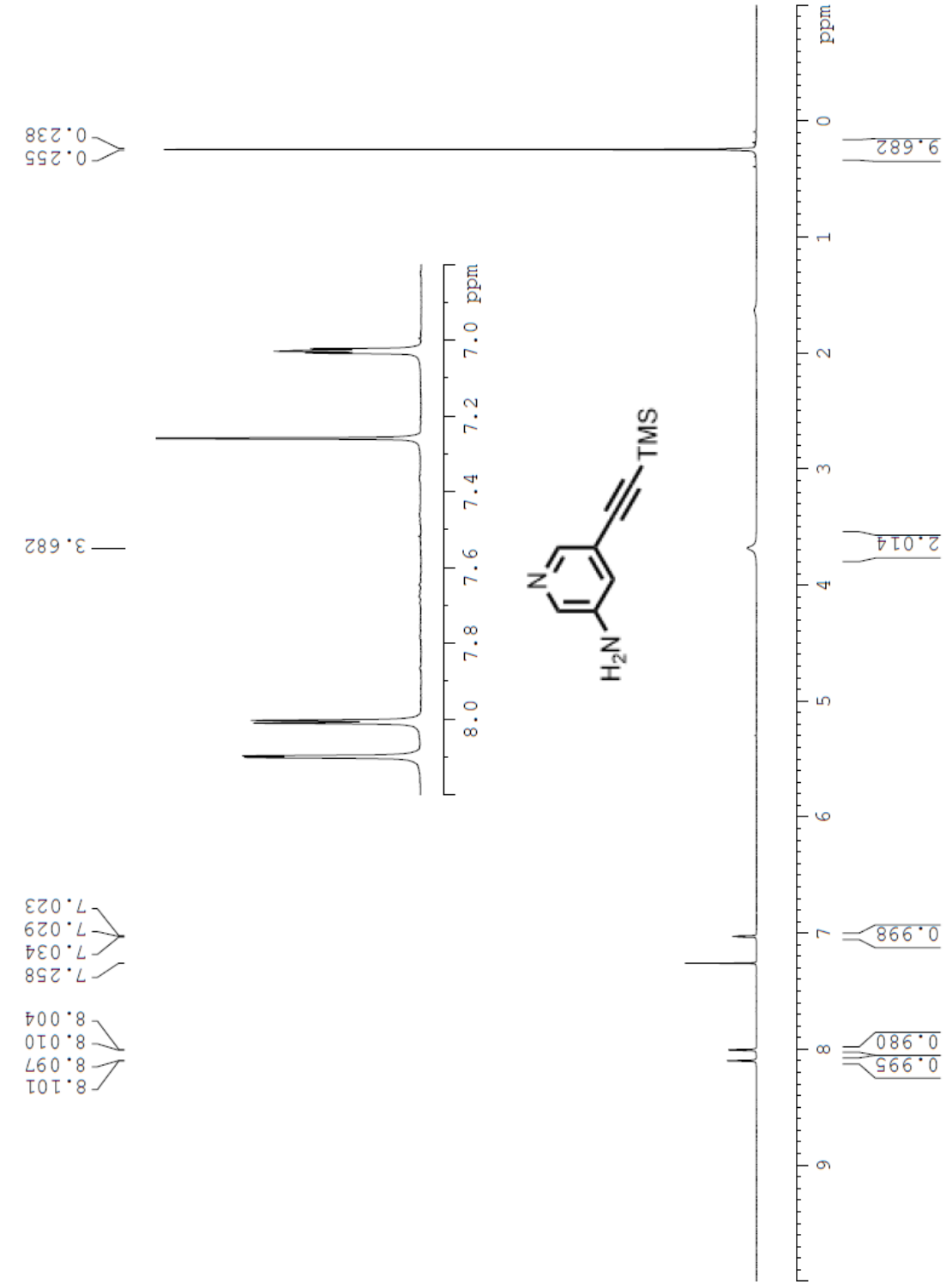

Figure A1. ^{1}H NMR of compound **5** in $CDCl_3$.

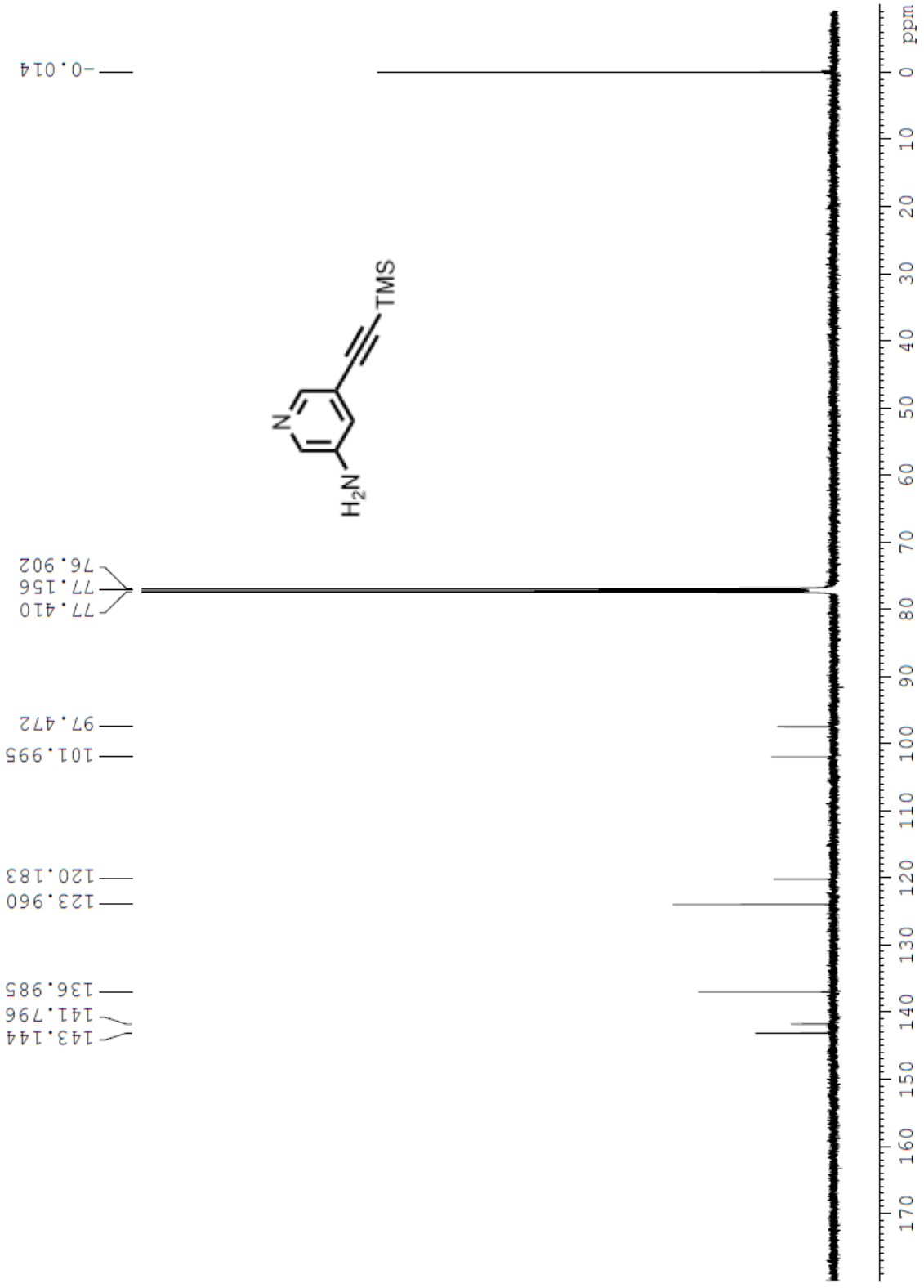

Figure A2. ^{13}C NMR of compound 5 in $CDCl_3$.

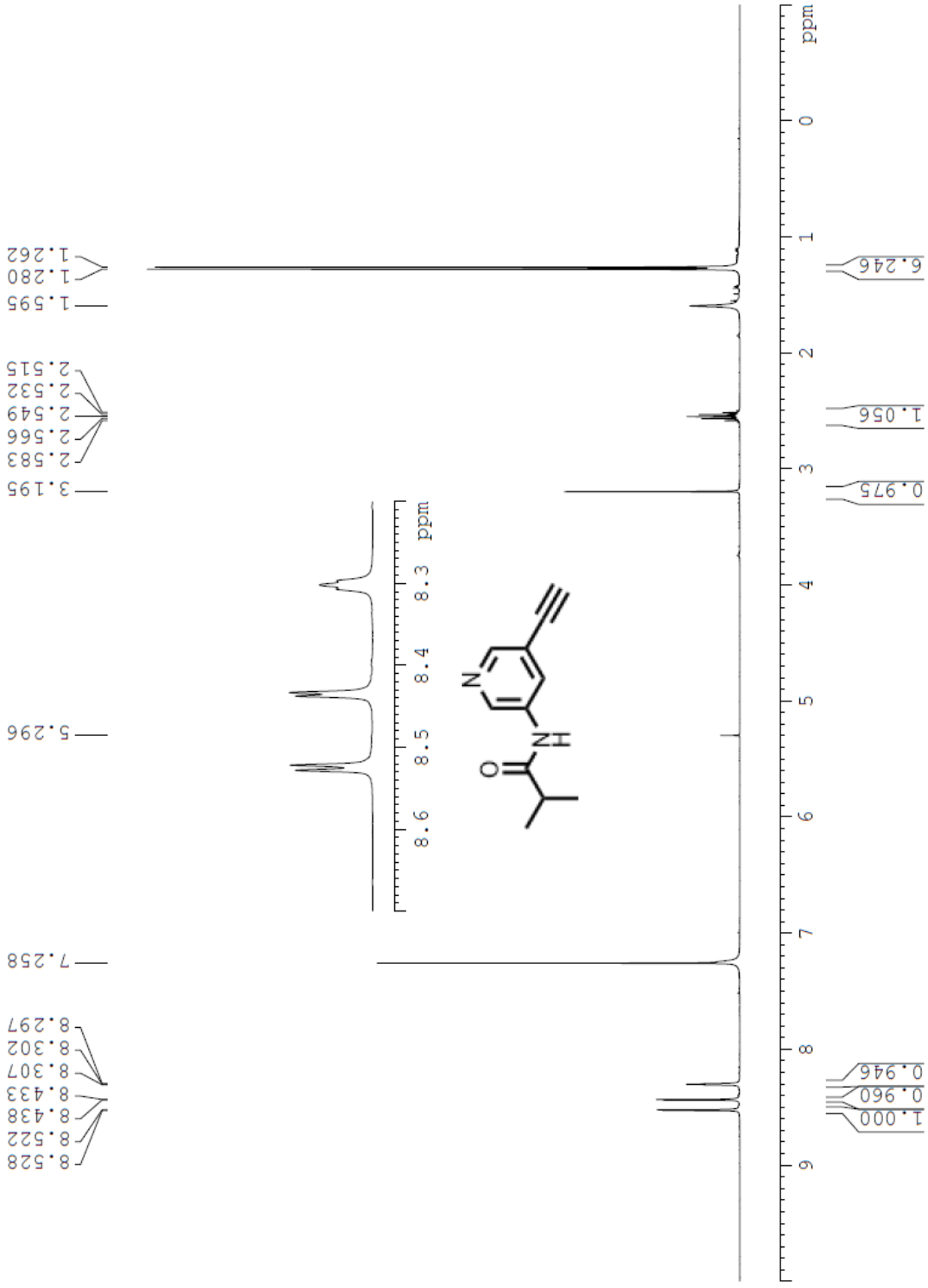

Figure A3. ^{1}H NMR of compound **6a** in $CDCl_3$. (Note: the NH proton is completely missing in the spectrum, in a very unusual occurrence)

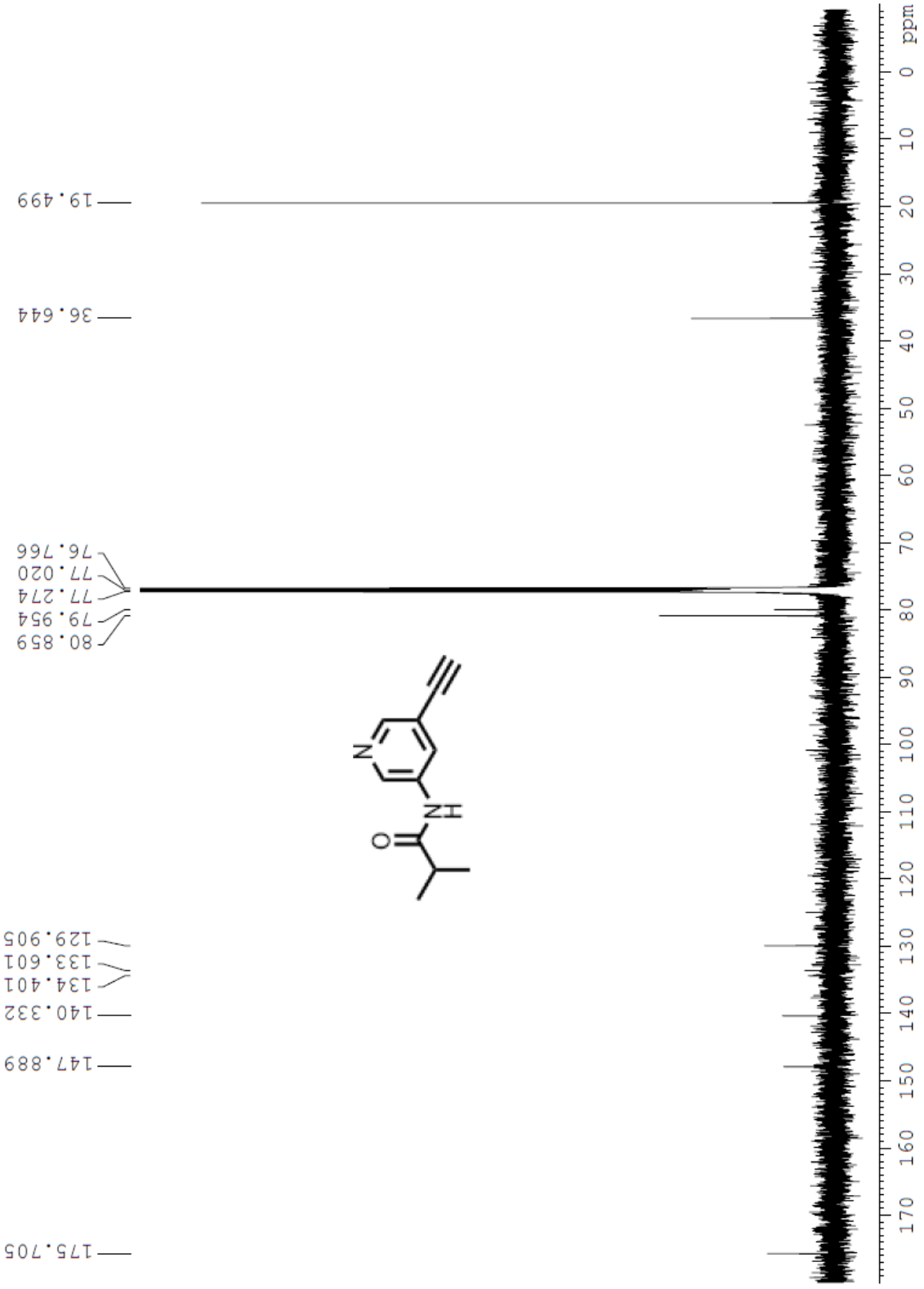

Figure A4. ^{13}C NMR of compound **6a** in $CDCl_3$.

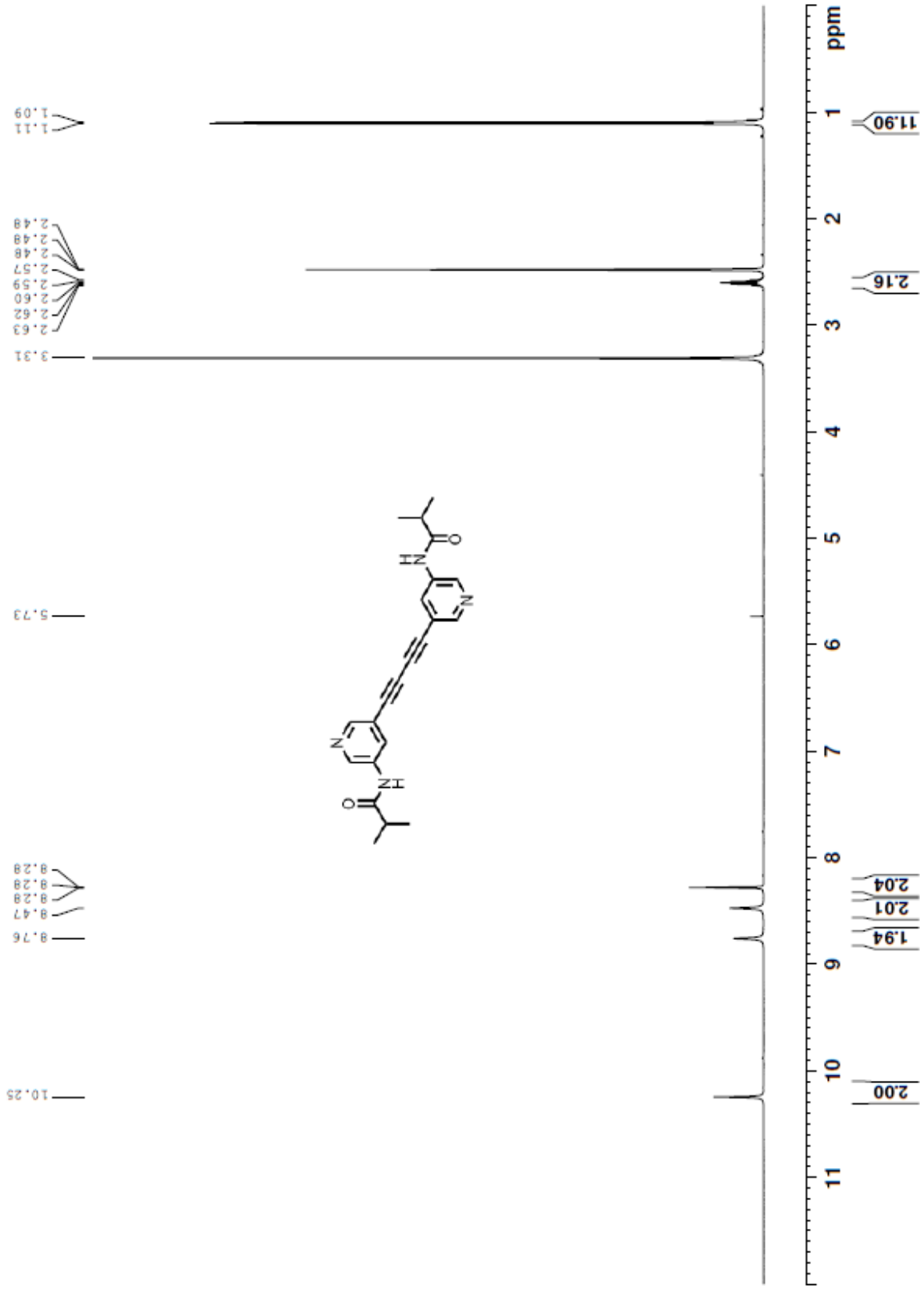

Figure A5. ^{1}H NMR of compound **3a** in d_6-DMSO.

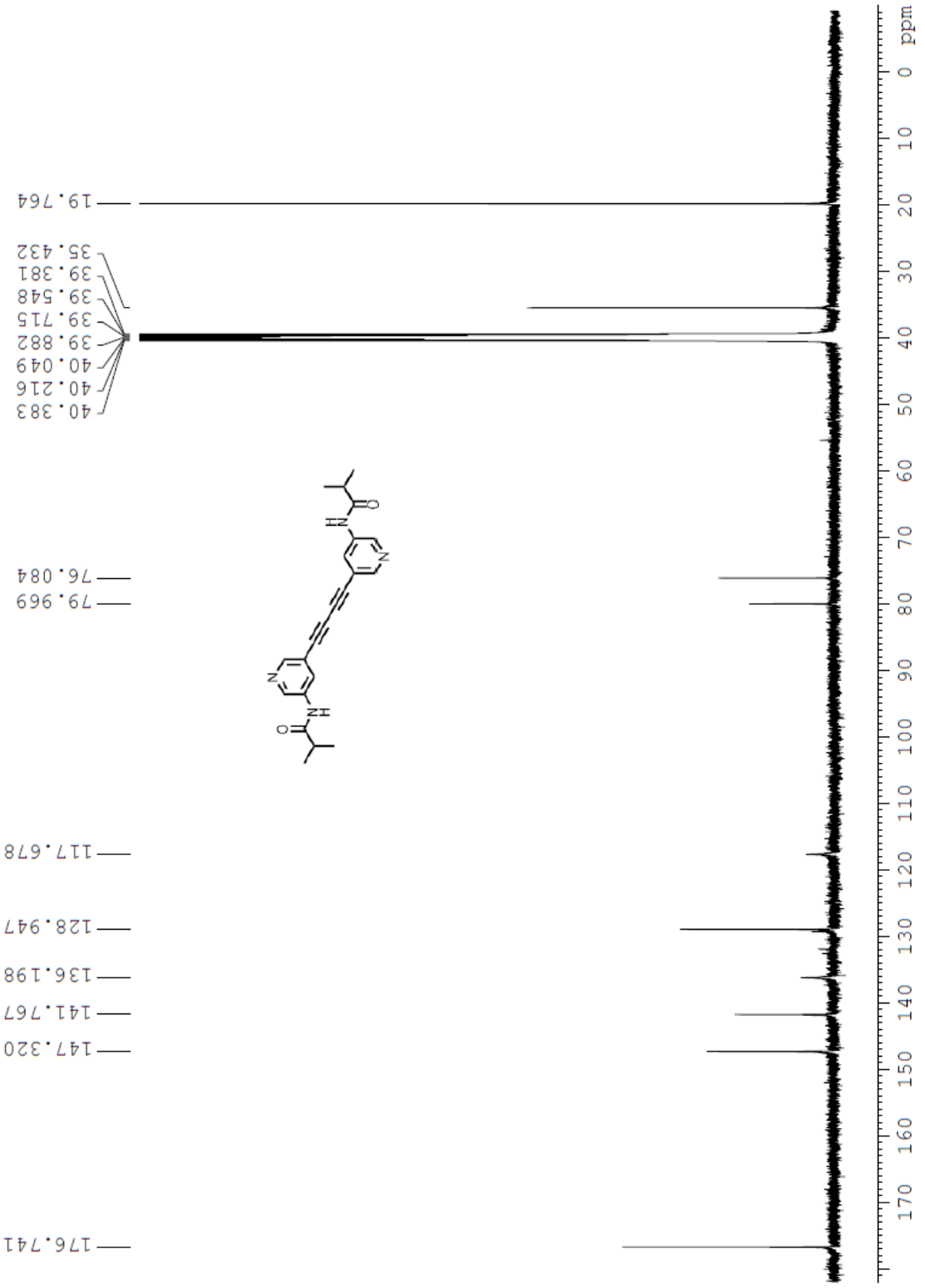

Figure A6. ^{13}C NMR of compound **3a** in d_6-DMSO.

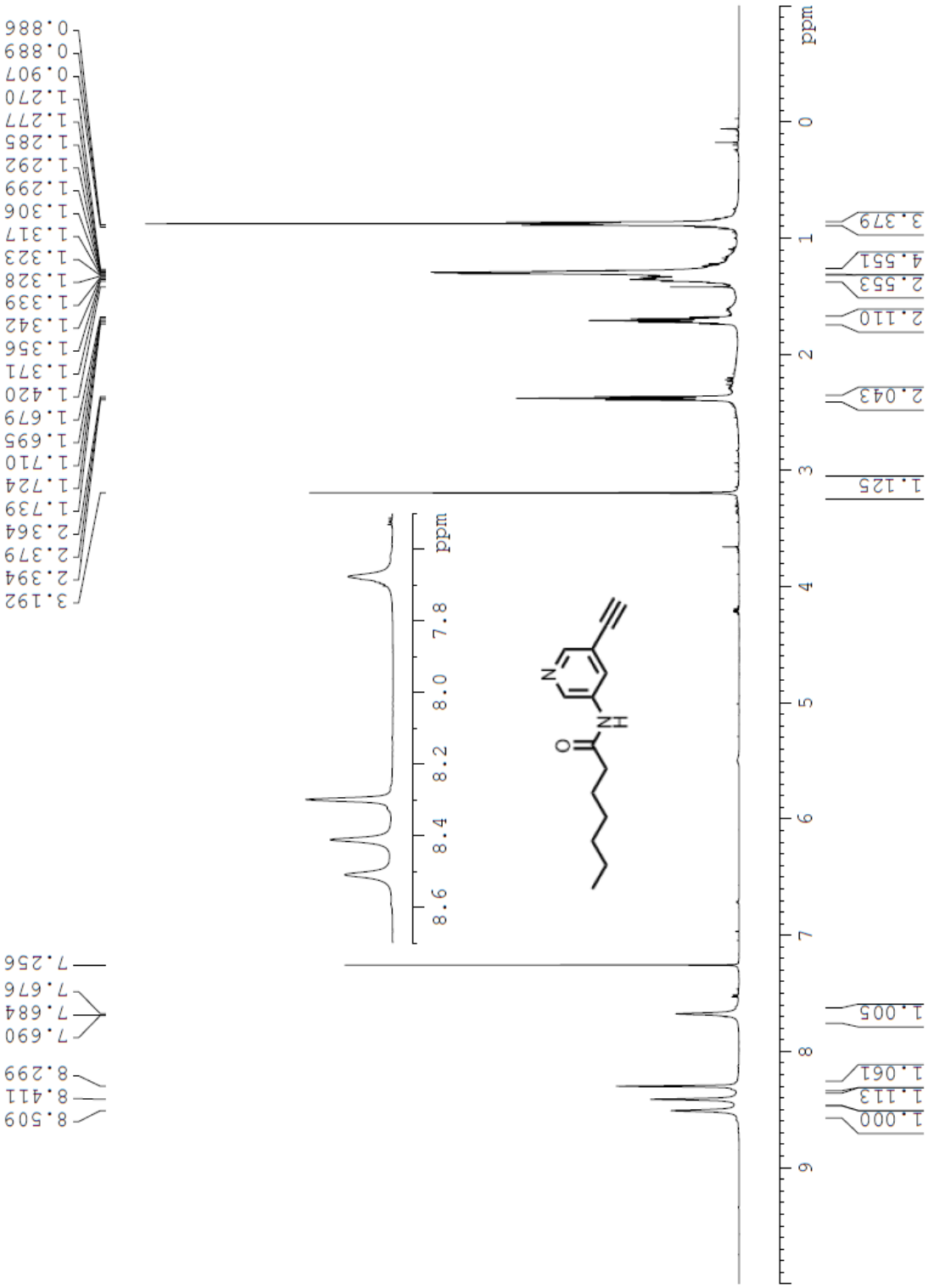

Figure A7. ^{1}H NMR of compound **6b** in $CDCl_3$.

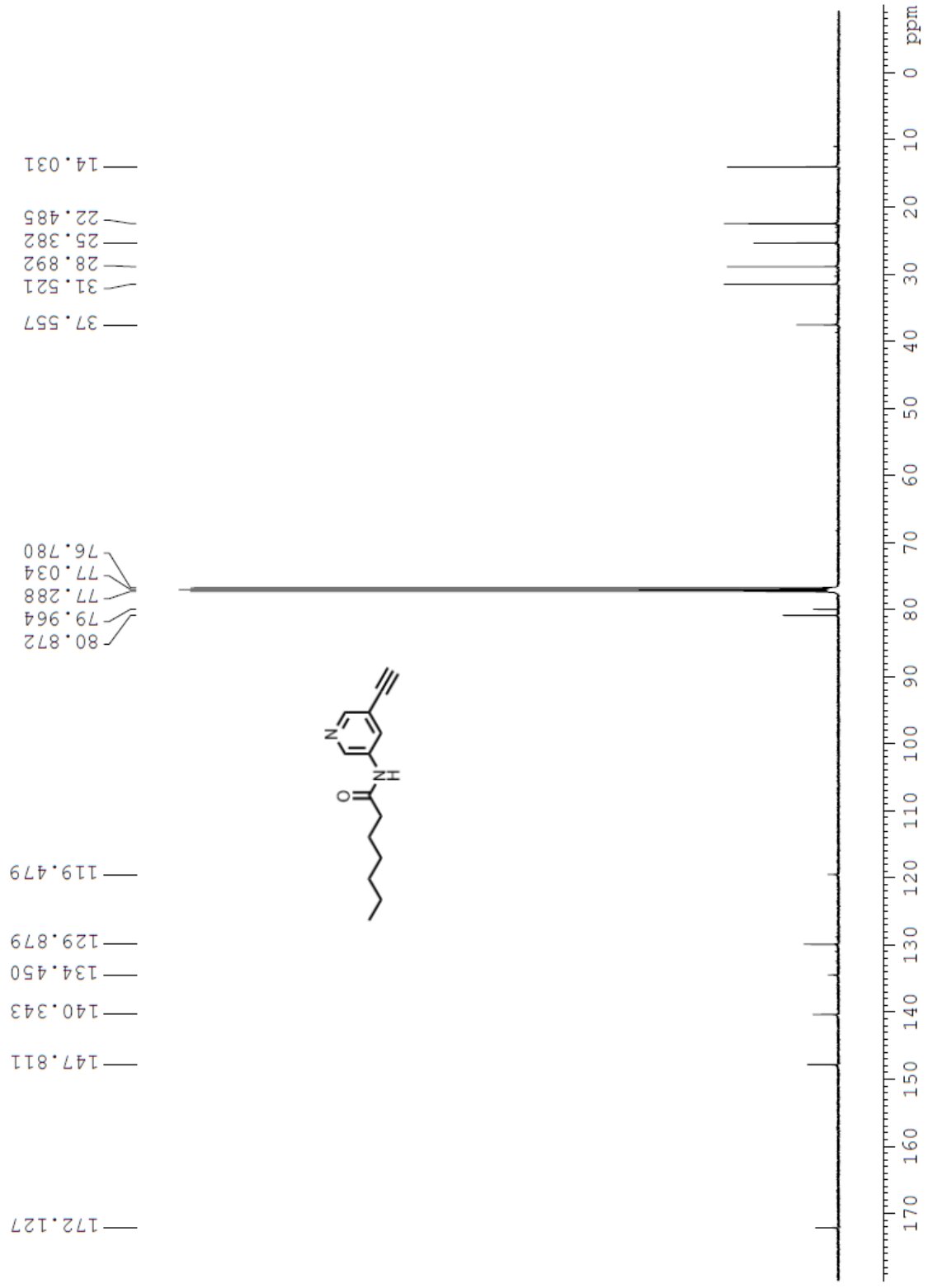

Figure A8. ^{13}C NMR of compound **6b** in $CDCl_3$.

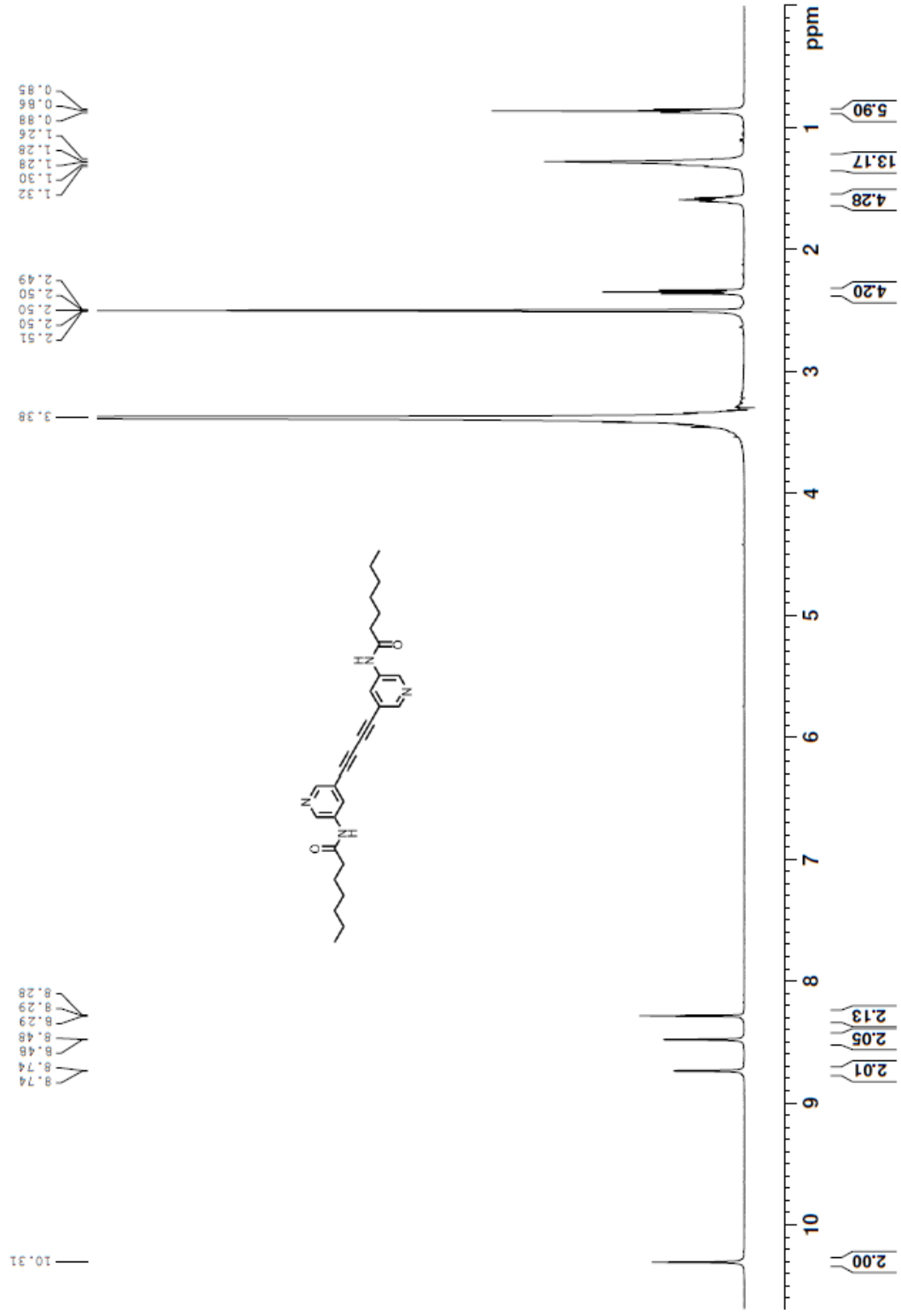

Figure A9. ^{1}H NMR of compound **3b** in d_6-DMSO.

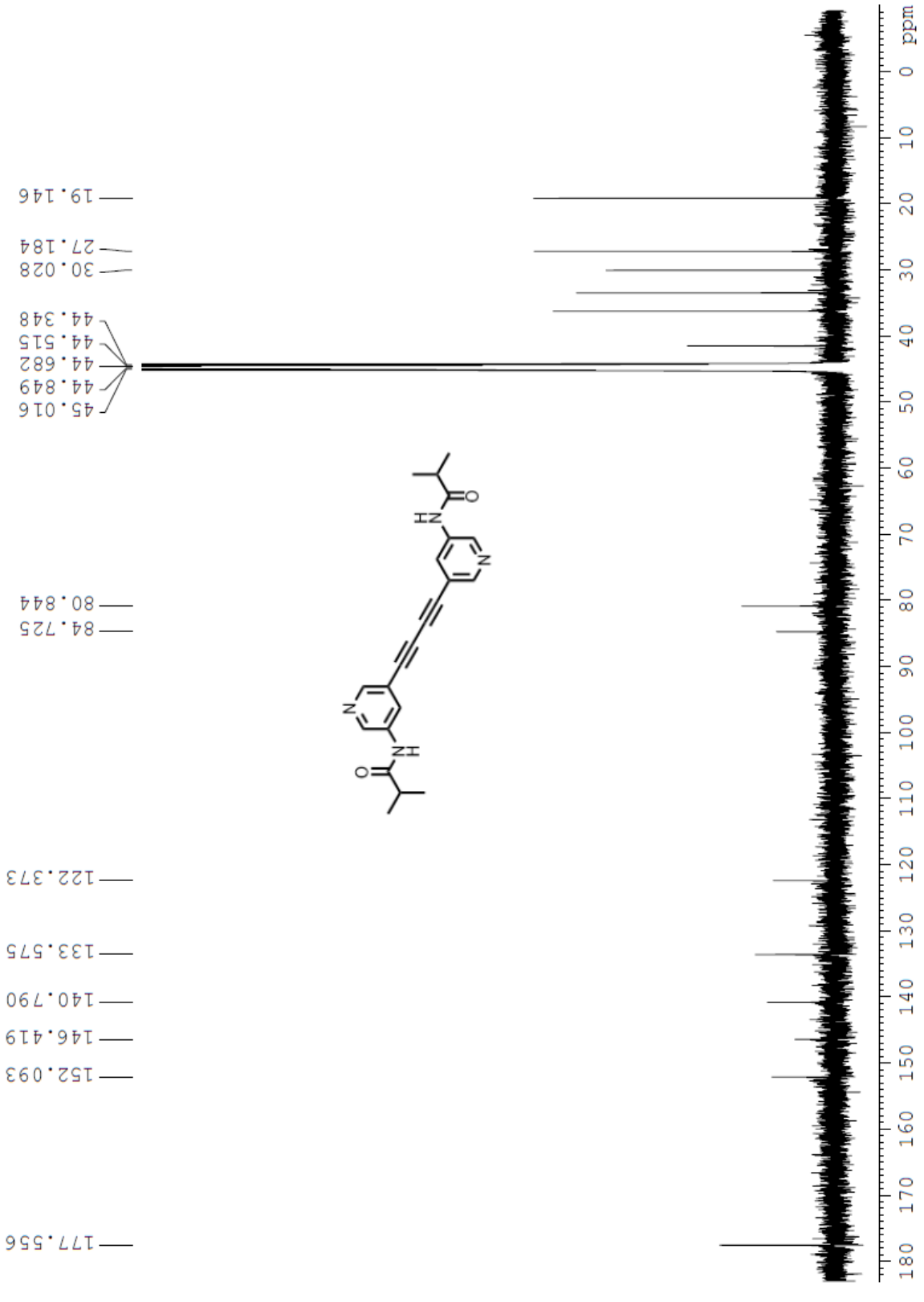

Figure A10. ^{13}C NMR of compound **3b** in d_6-DMSO.

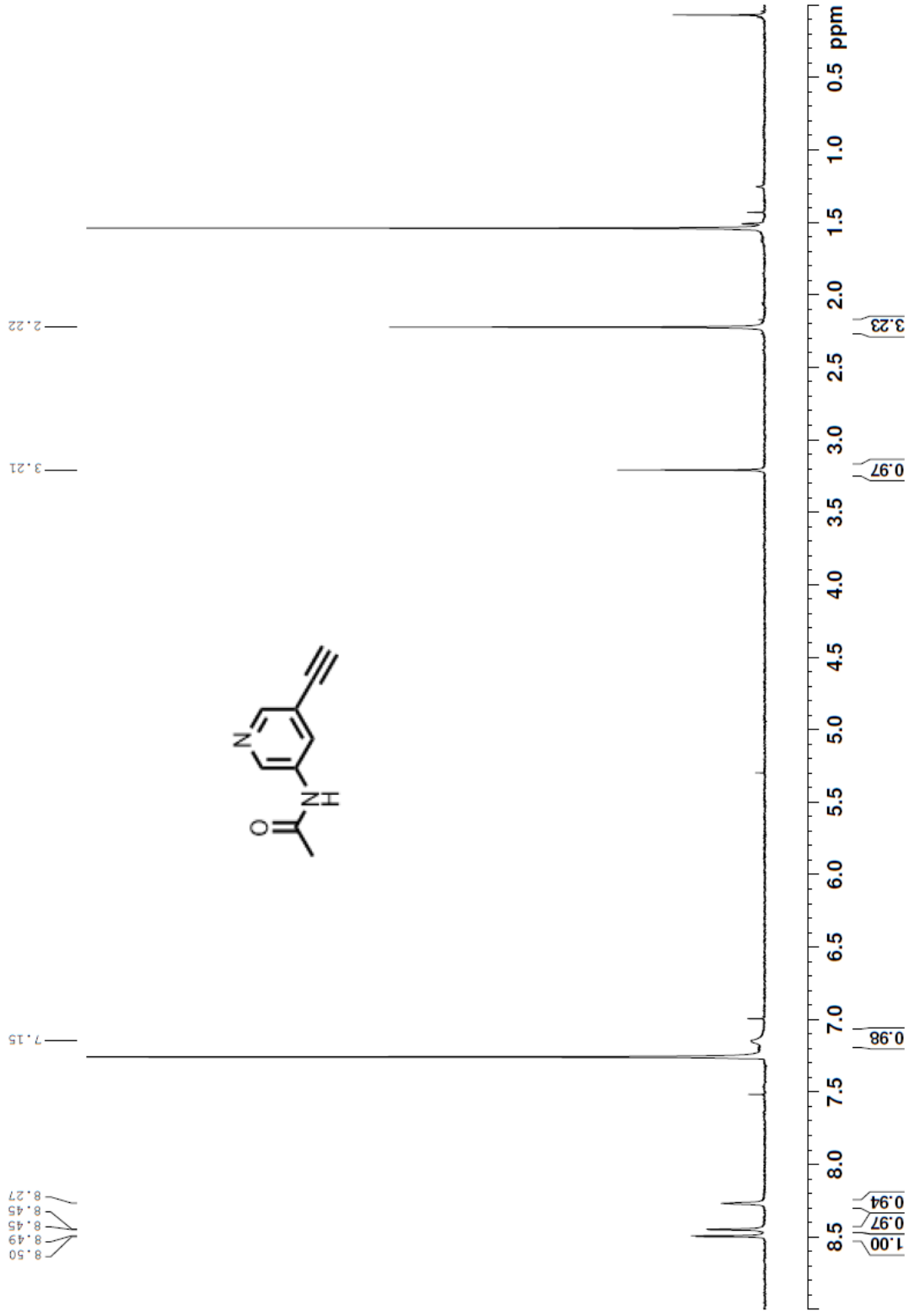

Figure A11. ^{1}H NMR of compound **6c** in $CDCl_3$.

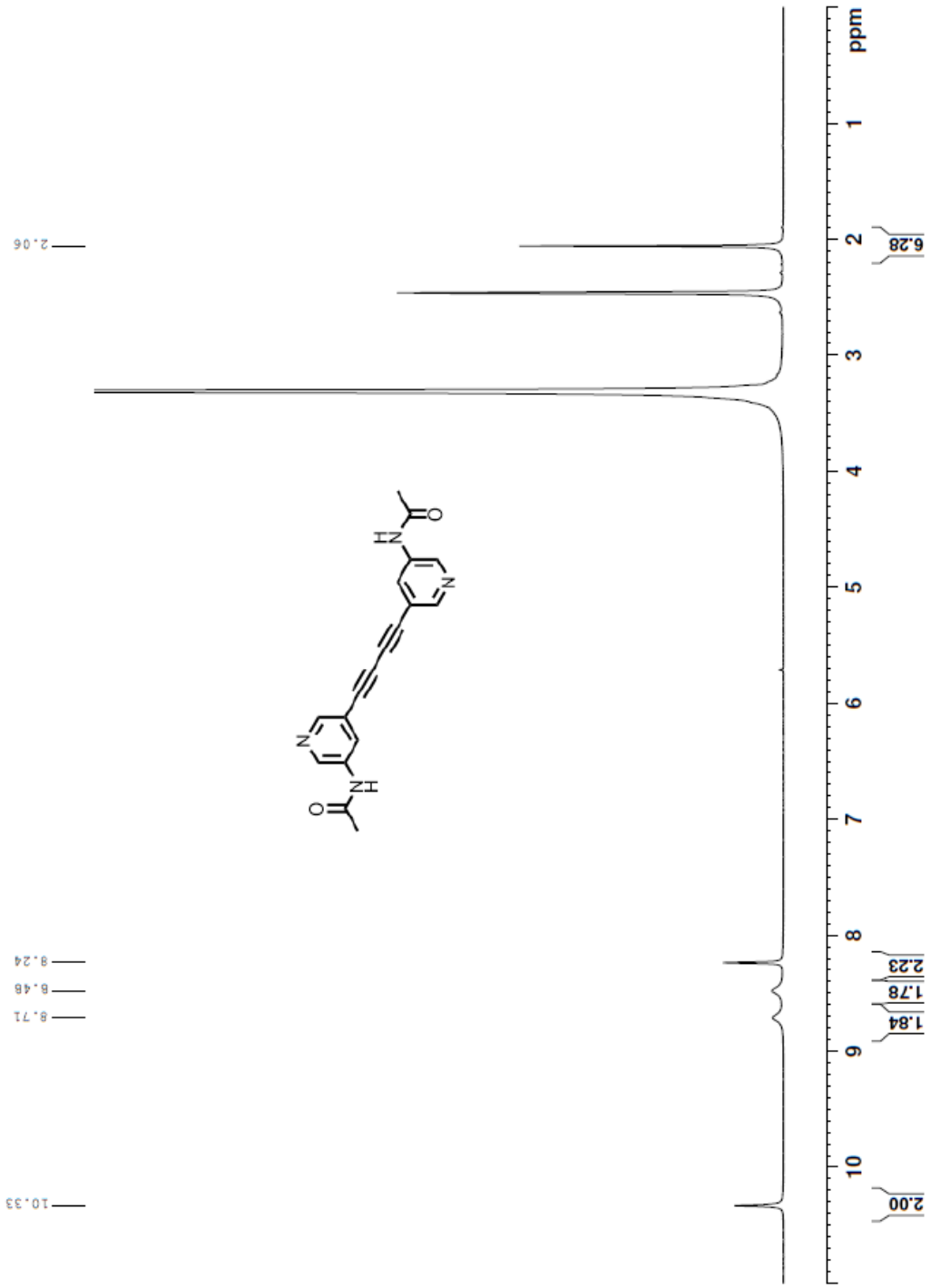

Figure A12. ^{1}H NMR of compound **3c** in d_6-DMSO.

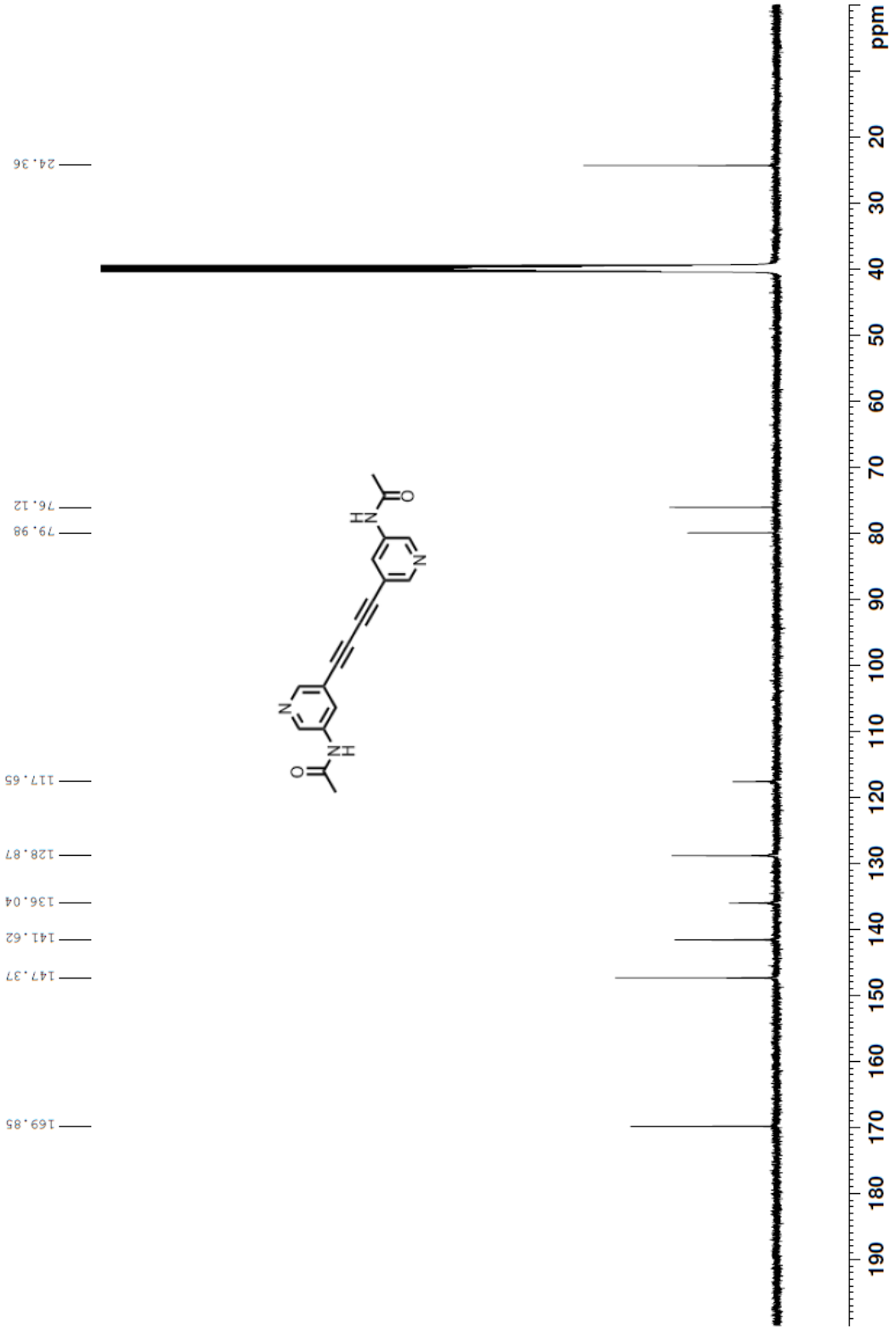

Figure A13. ^{13}C NMR of compound **3c** in d_6-DMSO.

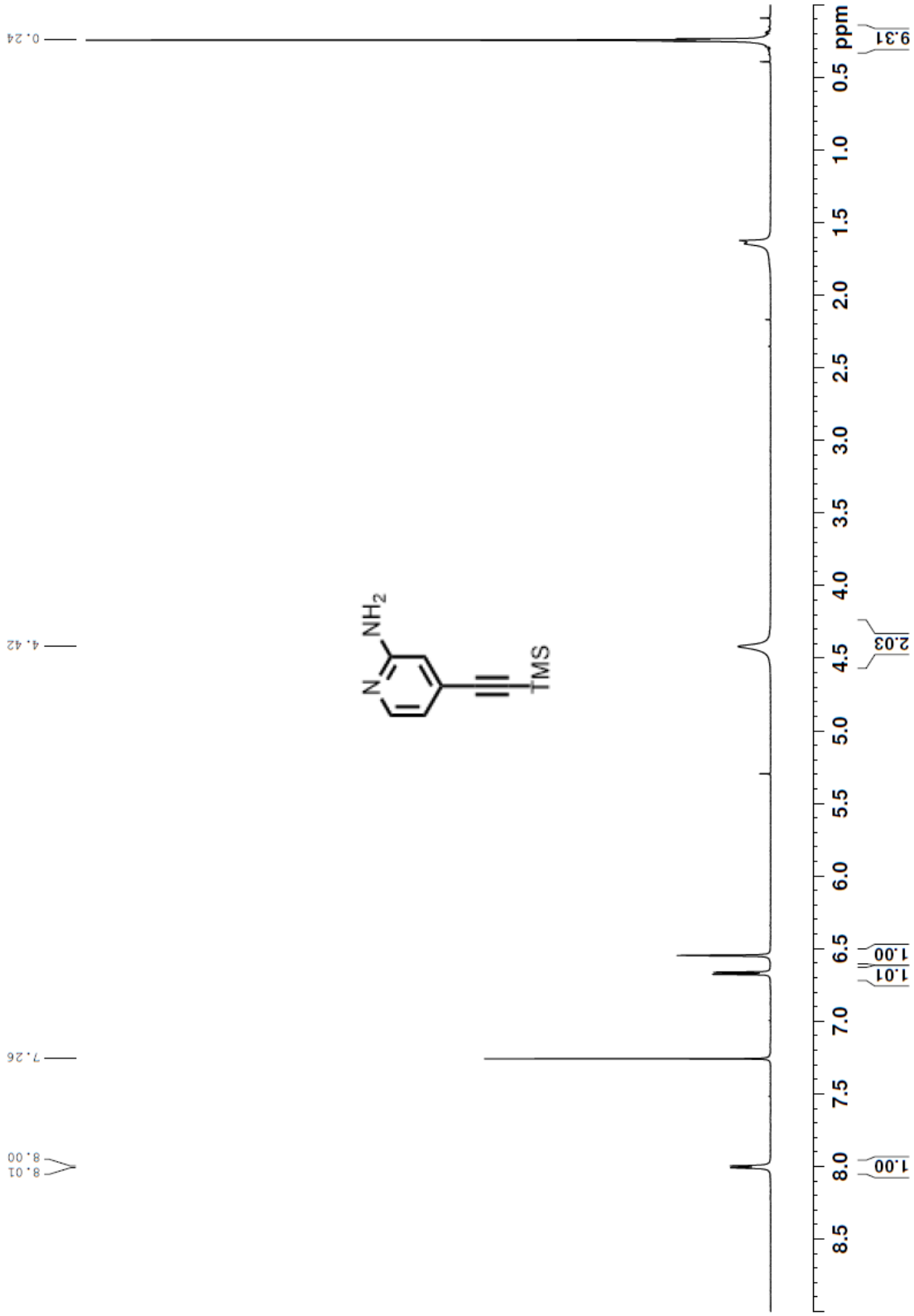

Figure A14. ^{1}H NMR of compound **11** in $CDCl_3$.

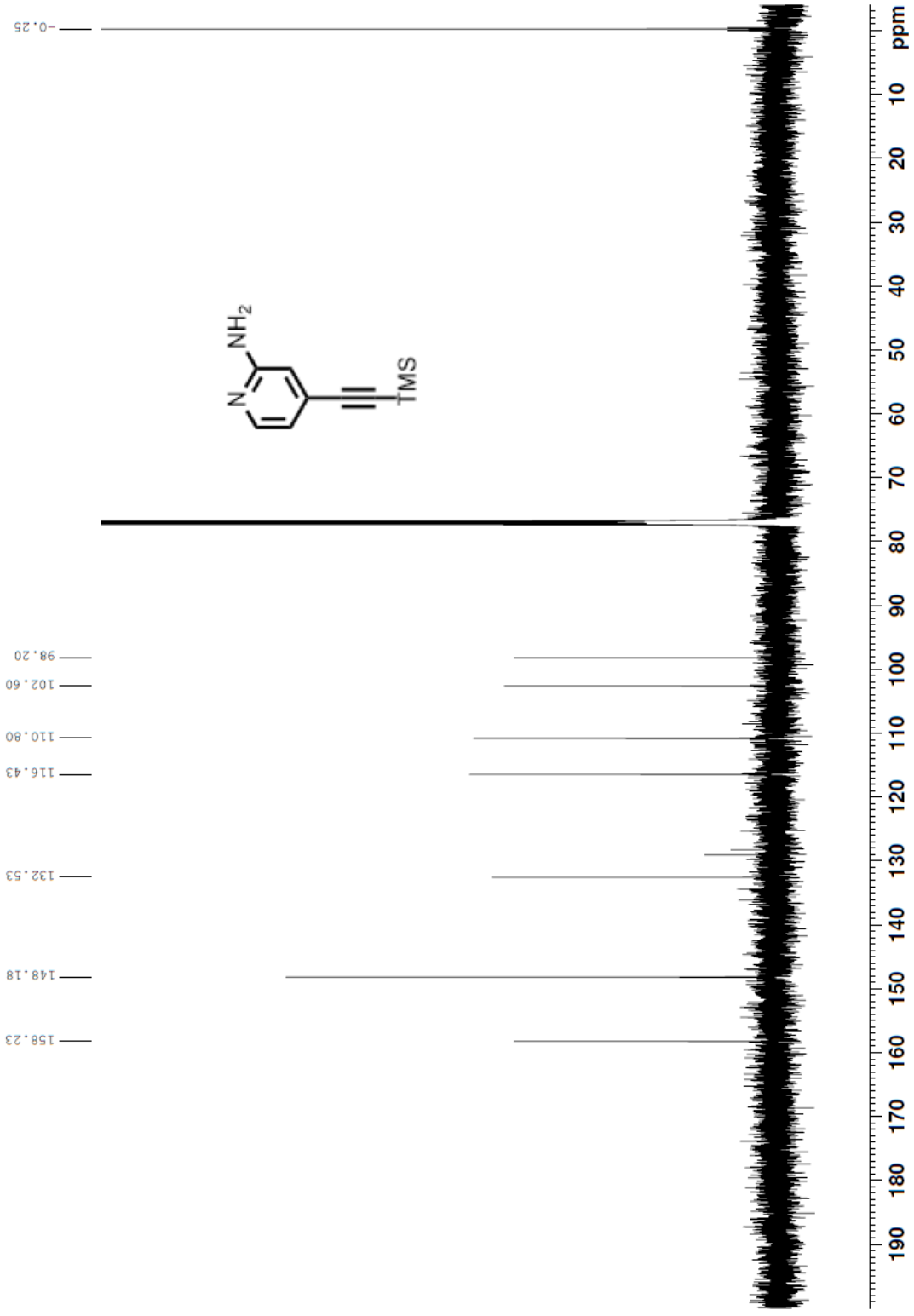

Figure A15. ^{13}C NMR of compound **11** in $CDCl_3$.

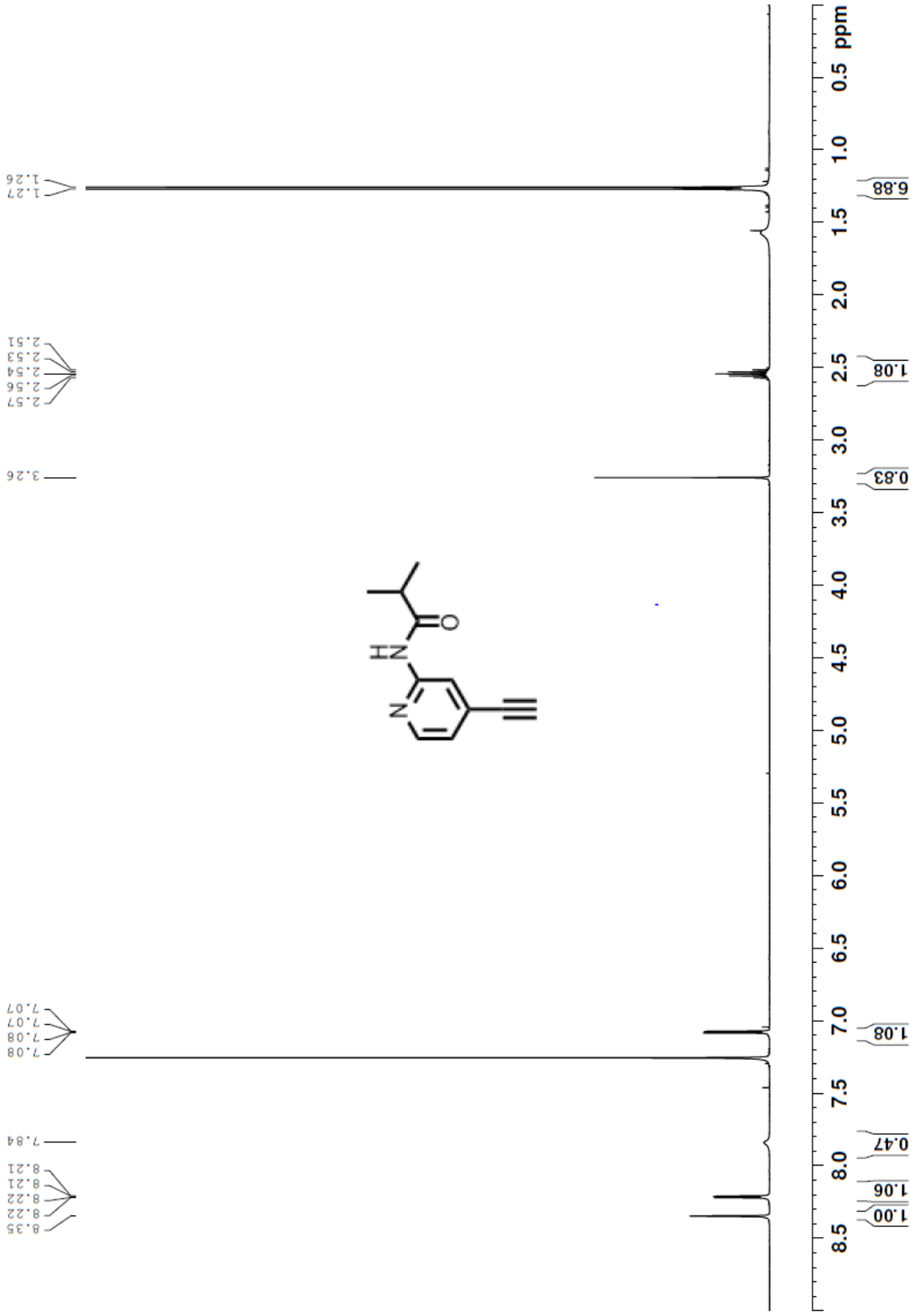

Figure A16. ^{1}H NMR of compound **12** in $CDCl_3$.

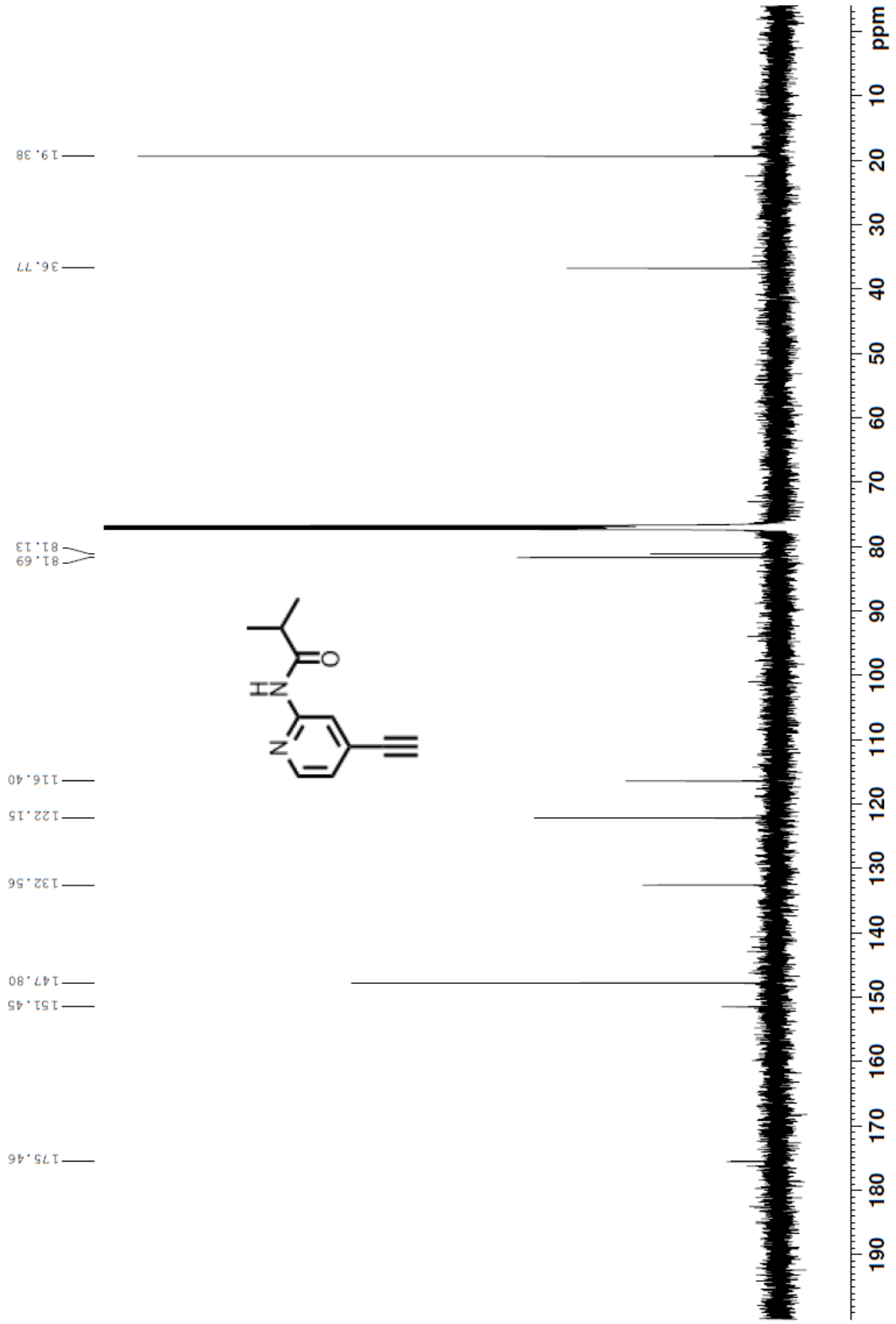

Figure A17. ^{13}C NMR of compound **12** in $CDCl_3$.

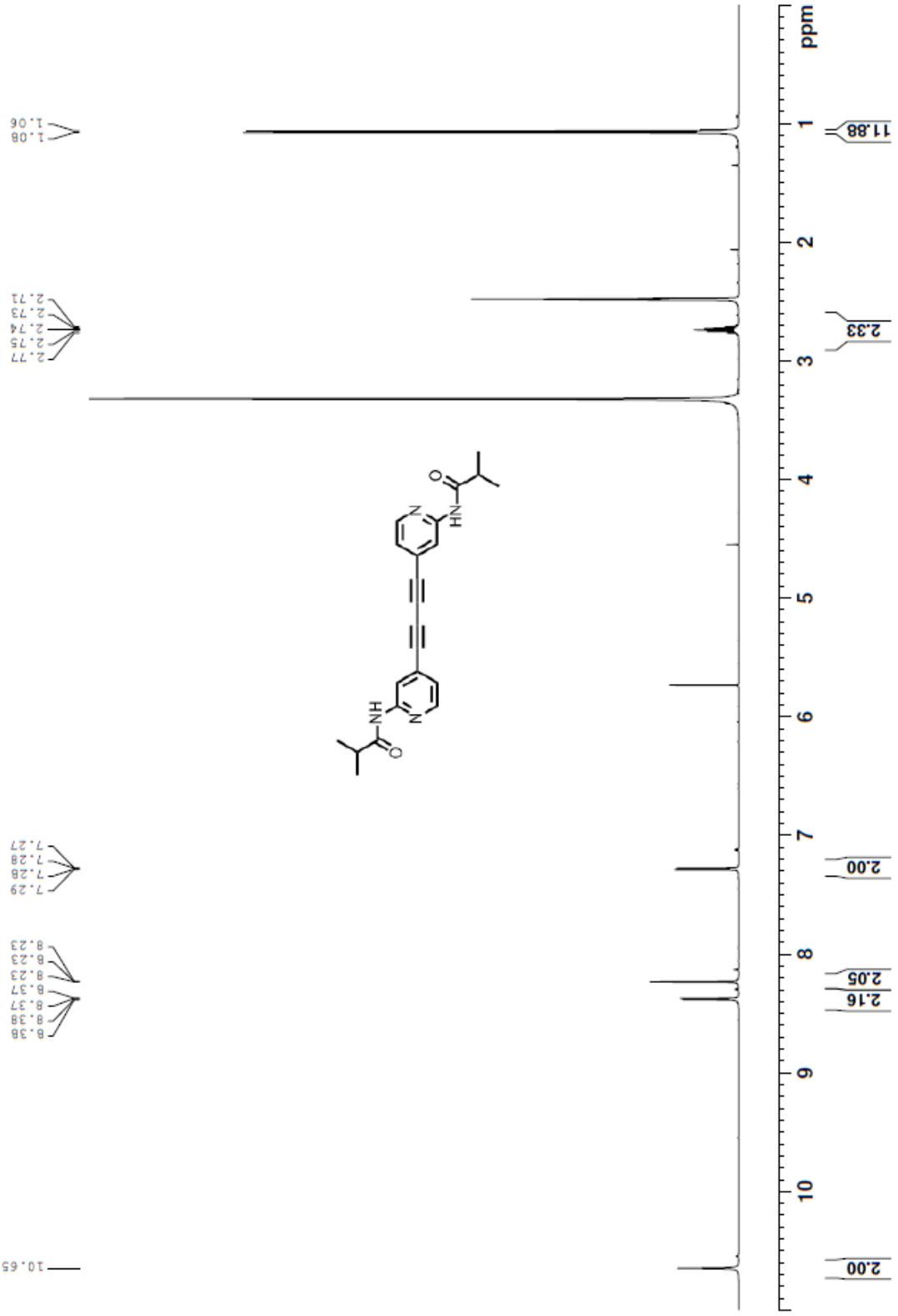

Figure A18. ^{1}H NMR of compound **13** in d_6-DMSO.

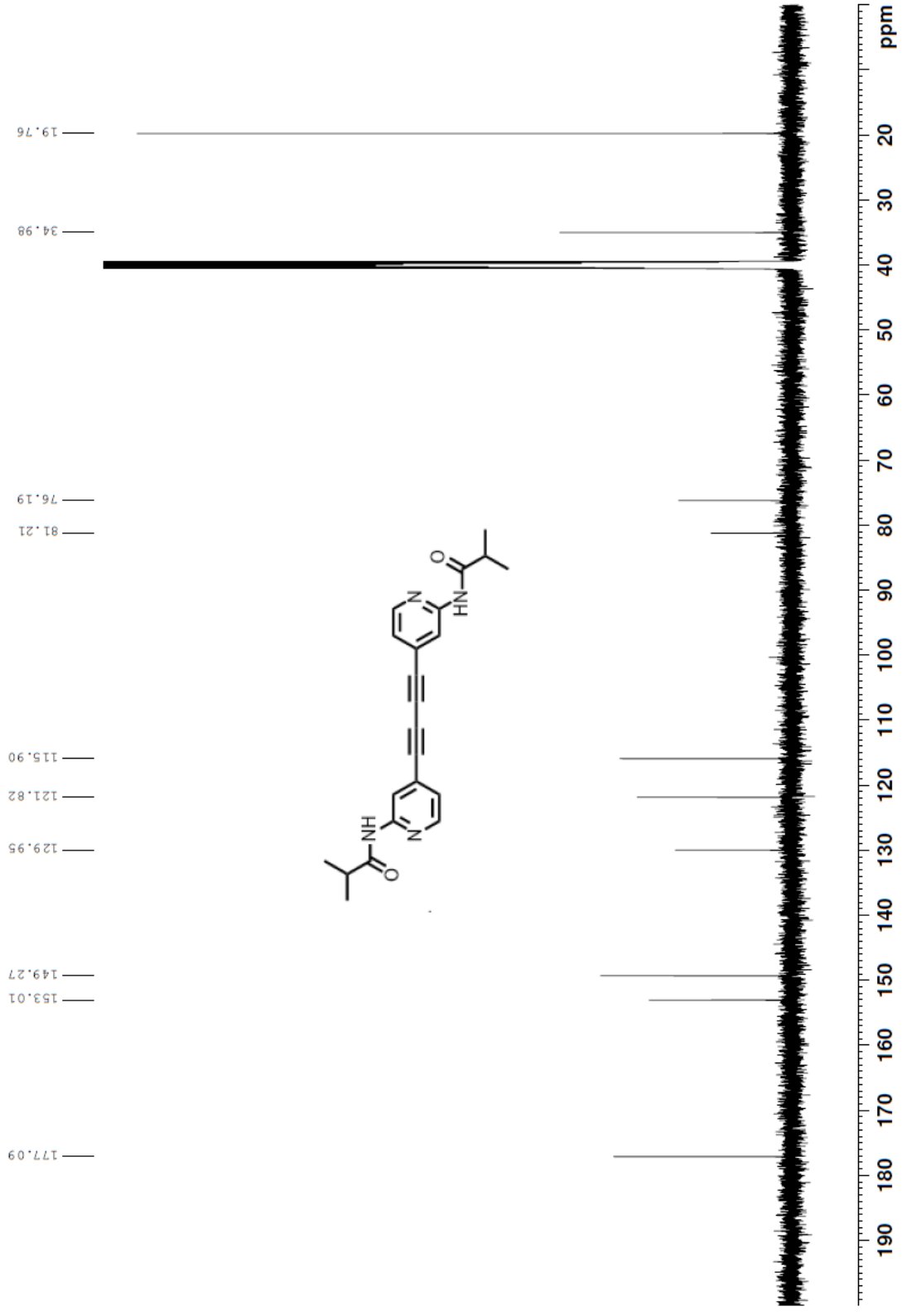

Figure A19. ^{13}C NMR of compound **13** in d_6-DMSO.

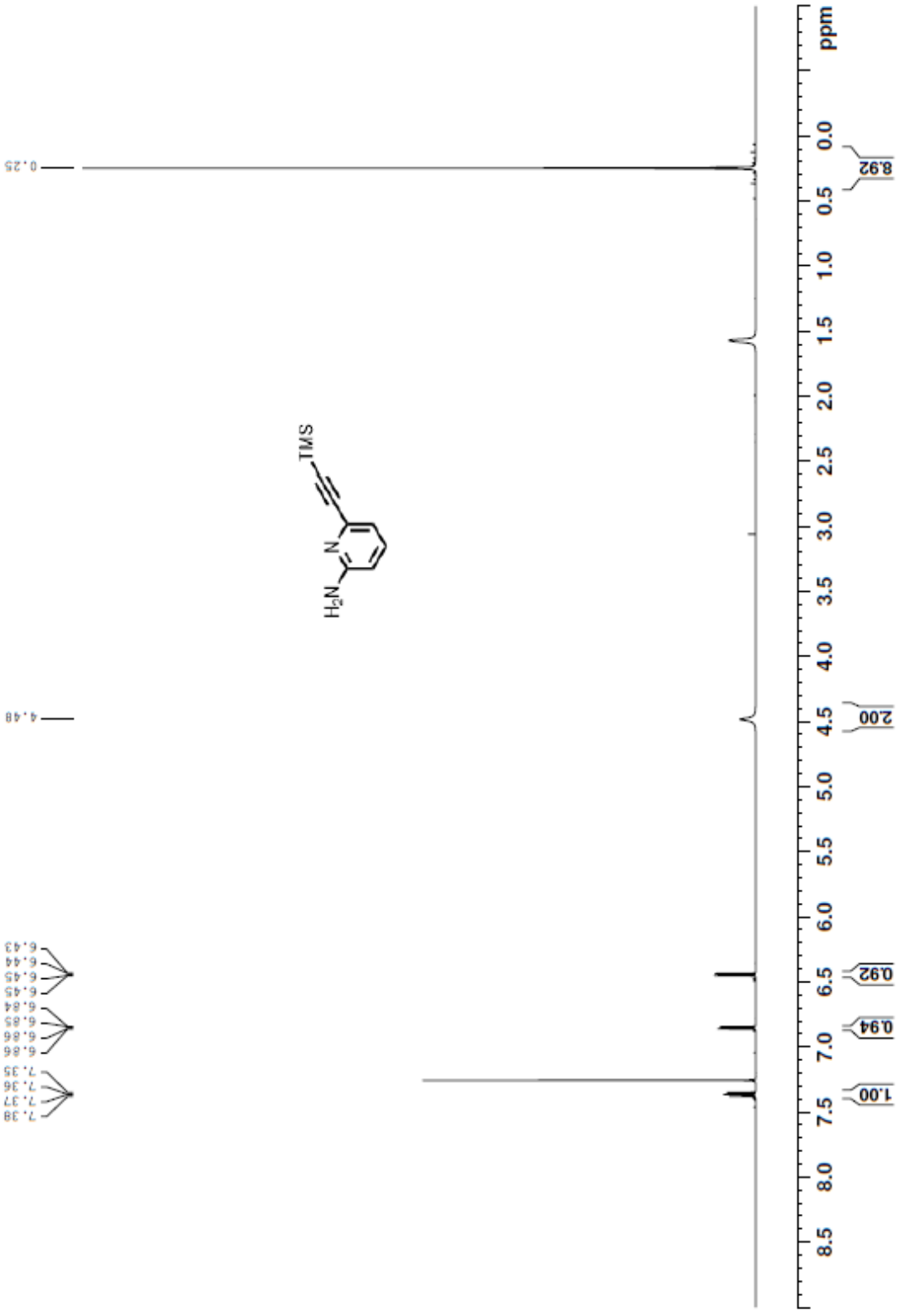

Figure A20. ^{1}H NMR of compound **14** in $CDCl_3$.

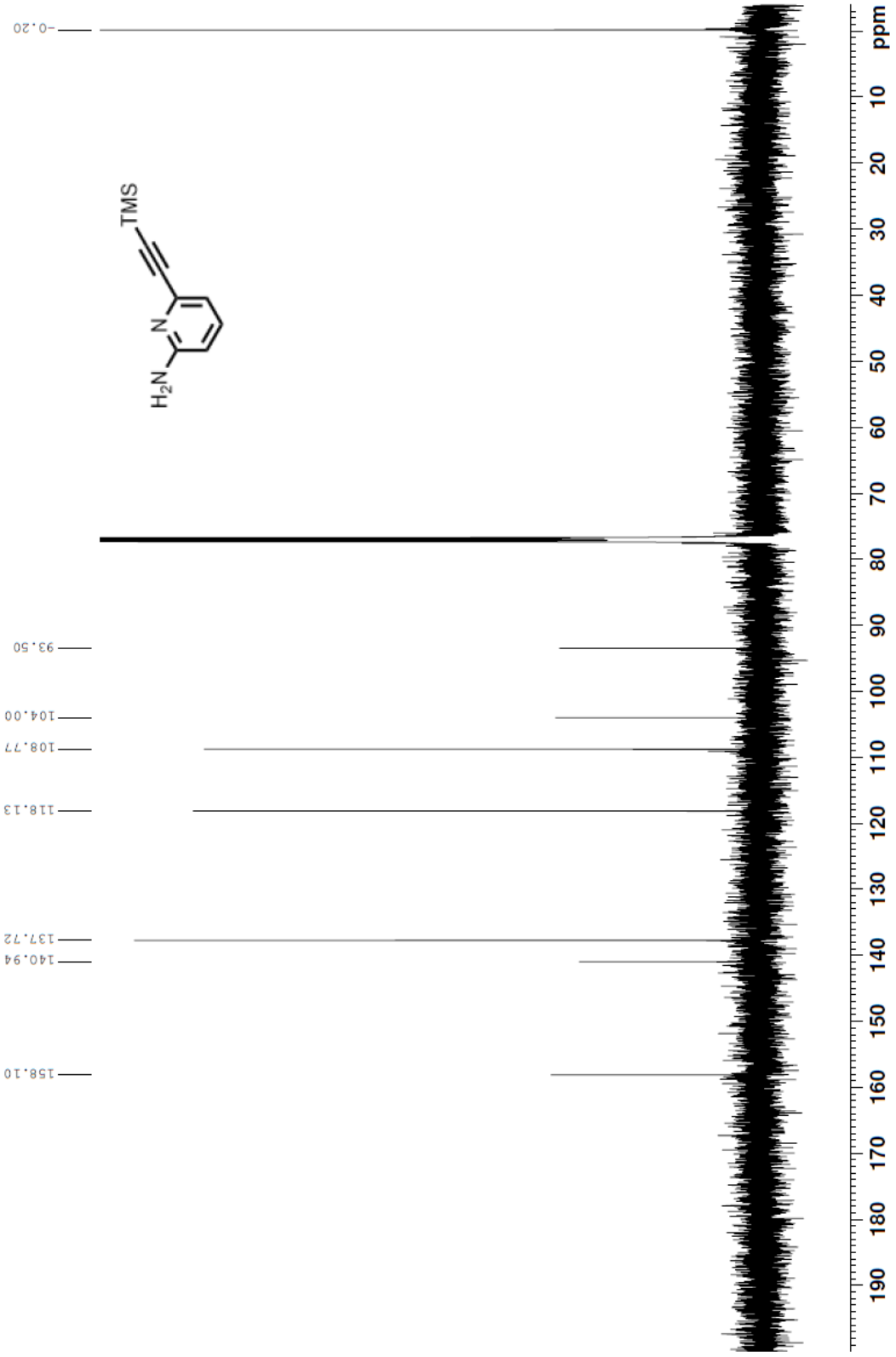

Figure A21. ^{13}C NMR of compound **14** in $CDCl_3$.

Figure A22. ^{1}H NMR of compound **15** in $CDCl_3$.

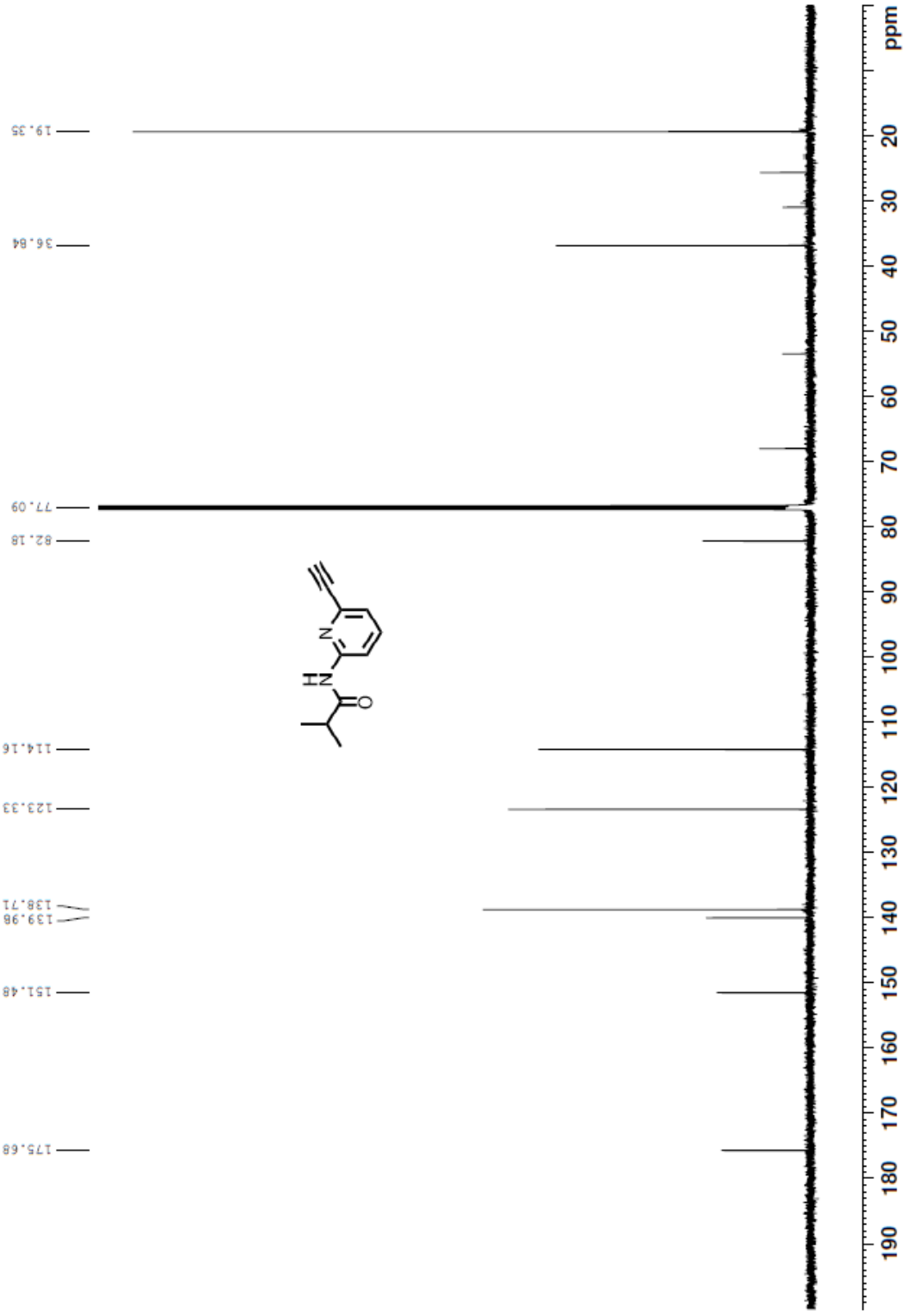

Figure A23. ^{13}C NMR of compound **15** in $CDCl_3$.

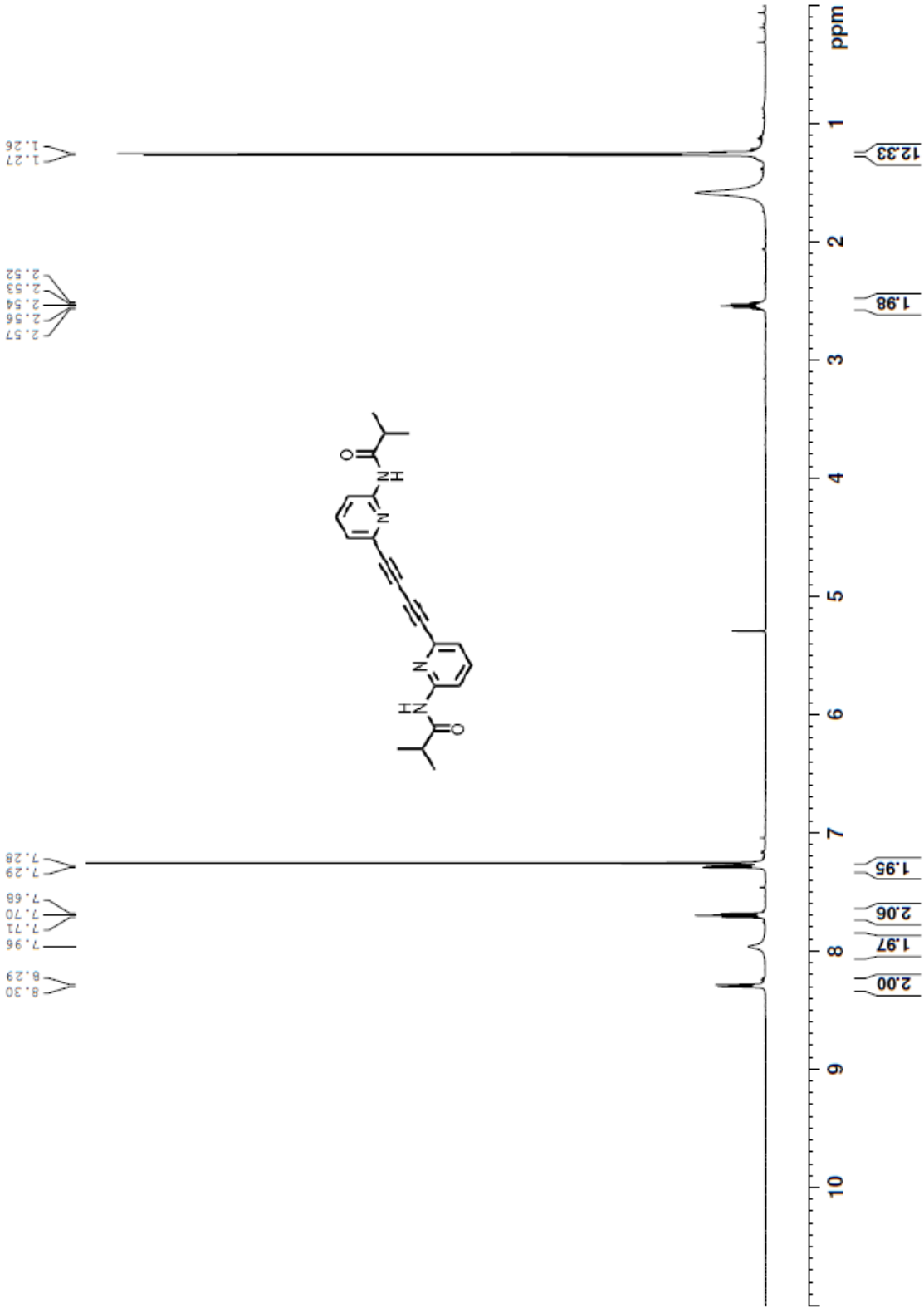

Figure A24. ^{1}H NMR of compound **16** in $CDCl_3$.

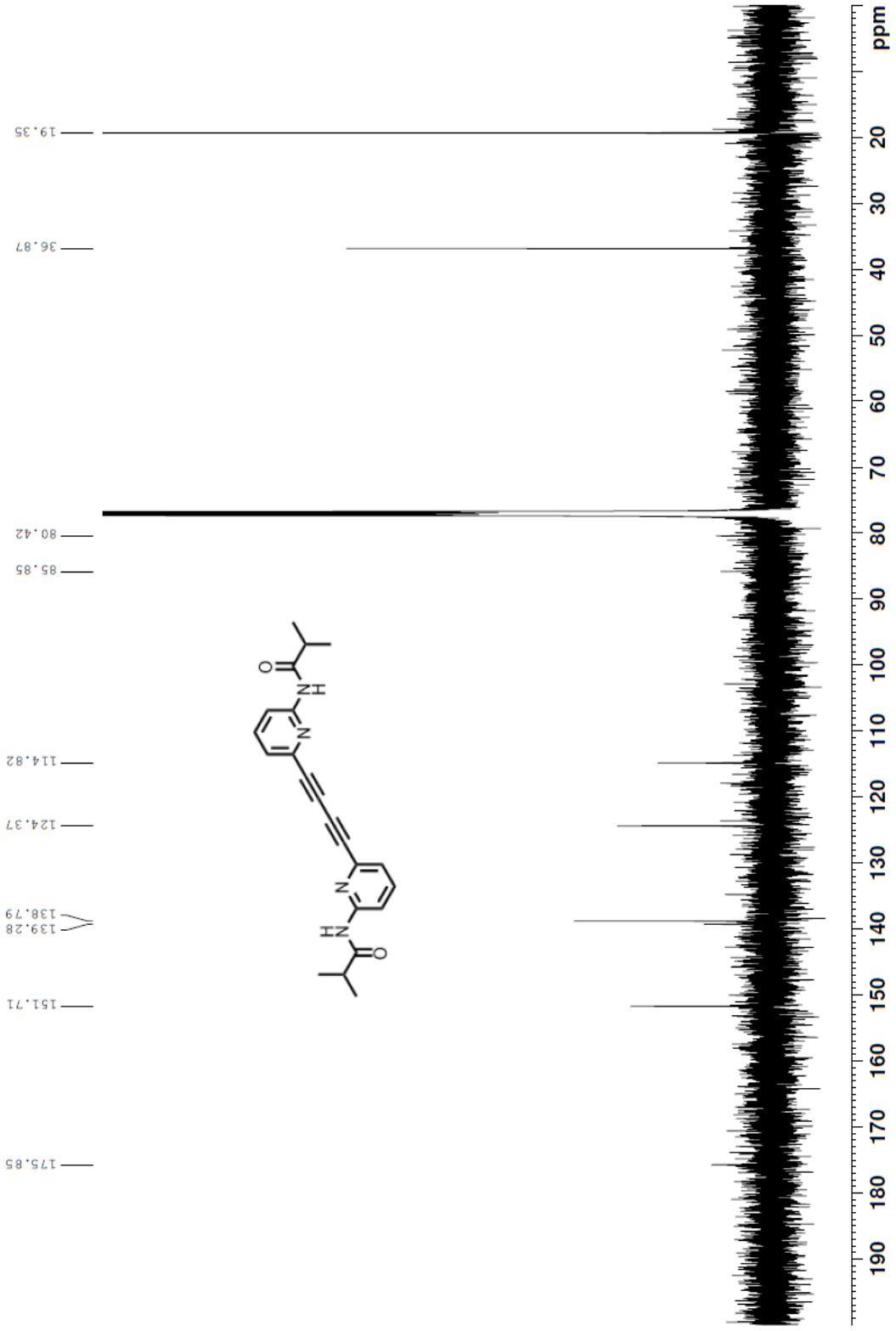

Figure A25. ^{13}C NMR of compound **16** in $CDCl_3$.

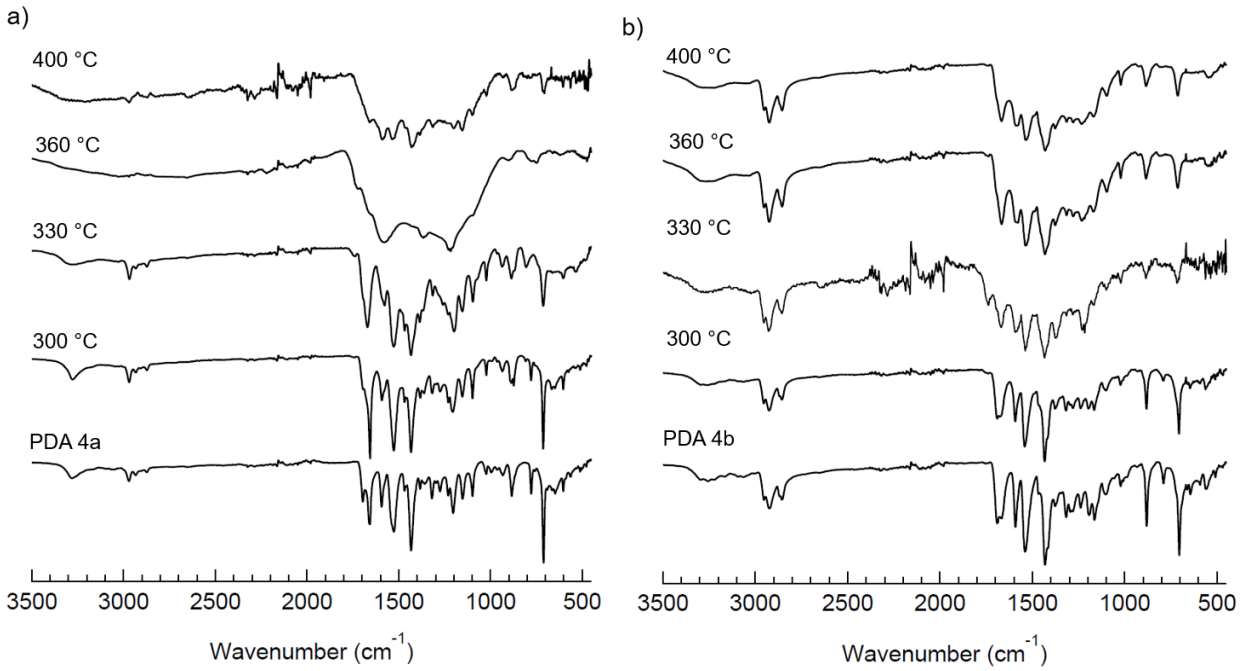

Figure A26. FT-IR Spectra of PDAs **4a,b** and their thermally generated intermediates during their conversion to GNRs **1a,b**.

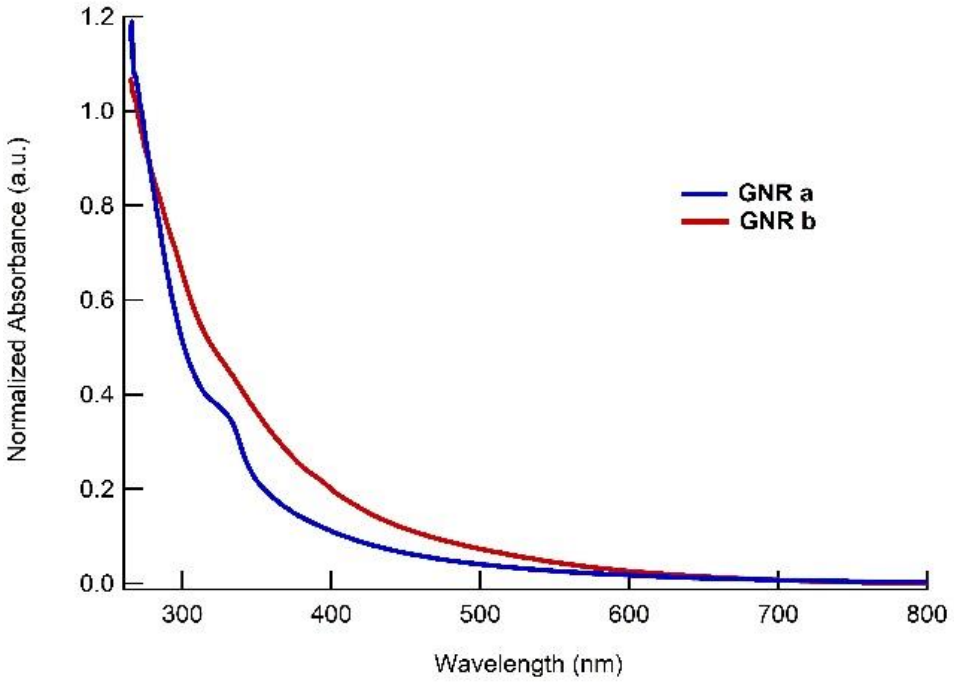

Figure A27. Normalized UV-Vis spectra of GNRs **1a,b** in N-methyl-2-pyrrolidone. 1 mg/mL solutions were sonicated overnight then passed through a 0.2 μm filter.

Crystallography Details

Microfocus X-ray data collection and structure determination

To obtain crystals of appropriate size and order for diffraction, crude product was dissolved in boiling methanol at 1 mg/mL and filtered while hot through packed cotton. The filtrate was sealed in a standard 20-mL scintillation vial and protected from light with aluminum foil. Large crystal clusters formed after about a week (Figure A11a). For extraction, the crystal clusters were transferred to glass 9-well spot plates with fresh methanol constantly added to prevent the crystals from drying. During extraction, crystals were mounted on CryoLoops™ from Hampton Research after dragging them through Parabar 10312 (Paratone®) for cryoprotection and flash-cooled in liquid nitrogen.

Diffraction data were collected under cryogenic conditions (100 K) on beamline 24-ID-C at the Advanced Photon Source (APS) equipped with a Dectris PILATUS 6MF pixel detector array using a 10 μm beam with wavelength 0.775 Å at a detector distance of 150 mm (0.85 Å resolution at detector edge). 720 diffraction images were collected with an oscillation range of 0.5° from a single crystal. 3 image ranges, consisting of 542/720 frames, were indexed and integrated separately by *XDS*[66]. The outputs from *XDS* were sorted and merged in *XSCALE* and yielded *ab initio* solutions using *SHELXD*[67] and *SHELXT*[68]. The atomic positions were refined against measured data using *SHELXLE*[69].

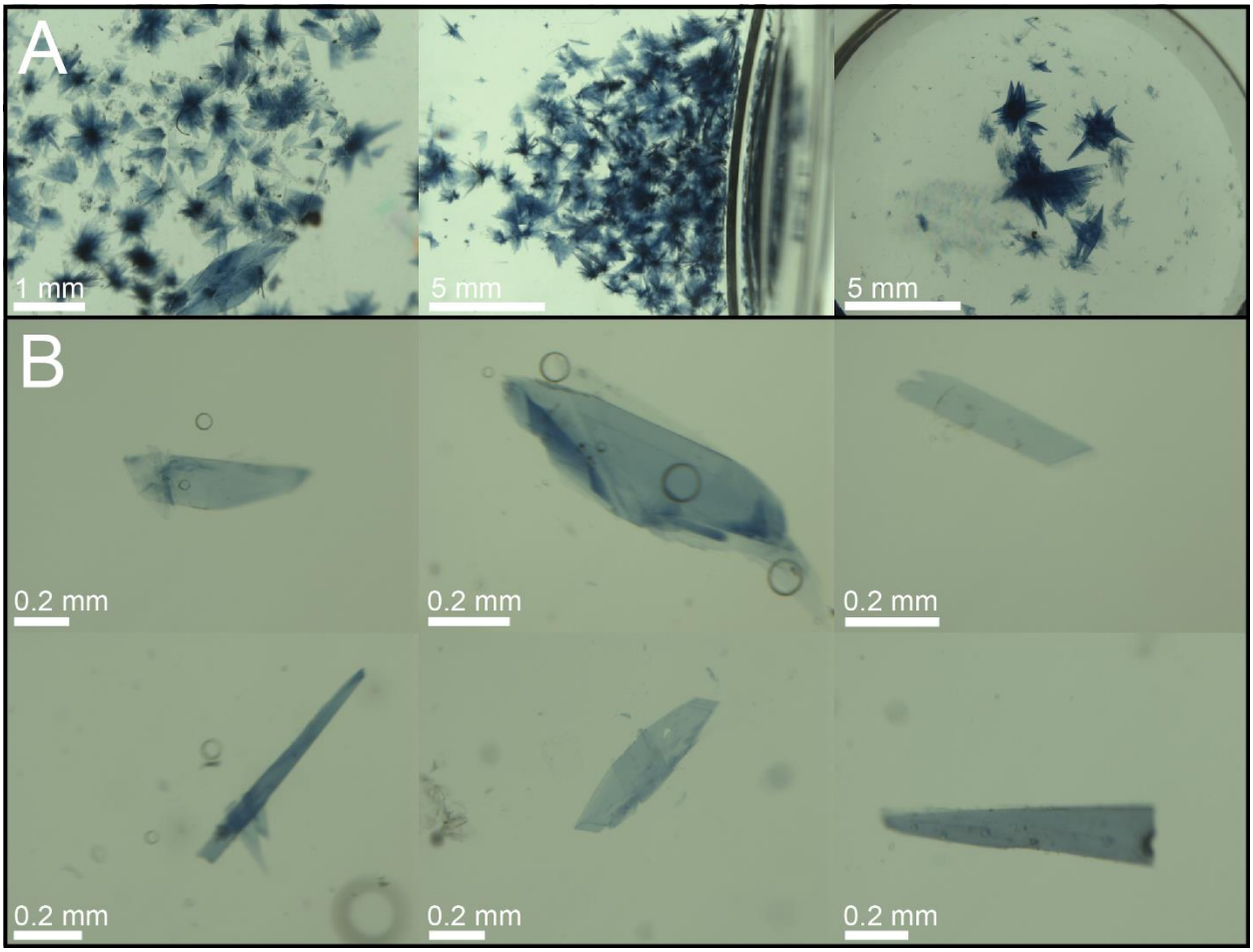

Figure A28. A) Crude compound **3a** was recrystallized in methanol, resulting in large crystal clusters. B) Individual crystals were isolated from the crystal clusters and flash-frozen for microfocus x-ray data collection. The plate-like morphology suggest preferential growth in two unit cell vectors.

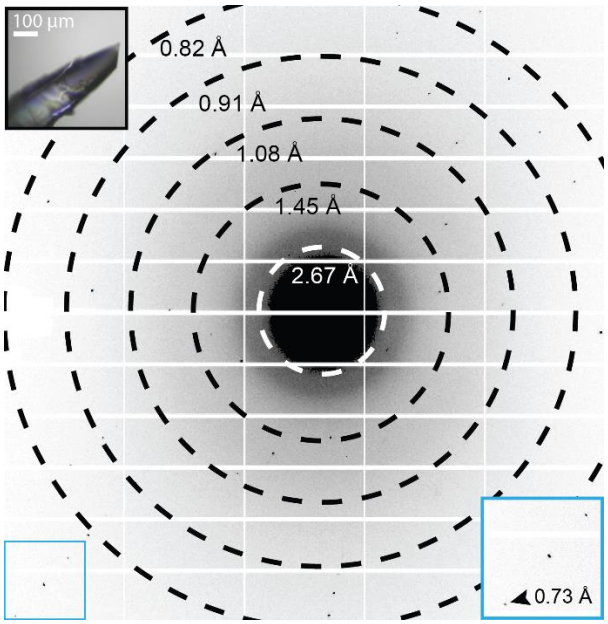

Figure A29. Single crystal diffraction pattern of compound **3a** measured during microfocus x-ray data collection. The pattern corresponds to a 0.5° wedge of reciprocal space. The blue inset on the bottom right shows a magnified image of the boxed region at the bottom left of the diffraction pattern. Diffraction was observed to the corners of the detector. The black inset contains the in-line crystal image with a scale bar corresponding to 100 µm. Resolution circles are indicated by the dotted rings.

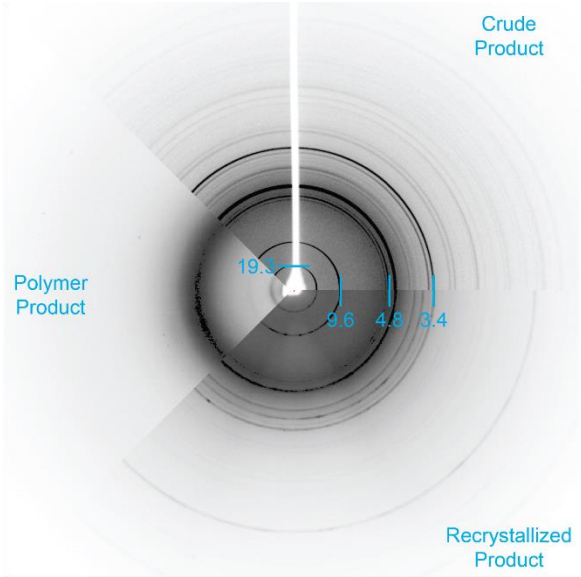

Figure A30. Comparison of powder diffraction patterns of compound **3a**, measured from crude product (top right), recrystallized product (bottom right), and polymer product (left). Powder rings at 4.8 Å, 9.6 Å, and 19.3 Å correspond to unit cell vectors *a* and *c* while rings related to unit cell vector *b* are notably missing, suggesting that the intermolecular interactions in the direction of vector *b* are significantly weaker than those associated to vectors *a* and *c*. In addition to the rings corresponding to the unit cell dimensions, a ring at 3.4 Å reflects arrangement of the diynes into a polymer growth axis.

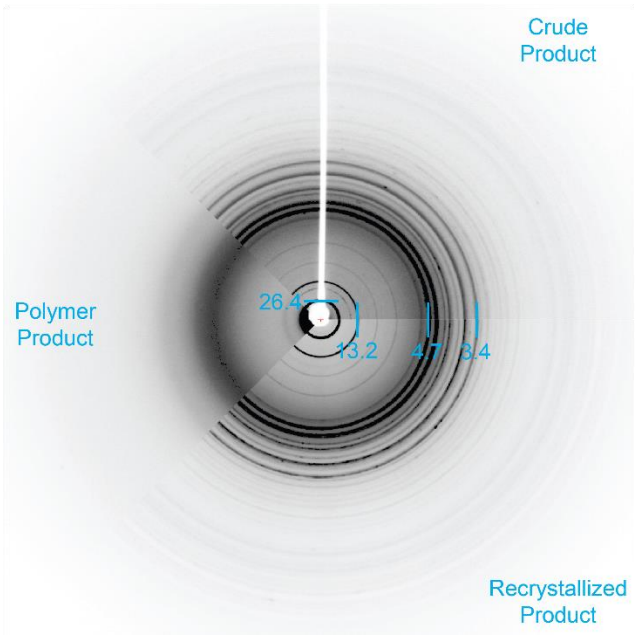

Figure A31. Comparison of powder diffraction patterns of compound **3b**, measured from crude product (top right), recrystallized product (bottom right), and polymer product (left). Strong powder rings at 4.7 Å and 26.4 Å possibly correspond to unit cell vectors. The rings in the lower resolution region are commensurate to the presence of a larger R-group in **2b** compared to **2a**. Furthermore, a ring at 3.4 Å suggests a similar arrangement of diynes into a polymer growth axis seen in **2a**.

Table A1. Crystallographic Data for **3a**.

Data Collection and Processing	
Molecular Formula	$C_{22}H_{22}N_4O_2$
No. of crystals merged	1 (3 wedges)
Space Group	P -1
Cell dimensions	
a, b, c (Å)	4.80 5.29 19.31
α, β, γ (°)	89.882 87.884 76.199
Resolution Limit (Å)	0.85 (0.88-0.85)
Wavelength (Å)	0.77490
Rmerge (%)	3.1 (4.6)
I/σ_I	25.57 (21.32)
Completeness	83.0 (81.7)
$CC_{1/2}$	99.9 (99.5)
No. total reflections	3822 (478)
No. unique reflections	1356 (165)
Multiplicity	2.82 (2.90)
Refinement	
Resolution (A)	0.85
No. of Reflections	1356
R1 (%)	4.58
wR2 (%)	13.14
GooF (Restrained GooF)	1.087 (1.087)

Computational Details

Computational Methods

All geometries were fully optimized at the B3LYP/6-31G(d) level of theory in the gas phase.[70-73] All optimized geometries were verified by frequency computations as minima (no imaginary frequencies) or transition structures (one imaginary frequency). Frequency analysis was performed at 298.15 K. Free energy corrections were calculated using Truhlar's quasiharmonic approximation, which sets all the real vibrational frequencies that are lower than 100 cm^{-1} to 100 cm^{-1} to correct entropies for the breakdown of the harmonic oscillator approximation.[74,75] Subsequent single-point energy calculations on the optimized structures were performed using the M06-2X/6-311+G(d,p) level of theory.[76] The thermal corrections calculated from vibrational frequencies at the B3LYP/6-31G(d) level on the optimized geometries were then added to the M06-2X/6-311+G(d,p) electronic energies to obtain the Gibbs free energies. All quantum chemical computations were performed using Gaussian 09.[77] All graphics on optimized structures were generated with CYLview.[78]

Conformational searches were carried out with *MacroModel* from *Schrödinger* using OPLS_2005 and an energy window of 10.0 kcal mol^{-1}.[79] A redundant conformer elimination was performed using an energy window of 10.0 kcal mol^{-1} and a maximum atom deviation cutoff of 0.5 Å. The lowest energy conformers were optimized with B3LYP/6-31G(d) to locate the global minimum for each reaction.

XYZ Geometries

Substituted model system

7

C	-3.85523	-2.54708	-0.66947
C	-3.89940	-1.26503	-0.10302
C	-2.69048	-0.61468	0.16611
C	-1.57334	-2.55580	-0.70740
C	-0.14679	-0.66674	0.09873
C	0.14686	0.66670	-0.09904
C	1.49099	1.26511	0.15479
C	0.83569	-1.58997	0.56037
C	1.62780	-2.42573	0.94597
C	1.57319	2.55609	0.70661
C	3.85509	2.54738	0.66933
C	3.89944	1.26510	0.10339
C	2.69060	0.61464	-0.16581
H	2.69787	-0.36501	-0.61714
H	0.66376	3.09740	0.95291
H	-0.66397	-3.09702	-0.95412
H	-2.69759	0.36480	0.61780
C	-1.49098	-1.26505	-0.15509
C	-1.62799	2.42533	-0.94653
C	-0.83571	1.58978	-0.56082
C	-2.64500	3.37910	-1.37144
H	-2.37428	4.40286	-1.08607
H	-2.77498	3.36232	-2.46116
H	-3.60589	3.13178	-0.90476
C	2.64466	-3.37973	1.37071
H	2.37428	-4.40327	1.08421
H	3.60584	-3.13188	0.90490
H	2.77389	-3.36396	2.46054
H	4.78320	3.07976	0.88767
H	-4.78340	-3.07936	-0.88778

N	5.17023	0.72266	-0.18174
N	-5.17010	-0.72268	0.18277
C	5.49977	-0.57637	-0.49528
C	-5.49957	0.57644	0.49606
H	5.94111	1.36633	-0.06459
H	-5.94101	-1.36637	0.06591
O	4.67979	-1.47632	-0.62181
O	-4.67954	1.47642	0.62206
C	6.98977	-0.82605	-0.68162
H	7.14909	-1.26088	-1.67284
H	7.61193	0.06896	-0.58337
H	7.31661	-1.56660	0.05525
C	-6.98953	0.82617	0.68257
H	-7.31704	1.56469	-0.05606
H	-7.14841	1.26354	1.67273
H	-7.61145	-0.06928	0.58697
N	2.72348	3.18465	0.96219
N	-2.72370	-3.18425	-0.96290

SCF energy: -1219.57775 hartree
zero-point correction: +0.377081 hartree
enthalpy correction: +0.406316 hartree
free energy correction: +0.314572 hartree
quasiharmonic free energy correction: +0.322698 hartree

8

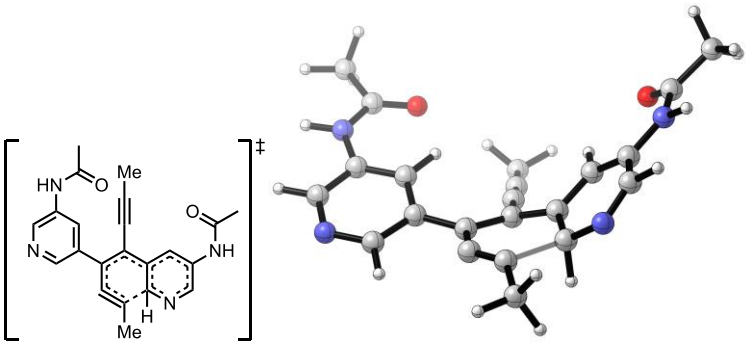

C	-4.62537	1.46473	-0.59909
C	-3.92755	0.24961	-0.50853
C	-2.56846	0.28256	-0.18551
C	-2.77531	2.67509	-0.04145
C	-0.53361	1.72213	0.38097

C	0.33145	0.71619	0.89156
C	1.74069	0.81559	0.59301
C	0.05629	2.94554	0.02475
C	1.25114	3.40277	-0.06328
C	2.41253	2.10939	0.42141
C	4.19628	1.06522	-0.63766
C	3.70411	-0.24126	-0.33358
C	2.47422	-0.35104	0.29888
H	2.04707	-1.32556	0.48875
H	2.46850	2.68012	1.35744
H	-2.34075	3.64972	0.16599
H	-2.00807	-0.63776	-0.14626
C	-1.96398	1.52649	0.06416
C	-0.52405	-1.55523	1.92298
C	-0.15319	-0.51001	1.42835
C	-1.02180	-2.81548	2.45994
H	-1.85728	-3.17641	1.84879
H	-0.23621	-3.58032	2.46096
H	-1.37436	-2.69576	3.49233
C	1.93199	4.72667	-0.10448
H	2.41405	4.96101	0.85494
H	2.72033	4.73506	-0.86521
H	1.20457	5.51127	-0.32788
H	-5.68447	1.46699	-0.86565
H	5.12600	1.15934	-1.20705
N	3.64304	2.17262	-0.23331
N	-4.06671	2.65160	-0.37740
N	4.49941	-1.32384	-0.73833
C	4.29667	-2.67158	-0.51023
H	5.33001	-1.07423	-1.25837
O	3.34397	-3.11514	0.11244
C	5.35637	-3.58135	-1.11480
H	4.89464	-4.18515	-1.90316
H	6.21581	-3.05114	-1.53725
H	5.70759	-4.26922	-0.34063
N	-4.64878	-0.93161	-0.78248
C	-4.26973	-2.23928	-0.58121
H	-5.59260	-0.78347	-1.11326
O	-3.17296	-2.57316	-0.15324
C	-5.33115	-3.27018	-0.93904
H	-5.56370	-3.85831	-0.04573
H	-6.25889	-2.84351	-1.33283

H	-4.91433	-3.95717	-1.68171

SCF energy: -1219.500711 hartree
zero-point correction: +0.375505 hartree
enthalpy correction: +0.403605 hartree
free energy correction: +0.314993 hartree
quasiharmonic free energy correction: +0.322328 hartree

8’

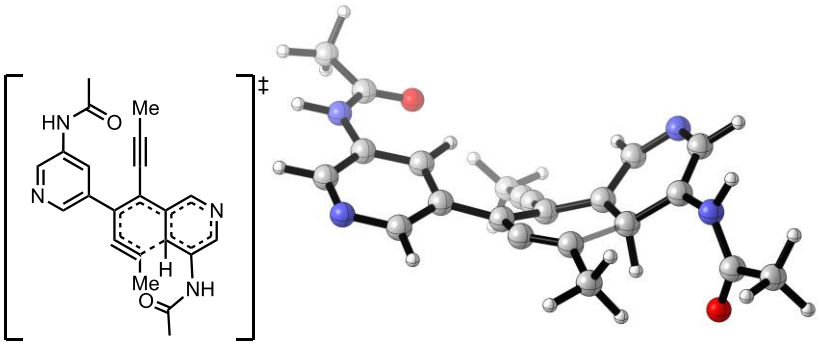

C	-3.92383	2.71154	-0.15660
C	-1.71504	2.79471	0.40432
C	-2.67641	0.65245	-0.11924
C	-0.19689	0.84528	0.45988
C	0.09222	-0.53184	0.71489
C	1.33447	-1.05116	0.21589
C	0.90704	1.65545	0.22370
C	2.17868	1.49271	0.09030
C	2.56407	-0.23867	0.12693
C	3.33169	-1.97375	-1.44731
C	1.30774	-2.31295	-0.43639
H	0.43087	-2.94266	-0.30794
H	2.99768	-0.03941	1.11648
H	-2.62227	-0.41372	-0.27133
H	-0.86676	3.39781	0.71884
C	-1.54993	1.40258	0.25681
C	-1.74706	-2.21288	1.57682
C	-0.90922	-1.44167	1.15443
C	-2.80369	-3.10533	2.03574
H	-3.71100	-2.94066	1.44260
H	-2.50869	-4.15677	1.93776

H	-3.04332	-2.92242	3.09085
C	3.33633	2.41441	0.31550
H	3.99854	2.04294	1.10397
H	3.93937	2.52625	-0.59368
H	2.96224	3.40191	0.59724
H	-4.85561	3.25682	-0.32047
H	4.07881	-2.36789	-2.13691
C	-3.89011	1.31668	-0.31448
N	-2.86398	3.43803	0.18891
N	2.22764	-2.74644	-1.27528
C	3.57889	-0.80835	-0.76770
N	4.84140	-0.18159	-0.93971
C	5.70187	0.14592	0.08906
H	5.25770	-0.28927	-1.85597
O	5.37744	0.09825	1.26823
N	-5.08853	0.67748	-0.69515
C	-5.38260	-0.66727	-0.69560
H	-5.84579	1.30342	-0.93393
O	-4.58142	-1.53948	-0.38664
C	-6.80087	-1.00757	-1.13006
H	-7.26834	-1.61683	-0.35088
H	-7.43288	-0.13607	-1.32705
H	-6.75204	-1.61929	-2.03654
C	7.06688	0.64746	-0.35435
H	7.34568	0.32868	-1.36385
H	7.07106	1.74347	-0.32680
H	7.81563	0.29469	0.35823

SCF energy: -1219.496056 hartree
zero-point correction: +0.375626 hartree
enthalpy correction: +0.403462 hartree
free energy correction: +0.316340 hartree
quasiharmonic free energy correction: +0.322810 hartree

9

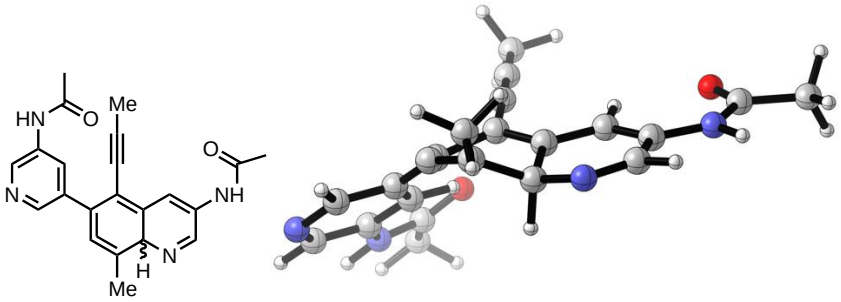

C	4.77247	1.39817	-0.44706
C	4.03514	0.20477	-0.47404
C	2.67026	0.25716	-0.17401
C	2.95894	2.61764	0.20780
C	0.68322	1.68094	0.48763
C	-0.28041	0.54009	0.69026
C	-1.51638	0.70591	0.09971
C	0.06385	2.87645	0.44526
C	-1.20960	3.17014	0.17836
C	-1.85802	2.04886	-0.61684
C	-4.06580	1.29781	-0.88635
C	-3.73243	-0.07453	-0.47973
C	-2.49860	-0.33539	0.04315
H	-2.26383	-1.31320	0.44185
H	-1.37622	1.98651	-1.60988
H	2.55785	3.57711	0.52685
H	2.07816	-0.64440	-0.20947
C	2.10624	1.49519	0.17365
C	0.48569	-1.69003	1.85946
C	0.10658	-0.66294	1.33233
C	0.98759	-2.93078	2.43650
H	1.82814	-3.30422	1.83864
H	1.33875	-2.78048	3.46527
H	0.20956	-3.70311	2.45691
C	-2.01553	4.29686	0.74664
H	-2.38800	4.95863	-0.04602
H	-2.90396	3.91443	1.26554
H	-1.41406	4.88676	1.44363
H	-5.10986	1.49622	-1.15869
H	5.83440	1.38976	-0.70090

N	-4.78209	-0.99199	-0.61262
N	4.72007	-0.97638	-0.82801
C	-4.79474	-2.33344	-0.27163
C	4.30603	-2.28299	-0.68983
C	-6.08862	-3.05935	-0.60864
H	-6.91572	-2.39563	-0.88020
H	-5.90393	-3.74608	-1.44198
H	-6.38354	-3.66303	0.25362
C	5.33593	-3.32192	-1.11170
H	4.88934	-3.96552	-1.87552
H	6.26667	-2.90031	-1.50394
H	5.56989	-3.95417	-0.24934
H	-5.62804	-0.62516	-1.02810
H	5.66977	-0.83686	-1.14548
O	-3.84503	-2.90306	0.24147
O	3.20496	-2.60861	-0.26795
N	4.25127	2.57922	-0.11477
N	-3.26720	2.29263	-0.91269

SCF energy: -1219.516951 hartree
zero-point correction: +0.377093 hartree
enthalpy correction: +0.405364 hartree
free energy correction: +0.316222 hartree
quasiharmonic free energy correction: +0.323958 hartree

9’

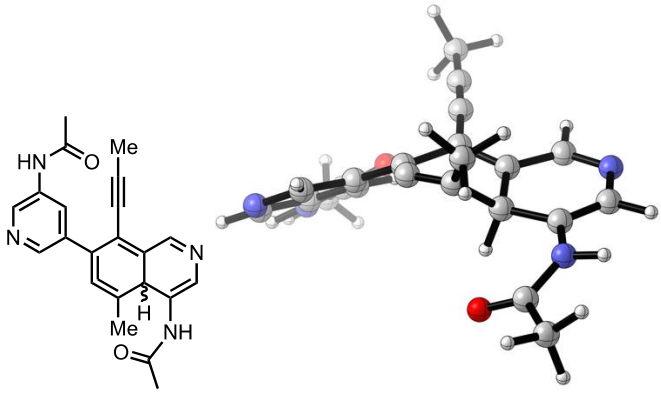

C	-3.53923	-2.83580	0.28388
C	-3.56652	-1.52075	-0.20289
C	-2.44291	-0.71224	-0.00327
C	-1.45704	-2.56491	1.17684

C	-0.11227	-0.49641	0.95965
C	0.05194	0.98691	0.69099
C	1.25838	1.35715	0.13996
C	1.05832	-1.05946	1.29553
C	2.31012	-0.63399	1.11369
C	2.35182	0.27297	-0.10987
C	3.66665	0.90048	-0.51775
C	3.76286	2.23371	-0.73577
C	1.57462	2.72771	-0.18472
H	0.79036	3.47175	-0.04807
H	2.01544	-0.32539	-0.97115
H	-0.64499	-2.98254	1.76824
H	-2.43373	0.29585	-0.38789
C	-1.35152	-1.24146	0.70262
C	-1.96544	2.61822	1.12584
C	-1.00665	1.89740	0.93064
C	-3.15147	3.44449	1.30956
H	-3.49024	3.42942	2.35308
H	-2.96037	4.48815	1.03306
H	-3.96432	3.06314	0.67934
C	3.42715	-0.76033	2.10210
H	4.22593	-1.41204	1.72580
H	3.88002	0.21964	2.30210
H	3.05960	-1.18466	3.04113
H	4.70805	2.66380	-1.06657
H	-4.39375	-3.49593	0.12316
N	-4.72539	-1.10120	-0.88917
C	-5.11677	0.18086	-1.20487
C	-6.46828	0.27896	-1.89827
H	-6.32807	0.76219	-2.87010
H	-6.96684	-0.68320	-2.05129
H	-7.12071	0.92608	-1.30401
H	-5.38770	-1.83712	-1.09397
O	-4.44739	1.17663	-0.96417
N	4.80386	0.09140	-0.69943
C	4.84496	-1.24152	-1.06962
H	5.67653	0.60034	-0.76715
C	6.24591	-1.77898	-1.32447
H	7.04023	-1.16523	-0.88807
H	6.30816	-2.79104	-0.91758
H	6.41136	-1.84851	-2.40577
O	3.84879	-1.93731	-1.19364

N	2.73428	3.15616	-0.57965
N	-2.51046	-3.35026	0.95817

SCF energy: -1219.511649 hartree
zero-point correction: +0.377185 hartree
enthalpy correction: +0.405382 hartree
free energy correction: +0.316992 hartree
quasiharmonic free energy correction: +0.324138 hartree

10

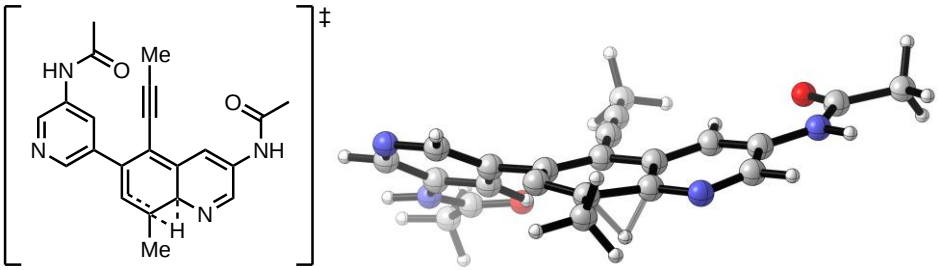

C	-4.76415	1.28642	-0.86972
C	-4.18288	0.25617	-0.11900
C	-2.80767	0.31247	0.13310
C	-2.77075	2.37656	-1.10126
C	-0.60855	1.56705	-0.15039
C	0.27408	0.45555	-0.12502
C	1.67178	0.67193	0.12143
C	-0.14956	2.91351	-0.08753
C	1.14761	3.15741	0.33240
C	2.12674	1.98779	0.50494
C	4.31843	1.29268	0.56627
C	3.97674	-0.04238	0.19650
C	2.63928	-0.34666	-0.00489
H	2.33785	-1.34823	-0.27615
H	1.47333	2.37964	1.46049
H	-2.22448	3.23750	-1.47284
H	-2.34108	-0.46484	0.71843
C	-2.07235	1.38958	-0.37998
C	-0.45175	-2.01683	-0.69494
C	-0.13642	-0.87088	-0.44854
C	-0.91301	-3.37550	-0.94968
H	-1.86235	-3.54722	-0.42848
H	-1.07080	-3.54506	-2.02226

H	-0.18230	-4.11418	-0.59989
C	1.70785	4.53461	0.59769
H	2.31549	4.58091	1.50685
H	2.36421	4.83106	-0.23123
H	0.88107	5.24339	0.66526
H	-5.83543	1.26781	-1.08235
H	5.36930	1.54398	0.73187
N	3.45832	2.26102	0.74281
N	-4.08203	2.32561	-1.35091
N	5.03686	-0.95286	0.07792
C	4.98141	-2.29663	-0.24586
H	5.95531	-0.56920	0.25594
O	3.94132	-2.88954	-0.48422
C	6.33217	-2.99592	-0.27603
H	7.18648	-2.33251	-0.10863
H	6.33917	-3.77934	0.48859
H	6.44877	-3.48692	-1.24653
N	-5.03341	-0.76738	0.35476
C	-4.69436	-2.00270	0.85397
H	-6.02066	-0.58729	0.23180
O	-3.54097	-2.38437	1.00983
C	-5.87860	-2.88604	1.22227
H	-6.85581	-2.44176	1.00889
H	-5.79225	-3.83158	0.67839
H	-5.82296	-3.11878	2.29035

SCF energy: -1219.488153 hartree
zero-point correction: +0.373174 hartree
enthalpy correction: +0.401112 hartree
free energy correction: +0.312864 hartree
quasiharmonic free energy correction: +0.320207 hartree

10’

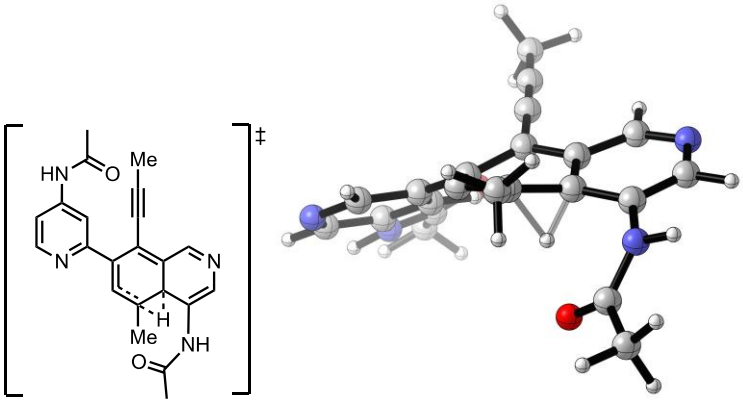

C	3.70653	-2.67984	-0.40376
C	3.61907	-1.41653	0.19990
C	2.43171	-0.69361	0.05618
C	1.60497	-2.51691	-1.28111
C	0.08464	-0.58132	-0.89036
C	-0.09113	0.84616	-0.76296
C	-1.37416	1.30920	-0.38555
C	-1.01862	-1.34351	-1.26375
C	-2.32103	-0.88042	-1.08183
C	-2.50217	0.38422	-0.29946
C	-3.84485	2.30751	0.38290
C	-1.64264	2.68550	-0.12708
H	-0.82165	3.39235	-0.22143
H	-2.35674	-0.62815	0.39549
H	0.81821	-2.95318	-1.88882
H	2.33097	0.27111	0.52981
C	1.39328	-1.24863	-0.70727
C	1.89401	2.53436	-1.16618
C	0.96500	1.77133	-0.99342
C	3.06188	3.39495	-1.31089
H	2.81838	4.44174	-1.09302
H	3.84867	3.07161	-0.61837
H	3.46269	3.35203	-2.33153
C	-3.49470	-1.61446	-1.66948
H	-3.97867	-2.28555	-0.95086
H	-4.25344	-0.93135	-2.06741
H	-3.09555	-2.24159	-2.47281

H	4.61682	-3.27336	-0.29370
H	-4.78801	2.74326	0.71175
N	2.72755	-3.22424	-1.12488
C	-3.74698	0.95025	0.19212
N	-2.81652	3.17830	0.20457
N	-4.83788	0.11551	0.53727
C	-4.70383	-1.01317	1.31444
H	-5.75494	0.54175	0.49918
O	-3.60582	-1.49238	1.59096
C	-5.99640	-1.63682	1.80206
H	-6.05405	-1.52378	2.88993
H	-6.89060	-1.19703	1.35077
H	-5.97527	-2.70840	1.58618
N	4.73353	-0.96609	0.94040
C	5.02511	0.31495	1.35058
H	5.44741	-1.66381	1.10080
O	4.28678	1.27421	1.16928
C	6.36000	0.46323	2.06776
H	6.90690	-0.47559	2.19987
H	6.98637	1.16118	1.50321
H	6.18020	0.90913	3.05057

SCF energy: -1219.479542 hartree
zero-point correction: +0.372581 hartree
enthalpy correction: +0.400220 hartree
free energy correction: +0.313616 hartree
quasiharmonic free energy correction: +0.320069 hartree

Results for Unsubstituted N-PDA

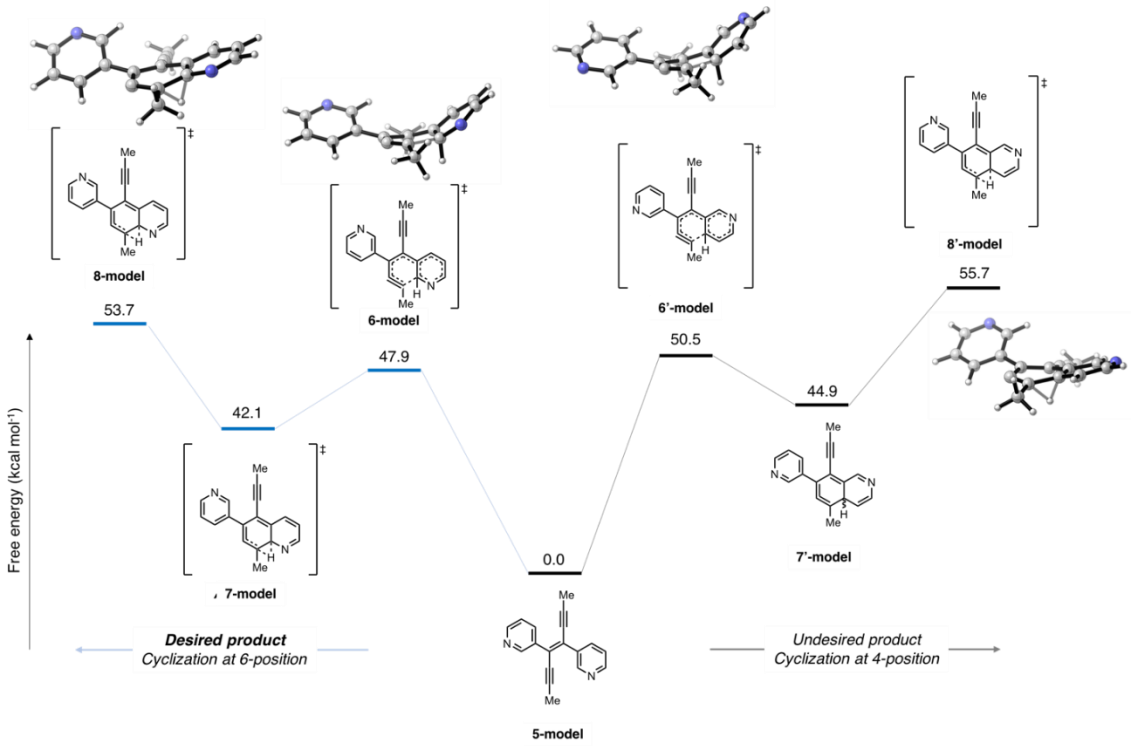

Figure A32. Potential energy surface of cyclization at 6- and 4-positions starting from structure **5-model**. Energies are free energies in kcal mol^{-1}.

Unsubstituted model system

5-model

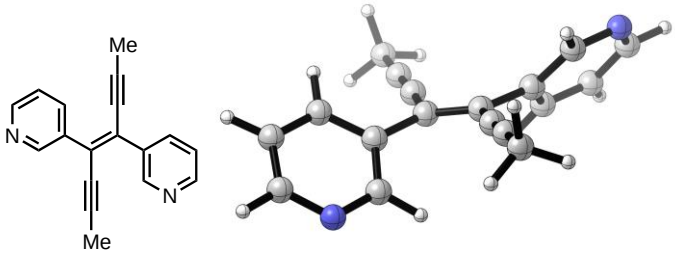

C	-4.63331	0.12295	-0.18864
C	-4.10560	1.05549	0.70480
C	-2.72401	1.20999	0.76611
C	-2.55269	-0.47185	-0.92773
C	-0.42290	0.55457	-0.02023

C	0.43047	-0.52753	-0.02218
C	1.91331	-0.39353	-0.06831
C	0.05817	1.89387	0.07139
C	0.37728	3.06115	0.17559
C	2.72537	-1.21927	0.72990
C	4.65886	-0.29494	-0.06171
C	3.95936	0.56105	-0.91225
C	2.56814	0.51148	-0.91529
H	1.99454	1.15312	-1.57520
H	2.25989	-1.95041	1.38744
H	-1.96419	-1.07568	-1.61313
H	-2.27320	1.93305	1.43948
C	-1.90610	0.41633	-0.05034
C	-0.39609	-3.02499	0.18056
C	-0.05844	-1.86323	0.07680
C	-0.84603	-4.40755	0.29056
H	-0.14703	-5.09452	-0.20137
H	-0.93164	-4.71504	1.34040
H	-1.83117	-4.53750	-0.17392
C	0.80232	4.45156	0.29163
H	0.83624	4.77118	1.34087
H	1.80561	4.59450	-0.12829
H	0.11740	5.12424	-0.23870
H	5.74734	-0.28071	-0.03407
H	-5.70949	-0.02564	-0.26287
N	4.05989	-1.17598	0.75003
N	-3.87757	-0.62433	-1.00342
H	4.49389	1.24463	-1.56566
H	-4.76306	1.64764	1.33477

SCF energy: -803.5793978 hartree
zero-point correction: +0.266766 hartree
enthalpy correction: +0.286689 hartree
free energy correction: +0.215898 hartree
quasiharmonic free energy correction: +0.222057 hartree

6-model

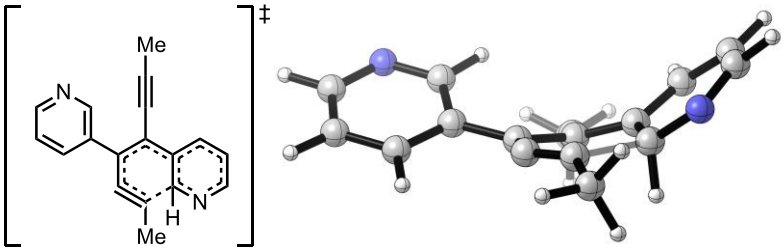

C	-4.49511	-0.97200	0.80217
C	-3.91628	-1.99716	0.05550
C	-2.58600	-1.86627	-0.33064
C	-2.54915	0.23265	0.82007
C	-0.43635	-0.61455	-0.32829
C	0.26733	0.61597	-0.46421
C	1.67332	0.62536	-0.16911
C	0.32908	-1.78208	-0.38848
C	1.57714	-2.07669	-0.42155
C	2.53527	-0.55085	-0.36889
C	4.14095	0.33003	1.06262
C	3.47328	1.58360	1.13155
C	2.25715	1.72663	0.49980
H	1.69186	2.64988	0.58102
H	3.90736	2.39824	1.70295
H	2.68986	-0.76655	-1.43503
H	-2.02906	1.11476	1.18007
H	-4.49697	-2.87157	-0.22372
H	-2.09302	-2.63089	-0.92360
C	-1.86273	-0.72032	0.04078
C	-0.96115	2.92624	-0.81235
C	-0.41065	1.86221	-0.61381
C	-1.66128	4.18586	-1.03762
H	-2.64784	4.17908	-0.55834
H	-1.09651	5.03460	-0.63360
H	-1.81323	4.36857	-2.10882
C	2.44036	-3.22386	-0.81639
H	2.90382	-3.05862	-1.79918
H	3.25624	-3.35633	-0.09774
H	1.84469	-4.13895	-0.86417
H	-5.53835	-1.02980	1.10878

H	5.06088	0.17978	1.62899
N	3.75093	-0.66346	0.30583
N	-3.82679	0.12333	1.19066

SCF energy: -803.5030161 hartree
zero-point correction: +0.265611 hartree
enthalpy correction: +0.284074 hartree
free energy correction: +0.218649 hartree
quasiharmonic free energy correction: +0.222060 hartree

6'-model

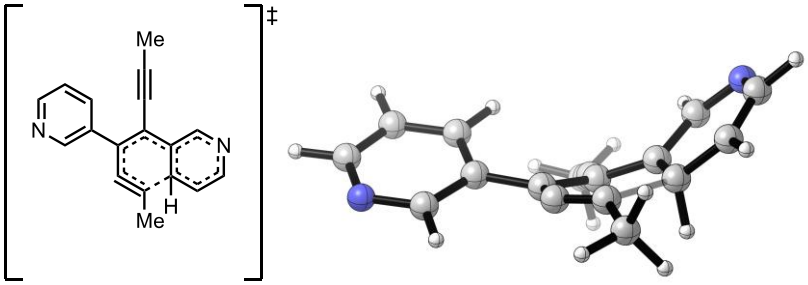

C	-4.51332	-1.08602	0.72826
C	-2.60963	-1.81841	-0.29537
C	-2.56186	0.30989	0.80164
C	-0.45162	-0.59947	-0.31801
C	0.28768	0.61295	-0.46121
C	1.69190	0.58281	-0.16554
C	0.28387	-1.78340	-0.37689
C	1.52819	-2.10128	-0.42222
C	2.51701	-0.61185	-0.37755
C	4.14251	0.44364	1.11620
C	2.28176	1.66292	0.54805
H	1.72033	2.59118	0.63462
H	2.65711	-0.81927	-1.44829
H	-2.05145	1.20637	1.13301
H	-2.11595	-2.59157	-0.88110
C	-1.87657	-0.66682	0.05937
C	-0.87839	2.95219	-0.82247
C	-0.35740	1.87526	-0.61348
C	-1.52283	4.23704	-1.06912
H	-2.56632	4.22987	-0.73157

H	-1.00421	5.04866	-0.54480
H	-1.52158	4.48006	-2.13906
C	2.31858	-3.29023	-0.85461
H	2.94405	-3.06546	-1.72962
H	2.99011	-3.63457	-0.05736
H	1.64622	-4.11246	-1.11212
H	-5.55400	-1.28278	0.98133
H	5.07030	0.42845	1.68449
C	-3.89569	0.09876	1.13379
H	-4.44618	0.83218	1.71601
N	-3.88576	-2.03734	0.02640
H	4.43369	-1.48393	0.25236
N	3.43520	1.61166	1.18459
C	3.77445	-0.62579	0.35002

SCF energy: -803.4989812 hartree
zero-point correction: +0.265520 hartree
enthalpy correction: +0.283912 hartree
free energy correction: +0.218703 hartree
quasiharmonic free energy correction: +0.222143 hartree

7-model

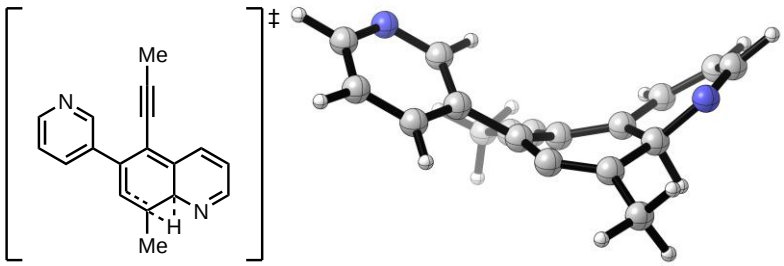

C	-4.32142	-1.05991	1.05513
C	-3.81853	-2.05342	0.21482
C	-2.54908	-1.88440	-0.32710
C	-2.41082	0.18612	0.87149
C	-0.43451	-0.59362	-0.52276
C	0.28835	0.68819	-0.53721
C	1.61311	0.61064	-0.11404
C	0.33741	-1.68271	-0.78751
C	1.64601	-1.87349	-0.75231
C	2.42750	-0.66892	-0.17281

C	3.79888	0.13588	1.53602
C	3.38074	1.50067	1.27158
C	2.30670	1.72761	0.46555
H	1.88851	2.72342	0.34901
H	3.88053	2.31622	1.78584
H	3.07690	-0.50668	-1.06077
H	-1.87168	1.07650	1.18180
H	-4.41618	-2.92917	-0.02131
H	-2.12038	-2.61222	-1.00961
C	-1.80245	-0.73924	-0.00059
C	-0.93568	2.99057	-0.93559
C	-0.36613	1.93860	-0.72590
C	-1.64213	4.24280	-1.18100
H	-2.68016	4.18254	-0.83232
H	-1.16183	5.08102	-0.66214
H	-1.66407	4.48267	-2.25147
C	2.43743	-2.95076	-1.43707
H	3.11388	-2.53565	-2.19780
H	3.06611	-3.48421	-0.71217
H	1.77167	-3.67160	-1.91854
H	-5.32012	-1.14676	1.48029
H	4.52939	-0.03696	2.32936
N	3.37348	-0.90316	0.90175
N	-3.63416	0.04219	1.38620

SCF energy: -803.5135248 hartree
zero-point correction: +0.266927 hartree
enthalpy correction: +0.285545 hartree
free energy correction: +0.219460 hartree
quasiharmonic free energy correction: +0.223345 hartree

7'-model

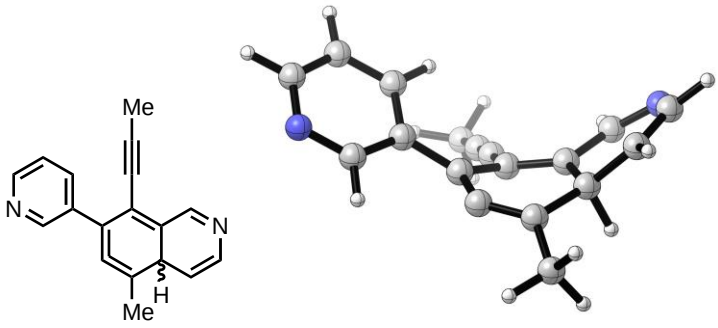

C	-4.33832	-1.16422	0.98995
C	-3.67994	0.00678	1.37078
C	-2.39707	0.24365	0.88871
C	-2.57929	-1.82699	-0.30597
C	-0.43998	-0.59213	-0.50673
C	0.31439	0.67397	-0.54235
C	1.63863	0.57196	-0.12626
C	0.30222	-1.69964	-0.77515
C	1.60989	-1.90640	-0.76511
C	2.42138	-0.72014	-0.18332
C	3.77463	0.26851	1.61515
C	2.33414	1.68251	0.48710
H	1.94620	2.68780	0.32417
H	3.07116	-0.57469	-1.07655
H	-2.16638	-2.55335	-1.00318
H	-4.15871	0.70951	2.04668
H	-1.85297	1.13106	1.19233
C	-1.80559	-0.69530	0.02661
C	-0.86880	2.99276	-0.96417
C	-0.31674	1.93443	-0.74064
C	-1.53640	4.26135	-1.23240
H	-2.62569	4.13821	-1.25385
H	-1.29664	5.00684	-0.46443
H	-1.22785	4.67318	-2.20132
C	2.35311	-2.98831	-1.50006
H	3.07743	-2.57171	-2.21396
H	2.92064	-3.62776	-0.80905
H	1.65310	-3.62697	-2.04515
H	-5.33763	-1.38363	1.36262
H	4.50112	0.21905	2.42234
N	-3.80326	-2.07222	0.16390
C	3.38035	-0.84287	0.95905
H	3.81127	-1.81375	1.18707
N	3.32974	1.55604	1.31625

SCF energy: -803.5089787 hartree
zero-point correction: +0.266651 hartree
enthalpy correction: +0.285277 hartree
free energy correction: +0.219136 hartree
quasiharmonic free energy correction: +0.223144 hartree

8-model

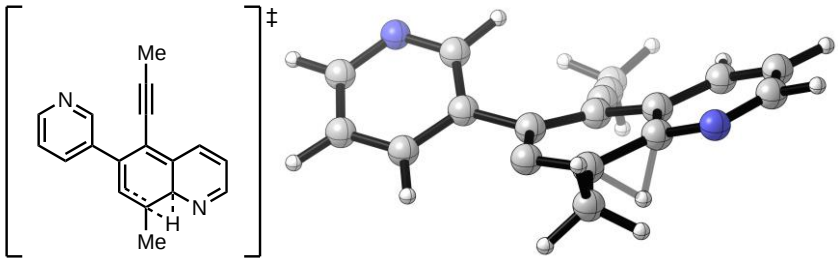

C	-4.60823	-0.83132	0.59379
C	-4.03948	-1.81511	-0.21530
C	-2.67544	-1.75081	-0.48132
C	-2.59490	0.21222	0.88437
C	-0.45001	-0.65756	-0.17992
C	0.26463	0.57983	-0.21489
C	1.66810	0.55763	0.01976
C	0.21261	-1.89242	-0.32854
C	1.60553	-1.95407	-0.34099
C	2.39787	-0.69818	-0.02655
C	4.35817	0.31325	0.63311
C	3.75814	1.60617	0.63303
C	2.42994	1.72130	0.31100
H	1.92964	2.68445	0.30906
H	4.35430	2.47627	0.88891
H	2.20512	-1.08739	-1.19375
H	-2.04741	1.01183	1.37616
H	-4.65402	-2.61034	-0.62787
H	-2.17012	-2.49319	-1.09032
C	-1.91414	-0.70337	0.06036
C	-0.90380	2.91082	-0.63492
C	-0.37223	1.84092	-0.41769
C	-1.59405	4.17186	-0.87955
H	-2.63425	4.12146	-0.53613
H	-1.10520	5.00299	-0.35734
H	-1.60665	4.41371	-1.94962
C	2.37211	-3.23791	-0.57122
H	3.35192	-3.07455	-1.03006
H	2.54837	-3.73637	0.38989
H	1.77074	-3.90783	-1.19107
H	-5.67504	-0.84235	0.81324

H	5.40854	0.21207	0.90691
N	3.73720	-0.79359	0.31045
N	-3.90362	0.16355	1.15024

SCF energy: -803.4921869 hartree
zero-point correction: +0.263518 hartree
enthalpy correction: +0.281690 hartree
free energy correction: +0.217089 hartree
quasiharmonic free energy correction: +0.220366 hartree

8'-model

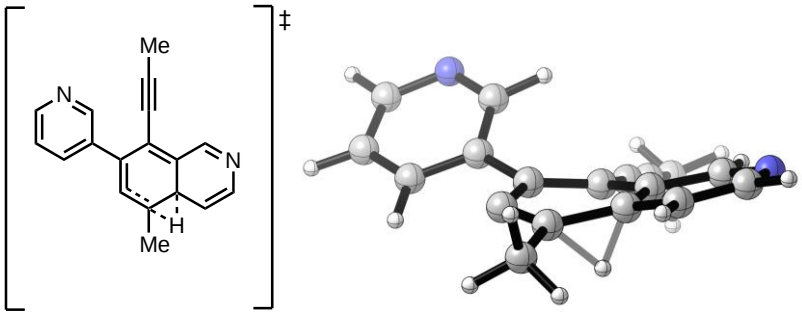

C	-4.60313	-0.80148	0.63445
C	-4.05477	-1.78778	-0.18564
C	-2.69366	-1.73624	-0.46860
C	-2.57573	0.22033	0.90450
C	-0.45410	-0.66599	-0.18672
C	0.27523	0.56593	-0.22471
C	1.67551	0.52755	0.01991
C	0.20024	-1.89842	-0.35928
C	1.59257	-1.97003	-0.37612
C	2.39248	-0.73291	-0.02125
C	4.35295	0.48403	0.71073
C	2.44213	1.69387	0.32331
H	1.93785	2.65801	0.30503
H	2.22017	-1.08775	-1.20091
H	-2.01390	1.01288	1.39175
H	-4.68276	-2.57434	-0.59448
H	-2.20512	-2.47975	-1.08981
C	-1.91493	-0.69967	0.06905
C	-0.88749	2.89165	-0.67817
C	-0.35262	1.82687	-0.44486
C	-1.56924	4.15321	-0.94018

H	-1.63851	4.34521	-2.01813
H	-2.58902	4.13886	-0.53731
H	-1.03552	4.99641	-0.48608
C	2.33310	-3.26347	-0.64859
H	3.28207	-3.11961	-1.18019
H	2.55899	-3.77837	0.29438
H	1.68922	-3.92169	-1.23664
H	-5.66719	-0.80216	0.86686
H	5.39222	0.52475	1.02900
N	-3.88143	0.18406	1.18560
C	3.77534	-0.71130	0.38739
H	4.34335	-1.63413	0.43312
N	3.71070	1.69378	0.66186

SCF energy: -803.4890542 hartree
zero-point correction: +0.263436 hartree
enthalpy correction: +0.281605 hartree
free energy correction: +0.216966 hartree
quasiharmonic free energy correction: +0.220398 hartree

References

[1] Zhou, X.; Yu, G. Modified Engineering of Graphene Nanoribbons Prepared via On-Surface Synthesis. *Adv. Mater.* **2019**, 32, 1905957.

[2] Llinas, J. P.; Fairbrother, A.; Barin G. B.; Shi, W.; Lee, K.; Wu,S.; Choi, B. Y.; Braganza, R.; Lear, J.; Kau, N.; Choi, W.; Chen,C.; Pedramrazi, Z.; Dumslaff, T.; Narita, A.; Feng, X.; Müllen, K.; Fischer, F.; Zettl, A.;Ruffieux, P.; Yablonovitch, E.; Crommie, M.; Fasel, R.; Bokor, J. Short-Channel Field-Effect Transistors with 9-Atom and 13-Atom Wide Graphene Nanoribbons. *Nature Commun.* **2017**, *8*, 633.

[3] Li, X.; Wang, X.; Zhang, L.; Lee, S.; Dai, H. Chemically Derived, Ultrasmooth Graphene Nanoribbon Semiconductors. *Science* **2008**, *319*, 1229–1232.

[4] Shen, H.; Shi, Y.; Wang, X. Synthesis, Charge Transport and Device Applications of Graphene Nanoribbons. *Synth. Met.* **2015**, *210*, 109–122.

[5] Rajaji, U.; Arumugam, R.; Chen, S.-M.; Chen, T.-W.; Tseng, T.-W.; Chinnapaiyan, S.; Lee, S.-Y.; Chang, W.-H. Graphene Nanoribbons in Electrochemical Sensors and Biosensors: A Review. *Int. J. Electrochem. Sci.* **2018,** *13*, 6643-6654.

[6] Cho, K. M.; Cho, S.-Y.; Chong, S.; Koh, H.-J.; Kim, D. W.; Kim, J.; Jung, H.-T. Edge-Functionalized Graphene Nanoribbon Chemical Sensor: Comparison with Carbon Nanotube and Graphene. *ACS Appl. Mater. Interfaces* **2018**, *10*, 42905–42914.

[7] Nakada, K.; Fujita, M.; Dresselhaus, G.; Dresselhaus, M. S. Edge State in Graphene Ribbons: Nanometer Size Effect and Edge Shape Dependence. *Phys. Rev. B* **1996**, *54*, 17954-17961.

[8] Fujita, M.; Wakabayashi, K.; Nakada, K.; Kusakabe, K. Peculiar Localized State at Zigzag Graphite Edge. *J. Phys. Soc. Jpn.* **1996**, *65*, 1920-1923.

[9] Hao, Z.; Zhang, H.; Ruan, Z.; Yan, C.; Lu, J.; Cai, J. Tuning Electronic Properties of Atomically Precise Graphene Nanoribbons by Bottom-up Fabrications. *ChemNanoMat* **2020**.

[10] Wang, X.-Y.; Yao, X.; Müllen, K. Polycyclic Aromatic Hydrocarbons in the Graphene Era. *Sci. China Chem.* **2019**, *62*, 1099–1144.

[11] Cai, J.; Ruffieux, P.; Jaafar, R.; Bieri, M.; Braun, T.; Blankenburg, S.; Muoth, M.; Seitsonen, A.; Saleh, M.; Feng, X.; Müllen, K.; Fasel, R. Atomically Precise Bottom-up Fabrication of Graphene Nanoribbons. *Nature* **2010**, *466*, 470–473.

[12] Bronner, C.; Durr, R.A.; Rizzo, D.J.; Lee, Y.-L.; Marangoni, T.; Kalayjian, A. M.; Rodriguez, H.; Zhao, W.; Louie, S. G.; Fischer, F. R.; Crommie, M. F. Hierarchical On-Surface Synthesis of Graphene Nanoribbon Heterojunction. *ACS Nano* **2018**, *12*, 2193-2200.

[13] Beyer, D.; Wang, S.; Pignedoli, C. A.; Melidonie, J.; Yuan, B.; Li, C.; Wilhelm, J.; Ruffieux, P.; Berger, R.; Müllen, K.; Fasel, R.; Feng, X. Graphene Nanoribbons Derived from Zigzag Edge-Encased Poly(para-2,9-dibenzo[bc,kl]coronenylene) Polymer Chains. *J. Am. Chem. Soc.* **2019**, *141*, 2843-2846.

[14] Radocea, A.; Sun, T.; Vo, T.; Sinitskii, A.; Aluru, N.; Lyding, J. Solution-Synthesized Chevron Graphene Nanoribbons Exfoliated onto H:Si(100). *Nano Letters* **2016**, *17*, 170–178.

[15] Gao, J.; Uribe-Romo, F. J.; Saathoff, J. D.; Arslan, H.; Crick, C. R.; Hein, S. J.; Itin, B.; Clancy, P.; Dichtel, W. R.; Loo, Y.-L. Ambipolar Transport in Solution-Synthesized Graphene Nanoribbons. *ACS Nano* **2016**, *10*, 4847−4856.

[16] Li, G.; Yoon, K.-Y.; Zhong, X.; Zhu, X.; Dong, G. Efficient Bottom-Up Preparation of Graphene Nanoribbons by Mild Suzuki–Miyaura Polymerization of Simple Triaryl Monomers. *Chem. - Eur. J.* **2016**, *22*, 9116−9120.

[17] Yang, W.; Lucotti, A.; Tommasini, M.; Chalifoux, W. A. Bottom-Up Synthesis of Soluble and Narrow Graphene Nanoribbons Using Alkyne Benzannulations. *J. Am. Chem. Soc*. **2016**, *138*, 9137−9144.

[18] Hayashi, H.; Yamaguchi, J.; Jippo, H.; Hayashi, R.; Aratani, N.; Ohfuchi, M.; Sato, S.; Yamada, H. Experimental and Theoretical Investigations of Surface-Assisted Graphene Nanoribbon Synthesis Featuring Carbon-Fluorine Bond Cleavage. *ACS Nano* **2017**, *11*, 6204-6210.

[19] Di Giovannantonio, M.; Deniz, O.; Urgel, J.I.; Widmer, R.; Dienel, T.; Stolz, S.; Sánchez-Sánchez, C.; Muntwiler, M.; Dumslaff, T.; Berger, R.; Narita, A.; Feng, X.; Müllen, K.; Ruffieux, P.; Fasel, R. On-Surface Growth Dynamics of Graphene Nanoribbons: The Role of Halogen Functionalization. *ACS Nano* **2018**, *12*, 74-81.

[20] Ruffieux, P.; Wang, S.; Yang, B.; Sánchez-Sánchez, C.; Liu, J.; Dienel, T.; Talirz, L.; Shinde, P.; Pignedoli, C. A.; Passerone, D.; Dumslaff, T.; Feng, X.; Müllen, K.; Fasel, R. On-Surface Synthesis of Graphene Nanoribbons with Zigzag Edge Topology. *Nature* **2016**, *531*, 489-492.

[21] Lee, Y-L.; Zhao, F.; Cao, T.; Ihm, J.; Louie, S. G. Topological Phases in Cove-Edged and Chevron Graphene Nanoribbons: Geometric Structures, z_2 Invariants, and Junction States. *Nano Lett.* **2018**, *18*, 7247-7253.

[22] Teeter, J. D.; Costa, P. S.; Pour, M. M.; Miller, D. P.; Zurek, E.; Enders, A.; Sinitskii, A. Epitaxial Growth of Aligned Atomically Precise Chevron Graphene Nanoribbons on Cu(111). *Chem. Commun.* **2017**, *53*, 8463-8466.

[23] Bronner, C.; Stremlau, S.; Gille, M.; Brauße, F.; Haase, A.; Hecht, S.; Tegeder, P. Aligning the Band Gap of Graphene Nanoribbons by Monomer Doping. *Angew. Chem. Int. Ed.* **2013**, *52*, 4422–4425.

[24] Liu, J.; Li, B.-W.; Tan, Y.-Z.; Giannakopoulos, A.; Sánchez-Sánchez, C.; Belijonne, C.; Ruffieux, P.; Fasel, R.; Feng, X.; Müllen, K. Toward Cove-Edged Low Band Gap Graphene Nanoribbons. *J. Am. Chem. Soc.* **2015**, *137*, 6097-6103.

[25] Verzhbitskiy, I. A.; De Corato, M.; Ruini, A.; Molinari, E.; Narita, A.; Hu, Y.; Schwab, M. G.; Bruna, M.; Yoon, D.; Milana, S.; Feng, X.; Müllen, K.; Ferrari, A. C.; Casiraghi, C.; Prezzi, D. Raman Fingerprints of Atomically Precise Graphene Nanoribbons. *Nano Lett.* **2016**, *16*, 3442-3447.

[26] Wu, J.; Gu, Y.; Muñoz-Mármol, R.; Wu, S.; Han, Y.; Ni, Y.; Díaz-García, M.; Casado, J. Cove-Edged Nanographenes with Localized Double Bonds. *Angew. Chem. Int. Ed.* **2020**.

[27] Yano, Y.; Mitoma, N.; Matsushima, K.; Wang, F.; Matsui, K.; Takakura, A.; Miyauchi, Y.; Ito, H.; Itami, K. Living Annulative π-Extension Polymerization for Graphene Nanoribbon Synthesis. *Nature* **2019**, *571*, 387-392.

[28] Moreno, C.; Vilas-Varela, M.; Kretz, B.; Garcia-Lekue, A.; Costache, M. V.; Paradinas, M.; Panighel, M.; Ceballos, G.; Valenzuela, S. O.; Peña, D.; Mugarza, A. Bottom-up Synthesis of Multifunctional Nanoporous Graphene. **2018**, *360*, 199–203.

[29] Wang, X.-Y.; Yao, X.; Narita, A.; Müllen, K. Heteroatom-Doped Nanographenes with Structural Precision. *Acc. Chem. Res.* **2019**, *52*, 2491-2505.

[30] Kawai, S.; Saito, S.; Osumi, S.; Yamaguchi, S.; Foster, A. S.; Spijker, P.; Meyer, E. Atomically Controlled Substitutional Boron-Doping of Graphene Nanoribbons. *Nature Commun.* **2015**, *6*, 8098.

[31] Wang, X.-Y.; Urgel, J. I.; Barin, G. B.; Eimre, K.; Di Giovannantonio, M.; Milani, A.; Tommasini, M.; Pignedoli, C. A.; Ruffieux, P.; Feng, X.; Fasel, R.; Müllen, K.; Narita, A.

Bottom-Up Synthesis of Heteroatom-Doped Chiral Graphene Nanoribbons. *J. Am. Chem. Soc.* **2018**, *140*, 9104-9107.

[32] Cao, Y.; Qi, J.; Zhang, Y.-F.; Huang, L.; Zheng, Q.; Lin, X.; Cheng, Z.; Zhang, Y.-Y.; Feng, X.; Du, S.; Pantelides, S.T.; Gao, H.-J. Tuning the Morphology of Chevron-Type Graphene Nanoribbons by Choice of Annealing Temperature. *Nano Research* **2018**, *11*, 6190-6196.

[33] Nguyen, G.D.; Toma, F. M.; Cao, T.; Pedramrazi, Z.; Chen, C.; Rizzo, D. J.; Joshi, T.; Bronner, C.; Chen, Y.-C.; Favaro,M.; Louie,S. G.; Fischer, F. R.; Crommie, M. F. Bottom-Up Synthesis of N=13 Sulfur-Doped Graphene Nanoribbons. *J. Phys. Chem. C* **2016**, *120*, 2684-2687.

[34] Kim, K. T.; Lee, J. W.; Jo, W. H. Charge-Transport Tuning of Solution-Processable Graphene Nanoribbons by Substitutional Nitrogen Doping. *Macromol. Chem. Phys.* **2013**, *214*, 2768-2773.

[35] Vo, T. H.; Perera, U. G. E.; Shekhirev, M.; Pour, M. M.;Kunkel, D.A.; Lu, H.; Gruberman, A.; Sutter, E.; Cotlet, M.; Nykypanchuk, D.; Zahl, P.; Enders,A.; Sinitskii, A.; Sutter, P. Nitrogen-Doping Induced Self-Assembly of Graphene Nanoribbon-Based Two-Dimensional and Three-Dimensional Metamaterials. *Nano Lett.* **2015**, *15*, 5770-5777.

[36] Kawai, S.; Nakatsuka, S.; Hatakeyama, T.; Pawlak, R.; Meier, T.; Tracey, J.; Meyer, E.; Foster, A. S. Multiple Heteroatom Substitution to Graphene Nanoribbon. *Science Advances* **2018**, *4*, eaar7181.

[37] Cloke, R. R.; Marangoni, T.; Nguyen, G. D.; Joshi, T.; Rizzo, D. J.; Bronner, C.; Cao, T.; Louie, S. G.; Crommie, M. F.; Fischer, F. R. Site-Specific Substitutional Boron Doping of Semiconducting Armchair Graphene Nanoribbons. *J. Am. Chem. Soc*. **2015**, *137*, 8872–8875.

[38] Piskun, I.; Blackwell, R.; Jornet-Somoza, J.; Zhao, F.; Rubio, A.; Louie, S.; Fischer, F. Covalent C-N Bond Formation through a Surface Catalyzed Thermal Cyclodehydrogenation. *J. Am. Chem. Soc.* **2020,** *142*, 3696-3700.

[39] Cai, J.; Pignedoli, C. A.; Talirz, L.; Ruffieux, P.; Sode, H.; Liang, L.; Meunier, V.; Berger, R.; Li, R.; Feng, X.; Mullen, K.; Fasel, R. Graphene Nanoribbon Heterojunctions. *Nat. Nanotechnol*. **2014**, 9, 896−900.

[40] Zhang, Y.; Zhang, Y.; Li, G.; Lu, J.; Lin, X.; Du, S.; Berger, R.; Feng, X.; Müllen, K.; Gao, H.-J. Direct Visualization of Atomically Precise Nitrogen-Doped Graphene Nanoribbons. *Appl. Phys. Lett*. **2014**, 105, 023101.

[41] Durr, R. A.; Haberer, D.; Lee, Y.-L.; Blackwell, R.; Kalayjian, A. M.; Marangoni, T.; Ihm, J.; Louie, S. G.; Fischer, F. R. Orbitally Matched Edge-Doping in Graphene Nanoribbons. *J. Am. Chem. Soc.* **2018**, *140*, 807-813.

[42] Vo, T. H.; Shekhirev, M.; Kunkel, D. A.; Orange, F.; Guinel, M. F.-F.; Enders, A.; Sinitskii, A. Bottom-Up Solution Synthesis of Narrow Nitrogen-Doped Graphene Nanoribbons. *Chem. Commun.* **2014**, *50*, 4172-4174.

[43] Wegner, G. Topochemical Polymerization of Monomers with Conjugated Triple Bonds. *Makromol. Chem.* **1972**, *154*, 35-48.

[44] Enkelmann V. (1984) Structural aspects of the topochemical polymerization of diacetylenes. In: Cantow HJ. (eds) Polydiacetylenes. Advances in Polymer Science, vol 63. Springer, Berlin, Heidelberg.

[45] Lauher, J.; Fowler, F.; Goroff, N. Single-Crystal-to-Single-Crystal Topochemical Polymerizations by Design. *Accounts of Chemical Research* **2008**, *41*, 1215–1229.

[46] Jordan, R. S.; Wang, Y.; McCurdy, R. D.; Yeung, M. T.; Marsh, K. L.; Kahn, S. I.; Kaner, R. B.; Rubin, Y. Synthesis of Graphene Nanoribbons via the Topochemical Polymerization and Subsequent Aromatization of a Diacetylene Precursor. *Chem* **2016,** *1*, 78-90.

[47] Jordan, R. S.; Li, Y. L.; Lin, C-W.; McCurdy, R. D.; Lin, J. B.; Brosmer, J. L.; Marsh, K. L.; Khan, S. I.; Houk, K. N.; Kaner, R. B.; Rubin, Y. Synthesis of *N* = 8 Armchair Graphene Nanoribbons from Four Distinct Polydiacetylenes. *J. Am. Chem. Soc.* **2017**, *139*, 15878-15890.

[48] See Appendix.

[49] See reference 47 for a similar observation on an intermediate stage to $[8]_A$GNR.

[50] Prall, M.; Krüger, A.; Schreiner,P. R.; Hopf, H. The Cyclization of Parent and Cyclic Hexa-1,3-dien-5-ynes—A Combined Theoretical and Experimental Study. *Chem. Eur. J.* **2001**, *7*, 4386-4394.

[51] Tian, Z.; Dai, S.; Jiang, D. Stability and Core-Level Signature of Nitrogen Dopants in Carbonaceous Materials. *Chem. Mater.* **2015**, *27*, 5775-5781.

[52] Kapteijn, F.; Moulijn, J.A.; Matzner, S.; Boehm H.-P. The Development of Nitrogen Functionality in Model Chars during Gasification in CO_2 and O_2. *Carbon,* **1999**, *37*, 1143-1150.

[53] Geng, J.; Si, L.; Guo, H.; Lin, C.; Xi, Y.; Li, Y.; Yan, X.; Wang, B.; Chen, L. 3D Nitrogen-Doped Graphene Gels as Robust and Sustainable Adsorbents for Dyes. *New J. Chem.* **2017**, *41*, 15447-15457.

[54] Kondo, T.; Casolo, S.; Suzuki, T.; Shikano, T.; Sakurai, M.; Harada, Y.; Saito, M.; Oshima, M.; Trioni, M. I.; Tantardini, G. F.; Nakamura, J. Atomic-Scale Characterization of Nitrogen-Doped Graphite: Effects of Dopant Nitrogen on the Local Electronic Structure of the Surrounding Carbon Atoms. *Phys. Rev. B* **2012**, *86*, 035436.

[55] Matanovic, I.; Artyushkova, K.; Strand, M. B.; Dzara, M. J.; Pylypenko, S.; Atanassov, P. Core Level Shifts of Hydrogenated Pyridinic and Pyrrolic Nitrogen in the Nitrogen-Containing Graphene-Based Electrocatalysts: In-Place vs Edge Defects. *J. Phys. Chem. C* **2016**, *120*, 29225-29232.

[56] Men, S.; Mitchell, D. S.; Lovelock, K. R. J.; License P. X-ray Photoelectron Spectroscopy of Pyridinium-Based Ionic Liquids: Comparison to Imidazolium- and Pyrrolidinium-Based Analogues. *ChemPhysChem* **2015**, *16*, 2211-2218.

[57] Jansen, R. J. J.; van Bekkum, H. XPS of Nitrogen-Containing Functional Groups on Activated Carbon. *Carbon* **1995**, *8*, 1021-1027.

[58] Ryu, S.; Maultzsch, J.; Han, M. Y.; Kim, P.; Brus, L. E. Raman Spectroscopy of Lithographically Patterned Graphene Nanoribbons. *ACS Nano* **2011**, *5*, 4123−4130.

[59] Ortiz-Medina, J.; García-Betancourt, M. L.; Jia, X.; Martínez-Gordillo, R.; Pelagio-Flores, M. A.; Swandon, D.; Elías, A.L. Gutiérrez, H. R. ; Garcia-Espino, E.; Meunier, V.; Owens, J.; Sumpter, B.G.; Cruz-Silva, E.; Rodríguez-Macías, F.J.; López-Urías, F.; Muñoz-Sandoval, E.; Dresselhaus, M. S.; Terrones, H.; Terrones, M. Nitrogen-Doped Graphitic Nanoribbons: Synthesis, Characterization, and Transport. *Adv. Funct. Mater.* **2013**, *23*, 3755-3762.

[60] Daigle, M.; Maio, D.; Lucotti, A.; Tommasini, M.; Morin, J.-F. Helically Coiled Graphene Nanoribbons. *Angew. Chem.* **2017**, *129*, 6309-6313.

[61] Zhang, C.; Fu, L.; Liu, N.; Lui, M.; Wang, Y.; Liu, Z. Synthesis of Nitrogen-Doped Graphene Using Embedded Carbon and Nitrogen Sources. *Adv. Mater.* **2011**, *23*, 1020-1024.

[62] Hu, X.; Bai, D.; Wu, Y.; Chen, S.; Ma, Y.; Lu, Y.; Chao, Y.; Bai, Y. A Facile Synthesis of Reduced Holey Graphene Oxide for Supercapacitors. *Chem. Commun.* **2017**, *53*, 13225-13228.

[63] Lu, Y.-F.; Lo, S.-T.; Lin, J.-C.; Zhang, W.; Lu, J.-Y.; Liu, F.-H.; Tseng, C.-M.; Lee, Y.-H.; Liang, C.-T.; Li, L-L. Nitrogen-Doped Graphene Sheets Grown by Chemical Vapor Deposition : Synthesis and Influence of Nitrogen Impurities on Carrier Transport. *ACS Nano* **2013**, *7*, 6522-6532.

[64] Liu, M.; Song, Y.; He, S.; Tjiu, W. W.; Pan, J.; Xia, Y.-Y.; Liu, T. Nitrogen-Doped Graphene Nanoribbons as Efficient Metal-Free Electrocatalysts for Oxygen Reduction. *ACS Appl. Mater. Interfaces* **2014**, *6*, 4212-4222.

[65] Wang, G.; Maiyalagan, T.; Wang, X. Review on Recent Progress in Nitrogen-Doped Graphene: Synthesis, Characterization, and Its Potential Applications. *ACS Catal.* **2012**, *2*, 781-794.

[66] Kabsch, W. (2010). *Acta Cryst.* D**66**, 125-132.

[67] Sheldrick, G. M. (2008). Acta Cryst. A**64**, 112-122.

[68] Sheldrick, G. M. (2015). Acta Cryst. A**71**, 3-8.

[69] Sheldrick, G. M. (2015). Acta Cryst. C**71**, 3-8.

[70] Becke, A. D. Density-Functional Thermochemistry. III. The Role of Exact Exchange. *J. Chem. Phys.* **1993**, *98*, 5648−5652.

[71] Lee, C.; Yang, W.; Parr, R. G. Development of the Colle-Salvetti Correlation-Energy Formula into a Functional of the Electron Density. *Phys. Rev. B* **1988**, *37*, 785−789.

[72] Stephens, P. J.; Devlin, F. J.; Chabalowski, C. F.; Frisch, M. J. *Ab Initio* Calculation of Vibrational Adsorption and Circular Dichroism Spectra Using Density Functional Force Fields. *J. Phys. Chem.* **1994**, *98*, 11623−11627.

[73] Vosko, S. H.; Wilk, L.; Nusair, M. Accurate Spin-Dependent Electron Liquid Correlation Energies for Local Spin Density Calculations: A Critical Analysis. *Can. J. Phys.* **1980**, *58*, 1200−1211.

[74] Zhao, Y.; Truhlar, D. G. Computational Characterization and Modeling of Buckyball Tweezers: Density Functional Study of Concave-Convex π-π Interactions. *Phys. Chem. Chem. Phys.* **2008**, *10*, 2813-2818.

[75] Ribeiro, R. F.; Marenich, A. V.; Cramer, C. J.; Truhlar, D. G. Use of Solution-Phase Vibrational Frequencies in Continuum Models for the Free Energy of Solvation. *J. Phys. Chem. B* **2011**, *115*, 14556-14562.

[76] Zhao, Y.; Truhlar, D. G. The MO6 Suite of Density Functionals for Main Group Thermochemistry, Thermochemical Kinetics, Noncovalent Interactions, Excited States, and Transition Elements: Two New Functionals and Systematic Testing for Four MO6-Class Functionals and 12 Other Functionals. *Theor. Chem. Acc.* **2008**, *120*, 215.

[77] Frisch, M. J.; Trucks, G. W.; Schlegel, H. B.; Scuseria, G. E.; Robb, M. A.; Cheeseman, J. R.; Scalmani, G.; Barone, V.; Mennucci, B.; Petersson, G. A.; Nakatsuji, H.; Caricato, M.; Li, X.; Hratchian, H. P.; Izmaylov, A. F.; Bloino, J.; Zheng, G.; Sonnenberg, J. L.; Hada, M.; Ehara, M.; Toyota, K.; Fukuda, R.; Hasegawa, J.; Ishida, M.; Nakajima, T.; Honda, Y.; Kitao, O.; Nakai, H.; Vreven, T.; Montgomery, J. A., Jr.; Peralta, J. E.; Ogliaro, F.; Bearpark, M.; Heyd, J. J.; Brothers, E.; Kudin, K. N.; Staroverov, V. N.; Kobayashi, R.; Normand, J.; Raghavachari, K.; Rendell, A.; Burant, J. C.; Iyengar, S. S.; Tomasi, J.; Cossi, M.; Rega, N.; Millam, N. J.; Klene, M.; Knox, J. E.; Cross, J. B.; Bakken, V.; Adamo, C.; Jaramillo, J.; Gomperts, R.; Stratmann, R. E.; Yazyev, O.; Austin, A. J.; Cammi, R.; Pomelli, C.; Ochterski, J. W.; Martin, R. L.; Morokuma, K.; Zakrzewski, V. G.; Voth, G. A.; Salvador, P.; Dannenberg, J. J.;

Dapprich, S.; Daniels, A. D.; Farkas, Ö.; Foresman, J. B.; Ortiz, J. V.; Cioslowski, J.; Fox, D. J. *Gaussian 09, Revision B.01*; Gaussian, Inc.: Wallingford, CT, 2009.

[78] Legault, C. Y. *CYLview, 1.0 b*; *Université de Sherbrooke* (http://www.cylview.org), 2009.

[79] Watts, K. S.; Dalal, P.; Tebben, A. J.; Cheney, D. L.; Shelley, J. C. Macrocycle Conformational Sampling with MacroModel. *J. Chem. Inf. Model*. **2014**, 54, 2680.

Chapter 4: Lowering the Barrier for the Hopf Reaction – Graphene Nanoribbons Fabricated at Room Temperature

Section 4.1. Abstract

The synthesis of solution-processable graphene nanoribbons (GNRs) remains one of the primary challenges surrounding these semiconducting materials. Our solid-state approach to GNRs follows a two-step process: topochemical polymerization of 1,3-butadiynes to a polydiacetylene (PDA) polymer followed by Hopf cyclization to afford GNRs. These PDAs contain embedded dienyne moieties which are optimally positioned to undergo dual Hopf cyclizations upon heating. Unfortunately, the high annealing temperatures necessary for this second conversion result in sidechain fragmentations, and therefore completely insoluble GNRs. Our prior work with fjord-edge N_2-[8]GNR showed that lower cyclization temperatures help retain these solubilizing sidechains. In this work, we present two norbornadiene based precursors, each ultimately capable of forming a PDA, containing high levels of ring strain designed to lower the energetic barrier of the Hopf cyclization. The synthesis of bis(norbornadienyl)1,3-butadiyne and *trans*-bis(norbornadienyl)enediyne and the application of these and other enediynes to our solid-sate method are discussed.

Section 4.2. Introduction

Since the beginning of modern organic chemistry, scientists have developed a myriad of ways to make carbon-carbon bonds. Among them, alkenes are a particularly common synthetic

handle due to their ease of preparation. Reactions of strained alkenes typically have lower reaction barriers than conventional alkenes, enabling room temperature or catalyst-free transformations that make them synthetically desirable. For example, benzo-fused cycloheptene isomerizes solely into the *trans* form using visible light, introducing ring strain into the molecule.[1] The subsequent fast [3+2] cycloaddition with a variety of hindered azides, including insulin derivatives, to ligate biologically relevant molecules, highlights the versatility of this strained alkene. Within materials chemistry, strained rings have long been a popular choice for ring-opening polymerization of cyclic hydrocarbons such as norbornene, cyclobutene, cyclopropane or cyclooctenes.[2,3] Strained alkenes are also common in cycloadditions and rearrangements, capable of forming complex natural products.[4] To help rationalize the factors that affect alkene reactivity, Houk and Bickelhaupt proposed an activation strain model that predicts reactivity and transition state geometries as a function of activation and distortion.[5,6] They have recently applied this model to analyze reaction rates for transition metal catalyzed reactions, cycloadditions and other cyclizations, reinforcing the importance of strain in alkenes as a synthetic handle.[7] In this work, we sought to utilize strained alkenes as a method of lowering the reaction barrier in the synthesis of graphene nanoribbons (GNR).

Our group has developed a solid-state method for producing GNRs from assembled 1,3-butadiynes via diaryl polydiacetylene (PDA) intermediates.[8] These PDAs are characterized by an alternating enyne backbone and combined with pendant aryl groups, the embedded 1,3-hexadien-5-ynes are crucial to GNR formation (Figure 4.1). Heating the PDAs cause the dienynes to undergo Hopf cyclization and cyclodehydrogenation to form the aromatic core of the GNR. Musso and Hopf first described the cyclization of 1,3-hexadien-5-yne to benzene at 274 °C in 1969.[9] Hopf

later proposed that the dienyne specifically undergoes a 6 π-electrocyclization mechanism to form benzene when heated below 550 °C.[10] He went on to calculate energies for cyclizing the parent

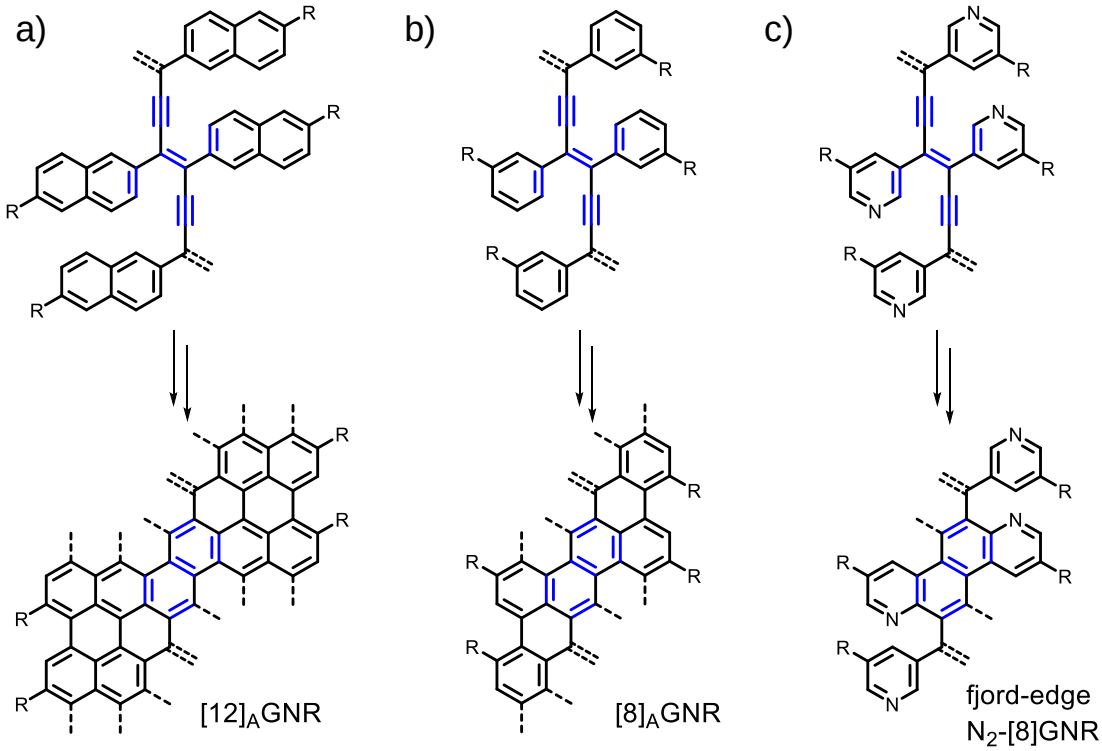

Figure 4.1. Diaryl PDA polymers with embedded dienynes. a) Bis(naphthyl) PDA to $[12]_A$GNR, b) bis(phenyl) PDA to $[8]_A$GNR and c) bis(pyridyl) PDA to fjord-edge N_2[8]GNR.

1,3-hexadien-5-yne, along with benzannulated and cyclic analogues, in effect studying how variations to one of the alkenes affected the overall reaction (Figure 4.2). Relative to the parent 1,3-hexadien-5-yne, the benzannulated system has a higher barrier of about 6 kcal mol^{-1}, likely due to the loss of aromaticity in forming an o-quinoide structure on the way to naphthalene. In contrast, tethering the dienyne into a cyclic system can lower the barrier to room temperature for select rings, 9- and 10- membered cyclic dienynes, as the resulting product contains less ring strain and gains aromaticity. Thus we can see early evidence that subtle changes to the dienyne have

drastic effects on their reactivity. By designing a cyclic strained dienyne with a low reaction battier, we hypothesized that GNRs could be synthesized at room temperature or not much above, rather than at the high temperatures currently required.

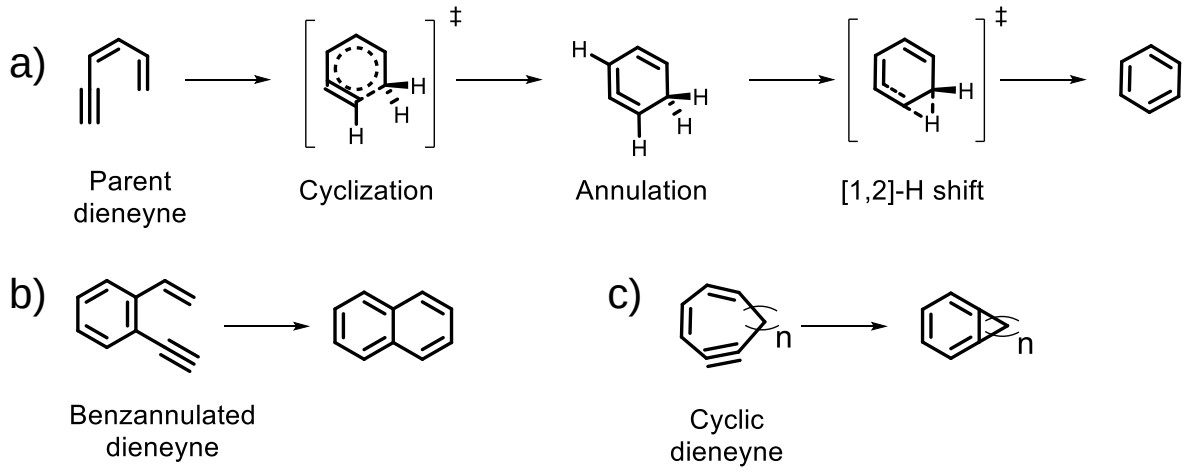

Figure 4.2. a) Mechanism of the Hopf cyclization from the parent 1,3-hexadien-5-yne, b) cyclization of the benzannulated dienyne and c) cyclization of a tethered cyclic dienyne

Lowering the reaction temperature needed for GNR synthesis has dual purpose. From a manufacturing perspective, lower temperatures simplify conditions and reduce energy waste. From a processing standpoint, low annealing temperatures will help retain sidechains on the GNR, keeping them soluble and solution processable. Early comparisons between our work on $[8]_A$GNR[11] and *fjord*-edge N_2[8]GNR (Chapter 3) show that sidechain retention is a function of annealing temperature. Using cross-polarization/magic angle spinning (CP/MAS) ^{13}C solid-state NMR, we could track the loss of the alkynyl carbons as the PDA underwent Hopf cyclization. $[8]_A$GNR completely cyclized after heating to 500-600 °C for 1h, but this was unfortunately concomitant with loss of solubilizing keto and amide sidechains. In contrast our fjord-edge GNRs with nitrogen substitutions cyclized at 330-360 °C after heating for 1h, and thus were able to retain their amide sidechains. UV-vis of a filtered solution of these fjord GNRs in N-methylpyrrolidone

demonstrated the continued solubility of GNRs with sidechains. This would overcome one of the barriers to efficient processing of GNRs, allowing for uniform deposition of individual GNRs for devices or other applications. Thus we designed a strained PDA which could undergo Hopf cyclization.

For each dienyne moiety within the strained PDA, an alkyne and one alkene are formed through polymerization and one the remaining alkene is retained as part of the pendant group. Our approach to GNRs begins with the topochemical polymerization 1,3-butadiynes to form the PDA. Wegner initially reported on a series of 1,3-butadiynes in 1971, which formed PDA polymers under UV light, provided the C_1-$C_{4'}$ distance between alkynyl carbons of neighboring alkynes is within 3.5 Å.[12] Thus the first step to our GNR synthesis begins with identifying 1,3-butadiynes capable of undergoing topochemical polymerization. Over the last few years, we have successfully identified seven different diarylbutadiynes which could be polymerized into $[12]_A$GNR, $[8]_A$GNR and fjord-edge N_2[8]GNR (Figure 4.3). However, these were the product of synthesizing and crystallizing a diverse library of diarylbutadiynes, since no universal method for engineering molecular packing exists. In the case of $[12]_A$GNR, we started from bis(naphthyl)butadiynes and screened the free alcohol, propoxy and methylmethoxy ether sidechains. Only naphthalene substituted with the latter moiety produced crystals with C_1-C_4' within 3.5 Å and, surprisingly, bis(phenyl)butadiyne with methylmethoxy ether sidechains did not crystallize properly. For $[8]_A$GNR, a variety of substitution patterns, *para* vs. *meta*, and sidechain functionalities, keto vs. amido, and sidechain length, methyl, isobutyl, tert-butyl, heptyl and branched were screened before four butadiynes were found to be successful. Dipyridylbutadiyne proved to be the most challenging, as variations on pyridine substitution patterns dominated the success of polymerizations. Although we were able to identify appropriate butadiynes in each case, screening

the various substitutions is time consuming and synthetically laborious. It would instead be preferably to access the PDA via an alternative route. More specifically, a monomer unit capable of forming the PDA, independent of solid-state packing parameters would be desirable. As a result, the corresponding PDA should always be synthetically attainable either via topochemical polymerization of 1,3-butadiynes, or through this alternative monomer.

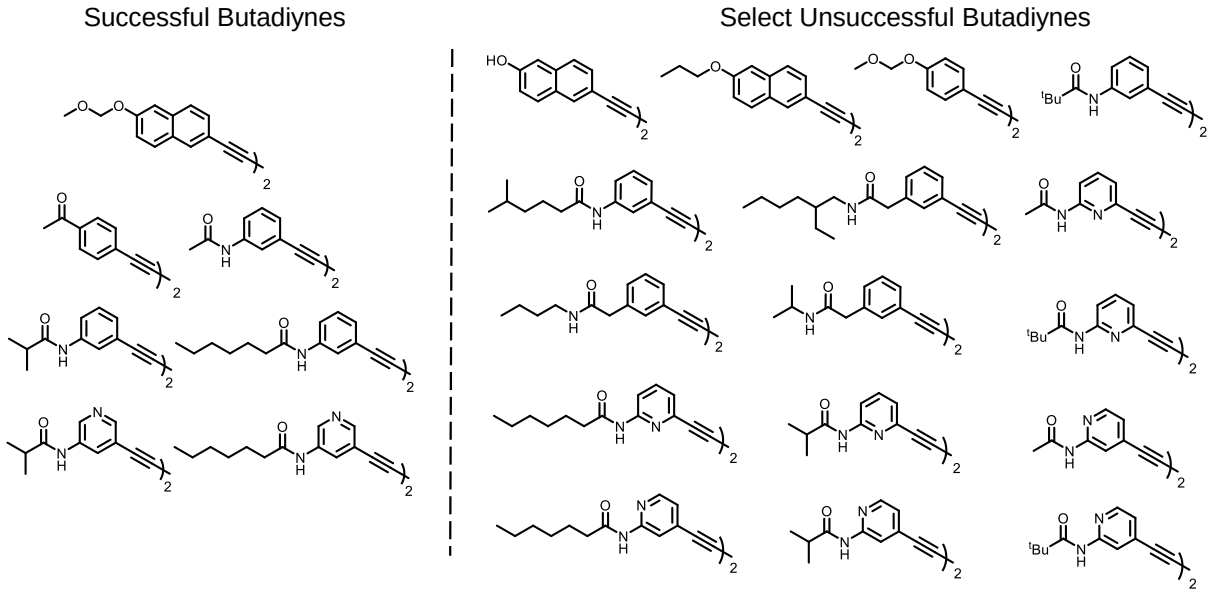

Figure 4.3. Butadiynes that successfully undergo topochemical polymerization and examples of some butadiynes that were unsuccessful.

PDA polymers have an alternating enyne backbone which yields two possible retrosynthetic disconnections: alkene or alkyne. Disconnection at the alkene would undo the topochemical polymerization reaction, as it can be thought of as a 1,4-addition between butadiynes where the newly formed bond is an alkene (Figure 4.4a). Alternatively, disconnection at the alkyne could be the product of alkyne metathesis. This disconnection would require a *trans*-enediyne

monomer unit that allows us to build in the stereochemistry of the PDA. Zhang *et al.* recently developed a molybdenum catalyst for alkyne metathesis, specifically capable of synthesizing PDAs in solution from *trans*-dialkyl enediynes while suppressing formation of smaller dimerized alkynes (Figure 4.4b).[13,14] They have since used the same molybdenum catalyst to synthesize porous poly(aryleneethynylene) networks from the sterically bulky phenyl and adamantly triynes, demonstrating the ability of their catalyst to handle a sterically diverse alkynes.[15] This would allow us to compare our GNR synthesis starting from a strained cyclic 1,3-butadiyne and a strained cyclic enediyne. Success of the latter would serve to diversify the range of accessible PDAs we could convert into GNRs.

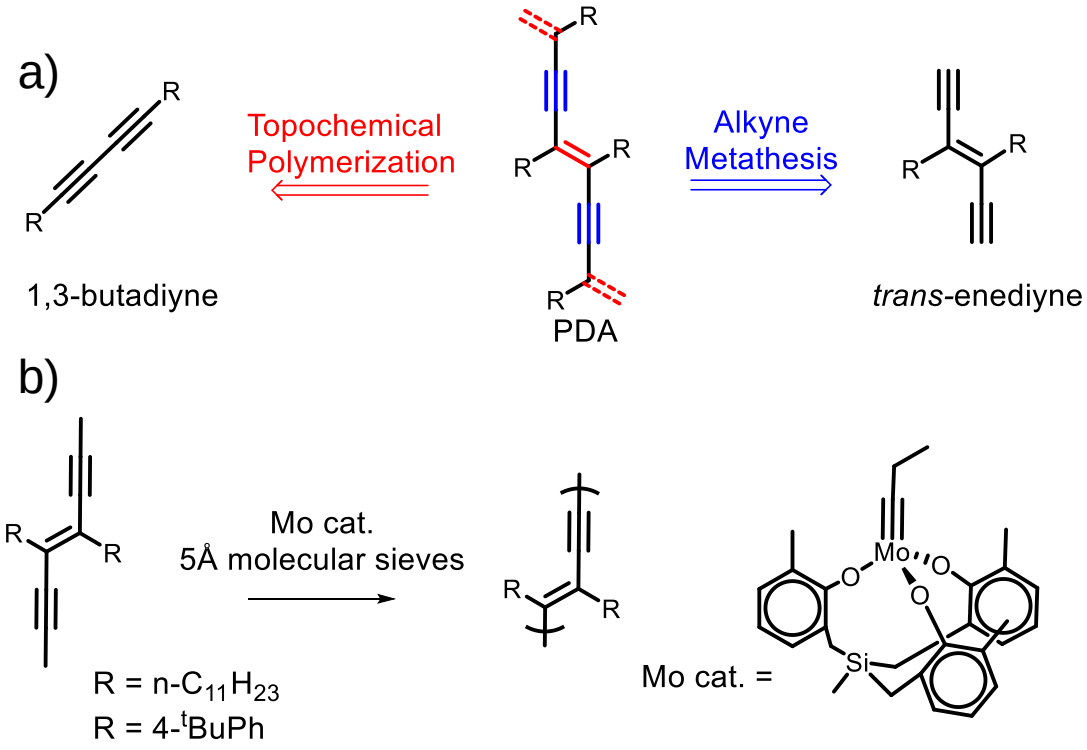

Figure 4.4. a) Retrosynthetic pathways of PDA formation either to 1,3-butadiynes or *trans*-enediynes. b) Solution polymerization of *trans*-enediynes into soluble PDAs.[14]

In this work, we show that calculations on a series of strained cyclic *trans*-enediyne model compounds suggest norbornadiene has a much lower barrier to cyclization than the corresponding diphenyl model, synonymous with our previous work on $[8]_A$GNR. We then proceed to show the synthesis of a bis(norbornadienyl)1,3-butadiyne and a bis(norbornadienyl) *trans*-enediyne as two comparable PDA synthons. Suggestions of further mechanistic studies using this and other *trans*-enediyne monomers are then discussed.

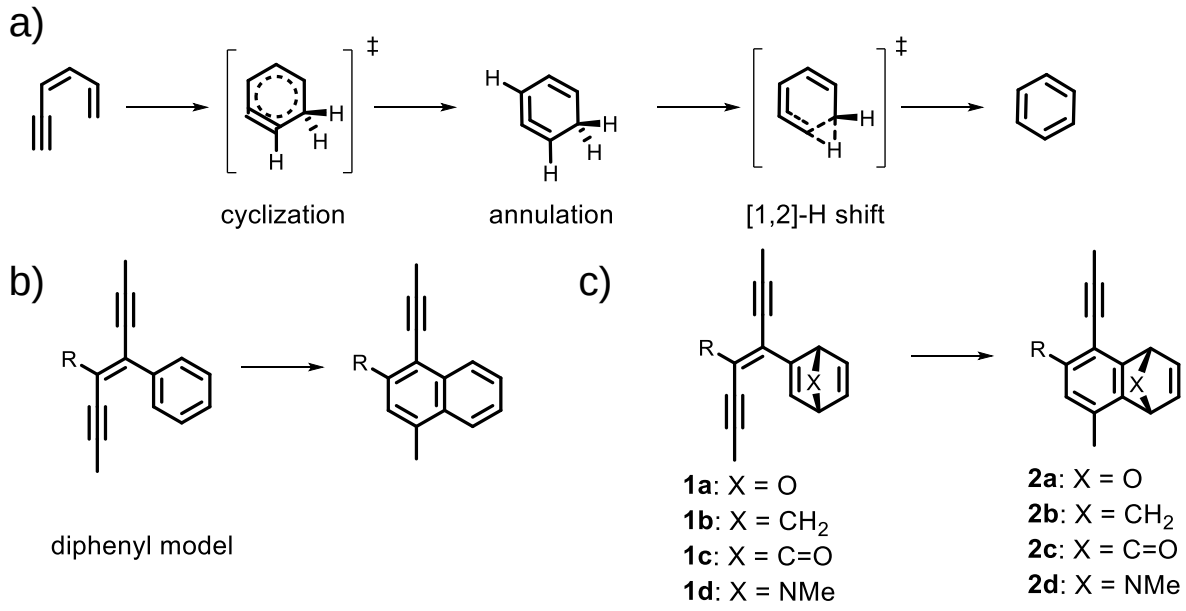

Figure 4.5. a) Intermediates and transition states evaluated during calculations. b) Diphenyl system evaluated by Prall *et al.*[10] c) Strained cyclic *trans*-enediynes evaluated. R = Ph.

Section 4.3. Results and Discussion

Monomer Design. We began with bicyclic rings as an ideal strained alkene due to their tendency to contain higher ring strain, which makes the embedded alkenes more reactive over their monocyclic counterparts.[16,17] Next we evaluated which types of strained bicycles would make an ideal dienyne by using the 6-π electrocyclization mechanism Hopf proposed (Figure 4.5a).[10]

Initial cyclization of the *trans*-1,3-hexadien-5-yne yields an isobenzene intermediated labelled annulation, before undergoing the rate-determining [1,2]-H shift and then rearomatizing to benzene. Their work went on to evaluate the cyclization of the benzannulated system to naphthalene, whose initial [1,2]-H was also the rate-determining step, and more closely relates to the structures found within our PDAs. Our collaborator in the Houk group at UCLA was able to verify the free energies calculated by Hopf and co-workers for the benzannulated enediyne and further calculate free energies for a series of strained cyclic dienynes.[18] Specifically we included the diphenyl model system both to benchmark against the calculation by Hopf and co-workers, and as an analogue for our work with $[8]_A$GNR. Because the temperature needed to cyclize the diphenyl PDA to $[8]_A$GNR is already known, comparing between the diphenyl and strained model systems should provide an estimate differences in cyclizing the strained cyclic PDA. The series of strained bicyclohexadienes was chosen by varying the bridgehead group to O, CH_2, C=O, and NMe. Geometries of the cyclization, annulation, and [1,2]-H shift structures were optimized along the transition from **1a-d** to **2a-d** (Figure 4.5b). As seen in **Table 4.1**, replacing a single phenyl group with these strained systems has an almost 30 kcal mol^{-1} decrease in the rate-limiting [1,2]-H shift step versus the diphenyl system. While all the strained cycles had rate-determining steps within 5 kcal mol^{-1} of each other we decided to pursue the norbornadiene, **1b**, as it is known to undergo cycloaddition reactions under UV light. This known reactivity implies that topochemical polymerization of a bis(norbornadienyl)1,3-butadiyne should not return a PDA with embedded dienynes and reinforce the need for an alternative PDA synthon. If successful, oxanorbornadiene would be another strained cycle of interest due to its similarly low [1,2]-H shift barrier and propensity to form benzene via deoxygenation.[19]

Table 4.1. Calculated Free Energies of the Hopf Cyclization of Model Enediynes.[18] All energies are in kcal mol^{-1}. Structures were optimized in the gas phase using B3LYP/6-31G(d),[20] and single-point calculations were performed using M06-2X/6-311+G(d,p).[21]

	Diphenyl	***1a***	***1b***	***1c***	***1d***
cyclization	52.6	31.5	32.2	36.1	29.8
Annulation	45.5	4.2	3.5	10.4	1.4
H shift	58.4	36.9	39.9	42.2	37.2

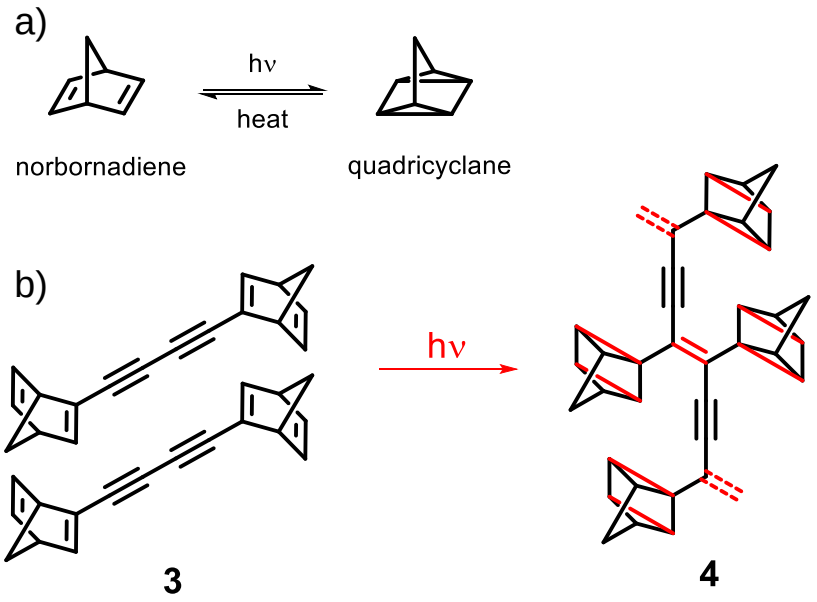

Figure 4.6. a) Interconversion of norbornadiene and quadricyclane. b) Expected result if bis(norbornadienyl)butadiynes underwent topochemical polymerization.

Norbornadienes are known to under cycloaddition reactions in the presence of UV light, as mentioned above. The ring strain and high level of π-orbital overlap between alkenes allow the reversible transformation from norbornadiene to quadricyclane (Figure 4.6a).[22] The conversion

proceeds with high quantum yield and has rendered norbornadienes a popular candidate among Molecular SOlar-Thermal (MOST) energy storage materials.[23,24] This light-induced reaction is potentially problematic as both cycloaddition and topochemical polymerization could occur upon exposure. This would result in PDA **4**, which lacks the 1,3-hexadien-5-yne moiety necessary for Hopf cyclization. Quadricyclane half-life is days to weeks, and thus would prevent conversion of the PDA to GNR.[25] Despite these challenges and because polymerization of the 1,3-butadiyne, **3**, was potentially problematic, norbornadienyl substituents represented an ideal case study for comparing the two PDA synthons. Norbornadienes have mostly been functionalized at the alkenyl positions using electron accepting and donating substituents to create push-pull systems which can tune the absorption window for MOST applications. Common pairings of substituents such as ethynyl-cyano, ethynyl-phenyl, and some ethynyl-linked oligomers has developed a varied library of norbornadiene derivatives.[26,27] Although none of these examples utilized monosubstituted ethynylnorbornadienes, we predicted that similar conditions could be applied to synthesize **3** in a straightforward fashion.

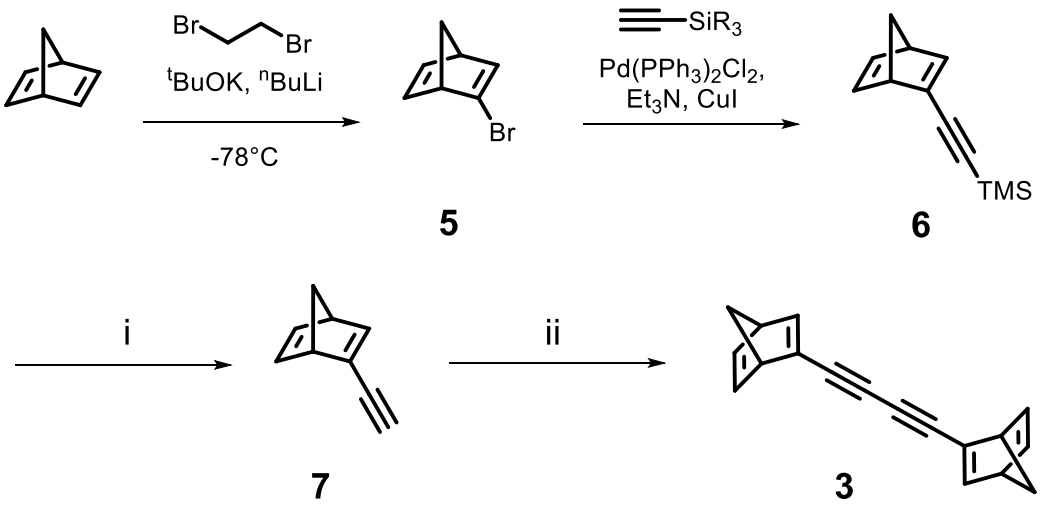

Scheme 4.1. Synthetic plan for bis(norbornadienyl)butadiyne **3**. Reaction conditions: i) TBAF in THF at either 25 °C or -78 °C. ii) CuI and TMEDA in DCM or Acetone; $Cu(OAc)_2$ in pyridine.

Synthesis of bis(norbornadienyl)1,3-butadiyne **(3)**: Initially we brominated norbornadiene through radical addition using 1,2-dibromoethane as the bromine source. This was followed by addition of ^{t}BuOK to dehydrobrominate and give exclusively the monobrominated norbornadiene **2**. Next we were able to attach the alkyne using a standard Sonogashira reaction with TMS acetylene to form **5**. Our initial attempt to deprotect the TMS group with TBAF at 25 °C resulted in isolation of no mass, suggesting the terminal alkyne **7** was potentially volatile. Subsequently we attempted to deprotect the alkyne in the presence of alkyne coupling reagents by adding titrating in a solution of TBAF. Both Hay, CuI and TMEDA, and Glaser, $Cu(OAc)_2$ and pyridine, conditions were tested also at both 25°C and at -78 °C, but none yielded the desired diyne **3**. Referencing the synthetic work done with ethynyl-substituted norbornadienes for MOST applications, the chromophores were di- or tri-substituted systems, whose larger molecular weight potentially reduced the volatility of the corresponding terminal alkyne. Some groups noted in passing that the terminal alkyne of di- and trisubstituted norbornadiene was entirely avoided.[24]

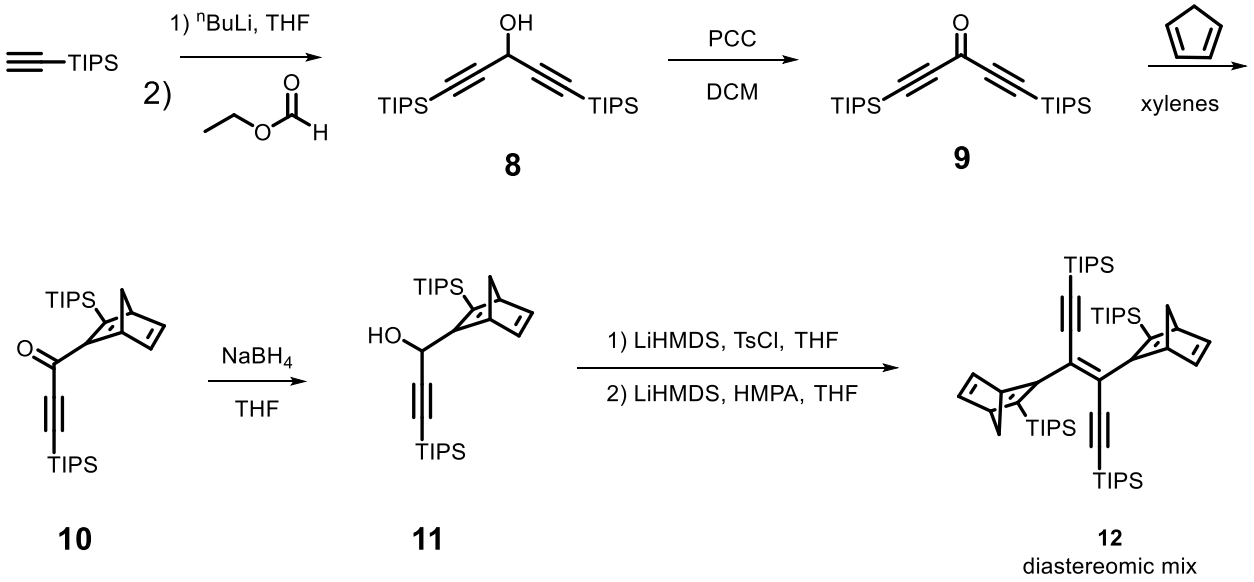

Scheme 4.2. Synthetic plan for bis(norbornadienyl) *trans*-enediyne **12**.

This provided the rationale for our unsuccessful attempts to synthesize diyne **3,** and gave an example of a 1,3-butadiyne which is synthetically unattainable and thus motivates the need for an alternative PDA synthon.

Synthesis of bis(norbornadienyl) trans-enediyne: We then turned our attention to synthesizing the related bis(norbornadienyl) *trans*-enediyne, based on work from Jones and Hynd on stereoselectively coupling propargyl halides to enediynes.[28,29] To avoid expensive palladium-catalyzed routes to enediynes, they utilized a metallocarbenoid intermediate to initially couple propargyl halides to halodiynes.[30] Dehydrohaloelimination of the halodiyne yields predominantly the *trans*-enediyne. Jones and Hynd rationalized the high levels of stereoselectivity in the elimination reaction was caused by steric interactions of the vinyl groups in the halodiyne intermediate. Syn-elimination of the halodiyne would result in gauche interactions between the vinyl groups whereas anti-elimination avoids them entirely. As the vinyl substituents become sterically more cumbersome, the gauche interaction become increasing unfavorably, resulting in predominantly anti-elimination to the *trans*-enediyne. As expected, the authors found that TIPS and bulkier cyclic groups demonstrated greater stereocontrol than TES, TMS, or linear alkanes with preference for the *trans*-enediyne stereoisomer.

To attain the appropriate propargyl bromide for the above coupling, we began by synthesizing a diyne which could later act as the dienophile in a Diels-Alder reaction to yield a norbornadiene (Scheme 4.2). TIPS acetylide underwent nucleophilic attack of ethyl formate to yield the symmetric diyne **8**. This was then oxidized using PCC to the corresponding ketone, **9**, in order to activate the dienophile for the subsequent Diels-Alder reaction. Refluxing **9** with cyclopentadiene in xylenes overnight installed the norbornadiene moiety. During the course of this reaction, we observed solely addition of cyclopentadiene to one alkyne and not both, likely due to

large steric hindrance after the first bicycle is attached. Reduction of **10** to the propargyl alcohol proceeds in moderate yield, ~50 %, and is isolated as a mixture of diastereomers. Attempts to drive the reduction step with additional $NaBH_4$ were unsuccessful, likely due to steric shielding around the ketone. Conversion of the propargyl alcohol to the propargyl bromide was assumed to proceed with Br_2 and PPh_3, but the bromide could not be isolated. Attempts to brominate and couple in one pot were also unsuccessful, prompting us to consider changing the propargyl leaving group. We opted to transform the alcohol to a tosyl group and, without isolating, subject the new alkyne to coupling conditions. In line with the work by Jones and Hynd, we believed this would give exclusively the *trans*-enediyne. We were able to produce small amounts of the *trans*-enediynes, using the tosyl intermediate, but could not unfortunately isolate the enediyne. As such we were unable to attempt polymerization to the PDA using alkyne metathesis, but instead are evaluating alternative routes that would increase the yield.

Some alternative routes we are considering include removal of the alkynyl TIPS group prior to forming the propargyl alcohol. This is expected to both increase the yield of the reduction and reduce the stabilization of the metallocarbenoid formed during halodiyne formation. Alternatively, should this not have improvements on the coupling yield, we could convert ketone **10** into an imine and a thioketone. A Barton-Kellog reaction between these fragments produces an episulfide, which can be oxidized to yield the alkene. These conditions have been successful in forming hindered alkenes, which is ideal for our substrate.[31,32] Beyond polymerization to the PDA, we can directly heat the bis(norbornadienyl) *trans*-enediyne to validate the calculations performed on the energetic barrier to Hopf cyclization.

Section 4.4. Conclusion

Here we have shown the synthesis of an alternative PDA synthon which avoids the solid-state requirements necessary for topochemical polymerization. Alkyne metathesis of an analogous enediyne would form the alternating enyne backbone of PDAs. To achieve this, we synthesized a bis(norbornadienyl)*trans*-enediyne through a metallocarbenoid coupling reaction that circumvents the need for more costly palladium catalysts. Current work is under way to optimize the yield of the final coupling reaction for gram-scale synthesis. This norbornadienyl PDA should have a lower cyclization barrier to the GNR, which would broaden the possible types of solution-processable GNRs attainable using our group's solid-state approach.

Section 4.5. Experimental Details

General procedures: Chemical reagents were obtained from commercial sources and used without further purification. Unless otherwise noted, all reactions were performed under argon at 25 °C. Silicycle (Siliflash P60) silica gel 60 (240-400 mesh) was used for all column chromatography. Solution NMR spectra were obtained on a Bruker AV500 instrument.

(1S,4R)-2-bromobicyclo[2.2.1]hepta-2,5-diene (5)

Norbornadiene (5.00 mL, 59.9 mmol, 1.0 eq) was added to a flame dried flask at -35 °C with THF (60 mL). ^{t}BuOK (6.73 g, 59.9 mmol, 1.0eq) was added slowly before cooling the reaction to -78 °C. n-BuLi (59.9 mmol, 1.0 eq) was added dropwise then the reaction stirred for 30 minutes and allowed to warm to -60 °C. Dibromoethane (6.22 mL, 71.9 mmol. 1.2 eq) was added dropwise and

allowed to warm to room temperature over 6 hours. H_2O and Et_2O were added to quench the reaction. The organic phase was then washed with brine twice and water twice, dried over $MgSO_4$ and concentrated. The product was used without purification, 9.88g (96%). ^{1}H NMR (400 MHz, $CDCl_3$): δ (ppm) 6.89 (dd, *J* = 5.1, 3.2 Hz, 1H), 6.77 (dd, *J* = 5.1, 3.2 Hz, 1H), 6.64 (d, *J* = 3.2 Hz, 1H), 3.58-3.62 (m, 1H), 3.46-3.49 (m, 1H), 2.66 (dt, *J* = 6.1, 1.7 Hz, 1H), 2.07 (dt, *J* = 6.1, 1.7 Hz, 1H); ^{13}C NMR (125 MHz, $CDCl_3$): δ (ppm) 142.8, 141.8, 139.6, 136.7, 73.8, 58.3, 51.6.

(((1S,4R)-bicyclo[2.2.1]hepta-2,5-dien-2-yl)ethynyl)trimethylsilane (6)

To a crude solution of **5** (1.36 g, 7.89 mmol, 1.0 eq) in toluene (20 mL) was added $Pd(PPh_3)_2Cl_2$ (140 mg, 0.20 mmol, .025 eq) and CuI (38 mg, 0.20 mmol, .025 eq). The reaction was sparged with argon for 20 minutes before TMS acetylene (2.27 mL, 15.9 mmol, 2.0 eq) and DIPA (15.9 mmol, 2.0 eq) were added. The reaction was monitored by TLC and once complete, passed through celite. The filtrate was concentrated and purified on silica gel using hexanes as eluent to give 535 mg (36%) of the pure product as a clear oil. ^{1}H NMR (400 MHz, $CDCl_3$): δ (ppm) 6.97 (d, *J* = 3.2 Hz, 1H), 6.6 (dd, *J* = 5.3, 3.2 Hz, 1H), 6.69 (dd, *J* = 5.3, 3.2 Hz, 1H), 3.61-3.65 (m, 1H), 3.56-3.59 (m, 1H), 2.11 (dt, *J* = 6.4, 1.6 Hz, 1H), 2.04 (dt, *J* = 6.4, 1.6 Hz, 1H), 0.19 (s, 9H); ^{13}C NMR (125 MHz, $CDCl_3$): δ (ppm) 149.5, 142.8, 142.1, 138.2, 102.4, 101.6, 73.6, 55.7, 51.0, 0.04.

1,5-Bis(triisopropylsilyl)penta-1,4-diyn-3-ol (8)

To a flame dried flask under argon was added ethynyltriisopropylsilane (3.00 mL, 13.3 mmol, 2.1 eq) and THF (22 mL). The flask was cooled to -78 °C before n-BuLi (13.3 mmol, 2.1 eq) was

added dropwise and allowed to stir for 10 minutes. A solution of ethyl formate (0.51 mL, 6.35 mmol, 1.0 eq) in THF (4 mL) was added dropwise at -78 °C. The flask was allowed to warm to room temperature and stirred for 20 minutes before quenching with saturated NH_4Cl. The solution was extracted with CH_2Cl_2 three times; organic layers were pooled and then washed with H_2O. The organic layer was dried over $MgSO_4$ before concentrating. The mixture was purified on silica using 10:1 hexanes: ethyl acetate to give 2.31 g (93%) of the title compound as a clear oil. ^1H NMR (400 MHz, $CDCl_3$): δ (ppm) 5.10 (d, *J* = 7.9 Hz, 1H), 2.18 (d, *J* = 7.9 Hz, 1H), 1.09-1.11 (m, 42H).

1,5-Bis(triisopropylsilyl)penta-1,4-diyn-3-one (9)

1,5-Bis(triisopropylsilyl)penta-1,4-diyn-3-ol, **8**, (1.01 g, 2.58 mmol, 1.0 eq) was dissolved in CH_2Cl_2 (25 mL) at room temperature. Pyridinium Chlorochromate (1.11 g, 5.15 mmol, 2.0 eq), celite (1.00 g) and powdered molecular sieves (1.00 g) were added and everything stirred at room temperature for 3 hours. After completion measured by TLC, the mixture was filtered through a silica plug and concentrated. The title compound, **9**, 958 mg (95%), collected as a clear oil. ^1H NMR (400 MHz, $CDCl_3$): δ (ppm) 1.09-1.11 (m, 42 H); ^{13}C NMR (125 MHz, $CDCl_3$): δ (ppm) 159.9, 105.3, 97.6, 18.4, 11.0.

3-(Triisopropylsilyl)-1-((1R,4S)-3-(triisopropylsilyl)bicyclo[2.2.1]hepta-2,5-dien-2-yl)prop-2-yn-1-one (10)

Freshly distilled cyclopentadiene (0.41 mL, 4.88 mmol. 2.0 eq) was added to a solution of **9** (951 mg, 2.44 mmol, 1.0 eq) in xylenes (12 mL) and heated to 140 °C under argon to stir for 24 hours. The mixture was cooled to room temperature and concentrated before purifying on silica gel column chromatography with 2% ethyl acetate in hexanes. 998 mg (91%) of the product was collected. ^{1}H NMR (400 MHz, $CDCl_3$): δ (ppm) 6.89 (dd, *J* = 5.4, 3.2 Hz, 1H), 6.68 (dd, *J* = 5.4, 3.2 Hz, 1H) 4.16-4.18 (m, 1H), 4.06-4.09 (m, 1H), 2.00 (qt, *J* = 6.6, 1.5 Hz, 2H), 1.09-1.11 (m, 42H) ; ^{13}C NMR (125 MHz, $CDCl_3$): δ (ppm) 175.9, 170.9,165.9, 142.4, 141.8, 105.3, 95.7, 71.7, 58.6, 54.7, 18.9, 18.9, 18.5, 11.9, 11.08.

3-(Triisopropylsilyl)-1-((1R,4S)-3-(triisopropylsilyl)bicyclo[2.2.1]hepta-2,5-dien-2-yl)prop-2-yn-1-ol (11)

A solution of **10** (238 mg, 0.529 mmol, 1.0 eq) in THF (1.5 mL) was chilled to 0 °C under argon. $NaBH_4$ (40 mg, 1.06 mmol, 2.0 eq) was added slowly and the mixture allowed warm to room temperature then stirred for 30 min. The mixture was quenched with saturated NH_4Cl and extracted three times with ethyl acetate. The organic layers were pooled and washed with brine before drying over $MgSO_4$ and concentrating. After purification using column chromatography in 1% ethyl acetate in hexanes, 155 mg (64%) of clear oil was isolated as a mixture of diastereomeric products. ^{1}H NMR (400 MHz, $CDCl_3$): δ (ppm) 6.86 (dd, *J* = 5.1, 3.1 Hz, 1H), 6.78 (dd, *J* = 5.1, 3.1 Hz, 1H), 6.68 (dd, *J* = 5.2, 3.0 Hz, 1H) 6.56 (dd, *J* = 5.2, 3.0 Hz, 1H), 5.22 (d, *J* = 1.7 Hz, 2H) 3.88-3.91 (m, 1H), 3.82-3.84 (m, 1H), 3.74-3.77 (m, 2H) 1.89 (dd *J* = 5.5, 1.3 Hz, 2H) 1.04-1.08 (m,

42H); ^{13}C NMR (125 MHz, $CDCl_3$): δ (ppm) 142.9, 141.9, 123.6, 104.2, 85.6, 72.6, 61.9, 53.0, 18.6, 18.5, 11.1.

((E)-3-((1R,4S)-3-(triisopropylsilyl)bicyclo[2.2.1]hepta-2,5-dien-2-yl)-4-(3-(triisopropylsilyl)bicyclo[2.2.1]hepta-2,5-dien-2-yl)hexa-3-en-1,5-diyne-1,6-diyl)bis(triisopropylsilane) (12)

To a solution of **11** (92 mg, 0.20 mmol, 1.0 eq) in THF (0.6 mL) at 0 °C LiHMDS (0.22 mL, 0.22 mmol, 1.1 eq) was added dropwise. Then p-toluenesulfonyl chloride (43 mg, 0.22 mmol, 1.1 eq) was added and the mixture allowed to warm to room temperature before stirring for 30 min. In a separate flask, LiHMDS (0.22 mL, 0.22 mmol, 1.1 eq) and HMPA (0.04 mL, 0.22 mmol, 1.1 eq) were mixed in THF (0.5 mL) for 10 minutes. This mixture was added dropwise to the original flask at – 90 °C and stirred for 30 min at – 90 °C. After warming to room temperature, the reaction was quenched with aqueous NH_4Cl, diluted with H_2O and extracted three times with Et_2O. The organic layers were pooled and washed with brine before drying over $MgSO_4$ and concentrating. The crude mixture contained small amounts of **12** as detected by NMR. ^{1}H NMR (400 MHz, $CDCl_3$): δ (ppm) 6.82-6.87 (m, 2H), 6.53-6.58 (m, 2H), 3.80-3.85 (m, 2H), 3.73-3.78 (m,2 H), 2.16 (t, *J* = 7.8 Hz, 4H), 1.49-1.63 (m, 84H).

Section 4.6. Appendix C

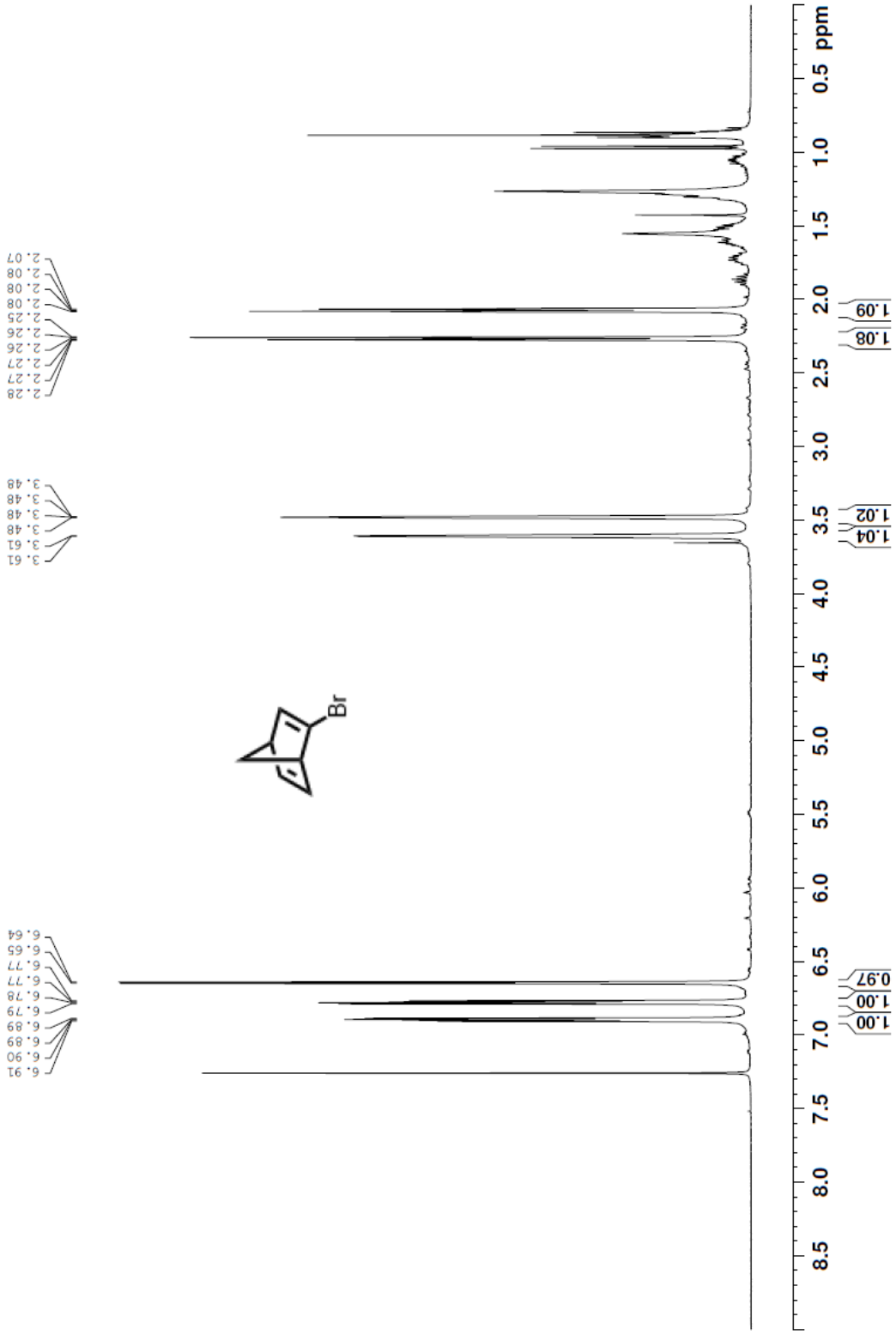

Figure A1. ^{1}H NMR spectrum of compound **5** in $CDCl_3$.

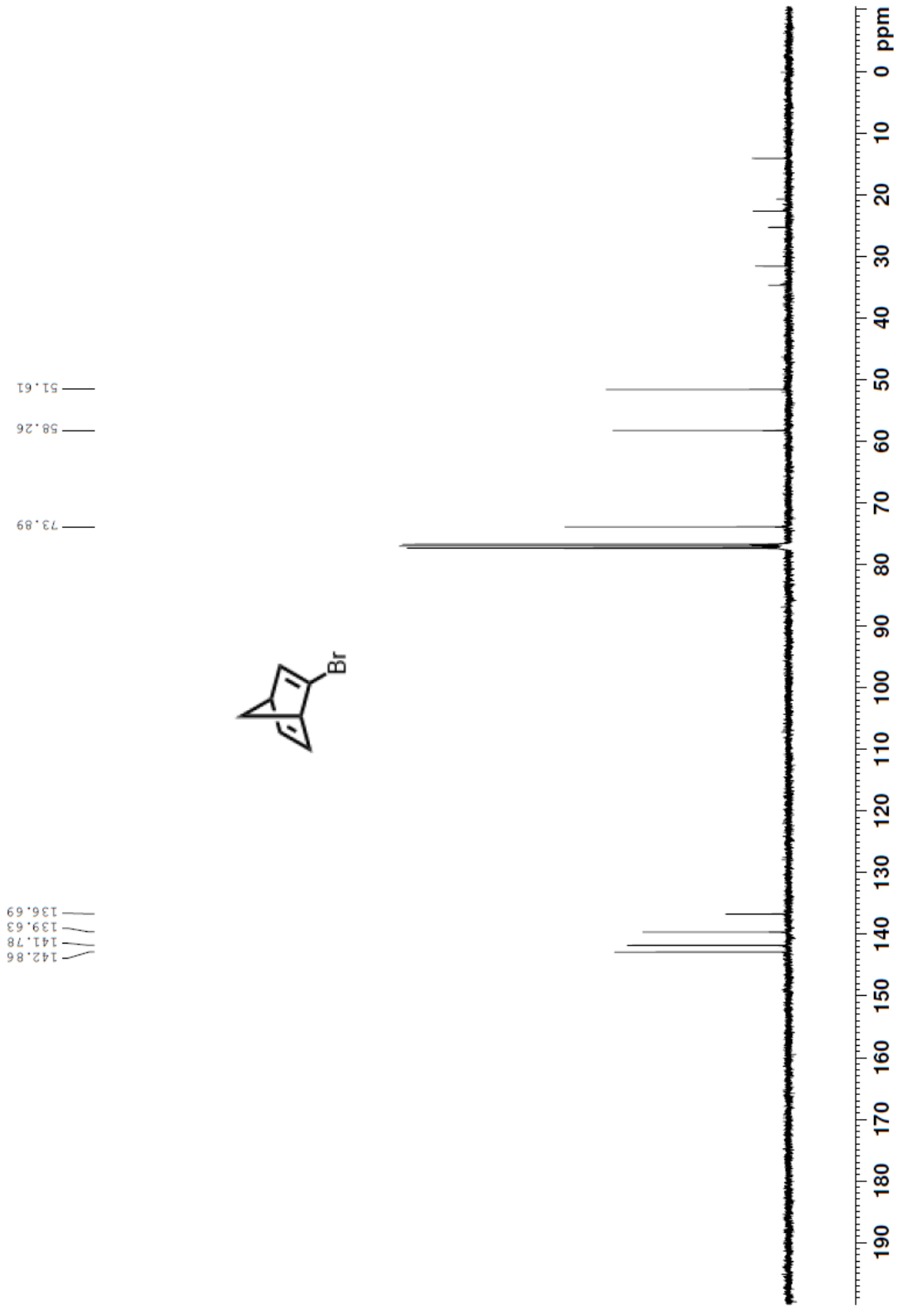

Figure A2. ^{13}C NMR spectrum of compound **5** in $CDCl_3$.

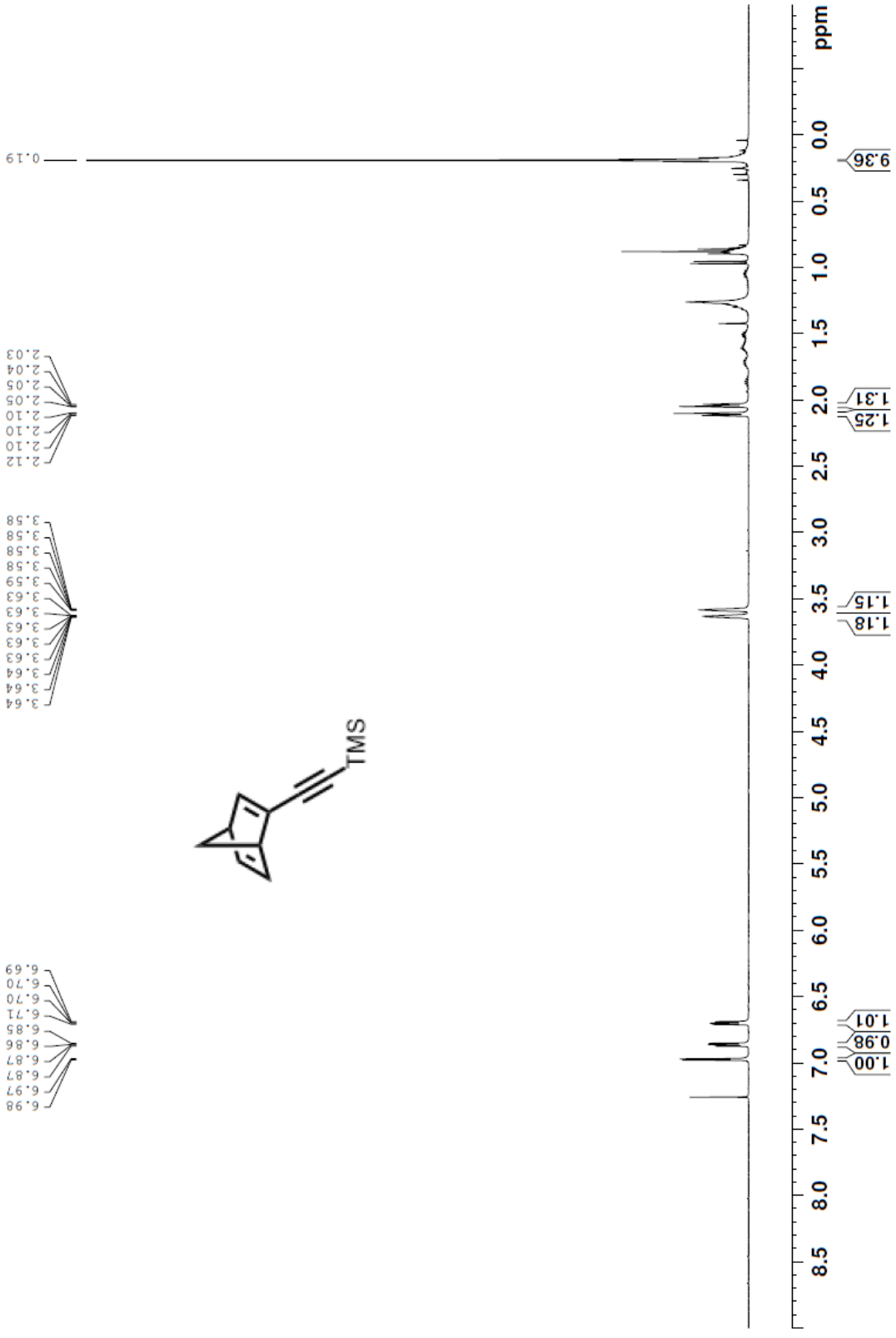

Figure A3. ^{1}H NMR spectrum of compound **6** in $CDCl_3$.

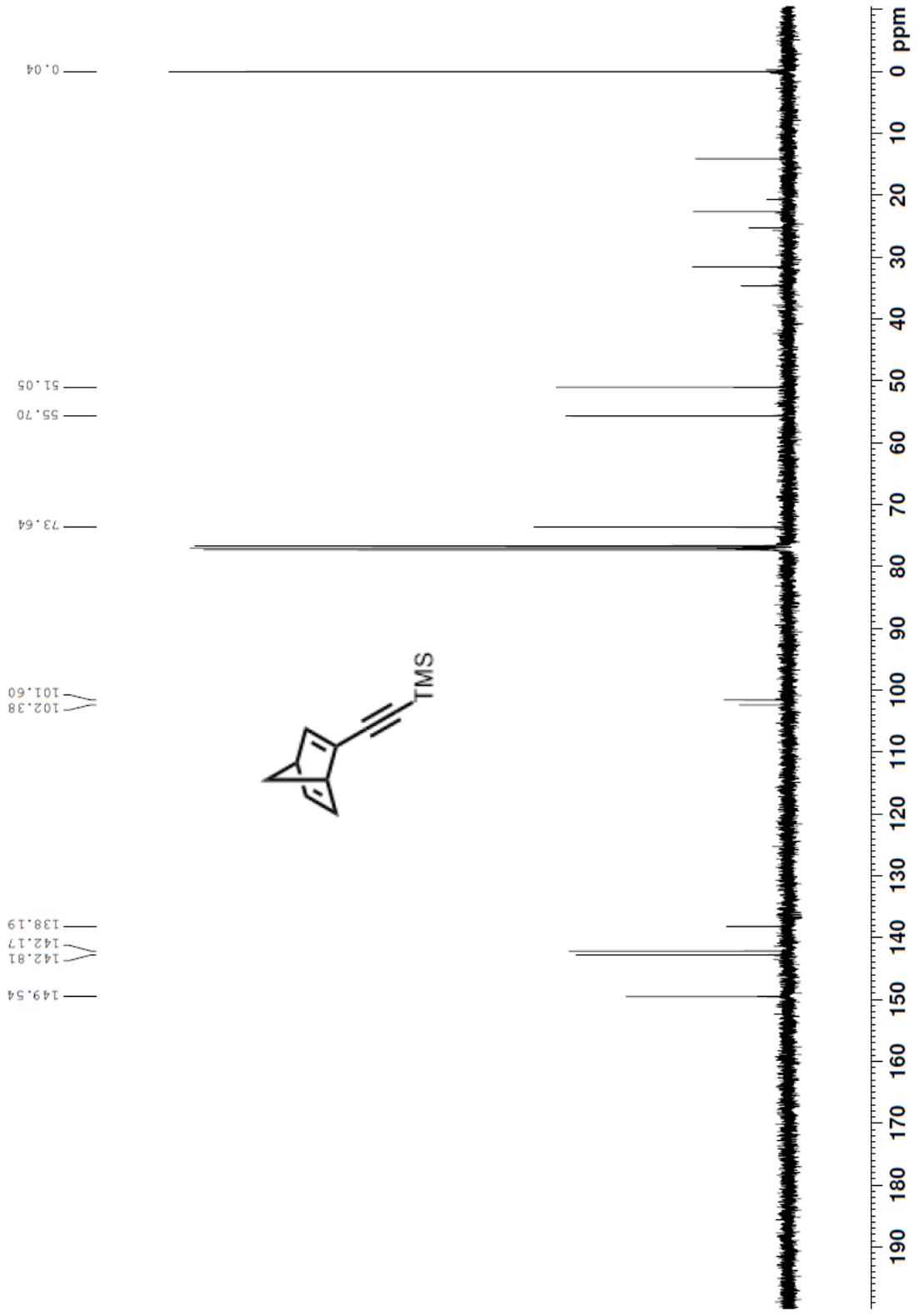

Figure A4. ^{13}C NMR spectrum of compound **6** in $CDCl_3$.

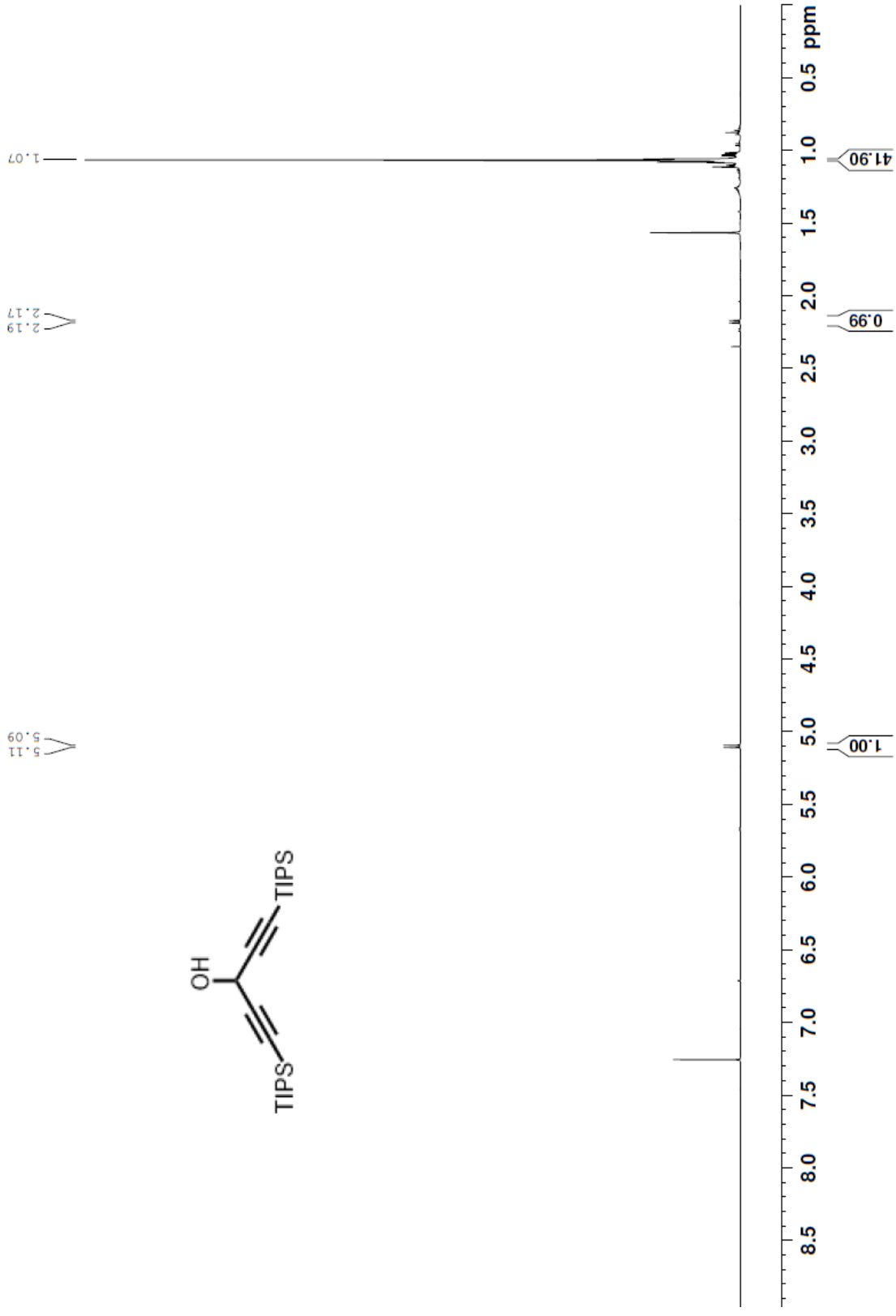

Figure A5. ^{1}H NMR spectrum of compound **8** in $CDCl_3$.

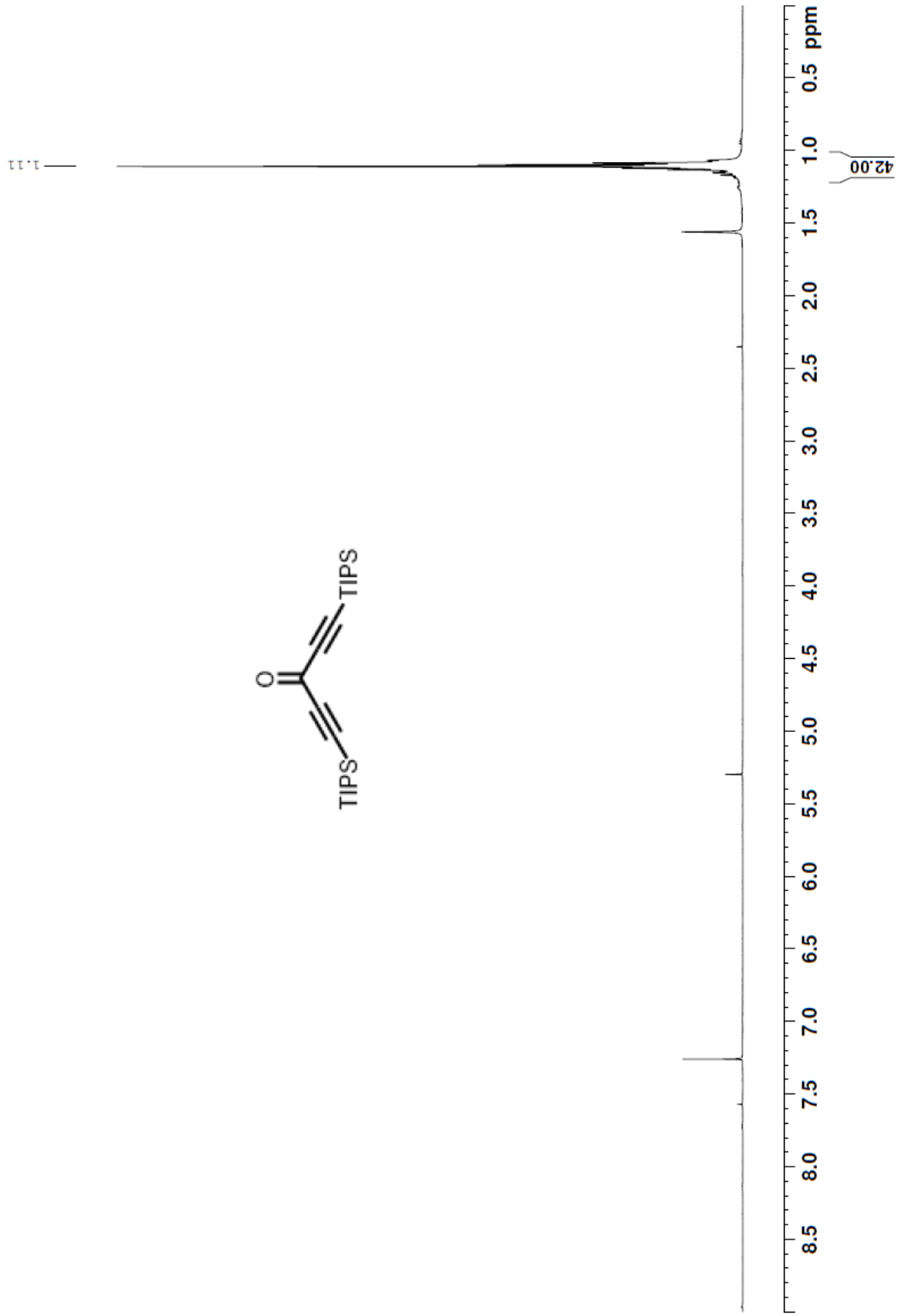

Figure A6. ^{1}H NMR spectrum of compound **9** in $CDCl_3$.

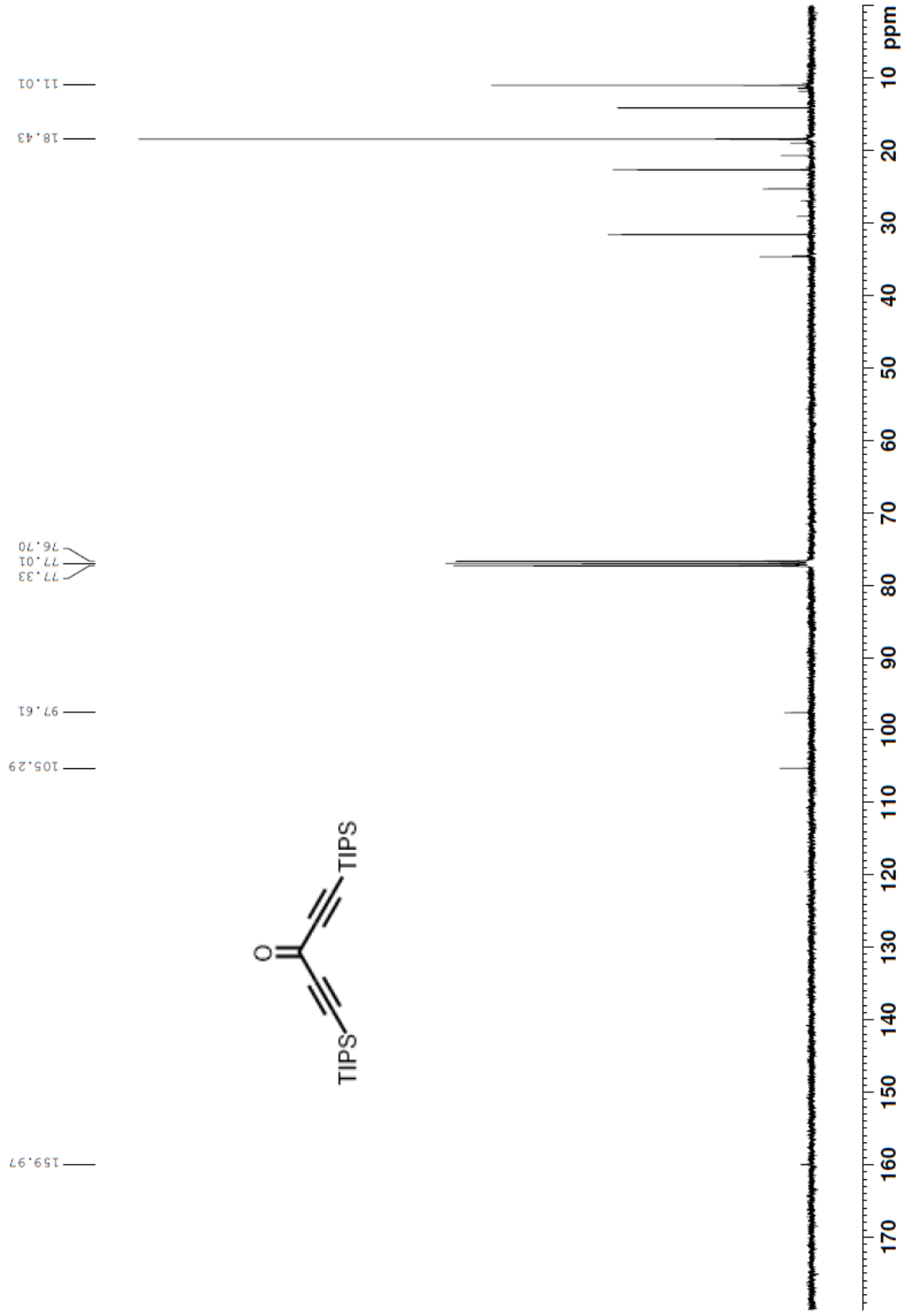

Figure A7. ^{13}C NMR spectrum of compound **9** in $CDCl_3$.

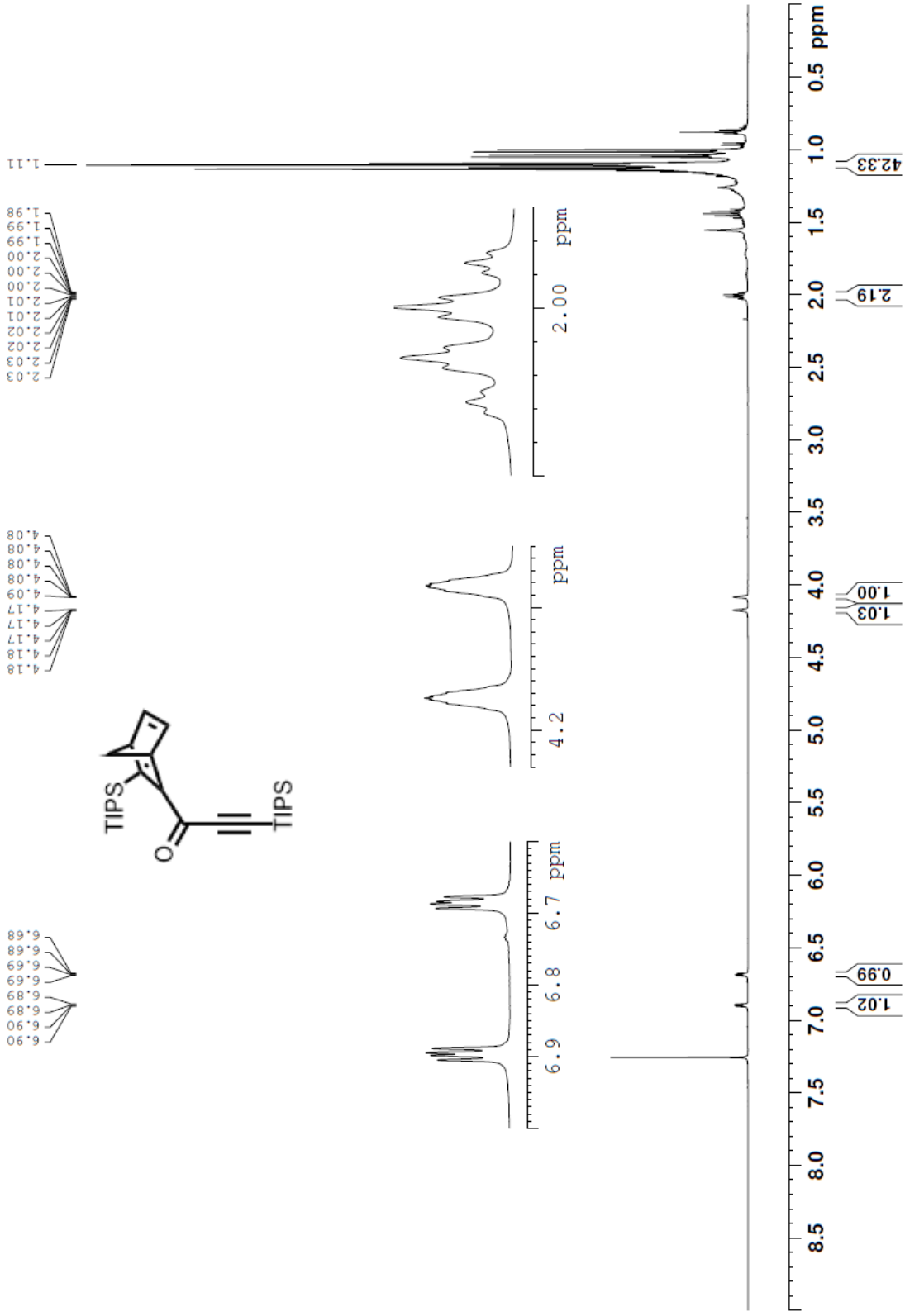

Figure A8. ^{1}H NMR spectrum of compound **10** in $CDCl_3$.

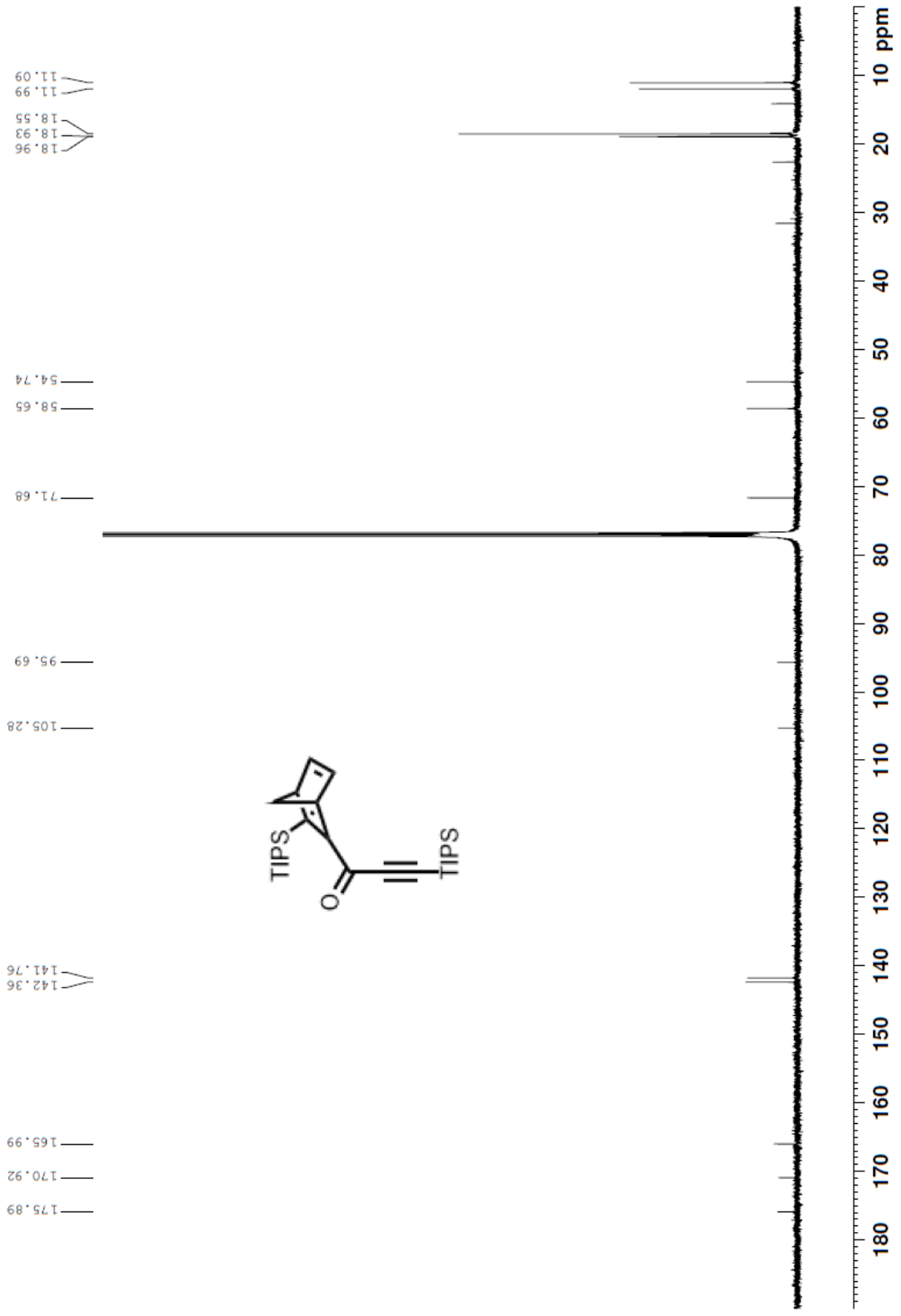

Figure A9. ^{13}C NMR spectrum of compound **10** in $CDCl_3$.

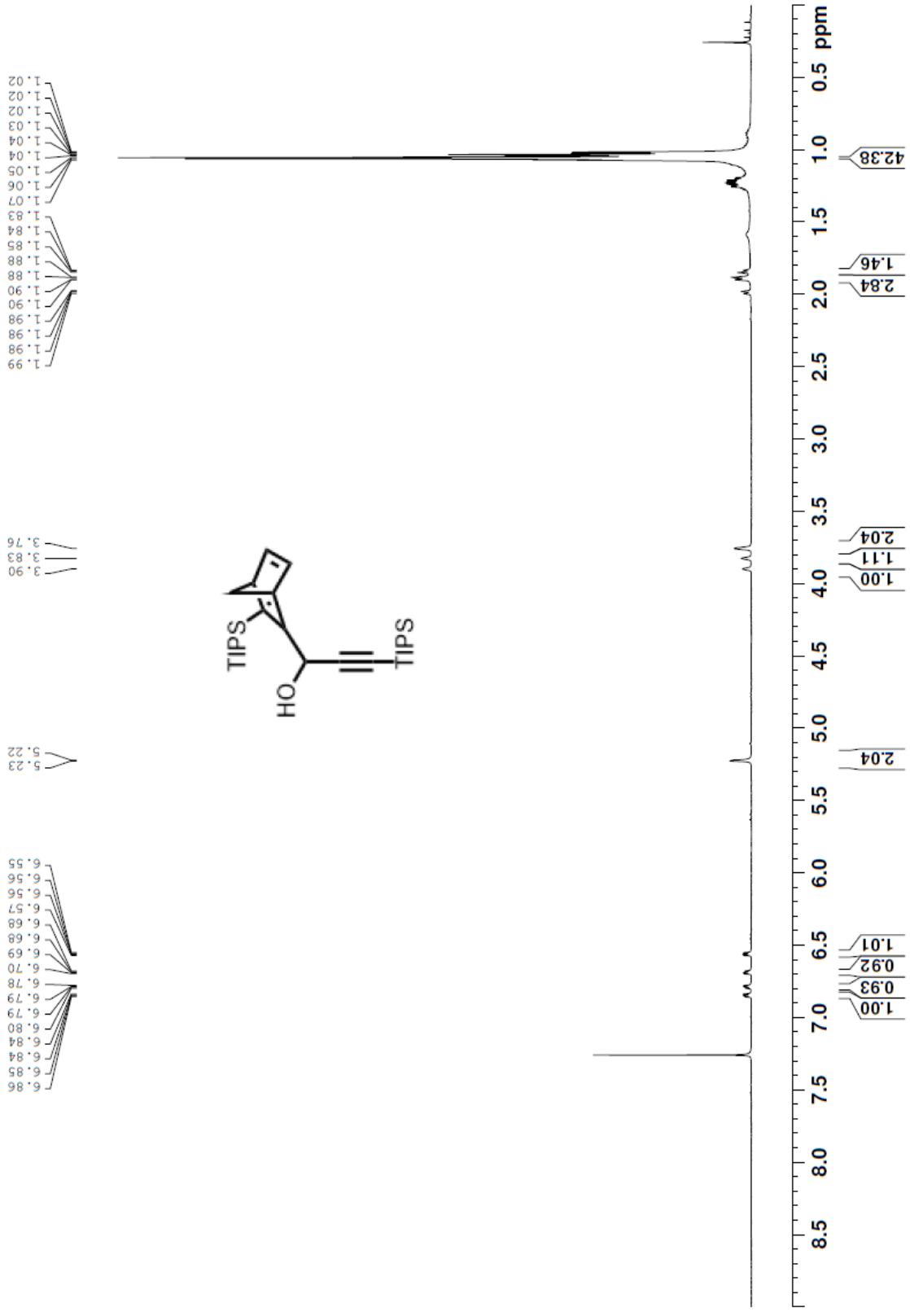

Figure A10. ^{1}H NMR spectrum of compound **11** in $CDCl_3$.

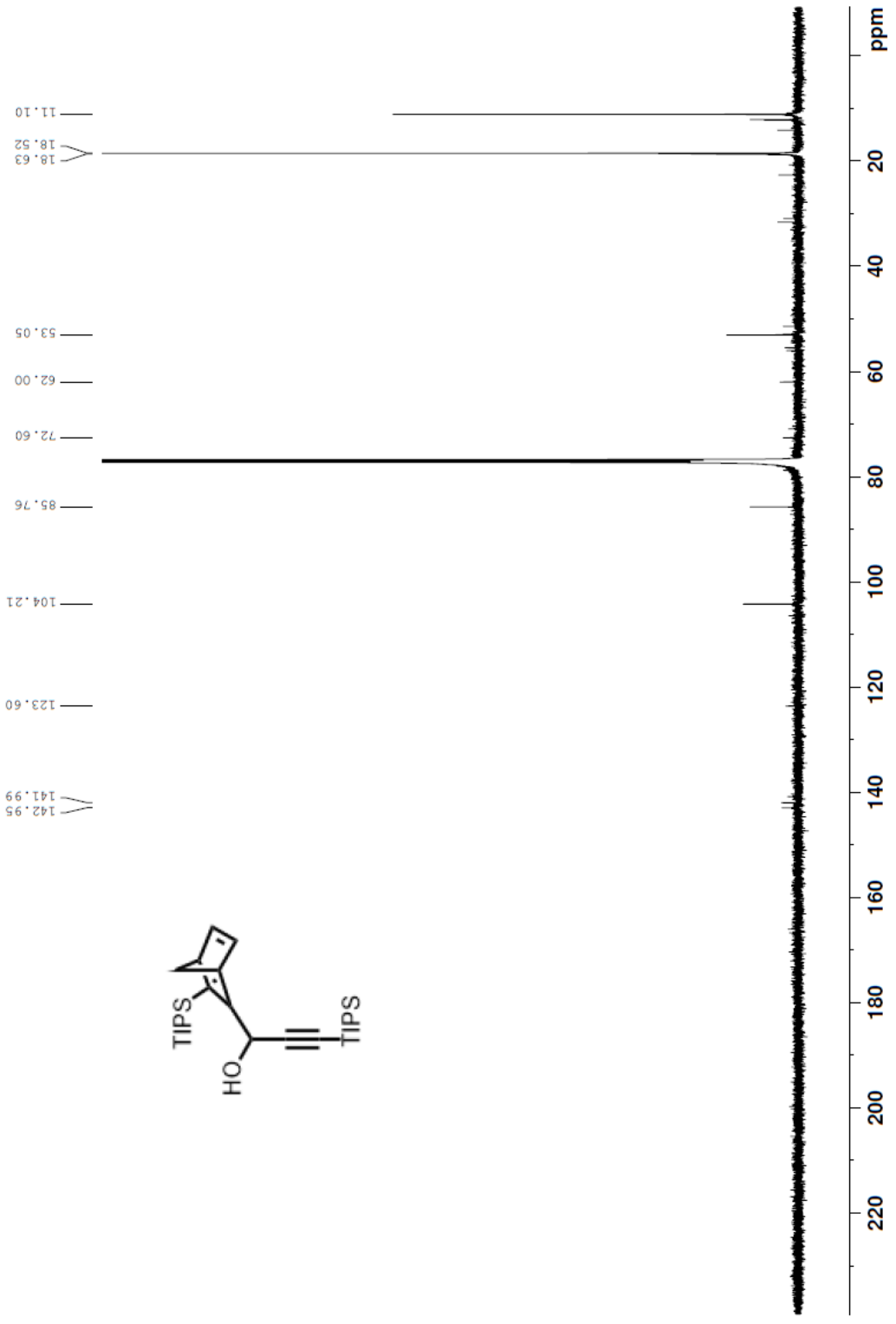

Figure A11. ^{13}C NMR spectrum of compound **11** in $CDCl_3$.

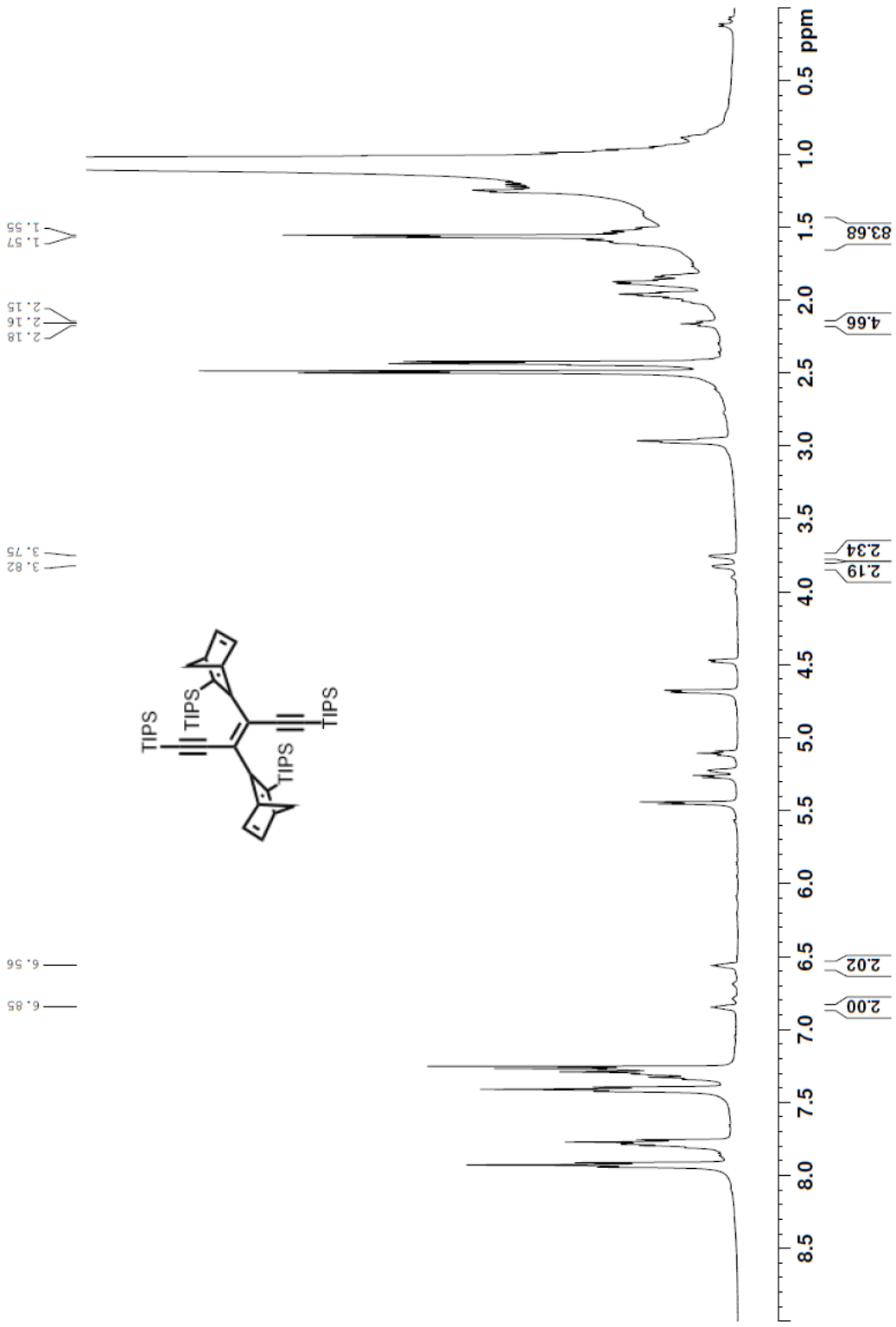

Figure A12. ^{1}H NMR spectrum of crude compound **12** in $CDCl_3$. Selected and integrated peaks correspond to compound **12**.

References

[1] Singh, K.; Fennell, C. J.; Coutsias, E. A.; Latifi, R.; Hartson, S.; Weaver, J. D. Light Harvesting for Rapid and Selective Reactions: Click Chemistry with Strain-Loadable Alkenes. *Chem* **2018**, *4*, 124-137.

[2] Bielawski, C. W.; Grubbs, R. H. Living Ring-Opening metathesis Polymerization. *Prog. Polym. Sci.* **2007**, *32*, 1-29.

[3] Lynde, B. E.; Maust, R. L.; Li, P.; Lee, D. C.; Jasti, R.; Boydston, A. J. Ring-Opening Metathesis Polymerization of a Strained Stilbene-Based Macrocyclic Monomer. *Mater. Chem. Front.* **2020**, *4*, 252-256.

[4] Wilson, M. R.; Taylor, R. E. Strained Alkenes in Natural Product Synthesis. *Angew. Chem. Int. Ed.* **2013**, *52*, 4078-4087.

[5] Van Zeist, W.-J.; Bickelhaupt, F. M. The Activation Strain Model of Chemical Reactivity. *Org. Biomol. Chem.* **2010**, *8*, 3118-3127.

[6] Schoenebeck, F.; Ess, D. H.; Jones, G. O.; Houk, K. N. Reactivity and Regioselectivity in 1,3-Dipolar Cycloadditions of Azides to Strained Alkynes and Alkenes: A Computational Study. *J. Am. Chem. Soc.* **2009**, *131*, 8121-8133.

[7] Bickelhaupt, F. M.; Houk, K. N. Analyzing Reaction Rates with the Distortion/Interaction-Activation Strain Model. *Angew. Chem. Int. Ed.* **2017**, *56*, 10070-10086.

[8] Jordan, R. S.; Wang, Y.; McCurdy, R. D.; Yeung, M. T.; Marsh, K. L.; Khan, S. I.; Kaner, R. B.; Rubin, Y. Synthesis of Graphene Nanoribbons via the Topochemical Polymerization and Subsequent Aromatization of a Diacetylene Precursor. *Chem* **2016**, *1*, 78-90.

[9] Hopf, H.; Musso, H. Preparation of Benzene by Pyrolysis of *cis*- and *trans*-1,3-Hexadien-5-ynes. *Angew. Chem. Int. Ed.* **1969**, *8*, 680.

[10] Prall, M.; Krüger, A.; Schreiner, P. R.; Hopf, H. The Cyclization of Parent and Cyclic Hexa-1,3-dien-5-ynes – A Combined Theoretical and Experimental Study. *Chem. Eur. J.* **2001**, *7*, 4386-4394.

[11] Jordan, R. S.; Li, Y. L.; Lin, C.-W.; McCurdy, R. D.; Lin, J. B.; Brosmer, J. L.; Marsh, K. L.; Khan, S. I.; Houk, K. N.; Rubin, Y. Synthesis of $N = 8$ Armchair Graphene Nanoribbons from Four Distinct Polydiacetylenes. *J. Am. Chem. Soc.* **2017**, *138*, 15878-15890.

[12] Wegner, G. Topochemical Reactions of Monomers with Conjugated Triple-Bonds. *Makromolekul. Chem.* **1972**, *154*, 35-48.

[13] Yang, H.; Liu, Z.; Zhang, W. Multidentate Triphenolsilane-Based Alkyne Metathesis Catalysts. *Adv. Synth. Catal.* **2013**, *25*, 885-890.

[14] Hu, K.; Yang, H.; Zhang, W.; Qin, Y. Solution Processable Polydiacetylenes (PDAs) Through Acyclic Enediyne Metathesis Polymerization. *Chem. Sci,* **2013**, *4***,** 3649-3653**.**

[15] Yang, H.; Zhu, Y.; Du, Y.; Tan, D.; Jin, Y.; Zhang, W. Aromatic-Rich Hydrocarbon Porous Networks through Alkyne Metathesis. *Mater. Chem. Front.* **2017**, *1*, 1369-1372.

[16] Khoury, P. R.; Goddard, J. D.; Tam, W. Ring Strain Energies: Substituted Rings, Norbornanes, Norbornenes, and Norbornadienes. *Tetrahedron* **2004**, *60*, 8103-8112.

[17] Howell, J.; Goddard, J. D.; Tam, W. A Relative Approach for Determining Ring Strain Energies of Heterobicyclic Alkenes. *Tetrahedron* **2009**, *65*, 4562-2568.

[18] Lin, J. B. (2018). *Computational Studies of Organic Electronic Materials* [Doctoral dissertation, University of California, Los Angeles]. ProQuest ID: Lin_ucla_0031D_17403.

[19] Xing, Y. D.; Huang, N. A. Deoxygenation of 7-oxabicyclo[2.2.1]hepta-2,5-diene Systems to Substituted Benzenes by Titanium Tetrachloride-Lithium Aluminum Hydride. *J. Org. Chem.* **1982**, *47*, 140-142.

[20] (a) Becke, A. D. *J. Chem. Phys.* **1993**, *98*, 5648−5652. (b) Lee, C.; Yang, W.; Parr, R. G. Phys. Rev. B: *Condens. Matter Mater. Phys.* **1988**, *37*, 785−789. (c) Stephens, P. J.; Devlin, F. J.; Chabalowski, C. F.; Frisch, M. J. *J. Phys. Chem.* **1994**, *98*, 11623−11627. (d) Vosko, S. H.; Wilk, L.; Nusair, M. *Can. J. Phys.* **1980**, *58*, 1200−1211.

[21] Vosko, S. H.; Wilk, L.; Nusair, M. *Can. J. Phys.* **1980**, *58*, 1200−1211.

[22] Hammond, G. S.; Turro, N. J.; Fisher, A. Photosensitized Cycloaddition Reactions. *J. Am. Chem. Soc.* **1961**, *83*, 4674-4675.

[23] Quant, M.; Lennartson, A.; Dreos, A.; Kuisma, M.; Erhart, P.; Börjesson, K.; Moth-Poulsen, K. Low Molecular Weight Norbornadiene Derivatives for Molecular Solar-Thermal Energy Storage. *Chem. Eur. J.* **2016**, *22*, 13265-13274.

[24] Mansø, M.; Petersen, A. U.; Wang, Z.; Erhart, P.; Nielsen, M. B.; Moth-Pouslen, K. Molecular Solar Thermal Energy Storage in Photoswitch Oligomers Increases Energy Density and Storage Times. *Nat. Commun.* **2018**, *9*, 1945.

[25] Peterson, A. U.; Hofmann, A. I.; Fillols, M.; Mansø, M.; Jevric, M.; Wang, Z.; Sumby, C. J.; Müller, C.; Moth-Poulsen, K. Solar Energy Storage by Molecular Norbornadiene-Quadricyclane Photoswitches: Polymer Film Devices. *Adv. Sci.* **2019**, *6*, 1900367.

[26] Peterson, A. U.; Jevric, M.; Moth-Poulsen, K. Triazole-Functionalized Norbornadiene-Quadricyclane Photoswitches for Solar Energy Storage. *Eur. J. Org. Chem.* **2018**, *32*, 4465-4474.

[27] Tebikachew, B. E.; Li, H. B.; Pirrotta, A.; Börjesson, K.; Solomon, G. C.; Hihath, J.; Moth-Poulsen, K. Effect of Ring Strain on the Charge Transport of a Robust Norbornadiene-Quadricyclane-Based Molecular Photoswitch. *J. Phys. Chem. C.* **2017**, *121*, 7094-7100.

[28] Hynd, G.; Jones, G. B.; Plourde II, G. W.; Wright, J. M. Stereoselective Access to Substituted Enediyne Building Blocks. *Tet. Lett.* **1999**, *40*, 4481-4484.

[29] Jones, G. B.; Wright, J. M.; Plourde II, G. W.; Hynd, G.; Huber, R. S.; Mathews, J. E. A Direct and Stereocontrolled Route to Conjugated Enediynes. *J. Am. Chem. Soc.* **2000**, *122*, 1937-1944.

[30] Huber, R. S.; Jones, G. B.; A Mild and Efficient Route to the Pharmacophore of the Enediyne Antitumor Agents – (Z)-1,6-[Bis(trimethylsilyl)]-Hex-3-ene-1,5-diyne via a Novel Carbenoid Coupling Reaction. *Tet. Lett.* **1994**, *35*, 2655-2658.

[31] Mussons, M. J.; Raposo, C.; Anaya, J.; Grande, M.; Morán, J. R.; Caballero, M. C. Molecular Receptor Design for the Complexing of Dibutylmalonic Acid. *J. Chem. Soc., Perkin Trans. 1*, **1992**, 3125-3127.

[32] Barton, D. H. R.; Guziec, F. S.; Shahak, J.; Shahak, I. Olefin Synthesis by a Two-Fold Extrusion Processes. Part II. Synthesis of Some Very Hindered Olefins. *J. Chem. Soc., Perkin Trans. 1*, **1974**, 1794-1799.

Chapter 5: Design Rules for Straightening Conjugated Polymer Electrolyte Chains for OPV Applications

Section 5.1. Abstract

Semiconducting polymers are a versatile class of materials for many (opto)electronic applications, including organic photovoltaics (OPVs). These polymers, however, are inherently disordered and suffer from poor conductivities due to bends and kinks in the polymer chain along the conjugated backbone. In an effort to address polymer disorder we have been developing methods to straighten polymer chains by creating amphiphilic conjugated polyelectrolytes (CPEs) that self-assemble in water into cylindrical micelles. Initial work utilized an alternating thiophene-fluorene copolymer that was partly ordered, and this work refines our design rules for polymer assembly with the synthesis and characterization of the more ordered, micelle-forming polymer, poly(cyclopentadithiophene-alt-thiophene) (PCT). Solution phase self-assembly into micelles is observed using small-angle X-ray scattering (SAXS) and cryo-TEM. Both inter-micelle aggregation and disorder are characterized using a range of SAXS fitting methods. We find that refining our previous design rules by pairing the subunit bond angles between the alternating, non-identical monomers in the copolymer increases the propensity for the polymer to assemble into well-ordered cylindrical micelles.

Section 5.2. Introduction

Semiconducting polymers are a useful class of optoelectronic materials because of their solution processability, low cost, and structural tunability. These factors make them widely accessible across a range of organic electronic devices including photovoltaics, thermoelectrics, light-emitting diodes, and transistors.[1-4] However, semiconducting polymers suffer from intrinsic disorder that disrupts their conjugated π-system, resulting in decreased conductivity and overall device performance. Because disorder can be so detrimental to polymer device performance, extensive efforts across the field have been made to induce order in semiconducting polymers. In general, semiconducting polymers conduct charge carriers via two methods: along the backbone of the polymer chain through π-conjugation or by chain-to-chain hopping within ordered crystalline π-stacked domains. As such, many of the efforts to increase the order in semiconducting polymers approach this problem either by increasing the polymer crystallinity to encourage π-overlap, or by straightening polymer chains to facilitate along the chain transport.

Many groups have aimed to increase the overall crystallinity of semiconducting polymer films, as crystallinity, and therefore π-stacking and conductivity through the π-stacks, has long been demonstrated to be strongly correlated.[5,6] Film processing conditions including solvent choice, substrate choice, deposition speed, and temperature have all been used to tune polymer crystallinity.[7,8] Furthermore, post-casting treatments including thermal and solvent annealing are used as routine methods to increase polymer crystallinity.[9] Alternatively, polymer morphology can be tuned at the monomer level through sidechain engineering. This approach has demonstrated an increase in crystallinity, and therefore device performance for a variety of applications.[10-13] Alternatively, polymer order and intrinsic carrier mobility can be increased by straightening the polymer chains to eliminate inherent trap states where the conjugation is broken. For example,

polymer chains have been straightened by incorporating them into host-guest systems of aligned nanopores, or via mechanical rubbing, which can increase conductivity by up to three orders of magnitude relative to analogous unaligned systems.[14-16]

While these post-synthetic processing methods have been shown to be promising in increasing polymer order and conductivity, they are not likely to be applicable at a larger scale, because they require special processing that negates many of the attractive aspects of easily processable plastic electronics. In this work, we thus expand upon our previous set of design rules to synthesize a conjugated polyelectrolyte (CPE) that will spontaneously self-assemble into straight polymer micelles in solution as a route to introduce intrinsic order into polymer system. CPEs are polymers that consist of a π-conjugated backbone with charged sidechains, allowing for processing and self-assembly in polar solvents. CPEs are also commonly used as fluorescent sensors in biological systems, thanks to their unique combination of water solubility and easy to measure optical properties.[17-20] In addition, their ion conducting abilities make CPEs effective interlayer agents in organic electronics such as solar cells and FETs.[21,22]

We previously implemented a set of design rules that take advantage of the unique properties of CPEs to create a conjugated system that self-assembles into inherently straight micelles and can be applicable in organic electronics.[23-25] The design rules for our polymer system were as follows: 1) a hydrophobic conjugated backbone and charged sidechains to create amphiphilic behavior, 2) an alternating copolymer system so that the charged sidechains are all on one side of the polymer, when the subunits lie in a perfect coplanar conformation, 3) sidechains that are branched off an sp3 hybridized carbon within the π-conjugated backbone hinders π-stacking and create a 3D wedge-shape that can assemble into a cylindrical structure. With these design rules in mind, we have extensively studied poly(fluorene-alt-thiophene) (PFT, Figure 5.1),

an alternating copolymer with a rigid hydrophobic conjugated backbone and charged hydrophilic sidechains that are all on the same side of the polymer chain.[23-25] This alternating copolymer CPE structure creates a driving force for the formation of cylindrical micelles in aqueous solutions. Studies of the optical and structural properties of PFT revealed the expected cylindrical micelle assembly, along with efficient charge transfer properties to acceptor molecules interacting with these micelles.

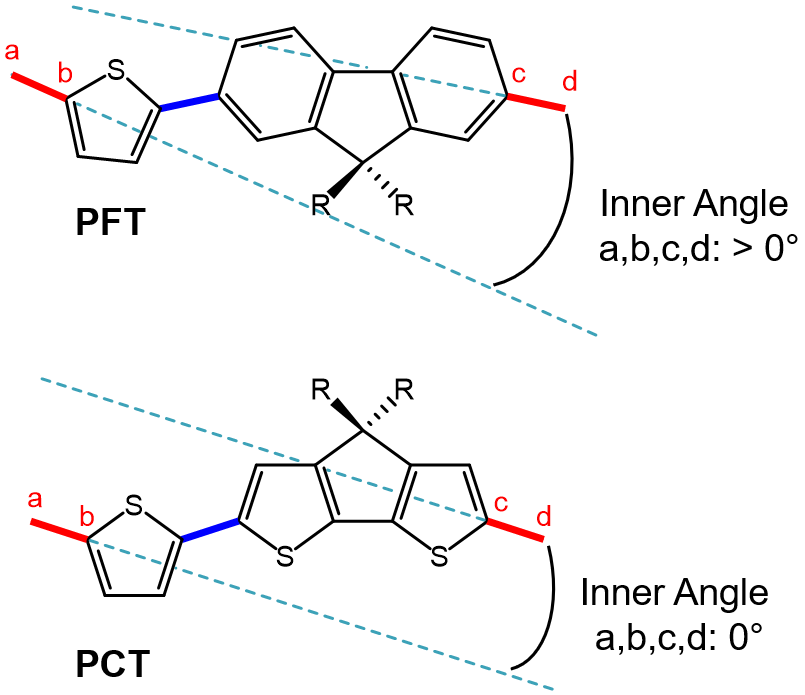

Figure 5.1. Comparison of bond angle matching between PFT and PCT demonstrating that the bond angles of the monomer units in PCT result in an internal angle of 0º

In the present work, we expand on this alternating copolymer amphiphilic design rule to develop a new polymer system by adding a 4th rule: matching alternating monomer bond angles such that the internal angle of the polymer chain is 0º, thus forcing the individual polymer chains to be as straight as possible within the self-assembled micelle. For this new work, by exchanging the fluorene with cyclopentadithiophene subunits, we synthesized poly(cyclopentadithiophene-alt-

thiophene) (PCT), whose structure is shown in Figure 5.1. We hypothesize that this new structure will demonstrate two advantages over the previously studied PFT. As compared to the fluorene unit in PFT, the cyclopentadithiophene subunit and thiophene moieties have matched connecting angles, resulting in a straighter polymer backbone as demonstrated in Figure 5.1. Upon self-assembly, this straighter backbone should result in less disordered cylindrical micelles, in comparison to what we observed in the PFT system. In addition to straightening the polymer chains, cyclopentadithiophene units absorb well in the visible spectrum,[26] making this polymer much more applicable for use in organic photovoltaics.

Herein, we study the expansion of our design rule for straight cylindrical CPE self-assembly in water using a combination of cryo- electron microscopy (cryoEM), solution small-angle X-ray scattering (SAXS), and Dammin bead modeling of the SAXS scattering data. Overall, we demonstrate that our design rules allow for making straighter amphiphilic polymer chains having a tunable band gap.

Section 5.3. Results and Discussion

As demonstrated in Scheme 1, the colinear structure of amphiphilic PCT is achieved by using cyclopentadithiophene as one of the monomeric units and by incorporating hydrophilic ammonium sidechains along the backbone of the polymer. We found that it is much easier to introduce these sidechains via a double Michael addition of N,N-dimethylacrylamide at the sp3 carbon of the cyclopentadithiophene moiety, which considerably enhances the yields of the intermediates compared to the more traditional double alkylation approach with $ClCH_2CH_2CH_2NMe_2$.[21-23] The latter, in our case, resulted in complete loss of the expensive

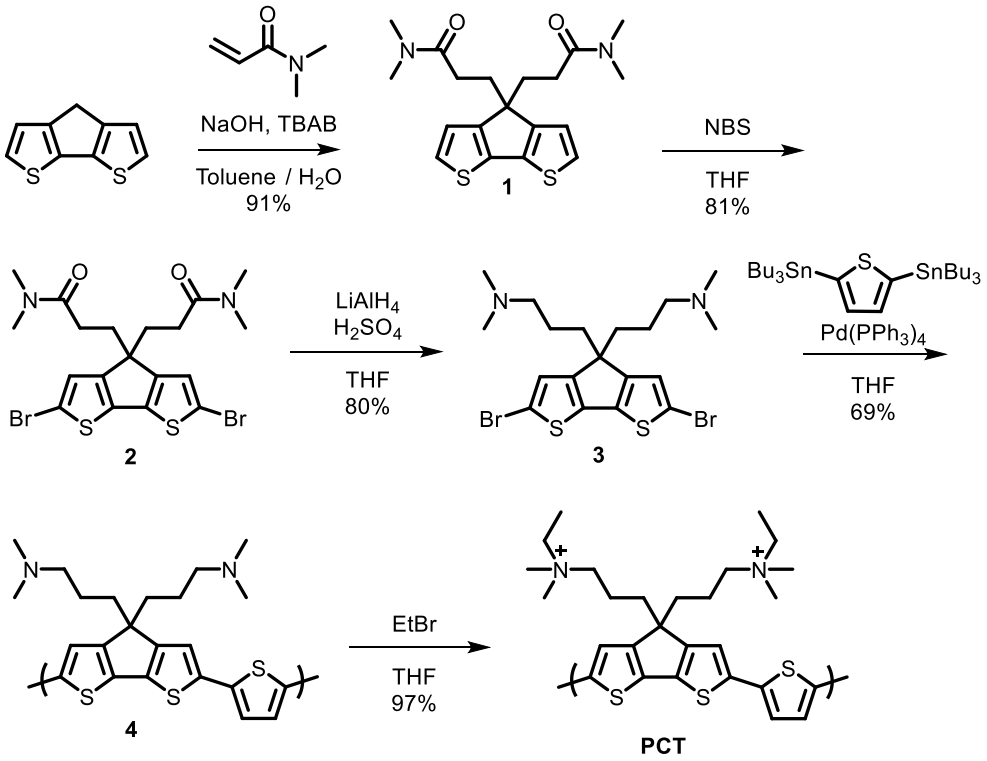

Scheme 5.1: An improved synthetic approach to PCT making use of a double Michael addition of N,N-dimethylacrylamide with cyclopentadithiophene.

cyclopentadithiophene starting material. We have also shown that introducing the sidechains via double Michael addition works on fluorene rings (Figures A9-A10). Subsequent bromination of the outer cyclopentadithiophene rings, followed by reduction of the N,N-dimethylamide to N,N-dimethylamine groups using in situ generated AlH3 yielded the monomeric core of PCT. After polymerization with 2,5-bis(tributylstannyl)thiophene, the final polymer was quaternized with excess bromoethane to generate the hydrophilic N,N-dimethyl-N-ethylammonium functions. The versatility of this strategy allows for straightforward changes to the core or sidechains of these linker units, and thus, allow to us to obtain a potential library of amphiphilic polymers. The characterization data for these intermediates and final products can be found in Figures A1-A8.

The optical characterization of PCT is shown in Figure 5.2a. We see that a large red-shift in the band gap as compared to PFT, caused by the exchange of fluorene for the cyclopentadithiophene units. As expected, the emission spectrum is also red-shifted, opening up the possibility of incorporating a variety of electron acceptor molecules to study charge transfer characteristics. These optical spectra demonstrate that the band gap of the CPEs created using our design rules can easily be tuned, with only minor changes in the linker structure.

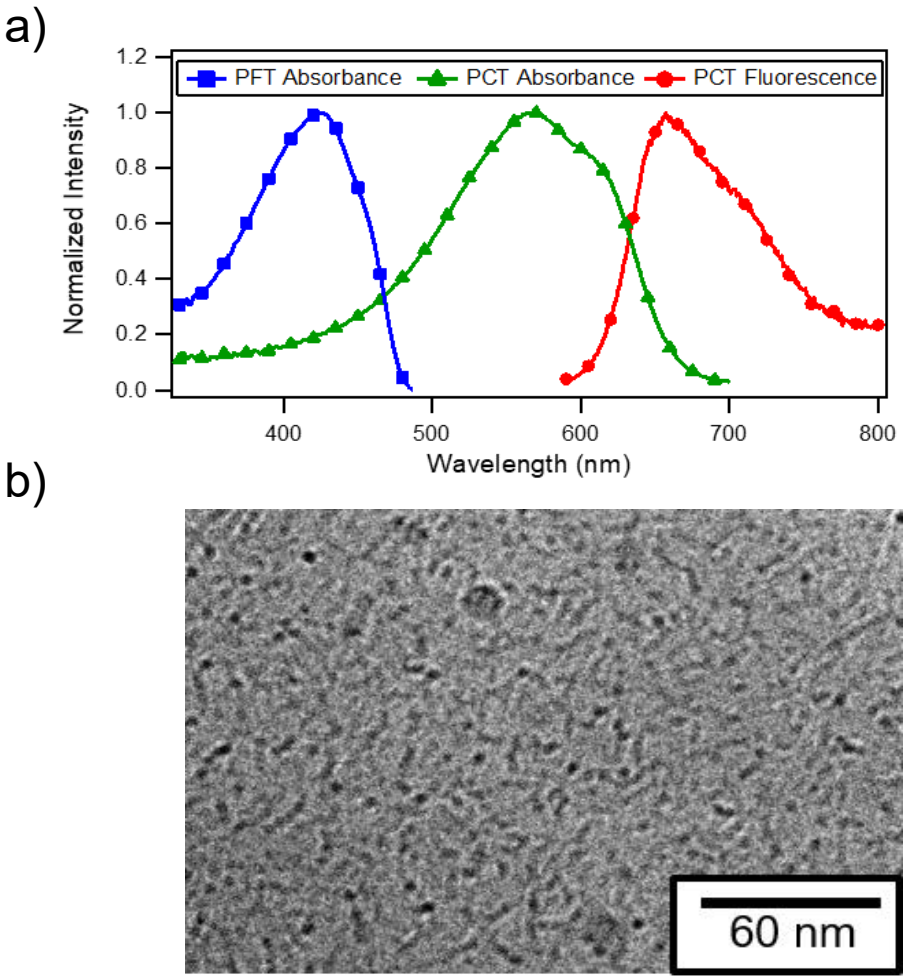

Figure 5.2. a) Optical characterization of PCT demonstrating visible-region band gap absorption. b) CryoEM image of PCT solution showing micelle-like structures with average diameters of 2 nm.

Self-assembly of PCT into cylindrical micelles was first demonstrated using CryoEM on flash-frozen dilute aqueous solutions of PCT, as seen in Figure 5.2b. The cryoEM samples were prepared by the standard method – producing thin-films of vitreous solution suspended across holey-carbon grids. This produces a network of PCT micelles, with many individual micelles overlapping one another; each micelle measures about 2 nm in diameter. While the formation of a micellar-network makes distinguishing individual micelles difficult, we estimate that the average length of each micelle is roughly several-tens-of-nanometers. Most importantly, the cryoEM data provides clear evidence for PCT micelle formation.

To complement the images of our cylindrical micelles, we used solution SAXS to provide more quantitative information on the size and shape of self-assembled micelles and aggregates in solution. All samples measured by solution SAXS underwent size-selective precipitation to separate high- and low-molecular weight (MW) polymers prior to micelle formation. We expected low–MW polymer chains to demonstrate more ideal cylindrical self-assembly behavior, while high-MW chains would give us insight on the behavior that would be observed for polymers of a size that is more commonly used in device applications. The raw scattering curves in Figure 5.3a for both high- and low-MW samples (red and blue curves, respectively) are fairly featureless, which is expected for cylindrical micelles in solution.[24,27,28] The general shape of the solution self-assembly can be determined by fitting to a Guinier-region power law, wherein the power law slope is indicative of the polymer fractal structure.[29] In essence, this power law slope is representative of the dimensionality of the average shapes in solution: slopes of 1, 2, and 3 correlate to rigid rod, flat disk, and spherical structures, respectively. Interactions between molecules, or branching/bending in the case of rigid rods, should result in deviations from a slope of 1.

As can be seen in Figure 5.3a, both high- and low-MW scattering profiles have slopes near 1, with the low-MW scattering profile fitting exactly to 1. For comparison, the power-law slope of PCT with a similar molecular weight is 1.4 (Figure A11). This confirms that using the cyclopentadithiophene unit to match the bond angles between thiophene/ cyclopentadithiophene units, indeed straightens the polymer chain and results in well-ordered micelles at low-MW. For the high-MW sample, the increase in the power law slope to 1.3 can be explained by the presence of longer chains that should produce longer micelles with more propensity to bend in solution. Disorder from misaligned polymer chains could also result in some micelle branching. While high-MW PCT does show deviation from perfect one-dimensional behavior, these micelles all have a Porod slope much closer to 1 than our previous polymer, PFT, which did not have a matching bond angle between the fluorene and thiophene monomer units. The scattering patterns of high-MW PFT micelles fit to a power law slope of 1.5, indicating the importance of bond angle matching for inducing order in this amphiphilic system.

The radially averaged scattering data shown in Figure 5.3a can be Fourier-transformed to a pair-distance distribution function, P(r), as seen in Figure 5.3b. These P(r) functions represent the radially averaged distribution of electron density correlations as a function of the separation distance, r, within a solution-phase aggregate.[30-32] We note that if the interparticle spacing is regular, such as in a lyotropic liquid crystal, we would observe distinct peaks corresponding to the average interparticle distance in both the raw and Fourier-transformed data.[33,34] Partial ordering would not produce peaks in the raw data, but can still produce broad correlation peaks in the P(r) data. Because the P(r) function averages over all electron density correlations with equal probability, it cannot distinguish between interparticle and intraparticle correlations. The P(r) functions of the SAXS data in Figure 5.3b confirm the cylindrical scattering profile, with a sharp

peak produced by the diameter of the cylinder (region 1), followed by a linear decay (region 2) related to the long axis of the cylinder. For both high- and low-MW PCT samples (red and blue

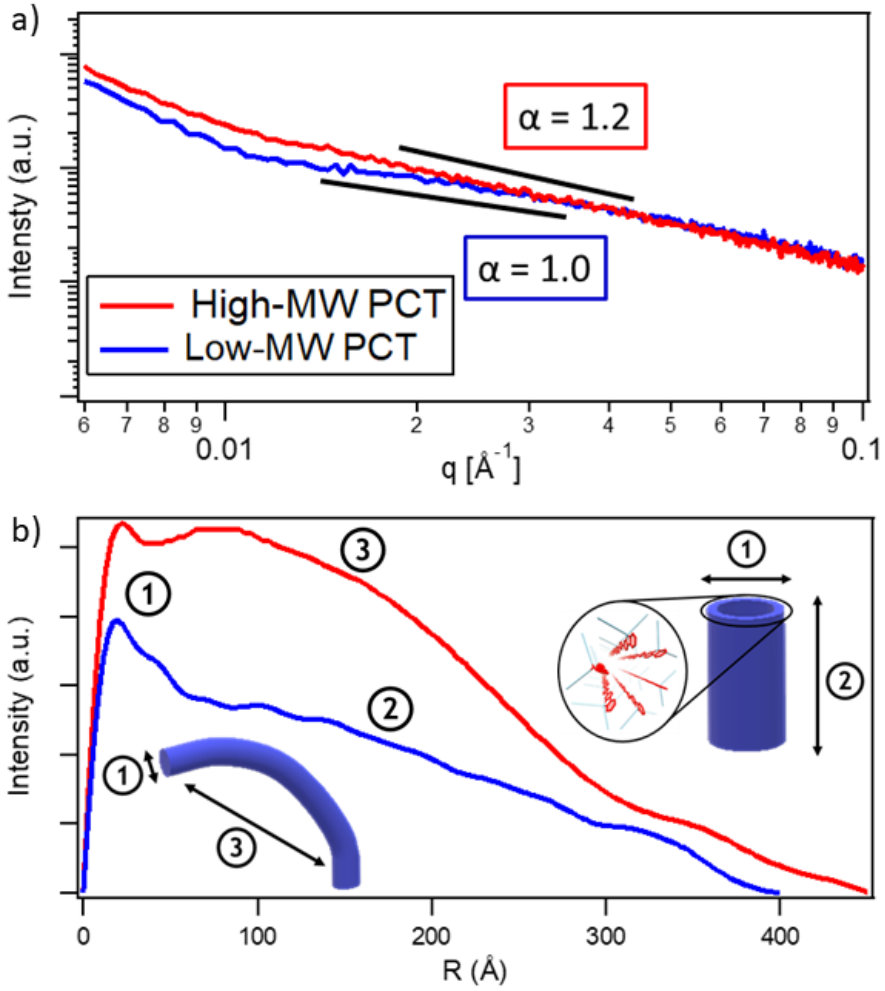

Figure 5.3. a) Radially averaged SAXS data with power-law fits, and b) P(r) transformations of the SAXS data confirming rod-like micelle structures for both high- (red) and low- (blue) MW PCT in water.

curves, respectively), there is a sharp peak at r = ~20 Å. Particularly in the case of low-MW, the P(r) demonstrates a shape nearly identical to that of a perfect rigid rod, further indicating that matching the bond angles between the alternating units within the copolymer is crucial for creating straight polymer chains. For the high-MW sample, there is also a broad peak centered at ~100 Å

(red curve, region 3), suggesting that some intraparticle correlation is possible at longer chain lengths due to bending fluctuations within the micelle, a phenomenon which will be discussed in more detail below.

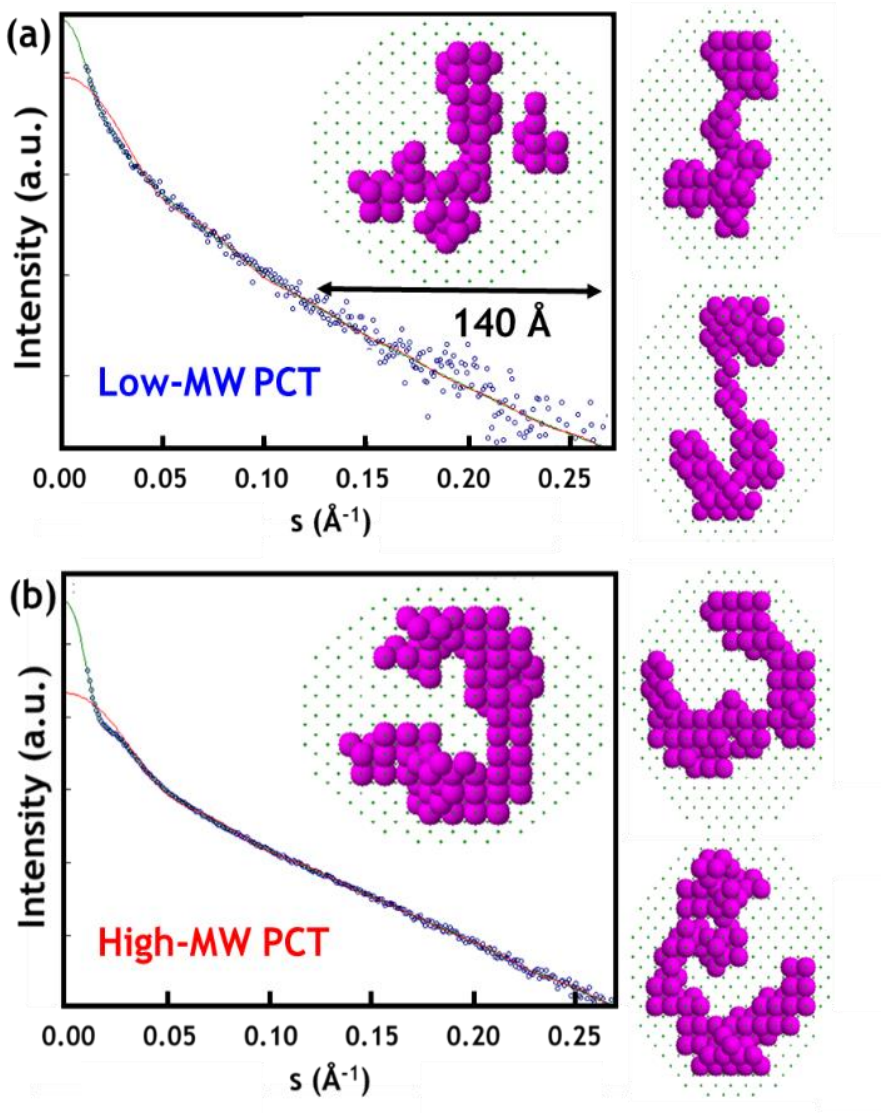

Figure 5.4. Dammin bead model fits and structures for a) 1 mg/mL high-MW PCT, and b) 1 mg/mL low-MW PCT confirming rod-like micelle shapes; the curvature in the high-MW PCT is due to the broad correlation peak seen in the P(r) function from Figure 5.2c.

To further explore the structure of our amphiphilic polymer assemblies, we also utilized Dammin bead modeling, which is a Monte Carlo based optimization, to fit our SAXS data. In the fitting process, the radially averaged SAXS was fist fit to a smoothly varying function (green line in Figure 5.4) so that the Monte-Carlo routing does not try to fit structure to the noise in the data. A set of beads in a simulation box are then moved using Monte-Carlo methods to create structure whose scattering profiles best match the fit to the scattering data.[35] The fits are usually not unique, so a series of best fit structures are use define the probably structure in solution. Note that due to computational limitation, we have not been able to use simulations boxes larger than 140 Å, which is smaller than some of the correlation distances shown in Figure 5.3.

Three-dimensional reconstructions generated for low-MW PCT (Figure 5.4a) generally show straight, rod-like chains that agree with both the Guinier region fits and the P(r) data presented above. Upon moving to the high-MW PCT samples, he overall shape of the reconstructions is still cylindrical, but now all cylinders show some curvature (Figure 5.4b). This curvature is simply another visualization of the 100 Å correlation peak that is observed in the P(r) data and of the deviation of the Porod slope from a value of 1.0. We note that the structural heterogeneity in the Dammin fits may be artificially small, given that the intramicelle correlation distance is 100 Å and the simulation box is only 140 Å. The c-shaped micelles in all reconstructions likely results because this is the only way to generate a 100 Å correlation within the limited box, and a broader range of conformation likely exist in the real system. Overall, both the high- and low-MW Dammin bead models reconstructions further demonstrate that PCT forms rod-like micelles in solution. For both samples, more examples of bead models are shown in Figures A12 and A13.

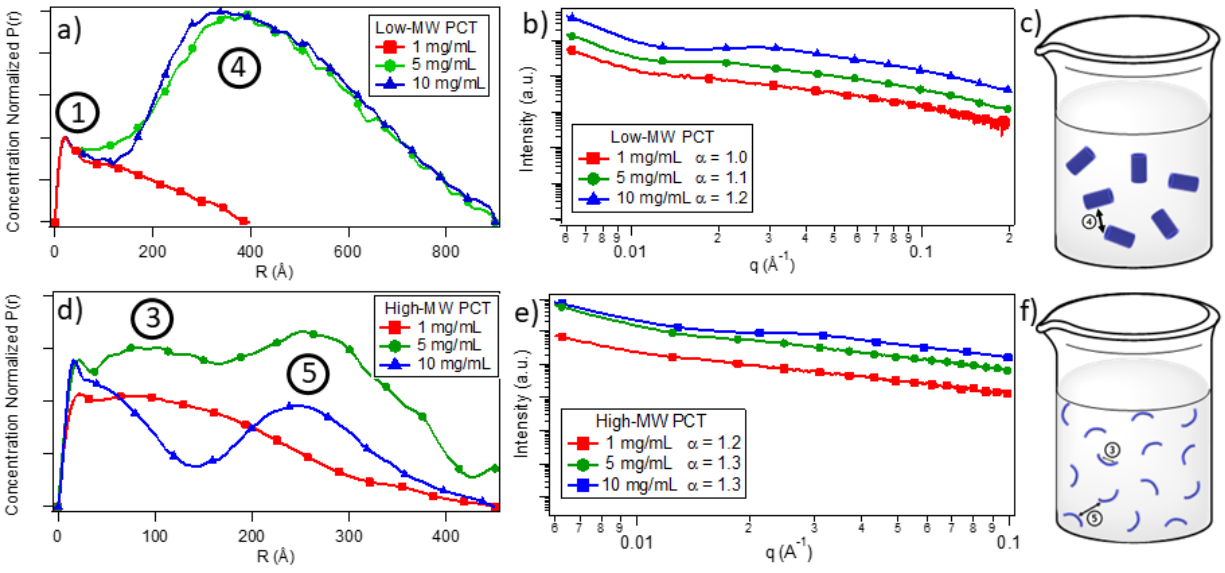

Figure 5.5 Concentration-dependent studies of low-MW PCT (a-c) and high-MW PCT (d-f) demonstrating that cylinder shape is maintained while micelles interact with each other in solution.

In order to ensure that the above discussed SAXS results are not due to aggregation effects, and to observe the interaction of polymer chains in solution, we further examined both low- and high-MW samples at varying concentrations, as seen in Figure 5.5. In non-interacting systems, the scattering profiles do not change shape as the concentration changes, and only the scattering intensity increasing with increasing concentration.[36,37] Either repulsive or attractive interactions will result in new inter-aggregate correlation peaks as concentrations increases. Figure 5.5a shows concentration-normalized P(r) transformations for the low-MW fraction of PCT. The peak at 20 Å remains the same for all concentrations, indicating that the rod-like shape of the individual micelles remains unchanged, and that all measurements were performed above the critical micelle concentration.[38] However, as the concentration increases, a broad peak appears at ~400 Å, likely corresponding to electron density correlations between neighboring micelles in solution. These changes are also reflected in the Guiner-region power law fits shown in Figure 5.5b. The increase

in slope from 1.0 to 1.2, can thus be explained by the interaction between neighboring polymer micelles. These intermicelle correlations observed in the SAXS data are represented as region 4 in the schematic shown in Figure 5.5c.

The P(r) data for the high-MW PCT (Figure 5.5d) show three distinct peaks that appear at different concentrations. As with the low-MW samples, the first peak at ~20 Å corresponds to the cylinder diameter (region 1). The peak at ~100 Å (region 3), as previously discussed, relates to curvature fluctuations in longer micelles, and likely stems from intra-micelle density correlation that can occur because the increased length of the micelle allows for some bending in solution. However, as the concentration increases, an additional peak at ~300 Å (region 5) appears. Similar to what is seen for the low-MW PCT, this new peak is likely due to inter-micelle correlation because neighboring micelles are now closer to each other. It is also interesting to note that the inter-micelle correlation peak appears at longer distances for low-MW as compared to high-MW PCT. We hypothesize that in the low-MW system, the micelles are short enough that they are able to minimize repulsive forces more effectively with increased distance between micelles. However, at higher-MW, there is increased disorder caused by fluctuations of the longer polymer micelles, leading to closer contacts. Interestingly, as the concentration increase, the curvature peak at ~100 Å appears to decrease in intensity, indicating that repulsion from neighboring micelles can help to straighten out the micelles in the high-MW samples. While the radially averaged data and corresponding Guinier-Porod fits seen in Figure 5.5e show little change with increasing concentration, a small increase is observed going from 1 mg/ml to 4 mg/ml.

Section 5.4. Conclusions

With this work, we have demonstrated the utility of our design rules for straightening polymer chains using self-assembling amphiphilic CPEs by demonstrating the formation of well-ordered cylindrical micelles in our new PCT polymer. We are able to move the band gap ~150 nm into the visible region from our previous micelle forming PFT polymer, making this polymer better suited for future optoelectronic applications. Solution SAXS characterization of PCT demonstrates that low molecular weight versions of this polymer are able to form well-ordered cylindrical micelles in solution, as demonstrated by a Porod power law slope of 1 and corresponding P(r) profiles that match the theoretical shape for a cylinder. These results demonstrate that ensuring proper bond angle matching between monomer units is crucial for improving the overall order of the system, even at high molecular weights. Because of the added order of this amphiphilic polymer system, as compared to our previously studied PFT, we are now able to understand how molecular weight controls both intra- and inter-micelle interactions in ways that could not be determined in the more disordered PFT system. At high molecular weight, we can see that the polymer is able to maintain a largely cylindrical self-assembled structure, but it can bend, thus introducing intra-micelle interactions.

With the synthesis and characterization of PCT, we have been able to confirm and expand our design rules for amphiphilic self-assembly of charged conjugated polymers. This opens up exciting potential for new studies where these self-assembling polymers are combined with various excited state electron acceptors to study charge transfer properties, both in solution and in the solid-state. Together, our design rules include, (1) a hydrophobic core with hydrophilic sidechains, (2) an alternating copolymer in order to ensure that all polar substituents can reside on the same side of the polymer chain after self-assembly, (3) a substituent branching point at an sp3 carbon to

prevent random polymer aggregation and π-stacking, and lastly, (4) an internal angle of 0º between repeat units of co-monomers to produce a straight polymer chain. Due to the ease of structural tunability within these parameters, many other CPEs should be synthesizable using these design rules. This new class of water-soluble polymers with inherent order and straighter polymer chains may help reduce the many trap states which are typically seen in semiconducting polymers.

Section 5.5. Experimental Section

Synthetic Methods

General procedures: Chemical reagents were obtained from commercial sources and used without further purification. Unless otherwise noted, all reactions were performed under argon at 25 °C. Silicycle (Siliflash P60) silica gel 60 (240-400 mesh) was used for all column chromatography. Solution NMR spectra were obtained on a Bruker AV500 instrument.

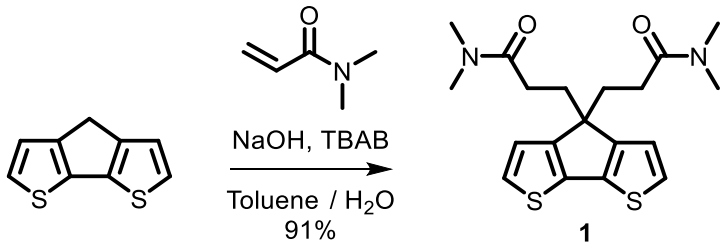

3,3'-(4H-cyclopenta[2,1-b:3,4-b']dithiophene-4,4-diyl)bis(N,N-dimethylpropanamide) (1)

Cyclopentadithiophene (1.50 g, 8.40 mmol, 1.0 eq) was dissolved with toluene (15 mL) along with tetrabutylammonium bromide (250 mg, 0.840 mmol, 0.1 eq) and N,N-dimethylacrylamide (3.33 g, 33.6 mmol, 4.0 eq) and sparged with argon for 15 minutes. At the same time a 50 % wt solution of sodium hydroxide (7.5 mL) was sparged under argon. The sodium hydroxide solution was then added to dropwise and the mixture heated at 65 °C overnight. The reaction was then cooled to room temperature and washed first with 1 M sodium hydroxide then brine. The organic layer was dried over $MgSO_4$ and concentrated *in vaccuo*. The precipitate was washed with pentane and filtered to yield the product as a tan solid (2.66 g , 91%). ^{1}H NMR (500 MHz, $CDCl_3$): 7.17 (d, *J* = 4.7 Hz, 2H), 6.93 (d, *J* = 4.7 Hz, 2H), 2.77 (s, 6H), 2.62 (s, 6H), 2.35 (t, *J* = 7.9 Hz, 4H), 1.73 (t,

J = 7.9 Hz, 4H). ^{13}C NMR (125 MHz, $CDCl_3$): 172.5, 155.9, 137.3, 125.4, 121.7, 52.4, 37.0, 35.3, 33.3, 27.8. HRMS (DART) Calculated for $C_{19}H_{24}N_2O_2S_2$: 377.1352; found: 377.1337.

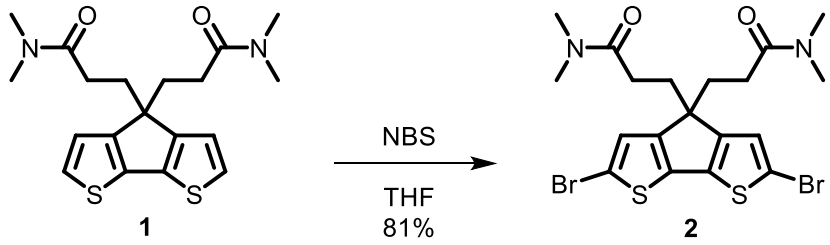

3,3'-(2,6-dibromo-4H-cyclopenta[2,1-b:3,4-b']dithiophene-4,4-diyl)bis(N,N-dimethylpropanamide) (2)

Compound **1** (4.00 g, 15 mmol. 1.0 eq) was dissolved in THF (100 mL) along with N-bromosuccinimide (4.29 g, 24.1 mmol. 2.1 eq). The reaction was covered in aluminum foil and stirred at room temperature overnight under argon. This mixture was concentrated *in vaccuo* and the residue redissolved in chloroform before washing with 10% aqueous sodium thiosulfate solution, 1 M sodium hydroxide, and brine. The organic layer was dried over $MgSO_4$ and evaporated on a rotovap before purifying on silica gel using hexanes/CH_2Cl_2/MeOH (1:1:0.1) as eluent to yield **2** as a tan solid (4.98 g, 81%). %). ^{1}H NMR (500 MHz, $CDCl_3$): 6.95 (s, 2H), 2.80 (s, 6H), 2.68 (s, 6H), 2.32 (t, *J* = 7.9 Hz, 4H), 1.73 (t, *J* = 7.9 Hz, 4H). ^{13}C NMR (125 MHz, $CDCl_3$): 171.9, 154.0, 137.07, 124.8, 112.0, 37.1, 35.4, 33.0, 27.5. HRMS (ESI) Calculated for $C_{19}H_{22}N_2O_2S_2$ [MH^+]: 532.9568; found: 532.9928.

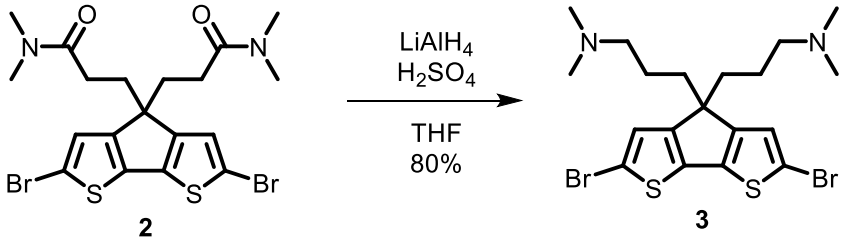

3,3'-(2,6-dibromo-4H-cyclopenta[2,1-b:3,4-b']dithiophene-4,4-diyl)bis(N,N-dimethylpropan-1-amine) (3)

Lithium aluminum hydride (874 mg, 23.0 mmol, 3.0 eq) was dissolved in THF (52 mL) in a flame dried flask then cooled to 0 °C before concentrated sulfuric acid was added dropwise (2.45 mL, 46.1 mmol, 6.0 eq). After stirring for 5 minutes, a solution of **2** (3.89 g, 7.68 mmol, 1.0 eq) in THF (77 mL) was added and allowed to reflux overnight under argon. The reaction was quenched with 1 M HCl at 0 °C then basified with 1 M NaOH. The precipitate was filtered and washed THF. The resulting filtrate was washed with brine and dried over $MgSO_4$ and evaporated on a rotovap. The product was purified on silica gel with 5% MeOH in CH_2Cl_2 to give 3.12 g of product as a white solid (80%). ^{1}H NMR (500 MHz, $CDCl_3$): 6.94 (s, 2H), 2.2-2.1 (m, 16 H), 1.83 (m, 4H), 1.07 (m, 4H). ^{13}C NMR (125 MHz, $CDCl_3$): 155.3, 136.6, 124.4, 111.5, 59.6, 54.6, 45.4, 35.2, 22.6. HRMS (ESI) Calculated for $C_{19}H_{26}N_2O_2S_2$ [MH^+]: 504.9982; found: 504.9826.

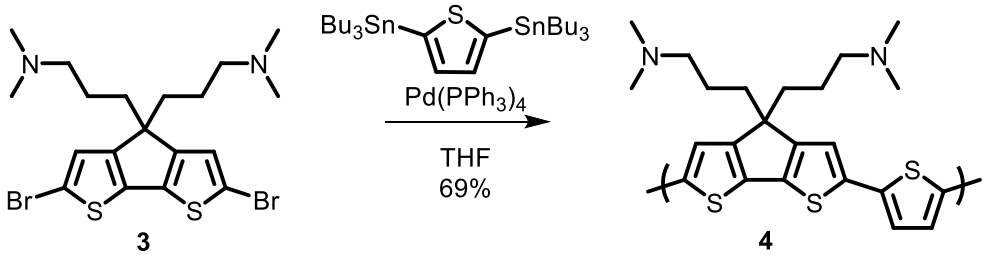

Poly{(4,4-bis(3'-(N,N-dimethylamino)propyl)cyclopenta[2,1-b:3,4-b']dithiophene)-2,6-diyl-alt-(thiophene-2,5-diyl)} (4)

2,5-bis(tributylstannyl)thiophene (4.08 g, 6.16 mmol, 1.0 eq) and **3** (3.12 g, 6.162, 1.0 eq) were dissolved in THF (175 mL) and sparged for 15 minutes under argon before tetrakis (triphenylphosphine)palladium (712 mg, 0.616 mmol, 0.1 eq) was added. The reaction was then refluxed for 3 days under argon. Upon cooling to room temperature, the polymer was precipitate with 700 mL of hexanes and centrifuged. The supernatant was decanted and the process repeated until the supernatant was light purple. The resulting polymer was vacuum dried to yield 1.85 g of purple solid as product (69%). ^{1}H NMR (500 MHz, $CDCl_3$): 7.9-6.0 (br s, 4H), 2.4-1.5 (m, 20H), 1.5-1.0 (br s, 4H). LS Analysis: Mn 9,760, PDI 2.193.

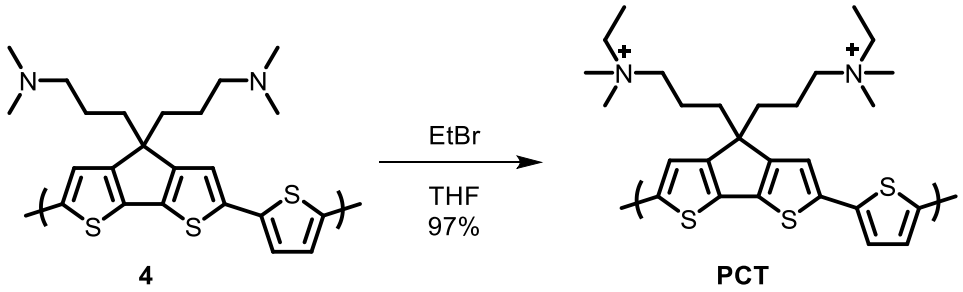

Poly{(4,4-bis(3'-(N-ethyl-N,N-dimethylamino)propyl)cyclopenta[2,1-b:3,4-b']dithiophene)-2,6-diyl-alt-(thiophene-2,5-diyl)} bromide (PCT)

Polymer **4** (100 mg, 1.0 eq) was dissolved in THF (30 mL) under argon. Ethyl bromide (15 mL) was added and the mixture allowed to reflux for 4 days. The mixture was then cooled and evaporated under pressure to yield a 146 mg of a purple powder (97%). ^{1}H NMR (500 MHz, DMSO-d_6): 7.6-7.2 (m, 4H), 3.0-2.8 (m, 12H), 2.51 (s, 8H), 1.9-1.7 (br s, 4H), 1.5-1.3 (br s, 4H), 1.1-1.0 (m, 6H).

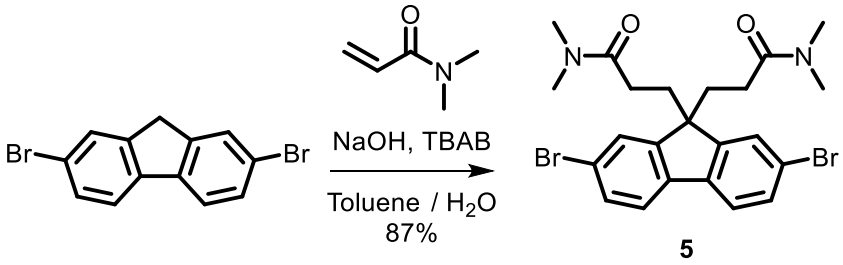

5

3,3'-(2,7-dibromo-9H-fluorene-9,9-diyl)bis(N,N-dimethylpropanamide) (5)

2,7-dibromo-9H-fluorene (10.00 g, 30.86 mmol, 1.0 eq) was dissolved with toluene (50 mL) along with tetrabutylammonium bromide (995 mg, 3.086 mmol, 0.1 eq) and N,N-dimethylacrylamide (9.790 g, 98.76 mmol, 3.2 eq) and sparged with argon for 15 minutes. At the same time a 50 % wt solution of sodium hydroxide (20 mL) was sparged under argon. The sodium hydroxide solution was then added to dropwise and the mixture stirred at room temperature for 30 min. The reaction was then cooled to room temperature and filtered. The solids were washed with toluene and water before drying. The title compound (14.02 g , 87%) without further purification. ^{1}H NMR (500 MHz, $CDCl_3$): 7.54 (d, J = 8.1 Hz, 2H), 7.51 (d, J = 1.5 Hz, 2H), 7.48 (dd, J = 8.1, 1.5 Hz, 2H),

2.78 (s, 6H), 2.56 (s, 6H), 2.41 (t, J = 2 Hz, 4H), 1.52 (d, J = 8.2 Hz, 4H); ^{13}C NMR (125 MHz, $CDCl_3$): 171.96, 150.5,138.9, 130.9, 126.6, 122.0, 121.2, 54.5, 36.8, 35.3, 34.9, 27.4.

Section 5.6. Appendix D

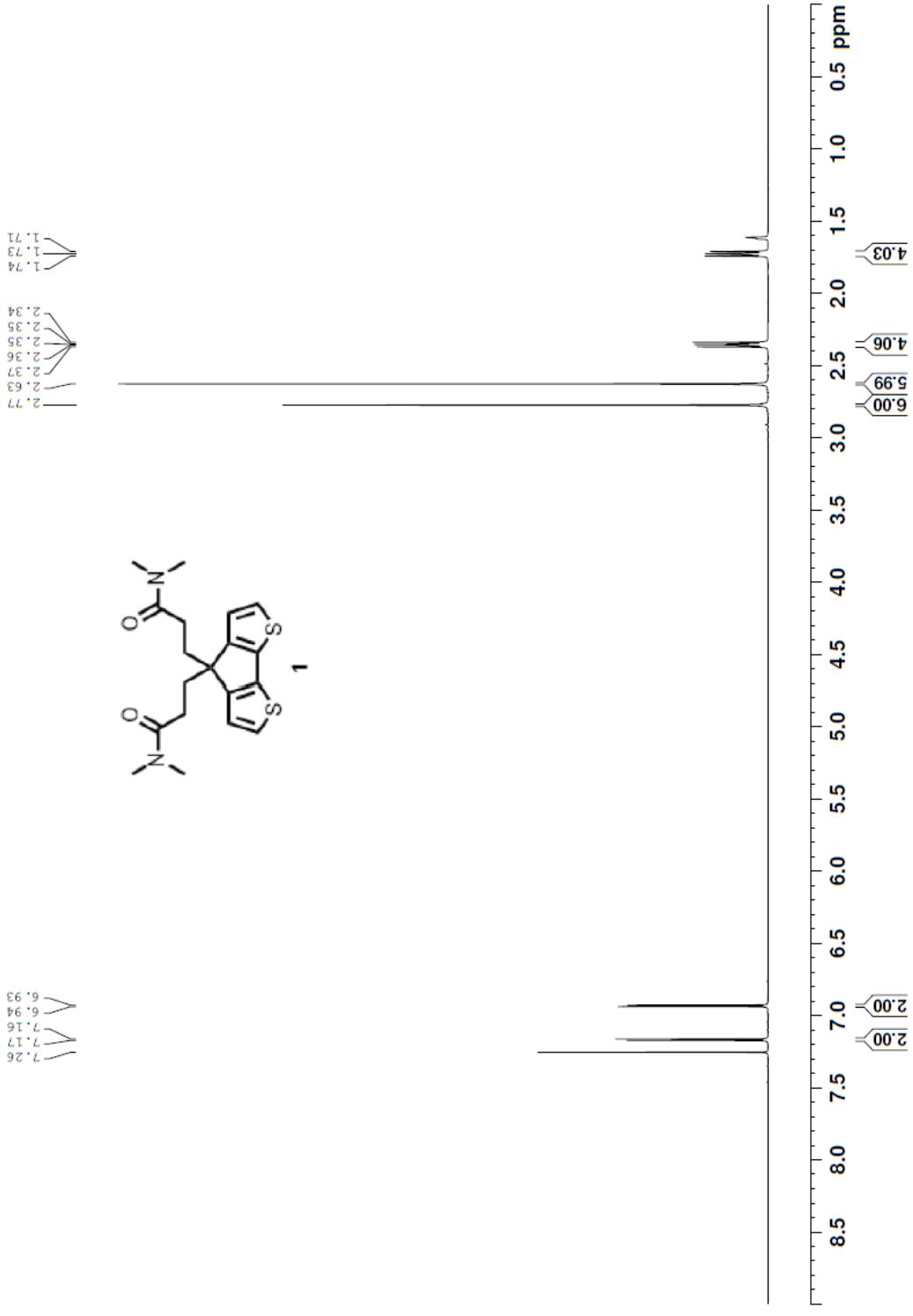

Figure A1 ^{1}H NMR spectrum of compound **1** in $CDCl_3$.

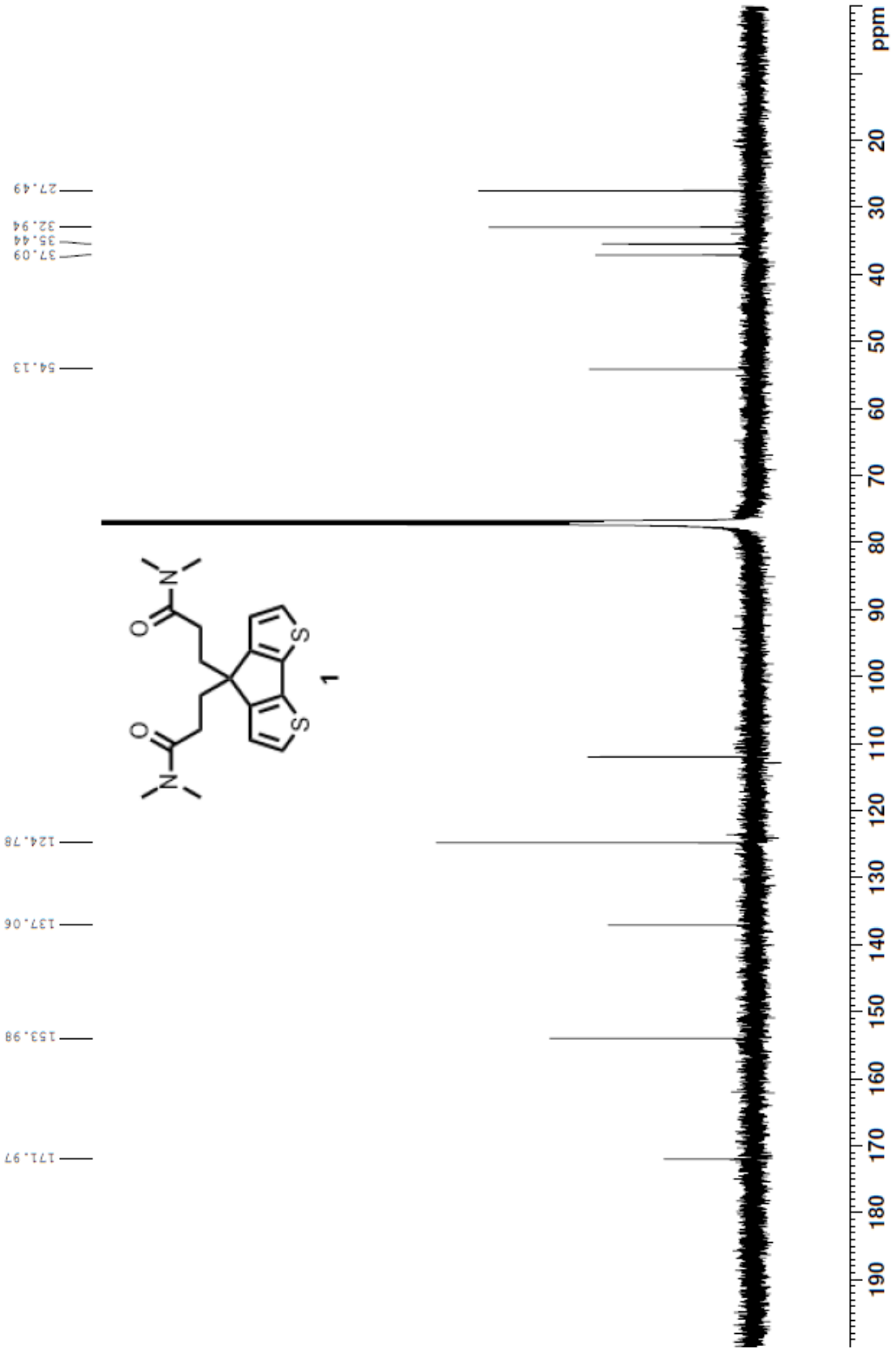

Figure A2 ^{13}C NMR spectrum of compound **1** in $CDCl_3$.

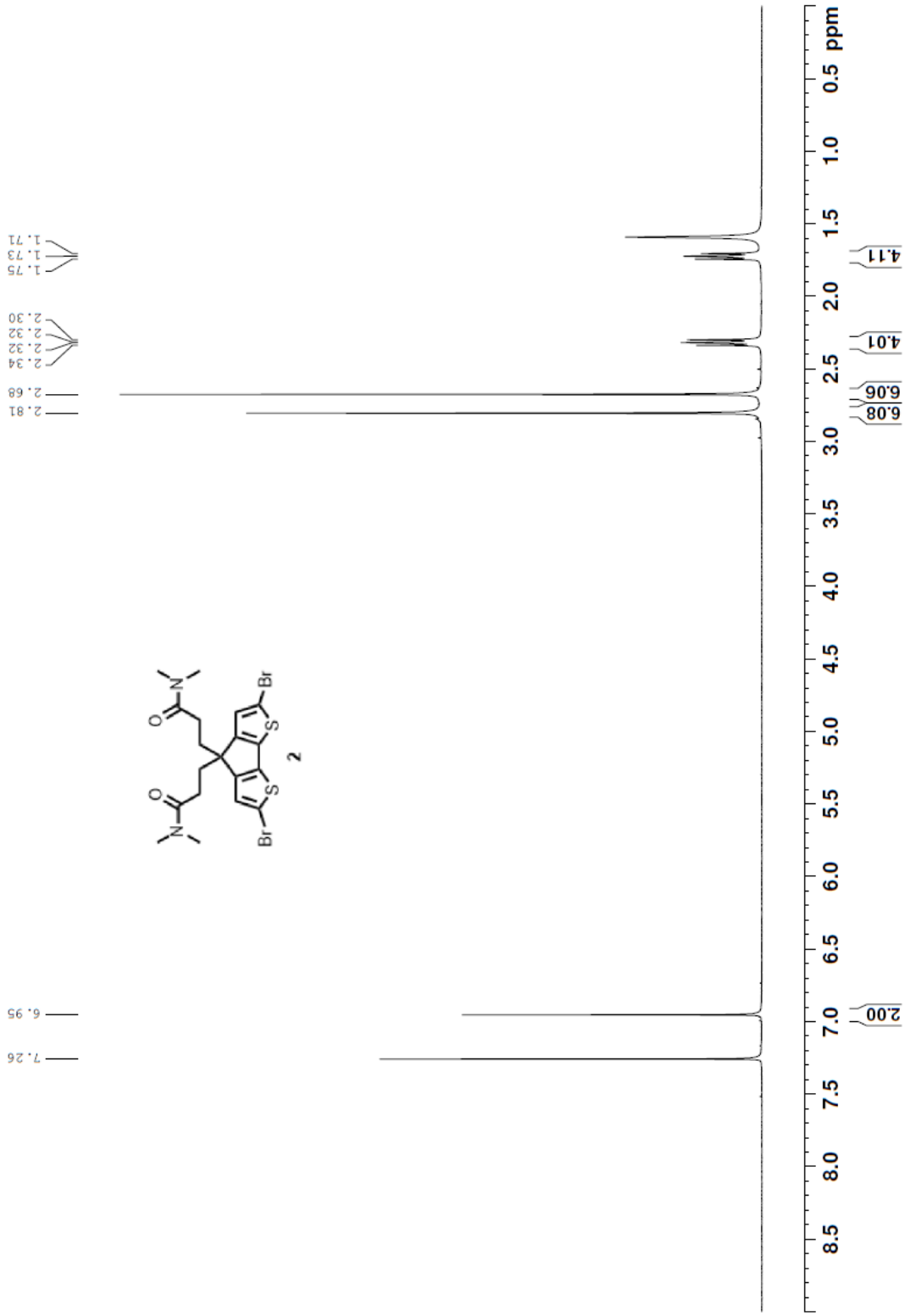

Figure A3 ^{1}H NMR spectrum of compound **2** in $CDCl_3$.

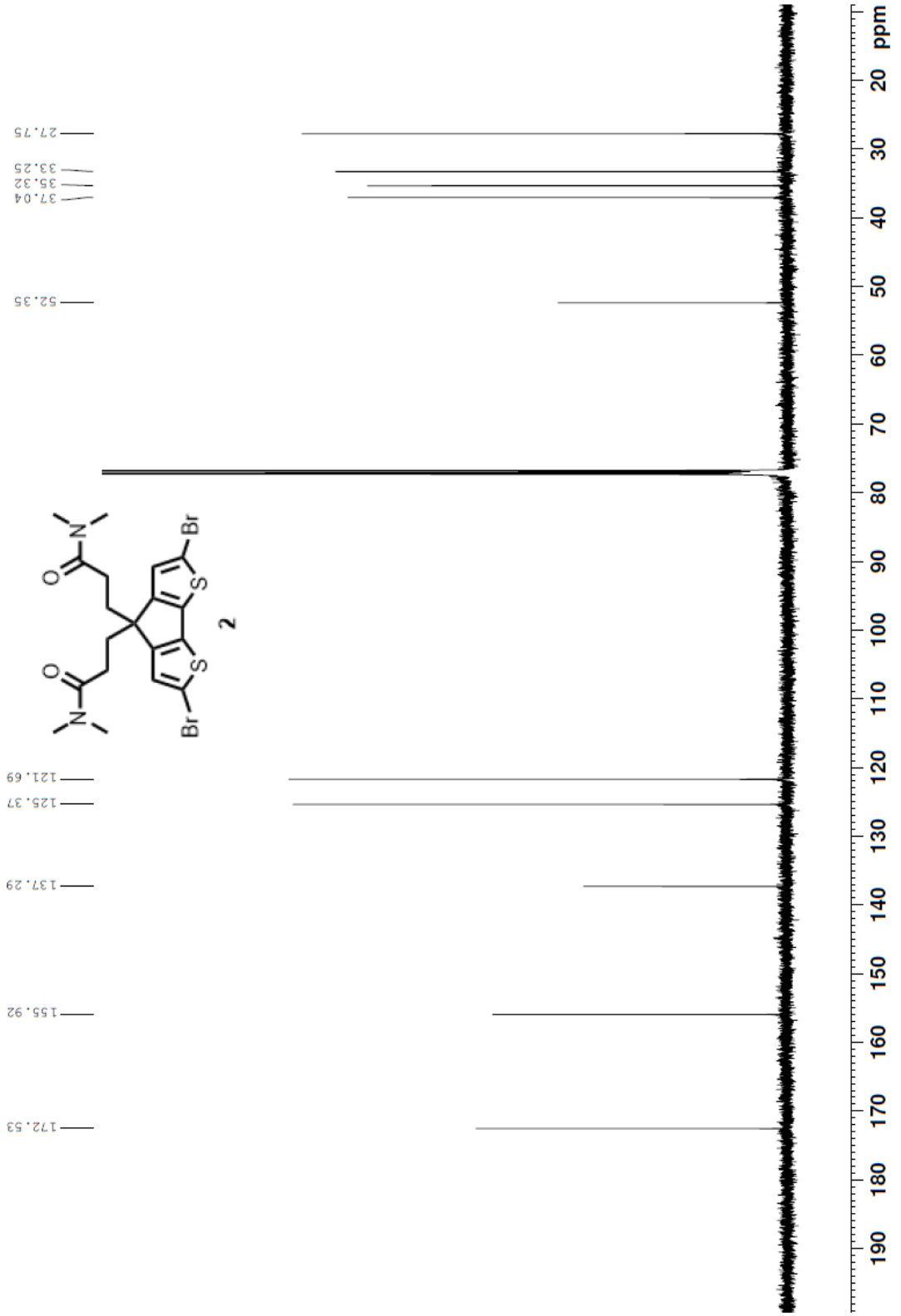

Figure A4. ^{13}C NMR spectrum of compound **2** in $CDCl_3$

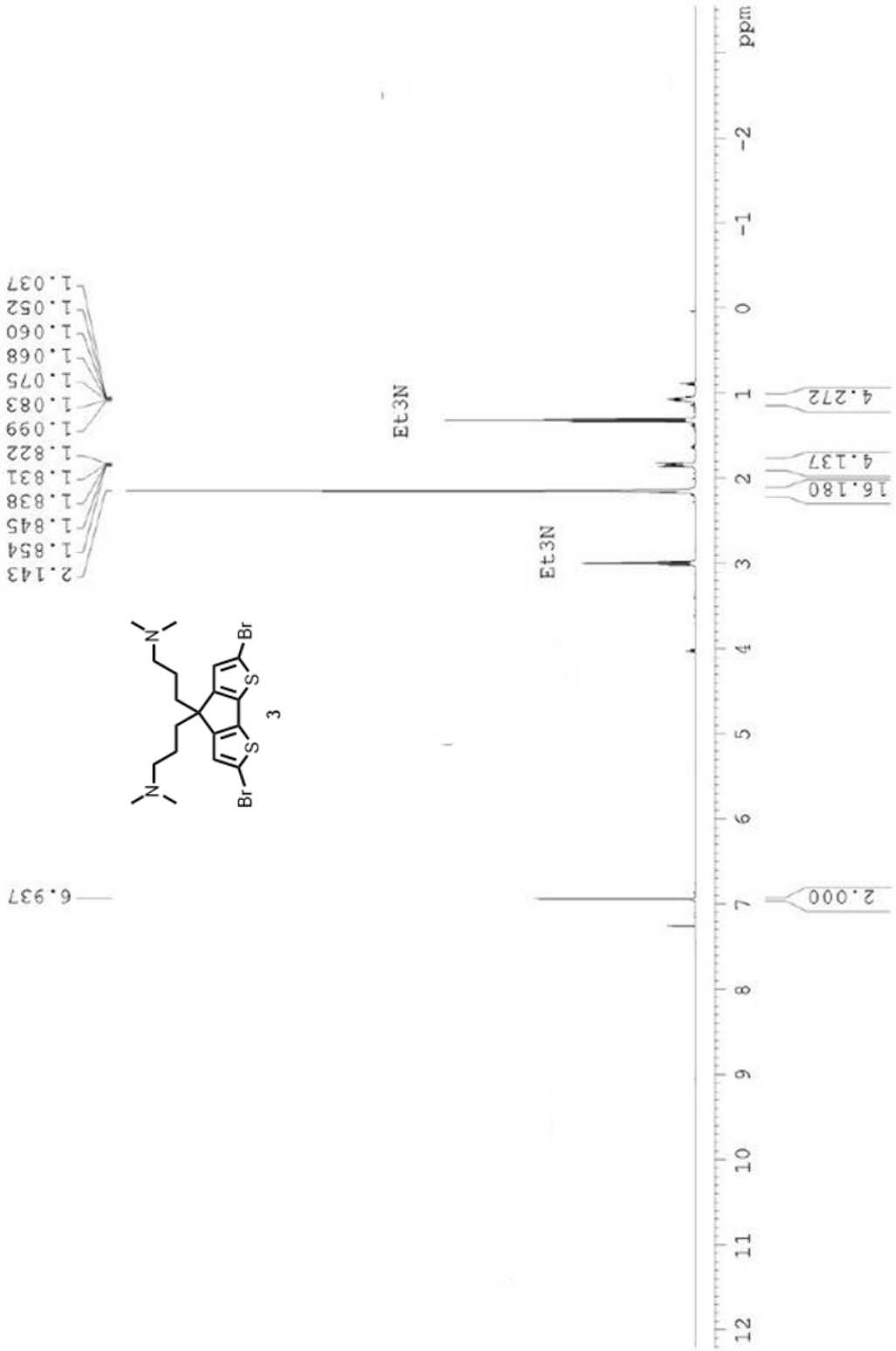

Figure A5 ^{1}H NMR spectrum of compound **3** in $CDCl_3$.

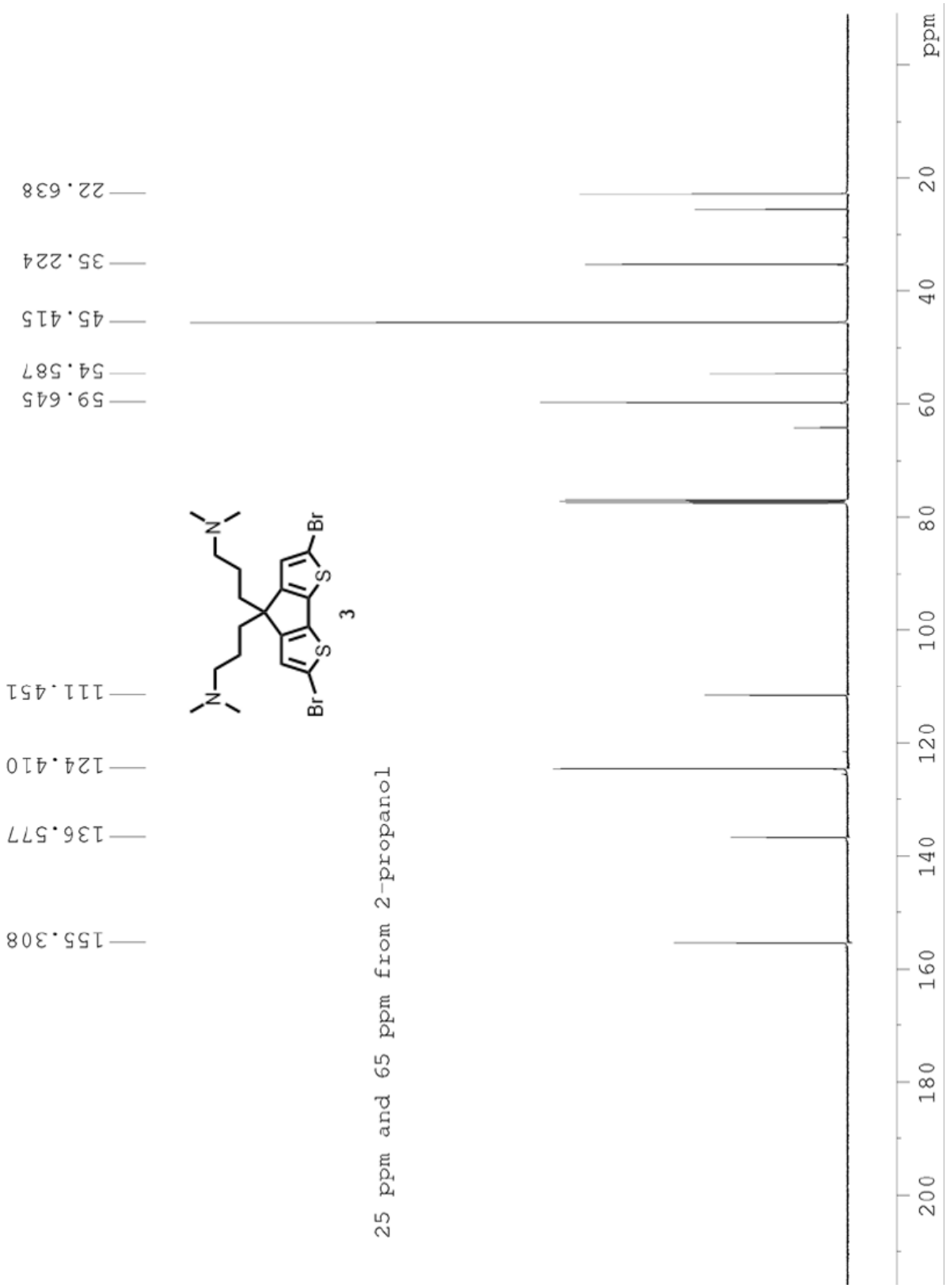

Figure A6 ^{13}C NMR spectrum of compound **3** in $CDCl_3$.

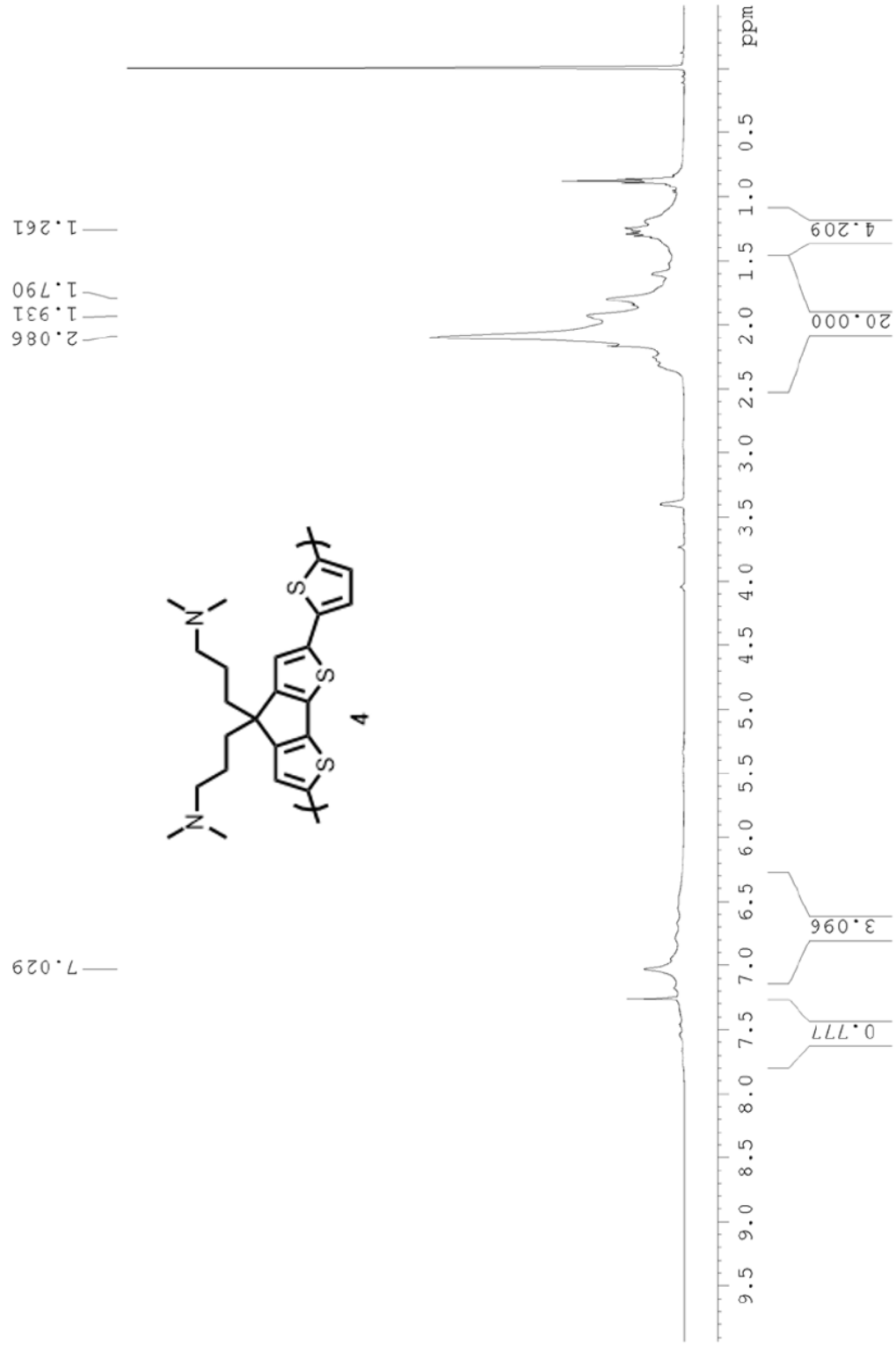

Figure A7 ^{1}H NMR spectrum of compound **4** in $CDCl_3$.

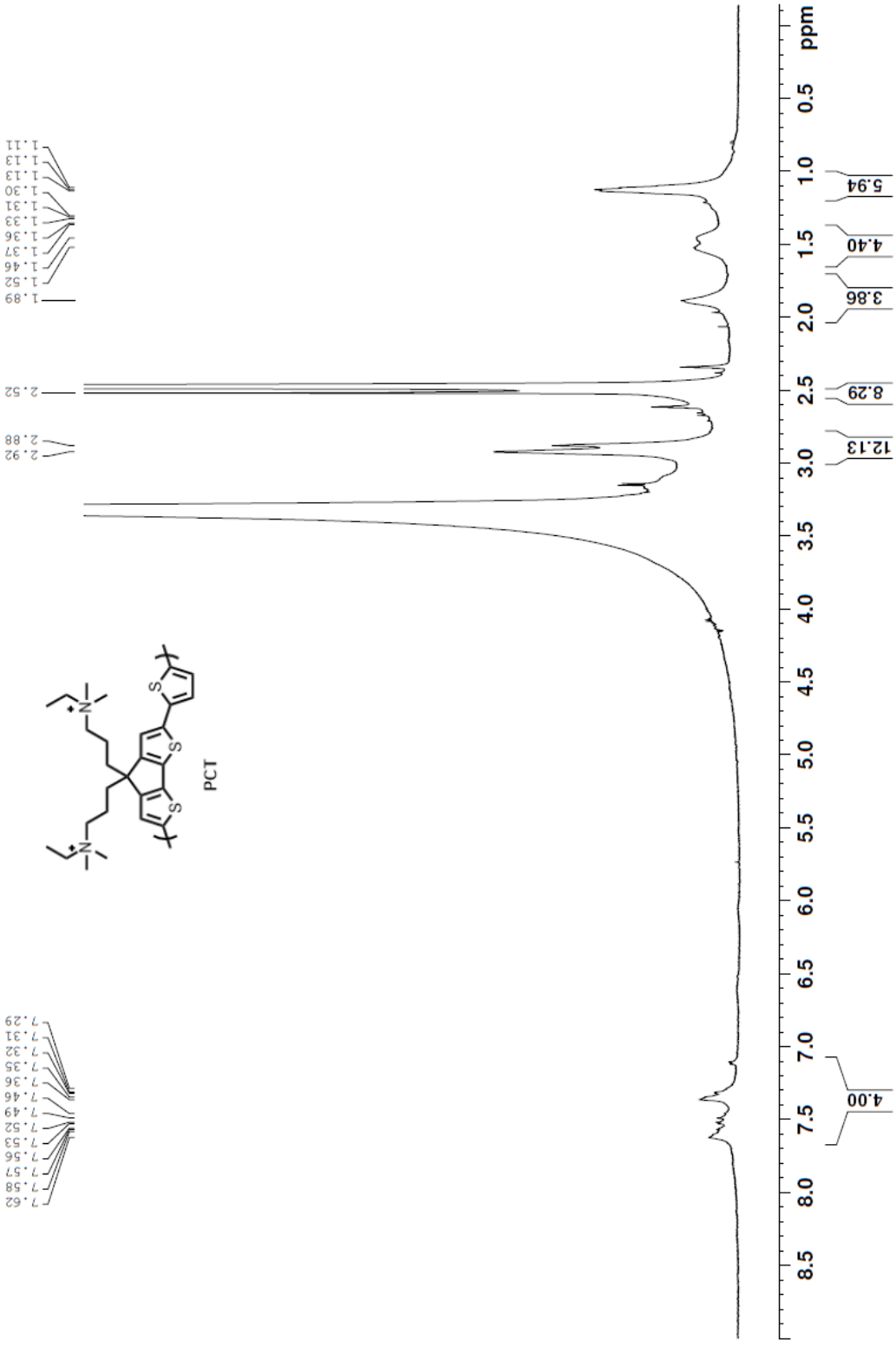

Figure A8. ^{1}H NMR spectrum of **PCT** in DMSO-d_6.

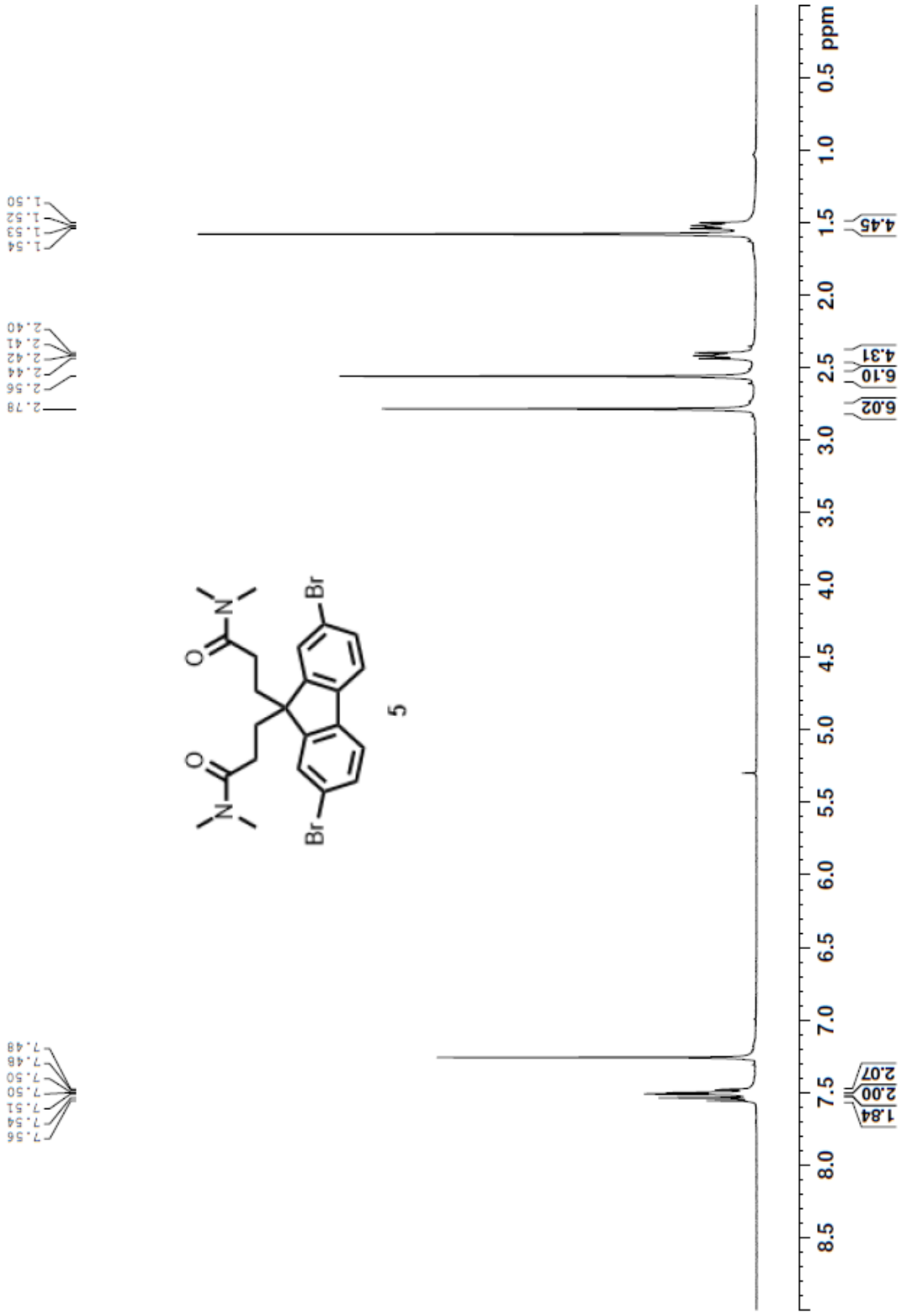

Figure A9 ^{1}H NMR spectrum of compound **5** in $CDCl_3$.

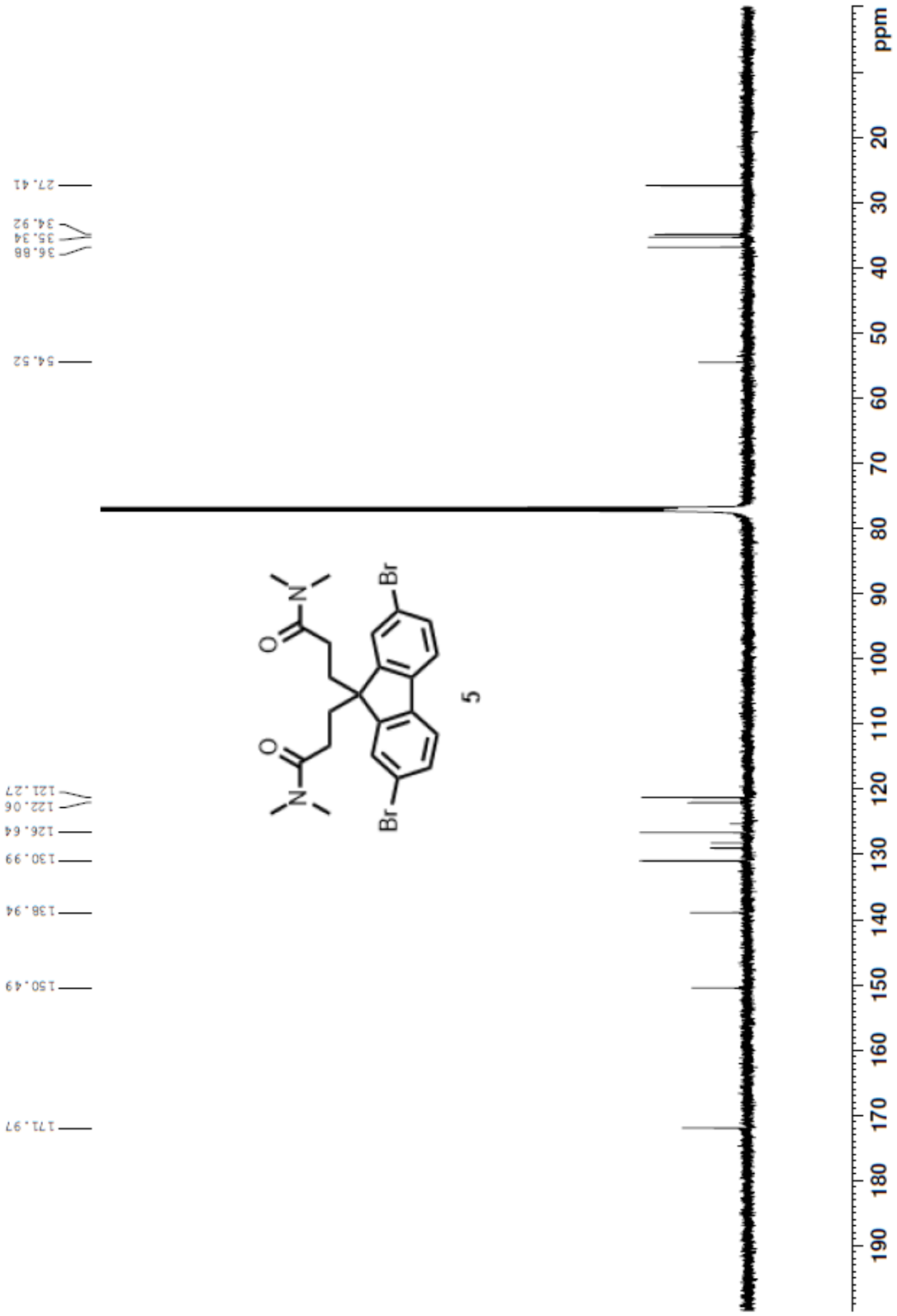

Figure A10 ^{13}C NMR spectrum of compound **5** in $CDCl_3$.

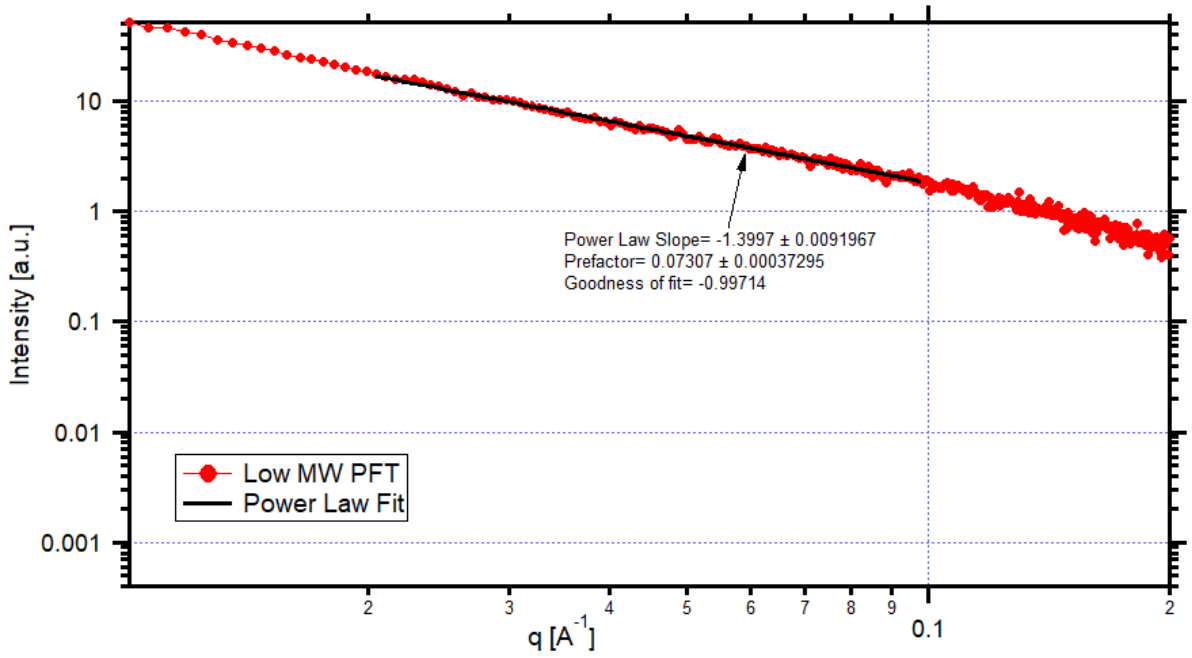

Figure A11 Power law fit of low MW PCT

DAMMIN Bead Modeling

DAMMIN INPUT PARAMETERS

Computation mode:	Expert
Maximum diameter of the particle :	350.0
Solution at Alpha = 0.221E+01 Rg : 0.105E+03 I(0):	0.175E+05
Radius of gyration read:	105.0
Number of GNOM data points:	343
Maximum s value [1/angstrom]:	0.3235
Number of Shannon channels:	30.89
Number of knots in the curve to fit:	55
A constant was subtracted:	9.234

Maximum order of harmonics:	20
Point symmetry of the particle:	P1
Sphere diameter [Angstrom]:	140.0
Packing radius of dummy atoms:	5.000
Radius of the sphere generated:	70.00
Number of dummy atoms:	1985
Number of equivalent positions:	1
Expected particle anisometry:	Unknown
Excluded volume per atom:	707.6
Radius of 1st coordination sphere:	14.10
Minimum number of contacts:	5
Maximum number of contacts:	12
Looseness penalty weight:	6.000e-3
No of non-solvent atoms:	1985
Initial DAM looseness:	7.571e-3
Disconnectivity penalty weight:	6.000e-3
Initial DAM # of graphs:	1742
Discontiguity value:	0.0
Center of the initial DAM:	0.0000 0.0000 0.0000
Peripheral penalty weight:	0.3000
Peripheral penalty value:	0.6029
Looseness fixing threshold:	0.0
R-factor fixing threshold:	0.0

*** The structure was randomized ***

No of non-solvent atoms:	1023
Randomized DAM looseness:	0.1022
Randomized DAM # of graphs:	911
Discontiguity value:	2.258
Randomized peripheral penalty value:	0.6033
Weight: 0=s^2, 1=Emphasis->0, 2=Log:	1

*** Porod weight with emphasis at low s ***

Initial scale factor:	9.153e-11
Scale factor fixed (Y=Yes, N=No):	N
Initial R^2 factor:	0.8020
Initial R factor:	0.8955
Initial penalty:	0.1952
Initial fVal:	0.9971
Variation of the target function:	1.574e-4
CPU per function call, seconds:	1.297e-4
Initial annealing temperature:	1.000e-3
Annealing schedule factor:	0.9500
# of independent atoms to modify:	1
Max # of iterations at each T:	138950
Max # of successes at each T:	13895
Min # of successes to continue:	46
Max # of annealing steps:	200

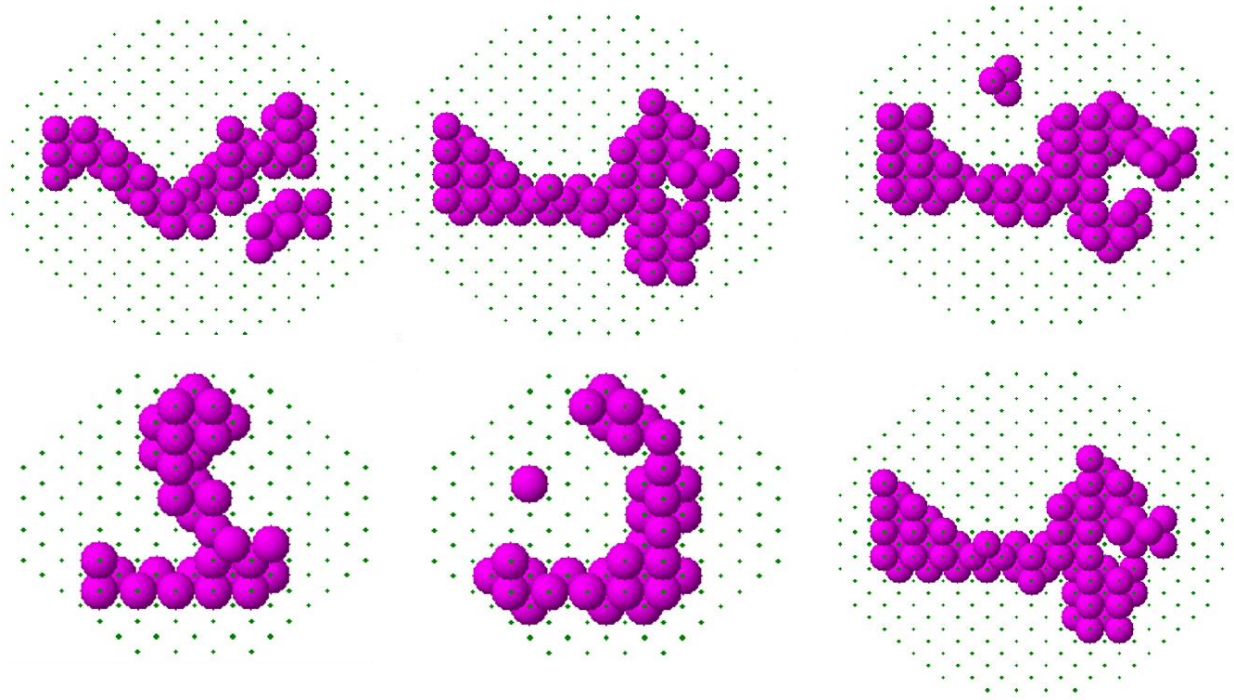

Figure A12. Additional representative DAMMIN bead models for low MW PCT

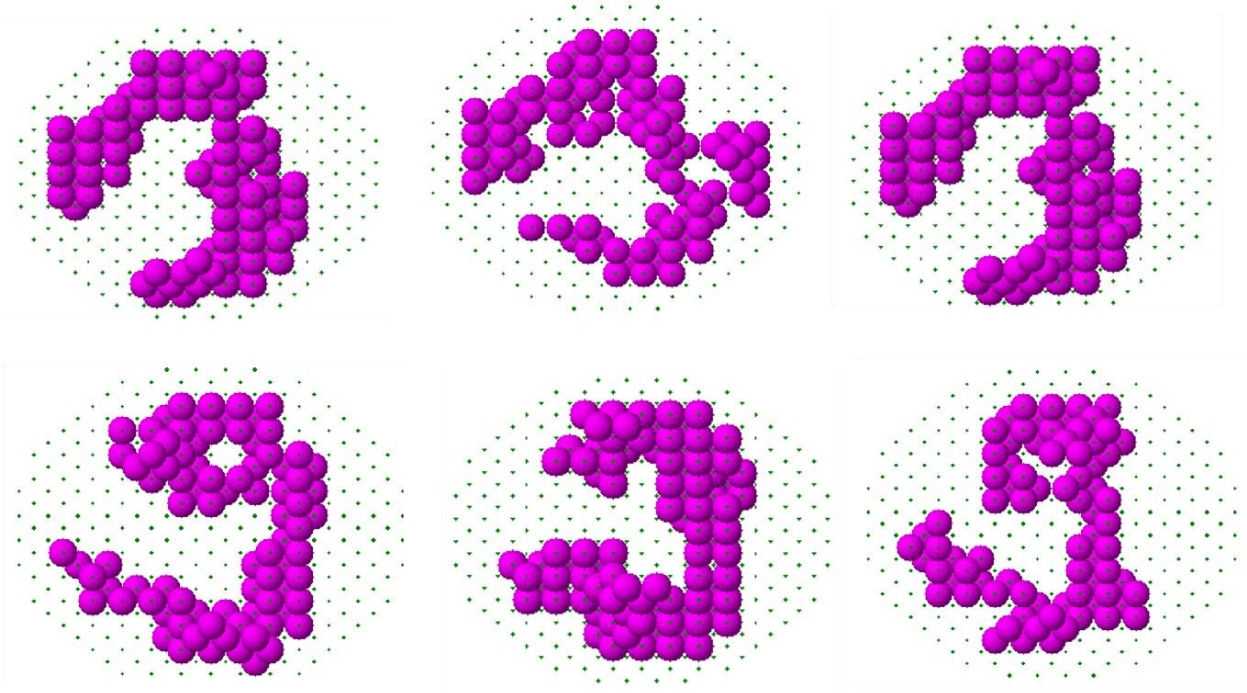

Figure A13. Additional representative DAMMIN bead models for high MW PCT

References

[1] Burroughes, J. H.; Bradley, D. D. C.; Brown, A. R.; Marks, R. N.; Mackay, K.; Friend, R. H.; Burns, P. L.; Holmes, A. B. Light-Emitting Diodes Based on Conjugated Polymers. *Nature* **1990**, *347*, 539–541.

[2] McNeill, C. R.; Greenham, N. C. Conjugated-Polymer Blends for Optoelectronics. *Adv. Mater.* **2009**, *21* 38–39, 3840–3850.

[3] Sirringhaus, H.; Bird, M.; Richards, T.; Zhao, N. Charge Transport Physics of Conjugated Polymer Field-Effect Transistors. *Adv. Mater.* **2010**, *22*, 3893–3898.

[4] Hamid Elsheikh, M.; Shnawah, D. A.; Sabri, M. F. M.; Said, S. B. M.; Haji Hassan, M.; Ali Bashir, M. B.; Mohamad, M. A Review on Thermoelectric Renewable Energy: Principle Parameters That Affect Their Performance. *Renew. Sustain. Energy Rev.* **2014**, *30*, 337–355.

[5] Hong, C. T.; Yoo, Y.; Kang, Y. H.; Ryu, J.; Cho, S. Y.; Jang, K. S. Effect of Film Thickness and Crystallinity on the Thermoelectric Properties of Doped P3HT Films. *RSC Adv.* **2015**, *5*, 11385–11391.

[6] Noriega, R.; Rivnay, J.; Vandewal, K.; Koch, F. P. V; Stingelin, N.; Smith, P.; Toney, M. F.; Salleo, A. A General Relationship between Disorder, Aggregation and Charge Transport in Conjugated Polymers. *Nat. Mater.* **2013**, *12*, 1–7.

[7] Luzio, A.; Criante, L.; D'Innocenzo, V.; Caironi, M. Control of Charge Transport in a Semiconducting Copolymer by Solvent-Induced Long-Range Order. *Sci. Rep.* **2013**, *3*, 1–6.

[8] Panzer, F.; Bässler, H.; Köhler, A. Temperature Induced Order-Disorder Transition in Solutions of Conjugated Polymers Probed by Optical Spectroscopy. *J. Phys. Chem. Lett.* **2017**, *8*, 114–125.

[9] Aloui, W.; Adhikari, T.; Nunzi, J. M.; Bouazizi, A.; Khirouni, K. Effect of Thermal Annealing on the Electrical Properties of P3HT:PC70BM Nanocomposites. *Mater. Sci. Semicond. Process.* **2015**, *39*, 575–581.

[10] Bridges, C. R.; Ford, M. J.; Thomas, E. M.; Gomez, C.; Bazan, G. C.; Segalman, R. A. Effects of Sidechain Branch Point on Self Assembly, Structure, and Electronic Properties of High Mobility Semiconducting Polymers. *Macromolecules* **2018**, *51*, 8597–8604.

[11] Wu, Y.; Schneider, S.; Walter, C.; Chowdhury, A. H.; Bahrami, B.; Wu, H. C.; Qiao, Q.; Toney, M. F.; Bao, Z. Fine-Tuning Semiconducting Polymer Self-Aggregation and Crystallinity Enables Optimal Morphology and High-Performance Printed All-Polymer Solar Cells. *J. Am. Chem. Soc.* **2019**, *142*, 392–406.

[12] Mei, J.; Bao, Z. Sidechain Engineering in Solution-Processable Conjugated Polymers. *Chem. Mater.* **2014**, *26* (1), 604–615.

[13] Strzalka, J.; Guo, J.; Chen, L. X.; Xu, T.; Yu, L.; Rolczynski, B. S.; Marks, T. J.; Loser, S.; Lee, B.; Liang, Y.; et al. When Function Follows Form: Effects of Donor Copolymer Sidechains on Film Morphology and BHJ Solar Cell Performance. *Adv. Mater.* **2010**, *22*, 5468–5472.

[14] Shaw, L.; Hayoz, P.; Diao, Y.; Reinspach, J. A.; To, J. W. F.; Toney, M. F.; Weitz, R. T.; Bao, Z. Direct Uniaxial Alignment of a Donor-Acceptor Semiconducting Polymer Using Single-Step Solution Shearing. *ACS Appl. Mater. Interfaces* **2016**, *8*, 9285–9296.

[15] Ghosh, R.; Luscombe, C. K.; Hambsch, M.; Mannsfeld, S. C. B.; Salleo, A.; Spano, F. C. Anisotropic Polaron Delocalization in Conjugated Homopolymers and Donor–Acceptor Copolymers. *Chem. Mater.* **2019**, *31*, 7033-7045. acs.chemmater.9b01704.

[16] Hamidi-Sakr, A.; Biniek, L.; Bantignies, J. L.; Maurin, D.; Herrmann, L.; Leclerc, N.; Lévêque, P.; Vijayakumar, V.; Zimmermann, N.; Brinkmann, M. A Versatile Method to Fabricate Highly In-Plane Aligned Conducting Polymer Films with Anisotropic Charge Transport and Thermoelectric Properties: The Key Role of Alkyl Sidechain Layers on the Doping Mechanism. *Adv. Funct. Mater.* **2017**, *27*, 1–13.

[17] Jiang, Y.; Cui, D.; Fang, Y.; Zhen, X.; Upputuri, P. K.; Pramanik, M.; Ding, D.; Pu, K. Amphiphilic Semiconducting Polymer as Multifunctional Nanocarrier for Fluorescence/Photoacoustic Imaging Guided Chemo-Photothermal Therapy. *Biomaterials* **2017**, *145*, 168–177.

[18] Pinto, M. R.; Schanze, K. S. Amplified Fluorescence Sensing of Protease Activity with Conjugated Polyelectrolytes. *Proc. Natl. Acad. Sci. U. S. A.* **2004**, *101*, 7505–7510.

[19] Liu, Y.; Ogawa, K.; Schanze, K. S. Conjugated Polyelectrolytes as Fluorescent Sensors. *J. Photochem. Photobiol. C Photochem. Rev.* **2009**, *10*, 173–190.

[20] Ambade, A. V.; Sandanaraj, B. S.; Klaikherd, A.; Thayumanavan, S. Fluorescent Polyelectrolytes as Protein Sensors. *Polym. Int.* **2007**, *56*, 474–481.

[21] Han, M. J.; McBride, M.; Risteen, B.; Zhang, G.; Khau, B. V.; Reichmanis, E.; Yoon, D. K. Highly Oriented and Ordered Water-Soluble Semiconducting Polymers in a DNA Matrix. *Chem. Mater.* **2020**, *32*, 688–696.

[22] Garcia, A.; Bakus, R. C.; Zalar, P.; Hoven, C. V.; Brzezinski, J. Z.; Nguyen, T. Q. Controlling Ion Motion in Polymer Light-Emitting Diodes Containing Conjugated Polyelectrolyte Electron Injection Layers. *J. Am. Chem. Soc.* **2011**, *133*, 2492–2498.

[23] Huber, R. C.; Ferreira, A. S.; Thompson, R.; Kilbride, D.; Knutson, N. S.; Devi, L. S.; Toso, D. B.; Challa, J. R.; Zhou, Z. H.; Rubin, Y.; et al. Long-Lived Photoinduced Polaron Formation in Conjugated Polyelectrolyte-Fullerene Assemblies. *Science* **2015**, *348*, 1340–1343.

[24] Clark, A. P. Z.; Shi, C.; Ng, B. C.; Wilking, J. N.; Ayzner, A. L.; Stieg, A. Z.; Schwartz, B. J.; Mason, T. G.; Rubin, Y.; Tolbert, S. H. Self-Assembling Semiconducting Polymers - Rods and Gels from Electronic Materials. *ACS Nano* **2013**, *7*, 962–977.

[25] Huber, R. C.; Ferreira, A. S.; Aguirre, J. C.; Kilbride, D.; Toso, D. B.; Mayoral, K.; Zhou, Z. H.; Kopidakis, N.; Rubin, Y.; Schwartz, B. J.; et al. Structure and Conductivity of Semiconducting Polymer Hydrogels. *J. Phys. Chem. B* **2016**, *120*, 6215–6224.

[26] Willot, P.; Govaerts, S.; Koeckelberghs, G. The Controlled Polymerization of Poly(Cyclopentadithiophene)s and Their All-Conjugated Block Copolymers. *Macromolecules* **2013**, *46*, 8888–8895.

[27] Svergun, D. I.; Koch, M. H. J. Small-Angle Scattering Studies of Biological Macromolecules in Solution. *Reports Prog. Phys.* **2003**, No. *66*, 1735.

[28] Putnam, D. K.; Lowe, E. W.; Meiler, J. Reconstruction of Saxs Profiles From Protein Structures. *Comput. Struct. Biotechnol. J.* **2013**, *8*, e201308006.

[29] Hammouda, B. A New Guinier-Porod Model. *J. Appl. Crystallogr.* **2010**, *43*, 716–719.

[30] Liu, H.; Zwart, P. H. Determining Pair Distance Distribution Function from SAXS Data Using Parametric Functionals. *J. Struct. Biol.* **2012**, *180*, 226–234..

[31] Svergun, D. I. Determination of the Regularization Parameter in Indirect-Transform Methods Using Perceptual Criteria. *J. Appl. Crystallogr.* **1992**, *25*, 495–503.

[32] Svergun, D. I.; Koch, M. H. J. Reports on Progress in Physics Related Content Small-Angle Scattering Studies of Biological Macromolecules in Solution Small-Angle Scattering Studies of Biological Macromolecules in Solution. *Reports Prog. Phys.* **2003**, No. 66, 1735.

[33] Xu, Z.; Gao, C. Graphene Chiral Liquid Crystals and Macroscopic Assembled Fibres. *Nat. Commun.* **2011**, *2*, 571–579.

[34] Wang, Z.; Liu, F.; Gao, Y.; Zhuang, W.; Xu, L.; Han, B.; Li, G.; Zhang, G. Hexagonal Liquid Crystalline Phases Formed in Ternary Systems of Brij 97-Water-Ionic Liquids. *Langmuir* **2005**, *21*, 4931–4937.

[35] Svergun, D. I. Restoring Low Resolution Structure of Biological Macromolecules from Solution Scattering Using Simulated Annealing. *Biophys. J.* **1999**, *76*, 2879–2886.

[36] Hirai, M.; Arai, S.; Iwase, H. Concentration Dependence of Thermal Structural Transition of Hen Egg-White Lysozyme under Constant Heating Rate Studied by Time-Resolved SAXS. *Thermochim. Acta* **2000**, *344*, 95–102.

[37] Chen, G.; Yu, W.; Singh, D.; Cookson, D.; Routbort, J. Application of SAXS to the Study of Particle-Size-Dependent Thermal Conductivity in Silica Nanofluids. *J. Nanoparticle Res.* **2008**, *10*, 1109–1114.

[38] Yu, D.; Huang, F.; Xu, H. Determination of Critical Concentrations by Synchronous Fluorescence Spectrometry. *Anal. Methods* **2012**, *4*, 47–49.

Chapter 6: Design and Control of Amphiphilic Polymer and Small Molecule Acceptor Co-Assemblies to Facilitate Excited State Electron Transfer

Section 6.1. Abstract

Excited state electron transfer has many applications including organic photovoltaics, sensors and water splitting. The efficiency of excited state electron transfer is largely influenced by both charge recombination and the molecular packing geometry between donor and acceptor. Here, we demonstrate how our unique amphiphilic, semiconducting polymers act as the scaffold for co-assemblies between electron donors and acceptors. These electron donating polymers form cylindrical micelles in water and provide a network for electron acceptor incorporation. We probe the excited state electron transfer in these co-assemblies by varying the acceptor size and solvation conditions necessary to form said co-assemblies. We find that tightly packed polymer micelles assemble more easily with flatter perylenediimide based acceptors than larger fullerene-based acceptors, as verified through a combination of photoluminescence (PL) spectroscopy and solution small angle X-ray scattering (SAXS). Initial geometric mismatch between tightly packed donor micelles and acceptors can be overcome by solvent annealing to drive additional acceptor incorporation. In contrast, looser and more disordered micelles form similar co-assembled structures, independent of acceptor shape. Our results demonstrate that we can achieve relatively precise control between electron donor and acceptor co-assemblies by varying the structural properties of component polymers and acceptors, which can provide guidelines for designing systems with controllable excited state electron transfers.

Section 6.2. Introduction

The photo-excited electron transfer (PET) process has many applications including catalysis, water splitting, organic photovoltaics (OPVs), etc.[1-4] For PET to occur, the first excited state of the electron donor must be aligned with a low-lying lowest unoccupied molecular orbital (LUMO) on the electron acceptor. Electron donors generate excitons after absorbing light, then charge separate to pass the electron to the acceptor, leaving behind a lone on the donor.

Biological photosynthesis is a representative PET system.[5] The precise packing of acceptor molecules around primary porphyrin-based electron donors enables charge separation with near unity quantum yield.[6] Inspired by this incredibly efficient natural process, researchers have made tremendous progress in mimicking many aspects of this process by building charge transfer complexes based on small light-absorbing molecules.[7,8] While many of these systems can achieve efficient charge transfer processes, there are two drawbacks. First, it is hard to control the crystallization process of small molecule charge transfer complexes. For example, tetrathiafulvalene (TTF) and tetracyanoquinodimethane (TCNQ) requires segregated stacking to have high conductivity, however, some conditions produce mixed stacking complexes. Among these charge transfer complexes, some produce integer charge transfer while others produce fractional charge transfer, thus further complicating matters. Second, small molecule charge transfer systems have low charge transport efficiency after charge separation due to the lack of an extended carrier propagating network. More often, the electron will transfer back to the donor molecule, resulting in charge recombination. Nature's photosynthesis is able to avoid this issue by utilizing a membrane as a heterogeneous matrix to facilitate long-range electron transfer and as

the structural connectivity that gives biological systems their unique functionality, rather than the fast excited-state electron transport.[9,10]

Similar designs can be achieved without a membrane by utilizing one charge transfer component as a matrix so it simultaneously acts as the electron donor (or acceptor), structure director, and transport medium. This advantageously provides a network where the electron transfer direction is different from the charge propagating direction, which can help mitigate photogenerated carrier recombination losses. Examples of such donor matrixes include carbon nanotubes and graphene,[11,12] semiconducting polymers,[13] and organogelator materials.[14] Among these materials, semiconducting polymers are particularly applicable due to their tunable extinction coefficients, narrow band gaps, and broad absorbance spectra that can be varied by harnessing the power of modern organic chemistry.[15-17] The charge transfer direction at the polymer donor-acceptor interface is typically different from the charge delocalization direction. Such anisotropy enables photogenerated carriers to delocalize along the conjugated polymer backbone, simultaneously increasing carrier mobility and helping to suppress charge recombination.[18,19]

Indeed, semiconducting polymers, as a class of PET electron donors have already been successfully used in various fields including: OPVs, sensors, water splitting catalyst etc., due to their solution-processable, low cost, structural and optical tunable properties.[20-22] For an OPV, a semiconducting polymer is usually paired with organic acceptors such as fullerene derivatives.[23,24] After the charge separation at the donor-acceptor interface, the charges transverse the polymer or the acceptor network and are eventually extracted to generate current.[25] However, one potential problem in these polymer-based devices is the high molecular inhomogeneity which makes it hard to study the specific molecular conformations that enhance device efficiency. Thus more control

over the final polymer structure and the way it packs with acceptors are needed. Various methods have been developed to control polymer structure including increasing molecular order through backbone and sidechain design,[26,27] increasing the overall crystallinity through enhanced π-stacking,[28,29] and straightening of polymer backbones via aligned nanopores or mechanical rubbing.[30,31] To control how polymers mix with acceptors, researchers have also developed methods including varying fabrication solvents, annealing conditions, and utilizing processing additives such as 1,8-diiodoctane (DIO) to tune the domains of the two components.[32-34] However, these post-processing methods have limited effect on controlling packing between polymer donors and acceptors. Methods that can precisely drive and control how semiconducting polymers co-assemble with acceptors are needed.

To address this issue, our work is based on two parts. First, we were able to increase the order of semiconducting polymers by synthesizing and studying two amphiphilic, cylindrical micelle–forming semiconducting polymers **PFT** and **PCT** previously reported from our groups (Figure 6.1).[35,36] These two semiconducting polymers are conjugated polyelectrolytes which consist of a conjugated backbone with charged alkyl sidechains capable of self-assembling into cylinder micelles in polar solvents such as water. Second, we used these ordered semiconducting polymers as electron donor scaffolds to study PET with acceptors. Our prior work utilizing **PFT** as a co-assembly scaffold for charged fullerene derivatives, both inside and outside the micelle leads us to believe **PCT** will also form similar assemblies.[37] This ordered and extended polymer micelle donor structure enables the precise positioning of the acceptors and even forms solution-phase polarons.

Here, we further explore control of the co-assembly process between these ordered polymers with acceptors, by expand on our previous work through use of different polymer micelle

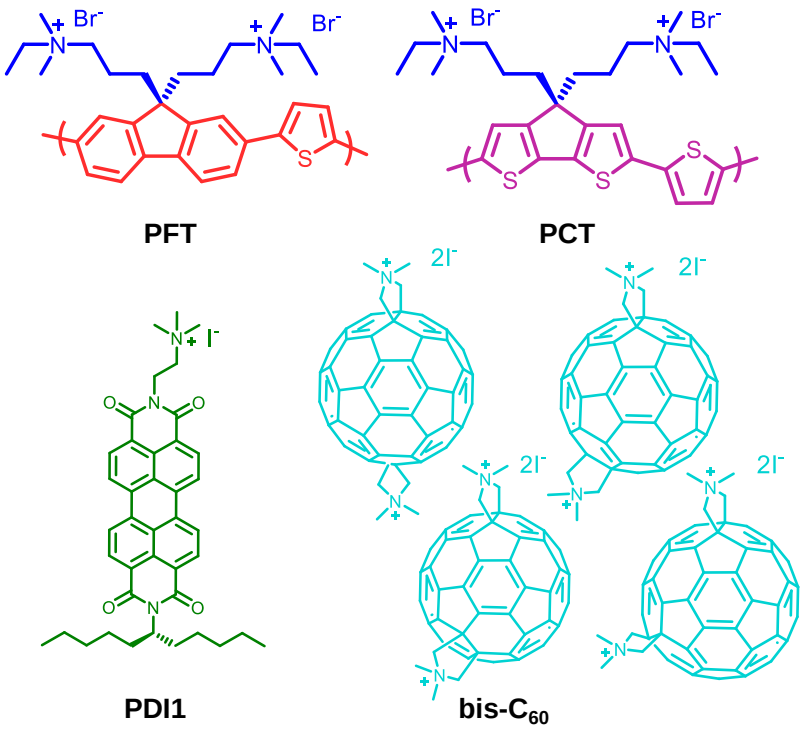

Figure 6.1. Molecular structure of poly(fluorine-*alt*-thiophene) (**PFT**), poly(cyclo-pentadithiophene-alt-thiophene) (**PCT**), charged perylenediimide (**PDI1**) and mixed-bischarged fullerenes (**bis-C60)**.

structures, acceptor sizes and geometries, and processing conditions that affect the co-assembled structures and excited electron transfer. We use two self-assembled semiconducting polymers with distinct micelle structures, as electron donors and co-assemble them with both flat PDI based and spherical fullerene based acceptor molecules in aqueous solutions (Figure 6.1). From photoluminescence (PL) quenching, we learn that loose and disordered polymer micelles form similar co-assemblies independent of acceptor type. However, tight and ordered polymer micelles, co-assemble with flat acceptors more easily than with spherical ones. After initial complexation, solvent annealing can be used to drive additional acceptors to the micelle, which were previously excluded due to size constraints. This phenomenon, along with native polymer and mixed co-

assemblies are characterized by solution small angle X-ray scattering (SAXS). We further drop-casted films of the co-assemblies to study the solid-state electron transfer. The grazing-incidence wide-angle X-ray scattering (GIWAXS) results reveal that these polymers do not π-stack like other conjugated polymers. PL quenching of these films indicates the co-assemblies are likely retained in the solid state. Overall, by manipulating polymer structure to form controlled micelles, we are able to probe structural factors that influence excited state electron transfer and provide insight into their systematic design.

Section 6.3. Results and Discussion

Characterization of Co-Assembled Structure and Electron Transfer in Solution

Structure of PFT and PCT in Water: A critical part of our design rules for controlling polymer and acceptor co-assemblies lies in controlling the chemical structure of individual components. Both of our polymers, **PFT** and **PCT**, contain a hydrophobic conjugated backbones and hydrophilic quatranized ammonium sidechains branched off a sp^3 carbon (Figure 6.1). This tetrahedral site forces the sidechains away from the backbone, resulting in a "pie-wedge" shape for each polymer chain. These individual chains assemble in water into cylindrical micelles, with the backbone forming the length of the micelle and the sidechains forming a hydrophilic sheath around the conjugated backbone. Since the backbone runs the length of the micelle, its geometry determines the longitudinal shape of the micelle. **PFT** and **PCT** are both alternating co-polymers containing thiophene and three-fused ring monomer units. The fluorene in **PFT** is functionalized at the 2 and 7-positions which causes the polymer to bend due to the nonlinear relation between those sites. In contrast, **PCT** contains cyclopentadithiophene whose three fused five-member rings have

complementary bond angles between the 5,5'-positions, resulting in a straighter backbone. This straightening of the backbone should give **PCT** a straighter, tighter micelle structure relative to **PFT**.

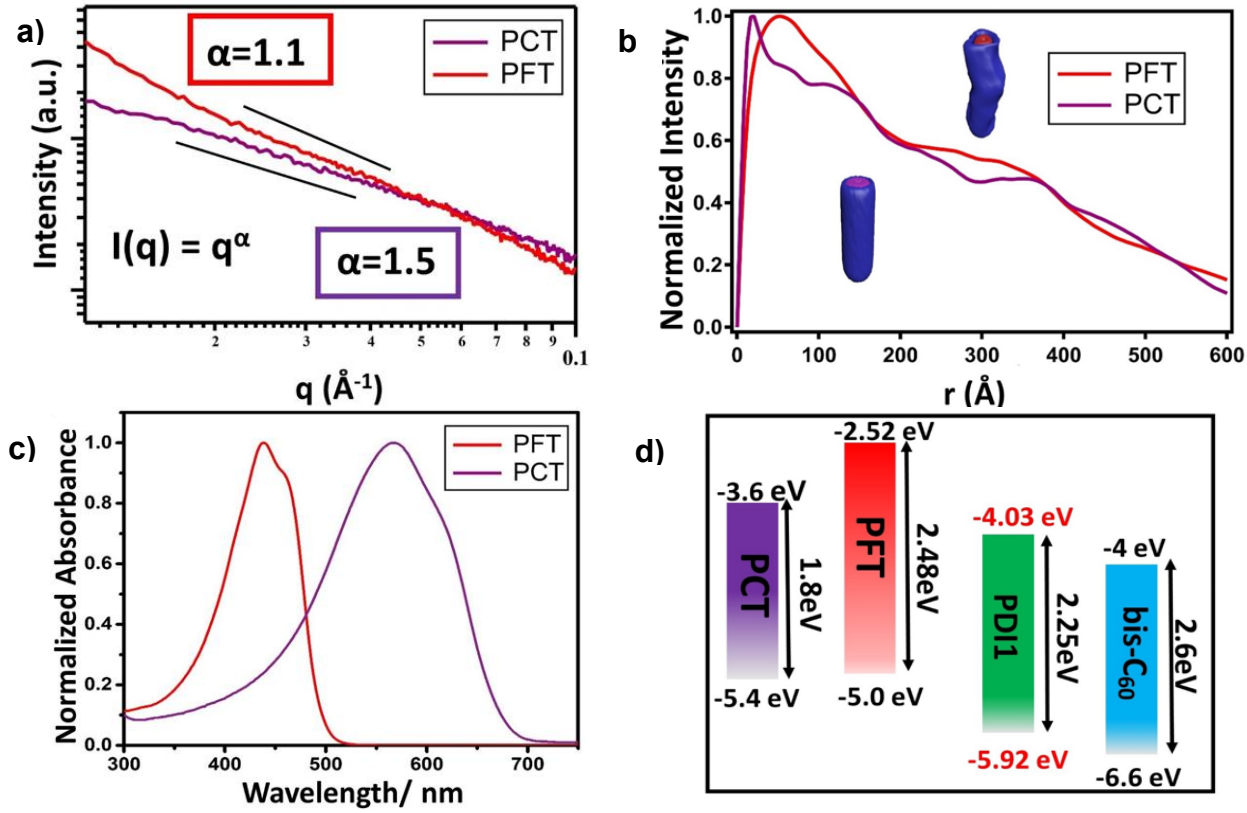

Figure 6.2. a) Solution SAXS of **PCT** and **PFT** in water. The power law fit of the curves show that **PCT** forms a straighter, cylindrical micelle compared to **PFT**. b) Fourier transform of the SAXS data in (a). Both **PCT** and **PFT** shows a cylinder shape profile, but **PCT** has a smaller micelle diameter. c) Absorbance spectrum of **PCT** and **PFT**. **PCT** absorbs more visible light than **PFT**. d) Energy levels of **PCT**, **PFT**, **PDI1** and **bis-C$_{60}$**. Excited electron transfer between the polymers and acceptors is possible given their LUMO levels.

Solution SAXS allows us to determine the shape and size of solution assemblies by analyzing the raw data and Fourier transformed data respectively. Fitting the raw data to a power law in the Guinier region can be used to extract the polymer fractal structure in solution. The slope

of the fit indicates the dimensionality of the object in solution, slopes of 1 indicate a rigid rod and 2 indicate a flat disk.[38,39] Figure 6.2a shows the raw SAXS data for **PCT** can be fit to a power law slope of nearly 1, whereas **PFT** has a slope of 1.5, which is consistent with our previous work.[36,37] This indicates that **PCT** forms a nearly straight, perfect cylinder in solution, while **PFT** is more disordered and bent, as predicted based on the rigidity of their respective backbones. Fourier transformation of the raw SAXS data gives the Pair-distance distribution functions, P(r), which are used to estimate the structure of the scattering object by presenting the distribution of electron densities along with the separation distance.[40,41] The combination of a peak at lower r and linear decay correlate to a cylindrical structure with the two r values indicating the cylinder diameter and longitude length respectively. **PCT** shows a narrower peak at lower r than **PFT**, indicating it forms tighter cylindrical micelle (Figure 6.2b). Other than the structure properties, **PCT** absorbs most range of the visible light and is more suitable for OPV related applications compared with **PFT** which only absorbs edge of the visible light (Figure 6.2c). Nevertheless, both amphiphilic polymers form cylindrical micelles, so they can be used as the scaffold for studying co-assembly structure and charge transfer.

Spectroscopy and Structure of Co-Assembled Polymers and Acceptors: To probe the effect of electron acceptor shape on cylindrical micelles, we synthesized two acceptors with drastically different geometries but similar LUMO levels (Figure 6.2d). **PDI1** is a small two-dimensional, flat acceptor with a single charged sidechain (Figure 6.1). Similar to **PFT** and **PCT**, it contains an ammonium sidechain on one end, but also has a long branched alkyl sidechain on the opposite end to help prevent self-aggregation. The opposing hydrophilicity of these sidechains gives **PDI1** its amphiphilicity. Our other acceptor, **bis-C_{60}**, is a mixture of four bis-pyrrolidiuim functionalized fullerenes, with placement of the two rings creating trans-like and cis-like adducts. These adducts

prefer to sit around different parts of the cylindrical micelle, and we have previously used them to study amphiphilic charge transfer with **PFT**.[37] Notably both **PDI1** and **bis-C$_{60}$** are insoluble in water on their own, and require the amphiphilic polymers to drive their co-assembly. This allows us to explore how acceptor size and shape affects co-assembly with the polymers.

Based on the energy levels shown in Figure 6.2d, both polymers should be able to undergo PET with both acceptors. Therefore, we can use PL as an indirect way of assessing how these assemblies are structured. Each polymer is mixed with each acceptor at two mass ratios to explore the effect of both shape and concentration. **PFT** PL shows no dependence on acceptor shape, only concentration (Figure 6.3a,b). In contrast, **PCT** PL is quenched 23% more with **PDI1** than **bis-C$_{60}$** for each ratio of acceptors (Figure 6.3c,d). We attribute this difference in quenching to structural differences in between the **PFT** and **PCT** micelle. **PCT** forms a more defined and tight micelle which leaves smaller pockets of space for addition acceptors compared with the more disordered and looser micelles of **PFT**. Since **PDI1** is a flat acceptor, it is able to fit into the tight spaces around the **PCT** micelle whereas the spherical bulk of **bis-C$_{60}$** is unable to pack into those same spaces. This results in more complementary assemblies between **PCT** with **PDI1** than **bis-C$_{60}$**. However, **PFT** micelles are more disordered and thus contain spaces which fit **PDI1** and **bis-C$_{60}$** equally well, resulting in similar abilities to quench **PFT**.

To further confirm the PL quenching difference of **PCT** by **PDI1** and **bis-C$_{60}$**, we turn to solution SAXS to obtain more structure information. Figure 6.4a,b show the P(r) curves for pure polymers, co-assemblies and pure acceptors with same concentrations in co-assemblies. The peak position correlated to cylinder diameter at low r is unchanged, indicating the **PCT** micelles retained

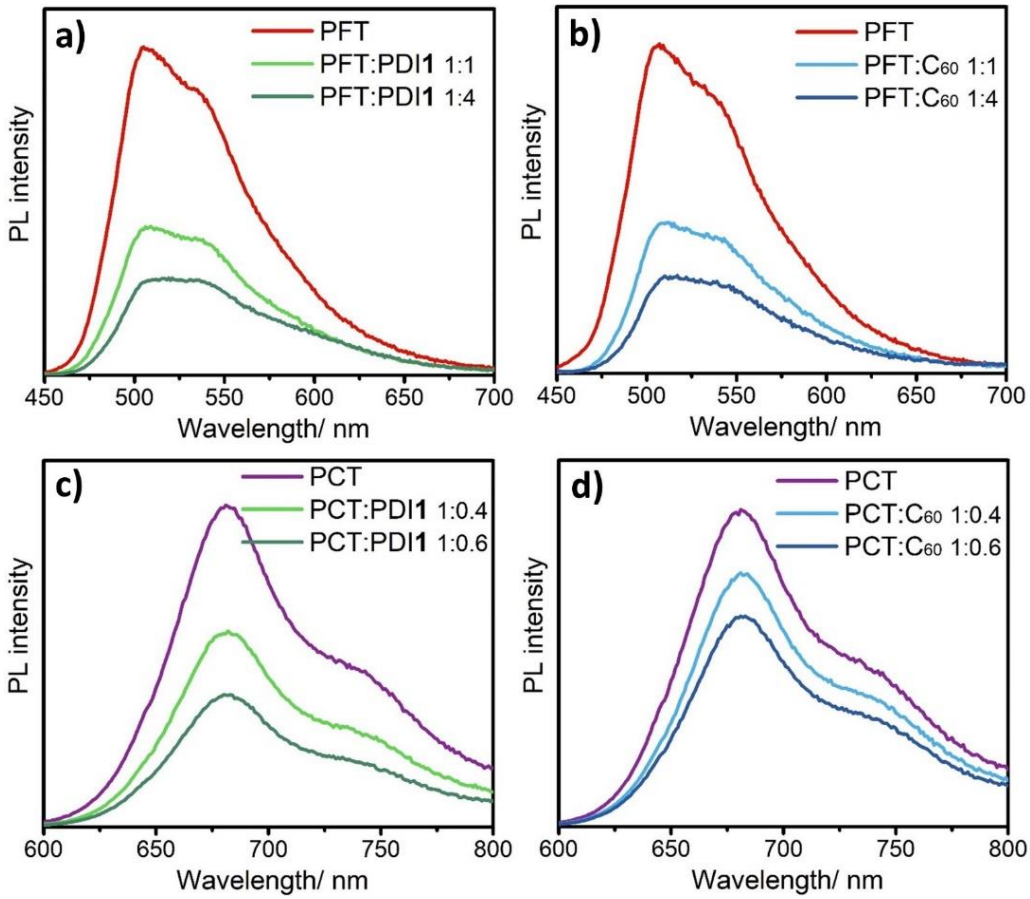

Figure 6.3. PL spectrum of a) **PFT** and **PDI1**, b) **PFT** and **bis-C$_{60}$**, c) **PCT** and **PDI1**, and d) **PCT** and **bis-C$_{60}$. PDI1** and **bis-C$_{60}$** quench **PFT** PL similarly, but quench **PCT** PL differently due to complementary micelle and acceptor geometry.

after incorporating both the acceptors. The appearance of correlation peaks at higher r is attributed to interactions between acceptors as compared with pure **PDI1** and **bis-C$_{60}$** P(r) curves in Figure 6.4a,b. Without polymers, both the acceptors form aggregates in solution due to the poor solubility. When co-assembled with polymers, both acceptor correlation peak intensities decrease, indicating the transformation of parts of the self-aggregation to co-assembly with polymer. However, **PDI1** shows a larger decrease of self-aggregation peak intensity than **bis-C$_{60}$**, which indicates that more **PDI1** co-assemble with **PCT** than **bis-C$_{60}$**. This trend is likely observed because the **PDI1** is better

able to fit into the **PCT** micelle due to small and flat geometry. This again affirms our earlier hypothesis that co-assembly is determined by how well the acceptors fit around the spaces of the pre-existing micelle network holds true.

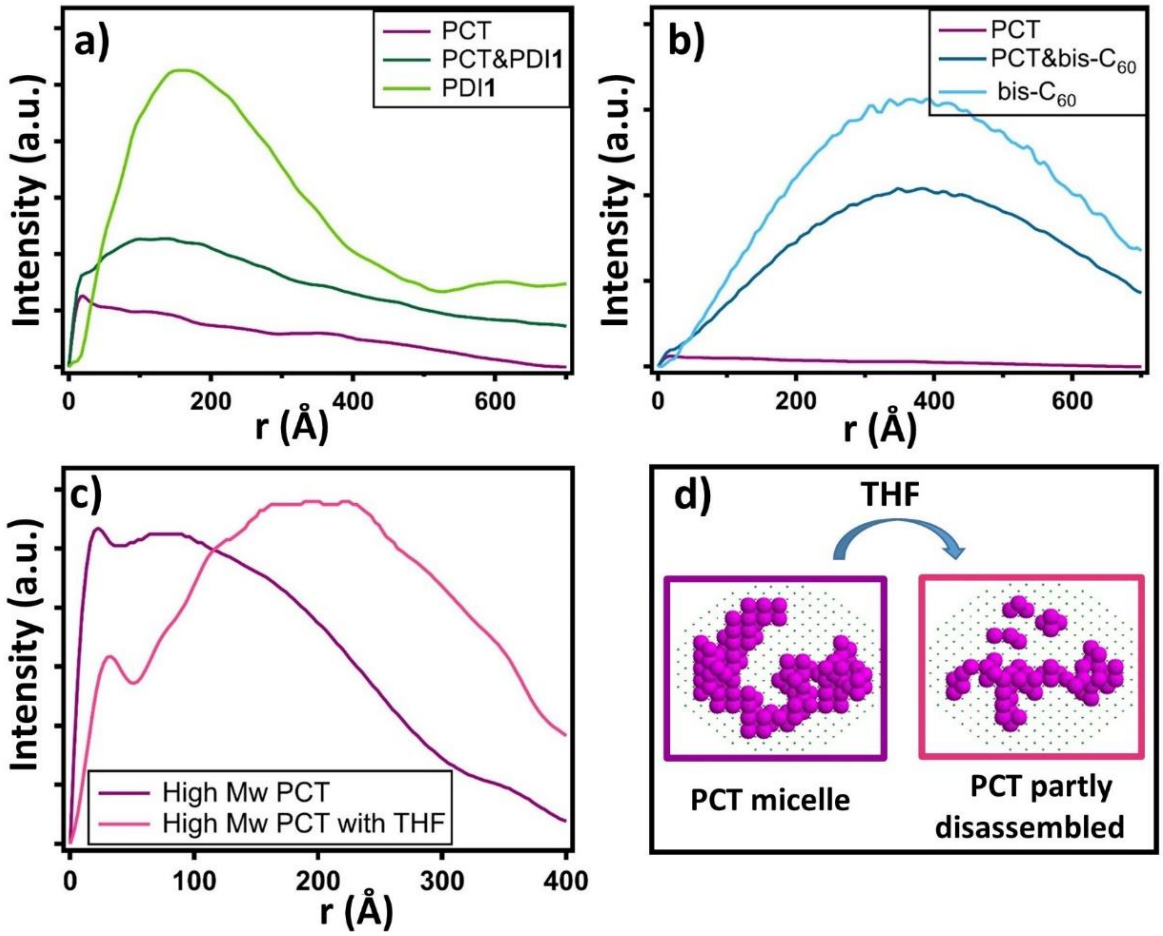

Figure 6.4. P(r) curves of a) **PCT, PDI1 and PCT** with **PDI1** b) **PCT**, **bis-C_{60}** and **PCT** with **bis-C_{60}**. The unchanged lower r peak position demonstrates that the micelle structure is conserved after acceptor co-assembly. c) P(r) of **PCT** without and with THF. Adding THF loosens the micelle structure and induces both intra- and intermicelle interaction. d) DAMMIN Beads modeling of **PCT** after adding THF shows a decrease in electron density.

The Effects of Solvent Annealing on Co-Assembled Structures: A potential drawback of the **PCT** micelles is its inability to accommodate acceptors of all shapes or sizes due to its tight structure. It

would be ideal if we could engineer a process that temporarily relaxes these micelles and allows the acceptors to incorporate into the newly opened spaces. Solvent annealing is a common method researchers use to tune polymer morphology.[34,42-44]Prior work from our groups showed that **PFT** cylindrical micelle networks in solution were relaxed upon addition of tetrahydrofuran (THF), but then become more robust once the THF was removed.[45] Seeing as **PCT** also forms cylindrical micelles, we chose to solvent anneal with THF for the co-assemblies studied in this work.

After the addition of THF to preassembled **PCT** without annealing in water, the main micelle peak intensity decrease, becomes broad and shift to higher r (Figure 6.4c). This means that the **PCT** micelle structure is not fully disrupted but appears to be partly dissolved as a loosening and disordering of the micelle. Meanwhile, a new broad correlation peak appears in the higher r region, which is assigned to intermicelle and intramicelle interactions due to disordering.[36] The structure of the partly dissolved micelles can be modeled using DAMMIN beads modeling to simulate the scattering structure corresponding to the solution SAXS data.[42] The modeling result in Figure 6.4d shows that the compact cylindrical micelles evolve into more diffuse scattering structures with less electron density. This validates our conclusion that THF partly dissolve and relax polymer micelle structure.

The effect of relaxing the micelles can be seen in the PL quenching data before and after THF annealing. **PFT** already forms loose micelles so THF annealing has no added effect on the co-assembly and the PL quenching remains unaffected (Figure 6.5a,b). In contrast, there is a noticeable decrease in PL after **PCT** co-assemblies are THF annealed. Both **PDI1** and **bis-C_{60}** decrease by 10% and 15% respectively for low and high acceptor ratios. **PDI1** is soluble in THF so solvent annealing simultaneously disrupts the acceptor aggregates (Figure A12) and relaxes the polymer micelle.[46] This allows the whole system to reassemble with closer donor-acceptor

interactions, resulting in increased quenching (Figure 6.5c,d). Co-assemblies of **PCT** and **bis-C$_{60}$** show similar trends to those of **PCT** with **PDI1** before and after solvent annealing (Figure 6.5e,f). The only difference is that increased quenching is purely due to reassembly after THF annealing and not also attributed to acceptor disaggregation. As **bis-C$_{60}$** is marginally soluble in neat THF, and does not disaggregate upon annealing, it merely fills in the spaces that open up as the polymer micelle relaxes. In general, this demonstrates that solvent annealing can be used to drive additional acceptors to co-assemble with the polymer micelles, which might have been previously excluded either due to steric hindrance or self-aggregation.

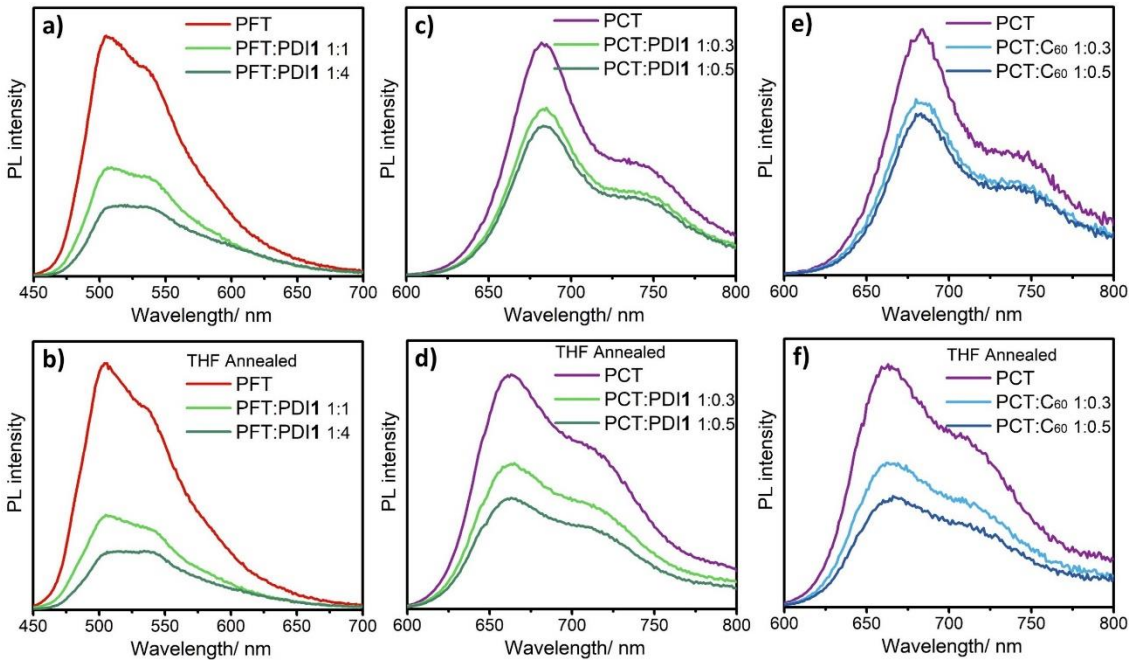

Figure 6.5. PL quenching spectrum of a) **PFT** and **PDI1**, b) **PFT** and **PDI1** after THF annealing, c) **PCT** and **PDI1**, and d) **PCT** and **PDI1** after THF annealing, e) **PCT** and **bis-C$_{60}$,** and f) **PCT** and **bis-C$_{60}$** after THF annealing. Consistent with the solution SAXS data, higher **PCT** concentrations are used so the **PDI1** ratios and quenching are less than those in Figure 6.3. THF annealing does not influence **PFT** PL quenching very much, but has a more obvious effect on **PCT** due to the structural difference between **PCT** and **PFT**.

Solid-State Structure of the Co-Assemblies

Up to now we have focused on the solution assembly, but transitioning the solution assemblies to solid-state would have potential applications in PET based devices. The PET efficiency in such devices, such as OPV, highly depends on the donor-acceptor interface molecular packing structure.[47,48] Since we were able to control the donor-acceptor packing structure in solution phase, the transition to solid-state could provide guidance on fabricating such devices with controllable structure, which will largely influence the device efficiency. We first use GIWAXS to characterize the pure polymer micelle structure in solid-state. Figure 6.6a shows the

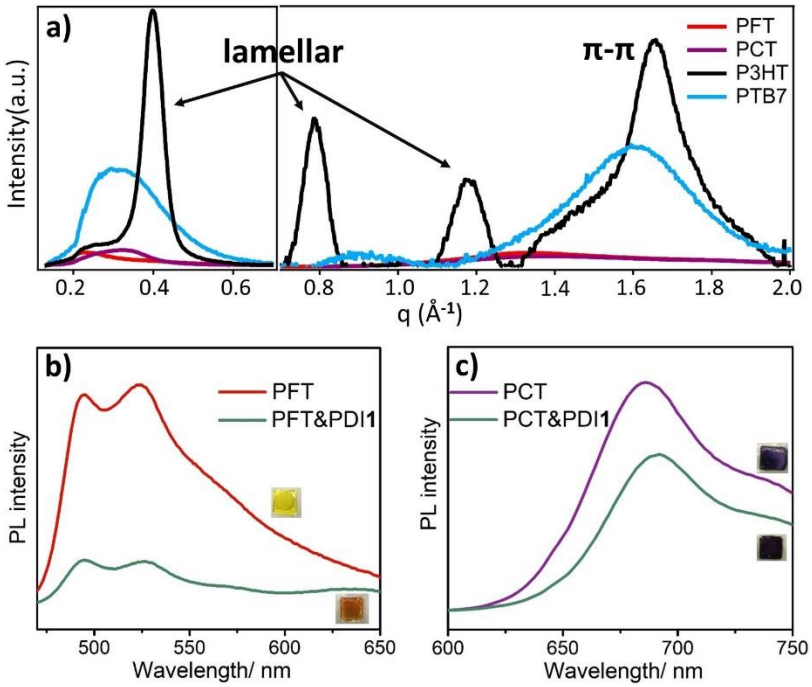

Figure 6.6. a) Full radially-integrated 2-D GIWAXS of **PFT, PCT,** P3HT, and PTB7 films. The intensity of **PFT** and **PCT** scattering are multiplicatively increased to be visible on the same scale of as P3HT and PTB7. Compared with common π-stacking polymers, **PFT** and **PCT** do not show the signature π-π stacking peaks, indicating likely retention of the micelles in the solid-state. b) **PFT** and c) **PCT** films co-assembled with **PDI1**, which show that the co-assembled structure is likely retained in solid-state.

integrated GIWAXS of neat **PFT** and **PCT** films plotted against films of poly(3-hexylthiophene) (**P3HT**) and poly[[4,8-bis[(2-ethylhexyl)oxy]benzo[1,2-b:4,5-b']dithiophene-2,6-diyl)[3-fluoro-2-[ethylhexyl)carbonyl]thieno[3,4-b]thiophenediyl (**PTB7**). **P3HT** is chosen as a typical semi-crystalline semiconducting polymer and **PTB7** as an amorphous polymer. Most of the conjugated semiconducting polymers, regardless of their crystallinity, show two peaks: the lamellar peak at lower q and a π-π stacking peak at higher q. However, both of our amphiphilic polymers do not show these characteristic GIWAXS patterns, indicating that micelle formation frustrates π-stacking, which bodes well for retaining the micelles in the solid state. By comparing PL of neat polymer films to those of the co-assemblies, we see that **PDI1** is still able to quench **PFT** and marginally quench **PCT** in the solid-state (Figure 6c,d). Specifically, in the case of **PFT**, we acknowledge that the increased amount of quenching is possibly due to energy transfer, as the **PFT** PL spectrum overlaps with the **PDI1** absorbance window. Nevertheless, the PL measurements show that these co-assemblies have potential in the solid-sate and provides an area for further study.

Section 6.4. Conclusions

To elucidate the effect of assembly structure on charge transfer, we studied the aqueous co-assemblies of two electron donor polymers and two small molecular acceptors. Our two amphiphilic, cylindrical micelle-forming, semiconducting polymers allowed us to probe the effect of micelle structure on charge transfer in conjunction with our two different acceptor geometries. For a loose polymer micelle, there is no selectivity with acceptor geometries. However, for a tight and ordered micelle, acceptors with matched geometry and miscibility form better co-assemblies.

These geometric constraints of acceptor molecules can be overcome by solvent annealing, which relaxes the polymer micelle and creates more space for the acceptor molecules. Overall, we were able to validate that control of co-assembly between semiconducting polymers and molecular acceptors can be tuned via polymer micelle structure by changing either changing the structure of the polymer itself or via through solvent annealing. These solution phase charge transfer assemblies show potential to stay in solid-state for potential device applications.

Section 6.5. Experimental Details

General procedures: Chemical reagents were obtained from commercial sources and used without further purification. Unless otherwise noted, all reactions were performed under argon at 25 °C. Silicycle (Siliflash P60) silica gel 60 (240-400 mesh) was used for all column chromatography. NMR spectra were obtained on a Bruker AV500 instrument. 2,9-di(undecan-6-yl)anthra[2,1,9-def:6,5,10-d'e'f']diisoquinoline-1,3,8,10(2H,9H)-tetraone **(1)**,[49] **PFT**,[35] the bis-C_{60} charged fullerenes,[37] and **PCT**[36] were synthesized according to published procedures.

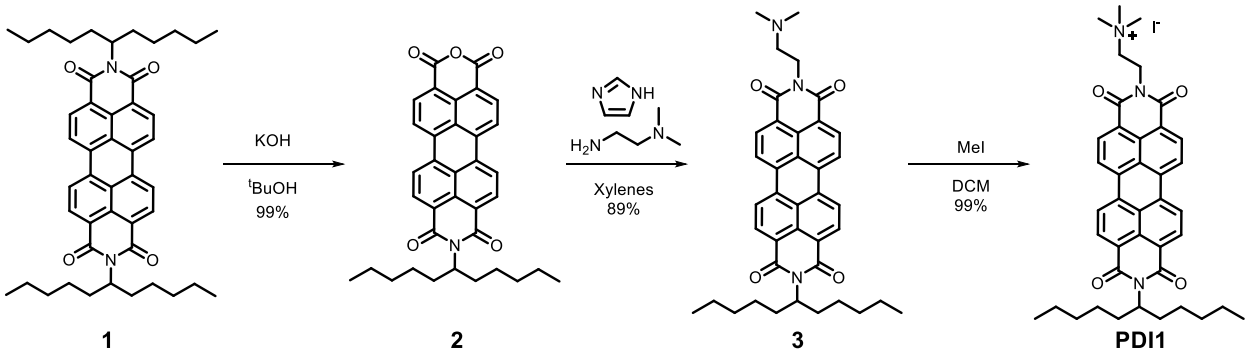

Scheme S1. Synthesis of PDI1.

9-(undecan-6-yl)-1H-isochromeno[6',5',4':10,5,6]anthra[2,1,9-def]isoquinoline-1,3,8,10(9H)-tetraone (2)

Compound **1** (1.000g, 1.432 mmol, 1.0 eq) was dissolved in tert-butanol (36 mL). Potassium hydroxide pellets (401 mg, 7.16 mmol, 5.0 eq) were added and the solution heated to 90 °C. After 1 hour, the reaction was checked by TLC and then poured into stirring glacial acetic acid (36 mL). This was allowed to stir for 2 hours at room temperature before 2N HCl (18 mL) was added and stirred for an additional 30 min. The mixture was then filtered and washed with H_2O until the filtrate was at neutral pH. The resulting red solid was then purified via column chromatography on silica gel using chloroform to chloroform with 10% acetic acid. 490 mg (63%) of the final compound was recovered. ^{1}H NMR (400 MHz, $CDCl_3$): δ (ppm) 8.69 (m, 8H), 5.18 (m, 1H), 2.23 (m, 2H), 1.86 (m, 2H), 1.27 (m, 12H), 0.83 (t, *J* = 4.7 Hz 6H); ^{13}C NMR (125 MHz, $CDCl_3$): δ (ppm) 160.0, 136.5, 133.6, 131.9, 129.5, 126.9, 126.6, 123.9, 123.2, 119.0, 54.9, 32.3, 31.7, 26.6, 22.6, 14.0; HRMS (DART) Calculated for $C_{35}H_{31}NO_5$ [M+H]: 545.22022; found 545.22104.

2-(2-(dimethylamino)ethyl)-9-(undecan-6-yl)anthra[2,1,9-def:6,5,10-d'e'f']diisoquinoline-1,3,8,10(2H,9H)-tetraone (3)

To a solution of compound **2** (481 mg, 0.882 mmol, 1.0 eq) in xylenes (2.0 mL) were added imidazole (481 mg, 7.66 mmol, 8.0 eq) and N,N-dimethylethylenediamine (0.145 mL, 1.32 mmol, 1.5 eq). The reaction was heated to 120 °C for 3.5 hours under argon. After cooling to room temperature, the mixture was poured into methanol (30 mL), sonicated and filtered. Purification by column chromatography in CH_2Cl_2 with 10% methanol and 2.5% trimethylamine afforded a red solid as the product (409 mg, 89%). ^{1}H NMR (400 MHz, $CDCl_3$): δ (ppm) 8.67 (d,

J = 4.0 Hz, 4H), 8.61 (d, *J* = 2.4 Hz, 2H), 8.59 (d, *J* = 2.4 Hz, 2H), 5.19 (m, 1H), 4.37 (t, J = 6.9 Hz, 2H), 2.75 (t, J = 6.9 Hz, 2H), 2.40 (s, 6H), 2.25 (m, 2H), 1.87 (m, 2H), 1.26 (m, 12H), 0.83 (t, *J* = 6.9 Hz, 6H); ^{13}C NMR (125 MHz, $CDCl_3$): δ (ppm) 163.5, 134,8, 134.4, 131.5, 129.6, 129.5, 126.5, 126.4, 123.2, 123.0, 56.9, 54.8, 45.8, 45.6, 38.1, 32.3, 31.8, 26.6, 22.6, 14.1; HRMS (DART) Calculated for $C_{39}H_{41}N_3O_4$ [M+H]: 615.30971; found 615.30508.

N,N,N-trimethyl-2-(1,3,8,10-tetraoxo-9-(undecan-6-yl)-3,8,9,10-tetrahydroanthra[2,1,9-def:6,5,10-d'e'f']diisoquinolin-2(1H)-yl)ethan-1-aminium iodide (PDI1)

Compound **3** (409 mg, 0.665 mmol) was dissolved in CH_2Cl_2 (14 mL) and iodomethane (0.91 mL) was added. The solution was allowed to stir at room temperature before concentrating to yield the final compound (425 mg, 99%) as a red solid. ^{1}H NMR (400 MHz, d_6-DMSO): δ (ppm) 8.70 (t, *J* = 8.8 Hz, 4H), 8.45 (br, 2H), 8.38 (d, *J* = 3.9, 2H), 5.05 (m, 1H), 4.45 (t, *J* = 7.1 Hz, 2H), 3.64 (t, *J* = 7.1 Hz, 2H), 3.22 (s, 9H), 2.17 (m, 2H), 1.80 (m, 2H), 1.23 (m, 12H), 0.75 (t, *J* = 6.9 Hz, 6H); ^{13}C NMR (125 MHz, d_6-DMSO): δ (ppm) 163.2, 134.6, 131.3, 128.9, 125.8, 124.6, 122.6, 62.3, 55.4, 54.0, 53.0, 34.2, 32.1, 31.6, 26.5, 22.4, 14.4, 7.9.

Sample Preparation.

The polymer solutions are made by weighing the polymer powders to vials and mixing with water on a hotplate. Co-assembly solutions were made by first dissolving the polymer in water before adding the acceptor powders. All polymer acceptor ratios are by mass, note that the two acceptors have similar molecular weights. THF annealing was performed by adding THF equal to ¼ volume of the original solution, and stirring overnight before slowly heating to 80 °c to evaporate the THF.

Polymer films were made by drop-casting either the polymer solutions or co-assembly solutions on a cleaned glass substrate. All sample preparations with **PCT** were done air-free due to **PCT** degradation in air. **PFT** does not degrade in air, thus all **PFT** experiments were performed ambient.

Spectroscopy Measurement.

The UV-vis absorption data were acquired using a Shimadzu UV- 3101PC UV-VIS-NIR Scanning Spectrophotometer for both solution and films. PL measurements were carried out using a Jobin Yvon Horiba Fluorolog-3 spectrofluorometer in front-face geometry. Solutions were measured using quartz cuvettes with 1 mm in path length.

Solution SAXS.

The solution SAXS data were collected at the Stanford Synchrotron Radiation Laboratory (SSRL) using beamline 4-2. The solution sample was loaded in a quartz capillary and held at room temperature. The scattering X-rays (12keV) were collected using a 2-D detector and radially averaged to obtain 1-D data. P(r) plots were obtained using the Gnom software from EMBL.

GIWAXS.

2-D GIWAXS data were collected at the SSRL using beamline 11-3. The beam wavelength is 0.9742 Å and the sample to detector distance is 250 mm. The sample chamber was flowed with helium to reduce noise and the incidence angle is 0.12°. All the samples were irradiated for 90 s. To reduce the 2-D diffractograms, we used the WAXStools in Igor pro. The diffractograms were radially integrated to reduce to 1-D diffraction curves.

Cyclic Voltammetry (CV)

Working electrodes were made by drop-casting **PFT**, **PCT** and **PDI1** on a clean ITO substrate. Both the counter and the reference electrode are Li.

Section 6.6. Appendix E

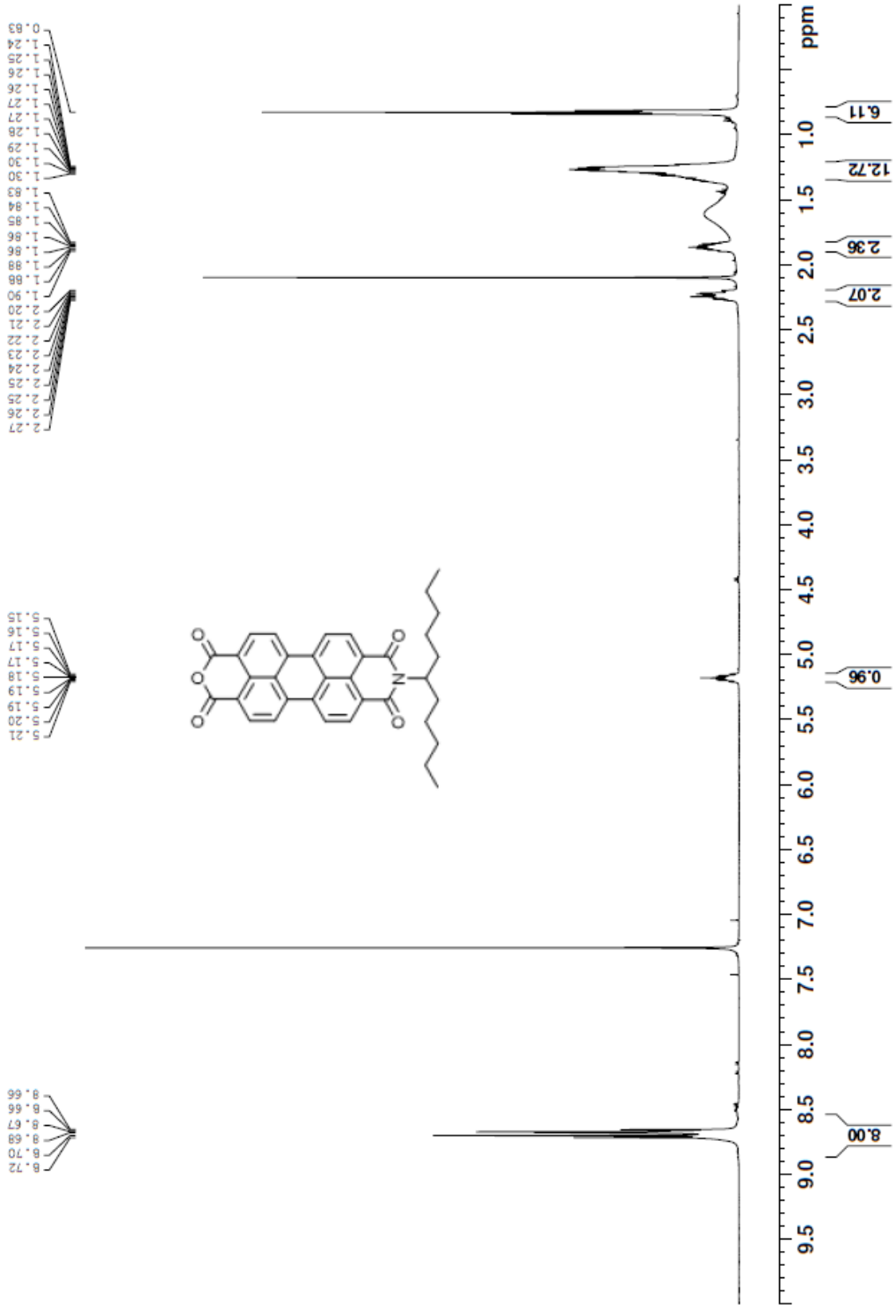

Figure A1. ^{1}H NMR spectrum of compound **2** in $CDCl_3$.

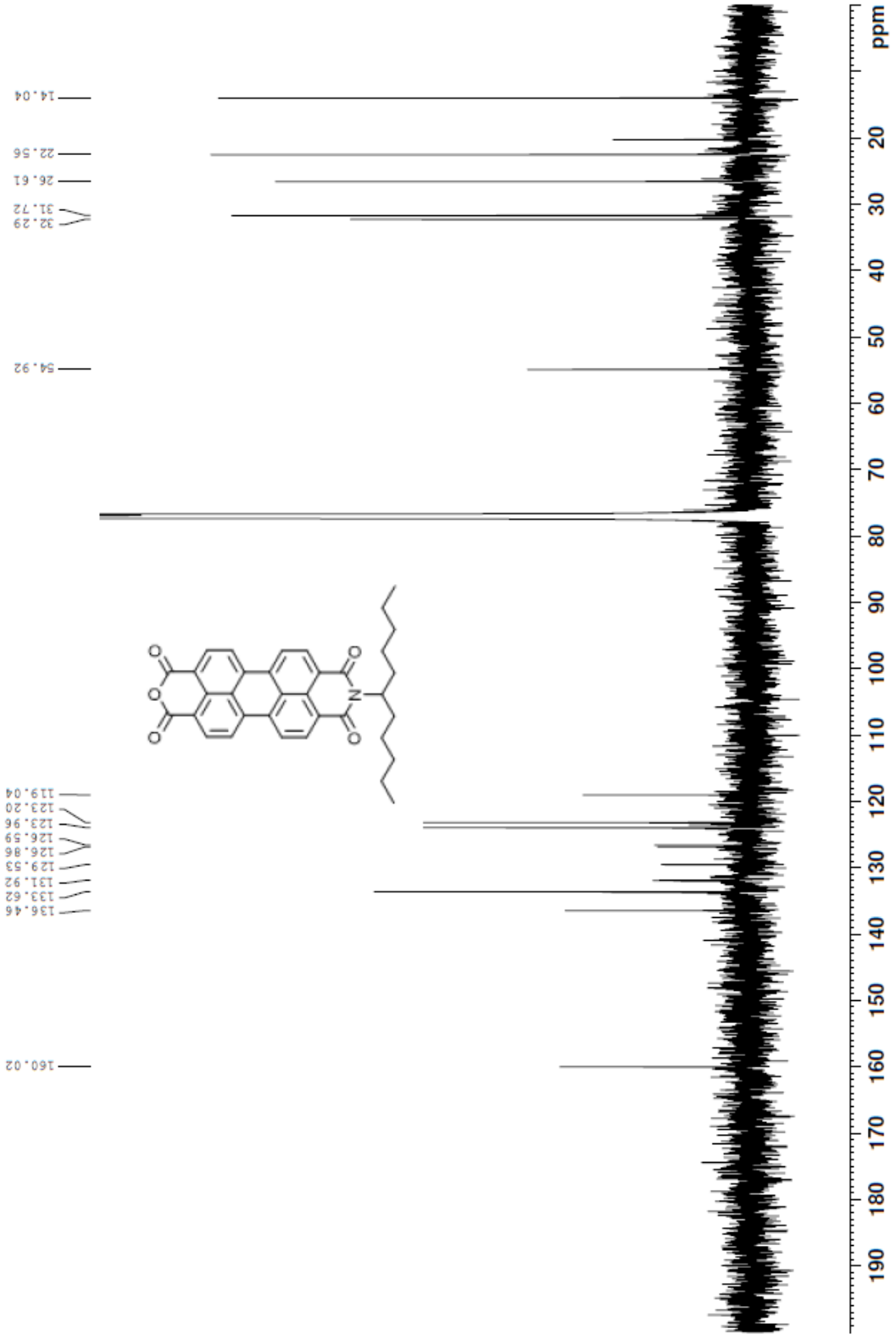

Figure A2. ^{13}C NMR spectrum of compound **2** in $CDCl_3$.

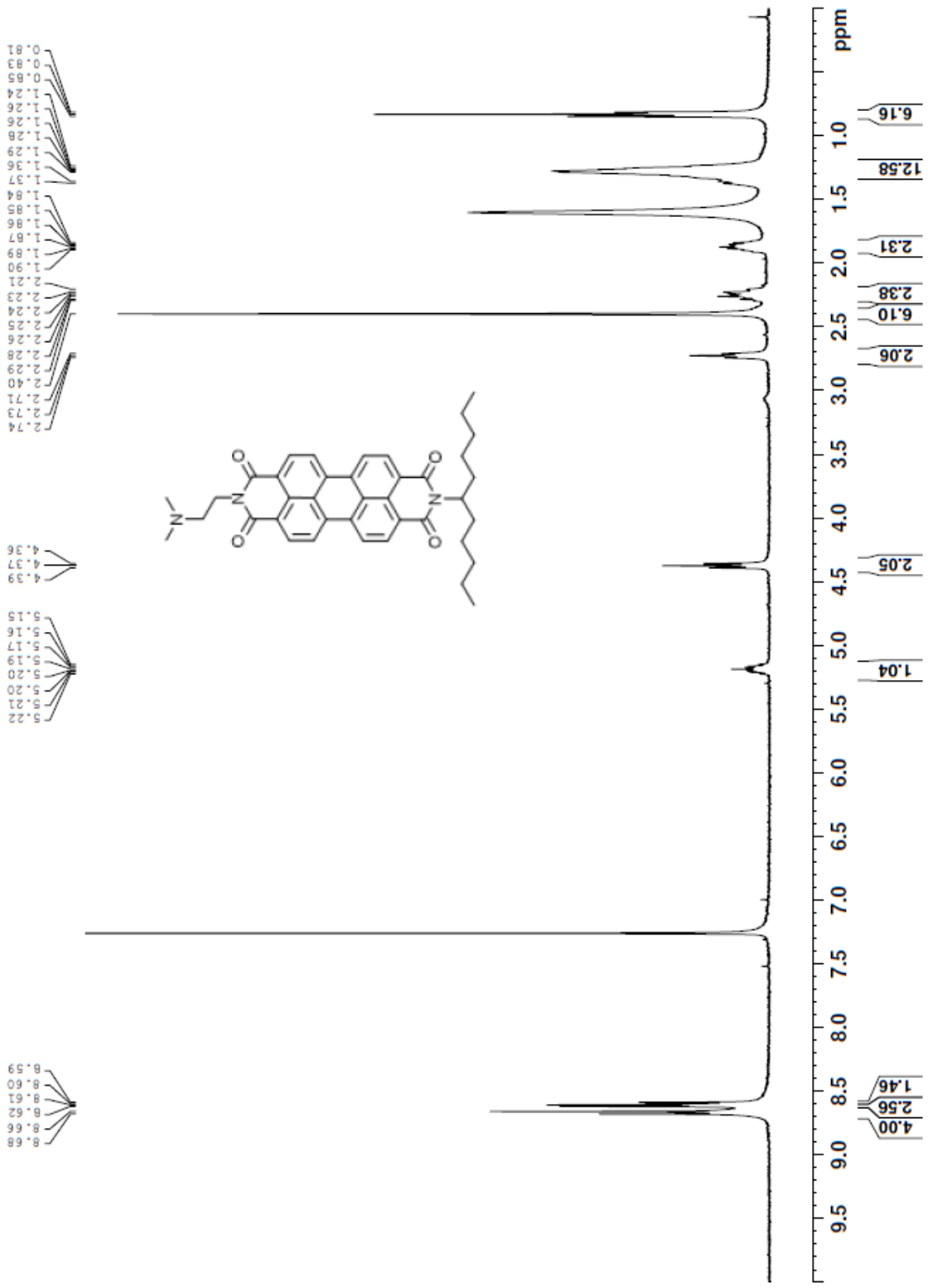

Figure A3. ^{1}H NMR spectrum of compound **3** in $CDCl_3$.

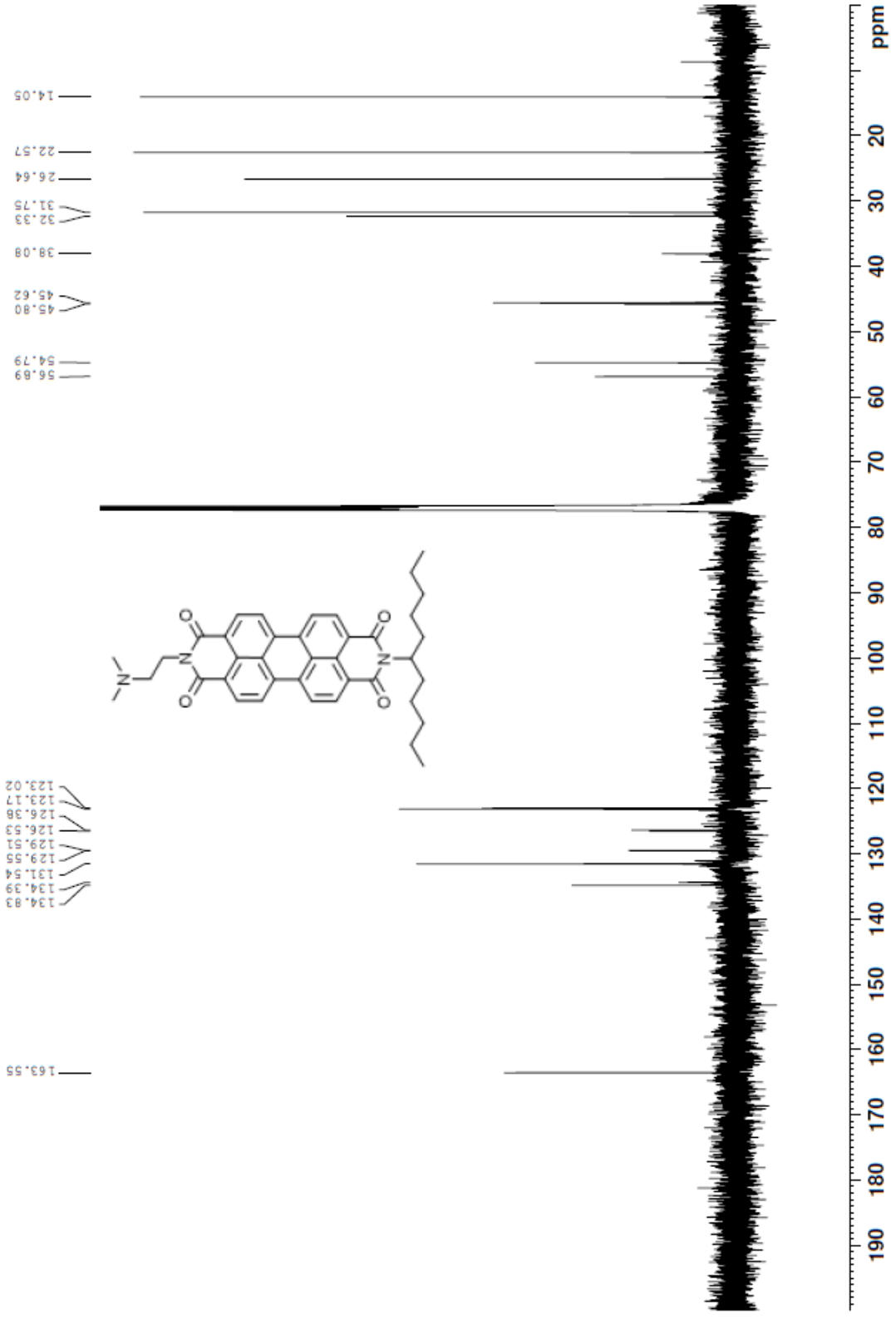

Figure A4. ^{13}C NMR spectrum of compound **3** in $CDCl_3$.

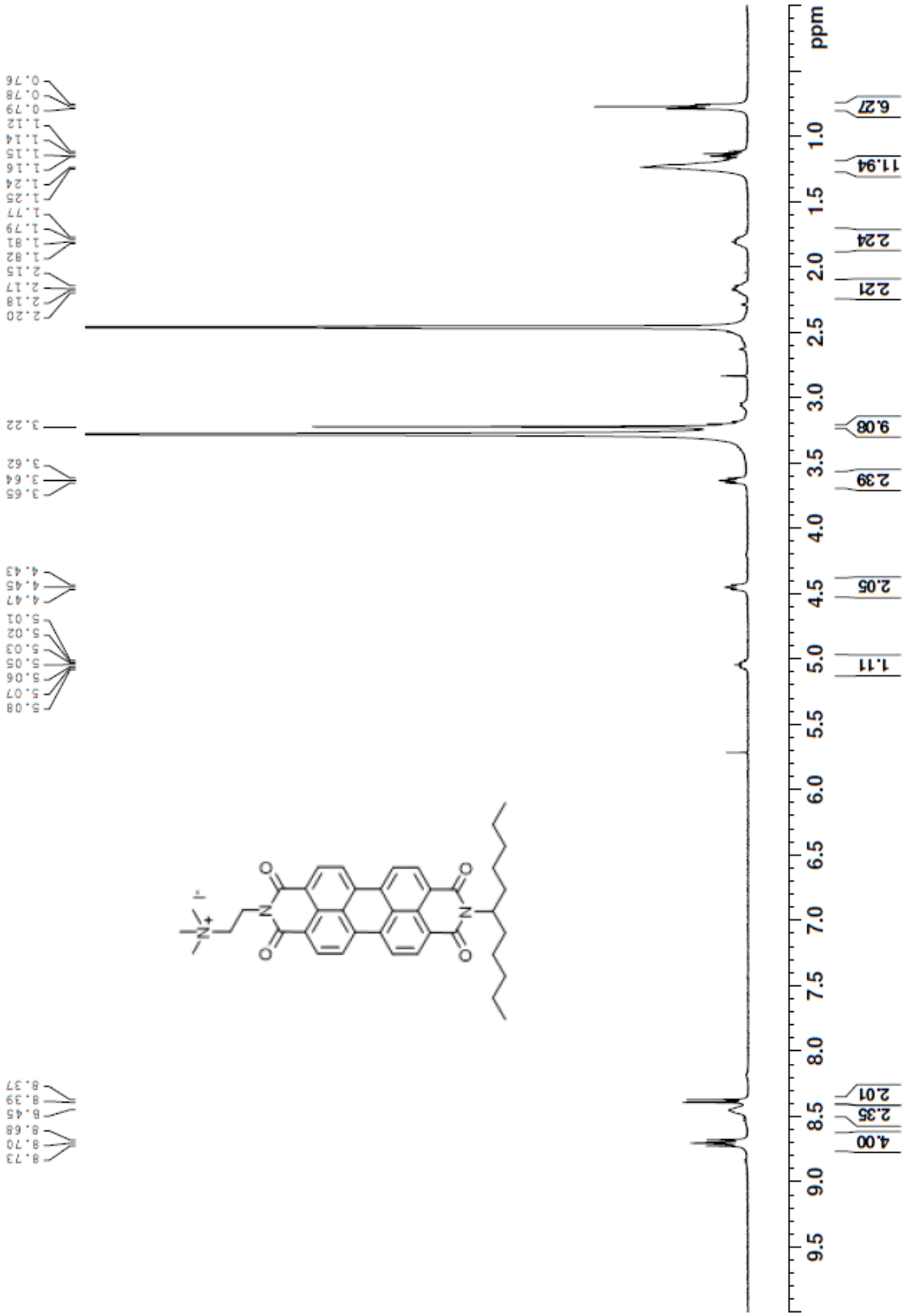

Figure A5. ^{1}H NMR spectrum of compound **PDI1** in d_6-DMSO.

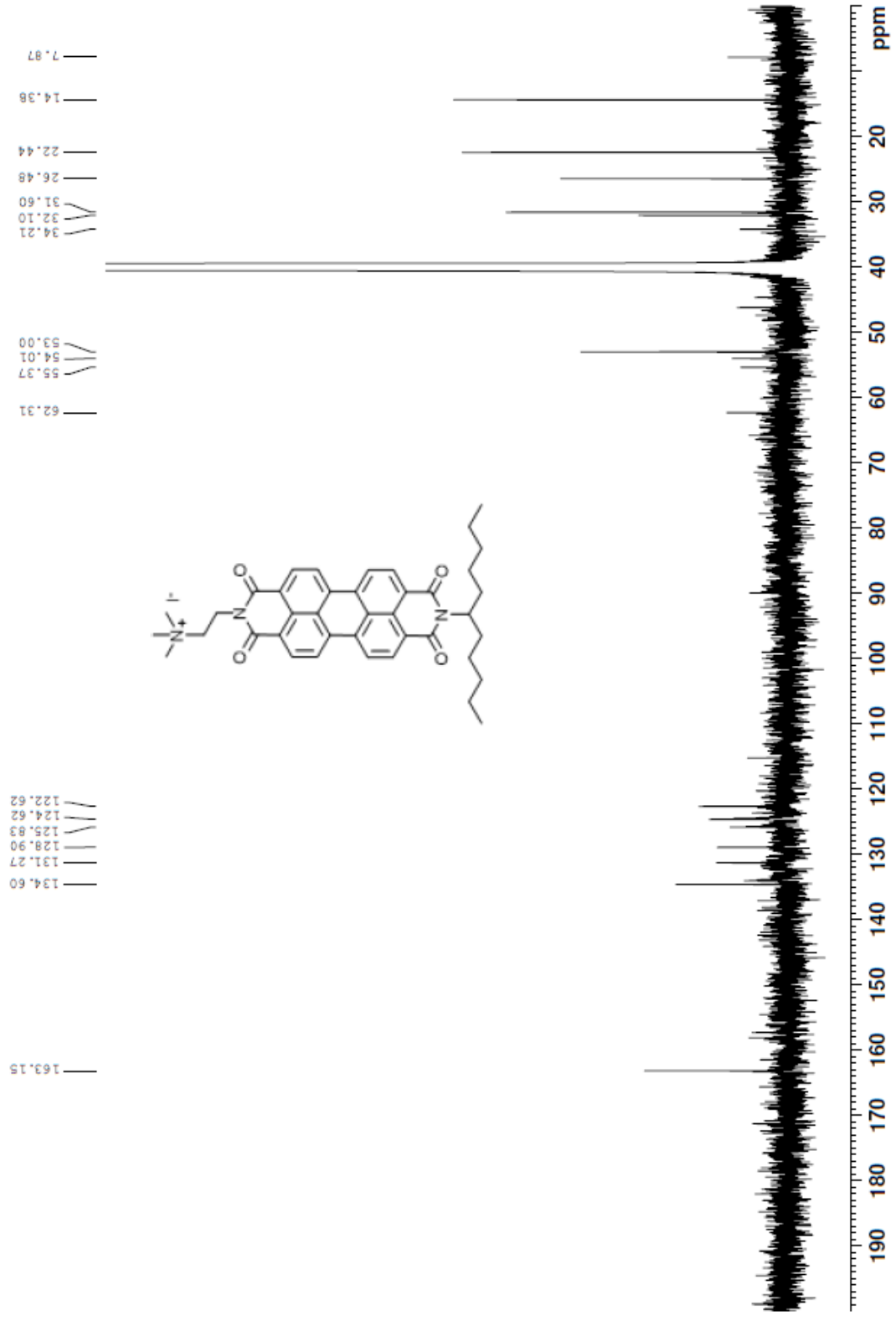

Figure A6. ^{13}C NMR spectrum of compound **PDI-1** in d_6-DMSO.

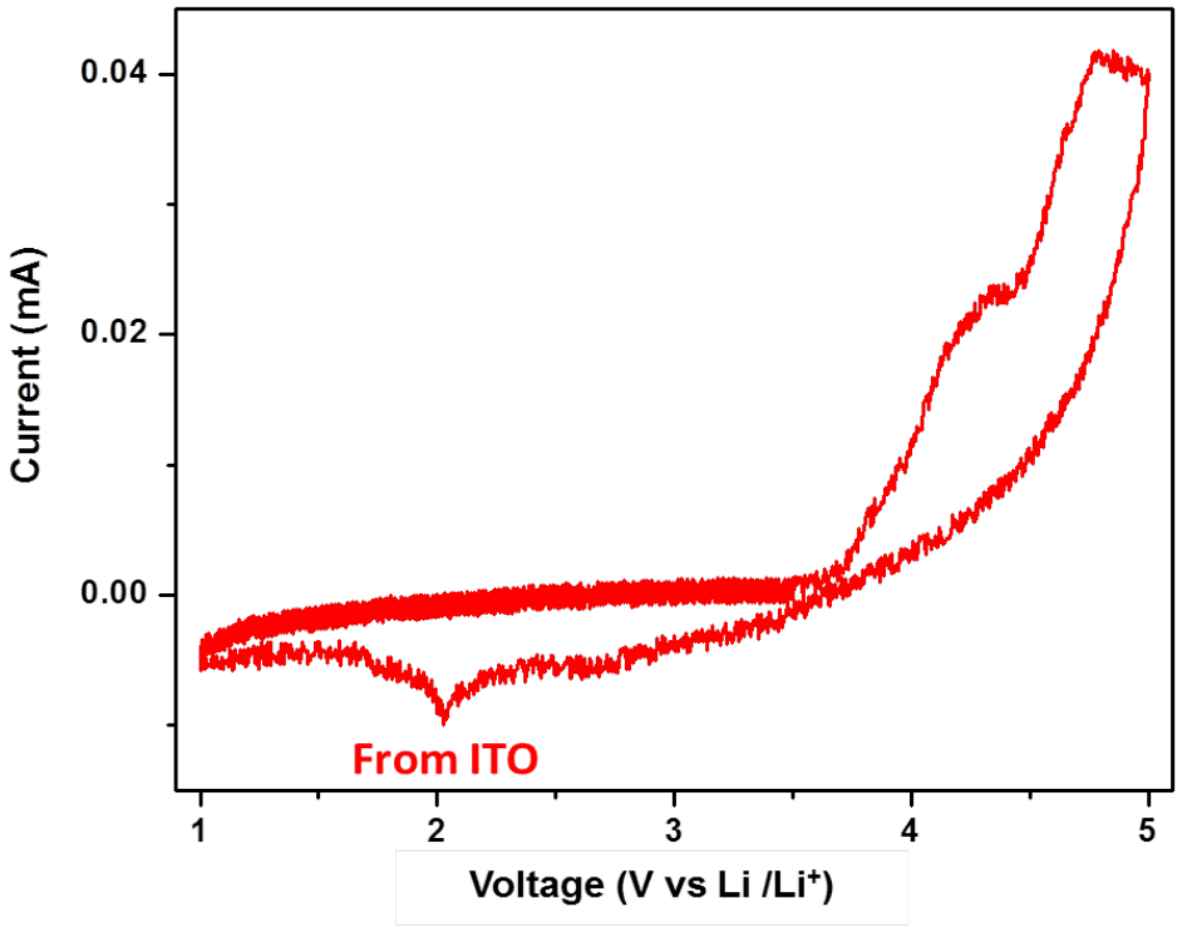

Figure A7. CV for **PCT**, measured in propylene carbonate with Li/Li+ as the reference electrode and ITO glass as the working electrode using a sweep rate of 0.5 mV/s. **PCT** exhibits two irreversible oxidation peaks at 4.1 and 4.5 V vs. Li/Li+. The reduction peak could not be measured, possibly due to the degradation of the polymer during oxidation. Absolute ionization potentials were calculated using –4.3 V as the absolute electrode potential for the standard hydrogen electrode and –3.0 V as the standard reduction potential of Li/Li+ vs. the standard hydrogen electrode.

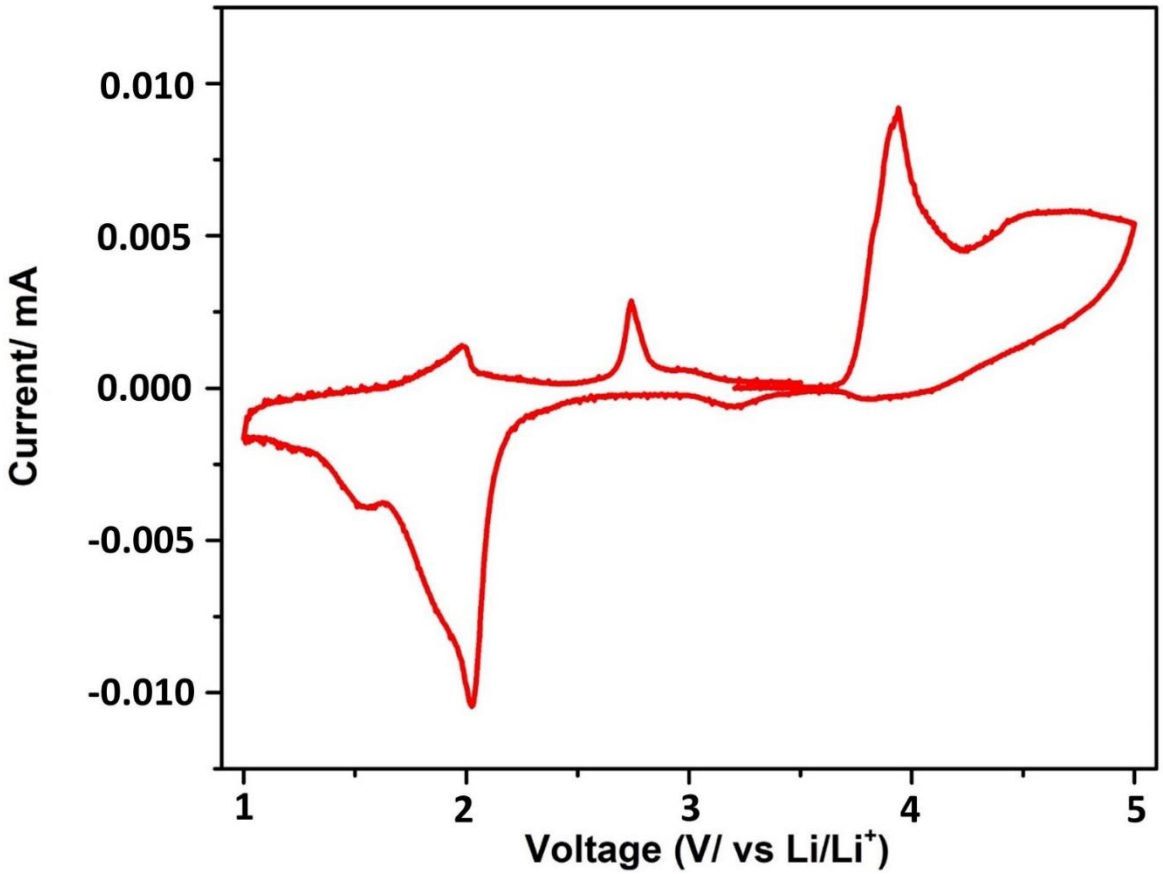

Figure A8. CV for **PFT**, measured in propylene carbonate with Li/Li+ as the reference electrode and ITO glass as the working electrode using a sweep rate of 5 mV/s. **PFT** exhibits two irreversible oxidation peaks at 3.75and 4.2 V vs. Li/Li+. The reduction peak could not be measured, possibly due to the degradation of the polymer during oxidation. Absolute ionization potentials were calculated using –4.3 V as the absolute electrode potential for the standard hydrogen electrode and –3.0 V as the standard reduction potential of Li/Li+ vs. the standard hydrogen electrode

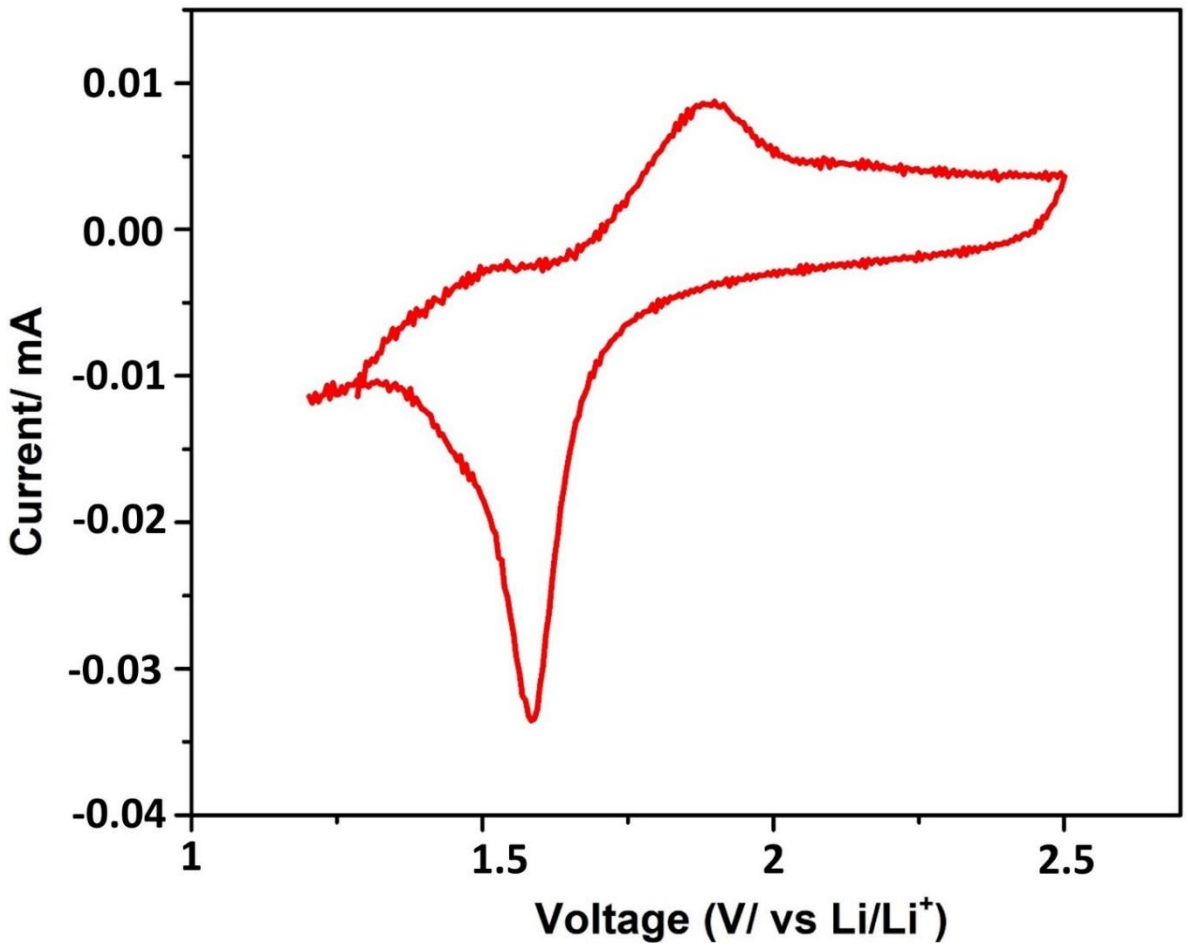

Figure A9. CV for **PDI1**, measured in $LiClO_4$ with Li/Li+ as the reference electrode and ITO glass as the working electrode using a sweep rate of 5 mV/s. **PDI1** exhibits one reversible reduction peak vs. Li/Li+. Absolute ionization potentials were calculated using –4.3 V as the absolute electrode potential for the standard hydrogen electrode and –3.0 V as the standard reduction potential of Li/Li+ vs. the standard hydrogen electrode.

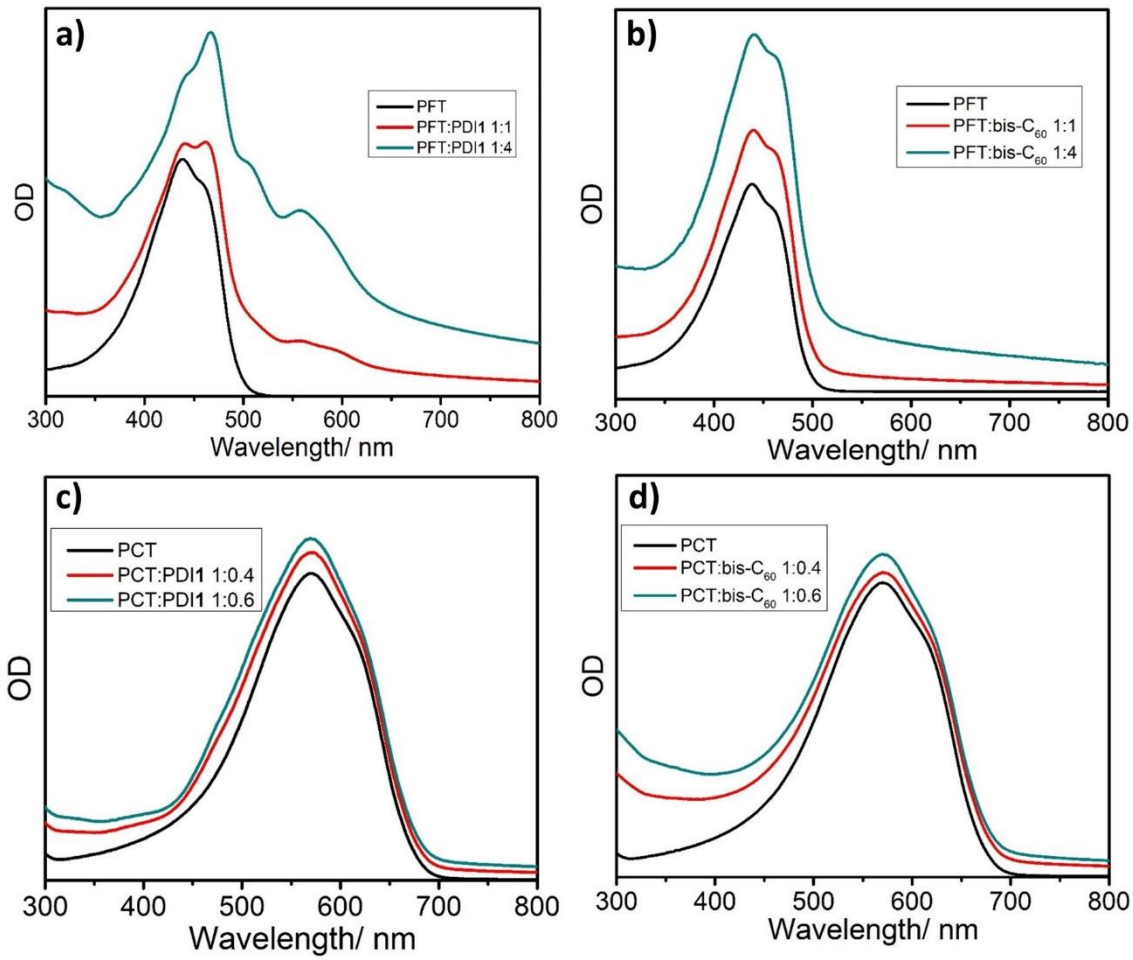

Figure A10. Absorbance of polymers with acceptors in water corresponding to Figure 6.2 in main text. a) **PFT** with **PDI1**. b) **PFT** with **bis-C$_{60}$** fullerenes. c) **PCT** with **PDI1**. b) **PFT** with **bis-C$_{60}$** fullerenes.

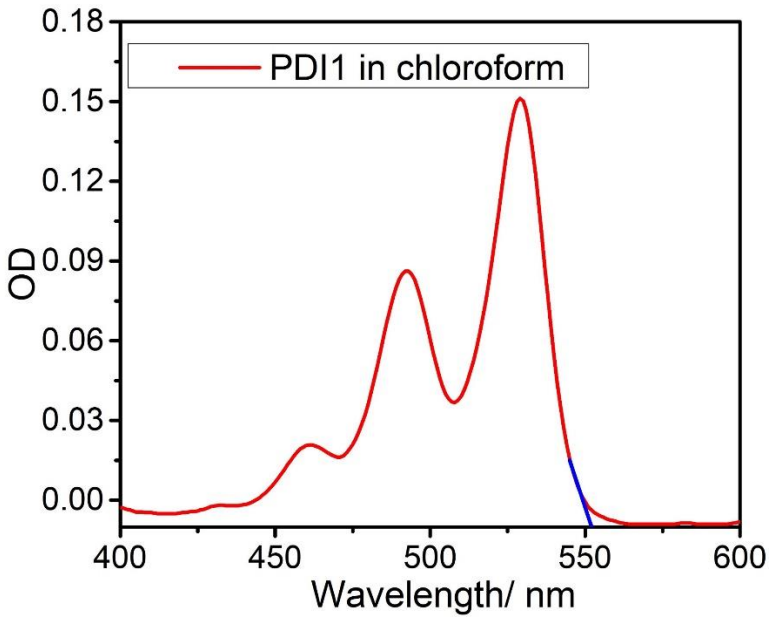

Figure A11. Absorbance of **PDI1** in chloroform after filtration. The bandgap of PDI1 is around 2.25eV (onset highlighted in blue).

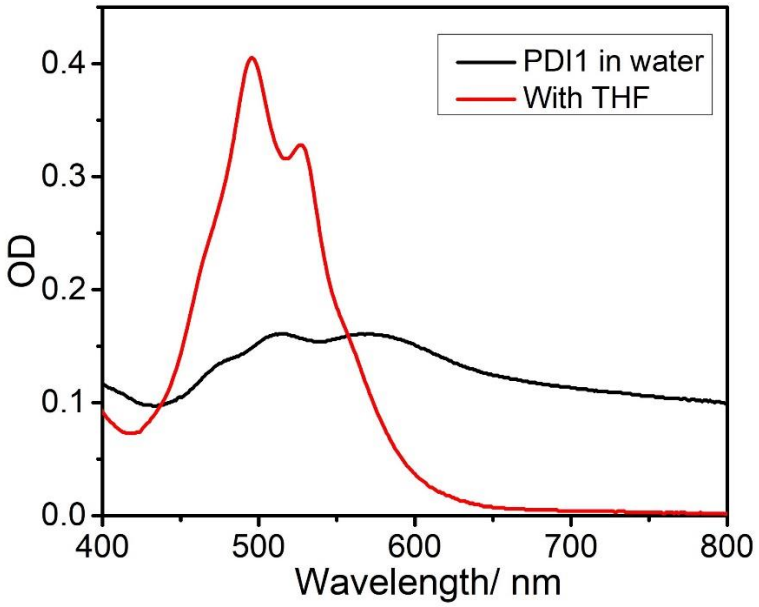

Figure A12. Absorbance of **PDI1** in water (black) and after adding ¼ volume THF to the solution (red).

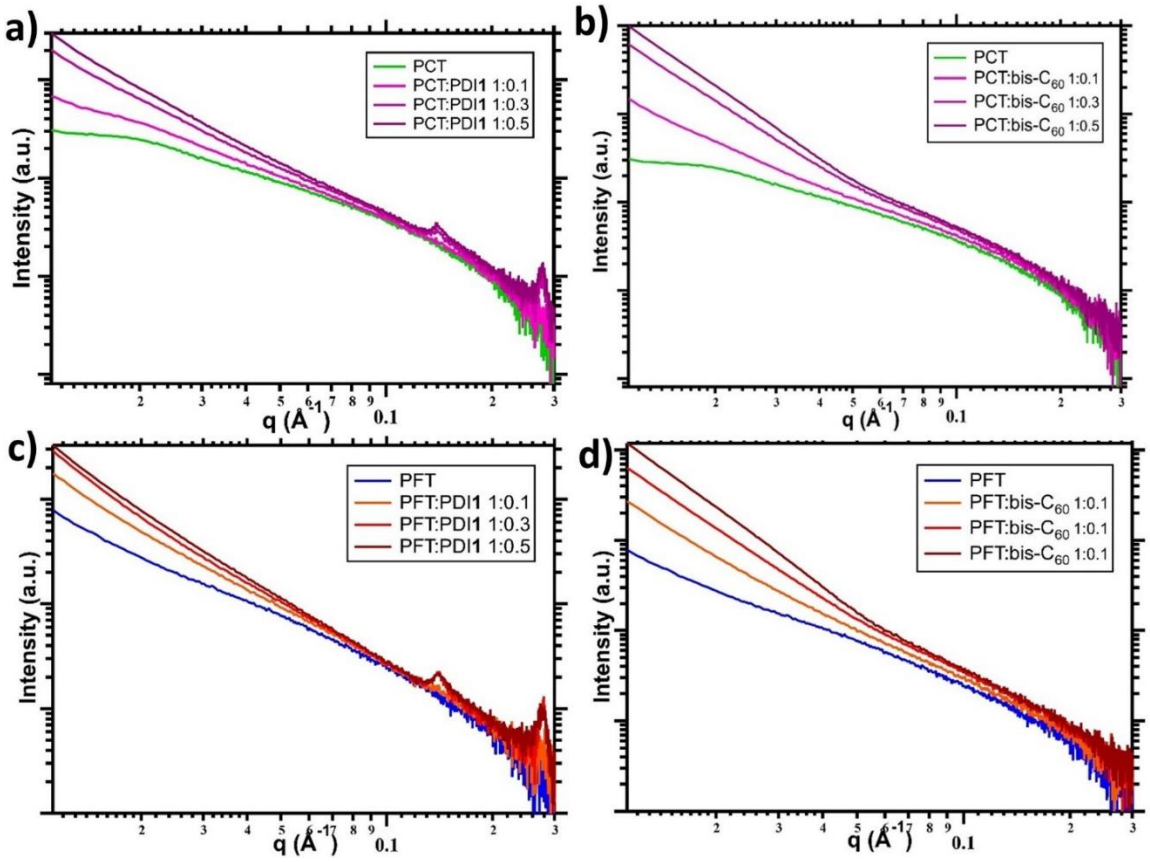

Figure A13. Solution SAXS of **PCT** and **PFT** co-assembled with acceptors with different ratios.

References

[1] Sumliner, J. M.; Lv, H.; Fielden, J.; Geletii, Y. V.; Hill, C. L. Polyoxometalate Multi-Electron-Transfer Catalytic Systems for Water Splitting. *Eur. J. Inorg. Chem.* **2014**, *2014*, 635–644.

[2] Choi, G. J.; Zhu, Q.; Miller, D. C.; Gu, C. J.; Knowles, R. R. Catalytic Alkylation of Remote C-H Bonds Enabled by Proton-Coupled Electron Transfer. *Nature* **2016**, *539*, 268–271.

[3] Nelson, J. Polymer: Fullerene Bulk Heterojunction Solar Cells. *Mater. Today* **2011**, *14*, 462–470.

[4] Tiwari, S.; Singh, A. K.; Joshi, L.; Chakrabarti, P.; Takashima, W.; Kaneto, K.; Prakash, R. Poly-3-Hexylthiophene Based Organic Field-Effect Transistor: Detection of Low Concentration of Ammonia. *Sensors Actuators, B Chem.* **2012**, *171–172*, 962–968.

[5] Rutherford, A. W. Photosystem II, the Water-Splitting Enzyme. *Trends Biochem. Sci.* **1989**, *14*, 227–232.

[6] Romero, E.; Augulis, R.; Novoderezhkin, V. I.; Ferretti, M.; Thieme, J.; Zigmantas, D.; Van Grondelle, R. Quantum Coherence in Photosynthesis for Efficient Solar-Energy Conversion. *Nat. Phys.* **2014**, *10*, 676–682.

[7] Ghosh, A. Quantum Chemical Studies of Molecular Structures and Potential Energy Surfaces of Porphyrins and Hemes. *ChemInform* **2003**, *34*.

[8] Gust, D.; Moore, T. A.; Moore, A. L. Molecular Mimicry of Photosynthetic Energy and Electron Transfer. *Acc. Chem. Res.* **1993**, *26*, 198–205.

[9] Melkozernov, A. N.; Barber, J.; Blankenship, R. E. Light Harvesting in Photosystem I Supercomplexes. *Biochemistry* **2006**, *45*, 331–345.

[10] Axelrod, H. L.; Okamura, M. Y. The Structure and Function of the Cytochrome C2: Reaction Center Electron Transfer Complex from Rhodobacter Sphaeroides. *Photosynth. Res.* **2005**, *85*, 101–114.

[11] Zhang, X. F.; Xi, Q. A Graphene Sheet as an Efficient Electron Acceptor and Conductor for Photoinduced Charge Separation. *Carbon* **2011**, *49*, 3842–3850.

[12] D'Souza, F.; Ito, O. Supramolecular Donor-Acceptor Hybrids of Porphyrins/Phthalocyanines with Fullerenes/Carbon Nanotubes: Electron Transfer, Sensing, Switching, and Catalytic Applications. *Chem. Commun.* **2009**, *33*, 4913–4928.

[13] Smilowitz, L.; Sariciftci, N. S.; Wu, R.; Gettinger, C.; Heeger, A. J.; Wudl, F. Photoexcitation Spectroscopy of Conducting-Polymer-C60 Composites: Photoinduced Electron Transfer. *Phys. Rev. B* **1993**, *47*, 13835–13842.

[14] Wicklein, A.; Ghosh, S.; Sommer, M.; Würthner, F.; Thelakkat, M. Self-Assembly of Semiconductor Organogelator Nanowires for Photoinduced Charge Separation. *ACS Nano* **2009**, *3*, 1107–1114.

[15] Zhou, H.; Yang, L.; You, W. Rational Design of High Performance Conjugated Polymers for Organic Solar Cells. *Macromolecules* **2012**, *45*, 607–632.

[16] Lu, L.; Yu, L. Understanding Low Bandgap Polymer PTB7 and Optimizing Polymer Solar Cells Based on IT. *Adv. Mater.* **2014**, *26*, 4413–4430.

[17] Hellmann, C.; Paquin, F.; Treat, N. D.; Bruno, A.; Reynolds, L. X.; Haque, S. A.; Stavrinou, P. N.; Silva, C.; Stingelin, N. Controlling the Interaction of Light with Polymer Semiconductors. *Adv. Mater.* **2013**, *25*, 4906–4911.

[18] Bakulin, A. A.; Dimitrov, S. D.; Rao, A.; Chow, P. C. Y.; Nielsen, C. B.; Schroeder, B. C.; McCulloch, I.; Bakker, H. J.; Durrant, J. R.; Friend, R. H. Charge-Transfer State Dynamics

Following Hole and Electron Transfer in Organic Photovoltaic Devices. *J. Phys. Chem. Lett.* **2013**, *4*, 209–215.

[19] Salleo, A. Charge Transport in Polymeric Transistors. *Mater. Today* **2007**, *10*, 38–45.

[20] Roy, A.; Beaupré, S.; Cho, S.; Lee, K.; Park, S. H.; Moses, D.; Moon, J. S.; Heeger, A. J.; Coates, N.; Leclerc, M. Bulk Heterojunction Solar Cells with Internal Quantum Efficiency Approaching 100%. *Nat. Photonics* **2009**, *3*, 297–302.

[21] Cao, X.; Li, Y.; Liu, B.; Gao, A.; Cao, J.; Yu, Y.; Hei, X. A Fluorescent Conjugated Polymer Photocatalyst Based on Knoevenagel Polycondensation for Hydrogen Production. *New J. Chem.* **2019**, *43*, 7093–7098.

[22] Li, H.; Dailey, J.; Kale, T.; Besar, K.; Koehler, K.; Katz, H. E. Sensitive and Selective NO2 Sensing Based on Alkyl- and Alkylthio-Thiophene Polymer Conductance and Conductance Ratio Changes from Differential Chemical Doping. *ACS Appl. Mater. Interfaces* **2017**, *9*, 20501–20507.

[23] Chen, D.; Nakahara, A.; Wei, D.; Nordlund, D.; Russell, T. P. P3HT/PCBM Bulk Heterojunction Organic Photovoltaics: Correlating Efficiency and Morphology. *Nano Lett.* **2011**, *11*, 561–567.

[24] Zhang, S.; Ye, L.; Hou, J. Breaking the 10% Efficiency Barrier in Organic Photovoltaics: Morphology and Device Optimization of Well-Known PBDTTT Polymers. *Adv. Energy Mater.* **2016**, *6*, 1–20.

[25] Street, R. A.; Song, K. W.; Northrup, J. E.; Cowan, S. Photoconductivity Measurements of the Electronic Structure of Organic Solar Cells. *Phys. Rev. B - Condens. Matter Mater. Phys.* **2011**, *83*, 1–13.

[26] Ferreira, A. S.; Aguirre, J. C.; Subramaniyan, S.; Jenekhe, S. A.; Tolbert, S. H.; Schwartz, B. J. Understanding How Polymer Properties Control OPV Device Performance: Regioregularity, Swelling, and Morphology Optimization Using Random Poly(3-Butylthiophene-Co-3-Octylthiophene) Polymers. *J. Phys. Chem. C* **2016**, *120*, 22115–22125.

[27] Steyrleuthner, R.; Di Pietro, R.; Collins, B. A.; Polzer, F.; Himmelberger, S.; Schubert, M.; Chen, Z.; Zhang, S.; Salleo, A.; Ade, H.; et al. The Role of Regioregularity, Crystallinity, and Chain Orientation on Electron Transport in a High-Mobility n-Type Copolymer. *J. Am. Chem. Soc.* **2014**, *136*, 4245–4256.

[28] Untilova, V.; Biskup, T.; Biniek, L.; Vijayakumar, V.; Brinkmann, M. Control of Chain Alignment and Crystallization Helps Enhance Charge Conductivities and Thermoelectric Power Factors in Sequentially Doped P3HT:F4TCNQ Films. *Macromolecules* **2020**, *53*, 2441-2453.

[29] Zhang, G.; Huber, R. C.; Ferreira, A. S.; Boyd, S. D.; Luscombe, C. K.; Tolbert, S. H.; Schwartz, B. J. Crystallinity Effects in Sequentially Processed and Blend-Cast Bulk-Heterojunction Polymer/Fullerene Photovoltaics. *J. Phys. Chem. C* **2014**, *118*, 18424–18435.

[30] Ghosh, R.; Luscombe, C. K.; Hambsch, M.; Mannsfeld, S. C. B.; Salleo, A.; Spano, F. C. Anisotropic Polaron Delocalization in Conjugated Homopolymers and Donor–Acceptor Copolymers. *Chem. Mater.* **2019**, *31*, 7033-7045.

[31] Hamidi-Sakr, A.; Biniek, L.; Bantignies, J. L.; Maurin, D.; Herrmann, L.; Leclerc, N.; Lévêque, P.; Vijayakumar, V.; Zimmermann, N.; Brinkmann, M. A Versatile Method to Fabricate Highly In-Plane Aligned Conducting Polymer Films with Anisotropic Charge Transport and Thermoelectric Properties: The Key Role of Alkyl Sidechain Layers on the Doping Mechanism. *Adv. Funct. Mater.* **2017**, *27*, 1–13.

[32] Gu, K. L.; Zhou, Y.; Gu, X.; Yan, H.; Diao, Y.; Kurosawa, T.; Ganapathysubramanian, B.; Toney, M. F.; Bao, Z. Tuning Domain Size and Crystallinity in Isoindigo/PCBM Organic Solar Cells via Solution Shearing. *Org. Electron.* **2017**, *40*, 79–87.

[33] Shao, M.; Keum, J. K.; Kumar, R.; Chen, J.; Browning, J. F.; Das, S.; Chen, W.; Hou, J.; Do, C.; Littrell, K. C.; et al. Understanding How Processing Additives Tune the Nanoscale Morphology of High Efficiency Organic Photovoltaic Blends: From Casting Solution to Spun-Cast Thin Film. *Adv. Funct. Mater.* **2014**, *24*, 6647–6657.

[34] Chen, H.; Hsiao, Y. C.; Hu, B.; Dadmun, M. Tuning the Morphology and Performance of Low Bandgap Polymer:Fullerene Heterojunctions via Solvent Annealing in Selective Solvents. *Adv. Funct. Mater.* **2014**, *24*, 5129–5136.

[35] Clark, A. P. Z.; Shi, C.; Ng, B. C.; Wilking, J. N.; Ayzner, A. L.; Stieg, A. Z.; Schwartz, B. J.; Mason, T. G.; Rubin, Y.; Tolbert, S. H. Self-Assembling Semiconducting Polymers - Rods and Gels from Electronic Materials. *ACS Nano* **2013**, *7*, 962–977.

[36] See Chapter 5

[37] Huber, R. C.; Ferreira, A. S.; Thompson, R.; Kilbride, D.; Knutson, N. S.; Devi, L. S.; Toso, D. B.; Challa, J. R.; Zhou, Z. H.; Rubin, Y.; et al. Long-Lived Photoinduced Polaron Formation in Conjugated Polyelectrolyte-Fullerene Assemblies. *Science* **2015**, *348*, 1340–1343.

[38] Boldon, L.; Laliberte, F.; Liu, L. Review of the Fundamental Theories behind Small Angle X-Ray Scattering, Molecular Dynamics Simulations, and Relevant Integrated Application. *Nano Rev.* **2015**, *6*, 25661.

[39] Hammouda, B. A New Guinier-Porod Model. *J. Appl. Crystallogr.* **2010**, *43*, 716–719.

[40] Liu, H.; Zwart, P. H. Determining Pair Distance Distribution Function from SAXS Data Using Parametric Functionals. *J. Struct. Biol.* **2012**, *180*, 226–234.

[41] Svergun, D. I.; Koch, M. H. J. Small-Angle Scattering Studies of Biological Macromolecules in Solution. *Rep. Prog. Phys.* **2003**, *66*, 1735

[42] Sinturel, C.; Vayer, M.; Morris, M.; Hillmyer, M. A. Solvent Vapor Annealing of Block Polymer Thin Films. *Macromolecules* **2013**, *46*, 5399–5415.

[43] Wu, C.; McNeill, J. Swelling-Controlled Polymer Phase and Fluorescence Properties of Polyfluorene Nanoparticles. *Langmuir* **2008**, *24*, 5855–5861.

[44] Sun, K.; Xiao, Z.; Hanssen, E.; Klein, M. F. G.; Dam, H. H.; Pfaff, M.; Gerthsen, D.; Wong, W. W. H.; Jones, D. J. The Role of Solvent Vapor Annealing in Highly Efficient Air-Processed Small Molecule Solar Cells. *J. Mater. Chem. A* **2014**, *2*, 9048–9054.

[45] Huber, R. C.; Ferreira, A. S.; Aguirre, J. C.; Kilbride, D.; Toso, D. B.; Mayoral, K.; Zhou, Z. H.; Kopidakis, N.; Rubin, Y.; Schwartz, B. J.; et al. Structure and Conductivity of Semiconducting Polymer Hydrogels. *J. Phys. Chem. B* **2016**, *120*, 6215–6224.

[46] Kim, Y.; Lee, Y.; Park, K.; Ahn, C. W.; Jung, H.; Jeon, H. Hierarchical Self-Assembly of Perylene Diimide (PDI) Crystals. *J. Phys. Chem. Lett.* **2020,** *11*, 3934-3940.

[47] Holcombe, T. W.; Norton, J. E.; Rivnay, J.; Woo, C. H.; Goris, L.; Piliego, C.; Griffini, G.; Sellinger, A.; Brédas, J. L.; Salleo, A.; et al. Steric Control of the Donor/Acceptor Interface: Implications in Organic Photovoltaic Charge Generation. *J. Am. Chem. Soc.* **2011**, *133*, 12106–12114.

[48] Kavarnos, G. J.; Turro, N. J. Photosensitization by Reversible Electron Transfer: Theories, Experimental Evidence, and Examples. *Chem. Rev.* **1986**, *86*, 401–449.

[49] Hu, Y.; Chen, S.; Zhang, L.; Zhang, Y.; Yuan, Z.; Zhao, X.; Chen, Y. *J. Org. Chem.* **2017**, *82*, 5926-5931.